UNIVERSITÀ DELLA CALABRIA

UNIVERSITA' DELLA CALABRIA

Dipartimento di Fisica

Scuola di Dottorato

Scienze, Comunicazione e Tecnologie "Archimede"

Indirizzo

Fisica e Tecnologie Quantistiche

Con il contributo di INFN

CICLO XXVII

Measurements of top-quark pair differential cross-sections in the lepton+jets channel in pp collisions at $\sqrt{s}$ = 8 TeV using the ATLAS detector

Settore Scientifico Disciplinare FIS/01

Direttore: Ch.mo Prof. Pietro Pantano

Firma _____

Supervisore: Ch.mo Prof. Enrico Tassi

Firma _____

Dottorando: Dott. Valerio Scarfone

Firma _____

Università della Calabria

Tesi PhD

Measurements of top-quark pair differential cross-sections in the lepton+jets channel in pp collisions at $\sqrt{s} = 8$ TeV using the ATLAS detector

Autore: Valerio SCARFONE

Supervisore: Prof. Enrico TASSI

Dottorato di ricerca in Fisica

Ciclo XXVII

Gruppo di ricerca di Fisica delle alte energie
Dipartimento di Fisica

November 2015

Abstract

I risultati presentati in questa tesi sono frutto del lavoro svolto in collaborazione con il *Top working group* di ATLAS [1], i quali sono stati descritti in un articolo pubblico di ATLAS [2], e sottomesso alla rivista internazionale di Fisica *European Physics Journal* volume C. Mi sono occupato della misura, con il rivelatore ATLAS, delle sezioni d'urto differenziali assolute e normalizzate, per la produzione di coppie top-antitop, nel canale semi-leptonico, in interazioni protone-protone all'energia del centro di massa di 8 TeV al Large Hadron Collider (LHC) di Ginevra. La misura di queste sezioni d'urto differenziali è di particolare importanza nell'ambito del programma di Fisica dell'esperimento ATLAS, sia da un punto di vista teorico poichè consente di eseguire dei test particolarmente stringenti delle predizioni della QCD perturbativa, fino all'ordine 'next-to-next-to-leading' (NNLO), sia da quello sperimentale poichè consente di migliorare la determinazione della densità gluonica del protone. L'alta massa del quark top suggerisce delle possibili connessioni con il meccanismo di rottura della simmetria elettrodebole, inoltre il quark top decade prima di adronizzare fornendo un'opportunità unica di studiare le proprietà di un quark "bare", come ad esempio gli effetti di spin attraverso le correlazioni angolari dei suoi prodotti di decadimento.

Nel contesto del *Modello Standard* il quark top decade quasi esclusivamente in un $b-$quark ed un bosone W. Dunque la segnatura sperimentale dello stato finale dipende dai modi di decadimento dei due bosoni W, in cui ciascuno, mediamente decade due volte su tre nel canale adronico ed una volta su tre leptonicamente. I possibili stati finali sono dunque tre: il canale dileptonico, caratterizzato da una bassa probabilità e da una segnatura sperimentale pulita, il canale semileptonico che risulta essere un buon compromesso tra una discreta probabilità ed un contributo di fondo non dominante rispetto al segnale, ed infine il canale completamente adronico che ha un'alta probabilità ma soffre di eventi multi-getti di QCD che rendono la sua segnatura sperimentale molto complessa.

Le misure di sezioni d'urto differenziali associate alla produzione di coppie di quark top-antitop vengono presentate come funzioni di osservabili cinematiche di singoli quark top e delle coppie top-antitop, scelte in modo tale da enfatizzare il processo di produzione delle coppie $t\bar{t}$, sensibili agli effetti di emissione di radiazione di QCD associati agli stati iniziali e finali del processo studiato, sensibili a processi non-risonanti e a termini correttivi a più alto ordine dello sviluppo perturbativo.

I dati analizzati sono relativi all'intero campione di dati collezionato nel 2012 con il rivelatore ATLAS presso i laboratori CERN di Ginevra, corrispondenti ad una luminosità integrata di 20.3 fb^{-1}.

Gli eventi sono selezionati nel canale semileptonico, richiedendo nello stato finale la presenza di un leptone carico con alto impulso trasverso, un neutrino ed almeno quattro getti adronici di cui due di tipo b. Gli effetti distorsivi che il rivelatore induce sulla misura, causati dalla limitata risoluzione ed accettanza di ATLAS, sono stati corretti, usando la procedura di *unfolding* con approccio iterativo bayesiano, al fine di confrontare le misure con diverse simulazioni MonteCarlo.

Le sezioni d'urto differenziali sono state misurate sia al livello di particelle stabili (cosidetto *particle level*) relativamente ad una regione fiduciale dello spazio delle fasi, che risulta più limitato rispetto al totale spazio delle fasi accessibile al rivelatore caratterizzato da contributi contenuti all'incertezza sistematica, sia al livello partonico (cosiddetto *parton level*) estrapolato all'intero spazio delle fasi, che risulta più ampio ed è esteso anche a regioni non accessibili al rivelatore caratterizzato da contributi di incertezza sistematica più significativi.

In generale i risultati sono in ragionevole accordo con le predizioni su un'ampia regione cinematica, tuttavia la maggior parte dei generatori MonteCarlo predicono i quark top più duri (ovvero con più alti valori in impulso trasverso) rispetto a quanto effettivamente si evince dalle misure. La regione centrale del rivelatore (cioè per bassi valori della variabile rapidità) viene descritta abbastanza bene dalle predizioni, invece relativamente alle regioni in avanti e all'indietro la descrizione non è ottimale. Questa difficoltà è stata investigata attraverso la dipendenza delle predizioni dai più recenti set di funzioni di distrubuzione partonica nel protone (PDFs), evidenziando un notevole miglioramento nella descrizione dei dati rispetto invece a set di PDFs più datati.

A livello partonico i risultati sono stati confrontati con le più recenti predizioni differenziali della QCD perturbativa, sino all'ordine next-to-next-to-leading, risolvendo il disaccordo osservato invece con le predizioni al NLO, sopratutto nelle code delle distribuzioni, dando indicazione del fatto che il disaccordo fosse dovuto alla mancanza di termini correttivi a più alto ordine dello sviluppo perturbativo nelle predizioni usate. Si evidenzia in particolare come quest'analisi sia la prima a mostrare un confronto tra le sezioni d'urto differenziali misurate per la produzione di quark top-antitop con le recentissime predizioni differenziali teoriche al NNLO.

Contents

List of Figures

List of Tables

Introduction

The top quark, discovered in 1995 by the CDF [21] and D0 [22] experiments at the Fermilab (USA) Tevatron proton-antiproton ($p\bar{p}$) collider, has completed the three generation structure of the Standard Model; it was the sixth quark to be observed opening up new physics scenario. The top quark can only be studied in high energy physics experiments.

Due to its very high mass and short life-time, since its discovery, the study of the top quark has represented one of the most interesting and investigated fields in particle physics. The top quark mass value $m_t = 173.2 \pm 0.9\ GeV$ [23] constitutes one of the Standard Model fundamental free parameters and makes the top quark the heaviest known fundamental particle. For this reason, in many beyond SM theories, the top quark is the preferred coupling partner for most of the predicted new particles, as the Z' boson.

In the Standard Model the top quark decays via the $t \to Wq$ process, where the produced q quark has bottom flavor in almost every cases, by implying that the $|V_{tb}|$ element of the Cabibbo-Kobayashi-Maskawa (CKM) matrix is close to one, so establishing an important experimental result for the Standard Model. The top quark has also the peculiarity to decay before its hadronization, by offering the unique opportunity to observe the properties of a bare quark, as for example the spin effects on the decaying products.

Top quark studies play an important role in the physics program of the Large Hadron Collider (LHC) and in particularly for the ATLAS experiment. Thanks to the very high luminosity and collision energy at LHC, the number of produced top quarks is considerably larger with respect to Tevatron, allowing to perform high-statistic precision measurements. The precise measurement of the top-quark mass provides insight to such fundamental questions as the stability of the electroweak vacuum [24]. Hence, knowing the properties of the top quark with high precision is important to improve our understanding about the essence of nature and is a direct gateway to potential new physics phenomena.

In proton-proton (pp) collisions, top quarks are produced in pairs or individually through the strong or the weak interaction respectively, allowing important tests on the features

of these two fundamental forces included in the SM. A large dataset of about 850000 (4.8M) top-quark pair events ($t\bar{t}$) at $\sqrt{s} = 7\ TeV$ ($8\ TeV$) has been recorded by the ATLAS and CMS collaboration respectively. It allows a detailed study of the top quark, its production mechanism and properties. The LHC is therefore a real Top Factory, facilitating an important step towards precision measurements in the top-quark sector, which allow to push back the boundaries of knowledge in this field of particle physics further than ever before.

Therefore large top-quark pair production cross-section at the LHC allows detailed studies of the characteristics of $t\bar{t}$ production to be performed with respect to different kinematic variables, providing a unique opportunity to test the Standard Model (SM) at the TeV scale. Furthermore, effects beyond the SM can appear as modifications of $t\bar{t}$ differential distributions with respect to the SM predictions [25] which may not be detectable with an inclusive cross-section measurement. A precise measurement of the $t\bar{t}$ differential cross-section therefore has the potential to enhance the sensitivity to possible effects beyond the SM.

The ATLAS [26] [27] [28] and CMS [29] experiments have published measurements of the $t\bar{t}$ differential cross-sections at a centre-of-mass energy $\sqrt{s} = 7$ TeV in pp collisions, both in the full phase space using parton-level variables and in fiducial phase-space regions using observables constructed from final-state particles (particle level); the CMS experiment also published measurements of the $t\bar{t}$ differential cross-sections with data taken at $\sqrt{s} = 8$ TeV [30]. The results presented here represent the natural extension of the previous ATLAS measurements of the $t\bar{t}$ differential cross-sections to the $\sqrt{s} = 8$ TeV dataset, and benefit from higher statistics and reduced detector uncertainties.

In the SM, the top quark decays almost exclusively into a W boson and a b-quark. The signature of a $t\bar{t}$ decay is therefore determined by the W boson decay modes. This analysis makes use of the lepton+jets $t\bar{t}$ decay mode, where one W boson decays into an electron or a muon and a neutrino and the other W boson decays into a pair of quarks, with the two decay modes referred to as the e+jets and μ+jets channel, respectively. Events in which the W boson decays to an electron or muon through a τ lepton decay are also included.

This PhD thesis presents a set of measurements of the $t\bar{t}$ production cross-section as a function of different properties of the reconstructed top quark and of the $t\bar{t}$ system at $\sqrt{s} = 8$ using the ATLAS detector. All spectra are unfolded both to a fiducial particle-level phase space and to the full phase space, and they are compared to the predictions of Monte Carlo (MC) generators and to next-to-leading-order (NLO) QCD calculations. The goal of unfolding to a fiducial particle-level phase space and to use variables directly related to detector observables is to allow precision tests of QCD, avoiding large model-dependent extrapolation corrections to the parton-level top-quark and to a phase space region outside the detector sensitivity. However, full phase-space measurements

represent a valid test of higher-order calculations for which event generation with subsequent parton showering is not yet available. Moreover, a subset of the observables under consideration has been measured by CMS [29].

In addition to the variables measured at $\sqrt{s}$ =7 TeV [26] [27] [28], a set of new measurements is presented. Angular rapidity-related variables are chosen in order to emphasize the central production region. These variables, similar to those used in dijet measurements at large jet transverse momentum [31] [32], are sensitive to effects of initial- and final-state radiation, to the different parton distribution functions (PDF), and to non-resonant processes including particles beyond the Standard Model [33]. Finally, observables constructed as a function of the transverse momenta of the W boson and the b-quark originating from the top quark have been found to be sensitive to interference and off-shell effects, non-resonant backgrounds [34] and non-factorizable higher-order corrections [35].

These results are collected in a public preprint [2], submitted to Eur. Phys. J. C, of which I am one of the main authors. I'm also a co-author of an internal ATLAS note [36] which contains additional technical details.

This PhD thesis is organized as follows: Chapter 1 provides an overview of the theoretical features of the top quark physics, Chapter 2 briefly describes the ATLAS detector, while Chapter 3 describes the data and simulation samples used in the measurements, as well as the background processes affecting these measurements. The reconstruction of physics objects and the event selection is explained in Chapter 4, together with the event yields for both the signal and background samples. Chapter 5 describes the kinematic reconstruction of the $t\bar{t}$ pairs using the pseudo-top algorithm and distributions of measured quantities before unfolding. Chapter 6 discusses in detail the analysis strategy, *i.e.* the measurements of the cross-sections, the unfolding technique, and statistical and systematics uncertainties affecting these measurements.

Last, the results are presented in Chapter 7, where the comparison with theoretical predictions is also discussed. Finally, a summary is presented in the last Chapter.

Chapter 1

The top quark

1.1 The Standard Model

The *Standard Model* (SM) theory includes all the known subnuclear particles and their interactions into a coherent scheme, except the gravitational force. The key idea of the SM is that elementary particles are the fundamental building blocks of nature, so they are indivisible, structureless objects, characterised by their intrinsic properties: mass, spin and the quantum numbers, which describe the dynamics of each particle.
The SM is based on fermions with spin $\frac{1}{2}$ and bosons with integer spin. The twelve fermions are ordered by their mass into three generations. Within each generation, one distinguishes two quarks and the two leptons. Quarks are characterised by their colour charge C, another quantum number is the elementary electrical charge (Q).
Quarks have either $Q = +\frac{2}{3}$ (up-type: up quark u, charm quark c, top quark t) or $Q = -\frac{1}{3}$ (down-type: down quark d, strange quark s, bottom quark b). Leptons have either $Q = +1$ (electron, muon, tauon) or $Q = 0$ (neutrinos).
In addition, an antiparticle exist for each particle, that is characterised by inverted quantum numbers (e.g. $Q_{antiparticle} = -1 \cdot Q_{particle}$) but at same time identical properties (e.g. mass, spin) with respect to the particle. The elementary particles are dynamic objects which can interact with each other depending on their quantum numbers. Within these interactions, particles can be converted into different particles or form stable states of matter. These processes follow several rules, e.g. energy, spin, momentum and charge conservation. The dynamics of each particle is described by its properties. The lightest particles are stable while single particles with larger masses are only short-lived. Therefore, the fermions of the first generation are stable.
In a simplified picture, they represent the toolkit to build up stable matter. Up- and down-quarks form the proton ($p = uud$) and the neutron ($n = udd$). Together with the

electron, they are the building blocks of all atoms which form more complex objects. Hence, the SM is based on a collection of elementary particles, well pictured in Figure 1.1, the interactions between particles are described as gauge quantum fields that interact via gauge bosons; the quarks interact via *strong*, *weak* and *electromagnetic* forces, the leptons only via *electromagnetic* and *weak* ones, while neutrinos interact only via the *weak* force.

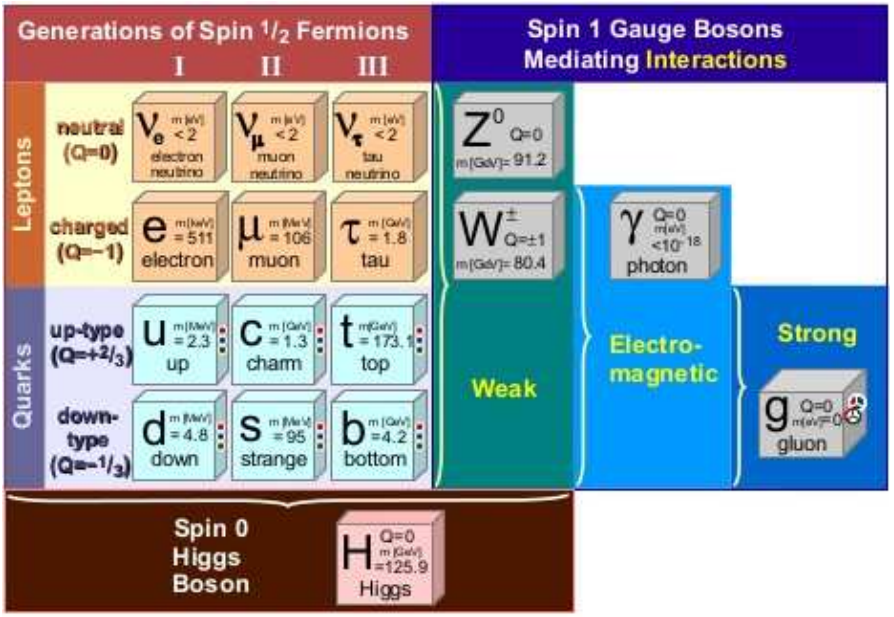

FIGURE 1.1: Standard model constituent summary.

In contrast to the gauge bosons, the Higgs boson is a spin 0 particle. Since the latest discovered particle of the SM [37] [38], it is the physical manifestation of the *Higgs* field that explains the masses of all elementary particles via the Higgs mechanism. For fermions, the coupling strength for the interaction with the Higgs boson scales linearly with the particle mass, therefore the coupling strength of the top quark to the Higgs boson is the largest of all known SM particles. The discovery of the predicted Higgs boson is the latest success of the SM. An overview of the SM will be given in the following.

1.1.1 Quantum Electrodynamics

The *Quantum Electrodynamics* (QED) [39] is a gauge field theory that describes the electromagnetic force in which the force mediator is represented by the photon, a massless gauge boson. The SM allows other gauge theories that are an extension of the QED. Its Lagrangian is:

$$\mathcal{L} = i\bar{\Psi}\gamma^{\mu}D_{\mu}\Psi - m\bar{\Psi}\Psi - \frac{1}{4}F_{\mu\nu}F^{\mu\nu} \tag{1.1}$$

where Ψ is the QED quantum field and m is mass constant, $\mathcal{D}_{\mu} = \partial_{\mu} + ieA_{\mu}(x)$ and $F_{\mu\nu} = \partial_{\mu}A_{\nu} - \partial_{\nu}A_{\mu}$, e is the elementary charge unit, by relating it to the electromagnetic interaction coupling constant α_e via $e = \sqrt{4\pi\alpha_e}$, while A_{μ} is the electromagnetic vector potential. The QED Lagrangian is invariant under the gauge transformation

$$A_{\mu} \rightarrow A_{\mu} - \frac{1}{e}\partial_{\mu}\alpha(x) \tag{1.2}$$

and also under the local $U(1)$ rotation

$$\Psi = e^{i\alpha(x)}\Psi \tag{1.3}$$

with an arbitrary gauge field $\alpha(x)$.
By adding a non-zero mass term as $\frac{1}{2}m_{\gamma}A^{\mu}A_{\mu}$ in Equation 1.1 would leads to violate the request of the gauge symmetry (i.e. violating the experimentally observed massless of the photon). The global $U(1)$ symmetry of QED ensures the conservation of the electromagnetic charge.

1.1.2 Quantum Cromodynamics

The Quantum Cromodynamics (QCD) describes the strong interactions, by introducing a new quantum number called color, from which the name *cromodynamic*, having three possible states: red, blue and green. Color was introduced to explain two unexpected experimental results: the existence of degenerate baryon states like the Δ^{++} and the strange value of the K meson decay rate, by solving the problem of the apparent violation of the Fermi-Dirac statistic in Δ^{++}, a baryon formed by 3 quarks up (uuu).
Making use of the color quantum number in the cross section calculation, it justify the unexpected results in the K decay rate, by finding to be 3 times smaller than theoretical predictions.
The quarks have never been observed as free states but they can be only found in colorless confined states, that are mesons or baryons. The first ones are quark/anti-quark systems that form a color/anti-color state, while the second ones are composed by three quarks in a color singlet state.
The QCD gauge theory is invariant under transformations of the non-Abelian $SU(3)$ group that ensures the conservation of the color quantum number.

Its Lagrangian can be expressed as:

$$\mathcal{L}_{QCD} = i\bar{\Psi}\gamma^{\mu}(\partial_{\mu} - ig_s A_{\mu}^{\alpha} T_a)\Psi - m\bar{\Psi}\Psi - \frac{1}{2} tr[F_{\mu\nu}F^{\mu\nu}] \tag{1.4}$$

It looks like similar to the QED one with the proper coupling constant $g_s = \sqrt{4\pi\alpha_s}$, and with important differences with respect to QED Lagrangian, that are eight gauge fields, corresponding to the eight generators of $SU(3)$, the T^a matrices, where

$$T^a = \frac{1}{2}\lambda^a \tag{1.5}$$

λ^a are the not-commuting Gell-Mann matrices. The $F_{\mu\nu}$ tensor is:

$$F_{\mu\nu} = (\partial_{\mu} A_{\nu}^{a} - (\partial_{\nu} A_{\mu}^{a} - ig_s[A_{\mu}, A_{\nu}]) \tag{1.6}$$

with the last term that is responsible of interactions among the gauge fields. The gauge simmetry forbids massive gluons. The steeply increase in strength of the QCD coupling $\alpha_s = \frac{g_s^2}{4\pi}$ with the interaction distance is due to gluon-gluon interactions.
The dependency of strong coupling constant from the collision energy is shown in Figure 1.2 (in natural units $h = 1$ and $c = 1$), resulting an inverse relation between energy and distance. Because of the the small coupling at high energy scales (small length scales), quarks and gluons behave as quasi-free particles, known as *asymptotic freedom*, so QCD can be described perturbatively. The potential energy of the strong interaction field increases for low energies (large distances) instead, until the stored energy is large enough to create new particles out of the vacuum, so that gluons and quarks cannot be observed. The phenomena of *confinementf* leads to the formation of colour neutral states composed of several quarks (hadrons).
Colour neutral states are built by combining either a quarks and an antiquark with the respective anticolour or several quarks or antiquarks containing all three colours or anticolours. Free quarks or gluons will generate new colour charged objects until finally only colour neutral hadrons remain, known as *hadronisation*.
The dynamic between the two or three valence quarks results in a constant gluon exchange between them. These gluons can produce themselves gluons or virtual pairs of quark and antiquark (*sea quarks*) which will finally annihilate and be reabsorbed by the valence quarks. In comparison to the valence quarks the gluon and sea quark carries only a small amount of the total energy of the proton. The exact distribution of the proton energy to the underlying elementary particles, typically called partons, is described by the *Parton Distribution Functions* (PDFs).

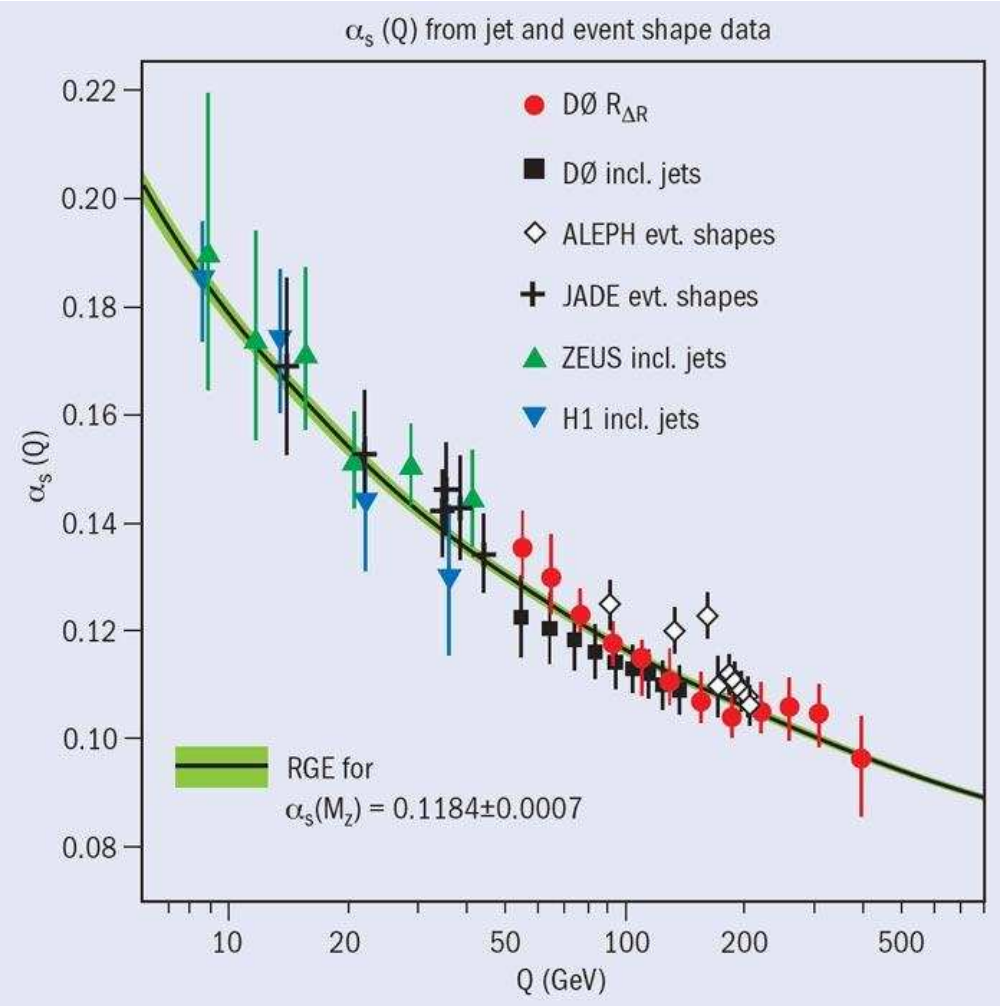

FIGURE 1.2: Strong running coupling constant distribution with respect to the collision energy.

1.1.3 The Weak Interaction

The *Weak* theory is based on the $SU(2)$ group of simmetry, it violates parity maximally. This means that its behaviour is not symmetric under spatial point-reflections defined by the chiral symmetry. Hence, this theory has a $V-A$ structure, that is vector - axial vector that implies the weak field can be decomposed into a left-handed $\Psi_L = \frac{1}{2}(1-\gamma_5)\Psi$ and a right-handed $\Psi_R = \frac{1}{2}(1+\gamma_5)\Psi$ components.

An important feature of the weak field is to change the flavor of quarks also between different generations during interactions; even if intra-generation exchange occur with a smaller probability than inter-generation ones. Interactions are only possible between up-like and down-like quarks ($u/c/t-$quarks $\rightarrow d/s/b-$quarks).

The interaction probability is proportional to the square of the Cabibbo-Kobayashi-Maskawa (CKM) [40][41] matrix elements $|V_{qq'}|^2$.

$$V_{CKM} = \begin{pmatrix} V_{ud} & V_{us} & V_{ub} \\ V_{cd} & V_{cs} & V_{cb} \\ V_{td} & V_{ts} & V_{tb} \end{pmatrix}$$

In general, the CKM matrix can be parametrised by three mixing angles and one (CP-violating) phase. The magnitudes of the single CKM elements are given by:

$$V_{CKM} = \begin{pmatrix} 0.97419 \pm 0.00022 & 0.2257 \pm 0.0010 & 0.00359 \pm 0.00016 \\ 0.2256 \pm 0.0010 & 0.97334 \pm 0.00023 & 0.0415^{+0.0010}_{-0.0011} \\ 0.00874^{+0.00026}_{-0.00037} & 0.0407 \pm 0.0010 & 0.99913^{+0.000044}_{-0.000043} \end{pmatrix}$$

If the weak interaction involves the exchange of electric charge, it is considered a *charged-current* interaction, mediated by $W^{\pm}$ bosons. If no electric charge exchange occurs, the weak interaction is defined as a *neutral-current* process mediated Z^0 boson exchange. The $W^{\pm}$ bosons couples only to left-handed particles and right-handed antiparticles. The Z^0 boson couples with different strengths to left-handed and right-handed particles.
Chirality is a fundamental property of the elementary particles. The two different states of chirality are for massless particles equal to the helicity, i.e. the projection of the spin onto the momentum. Weak neutral current and electromagnetic interactions interfere one each other as shown at the Large Electron-Positron Collider (LEP) experiment in the forward-background production asymmetry found of the $e^+e^- \to l^+l^-$ process [42]. This interference suggests a connection between electromagnetic and weak fields that leads to the electroweak unification.
An important difference between the weak interaction and the other ones is that the field quanta are massive, in contrast with the case of QED and QCD, where the gauge symmetry imposes that the photon and the gluons are instead massless. Massive gauge bosons suggest that the symmetry of the weak interaction is not perfect, i.e. that the Lagrangian and the physical vacuum do not obey to the same symmetry, that is the case of a spontaneously broken symmetry mechanism which justifies the $W^{\pm}$ and Z^0 mass trough the introduction of a scalar field.

1.1.4 Electroweak unification

The fundamental forces differ one to each other in the value of the coupling constant that determines the magnitude of the interaction mediated by that force, as well as in transformation properties and specific conservation rules, in fact these constants vary with the energy involved during the interaction and for this reason they are called *running constants*. Weinberg, Salam and Glashow developed a theory that includes both the weak and electromagnetic interactions as a single *electroweak* force.

This theory predicts the symmetry between electromagnetic and weak interactions would be manifest at a transferred momentum scale $q^2 >> 10^4\,\mathrm{GeV}^2$, that was a very large one in the late 1960s. The theory postulates the existence of four massless bosons arranged in one *weak isospin* triplet ($W_\mu = W_\mu^{(1)} W_\mu^{(2)} W_\mu^{(3)}$) and one *weak hypercharge* singlet (B_μ). This field has geometrical properties of a $SU(2)xU(1)$ group.
A spontaneous symmetry breaking mechanism is required to justify the existence of the observed massive bosons mediator of the weak force. By changing the reference frame and with the mediation of a scalar (Higgs) field, three massive vector bosons (W_μ^+, W_μ^- and Z^0) and one massless photon A_μ appears from the massless boson combination:

$$W_\mu^\pm = \frac{1}{\sqrt{2}} \left[W_\mu^{(1)} \pm W_\mu^{(2)} \right] \tag{1.7}$$

and

$$W_\mu^{(3)} = \frac{g Z_\mu - g' A_\mu}{\sqrt{g^2 + g'^2}} \tag{1.8}$$

$$B_\mu = \frac{-g' Z_\mu + g A_\mu}{\sqrt{g^2 + g'^2}} \tag{1.9}$$

with g and g' electroweak coupling constants. The electroweak Lagrangian assumes the following form:

$$\mathcal{L}_{ew} = \frac{g}{2} \left(J_\mu^- W_\mu^+ + J_\mu^+ W_\mu^- \right) + \frac{g}{\cos\theta_W} \left(J_\mu^{(3)} - \sin^2\theta_W J_\theta^{em} \right) Z_\theta + g \sin^2\theta_\mu J_\mu^{em} A_\mu \tag{1.10}$$

where J_μ^{em} is the electromagnetic current and $J_\mu^{(3)}$ is the third component of the isospin current J_μ. $J_\mu^\pm$ are instead a combination of the first and the second component of the isospin current J_μ:

$$J_\mu^\pm = J_\mu^{(1)} \pm i J_\mu^{(2)} \tag{1.11}$$

The relationship between the coupling constants g,g',e and the Weinberg angle θ_W can be expressed as:

$$\frac{g}{g'} = \tan\theta_W \tag{1.12}$$

$$e = g \sin\theta_W \tag{1.13}$$

1.1.5 Spontaneous symmetry breaking

Understanding the mechanism that generates the masses of the known SM particles represents one of the most important issues in particle physics. Because of the mass of $W^\pm$ and Z^0 bosons are different from zero the $SU(2)$ symmetry has to be broken.

A symmetry can be considered broken when the transformation is always invariant but for the vacuum state. How to solve this asymmetry for the weak interaction is well described by the *Higgs mechanism*.
Considere the Lagrangian of the SU(2) symmetry group describing the weak interaction:

$$\mathcal{L} = (\mathcal{D}_\mu \Phi)^+ (\mathcal{D}^\mu \Phi) - \mu^2 \Phi^+ \Phi - \lambda \left(\Phi^+ \Phi\right)^2 \tag{1.14}$$

with λ coupling term and μ^2 the mass term. A doublet of scalar complex fields Φ_α and Φ_β can be used to represents the field Φ as follows:

$$\Phi = \begin{pmatrix} \Phi_\alpha \\ \Phi_\beta \end{pmatrix} = \sqrt{\frac{1}{2}} \begin{pmatrix} \Phi_1 + i\Phi_2 \\ \Phi_3 + i\Phi_4 \end{pmatrix}$$

and $\mathcal{D}$ term in Lagrangian is:

$$\mathcal{D} = \partial_\mu + ig\frac{\tau_a}{2} W_\mu^a \tag{1.15}$$

with W_μ^a that are three gauge fields.
The weak Lagrangian is invariant under $SU(2)$ transformation

$$\Phi \to \Phi' = e^{\frac{i\alpha_a(x)\tau_a}{2}} \Phi \tag{1.16}$$

so that we have:

$$\Phi(x) \to \Phi'(x) = \left(1 + \frac{i\alpha(x)\tau}{2}\right) \Phi(x) \tag{1.17}$$

$$W_\mu \to W_\mu - \frac{1}{g}\partial_\mu \alpha - \alpha \times W_\mu \tag{1.18}$$

with a solution of the form with $\mu^2 > 0$ and $\mu^2 < 0$:

$$V(\Phi) = \mu^2 \Phi^+ \Phi + \lambda \left(\Phi^+ \Phi\right)^2 \tag{1.19}$$

The first solution leads to a system of four scalar massive particles interacting via three massless gauge bosons. The second and more interesting case has a manifold of potential minimum degeneracy in energy represented by

$$\Phi^+ \Phi = \frac{1}{2}\left(\Phi_1^2 + \Phi_2^2 + \Phi_3^2 + \Phi_4^2\right) = -\frac{\mu^2}{2\lambda} \tag{1.20}$$

While this solution can be rewritten as

$$\Phi_1 = \Phi_2 = \Phi_4 = 0 \tag{1.21}$$

$$\Phi_3 = -\frac{\mu^2}{\lambda} = \nu^2 \tag{1.22}$$

with the corresponding vacumm state that is

$$\Phi_0 = \sqrt{\frac{1}{2}} \begin{pmatrix} 0 \\ \nu \end{pmatrix}$$

If we expand the ground state we obtain the field:

$$\Phi(x) = \sqrt{\frac{1}{2}} \begin{pmatrix} 0 \\ \nu + h(x) \end{pmatrix}$$

and finally we have the Higgs scalar field $h(x)$. Using this result in the lagrangian we have that the system above described is composed by three massive vector bosons $W^{\pm}$ and Z^0 and by a fourth scalar particle, the Higgs boson.

1.1.6 Perturbation theory and renormalisation

In particle physics the cross section σ is the most important observable, being a measure of probability that a specific physics process (e.g. $gg \to t\bar{t}$) occurs. In principle, σ can be derived interpreting the Lagrangian density.
However, the exact calculation involves infinitly many contributions. Beacause of all contributions are not contribute in the same relevance and not all contributions can be taken into account, an approximation for the calculation of σ is performed. The solution for σ is expanded in orders of the coupling constant α, by using a perturbation theory. The single terms of the expansion are illustrated using Feynman diagrams.

With help of the Figure 1.3 the most simple process is represented by the leading order contribution (left) while higher orders correspond to processes that involve additionally produced particles (middle) or loops (right). The cross section σ can be expanded per-

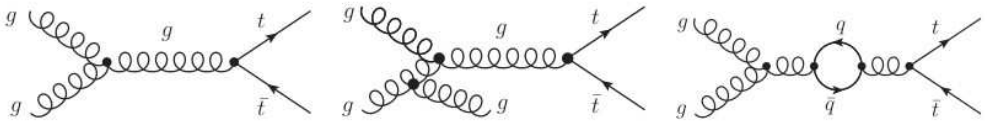

FIGURE 1.3: Graphical represention of Feynman diagrams for the process $gg \to tt$ in the s-channel: LO contribution (tree level, left) and higher order contributions with a real emission (additional gluon from initial state radiation, middle) and a virtual loop correction (qq loop, right).

turbatively for $\alpha << 1$ by calculating only the first terms of the expansion giving a good approximation for the result; but this approach leads to divergences appearing in the

calculation of separate contributions, as the virtual loop contributions. If all orders of the expansion would be taken into account these divergences would cancel with other contributions.

To allow the calculation of finite solutions at any order of perturbation theory, a *renormalisation* procedure is adopted. It involves the introduction of a renormalisation scale μ_R which sets a cut-off scale for the considered momenta in the calculation of the loop contributions. The remaining divergences are absorbed in the renormalised quantities, e.g. coupling constants, therefore becoming dependent on renormalization scale μ_R. The renormalised coupling constants $\alpha(\mu_R)$ are the measurable observables, their value is finite and divergences occur only in the non-physical, bare parameters of the Lagrangian density.

Usually, μ_R is identified with the typical energy or momentum scale of the process, e.g. the momentum transferred Q or the invariant mass m of a produced particle. At leading order of QCD the renormalized coupling constant is given by:

$$\alpha_S\left(Q^2\right) = \frac{12\pi}{(33-2n_f)ln\frac{Q^2}{\Lambda^2_{QCD}}} \tag{1.23}$$

where Λ_{QCD} is:

$$\Lambda^2_{QCD} = \mu^2 exp\left(\frac{-12\pi}{(33-2n_f)\alpha_s(\mu^2)}\right) \tag{1.24}$$

in which μ denotes a reference scale and $\alpha_S(\mu^2)$ the value assumed at that scale, e. g. $\alpha_S(m_Z^2) \approx 0.118$[43], n_f denotes the number of quark flavours contributing to the virtual loops and depends on the energy scale such that $(2m_q)^2 \leq Q^2$.

Actually the physical couplings $\alpha(Q^2)$ have to be measured because they are not predicted by the theory of the SM. The charge determines the measured coupling strength α. Each particle can create additional particles which carry themselves charge, through loop processes. This leads to a screening of the bare charge. When measuring α, the energy scale Q^2 is a measure of the probed distance, with dependency of the effective charge seen and therefore the measured value of α depends on the probed distance. For small distances (large Q^2) more of the bare charge is seen.

1.2 Top quark phenomenology

Within the SM, the existence of a third quark generation was theoretically motivated to explain CP violation in 1973 [41]. This theoretical hypothesis was confirmed by the direct experimental discovery of the top quark almost 20 years later by the Tevatron experiments CDF [21] and D0 [22] at Fermilab (USA) that observed the direct production of top-quark pairs in proton-antiproton ($p\bar{p}$) collisions at $\sqrt{s} = 1.8\,\text{TeV}$ with a five sigma significance. The Tevatron collider was the only tool allowing the study of top quarks for more than 15 years.

Among all known particles of the SM, the top quark plays a special role. The main reason is due to its mass, $m_t \approx 173\,\text{GeV}$, which is larger than for all other elementary particles currently known.

Since 2010, top quarks are also produced in pp collisions at the LHC. The datasets recorded at a centre-of-mass energies of $\sqrt{s} = 7\,\text{TeV}$ (2010-2011) and $\sqrt{s} = 8\,\text{TeV}$ (2012) contain about 1 and 5 million and top-quark pairs per experiment respectively.

An overview of top-quark phenomenology will be given in the following, starting with the top-quark production in hadron collider machines with focus on the production of top-quark pairs in pp collider experiments, the decay of the top quark and the observable final states of top-quark pairs, the top-quark mass and finally the relevance of the top quark in consideration of the Higgs discovery and physics beyond the SM.

A more detailed overview on top-quark physics can be found e.g. in [44][45].

1.2.1 Production mechanisms at hadron colliders

The top quarks which are studied in hadron collider experiments are produced mainly in pairs (one top quark and one antitop quark) but also the production of single top quarks can be observed. Other processes involving the top quark like the production of two top-quark pairs is very rare and will not be discussed further.

1.2.1.1 Top quark pair production

The production of top-quark pairs in pp and $p\bar{p}$ collider experiments is characterised by the strong interaction. The initial state allows for quark-antiquark ($q\bar{q}$) annihilation and gluon-gluon (gg) fusion production modes in LO, which Feynman diagrams are shown in Figure 1.4.

At NLO, top-quark pairs can also be produced from quark-gluon initial states, Figure 1.5

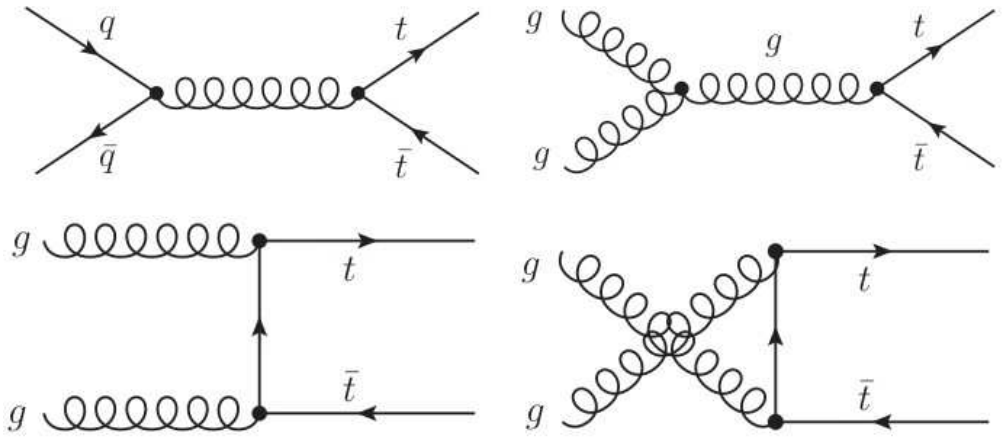

FIGURE 1.4: Feynman diagrams of LO top-quark pair production from the $q\bar{q}$ initial state (top left) and from the gg initial state (top right, bottom).

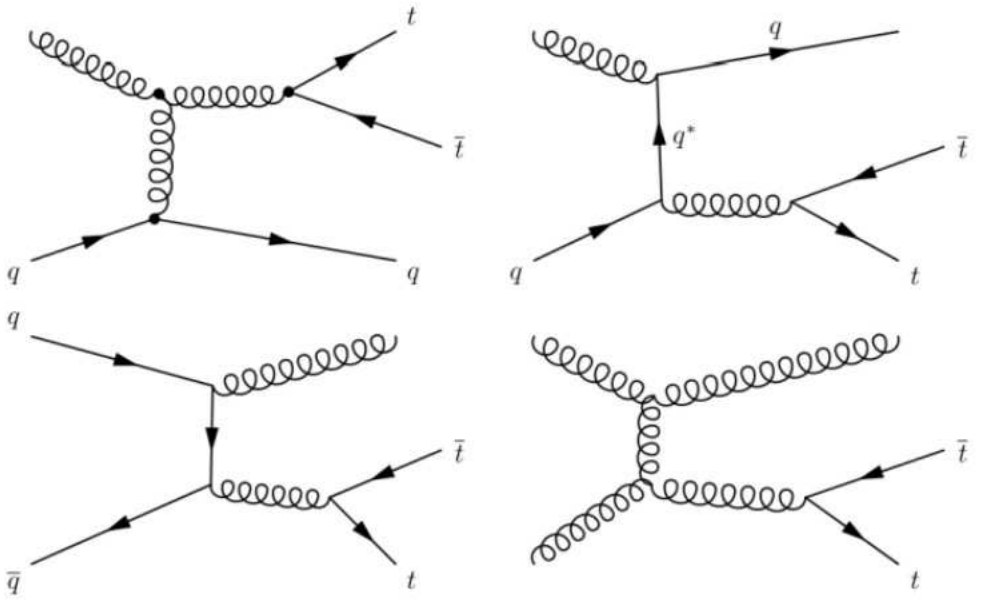

FIGURE 1.5: Feynman diagrams of NLO top-quark pair production via gluon fusion and quark/anti-quark annihilation processes.

For higher order processes with additionally produced real quarks or gluons one differentiates between initial state radiation (ISR) and final state radiation (FSR). ISR involves the initial state partons and FSR the final state top quarks or their decay products.

To quantify the $t\bar{t}$ production, as for any other particle production, it is necessary to measure the cross section of the process. In classical mechanics the cross section is related to the effective area of collision of two, or more, bodies.

In particle physics the cross section is a more complicated quantity including wavelength probability terms from quantum mechanics, but it is still proportional to the interaction probability. In high energy colliders such as the LHC, the protons can scatter inelastically producing new particles, as in the $pp \to t\bar{t}$ case, in addition to the elastic $pp \to pp$ scattering; all those possible scattering processes are considered in the total inclusive cross section. The exclusive cross section for a process can be thought of as the probability for that process to happen.
The cross section formula for a general process is given by:

$$\sigma = \frac{N_{events}}{\epsilon \int \mathcal{L} dt} \tag{1.25}$$

where N_{events} is the number of observed events, ϵ is the efficiency of the detector and of the particle selection cuts that are applied; $\int \mathcal{L} dt$ is the integrated luminosity, meaning the total luminosity obtained during the data acquisition; the instantaneous luminosity is a parameter of the collider given by the relation:

$$\mathcal{L} = f \frac{n_1 n_2}{4\pi \sigma_x \sigma y} \tag{1.26}$$

where f, n_1, n_2, σ_x and σ_y are the collision frequency, the number of particles forming the two bunches and the beam particle distribution along two orthogonal axis with respect to the beam direction respectively. The cross section is usually measured in barn (b); one barn is quantified in $10^{-24} cm^2$.

The total $t\bar{t}$ production rate for a pp collider experiment is given by the total inclusive cross section $\sigma_{pp \to t\bar{t}}$. In the asymptotic freedom regime, $\sigma_{pp \to t\bar{t}}$ can be factorised in the partonic cross section $\hat{\sigma}_{ij \to t\bar{t}}$ and the *Parton Distribution Functions* PDFs.
The partonic cross section describes the hard process (e.g. $ij = gg \to t\bar{t}t$) at small distances, calculated perturbatively, while the long-distance effects of the partons inside the hadrons are described by the PDFs. Both energy regimes are separated by the factorisation scale μ_F. An usual choice of μ_F is the energy transfer of the hard process (Q). So the total inclusive cross section $\sigma_{pp \to t\bar{t}}$ is given by the convolution of the partonic cross sections with the PDFs $f_i(x, Q)$, integrated over all momentum fractions x_1 and x_2 of the two partons interacting and summed over all possible initial state partons i and j (factorization theorem):

$$\sigma_{p_1 p_2 \to t\bar{t}} = \sum_{(i,j) \in (g,q,\bar{q})} \int_0^1 \int_0^1 \left(\hat{\sigma}_{ij \to t\bar{t}}\right) \cdot f_i^{p_1}(x_1, Q) \cdot f_j^{p_2}(x_2, Q) \cdot dx_1 dx_2 \tag{1.27}$$

Typically the total inclusive cross section $\sigma_{pp \to t\bar{t}}$ strongly depends on top mass m_t and the squared center of mass energy of the collider $s = 4E_{beam}^2$. The dependence from

the regularization scale arises from the fact that the partonic cross section is evaluated at a fixed perturbation order, neglecting higher order contributions. Such dependences become weaker as we add higher order corrections to calculation.
The factorization scale, on the other hand, indicates the transition between the perturbative regime, which belongs to the partonic cross section, and the non-perturbative one, included in the PDF definition. Of course the physical cross section should not depend on the two scales mentioned above, because of they are not physical parameters. The uncertainties on the scales is one of the major sources of uncertainty for the cross section prediction. As we said previously, typically the renormalization and factorization scales are set equal to the mass of the top $\mu = \mu_R = \mu_F = m_t$, but in some cases, as the differential cross sections studies, these scale factors may assume other values, for example the transverse momentum of a jet ($p_{T,jet}$) or the top quark pair invariant mass ($m_{t\bar{t}}$). In order to estimate the uncertainty coming from this arbitrary choice, the scale factors are changed within a certain range, often $[\frac{\mu}{2}, 2\mu]$ is used.

For $\sqrt{s} = 8\,\text{TeV}$, the total inclusive cross section is $\sigma_{pp\to t\bar{t}} = 245.8$ pb [46], mainly depending on the choice of the scales ($\mu_F = \mu_R = m_t$), the top-quark mass ($m_t = 173.3\,\text{GeV}$), and the PDFs ($MSTW2008nnlo$).

The PDFs describe the number density of gluons and all specific quark types as function of the proton momentum fraction x they carry for a given energy scale Q. In Figure 1.6, the PDFs for an energy scale in the order of top-quark production are shown. In a simplified picture, the three valence quarks of the proton (uud) carry $x = \frac{1}{3}$ of the proton momentum. The presence of additional gluons and quarks leads to a more complicated situation. In processes which large energy Q transferred, more gluons and sea quarks can be resolved and dominate the PDFs for low values of x.
PDFs have been measured experimentally e.g. in deep-inelastic scattering processes at the electron-proton collider HERA [47].
In pp collider experiments like the LHC, the predominant $t\bar{t}$ production mechanism is via gg fusion (about 90%). The $q\bar{q}$ annihilation production mode is suppressed in comparison to $p\bar{p}$ collider experiments because antiquarks occur only as sea quarks. Because of the top quark is the heaviest known SM particle, a minimal centre-of-mass energy $\sqrt{s}$ for its production is needed with respect to other particles, that is $\sqrt{\hat{s}} = 2 \cdot m_t \approx 345\,\text{GeV}$. The centre-of-mass energy of the colliding hadrons is related to the partonic centre-of-mass energy $\sqrt{\hat{s}}$ via the proton momentum fractions x_1 and x_2 of the two initial state partons $\sqrt{\hat{s}} = \sqrt{x_1 x_2 s}$.

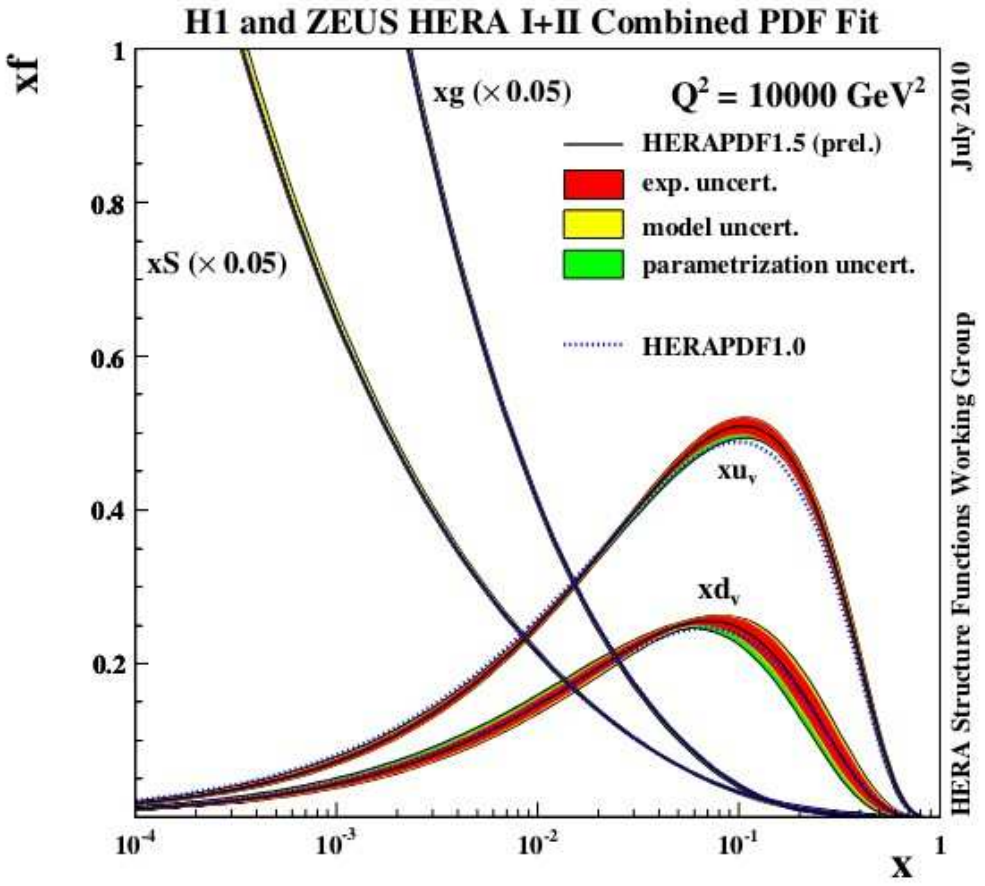

FIGURE 1.6: Parton Distribution Functions (PDFs) of the proton. The PDFs for the *valence quarks* (u_v, d_v), *sea quarks* (S) and the gluons (g) are shown as function of the proton momentum fraction x for an energy scale of $Q = 100\,\text{GeV}$. The values correspond to the HERAPDF1.5 NLO PDF set [3].

1.2.1.2 $t\bar{t}$ pair cross section studies

The $t\bar{t}$ cross section has been experimentally measured for the first time at Tevatron by the CDF[4] and D0[5] collaborations; the result for a top quark mass of $m_t = 173\,\text{GeV}$ is:

$$\sigma_{t\bar{t}}\,(p\bar{p}, 1.96\,\text{TeV}) = 7.08 \pm 0.36\ pb \tag{1.28}$$

The measured cross section is compared with the exact NLO and the approximate NNLO predictions showing the last one is in better agreement with data, as shown in Figure 1.7. Because of its strong dependence of the collision energy, the theoretical $t\bar{t}$ production cross section at the higher energies of LHC is greater than the one at Tevatron.
The best NNLO+NNLL theoretical predictions for the operating LHC energies up to now are [46]:

$$\sigma_{t\bar{t}}^{theory}(7\,\text{TeV}) = 172.0^{+4.4}_{-5.8}(scales)^{+4.7}_{-4.8}(PDF)\ pb \tag{1.29}$$

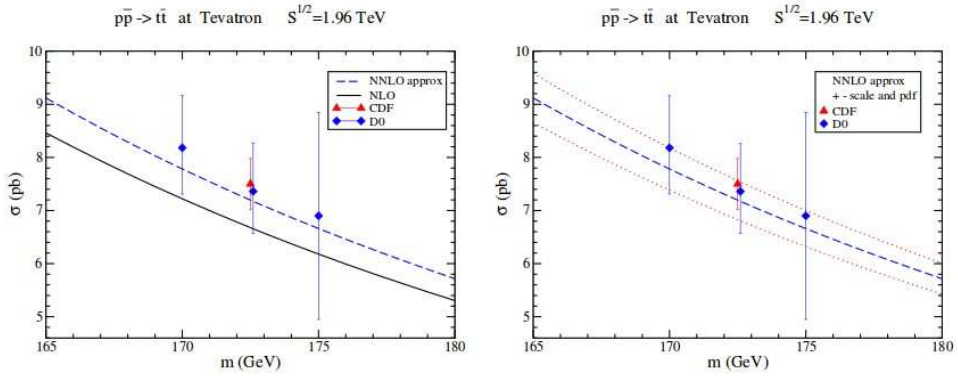

FIGURE 1.7: Tevatron $t\bar{t}$ cross section measurements compared, on the left plot, with NLO and NNLO prediction and, on the right, with NNLO scale variation uncertainties estimated varying PDF scale ($\mu = m_t$) of a factor two [4] [5] [6] [7].

$$\sigma_{t\bar{t}}^{theory}(8\,\text{TeV}) = 245.8^{+6.2}_{-8.4}(scales)^{+6.2}_{-6.4}(PDF)\ pb \tag{1.30}$$

The ATLAS[8] and CMS[9] collaborations measured the $t\bar{t}$ cross section in pp collisions at a center of mass energy of 7 TeV:

$$\sigma_{t\bar{t}}^{ATLAS}(7\,\text{TeV}) = 177^{+8}_{-7}(sys) \pm 3(stat) \pm 7(lumi)\ pb \tag{1.31}$$

$$\sigma_{t\bar{t}}^{CMS}(7\,\text{TeV}) = 165 \pm 10.6(sys) \pm 2.2(stat) \pm 7.8(lumi)\ pb \tag{1.32}$$

These experimental results, obtained combining the measurements performed in different decay channels, are in good agreement with the theoretical predictions as can be seen from plots in Figure 1.8, where results are compared with the NLO and NNLO predictions respectively. Once again the NNLO prediction better match the experimental measurements.

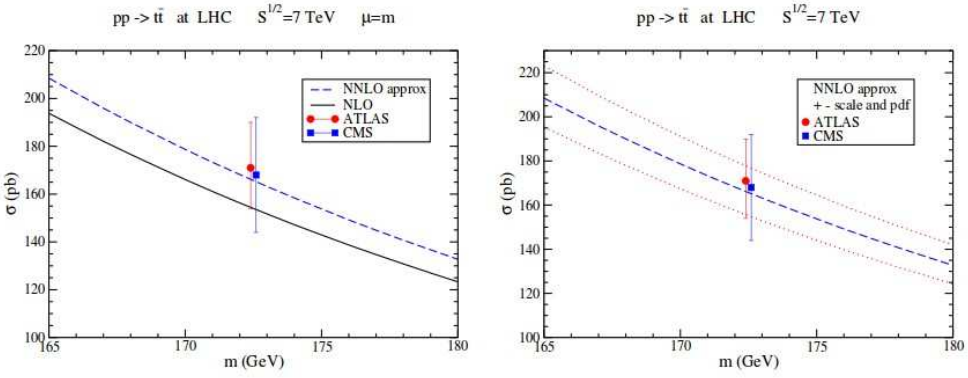

FIGURE 1.8: LHC $t\bar{t}$ cross section measurements compared, on the left plot, with NLO and NNLO prediction and, on the right, with NNLO scale variation uncertainties estimated varying PDF scale ($\mu = m_t$) of a factor two [8][9].

All the recent ATLAS and CMS results for each channel considered are shown in Figure 1.9. In Figure 1.10 both NNLO theoretical $t\bar{t}$ cross section distribution for pp and

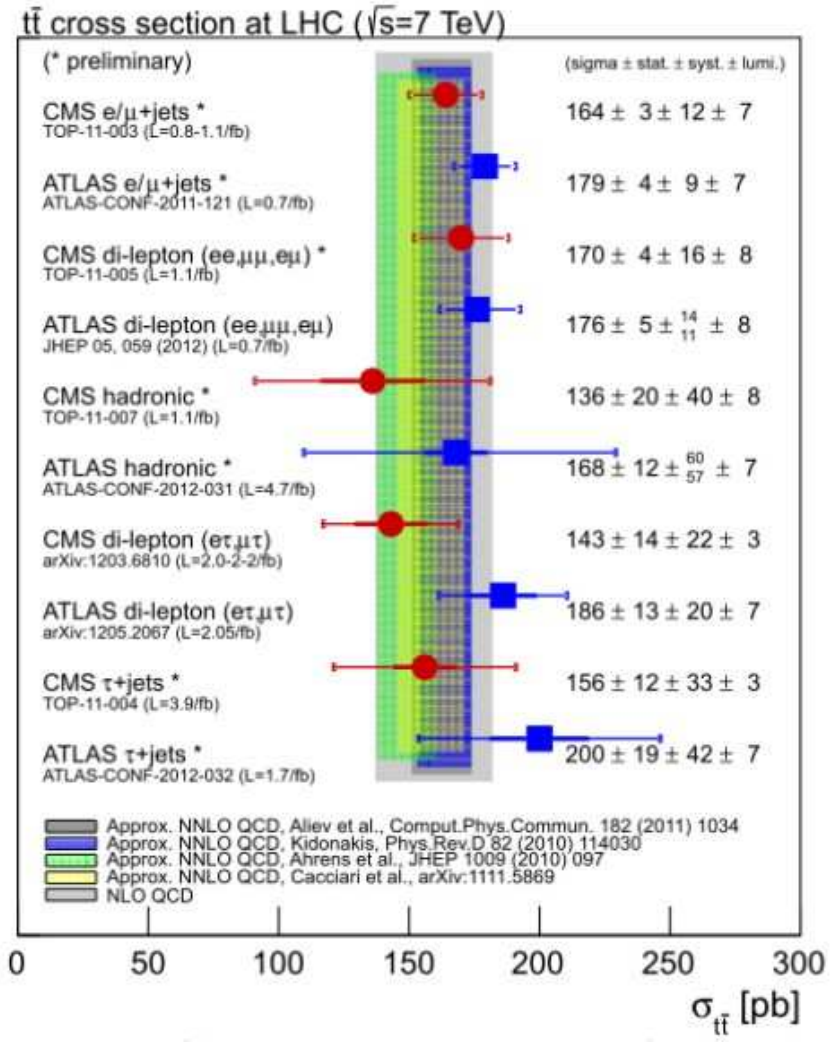

FIGURE 1.9: Compilation of the most precise measurements of $\sigma_{t\bar{t}}$ per decay mode and experiment, compared with several theory predictions at NLO and approximate NNLO QCD.

$p\bar{p}$ interactions with respect to the center of mass energy are shown together with the Tevatron and LHC experimental results. In both cases the experimental measurements are in good agreement with predicted cross sections.

The $\sigma_{t\bar{t}}$ measurement has been also performed at a center of mass energy of 8 TeV by both ATLAS[48] ($\mathcal{L} = 5.8fb^{-1}$) and CMS[10] ($\mathcal{L} = 5.8fb^{-1}$) in the $lepton + jets$ channel obtaining results compatible with the theoretical expectations:

$$\sigma_{t\bar{t}}^{ATLAS}(8\,\text{TeV}) = 241 \pm 31(sys) \pm 2(stat) \pm 9(lumi)\ pb \tag{1.33}$$

$$\sigma_{t\bar{t}}^{CMS}(8\,\text{TeV}) = 228^{+29}_{26}(sys) \pm 9(stat) \pm 10(lumi)\ pb \tag{1.34}$$

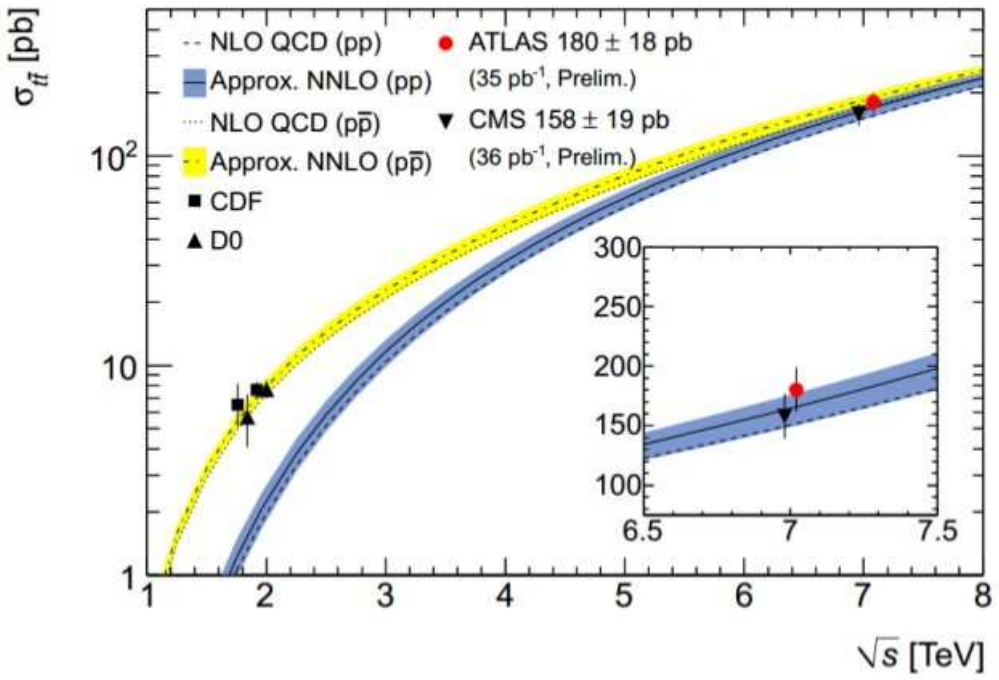

FIGURE 1.10: Inclusive top/anti-top production cross section predicted for LHC and compared with ATLAS and CMS measurements [8] [10].

1.2.1.3 Differential $t\bar{t}$ cross section

The differential $t\bar{t}$ production cross section constitutes a very important test of the Standard Model predictions and a sensitive channel for the presence of new physics, e.g. the role of the $t\bar{t}$ invariant mass distribution, which may be sensitive to the presence of resonances that decay into top pairs.

Theoretical predictions for differential distributions exist in fixed order QCD showing theoretical uncertainties between 10% and 15%, depending on the $m_{t\bar{t}}$, also the dependence on the transverse momentum p_T of the top quark has similar role for searching the new signal physics.

The corresponding theoretical prediction [50] for the LHC data taking at $\sqrt{s} = 14\,\text{TeV}$ is shown in Figure 1.11. Usually the differential cross section may be calculated either after extrapolation to the full phase space, at the level of partons before hadronization (*parton level*), or only within a reduced, or fiducial, phase space considering only objects visible by the detector (*particle level*); in this last case only the detector response correction is used. The parton level definition may be needed in order to compare with fixed order QCD calculations, while the particle level definition is closer to what is measured experimentally and can be compared with MC simulations.

The first measurements of the differential cross section has been performed by the Tevatron experiments resulting in the measurements of the cross section as a function of

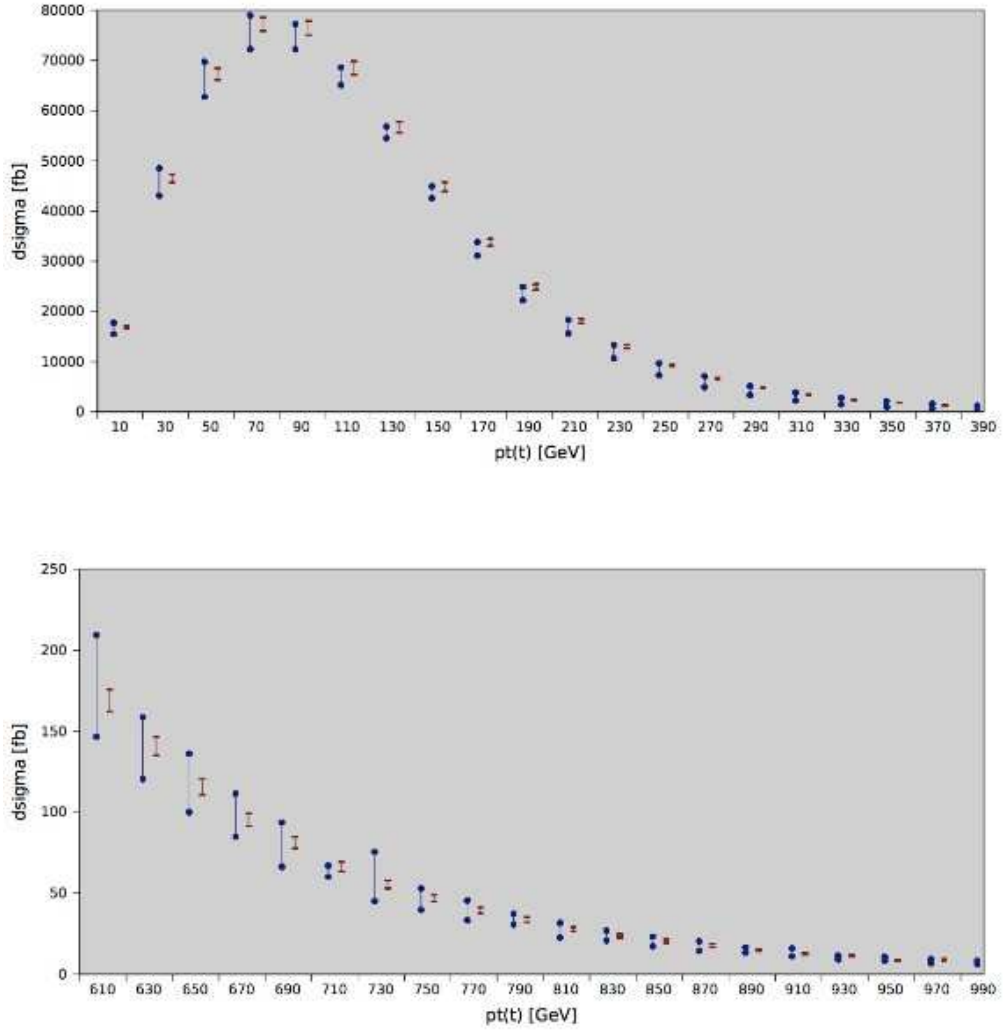

FIGURE 1.11: NLO QCD predictions [11] for the transverse momentum of the top quark at the 14 TeV LHC. Blue error bars correspond to the central MSTW pdf set and scale variation by a factor of two around $\mu = m_t$. Dark red error bands correspond to 1 standard deviation of MSTW pdf error sets for fixed renormalization and factorization scale at $\mu = m_t$. Note that the red and blue bars can be off-set because at NLO the central scale does not necessarily corresponds to the center of the blue bar. In this case, it seems that it is towards the upper value of the blue bar.

the transverse momentum of the top quark by $D0$ [12] with an integrated luminosity of $\mathcal{L} = 1fb^{-1}$ and as a function of the invariant mass of the $t\bar{t}$ system by CDF [13] with an integrated luminosity of $\mathcal{L} = 2.7fb^{-1}$. Both results are consistent with the standard model predictions as shown in Figure 1.12. Thanks to the large abundance of top quark pair production due to the high cross section, at the LHC collider differential cross section measurements can be performed with increased precision as a function of several kinematic variables. This improves the reliability of the measurements and widens the horizon for new physics searches. Several measurements with increasing statistic have been performed by the ATLAS and CMS collaboration on different decay channels.

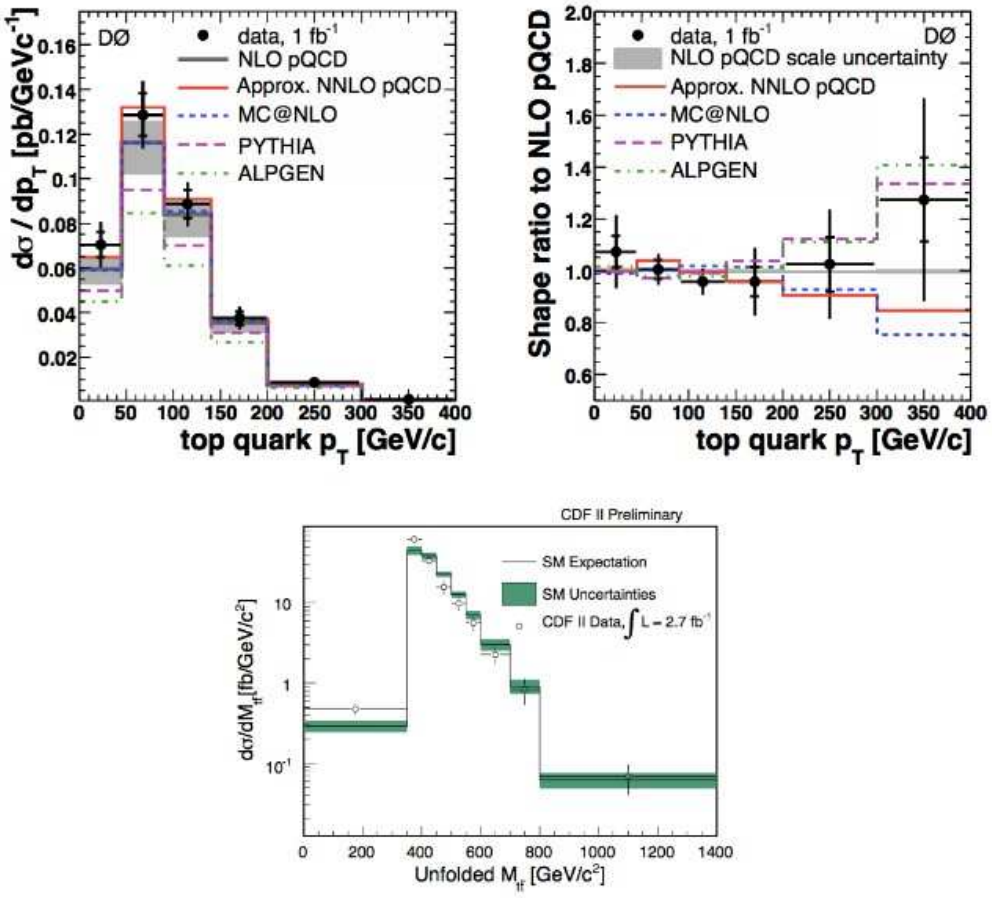

FIGURE 1.12: Differential cross section (top-left) and relative ratio (top-right) data obtained by the D0 experiment as a function of top-quark p_T (two entries per event) [12] compared with expectations from NLO, from an approximate NNLO calculation, and for several event generators. In the bottom plot it is shown the differential $t\bar{t}$ cross section obtained by the CDF collaboration as a function of $m_{t\bar{t}}$ [13] compared to the SM expectation.

In this thesis the results in the $lepton + jets$ obtained with 2012 data, corresponding to an integrated luminosity $\mathcal{L} = 20.3\ fb^{-1}$ and collected at a center of mass energy $\sqrt{s} = 8\,\text{TeV}$, will be described in detail in the following chapters together with the analysis method used. The previously measured differential cross section [14], relating to the $lepton + jets$ channel, at $\sqrt{s} = 7\,\text{TeV}$ are shown in Figure 1.13 ($ATLAS$ [14]) and 1.14 (CMS [15]). A good agreement has been found with all the predictions considered.

1.2.1.4 Single top quark production

As well as the previously discussed production of top-quark pairs, also single top quarks can be produced in hadron colliders. The production cross section for these processes

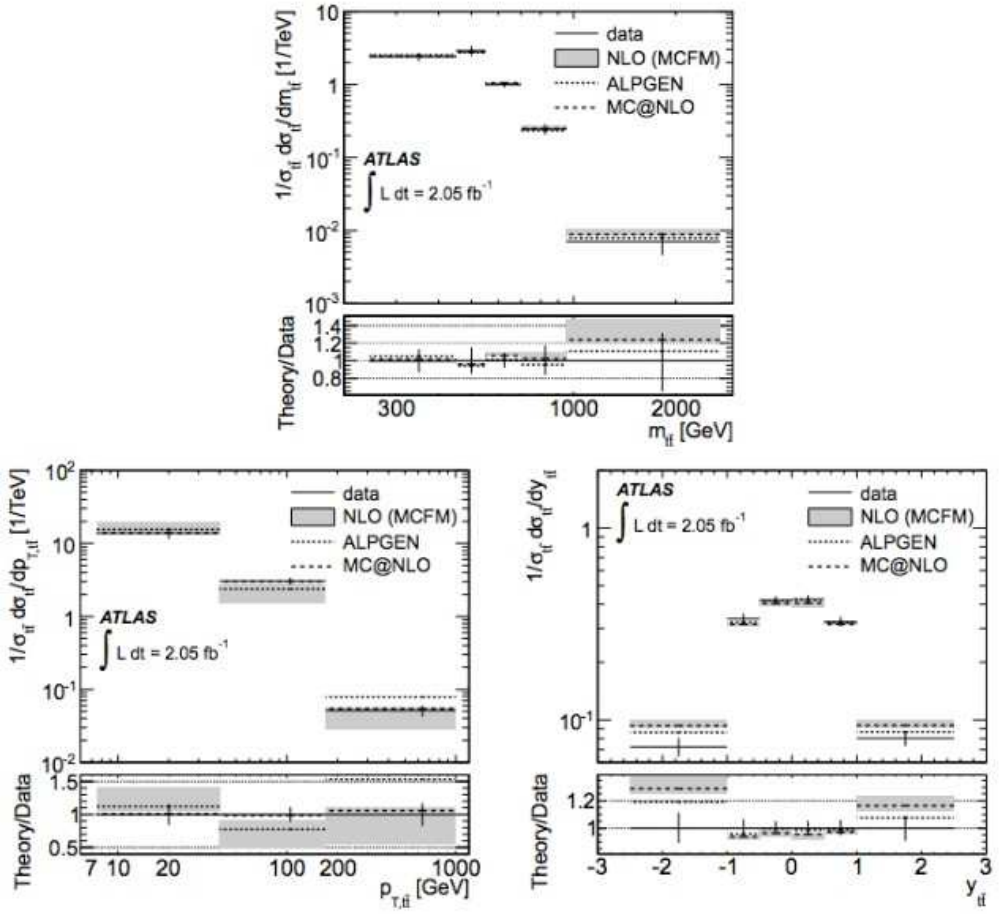

FIGURE 1.13: Electron and muon channels normalised differential $t\bar{t}$ production cross section obtained by the *ATLAS* collaboration as a function of the $m_{t\bar{t}}$ (top), $p_T^{t\bar{t}}$ (bottom-left) and $y_{t\bar{t}}$ (bottom-right). The inner (outer) error bars indicate the statistical (combined statistical and systematic) uncertainty. The measurements is compared to the *NLO* prediction from *MCFM* [14].

is lower because the production mechanism involves the weak interaction, i.e. Wtb vertices.

The first observation of single top quark production was achieved by the Tevatron experiments *CDF* and *D*0 in 2009 [51][52]. It constituted a very important result especially considering the extremely low cross section of the process at the Tevatron energy. This is not anymore true at LHC where the higher energies reached lead to a not negligible contribution form single top production.

The possible LO Feynman diagrams ($s-channel$, $t-channel$ and $tW-channel$) are shown in Figure 1.15. Via the t-channel, the top quark is created by a fusion of a b quark and a virtual W boson. This channel represents the predominant production mode for single top quarks at the LHC with $\sqrt{s} = 8\,\text{TeV}$. The charge of the initial state quark determines if a top quark or an antitop quark is produced.

For a pp collider, u quarks dominate the PDFs of the valence quark. Therefore, the

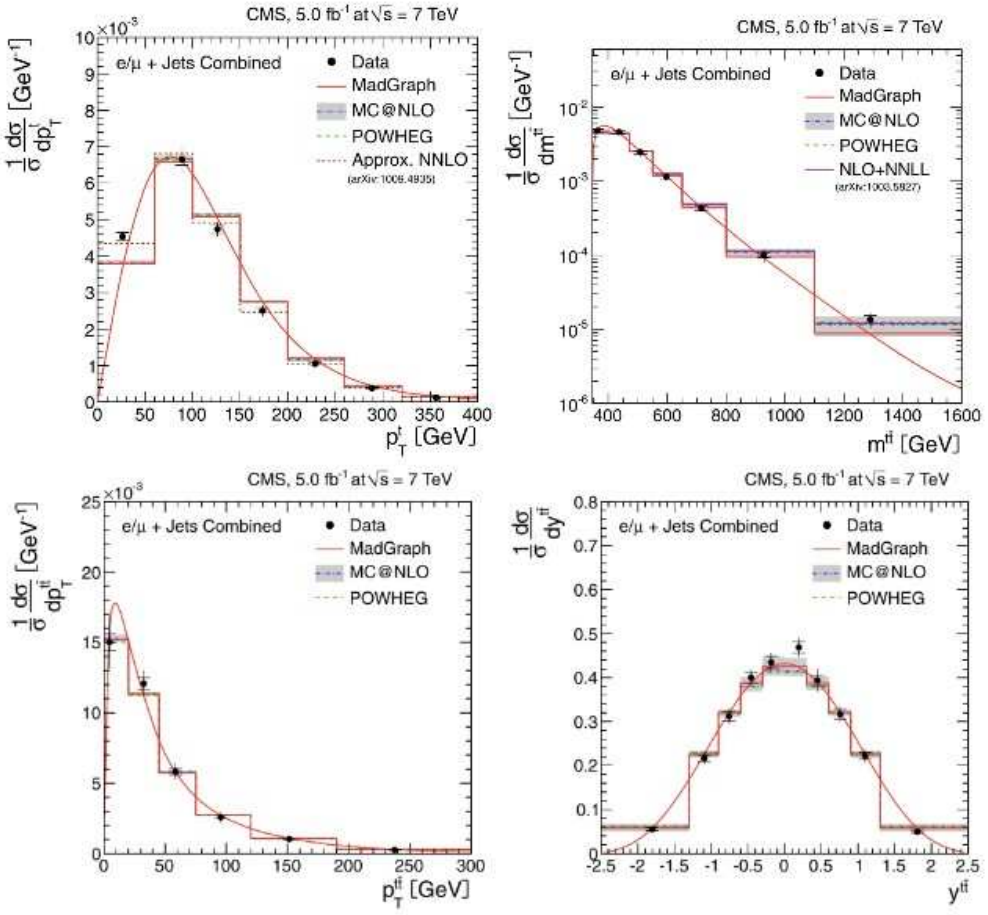

FIGURE 1.14: Electron and muon channels normalised differential $t\bar{t}$ production cross section obtained by the CMS collaboration as a function of the p_T^t (top-left), $m_{t\bar{t}}$ (top-right), $p_T^{t\bar{t}}$ (bottom-left) and $y_{t\bar{t}}$ (bottom-right). The inner (outer) error bars indicate the statistical (combined statistical and systematic) uncertainty. The measurements are compared to predictions from $MADGRAPH$, $POWHEG$, and $MC@NLO$. The $MADGRAPH$ prediction is shown both as a curve and as a binned histogram [15].

production of top quarks ($\sigma_{pp\to t,t-channel} \approx 56.4\ pb$) is preferred over the production of $\bar{t}$ quarks ($\sigma_{pp\to \bar{t},t-channel} \approx 30.7\ pb$) [53]. In the s-channel, a W boson creates either a t and a $\bar{b}$ quark or a $\bar{t}$ and a b quark. This depends on the charge of the W boson, which is determined by the charge of the initial state quarks. Therefore, the same argumentation as for the t-channel holds and the production of top quarks ($\sigma_{pp\to t,s-channel} \approx 3.8pb$) is preferred over the production of $\bar{t}$ quarks ($\sigma_{pp\to \bar{t},s-channel} \approx 1.8\ pb$) [53].
Last, through the tW-channel, the t ($\bar{t}$) quark is produced in association with a W boson. This production mode involves a gluon and a sea b ($\bar{b}$) quark in the initial state. Therefore, the cross section is charge-symmetric ($\sigma_{pp\to t,tW-channel} = \sigma_{pp\to \bar{t},tW-channel} \approx 11.1\ pb$) [53]. The expected cross sections at $\sqrt{s} = 7\,\text{TeV}$ and $\sqrt{s} = 8\,\text{TeV}$ are shown in Table 1.1.

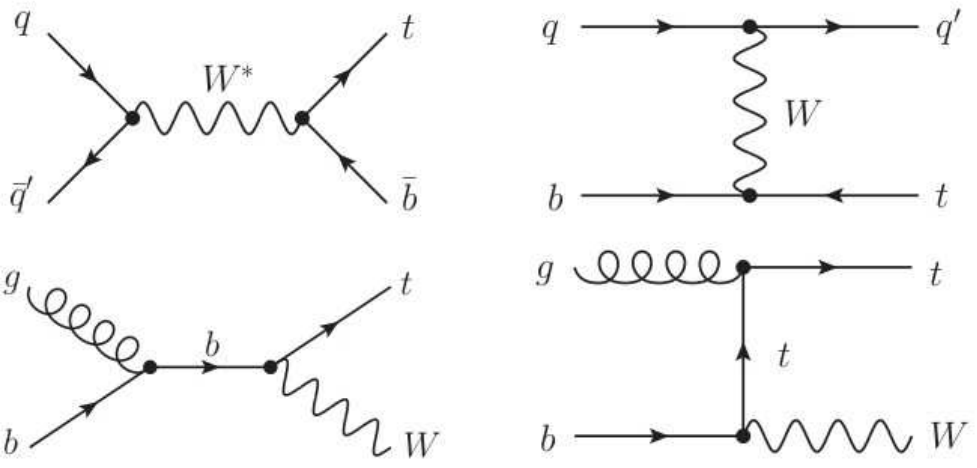

FIGURE 1.15: Feynman diagrams of the LO production of single top quarks in hadron colliders: $s-channel$ (top,right), $t-channel$ (top,left) and $tW-channel$ (bottom).

Channel	$7TeV[pb]$	$8TeV[pb]$
t-channel	$64.6^{+2.7}_{-2.0}$	$87.8^{+3.4}_{-1.9}$
s-channel	4.6 ± 0.2	5.6 ± 0.2
Wt	15.7 ± 1.1	22.4 ± 1.5

TABLE 1.1: Expected single top quark production cross sections in different channels at a center-of-mass energy of 7 TeV, given by approximate NNLO [17] [18] [19].

1.2.1.5 Kinematic quantities for leading order $t\bar{t}$ production

In this thesis the differential cross sections will be presented as a function of various kinematical quantities related to the top quarks and the $t\bar{t}$ system from top-quark pair production. Therefore, a short overview of these quantities and their connection with the underlying production mechanism in pp collisions is given in the following.
For simplicity, we discuss only the production of top-quark pairs at LO, where no additional partons occur in the partonic final state. The invariant mass of the $t\bar{t}$ system ($m_{t\bar{t}}$) is at LO equal to the centre-of-mass energy of the partonic interaction:

$$m_{t\bar{t}}^{LO} = \sqrt{\hat{s}} \geq 2 \cdot m_t \tag{1.35}$$

Hence $m_{t\bar{t}}$ is a measure of the momentum fractions of the initial state partons and the pp centre-of-mass energy. It is convenient to differentiate all momenta between a *longitudinal* and *transverse* component, in which the longitudinal component is chosen along the axis of the initial proton flight direction ($z-$axis).
The longitudinal momenta of initial state partons will depend on their x-Bjorken values. In contrast, the momentum of the initial state partons in the plane transverse to the

$z-$axis can be considered as zero, therefore, momentum conservation can be applied for this component and particle detectors are optimised for the measurement of transverse momenta.

Usually the longitudinal momentum p_z is expressed by using the rapidity y through the total energy E:

$$y = \frac{1}{2} ln \left(\frac{E + p_z}{E - p_z} \right) \tag{1.36}$$

Rapidity differences are invariant under Lorentz transformations. The rapidity of the $t\bar{t}$ system ($y_{t\bar{t}}$) describes its boost in longitudinal direction and at LO is determined by the ratio of the proton momentum fractions (x_1, x_2) of the initial state partons, infact if we use:

$$E_{t\bar{t}}^{LO} = E_{parton_1} + E_{parton_2} = \sqrt{s}(x_1 + x_2) \tag{1.37}$$

$$p_{t\bar{t}}^{z,LO} = p_{parton_1} - p_{parton_2} = \sqrt{s}(x_1 - x_2) \tag{1.38}$$

in the rapidity definition, we obtain:

$$y_{t\bar{t}}^{LO} = \frac{1}{2} ln \left(\frac{x_1}{x_2} \right) \tag{1.39}$$

The transverse momentum of the $t\bar{t}$ system ($p_{t\bar{t}}^{T}$) is a measure of the recoil against additionally produced particles and therefore vanishes at LO, ($p_{t\bar{t}}^{T,LO} = 0$. So, the produced top quarks are at LO back-to-back in the transverse plane to $z-$axis. Consequently, the difference in azimuthal angle of the two top quarks in this plane ($\Delta\phi(t, \bar{t})$) at LO is equals to π, $\Delta\phi(t, \bar{t})^{LO} = \pi$.

The transverse momentum of the top quarks in the $t\bar{t}$ rest frame (p_T^t) depends on the scattering angle (θ^*) in the $t\bar{t}$ rest frame and the magnitude of the top-quark momentum (p^t) is $p_T^t = p^t \cdot \sin\theta^*$.

For the LO process the magnitude of the top-quark momentum is given by the top-quark mass and the partonic centre-of-mass energy:

$$p_{LO}^t = \sqrt{\left(E_{LO}^t\right)^2 - \left(m^t\right)^2} \tag{1.40}$$

$$E_{LO}^t = \frac{1}{2}\sqrt{\hat{s}} \tag{1.41}$$

By substituting E_{LO}^t within p_{LO}^t :

$$p_{LO}^t = \sqrt{\frac{1}{4}\left(\sqrt{\hat{s}}\right)^2 - \left(m^t\right)^2} \tag{1.42}$$

The top-quark transverse momentum in the detector rest frame ($\hat{p_T^t}$) is a convolution of (p_T^t) and $p_T^{t\bar{t}}$. For $t\bar{t}$ production at LO $\hat{p_T^t}$ and p_T^t are equal.

1.2.2 Top quark decay

Because of the heaviest particle of the SM the top quark has the very short lifetime of approximately 10^{-24} seconds, which is short enough to decay before to hadronize. The top quark is unique in this feature. No free quark has ever been found so the top quark supplies the only probe of the behavior of bare quarks.

1.2.2.1 Decay of single top quarks

The decay of the top quark is characterised by the weak interaction. According to the CKM matrix the top quark decays almost exclusively into a W boson and a bottom quark ($V_{tb} \approx 1$). The top quark is besides the Higgs boson the only (currently known) particle which can decay into a real W boson, as shown in Figure 1.16.

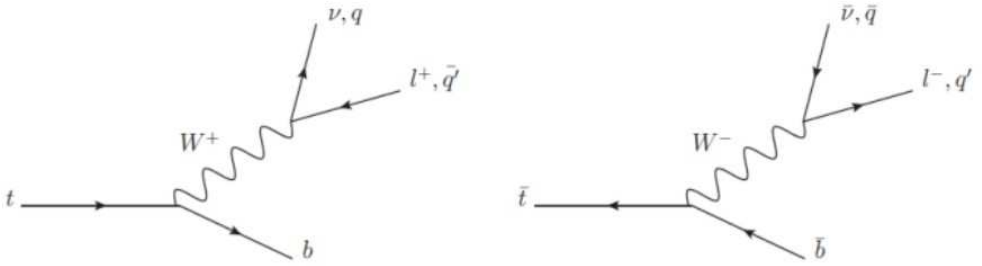

FIGURE 1.16: Feynman diagrams of top and anti-top quarks decay

Furthermore, the large mass leads to a large value of the decay width Γ_t, $\Gamma_t \propto m_t^3 \approx 1.3\,\text{GeV}$, which corresponds in a very short lifetime (τ_t) of $\tau_t = \frac{1}{\Gamma_t} \approx 5 \cdot 10^{-25} s$, that is ten times smaller than the *hadronisation* time scale ($\tau_{Had} \propto \frac{1}{\Lambda_{QCD}} \approx 3 \cdot 10^{-24} s$). Hence, top quarks decay befor hadronize and offer therefore the unique possibility to study bare quarks.
Top-quark properties are perturbatively calculable and can be directly studied experimentally, e.g. all spin information of the top quark is transmitted to its decay products and therefore experimentally accessible.

1.2.2.2 Top quark pair final states

The different $t\bar{t}$ final states are characterised by the decay of the two W bosons. Each W boson can decay either leptonically into a lepton and the corresponding antineutrino or hadronically into a quark and an antiquark. Considering the mass of the W boson and neglecting the flavour mixing, two different hadronic final states and three leptonic

final states are possible for each $W-$boson.
When both $W^{\pm}$ bosons decay hadronically the event is called a *fully hadronic* event ($BR \approx 0.46$). When both $W^{\pm}$ bosons decay leptonically the event is defined as a *dilepton* event ($BR \approx 0.09$). When one $W^{\pm}$ decays leptonically and the other hadronically the event is a *lepton + jets* event ($BR \approx 0.45$) (or *semileptonic*), as shown in Figure 1.17. The measured numbers for the branching ratios (BRs) are taken from [43] and assume

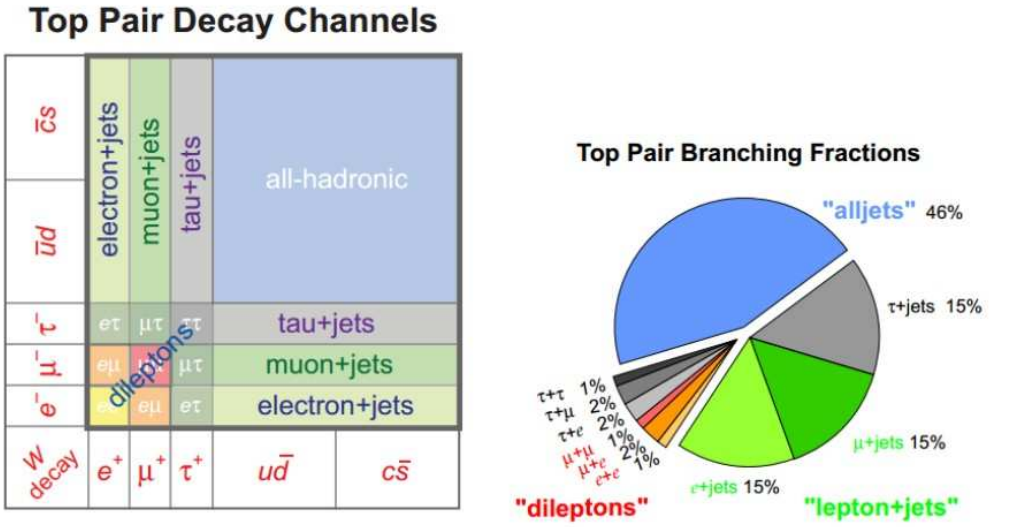

FIGURE 1.17: The $t\bar{t}$ pair decay channels (left) and branching ratios (right).

lepton universality. Counting all possible final states for the LO scenario, neglecting flavour mixing but considering the factor of three for quarks because of the three possible colour states, the probability is $\frac{6}{9}$ for a hadronic $W-$boson decay and $\frac{1}{9}$ for each of the three possible leptonic $W-$boson decays. This results at LO in an expected BR of $\frac{36}{81}$ for the fully hadronic and the semileptonic final state and a BR of $\frac{9}{81}$ for the dileptonic final state. The top quarks decay can be calculated using the same techniques as for the partonic production cross section.
In principle, production and decay should be treated simultaneously. Although the absolute value of the top-quark width is large, its relative size with respect to the top-quark mass is small, $\frac{\Gamma_t}{m_t} \approx 0.0075$.
This allows the application of the *narrow width approximation*, i.e. the separation of the process into an *on-shell* top-quark production and the subsequent decay.

1.2.2.3 Characteristics of the semileptonic $t\bar{t}$ final state

The final state investigation object of this thesis is the semileptonic final state with one muon or electron (in the following called $l + jets$, $e/\mu + jets$ or simply signal). About 30% of all top-quark pairs are decaying into this final state. A Feynman diagram for

the semileptonic decay without additional radiation is shown in Figure 1.18. The final

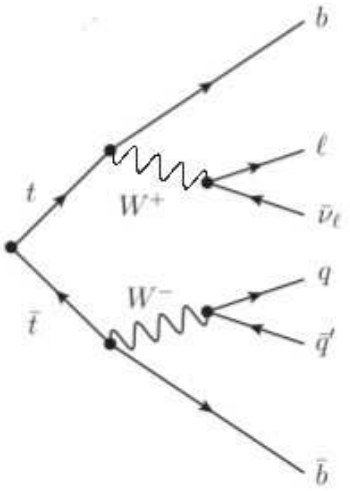

FIGURE 1.18: LO Feynman diagram for a semileptonic $t\bar{t}$ decay.

state objects of the LO decay are one lepton (e or μ) and one corresponding neutrino, two b quarks and two light quarks (u and d or s and c flavour).
In higher orders, additional particles can be produced, e.g. via FSR of the light and b quarks. For simplicity, this case will not be considered by remaining within LO scenario. The invariant mass of the two light jets and the invariant mass of the lepton and the neutrino form the W-boson mass of 80.4 GeV, and those of the W boson and the associated $b-$flavoured quark form the top-quark mass.
Tipically invariant masses are used experimentally as constraints for the reconstruction of the top quarks from the measured detector objects. The final state muon or electron is directly measured by the particle detectors, the neutrino, instead, is only detected indirectly via a momentum imbalance in the transverse plane (E_T^{miss}).
Due to confinement all final state quarks result in a bunch of colour neutral hadrons. Experimentally, the kinematics of each quark can be determined by clustering all its decay products into one object (called *jet*). The concept of a jet is illustrated in Figure 1.19. Furthermore, jets from b quarks (b-tagged jets) can be identified using the flight distance of the $B-$hadrons before their further decay, which is in the order of $c\tau = 500$ μm.
QCD processes beyond LO in perturbation theory can lead to additional partons in the final state, which result in additional jets. One kinematic quantity involving these additional jets is the distribution of the invariant mass of the $t\bar{t}$ pair and an additionally produced jet ($m_{t\bar{t}}^{jet}$). From this, the dimensionless observable ρ_S is constructed using a scale m_0 in the order of m_t, $\rho_S = \frac{2 \cdot m_0}{m_{t\bar{t}}^{jet}}$. The measured distribution of ρ_S is expected to

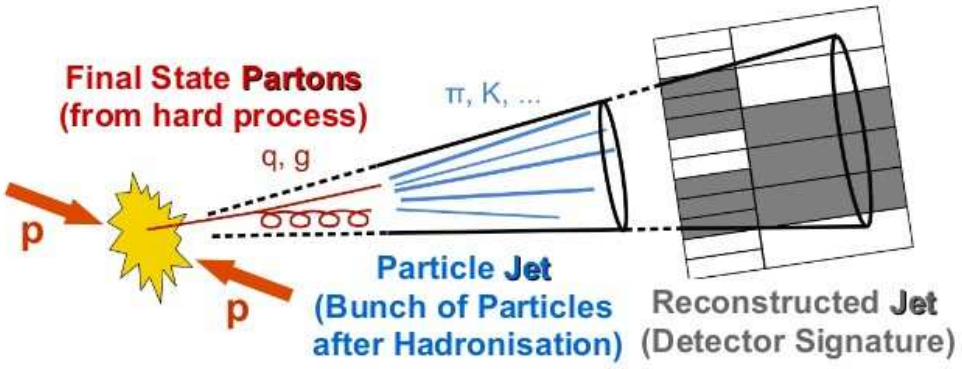

FIGURE 1.19: Sketch of proton-proton collision with a parton (quark or gluon) in the final state, resulting in a collimated spray of particles, a *jet*.

be sensitive to the top-quark mass [54].

The usual background processes for the $l + jets$ final state are the production of leptonically decaying W or Z bosons accompanied by additional jets, the production of QCD multi-jet final states or the production of single top quarks. Another background process are $t\bar{t}$ events that decay into a different final state.

The semileptonic final state is a good compromise between BR and experimentally manageable background processes. In comparison, the dileptonic final state has an intrinsic lower background contribution but a smaller BR, while the fully hadronic final state has a larger BR but suffers from a huge QCD multi-jet background. Semileptonic final states with a $\tau-$lepton are experimentally challenging because decay fastly and has to be reconstructed from its decay products, in contrast to a muon or electron. Moreover, the decay of $\tau-$leptons has a neutrino-component that make this final state particularly complicated.

1.2.3 Top quark mass

A precise determination of top quark mass m_t is important because quantum loops involving top quarks cause large corrections to theoretical predictions for many precision electroweak observables, like the mass of the Higgs boson. It consistutes a free parameter of the Standard Model and must be determined experimentally.

The most precise direct measurement of the top quark mass has been done by the Tevatron [16] experiments with a precision of 0.6% that makes the mass of a known quark with better precision among all the quarks: $m_t = 173.5 \pm 0.6(stat.) \pm 0.8(syst.)$ GeV.

The most recent direct m_t measurements are summarized in Figure 1.20. Besides the "active role" in putting constraints in many precision electroweak observables, indirect constraints on m_t can be obtained from precision measurements of the parameters of

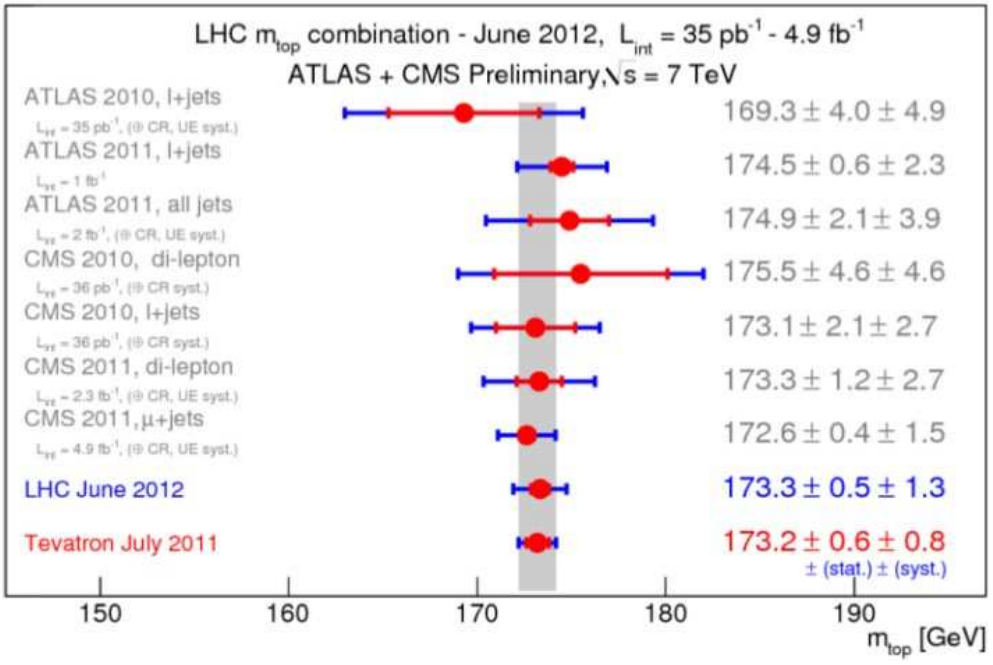

FIGURE 1.20: Overview of the top quark mass measurements from ATLAS and CMS, including the latest CDF and D0 combination [16].

the electroweak theory. In fact the mass of W boson can be expressed as:

$$m_W^2 = \frac{\pi\alpha\left(M_Z^2\right)/\sqrt{2}G_F}{\sin^2\theta_W \cdot (1-\delta_r)} \tag{1.43}$$

where $\alpha(M_Z^2)$ is the electromagnetic coupling constant, G_F is the Fermi constant and θ_W is the electroweak mixing angle ($\sin^2\theta_W = 1 - \frac{m_W^2}{m_Z^2}$). The correction factor δ_r expresses the dependency of m_W on the top quark mass m_t beacause contains contributions from higher order electroweak loop diagrams involving the top quark, which depend quadratically on m_t.

Actually the most recent indirect constraint on m_t based on electroweak precision measurements [55] is $m_t^{indirect} = 178.9^{+11.7}_{-8.6}$ GeV, which is in good agreement with the direct measurements, even if has a large uncertainty. Beacuse of the dependency of radiative correction factor δ_r on the Higgs mass (logarithmically), it is also possible to indirect constraints the Higgs mass m_H from global electroweak fits including direct measurements of top mass m_t.

The most recent determinations of those constraints fits with the Higgs boson discovery accomplished at LHC by the ATLAS[38] and CMS[37] experiments.

1.2.4 DGLAP equations and Hessian method

Measurements of *deep-inelastic scattering* (DIS) structure functions in lepton-hadron scattering and of lepton pair production cross sections in hadron-hadron collisions, as well as Drell-Yan processes and jet production from hadron-hadron experiments are needed to have informations in order to extract the probability density $f_i(x, Q_0^2)$ of finding a parton i with x momentum fraction at momentum tranfer scale Q_0, know as parton distribution functions. They are non-perturbative quantities. A very important feature of the PDF's is that they depend only on the hadron structure and are completely independent of the nature of the hard process, therefore this makes them universal so that can be used for the calculation of any hadronic cross section.
PDFs for the *valence* quarks are very different from the *sea* quarks, as the latter are abundant at low x but negligible at $x \approx 1$, while the valence quarks are peaked for larger values of x.
The gluons distribution is similar to that of sea quarks, incerases at low x, but gluons are more abundant. With respect to $q\bar{q} \to q\bar{q}, qq \to gg, qg \to qg$ the gluon gluon scattering $gg \to gg$ is also increased by large colour factors, related to the larger multiplicity of gluon states, so that it is the dominant process in pp or $p\bar{p}$ interactions at low x.
Given a functional dependence of x at a given scale Q_0^2, the PDFs are extracted from fits of data collected by hadron-hadron experiments described before. Perturbative QCD is able to predict the PDF via the Dokshitzer-Gribov-Lipatov-Altarelli-Parisi *evolution equations*[56][57][58] (DGLAP):

$$\frac{df_a(x,\mu^2)}{d\ln\mu^2} = \sum_b \int_0^1 \frac{dz}{z} P_{ab}(\alpha_s(\mu^2), z) f_a(\frac{x}{z}, \mu^2). \tag{1.44}$$

The kernels $P_{ab}(\alpha_s, z)$, known as the Altarelli-Parisi splitting functions, can be calculated as a power series expansion in α_s:

$$P_{ab}(\alpha_s, z) = \alpha_s P_{ab}^{(LO)}(z) + \alpha_s^2 P_{ab}^{(NLO)}(z) + \alpha_s^3 P_{ab}^{(NNLO)}(z) + \mathcal{O}(\alpha_s^4). \tag{1.45}$$

Various groups are very active in the determination of PDF from DGLAP fits, like CTEQ, MSTW, and H1 and ZEUS experiments at HERA.
As PDF parameters are fitted from experimental data, they are affected themselves by uncertainties which will propagate to any computation of cross section. These uncertainties affect mostly the gluon PDF. At the TeV center-of-mass energy scale the intercting partons have large momentum fractions and very high Q^2, so that the cross section predictions are dominated by PDF uncertainty.
There are various sources of uncertainty, but usually they can be divided into two classes: those which are associated with the *experimental* uncertainty on the data that are fitted

in the global analysis, and the *theoretical* uncertainty like neglected higher-order terms and higher-twist QCD corrections, electroweak corrections, nuclear corrections and so on.

To estimate the uncertainty, the CTEQ and MSTW groups, use the *Hessian* method, which consists in the study of the quadratic expansion of the χ^2 function about its global minimum.

The χ^2 function can be defined as:

$$\chi^2_{global} = \sum_n \sum_l \left(\frac{D_{nI} - T_{nI}}{\sigma_{nI}} \right)^2 \tag{1.46}$$

where T_{nI}, D_{nI} and σ_{nI} are the theory and data values, and uncertainty for data point I of data set n, respectively. To obtain a "best estimate" of the true PDFs we find the parameter set that minimizes the χ^2 function. Is needed to check the variation of χ^2_{global} in the neighborhood of its minimum, in an amount $\Delta\chi^2_{global}$, to study uncertainties.

Expanding χ^2_{global} with a Taylor series around its minimum and taking only the leading order terms we obtain:

$$\Delta\chi^2_{global} = \chi^2_{global} - \chi^2_0 = \sum_{i=1}^{d} \sum_{j=1}^{d} H_{ij}(a_i - a_i^0)(a_j - a_j^0) \tag{1.47}$$

where the Hessian matrix H_{ij} can be expressed as:

$$H_{ij} = \frac{1}{2} \frac{\partial^2 \chi^2_{global}}{\partial a_i \partial a_j}|_{min} \tag{1.48}$$

having a complete set of orthogonal eigenvectors v_{ik} defined by

$$\sum_{j=1}^{d} H_{ij} v_{jk} = \epsilon_k v_{ik} \tag{1.49}$$

with eigenvalues $\{\epsilon_k\}$.

The displacements from the minimum in terms of the eigenvectors are:

$$a_i - a_i^0 = \sum_{k=1}^{d} v_{ik} s_k z_k \tag{1.50}$$

where the scale factors s_k are introduced to normalize the new parameters z_k such that

$$\Delta\chi^2_{global} = \sum_{k=1}^{d} z_k^2 \tag{1.51}$$

where $\sum_{k=1}^{d} z_k^2 \leq T^2$ is the interior of a hypersphere of radius T.
Fitting groups produce the eigenvector PDF sets $S_k^{\pm}$, with parameters a_i shifted from the global minimum:

$$a_i(S_k^{\pm}) = a_i^0 \pm t e_{ik} \tag{1.52}$$

with t so that to have the desired $T = \sqrt{\Delta\chi^2_{global}}$.
The user can compute the value of a generic observable which depends on PDF by using the *central value*, that is the best fit estimate, and to evaluate the uncertainty it is necessary to evaluate O for each of the $2k$ set $(S_k^{\pm})$, and finally apply the following formula:

$$\Delta O = \frac{1}{2}\sqrt{\sum_k \left[O\left(S_k^+\right) - O\left(S_k^-\right)\right]^2}. \tag{1.53}$$

Actually there is another source of uncertainty in PDF sets: the global fits done to extrapolate PDFs are dependent on α_s value, which is not constant. Both CTEQ and MSTW agree to use a fixed value of $\alpha_s\left(M_Z^2\right)$, because the additional uncertainty associated to it is smaller if compared to other sources of PDF uncertainties [59].

Chapter 2

The LHC and the ATLAS detector

A Toroidal LHC ApparatuS, known as ATLAS, is one of the four main experiments at the Large Hadron Collider (LHC) installed within CERN laboratories. In this chapter a brief introduction to the LHC collider and its physics program is given, together with a description of the ATLAS detector.

2.1 The LHC collider

The *Large Hadron Collider* LHC [60] is the largest and highest-energy particle accelerator in the world. It has been built at CERN laboratories, in the circular tunnel where was the Large Electron Positron Collider (LEP). It is a 27 km long tunnel at a depth varying between 50 and 175 meters below the ground. The LHC had been designed to provide both proton-proton (pp) and heavy ion (HI) collisions. For pp collisions, the design instantaneous luminosity is $10^{34}\ cm^{-2}\ s^{-1}$ and the foreseen centre-of-mass energy for the collision is 14 TeV. During the 2010 and 2011 runs, collisions at 7 TeV centre-of-mass energy have been provided, instead 8 TeV for 2012 collisions. The instantaneous luminosity is defined as:

$$L = f \cdot \frac{n_1 \cdot n_2}{4 \cdot \pi \cdot \sigma^2} \cdot F \tag{2.1}$$

where σ is the transverse width of the beam (17 μm at the LHC at nominal conditions), assuming a gaussian particle distribution in the beam, f is the collision frequency defined as the reciprocal of the time delay between two collisions ($\frac{1}{25}\ ns = 40\ MHz$), n_1 and n_2 are the numbers of particles in the two colliding beams respectively.

The LHC is mainly composed by superconducting magnets, that operate at a temperature of 1.9 K, which is provided by a cryogenic system based on liquid helium. The LHC is equipped with a 400 MHz superconducting cavity system and it is composed with different types of magnets, that are dipole magnets (for a total of 1232 magnets) are used to keep the beams on their circular trajectory, while quadrupole magnets (for a total of 392) are necessary to keep the beams focused, in order to maximize the chances of interaction in the four different interaction points, where the two beams cross. Close to these four points, the LHC has straight sections, in which the two beam pipes, in which particles circulate, become one and the particles are then made to collide. Within this space, triplet magnets are used to squeeze the beam transversely, to focus it at the interaction point. These squeeze leads the beam to be significantly larger than it needs at the interaction point, reducing intra-beam interactions.
At the collision points, four big experiments have been built: ATLAS [20] at point 1, CMS [61] at point 5, LHCb [62] at point 8 and ALICE [63] at point 2. The first two are multi-purpose experiments, designed to study high transverse momentum events for the measurements of the Higgs physics and other phenomena beyond the Standard Model. LHCb has instead been designed especially to study b-physics, while ALICE was built to analyse mainly heavy ion collisions, to study the formation of a quark-gluon plasma. A schematic view of the LHC, the two beams and the four interaction regions is shown in Figure 2.1.

Along the ring there are sections dedicated to beam cleaning. They are located at points 3 and 7 and they include collimators that maintain the stability of the beam. They are designed to scatter particles with deviant momenta and large betatron[1] amplitudes. Furthermore, in point 6 a system is set up in order to dump the beams in case of problems or at the end of its lifetime during normal operation.
Colliding particles in the LHC are bunched together into bunches, made of $\sim 10^{11}$ protons. The design number of bunches is 2808, so that interactions happen every 25 ns.
Before being injected into the LHC, the particles are pre-accelerated step by step up to the injection energy of 450 GeV, by a series of accelerators. For protons the accelerating procedure starts with the linear accelerator LINAC2, which generates them at an energy of 50 MeV. The protons then go through the Proton Synchrotron Booster (PSB) and are accelerated to 1.4 GeV. After that they are injected into the Proton Synchrotron (PS), where they are accelerated up to 26 GeV. Finally, the Super Proton Synchrotron (SPS) is used to further increase their energy to 450 GeV, which corresponds to the adequate energy to be injected into the LHC ring. The complete accelerating system with every component is shown in Figure 2.2. The LHC started its operations on 10

[1] Betatron oscillations are transverse oscillations of particles in a circular accelerator about the equilibrium orbit.

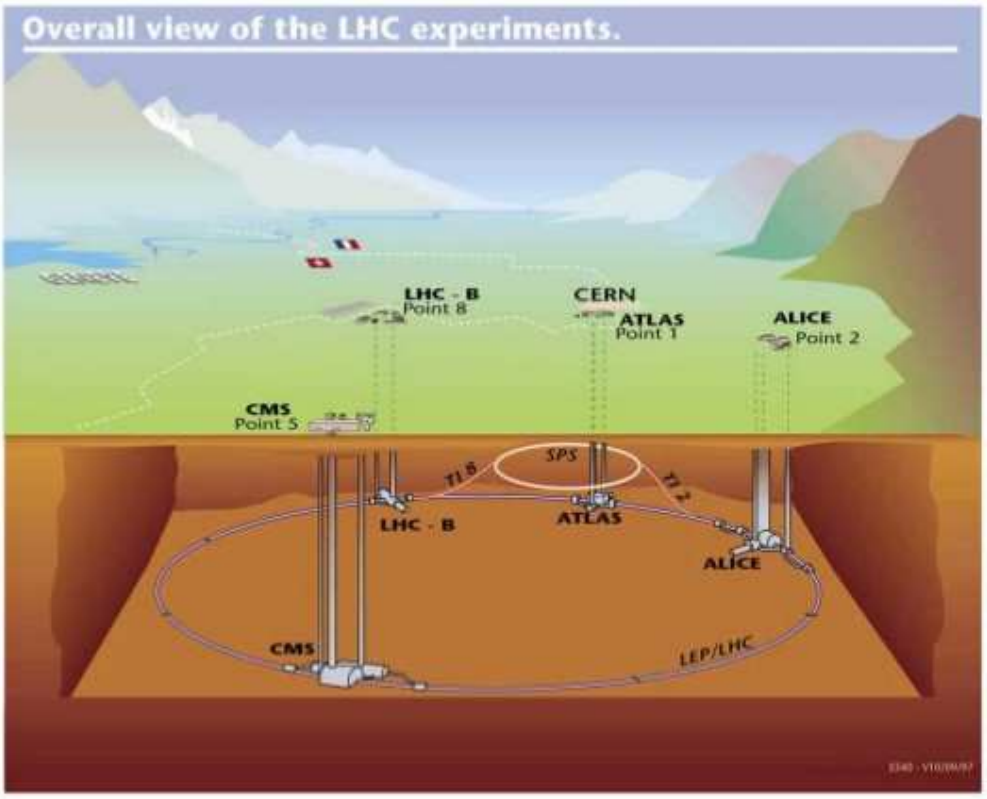

FIGURE 2.1: A schematic view of the LHC, its two beams and the four interaction regions.

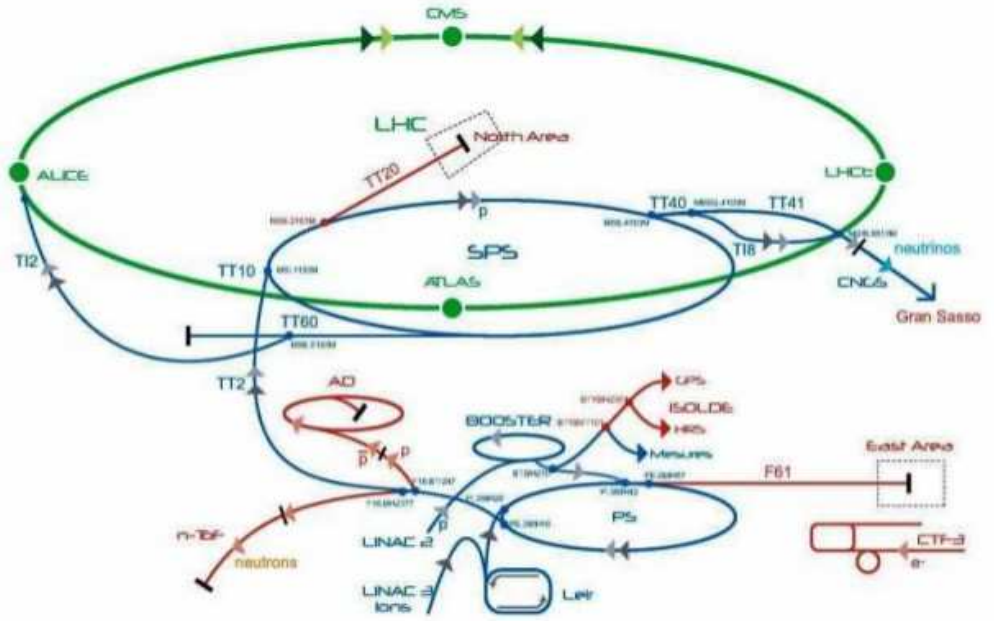

FIGURE 2.2: A schematic view of the acceleration chain at CERN.

September 2008, with the first beams circulating into the rings, in both directions, without collisions. After a commissioning phase, first collisions were expected few days later. Unfortunately, on 19 September of the same year a major accident happened, due to a defective electrical connection between two magnets. In the accident 53 magnets were damaged. This caused a long stop of the machine, to repair the damaged magnets, to check the electrical connections and to improve the safety systems. During Autumn 2009, after more than one year stop, the operations started again, with the first collisions at a centre-of-mass energy of 900 GeV recorded by the four experiments on 23 November 2009. After a 900 GeV collisions data taking, the centre-of-mass energy was further increased to 2.36 TeV, beating the Tevatron's previous record of 0.98 TeV per beam and giving therefore collisions at the highest energy ever reached before. After some months, the first collisions at $\sqrt{s} = 7\,\text{TeV}$ were registered, on 30 March 2010, starting a new running period that went on until the beginning of November, when the LHC provided the first heavy ion collisions. After the lead ions collisions period and a technical stop during the winter, *pp* collisions have started again on 13 March 2011 up to december of the same year (in which in november with HI mode). The latest data collection occurs in 2012, from February to December increasing the center-of-mass energy up to 8 TeV with instantaneous luminosity of $L = 0.7 \times 10^{34}\ cm^{34}s^{-1}$ that integrated corresponds to an amount between 20 fb^{-1} and 21 fb^{-1}.
The very high luminosity of the LHC is needed to pursue most of the studies of interest. This high luminosity regime introduces however some difficulties as well. One of them is characterized by the presence of pile-up, that is the superposition of high cross section inelastic events over the candidates for new physics. At the design luminosity 23 pile-up events per bunch crossing are expected. Another difficulty due to the nature of *pp* collisions is that the QCD processes will dominate over the physics processes of interest, so that imposes strong demands on the capability of the detectors to identify experimental signatures characteristic of the interesting processes.
For the these reasons there are some requirements fot the LHC machine, that can be summarized as follow:

- Fast response, high granularity and resistance to radiations

  The rates of events require a fast and sophisticated electronics, able to discriminate events and minimize the effect of pile-up. A high granularity of the detector is necessary to handle the high particle fluxes as well, moreover it must be resistant to high doses.

- Trigger

  The output bandwidth of the detector is limited and therefore the 40 MHz interaction rate must be reduced to few hundred Hz to perform the tape recording.

The capability of triggering efficiently on interesting events with a very high background rejection is therefore crucial.

- Full coverage

  In order to identify interesting events over the dominant QCD background, it is important to detect all particles produced in the collision. That requires a coverage over 2π in the azimuthal angle and pseudorapidity $|\eta| < 5$.

- Particle identification

  The capability to precisely reconstruct and identify electrons, muons, photons, tau leptons and jets is an essential requirement for the LHC experiments.

2.2 The ATLAS detector

The ATLAS detector is placed at Point 1, along LHC ring, in a cavern at a depth of 100 m. With its height of 25 m and its length of 44 m it represents one of the biggest detectors ever built. It weights about 7000 *tons* and it has a cylindric symmetry. The construction started in 2003 until July 2007, with the insertion of the innermost detector and the lowering of the last end-cap toroidal magnet. Since 2009 it has been recording cosmic-ray events and, since November 2009, proton-proton collision events at rates of up to 400 Hz [20]. A schematic view of the ATLAS detector is provided in Figure 2.3.
A brief summary of the coordinate system and nomenclature is given. The origin of the

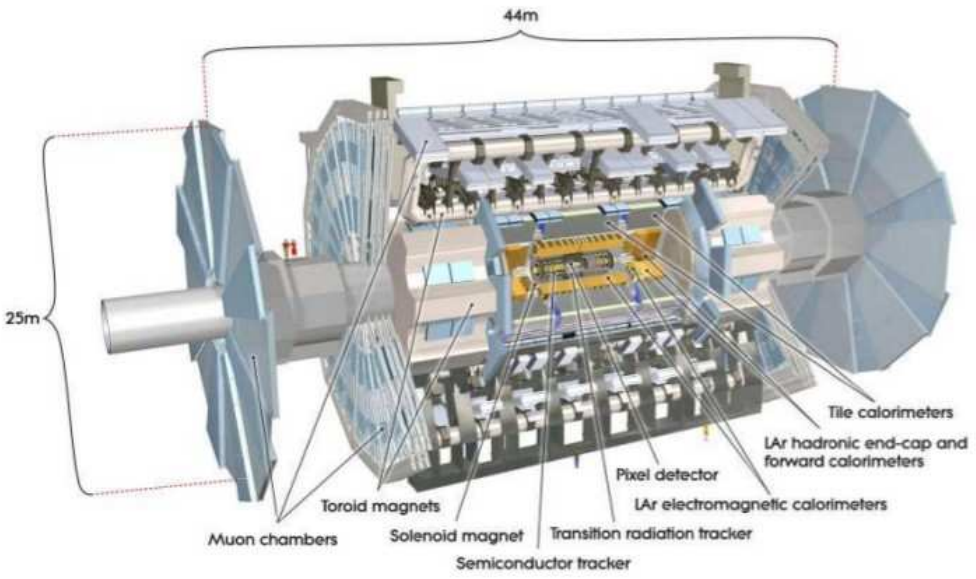

FIGURE 2.3: A schematic view of the ATLAS detector

coordinate system coincides with the nominal interaction point. The z-axis is parallel

to the beam and the x and y axes are othogonal to the beam forming a right-handed cartesian coordinate system where x points towards the centre of the LHC ring and y points upward. The x-y plane is called the transverse plane.
The azimuthal angle ϕ is measured around the z-axis, while the polar angle θ is measured from the z-axis.
Since pseudorapidity spectra are invariant under Lorentz boosts along z-axis, the pseudorapidity, defined as $\eta = -\ln\tan\frac{\theta}{2}$, is often preferable as a polar coordinate.
The distance ΔR in η-ϕ space is defined as $\Delta R^2 = \Delta\eta^2 + \Delta\phi^2$. Particles are often described by their transverse momentum p_T and transverse energy (projections in the transverse plane), as these variables could indicate interesting physics, if compared to the standard energy and momentum, because they are fixed to 0 in the initial state.
The ATLAS detector is composed of different subdetectors, as shown in Figure 2.3. Each of them plays an important role in the reconstruction of particles. The sub-detectors are organized in layers leading out from the interaction point.
Closest to the beam pipe there is the *Inner Detector*, used to reconstruct the trajectory of the charged particles. It is divided into *Pixel*, *SemiConductor Tracker* (SCT) and *Transition Radiation Tracker* (TRT) detectors. It covers $\eta < 2.5$. The whole system is enclosed by a solenoid magnet, which provides a magnetic field of 2 T that inflects the charged particles allowing a measurement of their momentum and charge. The lenghts of the inner and outer diameters of solenoid are 2.46 m and 2.56 m and its axial length is 5.8 m. The flux is returned by the steel of the ATLAS *Hadronic Calorimeter* (Had Calorimeter) and its girder structure. As result there is a negligible field within the *Electromagnetic Calorimeter* (EM Calorimeter) volume and a small field in the Had Calorimeter volume. To achieve the desired calorimeter performance, the solenoid layout has been carefully optimised to keep the material thickness in front of the calorimeter as low as possible: the solenoid assembly contributes a total of ~ 0.66 radiation lengths (X_0) at normal incidence.
The EM Calorimeter encloses the tracking chamber and is constructed in order to precisely measure the energy of electrons and photons. Outside the EM Calorimeter there is the Had Calorimeter, which measures the energy of hadronic particles. The calorimeter system is hermetic out to $|\eta| < 4.9$ and it is $\sim$ 9-13 radiation lengths thick, sufficient to detect the 99% of hadronic showers from single charged pions up to $\sim 500\,\text{GeV}$.
Finally, the calorimeters are enclosed by the Muon Spectrometer, designed to reconstruct and identify muons. It is located within in a magnetic field and it covers $|\eta| < 2.7$ with tracking chambers that provide precise measurements of momentum and charge. The system that generates the magnetic field for the Muon Spectrometer is composed of three large air-core toroids: one *barrel* component and two *end-caps*. The field is centred on the beam axis, perpendicular to the solenoidal field that serves the Inner Detector. The performance of the toroids in terms of bending power is characterized by

Subdetector	Radius[cm]	Element size	Spatial resolution[μm]	Hits/track	Readout channels
Pixel	$5-12$	$50\ \mu m \times 400\ \mu m$	$10\ (R-\phi) \times 115\ (z)$	3	80×106
SCT	$30-52$	$80\ \mu m$	$17\ (R-\phi) \times 580\ (z)$	8	6×106
TRT	$56-107$	$4\ mm$	130	30	3.5×105

TABLE 2.1: Summary of the main characteristics of the three ATLAS Inner Detector subdetectors [20]

the field integral $\int Bdl$, where B is the field component normal to the muon direction and the integral is computed along an infinite momentum muon trajectory, between the innerside and outerside muon-chamber planes. The barrel toroid provides 1.5 up to 5.5 Tm of bending power in the pseudorapidity range $0 < |\eta| < 1.4$, and the end-cap toroids approximately 1 up to 7.5 Tm in the region $1.6 < |\eta| < 2.7$. The bending power is lower in the transition regions where the two magnets overlap ($1.4 < |\eta| < 1.6$).
Finally, ATLAS includes a three-level trigger system for evaluating and recording only the most interesting events during a run. The trigger is configurable at every level to provide a constant stream of data under any beam conditions.
In the following the various systems composing the detector will be described in detail.

2.2.1 The Inner Detector

The Inner Detector is the innermost system of the ATLAS detector. Its schematic view is shown in Figure 2.4. It is composed by three subdetectors: two silicon detectors, the Pixel Detector and the SCT, and the TRT. It is immersed in an axial magnetic field of 2 T and its overall dimensions are 2.1 m in diameter and 6.2 m in length. The Inner Detector measures tracks from the passage of the charged particles. So it measures charged particles position and, being immersed in a magnetic field, also their p_T and charge [20]. A detailed description of the sub-detectors is given below and a summary of their main characteristics is also reported in Table 2.1.

- The Pixel Detector

  The Pixel Detector is the nearest system to the collision point and it is built directly onto the beryllium beam pipe in order to provide the best possible primary and secondary vertex resolution. It is composed by three cylindrical layers in the barrel region and two end-caps, each consisting of three disks (located at 495 mm, 580 mm and 650 mm from the detector centre). The Pixel Detector provides three precision measurement points for tracks with pseudorapidity $|\eta| < 2.5$ and it has a full coverage in ϕ. The detector structure is made of low-mass carbon fiber and integrates the cooling system, resulting in a total contribution to X_0 of about 3% per layer. Furthermore, all the detector components are designed to sustain a

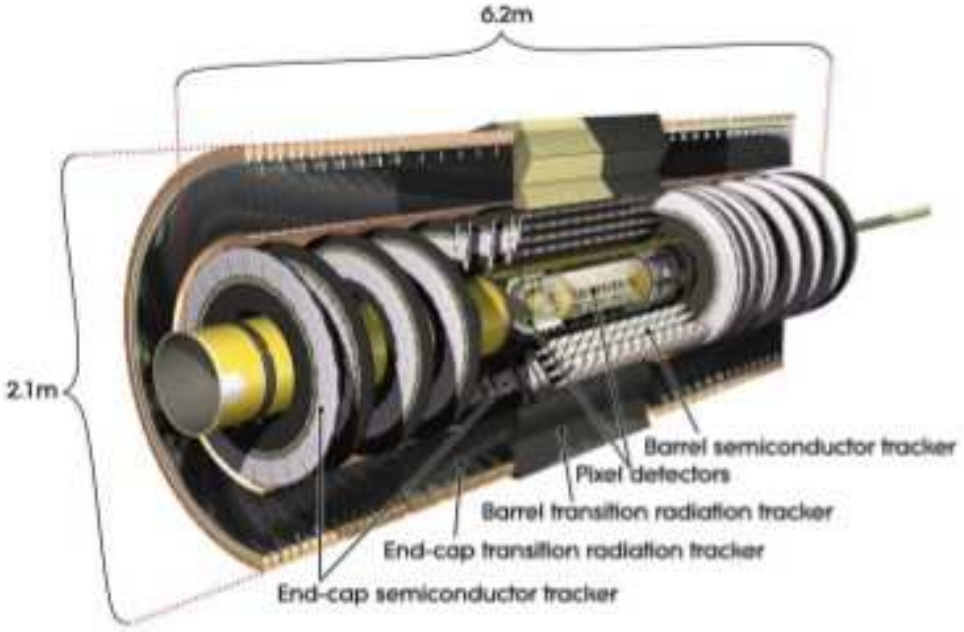

(a)

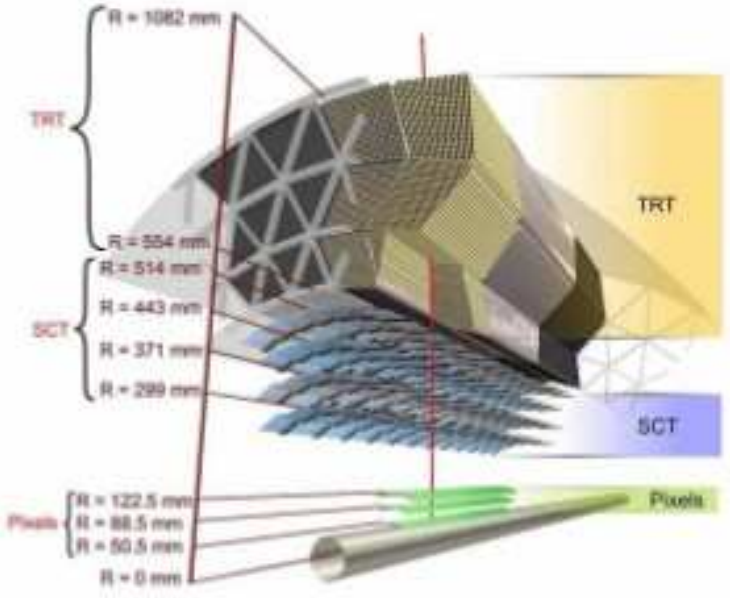

(b)

FIGURE 2.4: Schematic views of the ATLAS Inner Detector

radiation dose of $\sim 500\ kGy$, which is the dose expected during detector life time. The basic elements of the Pixel Detector are the silicon sensor *modules*, that are identical for barrel and disks. The 250 μm thick sensors are divided into pixels 50 μm wide and 400 μm long, with 47232 pixels on each of the 1744 modules. The total number of channels for the whole detector is $\sim$ 80.4 millions for the whole detector.

The design requirement was to achieve a resolution of 10 μm in the azimuthal direction and 115 μm along the beam direction. At present around 20 μm has been obtained in the azimuthal direction and 130 μm along the beam direction.

- The SCT Detector

  The SCT is the second element of the tracking system, going from the beam pipe outwards. It is composed by four cylinders in the barrel region, with full length of 1492 mm. Each of the two end-caps consists of 9 disks. It provides typically eight strip measurements (four space-points) for particles originating in the beam-interaction region. The detector consists of 4088 modules. The strips in the barrel have a constant pitch of 80 μm, while in the end-caps the strip direction is radial and of variable pitch. The intrinsic accuracies of the SCT are 17 μm in the azimuthal direction and 580 μm along the beam direction.

- The TRT Detector

  The TRT is the outermost system of the Inner Detector and its sensitive volume covers radial distances from 563 mm to 1066 mm. The detector is composed by 298304 proportional drift tubes (straws), 4 mm in diameter, read out by $\sim$ 351000 electronic channels. The straws in the barrel region are arranged in three cylindrical layers and 32 ϕ sectors; they have splitted anodes and they are read out from each side. The straws in the end-cap regions are radially oriented and arranged in 80 wheel-like modular structures. The TRT straw layout is made so that charged particles with transverse momentum $p_T > 0.5\,\mathrm{GeV}$ and with pseudorapidity $|\eta| < 2.0$ cross typically more than 30 straws.

  The spatial resolution of the TRT is 130 μm in all directions.

  The TRT can also be used for particle identification. Its tubes are combined with layers of polypropylene fibres and foils: a charged particle that passes through the boundary region between materials with a different refraction index emits X-ray radiation whose intensity is proportional to the relativistic factor. The TRT works with two threshold levels (defined at the level of the discriminator in the radiation-hard front-end electronics): the ratio of the high threshold hits versus all the hits can be used to identify electrons.

- The cooling system

For the Pixel Detector and the SCT, a cooling is necessary to reduce the effect of radiation damage to the silicon. They share a cooling system, using C_3F_8 fluid as a coolant. The target temperature for the silicon sensors after irradiation is 0 °C for the Pixel Detector and −7 °C for the SCT. Since the TRT operates at room temperature, a set of insulators and heaters isolate the silicon detectors from the environment of ATLAS.

2.2.2 The Calorimeters

The calorimeter system includes both the EM Calorimeter and the Had Calorimeter. The first is dedicated to the measurement of electrons and photons, while the latter to the measurement of hadrons. These calorimeters cover the range $|\eta| < 4.9$, using different techniques suited to the widely varying requirements of the physics processes of interest and of the radiation environment over this large η-range.
A schematic view of the calorimeter system is shown in Figure 2.5 [20]. The main pur-

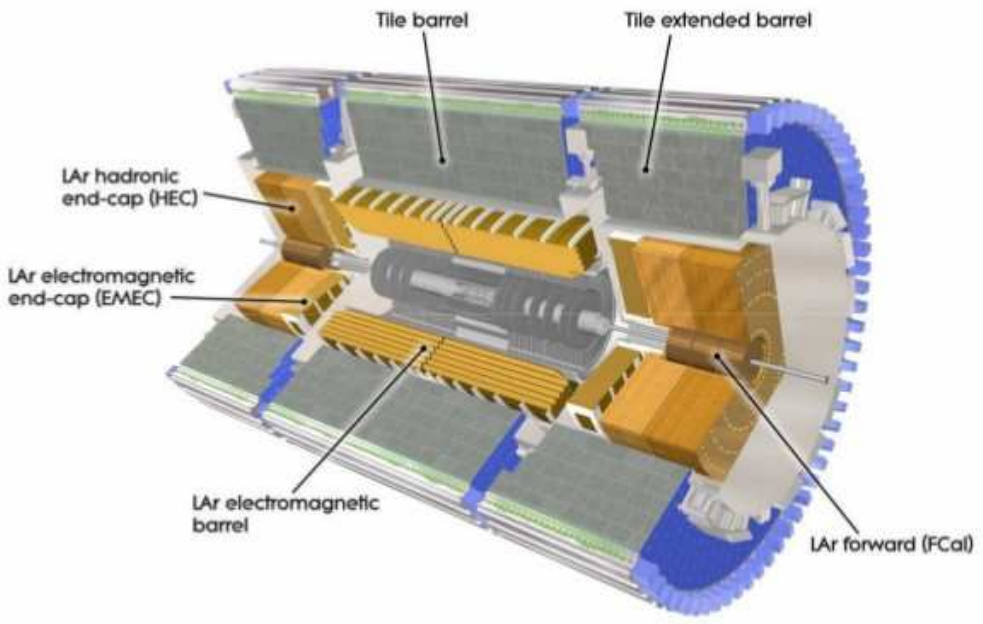

FIGURE 2.5: Schematic view of the ATLAS Calorimetric system

pose of the calorimeters is to measure the released energy of the particles and their position. One of the most important requirements for calorimeters is to provide good containment for electromagnetic and hadronic showers: the number of jets reaching the muon system (*punch-through*) has to be limited in order to have a good muon identification. Therefore, calorimeter depth is an important consideration. The total thickness of the EM calorimeter is more than 22 radiation lengths (X_0) in the barrel and more

Detector component	Required resolution (σ_E/E)	η coverage
EM calorimetry	$10\% \sqrt{E} \oplus 0.7\%$	$\|\eta\| < 3.2$ (< 2.5 for the trigger
Had calorimetry		
barrel and end-cap	$50\% \sqrt{E} \oplus 3\%$	$\|\eta\| < 3.2$
forward	$100\% \sqrt{E} \oplus 3.1\%$	$3.1 < \|\eta\| < 4.9$

TABLE 2.2: Nominal detector performance goals and coverage for the ATLAS detector [20].

than 24 X_0 in the end-caps. It contains electrons and photons showers up to $\sim 1\,\text{TeV}$ and it also absorbs almost $\frac{2}{3}$ of a typical hadronic shower. The approximate 9.7 (10) interaction lengths (λ) of active calorimeter (EM + Had) in the barrel (end-caps) are enough to provide good resolution for high-energy jets. The total thickness, including 1.3 λ from the outer support, is 11 λ at $\eta = 0$ and has been shown both by measurements and simulations to be sufficient to reduce punch-through well below the irreducible level of prompt or decay muons.

The ATLAS calorimetry is non-compensating, meaning that on average a hadron will deposit a smaller fraction of its energy in the active portion of the calorimeter with respect to an electron or photon. The difference must be taken into account by an additional correction applied to hadronic objects. There are several ways to select hadronic objects and correct their energy.

The performance of the calorimeter system is summarized in Table 2.2 [20]. Following some details on the different calorimeter regions are given.

- The EM Calorimeter

  The EM calorimeter is a lead liquid Argon (LAr) detector [64]. To ensure the maximum azimuthal coverage the EM Calorimeter was designed with an accordion geometry, as shown in Figure 2.6. The readout electrodes and the lead absorbers are laid out radially and folded so that particles can not cross the calorimeter without being detected. It is divided into one barrel part ($|\eta| < 1.475$) and two end-caps ($1.375 < |\eta| < 3.2$), each one with its own cryostat. The position of the central solenoid in front of the EM calorimeter demands optimisation of the material in order to achieve the desired calorimeter performance. As a consequence, the central solenoid and the LAr calorimeter share a common vacuum vessel, thereby eliminating two vacuum walls. The barrel calorimeter is composed of two identical half-barrels, separated by a small gap ($4\ mm$) at $z = 0$. Each endcap calorimeter is divided into two coaxial wheels: an inner wheel covering the region $1.375 < |\eta| < 2.5$, and an outer wheel covering the region $2.5 < |\eta| < 3.2$.

  Over the region optimized to precision physics ($|\eta| < 2.5$), the EM calorimeter

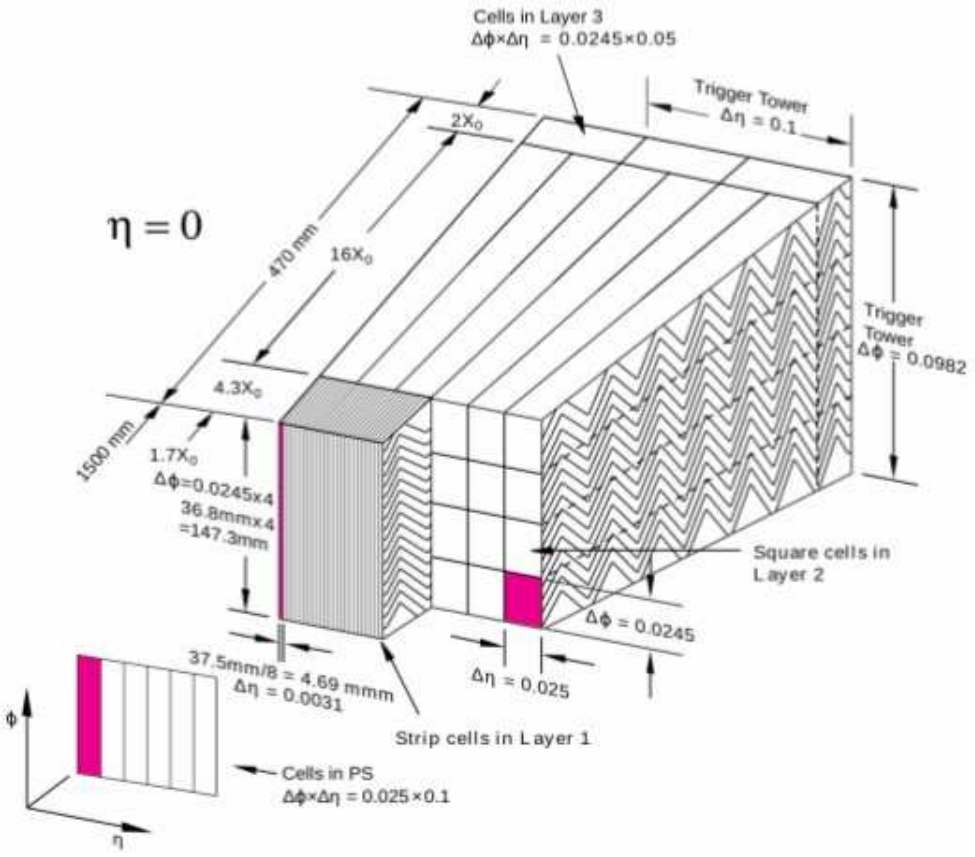

FIGURE 2.6: Schematic view of the accordion geometry

is segmented into three longitudinal sections: strips, middle and back. While most of the energy of electrons and photons is collected in the middle, the fine granularity of the strips is need to improve the γ - π^0 discrimination and the back measures the tails of highly energetic electromagnetic showers, and helps to distinguish electromagnetic and hadronic deposits. For the end-cap inner wheel, the calorimeter is segmented in two longitudinal sections and has a coarser lateral granularity than for the rest of the acceptance.

EM showers begin to develop well before they are measured in the calorimeter, because most of the central calorimetry sits behind the cryostat, the solenoid, and the $1-4$ radiation-lengths thick Inner Detector. In order to measure and correct for these losses, up to $|\eta| = 1.8$ there is an additional presampler layer in front of the sampling portion (*i.e.* accordion) of the calorimetry. The presampler is 11 mm (5 mm) thick in the barrel (end-cap) and includes fine segmentation in $\eta-$range. Unlike the rest of the calorimetry, the presampler has no absorber layer. It behaves almost like a single-layer LAr tracker. The transition region, that is region between the barrel and the end-cap EM calorimeters, with $1.37 < |\eta| < 1.52$, is expected to

have lower performance because of the large amount of passive material in front of the calorimeter, this region is often referred as *crack region*.

- The Hadronic Calorimeter

  The Hadronic Calorimeter is divided into three regions: central, end-cap and forward. In the central region there is the *Tile* Calorimeter (Tile) [65], which is placed directly outside the EM Calorimeter envelope. The Tile is a sampling calorimeter which uses steel as absorber and scintillating tiles as active material. It is divided into a barrel ($|\eta| < 1.0$) and two extended barrels ($0.8 < |\eta| < 1.7$). Radially, the Tile goes from a radius of 2.28 m up to 4.25 m. It is longitudinally segmented in three layers approximately 1.5, 4.1 and 1.8 interaction lengths thick for the barrel, and 1.5, 2.6, and 3.3 interaction length for the extended barrel. The Hadronic End-cap Calorimeter is composed of two independent wheels per end-cap, located behind the end-cap EM calorimeter and sharing the same LAr cryostats. It covers the region $1.5 < |\eta| < 3.1$, overlapping both with the Tiles and the Forward Calorimeter. It uses the LAr technology. Each wheel is divided into two longitudinal segments, it has four layers per end-cap. The wheels closest to the interaction point are built from 25 mm parallel copper plates, while those further away use 50 mm copper plates. The outer radius of the copper plates is 2.03 m, while the inner radius is 0.475 m (except in the overlap region with the forward calorimeter where this radius becomes 0.372 m). The copper plates are interleaved with 8.5 mm LAr gaps.
  The ATLAS hadronic calorimeter system has been designed with a thickness of about 10 interaction lengths. The large coverage in pseudo-rapidity allows good E_T^{miss} measurements. The Tile hadronic calorimeter performance on the measurements of the jet energy has been evaluated to be $\frac{\Delta E}{E} = \left(\frac{65}{\sqrt{E}} \oplus 2 \oplus \frac{5}{E}\right)\%$.

- The Forward Calorimeter

  The Forward Calorimeter (FCal) covers the $3.1 < |\eta| < 4.9$ region and is another LAr based detector. It is integrated into the end-cap cryostats, it is approximately 10 interaction lengths deep and consists of three 45 cm thick independent modules in each end-cap: the absorber of the first module is copper, which is optimised for electromagnetic measurements, while for other two is tungsten, which is used to measure predominantly the energy of hadronic interactions. The region where the FCal is set is very close to the beam pipe, so the expected radiation dose is very high. Therefore the electrode structure is different from the accordion geometry, consisting in a structure of concentric rods and tubes parallel to the beam axis. The LAr in the gap between the rod and the tube is the sensitive medium.
  The LAr electronic calibration is done using pulse height samples, while the tiles

signal is monitored in different ways. Cesium sources, which can scan within the detector, have been installed to check its response, e.g. the ratio of the reconstructed signal to the "true" signal. Charge can be injected into a single cell to test and calibrate the read-out electronics with lasers providing light to test the optical connections and photomultiplier tubes response.

2.2.3 The Muon Spectrometer

Because the muon particles that have high transverse momentum p_T are indicatives of the signature for many events category of physical interest the Muon Spectrometer plays an important role in ATLAS detector. The layout of MS is shown in Figure 2.7 [20]. It

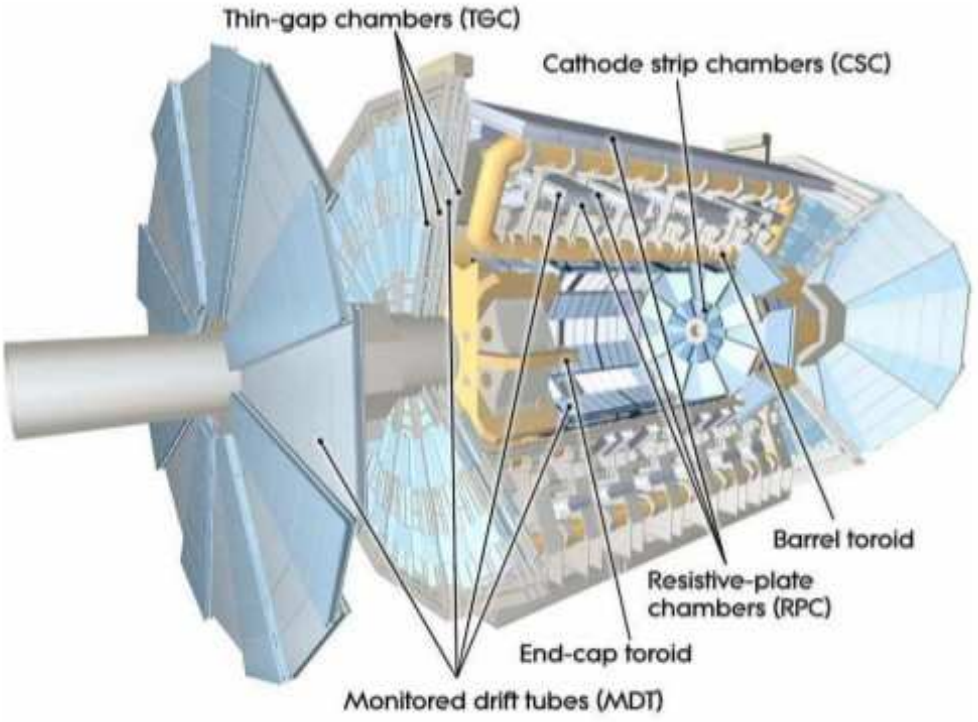

FIGURE 2.7: Schematic view of the Muon Spectrometer

represents the outermost ATLAS sub-detector measuring muons momentum in a pseudo-rapidity region of $1 \leq |\eta| \leq 2.7$. The different sub-detectors of which it is composed can be see in Figure 2.8: two trigger chambers, the Resistive Plate Chambers (RPC) and the Thin Gap Chambers (TGC), and two high-precision tracking chambers, the Monitor Drift Tubes (MDT) and the Cathode Strip Chambers (CSC). The momentum measurement is based on the magnetic deflection of muon tracks. Large volume magnetic field, which is necessary to bend the particle trajectories, is provided by the large barrel toroid

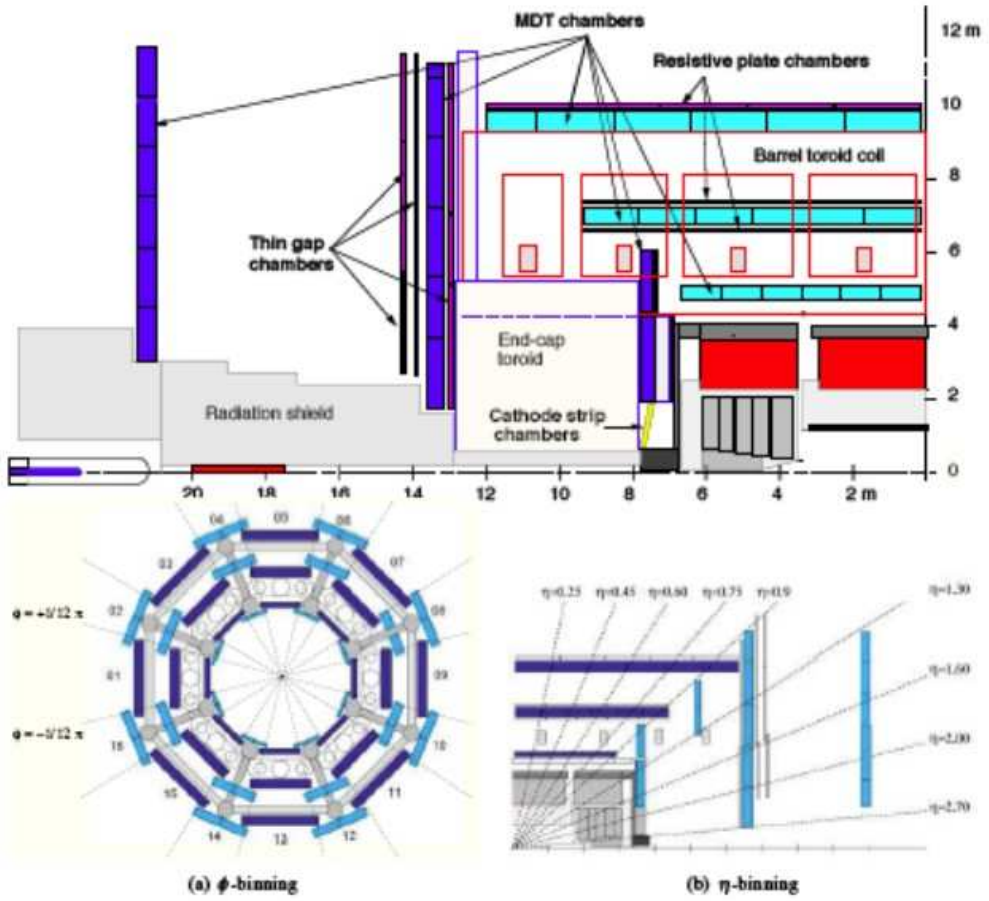

FIGURE 2.8: Muon Spectrometer layout (top) and his binning in η (down-left) and ϕ (down-right) projections.

in the region $|\eta| < 1.4$, by two smaller end-cap magnets in the $1.6 < |\eta| < 2.7$ region and by a combination of the two in the transition region ($1.4 < |\eta| < 1.6$). This magnet configuration provides a field which is mostly orthogonal to the muon trajectories minimising the degradation of the resolution due to multiple scattering.

ATLAS is able to acquire two independent measurements of a muons momentum, because the toroidal magnet system of the Muon Spectrometer is completely independent of the solenoid in the Inner Detector.

The measurement is performed over most of the η-range by the Monitored Drift Tubes (MDT). At large pseudorapidities and close to the interaction point, Cathode Strip Chambers (CSC) with higher granularity are used: they have been realized to withstand the demanding rate and background conditions. A sophisticated optical alignment system, that can be seen in Figure 2.9, have been designed to meet the stringent requirements on the mechanical accuracy and the survey of the muon chambers.

The MS performance on the transverse momentum measurement has been evaluated using muons of both $p_T = 10\,\text{GeV}$ and $p_T = 100\,\text{GeV}$ founding a resolution value of 3%

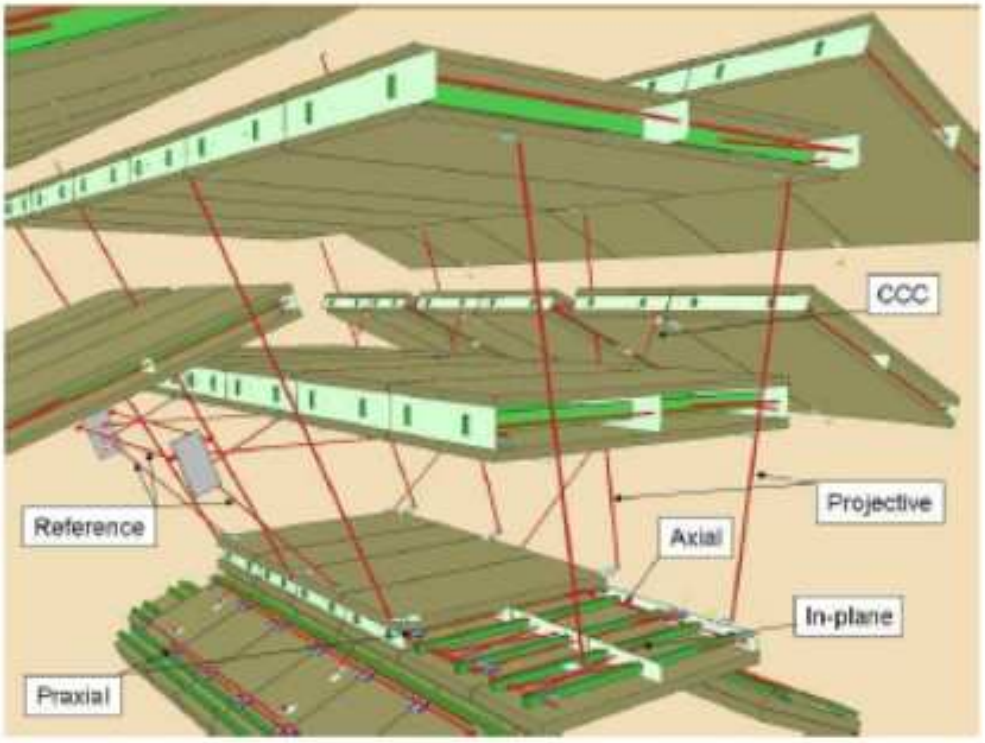

FIGURE 2.9: 3D representation of the Muon Spectrometer and his optical-alignment system.

and 12% respectively.

About the triggering system, it covers the pseudo-rapidity range $|\eta| < 2.4$. Resistive Plate Chambers (RPC) are used in the barrel and Thin Gap Chambers (TGC) in the end-cap regions. The trigger chambers for the Muon Spectrometer serve a three-fold purpose: to provide the bunch-crossing identification, to provide a well-defined transverse momentum thresholds and to measure the muon coordinate in the direction orthogonal to that determined by the precision-tracking chambers.

The RPC is a gaseous parallel electrode-plate detector arranged in strip elements that combines an adequate spatial resolution of 1 cm with an excellent time resolution of 1 ns. The number of strips (average strip pitch is 3 cm) per chamber is variable: 32, 24 or 16 in η and from 64 to 160 in ϕ. When a particle goes through an RPC chamber, the primary ionization electrons are multiplied into avalanches by a high electric field of typically 4.9 kV/mm. The signal is read out via a capacitive coupling of strips on both sides of the chamber.

The TGC are very thin multi-wire proportional chambers which characteristic is to have cathode-anode spacing smaller than the anode-anode (wire-wire) spacing. This feature justify the denomination *Thin Gap* and allows a very short drift time and an excellent response in time, less than 20 ns; this satisfy the requirement for the identification of bunch crossings at 40 MHz. The TGC are filled with a highly quenching gas mixture

of 55% of CO_2 and 45% of n-pentane (C_5H_{12}).
The MDT system is composed by drift chambers consisting of two multi–layer drift tubes (each multi-layer has three or four layer of tubes, depending on the position that the MDT chamber occupies in MS). The difference between MDT and traditional drift chambers is that each drift cell is enclosed in an aluminum tube, which provide mechanical stability to the chambers. A single MDT tube resolution is of 80 μm, while the all MDT system reach a resolution of 35 μm along the ϕ direction.
Finally the CSC chambers are proportional multi-wire chamber with segmented read out cathode. The drift cells are symmetric, *i.e.* the distance between the anode wires and the cathode is equal to the intra wire distance (2.54 mm). The cathodes are segmented in 1 mm strips, orthogonal to the anode wires, allowing to the measure the crossing point of incoming muon with resolution of 40 μm in the ϕ direction. In the η direction the cathode segmentation is coarser leading to a resolution of 5 mm.

2.2.4 Forward detectors

The luminosity measurement is one of the most important of ATLAS measurements for almost every physics analysis [66]. As it is a fundamental quantity, three different detectors help in its determination. Within a spatial distance of $\pm$ 17 m from the interaction region there is the LUminosity measurement using Cerenkov Integrating Detector (LUCID) [67]. It detects inelastic pp scattering in the forward direction and it is the main online relative-luminosity monitor for ATLAS. It is also used to check the beam losses before collisions are delivered by the LHC. For the beam monitoring, also another detector has been inserted: the Beam Condition Monitor (BCM).
The other detector used for luminosity measurement is called Absolute Luminosity For ATLAS (ALFA) [68]. It consists of scintillating fibre trackers located inside Roman pots which are designed to approach as close as 1 mm from the beam.
The last detector is Zero-Degree Calorimeter (ZDC) [68]. It is located beyond the point where the common straight-section vacuum-pipe divides back into two independent beam-pipes. The ZDC modules consist of layers of alternating quartz rods and tungsten plates which measure neutral particles at pseudorapidities $|\eta| \geq 8.2$.

2.2.5 Trigger

In 2011 collisions, protons collide in ATLAS every 50 ns. This correspond to LHC luminosities $> 10\%$ of the design value. An amount of 100 million channels in the ATLAS detector must be read out by the data acquisition software during the LHC operation, resulting in ~ 1.5 MB events. Without any filtering, ATLAS would need to process and

record $\sim 60\ TB$ of event data every second, currently an impossible task. This is not a dramatic limitation, since interesting physics occurs mostly at rates of 10, 1 or $< 0.1\ Hz$ and so we are actually interested in a tiny fraction of the total events produced. This is however a challenging task. Because only a small fraction of the events can be recorded, these events must be quickly searched for interesting signatures. A rapid decision must be made for each event. But rejected events are lost forever.

The ATLAS trigger system [69] is designed to record events at a rate of about 200 Hz, with a reduction of more than 5 orders of magnitude with respect to the collision rate. A three-level trigger system to handle the high-rate environment was implemented in ATLAS. At each level, physics objects are reconstructed with improved granularity and precision and over a larger fraction of the detector in order to have complete event reconstruction in the final trigger stage. The first level (Level1 or L1) trigger is a pure-hardware trigger that is designed to make a decision on each event in lower than 2.5 μs and provide output at a rate up to 75 kHz. It makes an initial decision based on the timing from an electrostatic beam pick-up (BPTX), the coarse detector information from muon trigger chambers and towers of calorimeter cells, together with the multiplicity information from the Minimum Bias Trigger Scintillators (MBTS) and very forward detectors. The L1 provides regions of interest (RoIs) to the following level. The second level (Level2 or L2) triggers make a decision in an amount lower than 40 ms and provide output at rates up to 3.5 kHz. The L2 triggers run a simplified version of the event reconstruction in the regions of interest defined by the calorimeter and muon systems. Improved selection criteria, such as distinguishing electrons from photons by track matching, and improved calibrations are applied. In the level-three trigger, called the *event filter* (EF), the complete offline event reconstruction makes a decision in under 4 s and provides output at 200-400 Hz. The L2 and EF are both software triggers and they are together referred to as the *high-level trigger* (HLT). One L1 item may seed many HLT triggers, and many L1 items may seed a single HLT trigger. A full sequence of triggers from L1 through the EF is called a *trigger chain*.

A specific configuration of possible trigger items is prepared for each data taking run, that defines a complete list of what trigger items will be evaluated, what values the parameters of those items will take, and how the lower-level trigger items map into higher-level triggers. Some items are run unprescaled, meaning that any time an event is accepted by the trigger it will be passed on to the next level (or written out in the case of the EF). Others, in particular low-p_T triggers, may be run with relatively high prescales, so that only some of the events which pass the trigger are accepted. Any of the HLT triggers can be run in pass-through mode, in which no events are rejected but each event is evaluated. This feature has been particularly useful during the initial trigger commissioning and will be used also for new trigger items. Because of the strict timing demands, if an event cannot be evaluated in the predicted time for each trigger

stage, it is passed and flagged for a later examination.
After the EF, the events are divided into "streams", each containing the output from several different trigger chains. These streams are transferred to the Tier0, where the full offine event reconstruction is run, and the output is saved for sending to computing centers around the world. Streams called the "express stream" and "calibration stream" contain an assortment of events which are deemed interesting or useful for calibration of the subdetectors. They are processed first in order to provide new calibrations to the detectors within 24-hour periods.
All the details about the trigger streams and chains used in my work are described in the next chapter.

Chapter 3

Data samples and Monte Carlo models for Signal and Background

The data collected by ATLAS and the Monte Carlo (MC) samples processed through fast or full detector simulation are processed through the same reconstruction chain. The output of the reconstruction are D3PD files, which format is a particular data structure file, typically used by ATLAS experiment that has the peculiarity to be easier handled with the official ATLAS software analysis framework. The analysis uses a particular type of D3PD called NTUP_COMMON which is the standard top group format. For both data and MC the combined_pdf_dijet_7 b-tagging calibration is used. This chapter aims to describe the data and MC samples used (Sec. 3.1) and (Sec. 3.3), to provide an overview of Monte Carlo programs (Sec. 3.2). Finally a detailed description of the background determination is provided in Sec. 3.4.

3.1 Data samples

The differential cross-sections are measured using a dataset collected by the ATLAS detector during the 2012 LHC pp run at $\sqrt{s} = 8\,\text{TeV}$, which corresponds to an integrated luminosity of $20.3 \pm 0.6\ \text{fb}^{-1}$. The luminosity is measured using techniques similar to those described in Ref. [70] with a calibration of the luminosity scale derived from beam-separation scans. The average number of interactions per bunch crossing in 2012 was 20. Data events are considered only if they are acquired under stable beam conditions and with all sub-detectors operational. The data used belongs to different periods corresponding to different LHC conditions, in fact the NTUP_COMMON file with version p1278, p1517 or p1562 depending on the data period are used. Since the analysis focuses on the ℓ+jets signal, data have been divided in an electron (*Egamma*) and a

muon (*Muons*) streams depending on the selected online triggers, analyzed respectively for the $e + jets$ and $\mu + jets$ channels. The trigger selection used, change depending on the data period to account for the continuous increasing of the instantaneous luminosity that leads to a corresponding increasing of the pile-up events. The data sample is collected using single-lepton triggers:

- electrons $EF\_e24vhi\_medium1$ OR $EF\_e60\_medium1$

  requiring a reconstructed *medium* electron of p_T greater than 24 or 60 GeV. Medium electrons are defined by the following requirements: $|\eta| < 2.47$, a certain ratio between energy deposit in EM and hadronic calorimeter, at least one hit in the detector pixel, and at least 7 hits in the SCT pixels; a minimum impact parameter of 5 mm is also required. The letters vh were added for those triggers seeded by $L1$ items with η-dependent thresholds and a hadronic leakage requirement;

- muons EF_mu24i_tight OR EF_mu36_tight

  asking for an isolated *tight* muon with $p_T > 36\,\text{GeV}$ or with $p_T > 24\,\text{GeV}$ in the muon channel. Tight muon requirements are similar to the medium requirements but more stringent; additional cuts on momentum and η are done depending on the reconstruction used for the muon.

For each lepton type the logical OR of the two triggers is used in order to increase the efficiency of isolated leptons at low transverse momentum. For electrons the two transverse momentum thresholds are 24 GeV and 60 GeV while for muons the thresholds are 24 GeV and 36 GeV.

3.2 Monte Carlo Simulation

Monte Carlo studies were used to optimise the design of the detector for the physics program and to perform feasibility studies for various specific physics processes, testing our comprehension of themselves. In this analysis, MC samples were used to provide detector smearing and acceptance and efficiencies correction factors for the particle level analysis and extrapolations of our results to the full top pair production phase-space from the fiducial volume of the detector. Monte Carlo programs are of fundamental importance because they allow to simulate the physical processes and the interactions of the final state particles with the detector by providing MC samples according to both theoretical predictions and phenomenological models. Typically a simulation consists of event generation and detector simulation. In event generation, the collision is simulated and partons are decayed to hadrons, which defines the *particle-level*. The detector simulation instead simulates the passage of particles through the detector and records the energy depositions. After this, the ATLAS reconstruction software can be applied, which reconstructs the physics objects to be used in the analysis from the detector output in the same manner as for real collisions. We provide a brief description of two simulation steps:

Event generation

This step of Monte Carlo simulations is performed with theoretical calculations of the elementary processes from the pp interaction to produce the final state stable particles. The first generation step is the calculation, at a fixed perturbative order of the QCD scheme, of the hard-process matrix element, followed by the *parton shower*, a QCD cascade generation. In the generation of the hard process, short lived but on-shell particles are usually decayed as part of the process. The Fig. 3.1 shows a simplified diagram of the gluon emission process in a generic process. The

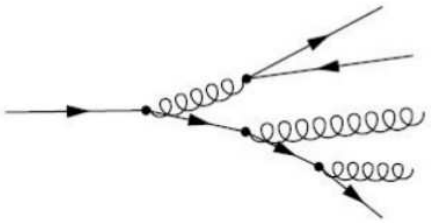

FIGURE 3.1: Example of a parton showering diagram.

parton shower is a space-like process for the initial state partons, where the QCD radiation emission progressively increases the virtuality of the initial state partons allowing them to access the hard scale needed for the hard scattering process, and

a time-like process when applied to the final-state partons. After the scattering, the time-like parton shower allows the high-virtuality partons coming out from the hard scattering to loose progressively their virtuality towards the hadronization phase, which is a non-perturbative process, performed using phenomenological models in order to produce the stable particles in the final state.
Then these final particles are passed through the detector simulator. A representation of the event generation chain is shown in Figure 3.2.

At the LHC, each bunch crossing usually produces multiple proton–proton col-

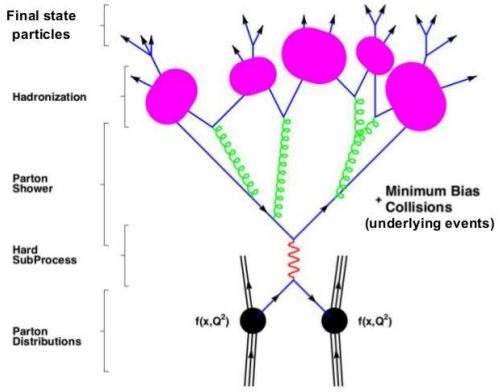

FIGURE 3.2: Pictorial representation of a Monte Carlo event generation chain.

lisions. These are generally *minimum bias* collisions, that is, they do not have a hard, perturbatively calculable collision, but only soft inelastic interactions. Therefore, to the proton–proton collision producing the hard event are also added minimum bias collisions before the event is passed to the detector simulation, referred to as *pileup*.

Detector simulation

After the generation of the final state hadrons, these particles are then passed into the detector simulation. At ATLAS, GEANT4 [71] is used as the standard detector simulator, representing the detector as a series of material volumes. It provides a model for the particle interaction through matter; for this reason a detailed description of the ATLAS detector geometry and of the trigger system is necessary, so it is continually updated as the detector is understood in better detail. GEANT4 takes the event generation output propagating them through the detector volumes, using small steps to simulate the various material interactions, by including multiple Coloumb scattering, the photoelectric effect, Compton scattering, ionisation, bremsstrahlung, conversion, annihilation, hadronic decays, and hadronic interactions. These processes are cut-off at a pre-determined energy scale, at which point the energy is considered to have been deposited in the current

detector volume.

The HITS file record the location and magnitude of the energy deposition in detector volumes, that is then passed to the ATLAS digitisation software, which reads these input files and than converts them into Raw Data Object (RDO): software objects which are the same as those used to store the actual detector output.

These RDOs are then passed through the full reconstruction algorithm chain, so simulating events equivalent to a real detector events. In addition, information from the underlying event generator is stored, so that the *truth*, that is the generator record before particles pass through the detector, may be analysed to derive corrections based on detector smearing and reconstruction efficiencies.

Due to computer elaboration time necessities, some Monte Carlo sample may not be processed using the full detector simulation but with an approximate and faster simulator, named AtlasFastII (AFII) [72].

Fast simulation

As said before a fast simulator can be also used, in addition to the standard GEANT4 simulation, that directly produces the RDO files that can then be passed to the reconstruction software.

For the inner detector usually can be used the FATRAS program, which performs the tracking extrapolation algorithm in reverse order, passing a particle through each element of the inner detector in turn and producing the RDO that would have been read in from the detector.

For the calorimeters, instead, FastCaloSim is used [73]. FastCaloSim uses a calorimeter response parameterisation for each of the individual electrons, photons and hadrons reaching the calorimetry. In order to generate a parameterisation of the longitudinal and lateral shower shape, with separate parameterisations based on the particle's energy and $|\eta|$, an amount of some millions of single particle GEANT4 simulated particles are used. Given the shower shape, the particle's energy is deposited into the calorimeter cells, the output RDOs, in a single step, without simulating the detailed interactions with the calorimeter, but still allows the full reconstruction software to be run on the output. The only advantage of using FastCaloSim is that can be reduced the simulation time by an order of magnitude.

MC events after the detector simulation process are reconstructed and analyzed with the same code used for the collision data.

3.3 MC Simulation sample

Those physical processes leading to a final signature similar to the $t\bar{t}$ one, constitute background sources affecting the $t\bar{t}$ pair production channel, due either to the similarity of the decay products themselves or to the not negligible probability of objects misidentification by the detector. As we will see below these background contributions can be evaluated either using standard Monte Carlo simulation models or via specifics data driven techniques. Data driven techniques are those that evaluates the background contributions directly from the data, taking into account only appropriate control regions. The processes giving a not negligible background contribution to the $t\bar{t}$ signal in the lepton+jets channel, are *single top* production, *multijets* events from QCD processes, $Z + jets$, $W + jets$ and diboson (WW, ZZ and WZ) events.
As well as to predict the background contributions from various processes, a series of simulated samples are used also to characterize the detector response and efficiency to reconstruct $t\bar{t}$ events, and to estimate systematic uncertainties. The response of the detector is simulated using a detailed model implemented in GEANT4 [71]. For the evaluation of a subset of the systematic uncertainties, generated samples are passed through a fast simulation using a parametrisation of the performance of the ATLAS electromagnetic and hadronic calorimeters [74]. Simulated events include the effect of multiple pp collisions from the same and previous bunch-crossings (in-time and out-of-time pileup) and are re-weighted to match the conditions of the data. All simulated samples are normalized to the data sample integrated luminosity based on the most precise theoretical cross-section calculations available.

$t\bar{t}$ sample

The nominal $t\bar{t}$ signal sample is generated using the POWHEG-BOX [75] generator, based on next-to-leading order QCD matrix elements. The CT10 [76] parton distribution functions (PDF) are employed and the top-quark mass (m_{t}) is set to 172.5 GeV. The h_{damp} parameter, which effectively regulates the high-p_{T} radiation in POWHEG, is set to the top-quark mass. Parton shower and hadronisation are simulated with PYTHIA [77] (version 6.427) using the Perugia 2011C tune [78].

The effect of the systematic uncertainties related to the PDF for the signal simulation are evaluated using samples generated with MC@NLO [79] (version 4.01) using the CT10nlo PDF set, interfaced to HERWIG [80] (version 6.520) for parton showering and hadronisation, and JIMMY [81] (version 4.31) for the modelling of multiple parton scattering. For the evaluation of systematic uncertainties due to the parton showering model, a POWHEG + HERWIG sample is compared to a POWHEG + PYTHIA sample. The uncertainties due to QCD initial and final

state radiation (ISR/FSR) modelling are estimated with samples generated with POWHEG-BOX interfaced to Pythia for which the parameters of the generation ($\Lambda_{\rm QCD}$, $Q^2_{\rm max}$ scale, transverse momentum scale for space-like parton-shower evolution and the $h_{\rm damp}$ parameter) are varied to span the ranges compatible with the results of measurements of $t\bar{t}$ production in association with jets [82–84].

The $t\bar{t}$ samples are normalized to the NNLO+NNLL cross-section of $\sigma_{t\bar{t}} = 253^{+13}_{-15}$ pb, evaluated using the Top++2.0 program [85] which includes the next-to-next-to leading order QCD corrections and resums next-to-leading logarithmic soft gluon terms [86–91]. The quoted cross-section corresponds to a top-quark mass of 172.5 GeV. Each $t\bar{t}$ sample is produced requiring at least one semileptonic decay in the top anti-top-quark pair. The complete list of $t\bar{t}$ samples can be consulted in Appendix A.1.

W+jets

Due to the high cross section and a signature very close to the $t\bar{t}$ one, especially in the high jet multiplicity case, the W+jets events constitute one of the largest background in this analysis. The W+jets samples come from the leptonic decays of vector bosons produced in association with several high-$p_{\rm T}$ jets, referred to as W+jets. Samples of simulated W+jets events with up to five additional partons in the LO matrix elements are produced with the Alpgen generator (version 2.13) [92] using the PDF set CTEQ6L1 and interfaced to Pythia (version 6.427) for parton showering. The complete list of these samples can be found in Appendix A.4. The overlap between samples is dealt with by using the MLM matching scheme [93]. Heavy-flavour quarks are included in the matrix element calculations to produce the $Wb\bar{b}$, $Wc\bar{c}$, Wc samples. The overlap between the heavy-flavour quarks produced by the matrix element and by the parton shower is removed. W+jets samples are normalized to the inclusive W boson NNLO cross-section [94, 95] and corrected by applying additional scale factors derived from data, as described in Section 3.4.

Z+jets

Z+jets events can be mismatched for $t\bar{t}$ processes in both the electron and muon Z boson decays ($Z \to e^+e^-$ and $Z \to \mu^+\mu^-$), where one lepton is not detected giving the needed fake E_T^{miss} contribution, and in the τ decay case ($Z \to \tau^+\tau^-$), where one τ decay is of a leptonic type and the other one is a hadronic type. The Z+jets samples come from the leptonic decays of vector bosons produced in association with several high-$p_{\rm T}$ jets, referred to as Z+jets. As well as the W+jets case, samples of simulated Z+jets events with up to five additional partons in the LO matrix elements are produced with the Alpgen generator (version 2.13) [92] using the PDF set CTEQ6L1 and interfaced to Pythia (version 6.427) for parton

showering. These samples are also available in the Appenadix A.5. The overlap between samples is dealt with by using the MLM matching scheme [93]. Heavy-flavour quarks are included in the matrix element calculations to produce the $Zb\bar{b}$ and $Zc\bar{c}$ samples. The overlap between the heavy-flavour quarks produced by the matrix element and by the parton shower is removed.

Single top

The background from electroweak single top quark production represents an important contribution to the total background contribution, even if its cross section is about a factor of two smaller than the $t\bar{t}$ cross section. Due to the lower number of jets with respect to the $t\bar{t}$ production, it contributes predominantly in low multiplicity events. The single top quark processes for the s-channel, t-channel and Wt associated production are simulated with POWHEG-BOX using the PDF set CT10 and showered with PYTHIA (version 6.427) calibrated with the P2011C tune and the PDF set CTEQ6L1. All possible production channels containing one lepton in the final state are considered. All samples are generated requiring the presence of a leptonically decaying W boson. The cross-sections multiplied by the branching ratios for the leptonic W decay employed for these processes are normalised to NLO+NNLL calculations [96–98]. All single top MC samples used are listed in the Appendix A.3.

Diboson

Diboson events $pp \to WW$, $pp \to WZ$ and $pp \to ZZ$ which decay products can have the same final topology as in $t\bar{t}$ events, give a small background contribution to the total one. The diboson production is modelled using HERWIG and JIMMY with CTEQ6L1 PDF set and the yields are normalized using the NLO cross-sections [99]. All possible production channels containing at least one lepton in the final states are considered. All diboson MC samples used can be found in the Appendix A.2.

3.4 Background determination

W+jets

This physics process represents one of the largest non-$t\bar{t}$ contribution to the final sample. After the event selection, approximately 3–4% of the total event yield is due to W+jets events. In Fig. 3.3 are shown the Feynman diagram on the W being produced in association with $t\bar{t}$ and b quarks and W+jets event; these diagrams respresent processes which have similar topology to the $t\bar{t}$ signal.

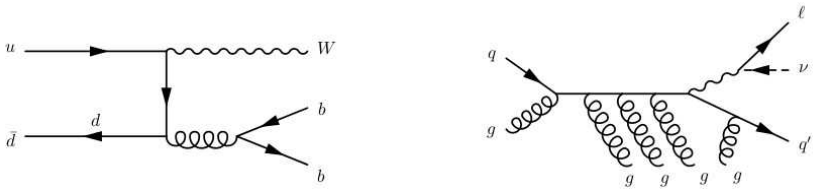

FIGURE 3.3: The Feynman diagram on the left shows the W being produced in association with $t\bar{t}$ and b quarks, while the right diagram shows a W+jets event.

The estimation of this background is performed using a combination of MC simulation and data-driven techniques. The ALPGEN+PYTHIA W+jets samples normalized to the inclusive W boson NNLO cross-section are used as starting point while the absolute normalisation through the *charge asymmetry* method and the heavy flavour fractions (HFF) of this process, which are affected by large theoretical uncertainties, are determined from data, with so called data-driven techniques, in order to reduce the Monte Carlo uncertainties. The corrections for the generator mis-modelling in the fractions of W boson production associated with jets of different flavour components ($W + b\bar{b}$, $W + c\bar{c}$, $W + c$) are estimated in a sample with the same lepton and $E_{\mathrm{T}}^{\mathrm{miss}}$ selections as the signal selection, but with only two jets and no b-tagging requirements. The b-jet multiplicity, in conjunction with the knowledge of the b-tagging and mistag efficiency, is used to extract the heavy flavour fraction. This information is extrapolated to the signal region using MC simulation, assuming constant relative rates for the signal and control regions. We give a description about the charge asymmetry and heavy floavour fraction methods.

- Charge asymmetry method

  This data-driven technique take advantage of the non-symmetric distribution of W^+ and W^- in the W+jets events from pp collisions, allowing the evaluation of a global normalization scale factor. By considering the possible $W^{\pm}$ production modes from parton level processes such as $u\bar{d} \to W^+$ or $c\bar{s} \to W^+$

or as well as $d\bar{u} \to W^-$ or $s\bar{c} \to W^-$; we know that the proton PDFs, from which the cross section depends, is different for the various quarks, *i.e.* the interaction probability of u-quarks coming from its PDF, is greater than the d-quarks one, therefore the cross section of $u\bar{d}$ processes ($\sim u(x_1) \cdot \bar{d}(x_2)$) is larger than the $d\bar{u}$ one ($\sim \bar{u}(x_1) \cdot d(x_2)$). These probability differences lead to an asymmetric production of $W^{\pm}$ bosons, resulting in an asymmetric lepton charge distribution.
If we call $N_{D^{+(-)}}$ the number of data events with a positive (negative) lepton and $N_{W^{+(-)}}$ the number of positive (negative) W from simulated W+jets events, with good approximation we can assume that:

$$N_{W^+} - N_{W^-} \approx N_{D^+} - N_{D^-}. \tag{3.1}$$

Therefore the total number of W+jets events can be evaluated as:

$$N_W = N_{W^+} + N_{W^-} = \frac{N_{W^+} + N_{W^-}}{N_{W^+} - N_{W^-}} \cdot (N_{D^+} - N_{D^-}) \tag{3.2}$$

that can be rewritten as:

$$N_W = \frac{R+1}{R-1} \cdot (N_D^+ - N_D^-) \tag{3.3}$$

where R is the known cross section ratio $\frac{\sigma(pp \to W^+ + X)}{\sigma(pp \to W^- + X)}$, estimated from the MC simulation [100]. If compared to the only MC background estimation, this procedure leads to a reduction of the total W+jets cross section uncertainty.

- Heavy flavour fraction

  The individual components forming the total W+jets background source are the heavy flavour components $Wb\bar{b}$, $Wc\bar{c}$ and Wc, and the light flavour one Wl. The determination of heavy flavour fraction (HFF) sources suffers from large theoretical uncertainties, having a strong impact on the final samples selected after b-tagging requirements, so it is important to decrease these uncertainties using a data-driven estimation. If we express the number of b-tagged events, $N_{i-jet}^{W,tag}$, as a function of the number of events before b-tagging $N_{i-jet}^{W,pretag}$, for each jet multiplicity sample i, we have:

$$N_{i-jet}^{W,tag} = N_{i-jet}^{W,pretag}(P_{b\bar{b},i}F_{b\bar{b},i} + P_{c\bar{c},i}F_{c\bar{c},i} + P_{c,i}F_{c,i} + P_{l,i}F_{l,i}) \tag{3.4}$$

where the b-tagging probabilities $P_x(x = b\bar{b}, c\bar{c}, c, l)$ for each flavour component can be estimated with MC studies, with the following condition about flavour fraction:

$$F_{b\bar{b}} + F_{c\bar{c}} + F_c + F_l = 1. \tag{3.5}$$

Now assuming that the number of total W+jets events in each i jet multiplicity sample is equal to the number of events in data after the non-W component subtraction:

$$N^{W}_{i-jet} = N^{data}_{i-jet} - N^{MCnon-W}_{i-jet} - N^{QCD}_{i-jet} \tag{3.6}$$

whereas the method estimates HFF from the 2-jet multiplicity sample, so substituting $i = 2$ in the Eq. 3.4, we obtain:

$$N^{W,tag}_{2-jet} = N^{W,pretag}_{2-jet}(P_{b\bar{b},2}F_{b\bar{b},2} + P_{c\bar{c},2}F_{c\bar{c},2} + P_{c,2}F_{c,2} + P_{l,2}F_{l,2}) \tag{3.7}$$

and by substituting $F_{c\bar{c}} = k_{c\bar{c}\to b\bar{b}}F_{b\bar{b}}$ in Eq. 3.7, it becomes:

$$N^{W,tag}_{2-jet} = N^{W,pretag}_{2-jet}(P_{b\bar{b},2}F_{b\bar{b},2} + P_{c\bar{c},2}k_{c\bar{c}\to b\bar{b}}F_{b\bar{b},2} + P_{c,2}F_{c,2} + P_{l,2}F_{l,2}) \tag{3.8}$$

where $k_{c\bar{c}\to b\bar{b}}$ represents the ratio between $Wc\bar{c}$ and $Wb\bar{b}$ components, taken from MC simulations.
Therefore processing separately the W^+ and W^- events and imposing that the number of b-tagged W events should be the same in data and MC, it is possible to evaluate the flavour fractions. These values are applied to MC events and the procedure is repeated in iterative-way until no significance variations are observed. The same procedure is applied to higher jet multiplicity samples starting from HFFs found from the 2-jet multiplicity bin.

In summary the overall W+jets normalisation is then obtained by exploiting the expected charge asymmetry in the production of W^+ and W^- bosons in pp collisions. This asymmetry is predicted precisely by theory, and other processes in the $t\bar{t}$ sample are symmetric in charge except for a small contamination from single-top and WZ events which is subtracted using MC simulation.

Fake leptons

This background source is due to QCD multi-jets events in correspondence to a lepton misidentification by the detector that deceives the single lepton triggers, that is commonly called QCD or fake-leptons background. These objects are long living mesons, as $\pi^{\pm}$ or $K^{\pm}$, photons and hadronic jets. The misidentification rate is very small but has a large multi-jets cross section that leads to a not negligible contribution. The QCD background is highly detector dependent, hence the better way for its estimation is via data driven methods, with the Matrix Method (MM) technique [101]. It has already been used by the CDF and D0 experiments at the

Tevatron [102]. It is based on the determination of the efficiency between signal-like and a fake-like events selected with different lepton requirements. It starts by defining two different event samples, called *tight* and *loose*, that differ only in the lepton cut definition. Typically the tight selection is exactly the one applied in standard analysis while the loose events are selected with a looser requirement in the leptonic cut.

The number of events surviving the tight and loose selection can be expressed as the sum of the correspondent number of real (true) signal events $\left(N_{real}^{tight(loose)}\right)$ plus the number of events from the lepton misreconstruction $\left(N_{fake}^{tight(loose)}\right)$:

$$N^{tight(loose)} = N_{real}^{tight(loose)} + N_{fake}^{tight(loose)}. \tag{3.9}$$

If we define the real and fake efficiencies ϵ_{real} and ϵ_{fake}, the Eq. 3.9 can be rewritten in terms of efficiencies such that:

$$N^{tight} = \epsilon_{real} N_{real}^{loose} + \epsilon_{fake} N_{fake}^{loose}. \tag{3.10}$$

We can now quantify the background source due to fake leptons as:

$$N_{fake}^{tight} = \frac{\epsilon_{fake}}{\epsilon_{real} - \epsilon_{fake}} \left(\epsilon_{real} N^{loose} - N^{tight}\right). \tag{3.11}$$

The non-prompt real leptons efficiency, ϵ_{real}, is extracted using a tag-and-probe technique using leptons from Z boson decays that do not contain fake lepton contamination. The ϵ_{fake} efficiency is determined from simulations of the $t\bar{t}$ signal sample by requiring exactly one loose lepton, defined by the ratio of events in which the selected loose lepton also pass the tight requirements, divided by the total number of loose events. The weight to be applied to the real data events is defined as $\bar{\omega_i}$:

$$\bar{\omega_i} = \frac{\epsilon_{fake}}{\epsilon_{real} - \epsilon_{fake}} \left(\epsilon_{real} t_i - (1 - t_i)\right) \tag{3.12}$$

where t_i is equal to 0 when the event i is tight-like and it is equal to 1 when the event i is loose-like.

QCD events (or fake-lepton events) contribute to the total event yield at approximately 1–2% level.

Other backgrounds

Other background sources like the Single-top, Z+jets and diboson events are simulated with MC generators and the event yields are normalized to the most recent theoretical calculations of their cross-sections. The single-top quark background

is one of the largest background contribution, amounting to approximately 4% of the total event yield and 36-40% of the total background estimate.

$t\bar{t}$ dilepton

The $t\bar{t}$ dilepton contribution, that is when the top quark pair events with both top and anti-top-quarks decaying semileptonically (including decays to τ), can sometimes pass the event selection and contributes approximately 5% of the total event yield. The fraction of dileptonic $t\bar{t}$ events in each p_{T} bin is estimated using the same MC sample used for the signal modelling. In the fiducial phase space definition, leptonic top quark decays to τ-leptons in lepton+jets $t\bar{t}$ events are considered as signal only if the τ lepton decays leptonically.

Chapter 4

Object Definition and Event Selection

The lepton+jets $t\bar{t}$ decay mode is characterized by the presence of a high-p_{T} lepton, two jets originating from b-quarks, two jets from the hadronic W boson decay, and missing transverse momentum due to the neutrino. So this analysis relies on the selection of electrons, muons and jets, the tagging of jets as b-jets, and the computation of missing transverse energy.

This chapter is structured as follows: the Sec. 4.1 describes the detector-level object definition, in Sec. 4.2 is presented the event selection strategy showing the event yelds and some control plots, Sections 4.3 4.4 are dedicated to the particle-level and the parton-level objects used to characterize the final state event topology and to define the fiducial phase-space region for the measurements. Last the matching criteria are described in Sec. 4.5.

4.1 Detector-level objects

Primary vertex

The primary vertex (PV) is the vertex reconstructed from charged particle tracks that originated from the hard collision event. Some of the calorimeter deposits and tracks reconstructed will be from pileup events unrelated to the primary, because of several proton–proton collisions will occur at each bunch crossing. Also, several of the objects will have their momenta corrected based on the assumption of the position of the primary vertex being the origin of the hard collision. The vertices reconstructed in a beam-crossing are found using an iterative vertex fitting

procedure [103]. An initial vertex seed is obtained by finding the global maximum in the distribution of the z coordinates of the tracks. Then, the position of the vertex is found using an adaptive vertex fitting algorithm [104]. This algorithm fits the vertex with a χ^2-based algorithm. Tracks which are incompatible with the primary by more than about 7σ (determined from the χ^2) are used to seed a new vertex. This procedure is repeated until all the tracks are associated with a vertex, or no new vertices are produced. The primary vertex of the event is to be distinguished from the pileup vertices, which are the vertices from proton–proton collisions in the bunch crossing that are not associated with the hard interaction, and secondary vertices, which are formed from particles in the hard collision which travel a measurable distance away from the primary vertex before decaying.

For the present analysis the requirements on the primary vertices in the event are that they are formed from reconstructed tracks such that they are spatially compatible with the luminous interaction region. The hard-scatter primary vertex is chosen to be the vertex with the highest $\sum p_{\mathrm{T}}^2$ where the sum extends over all associated tracks with $p_{\mathrm{T}} > 0.4\,\mathrm{GeV}$.

Electron

The electrons are reconstructed from energy deposits in the EM calorimeter using a sliding window algorithm [105] [106]: the EM calorimeter is divided into $\Delta\eta \times \Delta\phi = 0.025 \times 0.025$ segments (corresponding to the granularity of the middle layer of the calorimeter), and any 3×5 window of these segments which has a combined energy greater than 2.5 GeV is selected as an electron seed cluster. To select a cluster as an electron, a reconstructed track must be found, with condition that the track extrapolation is within $\Delta\eta < 0.05$ and $\Delta\phi < 0.1$ of the barycentre of the cluster on the side toward which the track bends and $\Delta\phi < 0.05$ on the other side. If multiple tracks match a cluster, the tracks are required to have hits in the silicon detectors and then the closest in ΔR is selected to be the matching track. For each selected electron, the cluster energy is then recalculated in 3×7 (3×5) towers of cells in the barrel (endcaps). The cluster energy is now corrected for estimated energy deposits in front of and leaked behind the EM calorimeter and energy estimated to be leaked outside the cluster. These corrections are derived from simulation of the detector. The final 4-momenta of electrons are then taken using the matched track for the η and ϕ parameters at the vertex, and the energy given by the cluster energy.

From the electron candidates, built with the above procedure, further selection requirements are needed to reject hadronic jets radiation misidentified like electrons, called "tight++", allowing only a certain fraction of energy in the hadronic calorimeter, a well collimated energy deposition found by comparing the cluster

energy to the energy in a larger tower area, requiring hits in the b-layer (the innermost pixel subdetector) and a minimum number of hits in the rest of the silicon, requiring a minimum number of high-threshold hits in the TRT and restrictions on the ratio of cluster energy to the track momentum. The cluster is also required to be isolated from hadronic activity in the rest of the event.

Because jets are reconstructed independently of electrons, for each electron there will be a corresponding jet reconstructed. Therefore, an overlap removal is performed, such that the jet closest to an identified electron and within $\Delta R < 0.4$ (approximately the size of reconstructed jets) is removed.

In summary the electron candidates are reconstructed as tracks in the inner detector associated with energy deposits in the EM calorimeter. They must pass identification criteria based on the shower shape in the EM calorimeter, on the track quality, and on the detection of the transition radiation produced in the TRT detector. The EM clusters are required to be in the pseudorapidity region $|\eta| < 2.47$, excluding the transition region between the barrel and the endcap calorimeters ($1.37 < |\eta| < 1.52$), because the EM calorimeter's barrel end-cap transition region contains a large amount of passive material and so there is a reduction of measurement precision. They must have a transverse energy $E_{\mathrm{T}} > 25\,\mathrm{GeV}$. The associated track must have a longitudinal impact parameter $|z_0| < 2$ mm with respect to the primary vertex. Isolation requirements, on both calorimeter and tracking variables, are used to reduce the background from non-prompt electrons. The calorimeter isolation variable is based on the energy sum of cells within a cone of radius $\Delta R < 0.2$ around the direction of each electron candidate. This energy sum excludes cells associated with the electron cluster and is corrected for leakage from the electron cluster itself and for energy deposits from pileup. The tracking isolation variable is based on the track p_{T} sum around the electron in a cone of radius $\Delta R < 0.3$, excluding the electron track. Both requirements are chosen in order to achieve a 90% electron selection efficiency for prompt electrons from Z boson decays.

Muon

The muon is identified as a charged particle leaving the track through the muon spectrometer (MS) [107]. Particle tracks are first reconstructed separately in the inner detector (ID) and the MS. The MS tracks are then back extrapolated to the interaction point and a compatible ID track is searched for. This is done by forming a χ^2 difference between the tracking parameters of the ID and MS tracks, and requiring a χ^2 probability greater than 0.001. When a compatible ID track is found, the track parameters are then refit using the hits in both the ID and MS and the energy deposits in the calorimeter along the muon path to obtain the

"combined" muon. If more than one ID track satisfies the χ^2 requirement, then all such tracks are refit, and the one with the best match after the refit is taken to be the muon candidate for a given MS track.

The track is required to have $|z_0| < 2$ mm and a transverse impact parameter significance, $|d_0/\sigma(d_0)| < 3$, consistent with coming from the hard interaction. Muons are required to have $p_{\mathrm{T}} > 25\,\mathrm{GeV}$ and be within $|\eta| < 2.5$. Muons must have at least one pixel hit and at least 5 SCT hits, and fewer than 3 holes in pixel and SCT layers combined. In the region $0.1 < |\eta| < 1.9$: $n_{\mathrm{TRT\,Hits}} + n_{\mathrm{TRT\,Outliers}} > 5$ and $n_{\mathrm{TRT\,Hits}} < 0.9 \times (n_{\mathrm{TRT\,Hits}} + n_{\mathrm{TRT\,Outliers}})$. To reduce the background from muons originating from heavy-flavour decays inside jets, muons are required to be separated by $\Delta R > 0.4$ from the nearest jet and to be isolated. They are required to satisfy the isolation requirement $I^{\ell} < 0.05$, where the isolation variable I^{ℓ} is the ratio of the sum of p_{T} of tracks, excluding the muon, in a variable-sized cone of radius $\Delta R = 10\,\mathrm{GeV}/p_{\mathrm{T}}(\mu)$ to the p_{T} of the muon [108]. The isolation requirement has an efficiency of about 97% for prompt muons from Z boson decays.

Jet

In perturbative QCD the high energy partons from the hard scattering process are described as a fragmentation into hadrons, called "jets", whose combined momenta carry out the parton's momentum. These particles leave energy deposits, or "clusters", in the hadronic calorimeter which are grouped together according to a jet algorithm.

The early jet algorithms were based only on a cone of a fixed radius R around the hardest single cluster found, and then removed all the clusters in that cone and repeated the procedure until all clusters greater than a fixed threshold are formed into a jet, bringing to theoretically instabilities in the algorithm. If a gluon splits into two collinear gluons that means a previously hard particle can become arbitrarily soft and therefore lead to different jet grouping, representing a problem when comparing to theoretical predictions based on a fixed-order perturbative expansion, since at each order, more radiation effects are allowed and so we can not apply these algorithms in the theoretical calculations. These considerations led to the requirement for jet algorithms to be "collinear safe". This property is guaranteed if instead of looking at cones based on p_T, one uses every particle or cluster in the event to build a cone and then uses a *split-merge* procedure in order to form final stable cones. The jet alghorithm must be in addition *infra-red* safe, that is it must be insensitive to the emission of soft gluons [109].

The more recent methods build jets step-by-step by repeatedly merging together nearby clusters of energy. The algorithm that the LHC experiments use is the anti-k_t algorithm [110], a method based on a sequential cluster recombination

algorithm that follows an iterative procedure; the intermediate reconstruction objects are called "pseudo-jets". First a distance d_{ij} is calculated between all the clusters i and j in the event, and a "beamline" distance d_{iB} is also calculated:

$$d_{ij} = \min(p_{T,i}^{2k}, p_{T,j}^{2k}) \frac{\Delta R_{ij}^2}{R^2} \tag{4.1}$$

$$d_{iB} = p_{T,i}^{2k} \tag{4.2}$$

where the parameter k is fixed equal to -1. This choice favours the clusterization around hard particles rather than soft ones, as it instead happens in the case of the k_T algorithm ($k = 1$). R is a free parameter of the algorithm, that has been set equal to 0.4; $\Delta R_{ij}^2 = (\eta_i - \eta_j)^2 + (\phi_i - \phi_j)^2$, and $p_{T,i}$, η_i and ϕ_i are the transverse momentum with respect to the beam axis, the pseudorapidity and the azimuthal angle of the cluster, respectively. After having calculated the distances between d_{ij} and d_{iB}; the minimum is chosen; if its value is d_{ij} then the objects i and j are combineb into a single pseudo-jet, otherwise we consider i as a final state object and do not consider it in further iterations. The procedure is iterated until all the clusters have been removed from the list.

The anti-k_t algorithm is an infrared and collinear safe algorithm (IRC) for its distance definition. IRC safety indicates that the set of hard jets found remains unchanged even in case of a collinear splitting or the addition of a soft emitted gluon. These properties also imply that the anti-k_t algorithm is pileup resistant.

The input energy deposits used to reconstruct jets are the *topoclusters* (topological clusters) defined from the detector output. The fine segmentation of the calorimeter means that a single high-energy particle can deposit its energy in several neighbouring cells. A topocluster is a set of neighbouring cells that have been grouped together by approximating the energy deposition of a single particle. Topoclusters are formed by finding all calorimeter cells with an energy deposition with signal-to-noise ratio greater than 4. For each cell, all its neighbouring cells with signal-to-noise greater than 2 are added to the seed to form a proto-cluster. If a neighbour could be added to two of these proto-clusters, then the two clusters are merged along with the neighbour into a single proto-cluster. Each neighbour is also added to a neighbour-seed list. If a neighbouring cell does not have a signal-to-noise greater than 2, then it is still added to the proto-cluster, but it does not get added to the neighbour-seed list. Once all the seed clusters have been processed, then the neighbour cell list is processed in the same way, with the new neighbours being added to the parent proto-cluster. This process continues until there are no more seed clusters in the list. Once the merging process is finished, each proto-cluster is searched in turn for local maxima. These are defined as cells

with a minimum value of energy of 500 MeV and with greater energy than any of their surrounding cells. If more than one such local maxima are found, then the clustering procedure is repeated with these local maxima as seeds, with the difference that only cells in the parent cluster are considered and no cluster merging occurs. This splits up topoclusters being formed from several close-by high energy particles, when it is possible to distinguish them. The topoclusters after splitting are then each assigned a 4-vector, such that the energy is the energy sum of the cells in the cluster, the mass is zero, and the direction is in the energy-weighted average of the direction of all the cluster cells.

The energy of the cells in the topoclusters are measured at the EM scale, that is the detector response corrected assuming that the total energy response is due to electromagnetic showers. The *EM jets* need to be corrected to the particle-level, that is corrected for the ratio of the reconstructed jet p_T with respect to the jet p_T of truth stable particles determined from simulation, that are jets formed using the same algorithm constructed from the underlying hadrons before detector interaction. This is done using the *EM+JES* (Jet Energy Scale) calibration scheme [111]. This scheme consists of three steps: subtract the energy estimated to be due to pileup, correct the jet direction so that the jet originates from the primary vertex of the interaction instead of the geometrical detector centre, and correct the energy and direction by calibration constants derived from simulation comparisons to truth jets. Each bunch crossing has several soft collision events that lead to a number of low momentum hadrons from pileup collisions entering the detector. If these hadrons occur in a particular region, an unrelated jet to the hard collision event can be reconstructed. In the ATLAS experiment, it was developed the *Jet Vertex Fraction* method (JVF) in order to reject these pileup jets [112]. The JVF algorithm first associates reconstructed tracks to a jet by matching tracks within $\Delta R < 0.4$ of the jet centre. The JVF is calculated as the sum of the p_T of the selected tracks originating from the selected primary over the sum of the p_T from all the selected tracks, resulting substantially in the fraction of the constituent tracks transverse momentum coming from the primary vertex. A value of the JVF close to 1 means that all the tracks in the jet can be associated to the primary vertex, viceversa a value close to 0 means that none of the tracks in the jet can be associated with the primary vertex and the jet was therefore likely to have come from pileup. The -1 value is instead assigned if no tracks can be associated to the jet.

Finally, for this analysis, jets are reconstructed using the above described anti-k_t algorithm [110] implemented in the FastJet package [113] with radius parameter $R = 0.4$. The jet reconstruction starts from topological clusters calibrated and

corrected for pileup effects using the jet area method [114]. A residual correction dependent on the instantaneous luminosity and the number of reconstructed primary vertices in the event [115] is then applied. They are calibrated using an energy- and η-dependent simulation-based calibration scheme, with *in situ* corrections based on data [116] and are accepted if $p_{\mathrm{T}} > 25\,\mathrm{GeV}$ and $|\eta| < 2.5$. To reduce the contribution from jets associated with pileup, jets with $p_{\mathrm{T}} < 50\,\mathrm{GeV}$ are required to satisfy $|\mathrm{JVF}| > 0.5$. Jets with no associated tracks or with $|\eta| > 2.4$ at the edge of the tracker acceptance are always accepted. To prevent double-counting of electron energy deposits as jets, the closest jet within $\Delta R < 0.2$ of a reconstructed electron is removed. If the nearest jet surviving the above cut is within $\Delta R < 0.4$ of the electron, the electron is discarded, to ensure it is cleanly separated from the nearby jet activity.

b-Jet

Jets containing b-quarks can be discriminated against light quark jets, due to the long lifetime of the B-hadrons, that combined with the large momenta of the objects produced at the LHC, results in a time of flight large enough to be identified from a reconstructed secondary vertex or the large impact parameters (the distance of closest approach of the track to the primary vertex) of its decay products. B-hadrons may also be identified from the large hadron mass and the large branching ratio into leptons. Because the relative rarity of events with b-jets in proton–proton collisions, the requiriment of at least two b-tagged jets in each event leads to a significant background reduction. Therefore the purity of the selected $t\bar{t}$ sample is improved by tagging jets containing b-hadrons, exploiting their long decay time and the large mass.

There are several b-tagging algorithms. $IP3D$ [117] is an impact parameter based algorithm, that works with individual tracks associated with a jet, that pass quality cuts. They must have at least 7 silicon hits (hits in the pixel or SCT detectors) with at least 2 pixel hits, one of which must be from the innermost layer, an impact parameters $\mid d_0 \mid < 1\ mm$ and $\mid z_0 \mid < 1.5\ mm$. d_0 is the impact parameter in the $r - \phi$ plane, z_0 along the beam axis, and both are signed with respect to the direction of the jet (positive if in front of the primary vertex, negative if behind). This requirement rejects most tracks which originate from the decays of long-lived mesons, such as K^0_S, Λ and the hyperons, and tracks produced by photon conversion after interaction with the beamline or detector, which would otherwise produce spurious tagging. Finally, they must have a $p_T > 1\,\mathrm{GeV}$. Tracks are associated to the jet with a jet p_T dependent ΔR. The tracks are required to be closer to the jet at higher p_T, since harder jets are more collimated, and so we can

reduce the number of tracks produced in pileup events by placing tighter cuts at higher p_T.

From these tracks, the $IP3D$ algorithm calculates the impact parameter significances $\frac{d_0}{\sigma_{d_0}}$ and $\frac{z_0}{\sigma_{z_0}}$, and finds a likelihood for the tracks to have originated from a b-jet, $\mathcal{L}_b$, and a likelihood for the track to have come from a light jet, $\mathcal{L}_l$. The $IP3D$ algorithm output is $\Sigma_i \frac{\mathcal{L}_b}{\mathcal{L}_l}$ where the i index runs on the number of tracks associated with the jet.

The $SV1$ algorithm is a secondary vertex-based algorithm. It takes the tracks associated to the jet and tries to fit a secondary vertex away from the primary vertex. It uses tracks similar to $IP3D$ but with looser cuts: tracks with $p_T > 400$ MeV, only 1 pixel hit which needs not be on the innermost layer $d_0 < 3.5$ mm and does not require the z_0 cut, but tracks are required to have an impact parameter significantly far from the vertex. From the tracks, it forms two-track vertices using every pair of tracks. If any of these two-track vertices have a mass compatible with a long lived particle (K^0_S, Λ, hyperons) it removes both of them from the list of tracks associated to the jet, then it combines the remaining two-track vertices into a single vertex, and then removes the worst fit track. It repeats this procedure until the overall χ^2 of the track errors to the vertex is below a quality threshold.

The JetFitter algorithm [118] uses the same tracks as $IP3D$, its idea is to find an axis along which the B-hadron decayed, possibly with an extra vertex due to a D-decay, and constrain the B-vertex position along this flight axis. Its starts with the position of the primary vertex and the flight axis from the PV in the direction of the jet momentum. It defines a distance d_i along the flight axis that corresponds to a vertex for the track along this axis. This vertex position d_i is found from the position of closest approach of the track to the axis. The algorithm proceeds by updating the flight axis direction and the d_i, by applying an iterative Kalman filter update of the input parameters, one track at a time, until the probability for the most probable two-vertex combination falls below a threshold.

In our analysis b-jets are identified using the $MV1$ b-tagger [119], called a multivariate discriminant, which combines the results of $IP3D$, $SV1$, and JetFitter into a single discriminant using a neural network, by combining information from the track impact parameters, secondary vertex location and decay topology. Jets are defined to be b-tagged if the MV1 discriminant value was larger than a threshold (working point) corresponding approximately to a 70% efficiency for tagging b-quark jets with $p_{\mathrm{T}} > 20\,\mathrm{GeV}$ from top decays in $t\bar{t}$ events, with a rejection factor of about 130 against light-quark and gluon jets, and about five against jets originating from charm quarks.

Missing Transverse Momentum

The momentum imbalance in the transverse plane with respect to the beam axis is due to one or more particles that are transparent to the detector. Within Standard Model these particles can only be neutrinos. But in new physics models, new particles can be produced which have small or no interactions with matter and so also contribute to missing transverse momentum. Typically, these particles are introduced as potential dark matter candidates. Thus, missing transverse momentum is an important quantity when searching for new physics.

This important kinematical quantity is symbolized by E_T^{miss}, where the transverse component of the energy $E_T = E \sin\theta$ is equal to the transverse momentum for massless particles or in the limit of very high energy processes if compared to the particle masses involved.

Bad calibrations of any detector component leads to mismeasurements of the missing transverse momentum, because in order to calculate the momentum imbalance it uses all the detector subsystems together in concert to build a complete picture of any event. We have to use some energy terms, each one related to each object category. The electron term, $E_{x,y}^{RefEle}$, uses electrons satisfying the tight++ criteria, as described above. The topoclusters associated with electrons are calibrated using the full electron energy scale excluding out-of-cluster corrections. Also we have the jet term ($E_{x,y}^{RefJet}$) that uses jet objects which have $p_T > 20\,\text{GeV}$ and the soft jet term ($E_{x,y}^{RefSoftJet}$) that uses jets with $7 < p_T < 20\,\text{GeV}$, the first ones calibrated with the full EM+JES corrections, as described above, and the last ones calibrated with the EM scale. Last, the muon term ($E_{x,y}^{RefMuon}$) includes muons, that adds the p_T as determined from track momentum, rather than the calorimeter topocluster since high-p_T muons are minimum ionising, so will not deposit their full energy in the calorimeter, while if the muon is isolated from a jet by at least $\Delta\, R = 0.3$, then the calorimeter energy is added to the muon term. Each calorimeter topocluster can be associated with: an electron, a jet, a soft jet, or a muon. If no associated object is found, the topocluster gets added to a separate term ($E_{x,y}^{CellOut}$), so called *Cell Out* topoclusters, calibrated to the EM scale.

Therefore by summing every energy component we have the total missing transverse momentum in the x and y directions:

$$-E_{x,y}^{miss} = E_{x,y}^{RefEle} + E_{x,y}^{RefJet} + E_{x,y}^{RefSoftJet} + E_{x,y}^{RefMuon} + E_{x,y}^{CellOut} \tag{4.3}$$

that in the transverse plane it becomes:

$$E_T^{miss} = \sqrt{(E_x^{miss})^2 + (E_y^{miss})^2}. \tag{4.4}$$

Furthermore E_T^{miss} allows to evaluate another useful kinematic quantity, that is the transverse W mass m_T^W:

$$m_T^W = \sqrt{2p_T^l E_T^{miss}(1 - \cos(\phi^l \phi^\nu))} \tag{4.5}$$

where p_T^l and ϕ^l are the transverse momentum and azimuthal angle of the lepton, while ϕ^ν that is the azimuthal angle of the neutrino, allowing a proxy for measuring the leptonically decaying W mass.
In conclusion, the missing transverse momentum $E_{\mathrm{T}}^{\mathrm{miss}}$ is computed from the vector sum of the transverse momenta of the reconstructed calibrated physics objects (electrons, photons, hadronically decaying τ-leptons, jets and muons) as well as the transverse energy deposited in the calorimeter cells not associated with these objects. Calorimeter cells not associated with any physics object are calibrated using tracking information before being included in the $E_{\mathrm{T}}^{\mathrm{miss}}$ calculation. The contribution from muons is added using their momentum. To avoid double counting energy, the parametrized muon energy loss in the calorimeters is subtracted in the $E_{\mathrm{T}}^{\mathrm{miss}}$ calculation.

4.2 Event selection at detector level

The event selection consists of a set of requirements based on the general event quality and on the reconstructed objects, defined in 4.1, that characterize the final state event topology. After the initial trigger selection described above, additional requirements are applied to the event sample in order to enhance the purity of the selected $t\bar{t}$ candidates. The event selection cuts in e+jets and μ+jets channels are similar to each other, leading to similar yields and distributions that allows an easier combination of the electron and muon channels. Each event must have a reconstructed primary vertex with five or more associated tracks. The events are required to contain exactly one reconstructed lepton candidate with $p_{\mathrm{T}} > 25\,\mathrm{GeV}$ geometrically matched to the trigger object and at least four jets with $p_{\mathrm{T}} > 25\,\mathrm{GeV}$ and $|\eta| < 2.5$. At least two of the jets have to be tagged as b-jets. The event selection is summarized in Table 4.1, the events yields are displayed in Table 4.2 for data, simulated signal, and backgrounds (the background determination is described in Sec. 3.4).

A series of control plots of the main quantities of physics interest have been produced to check that the Monte Carlo simulations are in good agreement with the detector results in both the electron and muon channels.

Event selection	
Trigger	Single lepton
Primary vertex	≥ 5 tracks with $p_{\mathrm{T}} > 0.4\,\mathrm{GeV}$
Exactly one	Muons: $p_{\mathrm{T}} > 25\,\mathrm{GeV}$, $\lvert\eta\rvert < 2.5$
isolated lepton	Electrons: $p_{\mathrm{T}} > 25\,\mathrm{GeV}$
	$\lvert\eta\rvert < 2.47$, excluding $1.37 < \lvert\eta\rvert < 1.52$
≥ 4 jets	$p_{\mathrm{T}} > 25\,\mathrm{GeV}$, $\lvert\eta\rvert < 2.5$
b-tagging	≥ 2 b-tagged jets at $\epsilon_b = 70\%$

TABLE 4.1: Summary of all requirements included in the event selection.

	e+jets	μ+jets
$t\bar{t}$	74000 ± 4700	92000 ± 5900
Single top	3600 ± 200	4400 ± 250
W+jets	3000 ± 300	4400 ± 400
Z+jets	1100 ± 550	570 ± 300
$WW/WZ/ZZ$	73 ± 40	67 ± 35
Non-prompt and fake lept.	2000 ± 900	1400 ± 600
Prediction	84000 ± 4900	103000 ± 6000
Data	85127	102952

TABLE 4.2: Event yields in the e+jets and μ+jets channels after the selection. The signal model, denoted $t\bar{t}$ in the table, is generated using POWHEG+PYTHIA. The quoted uncertainties represent the sum in quadrature of the statistical and systematic uncertainties on each subsample. Neither modelling uncertainties nor uncertainties on the inclusive $t\bar{t}$ cross-section are included in the systematic uncertainties.

Figures 4.1, 4.2 and 4.3 show data distributions compared to predictions for some kinematical key distributions of e+jets, μ+jets and combined channels, respectively, where real data are represented by black dots while MC contributions are differently colored depending on the specific contribution of the background or $t\bar{t}$ signal, and stacked to be comparable with the data.

The binning has been chosen in order to minimize the statistical fluctuations and migration effects, based on the resolution studies described in 6.2. The number of events in the plots are normalized to the corresponding bin width. All MC predictions distributions are also normalized with respect to the total integrated data luminosity, that is 20.3 fb^{-1}. In plots the uncertainty band includes the systematic uncertainties as described in Sec. 6.4.2, with statistical ones. The agreement between data and prediction is within the total uncertainty for all the distributions taken into account.
Others control plots are shown in Appendix B, for both signal and non-signal control regions: 3j0b, 4j0b and 4j1b (3 jets inclusive, 4 jets inclusive, 4 jets inclusive one of them

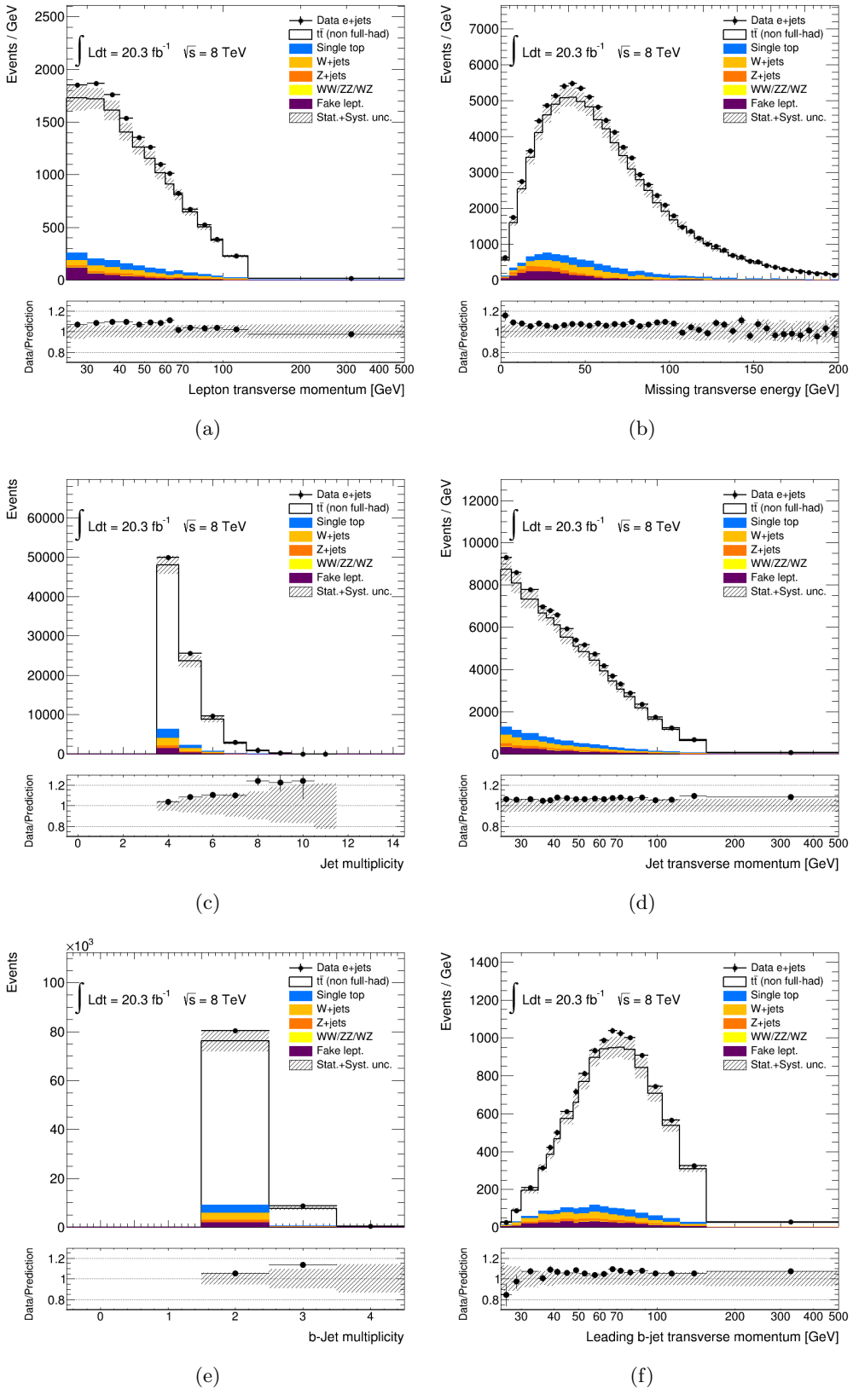

(a) (b)

(c) (d)

(e) (f)

FIGURE 4.1: Kinematic distributions at the detector level: 4.1(a) lepton transverse momentum and 4.1(b) missing transverse momentum $E_{\mathrm{T}}^{\mathrm{miss}}$, 4.1(c) jet multiplicity, 4.1(d) transverse momentum, 4.1(e) b-tagged jet multiplicity and 4.1(f) leading b-tagged jet p_{T}. The distributions for the e+jets channel are compared to predictions using POWHEG+PYTHIA as the $t\bar{t}$ signal model. The hashed area indicates the combined statistical and systematic uncertainties on the total prediction, excluding systematic uncertainties related to the modelling of the $t\bar{t}$ system. The lower parts of the figures show the ratios of the data to the predictions.

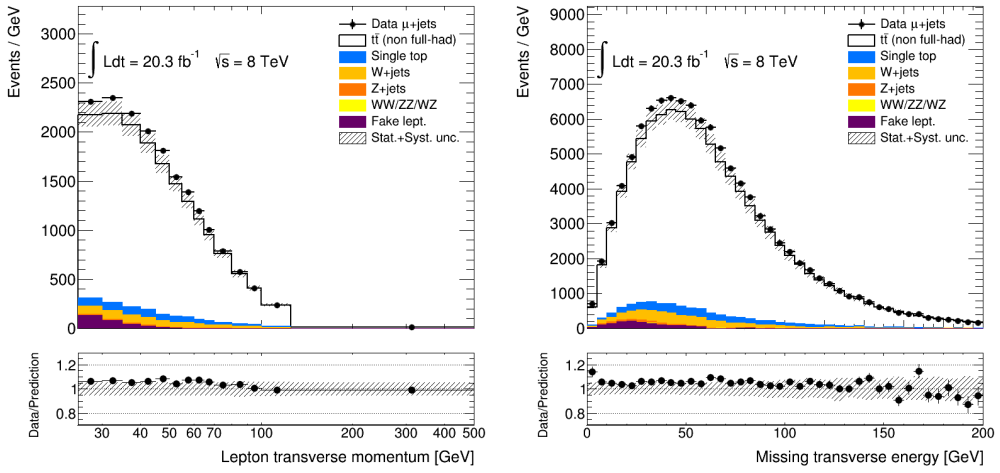

(a) (b)

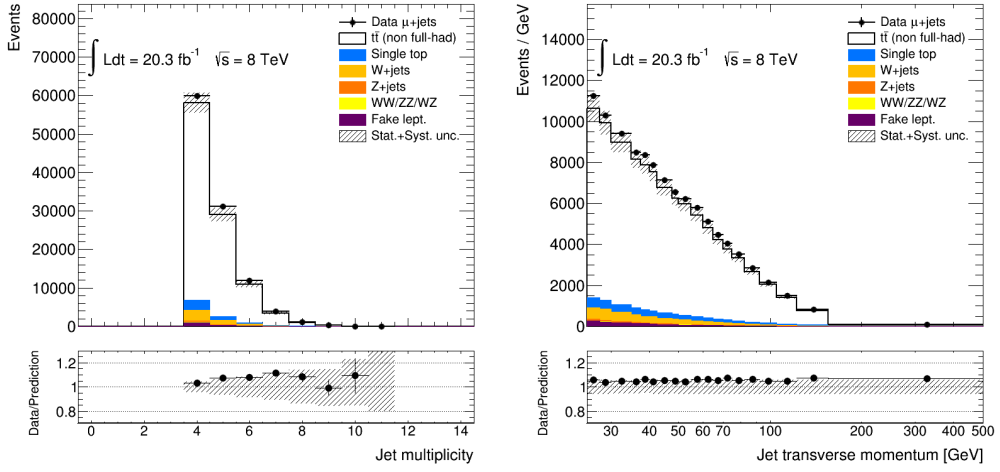

(c) (d)

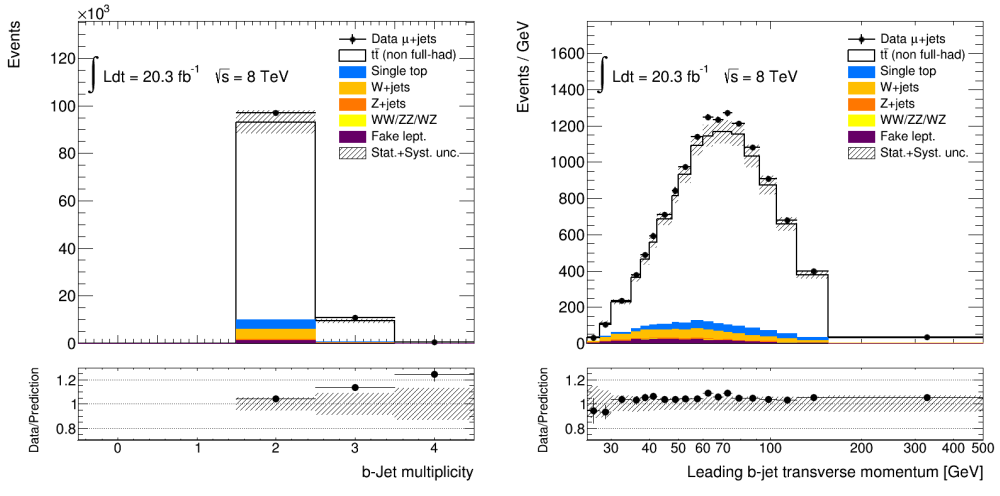

(e) (f)

FIGURE 4.2: Kinematic distributions at the detector level: 4.2(a) lepton transverse momentum and 4.2(b) missing transverse momentum $E_{\mathrm{T}}^{\mathrm{miss}}$, 4.2(c) jet multiplicity, 4.2(d) transverse momentum, 4.2(e) b-tagged jet multiplicity and 4.2(f) leading b-tagged jet p_{T}. The distributions for the μ+jets channel are compared to predictions using POWHEG+PYTHIA as the $t\bar{t}$ signal model. The hashed area indicates the combined statistical and systematic uncertainties on the total prediction, excluding systematic uncertainties related to the modelling of the $t\bar{t}$ system. The lower parts of the figures show the ratios of the data to the predictions.

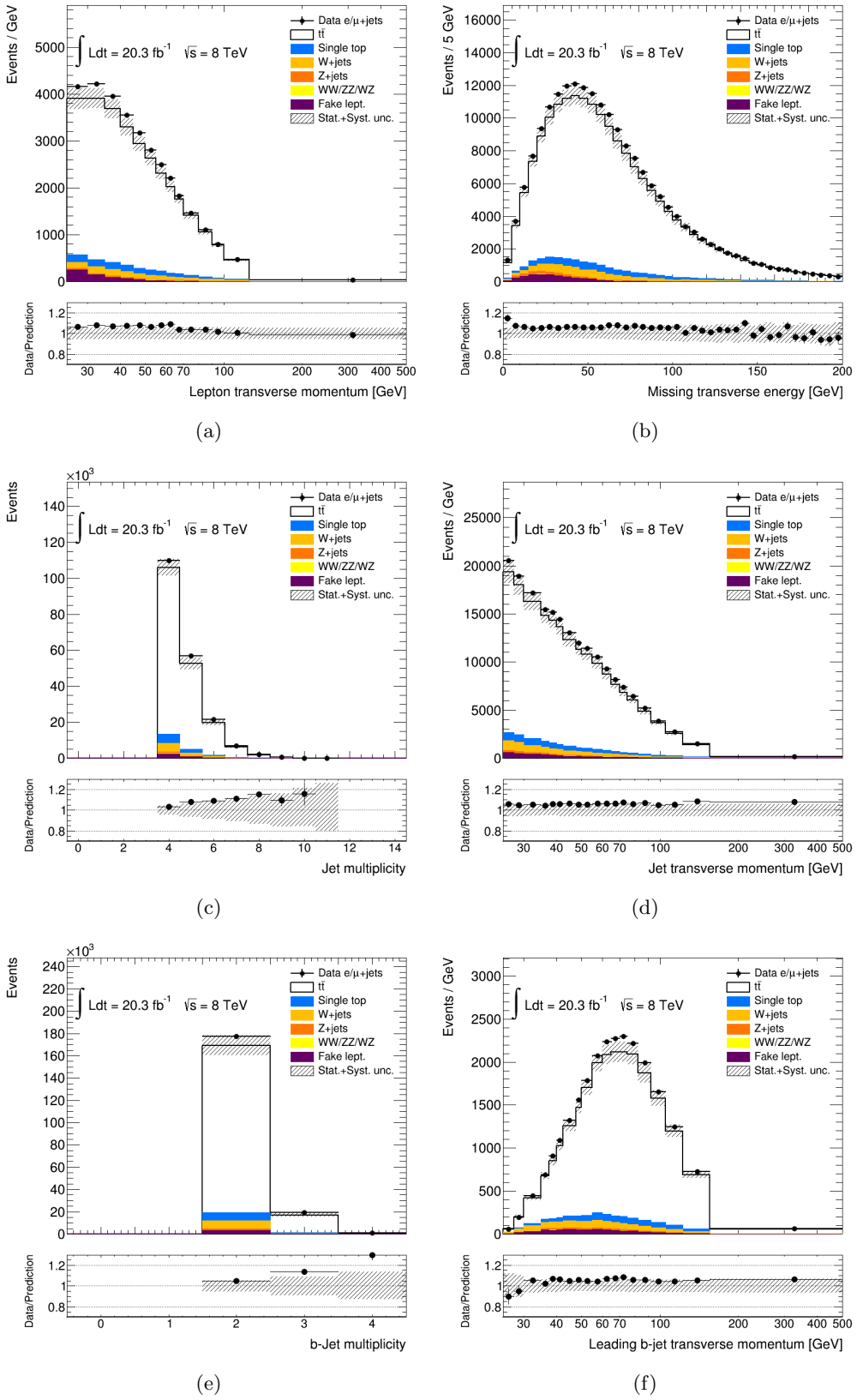

FIGURE 4.3: Kinematic distributions at the detector level: 4.3(a) lepton transverse momentum and 4.3(b) missing transverse momentum $E_{\mathrm{T}}^{\mathrm{miss}}$, 4.3(c) jet multiplicity, 4.3(d) transverse momentum, 4.3(e) b-tagged jet multiplicity and 4.3(f) leading b-tagged jet p_{T}. The distributions of the combined e+jets and μ+jets channels are compared to predictions using POWHEG+PYTHIA as the $t\bar{t}$ signal model. The hashed area indicates the combined statistical and systematic uncertainties on the total prediction, excluding systematic uncertainties related to the modelling of the $t\bar{t}$ system. The lower parts of the figures show the ratios of the data to the predictions.

b-jet).

4.3 Particle-level objects and fiducial phase space definition

Particle-level objects are defined for simulated events in analogy to the detector-level objects described above. Only stable final-state particles, *i.e.* particles that are not decayed further by the generator, and unstable particles[1] that are to be decayed later by the detector simulation, are considered. These particles are labelled by a status code 1 in the simulation.

The fiducial phase space for the measurements presented in this thesis is defined using a series of requirements applied to particle objects identical to those used in the selection of the detector-level objects. The procedure explained in this section is applied to the $t\bar{t}$ signal only, since the background subtraction is performed before unfolding the data.

Electrons and muons are required not to originate from a hadron in the MC particle record, either directly or through a tau decay. This ensures that the lepton is from an electroweak decay without requiring a direct W-boson match. The four-momenta of the bare leptons are then dressed by adding the four-momenta of all photons within $\Delta R = 0.1$. The dressed leptons are required to have $p_{\mathrm{T}} > 25\,\mathrm{GeV}$ and $|\eta| < 2.5$. Electrons in the transition region ($1.37 < \eta < 1.52$) are rejected at the detector level but accepted in the fiducial selection. This difference is accounted for by the efficiency correction described in Sec. 6.3.2.

The particle-level missing transverse momentum is calculated from the four-vector sum of the neutrinos, discarding neutrinos from hadron decays, either directly or through a tau decay.

Particle jets are clustered using the anti-k_t algorithm [110] with radius parameter $R = 0.4$, starting from all stable particles, except for selected leptons (e, μ, ν) and the photons used to dress the leptons. Particle jets are required to have $p_{\mathrm{T}} > 25\,\mathrm{GeV}$ and $|\eta| < 2.5$.

Hadrons containing a b-quark with $p_{\mathrm{T}} > 5\,\mathrm{GeV}$ are associated with jets through a ghost matching as described in Ref [114]. Particle b-tagged jets must have $p_{\mathrm{T}} > 25\,\mathrm{GeV}$, $|\eta| < 2.5$.

[1] Particles with a mean lifetime $\tau > 300$ *ps*

Particle objects are subject to analogous overlap removal criteria as detector-level objects, after dressing and jet reclustering: muons and electrons within $\Delta R < 0.4$ of a jet are excluded.

The events are required to contain exactly one reconstructed lepton candidate with $p_{\mathrm{T}} > 25\,\mathrm{GeV}$ and at least four jets with $p_{\mathrm{T}} > 25\,\mathrm{GeV}$ and $|\eta| < 2.5$. At least two of the jets have to be b-tagged.

Dilepton events where only one lepton passes the fiducial selection are by definition included in the fiducial measurement, but need to be corrected for in the parton-level measurements since the full phase space is only defined for true ℓ+jets events.

In summary, events with an isolated electron or a muon in the final state are selected, meaning that leptonic decays of the tau are also considered. In more detail, at particle level, a direct lepton–W match (where direct match means the lepton must come directly from a W decay) is not required, but we require an indirect W match (a W must be one of the ancestors of the lepton). With this requirement we accept the tau as a parent of the electron or a muon only if the tau itself comes from a W. We reject leptons that come from a quark or a hadron. In effect, the selected leptons come from a W without any hadron in between (i.e. $W \to \nu\tau(\to \text{hadron} \to \ell\nu)$ are not selected).

4.4 Parton-level objects and full phase-space definition

Parton-level objects are defined for simulated events. Only top quarks decaying directly to a W boson and a b-quark in the simulation are considered. These particles are labelled by a status code 155 in Herwig, 3 in Pythia and 22 in Pythia8 respectively. The full phase-space for the measurements presented in this paper is the one characterised by the $t\bar{t}$ pairs in which one top quark decays semileptonically (including τ leptons) and the other decays hadronically. Events in which both top quarks decay semileptonically define the dilepton background, and are thus removed from the signal simulation.

4.5 Matching

Matching between objects forming pseudotop quarks (see Section 5.2) at detector and particle levels is needed in order to define the matching correction (see Sec. 6.3.2) that corrects for resolution effects in the unfolding procedure. The simple geometric ΔR algorithm matches reconstructed objects constituting the pseudo-top quarks to particle-level

objects constituting the pseudo-top quarks at particle level and satisfying the fiducial requirements. Each particle-level e (μ) is matched to the closest reconstructed e (μ) within $\Delta R < 0.02$. Particle jets are geometrically matched to the closest reconstructed jet within $\Delta R_{\text{reco-jet,particle-jet}} < 0.4$. If a reconstructed jet is not matched to a particle jet, it is assumed to be either from pile-up or matching inefficiency and is treated as background. If two jets are reconstructed within $\Delta R_{\text{reco-jet,particle-jet}} < 0.4$ of a single particle jet, the reconstructed jet with smaller $\Delta R_{\text{reco-jet,particle-jet}}$ is matched to the particle jet and the other reconstructed jet is unmatched.

Chapter 5

Pseudo-top reconstruction algorithm

This chapter first gives an overview of the $t\bar{t}$ differential cross sections as function of several kinematical observables (Sec. 5.1), then it describes in details the top reconstruction algorithm (Sec. 5.2). Last, new kinematical variables besides the canonical ones are introduced with the aim to better study the central production region (Sec. 5.3).

5.1 Overview

In order to test perturbative QCD models that are used in the theory of top pair production in hadron colliders, more detailed measurements are needed with respect to the inclusive cross-section that gives a general indication of whether QCD can account for the total $t\bar{t}$ production. A precise measurement of the single differential cross-sections for the production of the top pair system will allows more stringet tests of the predictions of pQCD, known at to NNLO, and will gives us the possibility to better determine the gluon dendity in the proton.
For hadron collisions, incoming partons can be analysed in terms of the PDF values probed and their rapidity. For massless partons, their momenta can be written as $p_1^\mu = P(x_1, 0, 0, x_1)$, $p_2^\mu = P(x_2, 0, 0, -x_2)$ where x_1, x_2 are the fractions of the proton's momentum that they carry, P is the absolute value of the proton's momentum and s is the centre of mass energy squared. Then, the partonic centre of mass energy squared can be written as $\hat{s} = x_1 x_2 s$. The rapidity of the pair is given by $y = \frac{1}{2}\log\frac{x_1}{x_2}$ and we thus have $x_1 = \sqrt{\frac{\hat{s}}{s}}e^{y}$ and $x_2 = \sqrt{\frac{\hat{s}}{s}}e^{-y}$.
At leading order, the top pair is the only product of the collision and so the 4−momentum

of $t\bar{t}$ system will be equivalent to the 4-momentum of the partonic system, thus the rapidity of the top and anti-top quarks and their transverse mass can be related to the x-Bjorken values characterising the partons being probed for a given collision; for instance by referring to the transverse mass of top quark $m_T = \sqrt{m_t^2 + p_T^2}$, we have $x_1 = \frac{m_T}{\sqrt{s}}(e^{y_t} + e^{y_{\bar{t}}})$ and $x_2 = \frac{m_T}{\sqrt{s}}(e^{-y_t} + e^{-y_{\bar{t}}})$.

Of course, beyond leading order, extra radiation can be produced, resulting in non-zero transverse momentum p_T of the top pair. The measurements of differential cross-sections hence will also allow to test the initial and final state radiation models implemented in the MC programs used in this analysis. It is also interesting to compare the NLO matrix element generators matched to a shower MC with the LO multi-leg generators, which have explicit calculations for extra radiation.

To fully constraining the PDF, a complete knowledge of the kinematics of the system, as far as experimentally is achievable, is required. In this thesis, we consider the kinematic variables y, p_T and m of the top and anti-top and $t\bar{t}$ system.

Further motivation for measuring the kinematics of top pair production is that hints for physics beyond the standard model may show up in these distributions. For instance a high-mass resonance decaying to top quarks would produce an enhancement of the top cross-section at high $m_{t\bar{t}}$, and further probes of the angular distributions of the top pair would distinguish the spin of the resonances [120], while the p_T distributions of the individual top quarks has been shown to be sensitive to new physics effects [121]. Furthermore the top quark is an important background to most new physics searches. For instance, searches for supersymmetry (SUSY) typically concentrate on finding final states particles which decay through a chain of new particle states and produce a high p_T lepton [122]. The final experimentally observable decay products are then several high p_T jets, leptons and E_T^{miss}, which is of course the same as the final state produced by top production. Since SUSY particles are typically expected to be heavier than the top, the searches for these particles need to explore the high p_T tails of the spectra. Because in this regime there are large extrapolation uncertainties, it can be important to constraining the top pair modelling, because the uncertainties can be reduced.

5.2 Pseudo-top reconstruction algorithm

These measurements are carried out by means of a top-quark observable referred to as the pseudo-top quark, already deployed in a previous publication by the ATLAS Experiment on the same subject[28]. The pseudo-top quarks are defined by a combination of the final state objects, specifically jets, charged leptons (electrons or muons) and missing transverse energy. In this new measurement, we make use of a slightly revised version of

the pseudo-top algorithm, the only difference being in the reconstruction of the hadronically decaying W bosons (explained in details below). While in the older version of that algorithm the hadronic W boson was reconstructed from the two non-b tagged jets with the highest transverse momentum p_T, in the new version of the algorithm used in this analysis, it is reconstructed in a combination such that its invariant mass is as close as possible to the W mass.

The pseudo-top algorithm reconstructs the kinematics of the top quarks and their complete decay chain from a choice of final state objects, namely the charged lepton (electron or muon), missing transverse energy, and four narrow jets, two of which identified as coming from the hadronization of a b-quark. By running the same algorithm on detector- and particle-level objects, the degree of dependency on the details of the Monte Carlo simulation is strongly reduced compared to a parton-level kinematic fit with transfer functions while still keeping a strong correlation to the kinematics of the top quarks at the parton level.

The new and re-optimised version af the pseudo-top algorithm leads to a better correlation of pseudo-top objects to the parton level top quarks. The algorithm yields very good diagonality between particle and reco levels. The general idea is to keep the algorithm simple (e.g. for RIVET applications) and to remove the mass cuts on hadronic W or reconstructed top quark masses, in order to avoid issues of different scales and resolutions at particle and reco levels. RIVET is a tool used in phenomenology studies, whereby MC generator authors can automatically hook their generator up to compare with experimental data. It can also then be used to tune the phenomenological parameters that are needed to describe the non-perturbative shower evolution and other effects.

The pseudo-top algorithm is defined as follows:

1. Reconstruct the four-momentum of the neutrino which appears in the decay chain $t \to Wb \to \ell\nu b$:

   (a) Estimate the z-component of the neutrino momentum by applying the W boson mass constraint, using the measured W boson mass, $m_W = 80.399$ GeV [123], and the components of the missing transverse momentum vector (denoted as $p_{x,\nu}$, $p_{y,\nu}$) associated with the W boson decay neutrino. The $p_{z,\nu}$ of the neutrino can be constrained as follows:

   $$(E_l + E_\nu)^2 - (p_{x,l} + p_{x,\nu})^2 - (p_{y,l} + p_{y,\nu})^2 - (p_{z,l} + p_{z,\nu})^2 = m_W^2 \qquad (5.1)$$

   where the subscript l refers to either the electron or muon. Neglecting the

neutrino mass the $p_{z,\nu}$ of the neutrino is taken from the solution of the resulting quadratic equation:

$$p_{z,\nu} = \frac{-b \pm \sqrt{b^2 - 4ac}}{2a} \tag{5.2}$$

where

$$a = E_l^2 - p_{z,l}^2 \tag{5.3}$$
$$b = -2kp_{z,l} \tag{5.4}$$
$$c = E_l^2 p_{T,\nu}^2 - k^2 \tag{5.5}$$

and with

$$k = \frac{m_W^2 - m_l^2}{2} + (p_{x,l}p_{x,\nu} + p_{y,l}p_{y,\nu}). \tag{5.6}$$

If the resulting quadratic equation has two real solutions, take the one with smallest absolute value of $|p_z|$. If the determinant is negative, drop the imaginary part of the solution with smallest $|p_z|$. This is performed at both detector and particle levels, where in the latter the truth missing transverse energy is computed from neutrinos from the truth record, excluding those coming from the decay of hadrons. The particle-level true information on p_z^ν is not used.

(b) The components of the four-momentum of the neutrino in the $(p_x, p_y, p_z; m)$ representation are given by:

$$P^\nu = \left(E_x^{\text{miss}}, E_y^{\text{miss}}, p_z^\nu, 0\right) , \tag{5.7}$$

where $E_x^{\text{miss}} \equiv p_{x,\nu}$ and $E_y^{\text{miss}} \equiv p_{y,\nu}$, and with the p_z^ν coming from the $m_{\ell\nu} = m_W$ constrain, as we just saw, applied at both detector and particle levels.

2. Reconstruct the leptonic W boson which underwent the leptonic decay $W \to \ell\nu$ from the sum of the charged lepton and the neutrino;

3. Reconstruct the leptonic top quark from the sum of the leptonic W and the b-tagged jet closest in ΔR to the charged lepton;

4. Reconstruct the W boson which underwent the hadronic decay $W \to q\bar{q}'$ from the sum of the two non-b-tagged jets chosen in the combination in which the invariant mass of that system is the closest to the mass of the W boson, by imposing the usual W mass constraint:

$$(E_{lj_1} + E_{lj_2})^2 - (p_{x,lj_1} + p_{x,lj_2})^2 - (p_{y,lj_1} + p_{y,lj_2})^2 - (p_{z,lj_1} + p_{z,lj_2})^2 = m_W^2 \tag{5.8}$$

where the lj_1 and lj_2 indices are referred to the two light jets originating from the hadronically decaying W boson. This choice yields the best performance of the algorithm in terms of the correlation between detector, particle and parton levels.

5. Last, reconstruct the hadronic top quark from the sum of the hadronic W boson and the remaining b-jet.

In events with more than two b-tagged jets, only the two with the highest transverse momentum are considered.

Figures 5.1 and 5.2 show the determinant of the quadratic equation in solving the neutrino's longitudinal momentum, and the correlation between the reconstructed and particle levels.

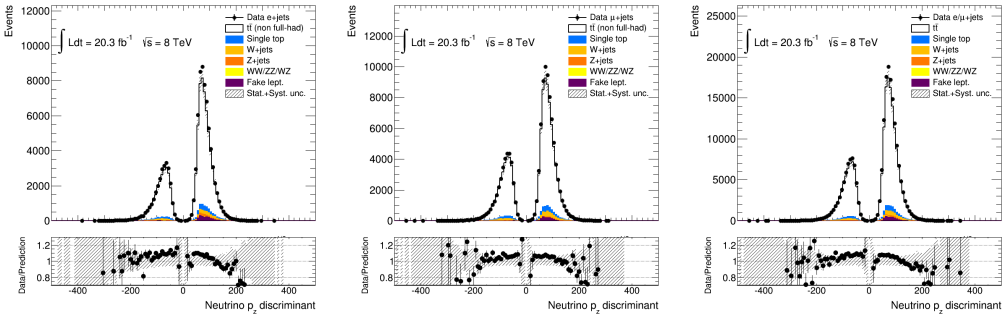

FIGURE 5.1: The determinant (D) of the quadratic equation used to measure the neutrino p_z momentum component.

A set of measurements of the $t\bar{t}$ production cross-sections is presented as a function of kinematic observables. In the following, the indices *had* and *lep* refer to the hadronically and leptonically decaying top quarks, respectively. The indices 1 and 2 refer respectively to the leading and sub-leading top quark, ordered by transverse momentum.

First, a set of baseline observables is presented: transverse momentum ($p_{\mathrm{T}}^{t,\mathrm{had}}$), absolute value of the rapidity ($\left|y^{t,\mathrm{had}}\right|$) and mass ($m_t^{had}$) of the hadronically decaying top quark (which was chosen over the leptonic top quark due to better resolution), and the transverse momentum ($p_{\mathrm{T}}^{t\bar{t}}$), absolute value of the rapidity $\left(\left|y^{t\bar{t}}\right|\right)$ and invariant mass ($m^{t\bar{t}}$) of the $t\bar{t}$ system. These observables, shown in Figures 5.3 and 5.4, have been previously measured by the ATLAS experiment using the 7 TeV dataset [27, 28] except for $\left|y^{t,\mathrm{had}}\right|$ which has not been measured in the full phase-space. The level of agreement between data and prediction is within the quoted uncertainties for $\left|y^{t,\mathrm{had}}\right|$, $m^{t\bar{t}}$ and $p_{\mathrm{T}}^{t\bar{t}}$. A trend is observed in the $p_{\mathrm{T}}^{t,\mathrm{had}}$ distribution, which is not well modelled at high values. A fair agreement between data and simulation is observed for large absolute values of the $t\bar{t}$ rapidity.

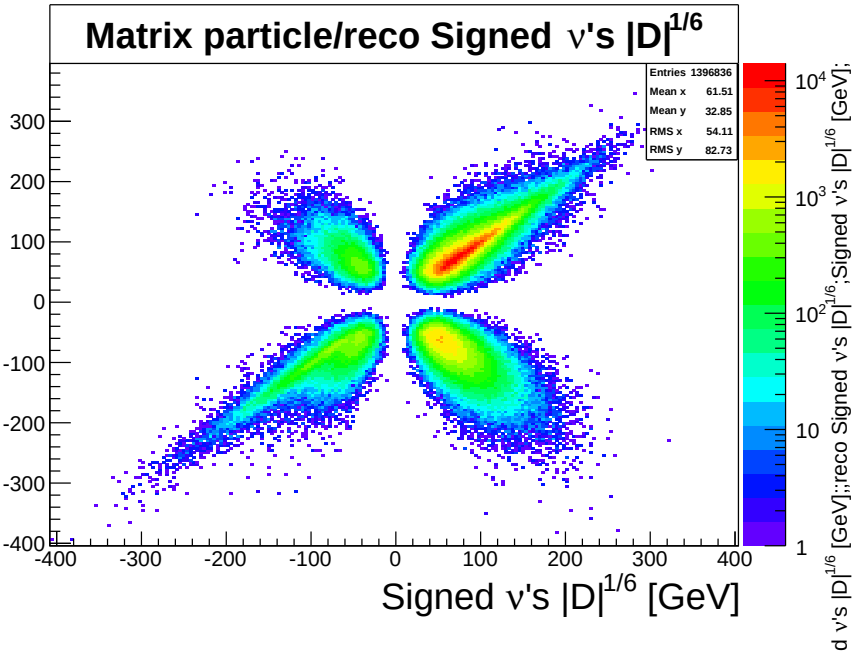

FIGURE 5.2: The correlation of the determinant of the quadratic equation between the particle (x-axis) and reconstructed (y-axis) levels. The signed $|D^{1/6}|$ is actually plotted, where the sign corresponds to the sign of the D.

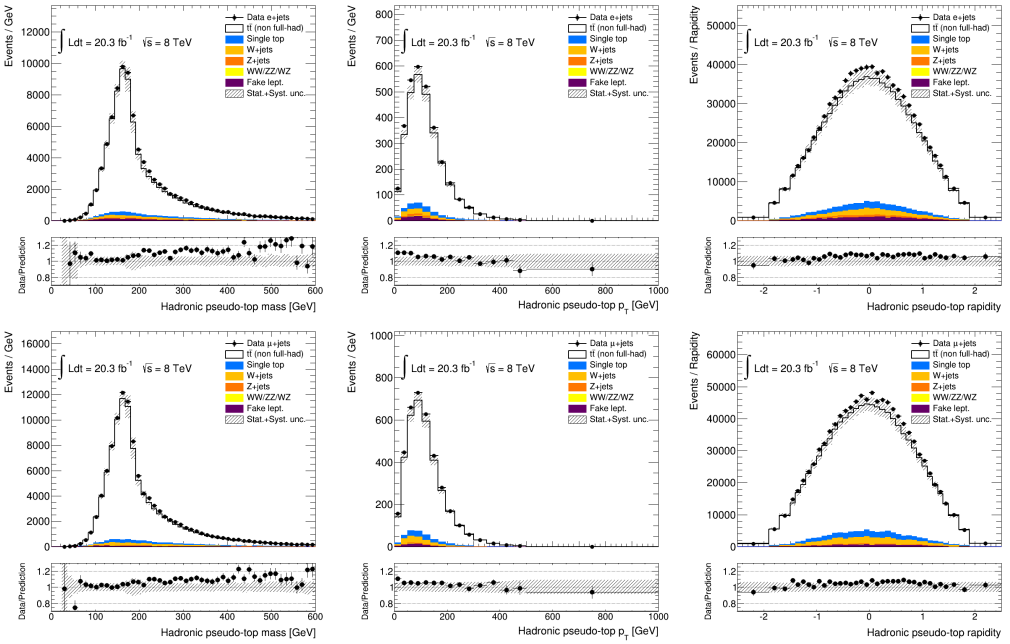

FIGURE 5.3: Mass (left), transverse momentum (center) and rapidity (right) of the reconstructed hadronic pseudo-top quark in the e+jets (top) and μ+jets (bottom) channels. The shaded area represents the total statistical and systematic uncertainties on the expected number of events.

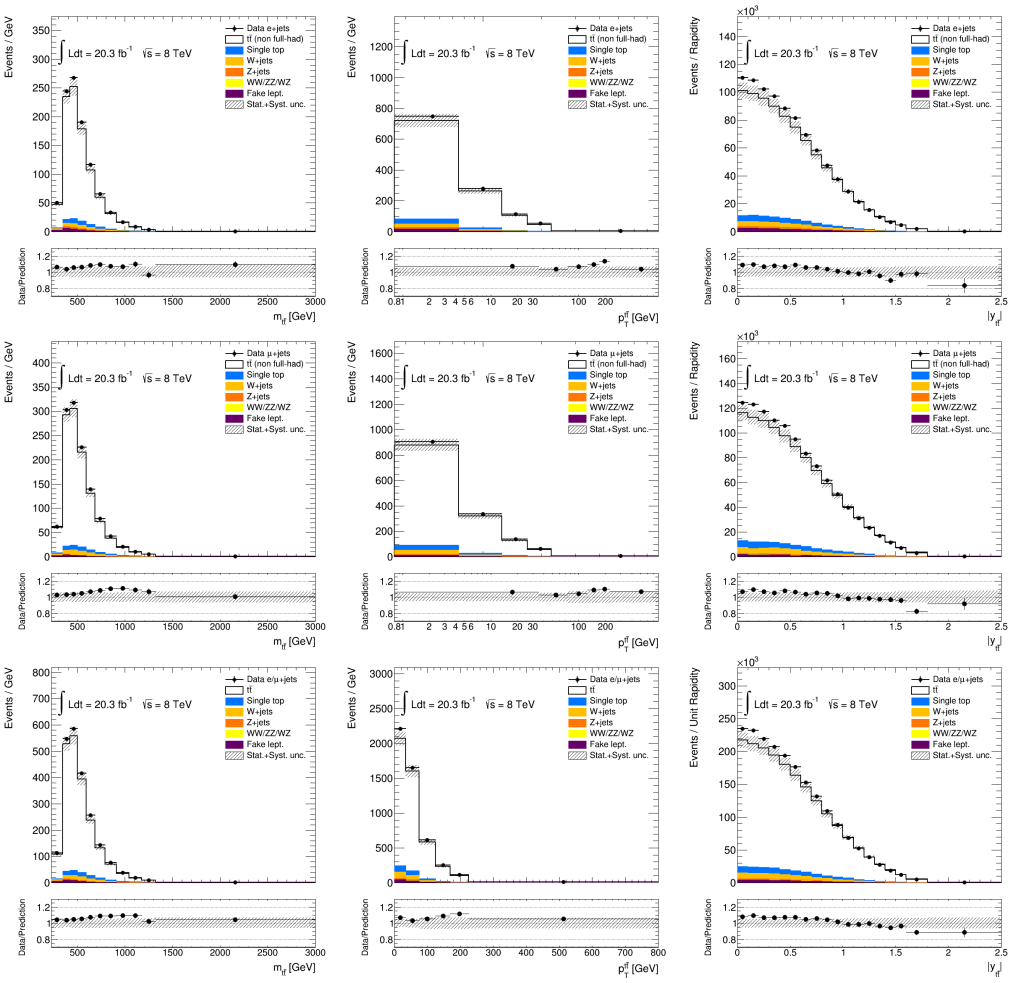

FIGURE 5.4: Invariant mass (left), transverse momentum (center) and the absolute value of the rapidity (right) of the reconstructed pseudo-$t\bar{t}$ system in the e+jets (top), μ+jets (center) and combined ℓ+jets (bottom) channels. The shaded area represents the total statistical and systematic uncertainties on the expected number of events.

For completeness in Figure 5.5 are also presented baseline kinematic variables related to the leptonically decaying top quark ($p_{\mathrm{T}}^{t,\mathrm{lep}}$,$\left|y^{t,\mathrm{lep}}\right|$, m_t^{lep}), while in Figures 5.6 and 5.7 both the leptonic- and hadronic-W ones ($p_T^{W,lep}$, $p_T^{W,had}$, $\mid y_W^{lep} \mid$, $\mid y_W^{had} \mid$, m_W^{lep} and m_W^{had}) are presented. The level of agreement between data and prediction is within the quoted uncertainties for absolute value of rapidity of both the hadronic and leptonic W, but for their transverse momentum and mass the agreement is worst in the tails of the distributions in which are present statistical fluctuations; the same behaviour is observed for the leptonic pseudo-top spectra ($p_{\mathrm{T}}^{t,\mathrm{lep}}$, $\left|y^{t,\mathrm{lep}}\right|$, m_t^{lep}).

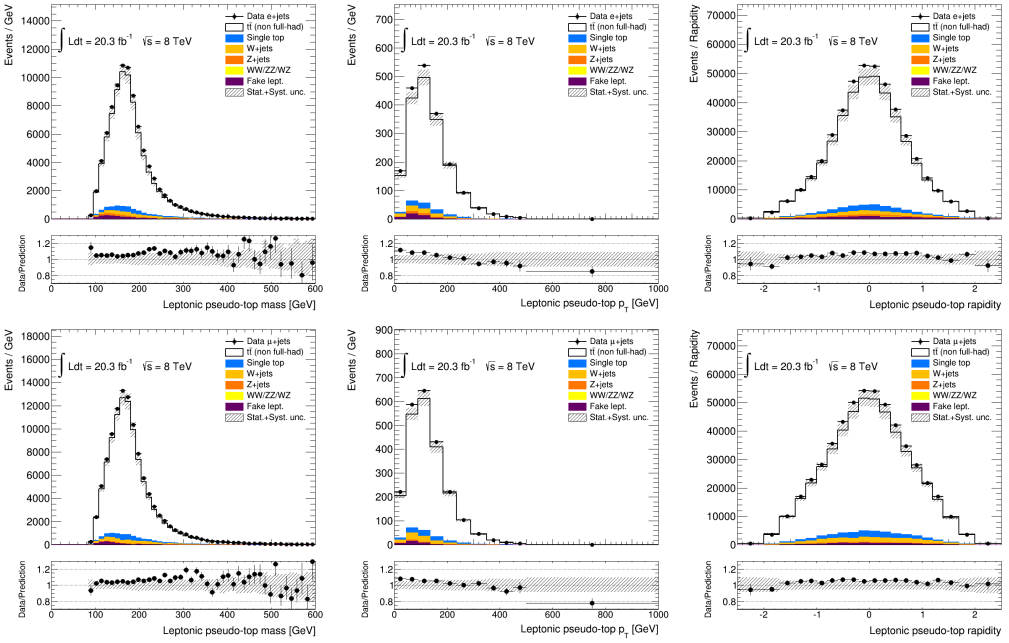

FIGURE 5.5: Mass (left), transverse momentum (center) and rapidity (right) of the reconstructed leptonic pseudo-top quark in the e+jets (top) and μ+jets (bottom) channels. The shaded area represents the total statistical and systematic uncertainties on the expected number of events.

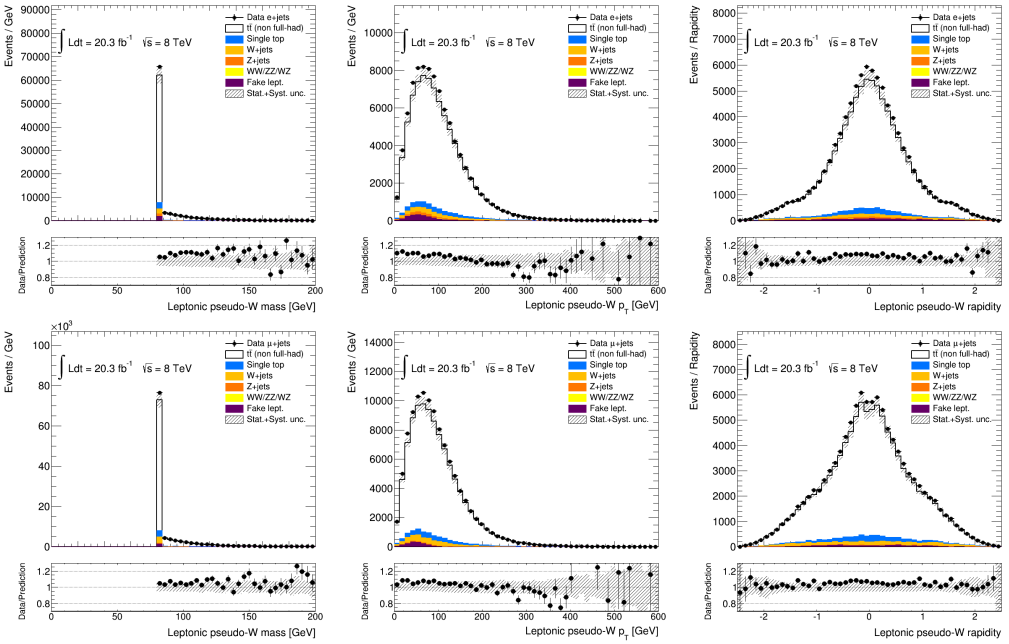

FIGURE 5.6: Mass (left), transverse momentum (center) and rapidity (right) of the reconstructed leptonic pseudo-W boson in the e+jets (top) and μ+jets (bottom) channels. The shaded area represents the total statistical and systematic uncertainties on the expected number of events.

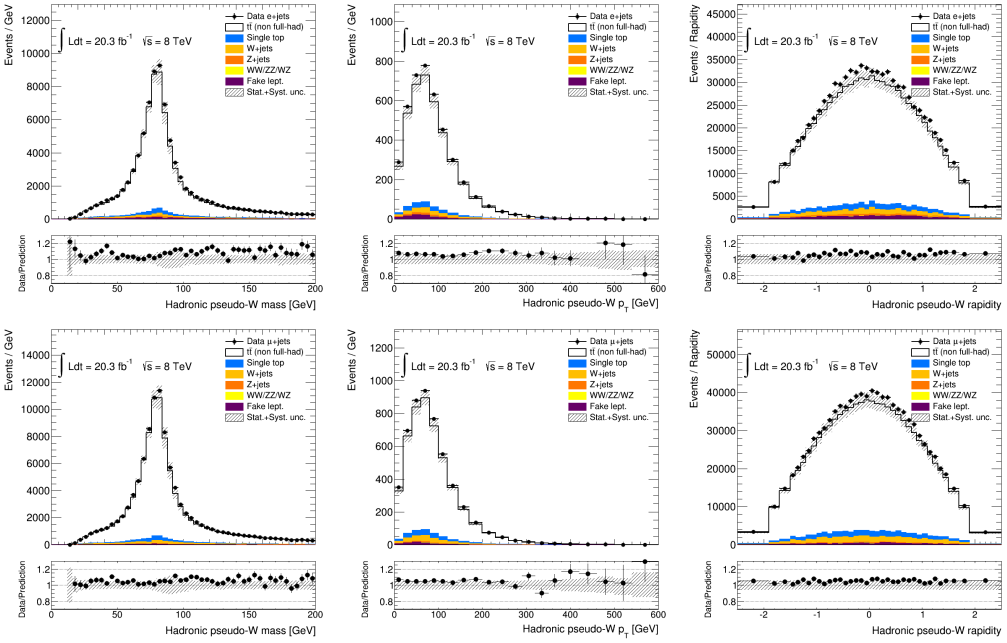

FIGURE 5.7: Mass (left), transverse momentum (center) and rapidity (right) of the reconstructed hadronic pseudo-W boson in the e+jets (top) and μ+jets (bottom) channels. The shaded area represents the total statistical and systematic uncertainties on the expected number of events.

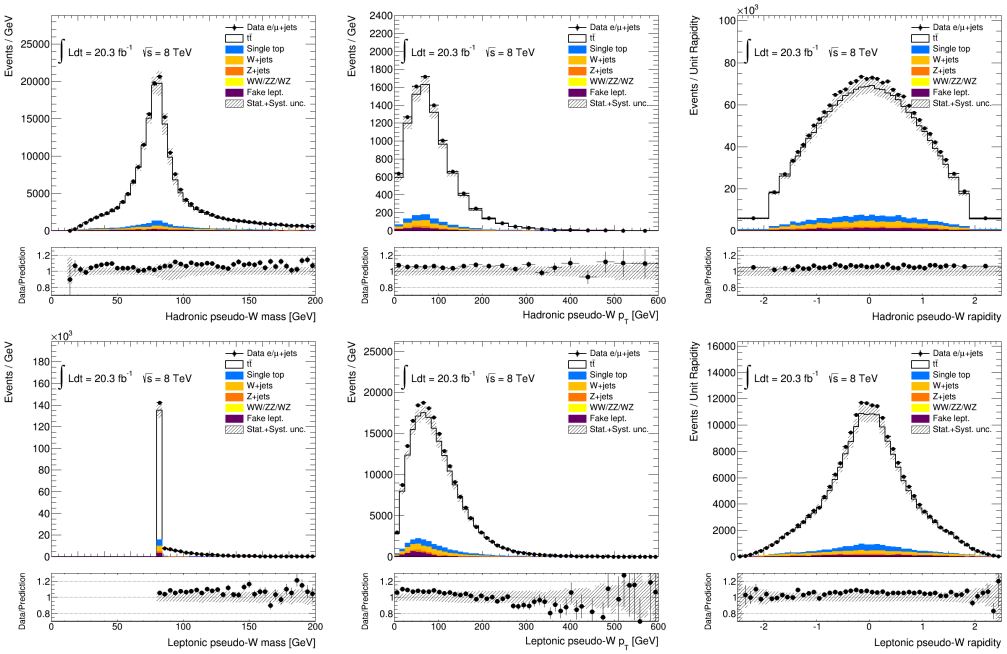

FIGURE 5.8: Mass (left), transverse momentum (center) and rapidity (right) of the reconstructed leptonic pseudo-W boson (top) and reconstructed hadronic pseudo-W boson (bottom) in the combined ℓ+jets channel. The shaded area represents the total statistical and systematic uncertainties on the expected number of events.

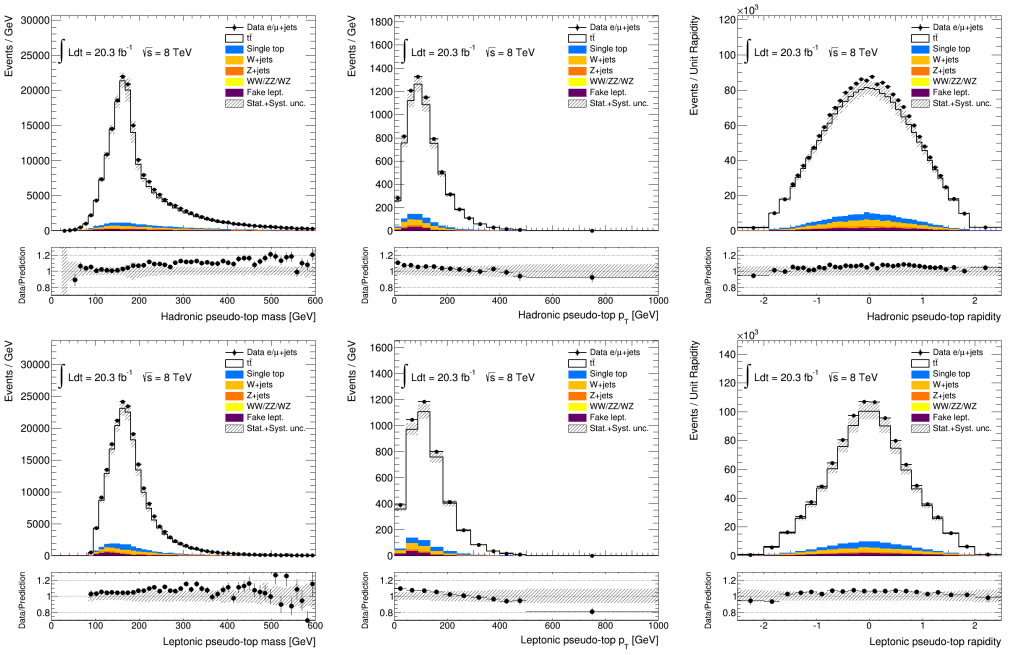

FIGURE 5.9: Mass (left), transverse momentum (center) and rapidity (right) of the reconstructed hadronic pseudo-top quark (top) and reconstructed leptonic pseudo-top quark (bottom) in the combined ℓ+jets channel. The shaded area represents the total statistical and systematic uncertainties on the expected number of events.

5.3 Extra observables

Besides the canonical kinematical variables of the hadronic-, leptonic-top and $t\bar{t}$ system, a set of new measurements is also presented. Angular variables sensitive to a p_{T} imbalance in the transverse plane, *i.e.* to the emission of radiation associated with the production of the top-quark pair, are employed to emphasize the central production region [32]. The angle between the two top quarks has been found to be sensitive to non-resonant contributions due to hypothetical new particles exchanged in the t-channel [31]. The rapidities of the two top quarks in the laboratory frame are denoted by $y^{t,1}$ and $y^{t,2}$, while their rapidities in the $t\bar{t}$ centre-of-mass frame are $y^{\star} = \frac{1}{2}\left(y^{t,1} - y^{t,2}\right)$ and $-y^{\star}$. The longitudinal motion of the $t\bar{t}$ system in the laboratory frame is described by the rapidity boost $y^{t\bar{t}}_{\mathrm{boost}} = \frac{1}{2}\left[y^{t,1} + y^{t,2}\right]$ and the production angle $\chi^{t\bar{t}} = e^{2|y^{\star}|}$. In particular, many signals due to processes not included in the Standard Model are predicted to peak at low values of $\chi^{t\bar{t}}$ [31]. Finally, observables depending on the transverse momentum of the decay products of the top quark have been found to be sensitive to higher-order corrections [34, 35].

Therefore the following additional variables are measured:

- the absolute value of the azimuthal angle between the two top quarks ($\Delta\phi^{t\bar{t}}$);
- the absolute value of the out-of-plane momentum ($\left|p^{t\bar{t}}_{\mathrm{out}}\right|$), *i.e.* the projection of top-quark three-momentum onto the direction perpendicular to a plane defined by the other top quark and the beam axis (z) in the laboratory frame [32]:

$$\left|p^{t\bar{t}}_{\mathrm{out}}\right| = \left|\vec{p}^{\,t,\mathrm{had}} \cdot \frac{\vec{p}^{\,t,\mathrm{lep}} \times \hat{z}}{|\vec{p}^{\,t,\mathrm{lep}} \times \hat{z}|}\right| ; \tag{5.9}$$

- the longitudinal boost of the $t\bar{t}$ system in the laboratory frame ($y^{t\bar{t}}_{\mathrm{boost}}$) [31];
- the production angle between the two top quarks ($\chi^{t\bar{t}}$) [31];
- the scalar sum of the transverse momenta of the two top quarks ($H^{t\bar{t}}_{\mathrm{T}}$) [34, 35]
- the p_{T} ratios of the decay products of the top quark:

$$R_{lb} = \frac{p_T^{lj,1} + p_T^{lj,2}}{p_T^{bj,1} + p_T^{bj,2}} \tag{5.10}$$

$$R_{Wb} = p_T^W / p_T^b \tag{5.11}$$

$$R_{Wt} = p_T^W / p_T^t \tag{5.12}$$

where the light jets 1 and 2 are coming from the hadronic W boson. The transverse momenta of these objects are indicated by the symbols $p_T^{lj,1}$ and $p_T^{lj,2}$ (light jets),

p_T^W (W boson), p_T^b (bottom quark) and p_T^t (top quark). These ratio variables are sensitive to higher-order QCD effects (R_{Wb}, R_{Wt}) [34, 35], as for example the exchange of gluons among quarks from the decay of the W boson and proton remnants, or to experimental uncertainties related to the b-jet energy scale (R_{lb}).

These observables are shown in Figures 5.10 5.11 5.12 5.13 at detector level.

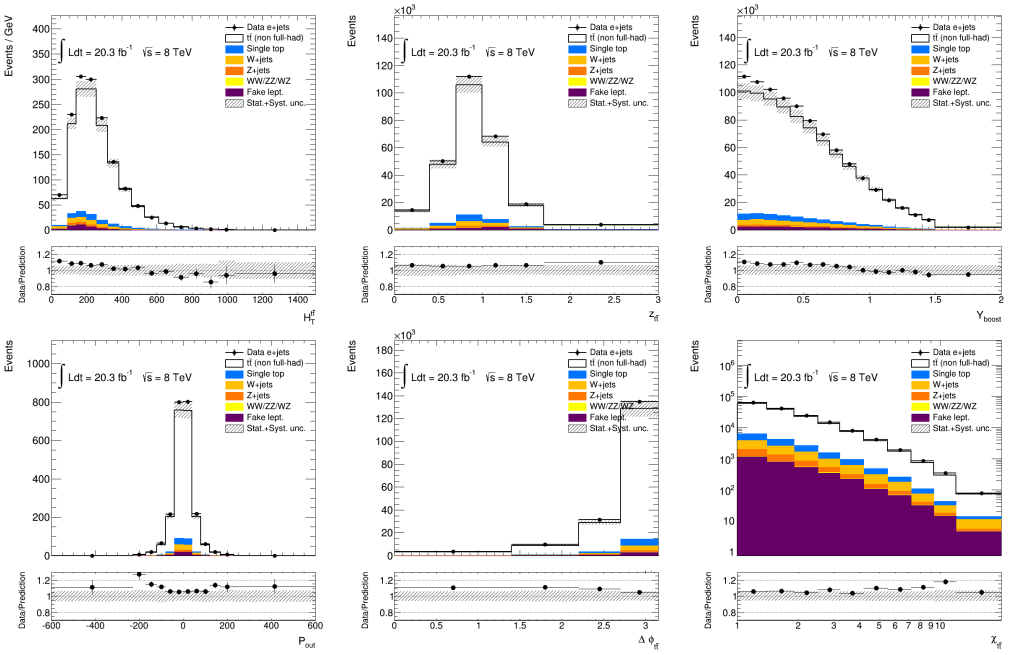

FIGURE 5.10: Additional observables describing the kinematics of top-antitop pairs in the e+jets channel. From the top-left to the bottom-right: $H_{\mathrm{T}}^{t\bar{t}}$, $z^{t\bar{t}}$, $y_{\mathrm{boost}}^{t\bar{t}}$, $p_{\mathrm{out}}^{t\bar{t}}$, $\Delta\phi^{t\bar{t}}$ and $\chi^{t\bar{t}}$. The shaded area represents the total statistical and systematic uncertainties on the expected number of events.

All these variables show only modest agreement with data. In particular, at high values of $H_{\mathrm{T}}^{t\bar{t}}$, fewer events are observed with respect to the prediction. The longitudinal boost $y_{\mathrm{boost}}^{t\bar{t}}$ is predicted to be less central than the data. Finally, R_{Wt} is predicted to be lower than what has been observed in the range 1.5–3.0.

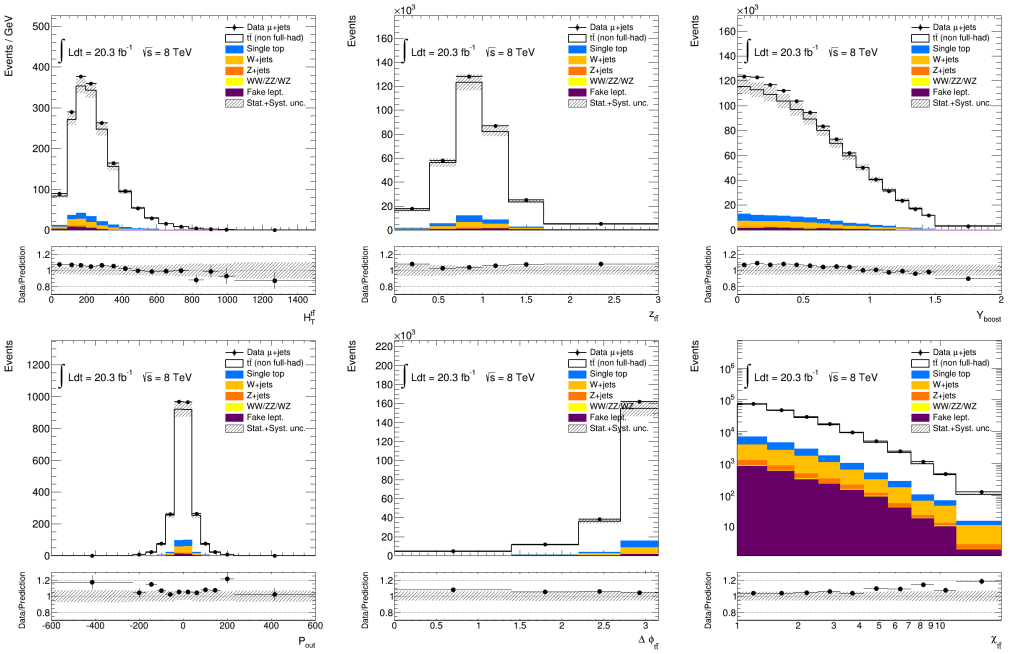

FIGURE 5.11: Additional observables describing the kinematics of top-antitop pairs in the μ+jets channel. From the top-left to the bottom-right: $H_{\mathrm{T}}^{t\bar{t}}$, $z^{t\bar{t}}$, $y_{\mathrm{boost}}^{t\bar{t}}$, $p_{\mathrm{out}}^{t\bar{t}}$, $\Delta\phi^{t\bar{t}}$ and $\chi^{t\bar{t}}$. The shaded area represents the total statistical and systematic uncertainties on the expected number of events.

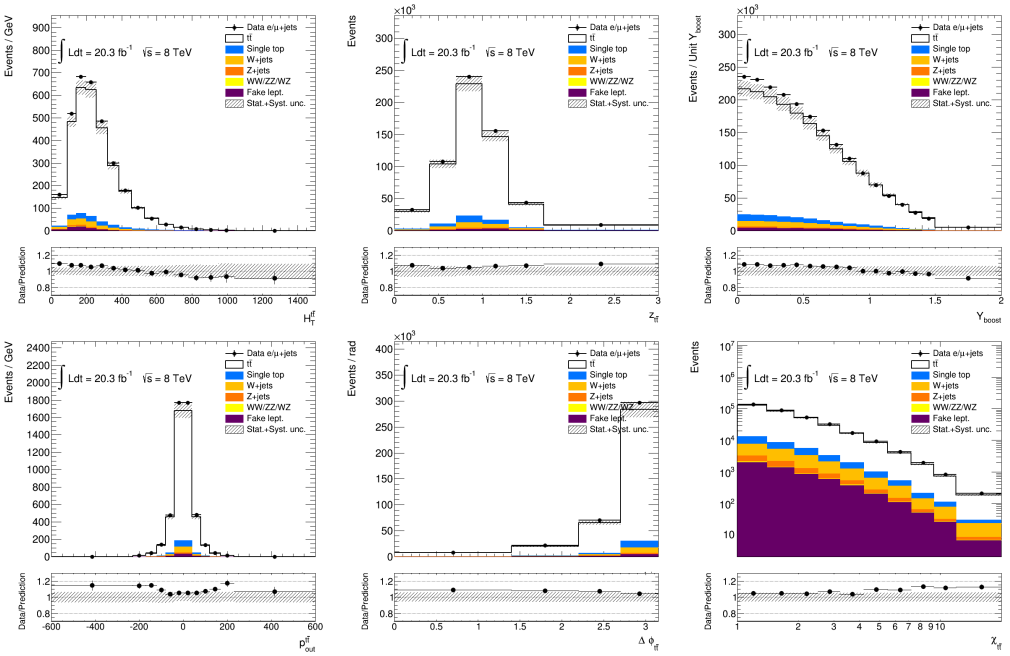

FIGURE 5.12: Additional observables describing the kinematics of top-antitop pairs in the ℓ+jets channel. From the top-left to the bottom-right: $H_{\mathrm{T}}^{t\bar{t}}$, $z^{t\bar{t}}$, $y_{\mathrm{boost}}^{t\bar{t}}$, $p_{\mathrm{out}}^{t\bar{t}}$, $\Delta\phi^{t\bar{t}}$ and $\chi^{t\bar{t}}$. The shaded area represents the total statistical and systematic uncertainties on the expected number of events.

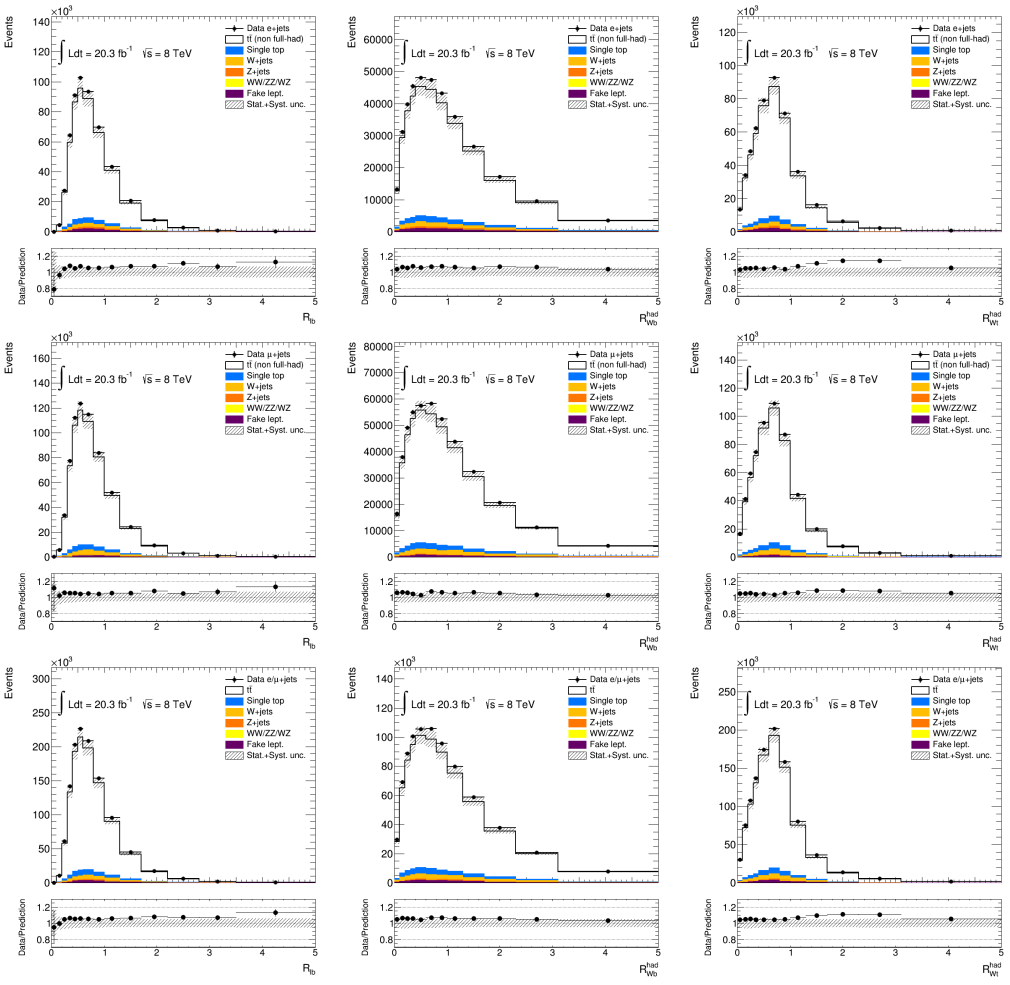

FIGURE 5.13: Additional observables describing the kinematics of the decay products of the top-antitop pairs in the e+jets (top), μ+jets (center) and ℓ+jets channels. From the left to the right: R_{lb}, R_{Wb}, R_{Wt}. The shaded area represents the total statistical and systematic uncertainties on the expected number of events.

Chapter 6

Analysis strategy

This chapter provides a detailed description of the analysis. In Sec. 6.1 and Sec. 6.2 the method used to combine the two different leptonic channels and the binning choice are described respectively; the unfolding technique used to measure the differential cross-sections in the fiducial and full phase-space is described in detail in Sec. 6.3. The systematics uncertainties affecting the measurements are described in Sec. 6.4, while in the last Section we describe the analysis framework (MAMbo [124]) used.

6.1 Combination of the analysis channel

Before applying any unfolding procedure the combination of the two channels is performed by adding together events of the two channels at the detector level in data in the proportion expected from the MC. Even though the e+jets and μ+jets efficiencies are slightly different, this simple combination method can be employed if their relative yield is the same in data and in MC, which is the case, as shown in Table 4.1. This method is further motivated by the fact that the efficiencies are comparable in e+jets and μ+jets channels.

In Figures 6.1 and 6.2 we show only a subsample of the efficiency corrections, with the remaining results of the efficiency corrections available in the Appendix C.1.2.

This approach properly accounts for all the correlations since the correlated uncertainties will add linearly while uncorrelated uncertainties, e.g. electron scale factors, will enter only through e+jets events and so will get properly added in quadrature to the other uncertainty sources. Since the largest uncertainties are common, the relative uncertainty on the combination is again similar to that observed in the individual channels.

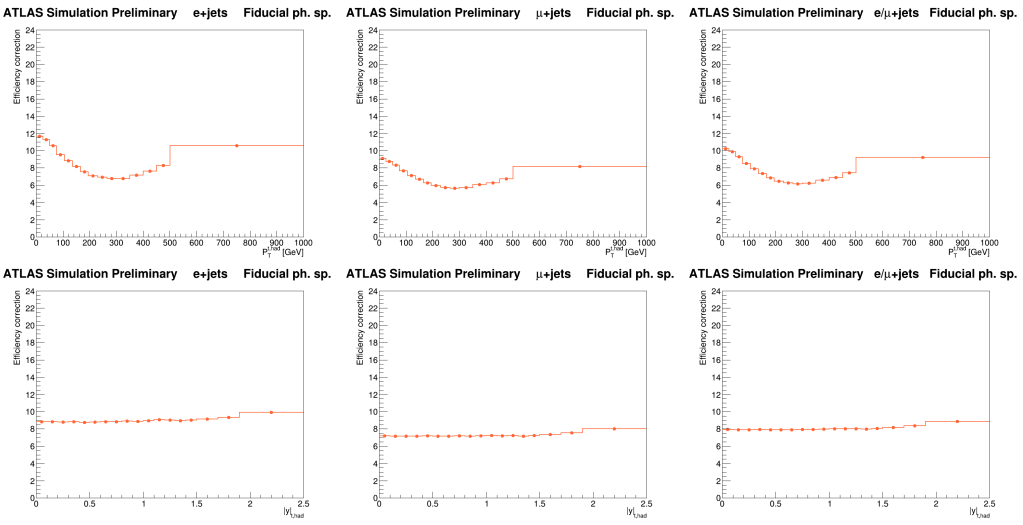

FIGURE 6.1: Efficiency corrections for the hadronic pseudo-top quark p_T (top) and absolute value of rapidity (bottom) in the e+jets (left), μ+jets (middle) and combined ℓ+jets channels.

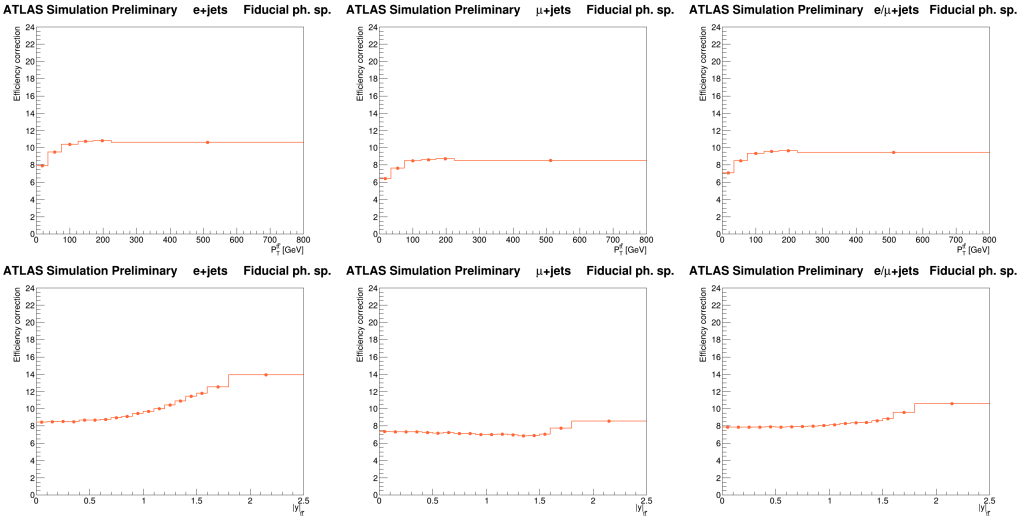

FIGURE 6.2: Efficiency corrections for the top quark pair p_T (top) and absolute value of rapidity (bottom) in the e+jets (left), μ+jets (middle) and combined ℓ+jets channels.

6.2 Binning choice

The binning optimization is based on the resolution of the ATLAS detector and is performed for each variable separately. The influence of the detector resolution is described by a migration matrix which relates a given variable at particle and reconstructed levels, for events passing also the matching criterion (see Section 6.3.2). Migration matrices were evaluated on simulation using a fine binning. The resolution is evaluated in each particle level bin of the migration matrix by looking at the profile distribution (binned in reconstructed quantities). The standard deviation of each profile is extracted using an iterative fit of a Gaussian distribution, see Figure 6.3.

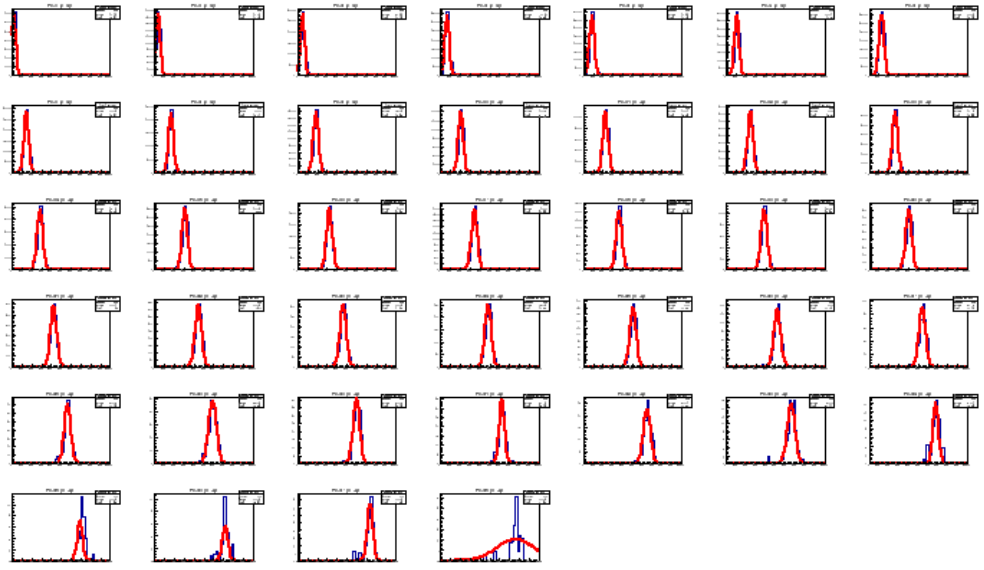

FIGURE 6.3: Example of fitted profiles for leptonic top transverse momentum with respect to particle level.

Each profile has been fitted three times, first by a Gaussian fit using mean value and standard deviation of the histogram as starting parameters. Next, a Gaussian fit using values of the mean and standard deviation from the preceding fit as starting parameters was performed. Finally, the variance parameter of the last Gaussian fit were plotted as a function of the particle-level quantity, and this resolution was fitted by a polynomial or exponential function. The choice of the function depended on further fit diagnostics. Example of a resolution fit taken from fitted profiles is shown in Figure 6.4.

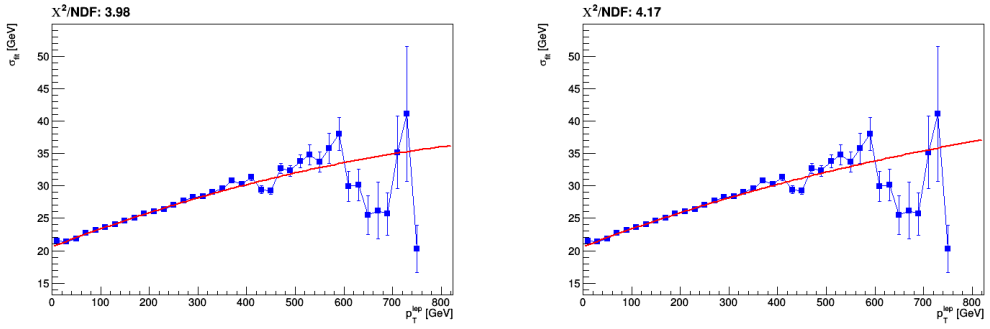

polynomial fit exponential fit

FIGURE 6.4: Final fit of the profiles standard deviation distributions of the leptonic top quark transverse momentum with respect to particle level.

This resolution-based binning has been derived by the following formula from the final fit of standard deviations of profile distributions:

$$\mathrm{Resol}(p_{\mathrm{N}-1}) = \frac{x_{\mathrm{N}} - x_{\mathrm{N}-1}}{2}, \tag{6.1}$$

where $\mathrm{Resol}(p_{N-1})$ is the resolution function for a given variable in the middle of the specified bin and x_N, x_{N-1} are bin edges. The factor of two on the right-hand side of the above equation stands for the fact that the bin width is required to be twice of the standard deviation of the profile, aiming to keep approximately 68% of events in the same reconstructed bin as was originally observed at the particle level.
Resulting matrices in optimized binning are plotted with labels describing how many events are in each bin in percentage. A couple of the optimized matrices is shown in Figures 6.5-6.6.

For each spectrum, the response matrix is constructed from all events that pass both the particle and detector level selection and the matching condition in the nominal $t\bar{t}$ MC sample. The migration matrix is then built from the response matrix by normalizing the detector bins in each particle-level bin to the sum of events in given particle-level bin. Therefore the main diagonal elements represents the probability for each generated event in a given bin to be effectively reconstructed in the same bin, viceversa off-diagonal elements represents the fraction of events that migrate into other bins. A collection of the remaining migration matrices of each spectrum is presented in the App. C.1.1. In general, good diagonality of the migration matrices is observed, with more than 50% of events staying on the diagonal. Bin edges were further rounded and sometimes the number of bins was reduced as a consequence of the result of the statistical fluctuations in MC closure tests as described in next subsection. Different binning is used for leptonic and hadronic top quarks, as the resolutions of their transverse momenta and rapidities is different. For the binning determination of the absolute rapidity, a fit to the resolution

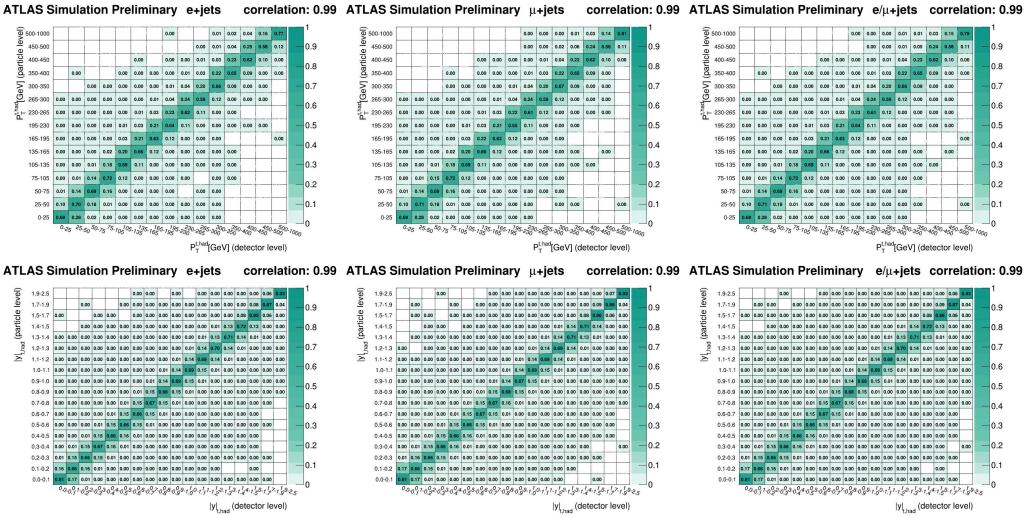

FIGURE 6.5: Migration matrix between detector and particle level for the hadronic pseudo-top quark p_T (top) and absolute value of rapidity (bottom) in the e+jets (left), μ+jets (middle) and combined ℓ+jets channel.

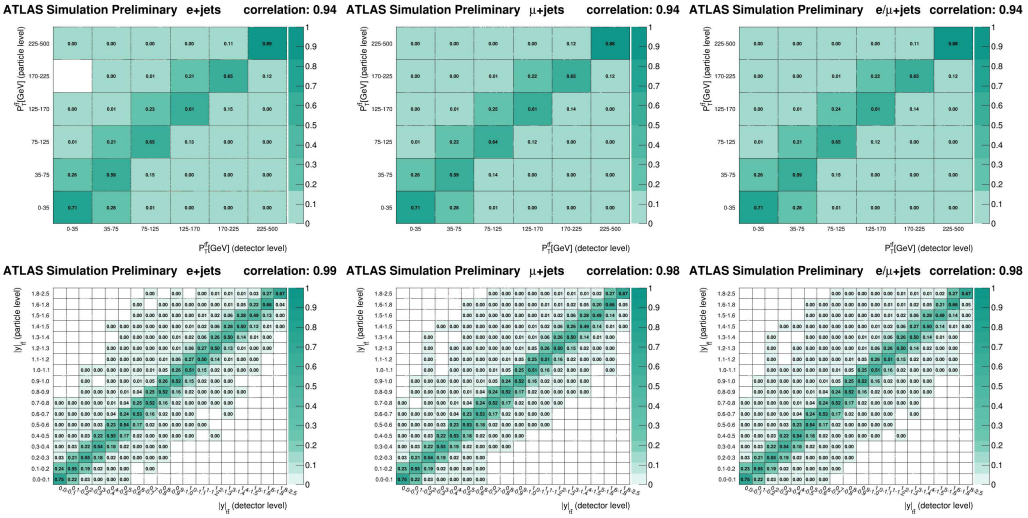

FIGURE 6.6: Migration matrix between detector and particle level for the top quark pair p_T (top) and absolute value of rapidity (bottom) in the e+jets (left), μ+jets (middle) and combined ℓ+jets channel.

was performed for the rapidity distribution, in order to avoid a non-Gaussian profile of the resolution as a function of $|y|$ when close to the origin.

6.3 Unfolding technique

In high energy physics experiments the measurement of a distribution $f(x)$ of some kinematical quantity x represents a standard task. In an ideal life one could measure the desired quantity x in every event and could obtain $f(x)$ as a simple histogram of the quantity x, but in the real life these measurements of physical observables are distorted or biased by the limited resolution and acceptance of the detector that does not allow a direct comparison of the measured distributions with the theoretical predictions. Therefore data must be corrected for these detector effects, making the measurements unconstrained from them and so allowing a comparison with theoretical predictions. This is performed through an *unfolding* technique. Therefore the determination of $f(x)$ is usually complicated by three effects: the *limited acceptance*, *transformation* and *finite resolution*.

The detector acceptance is the probability to observe a given event in the detector, less than 1, resulting in a certain loss of recorded events, depending on the kinematical observable x; it is treated by applying a bin dependent scale factor, evaluated from Monte Carlo, to rescale data to the predicted number of events. Transformation relates the "true" kinematical variable x with the measured one y, for instance these transformations can be caused by the non-linear response of a detector component. Last, the finite resolution effect is due to the limited accuracy of the detector and leads to a statistical smearing between the true kinematical variable x and the measured quantity y.

The relation between the distribution $f(x)$ of the true variable x, to be determined in an experiment, and the measured distribution $g(y)$ of the quantity y can be mathematically expressed by the integral equation:

$$g(y) = \int A(y,x) f(x) dx + b(y) \tag{6.2}$$

called a Fredholm integral equation of the first kind; where the distribution $b(y)$ has been added to the right-hand side representing a background contribution to the measured distribution $g(y)$. $A(y,x)$ is the resolution function and represents the detector effect, so that for a given value $x = x_0$ the resolution function $A(y,x_0)$ describes the response of the detector in the variable y for the fixed x_0 value.

The problem to determine the distribution $f(x)$ from measured ones $g(y)$, known the background distribution $b(y)$, is called unfolding, also known as *inverse problem*. Of course this technique requires the knowledge of the resolution function $A(y,x)$ that

contains all the effects of limited acceptance, transformation and finite resolution.
The inverse problem requires the calculatation of the inverse of the resolution function $A^{-1}(y,x)$. Furthermore, in high energy physics applications, the above approach is discretized so that the resolution function becomes a discrete matrix $(A(y,x) \rightarrow A)$ evaluated by Monte Carlo simulation; this is the Response Matrix (or Migration Matrix) previously described; this discretization approach also transform the functions $f(x)$ and $f(y)$ into histograms. Thus the integral (Eq. 6.2) is replaced by a system of linear equations:

$$y = Ax + b \tag{6.3}$$

which has to be solved for the vector x, given the vectors y and b. Usually the inversion problem is then aggravated by statistical and possible systematic errors of the response matrix itself.
In the following we describe the unfolding technique used in this analysis, the *Iterative Bayesian unfolding*.

Iterative bayesian

The starting point of the Bayesian unfolding method is to make the problem discrete and to treat the "cause" bins as independent degrees of freedom, i.e. without constraints among each other. Given the discretization of the problem, the Bayesian method relates causes and effects. In probabilistic terms, the purpose of the unfolding is to find the "true" number of events in each cause bin C_i, given the observed spectrum and assuming some knowledge about the smearing. Since the links cause→effects have a probabilistic nature, it follows that also the links effect→causes will be probabilistic, and therefore it will be uncertain the number of events to be attributed to the cause-cells. The algorithm can only attempt to rank in probability all possible spectra that might have caused the observed one. In other words, the realistic goal of the iterative bayesian unfolding is not to determine the true spectrum, but rather to assess the probability $P(C_i|E_j)$ that cause C_i is the real responsible for the effect E_j.
Therefore, the iterative bayesian method exploits the "cause and effect" problem [125]. Causes C_i correspond to the generated true values while effects E_j are the events effectively measured by the apparatus. Each cause can produce different effects, but for a given effect the exact corresponding cause is not known. However, the probability for a cause to generate a specific effect can be evaluated assuming some *a priori* knowledge, usually accomplished by Monte Carlo simulations. The Bayes Theorem allows to estimate the probability $P\left(x_C|x_E,\Lambda\right)$, given

the observation x_E and the smearing matrix Λ, as

$$P\left(x_C|x_E,\Lambda\right) = \frac{P\left(x_E|x_C,\Lambda\right)\cdot P_0\left(x_C\right)}{\sum_{x_C} P\left(x_E|x_C,\Lambda\right)\cdot P_0\left(x_C\right)} \tag{6.4}$$

where $P\left(x_E|x_C,\Lambda\right)$ is the so called *likelihood* while the left hand side of the Bayes' formula, Eq. 6.4, takes the name of *posterior*.
The basic trick of a practical algorithm to perform an independent-bin Bayesian unfolding [125], that it was used in this analysis work in order to obtain the differential cross sections, is to apply Bayes' theorem to causes and effects, instead than to the true and the observed spectrum, i.e. evaluating the probability $P(C_i|E_j)$ that the "cause" C_i is the real responsible for the effect E_j. In practice, instead of using of Eq.6.4 we start from:

$$P\left(C_i|E_j\right) = \frac{P\left(E_j|C_i\right)\cdot P_0\left(C_i\right)}{\sum_{k=1}^{n_C} P\left(E_j|C_k\right)\cdot P_0\left(C_k\right)} \tag{6.5}$$

where $P_0\left(C_i\right)$ is the prior probability for the cause C_i and n_C is the number of possible causes. The estimator for the number of causes in the $i-$th bin can be expressed as

$$\hat{n}\left(C_i\right) = \frac{1}{\epsilon_i}\sum_{j=1}^{n_E} n\left(E_j\right)\cdot P\left(C_i|E_j\right) \tag{6.6}$$

in which $n\left(E_j\right)$ represents the number of measured effects in the j-th bin and ϵ_i is the efficiency in each bin, evaluated with Monte Carlo simulations, that are defined as:

$$\epsilon_i = \sum_{j=1}^{n_E} \frac{n\left(E_j\right)^{MC}}{n\left(C_i\right)^{MC}}. \tag{6.7}$$

The $P\left(C_i \mid E_j\right)$ can be considered equivalents the ij-th element of an inverted migration matrix, expressed as follows:

$$M_{ij} = \frac{P\left(E_j|C_i\right)\cdot P_0\left(C_i\right)}{\sum_{h=1}^{n_E} P\left(C_i|E_h\right)\cdot\sum_{k=1}^{n_C} P\left(E_j|C_k\right)\cdot P_0\left(C_k\right)} \tag{6.8}$$

that leads to the following unfolding equation:

$$\hat{n}\left(C_i\right) = \sum_{j=1}^{n_E} M_{ij} n\left(E_j\right). \tag{6.9}$$

The new causes' probability can be expressed as

$$P_0'\left(C_i\right) = \frac{\hat{n}\left(C_i\right)}{\sum_{i=1}^{n_C}\hat{n}\left(C_i\right)} \tag{6.10}$$

by replacing the initial prior probability $P_0\left(C_i\right)$ for the cause C_i and the procedure

is reiterated n times until $P_0(C_i)$ and $P_0'(C_i)$ converge; for this analysis work the parameter of the iteration number n has been set equal to 4.

6.3.1 Unfolding validation

In order to find an optimal number of iterations for the Iterative Bayesian unfolding procedure, the dependence of a set of variables on the number of iterations n_{iter} has been studied. Furthermore a closure test is performed in order to demonstrate that the unfolding can recover the particle-level spectrum given the reconstructed spectrum.

6.3.1.1 Choice of the number of iterations for the iterative bayesian unfolding

With the aim to find an optimal number of iterations of the unfolding procedure the following quantities have been studied:

- bin-by-bin statistical error: $\sigma_i(n_{iter})$, where the index i runs over all bins;
- bin-by-bin posterior versus prior difference (called also residual): $\frac{N_i(n_{iter})-N_i(n_{iter-1})}{N_i(n_{iter})}$;
- posterior versus prior $\chi^2/NDF(n_{iter}, n_{iter}-1)$.

The number of iterations has been chosen as a compromise between low bin-by-bin statistical error (that tends to increase with the number of iterations) and low bin-by-bin residual (that tends to decrease with the number of iterations). This study has been performed for all the variables that are being unfolded and it has been observed that a choice of $n_{iter} = 4$ gives a general good compromise for all the spectra under study. An example of a such study, for $p_{\mathrm{T}}^{t\bar{t}}$, is shown in 6.7 (statistical error as a function of n_{iter}) and 6.8 (residual as a function of n_{iter}).

Finally, the posterior versus prior χ^2/NDF has been used as cross check. In general, for $n_{iter} = 4$, the $\chi^2(n_{iter}, n_{iter}-1)/NDF$ is below 1 and at the beginning of a *plateau*. The $\chi^2(n_{iter}, n_{iter}-1)/NDF$ for $p_{\mathrm{T}}^{t\bar{t}}$ is shown in 6.9.

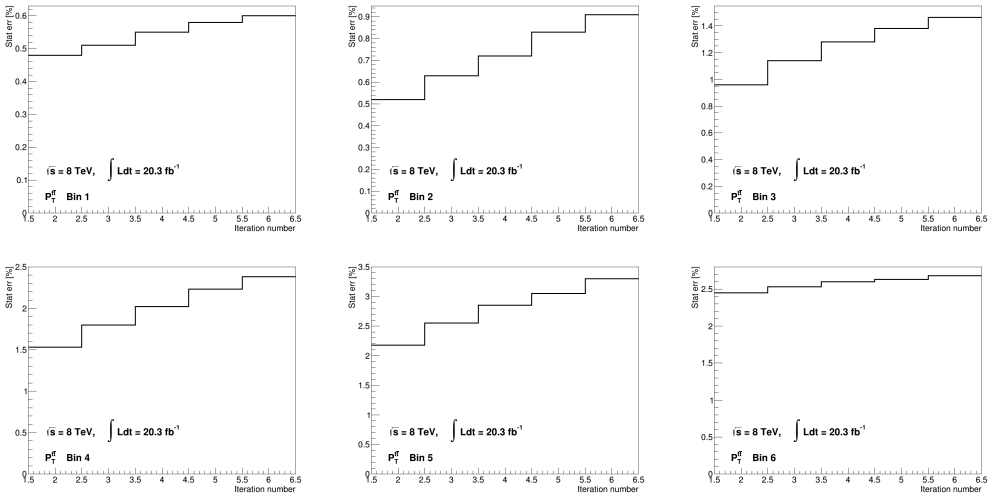

FIGURE 6.7: Bin by bin statistical error for $p_{\mathrm{T}}^{t\bar{t}}$ as a function of the number of iterations.

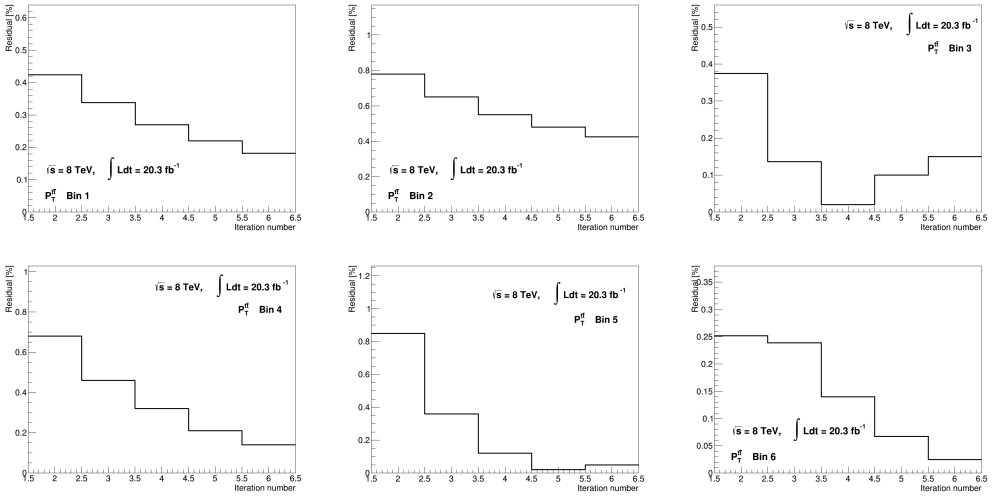

FIGURE 6.8: Bin by bin residual for $p_{\mathrm{T}}^{t\bar{t}}$ as a function of the number of iterations.

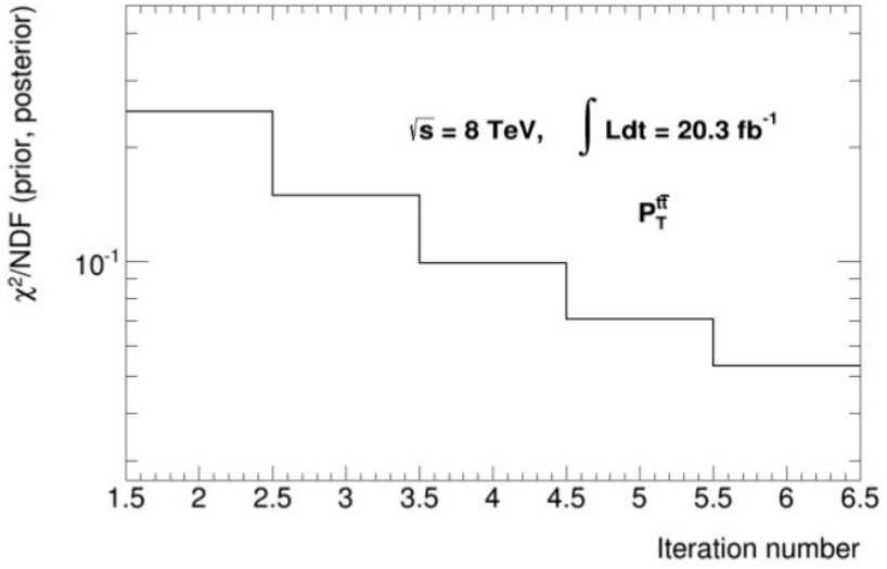

FIGURE 6.9: Posterior versus prior χ^2/NDF for $p_{\mathrm{T}}^{t\bar{t}}$ as a function of the number of iterations.

6.3.1.2 Closure test

The POWHEG + PYTHIA (id: 110404) $t\bar{t}$ sample is used to demonstrate that the unfolding as described above can recover the particle-level spectrum given the reconstructed spectrum. From this sample, two statistically independent subsamples are generated by randomly assigning each event in the sample to one of the two subsamples. One of these subsamples is considered as pseudo-data, and the other used to fill the migration matrix. The pseudo-data sample is then unfolded using the independent subsample as a training sample for the unfolding algorithm by applying only the matrix inversion correction. The comparisons between the unfolded pseudo-data and the particle-level pseudo-data spectra are presented in Figures 6.10 6.11 6.12 showing good closure within the statistical uncertainties. In App. G additional stress tests, with the aim to futher study the validity of the unfolding procedure are also presented.

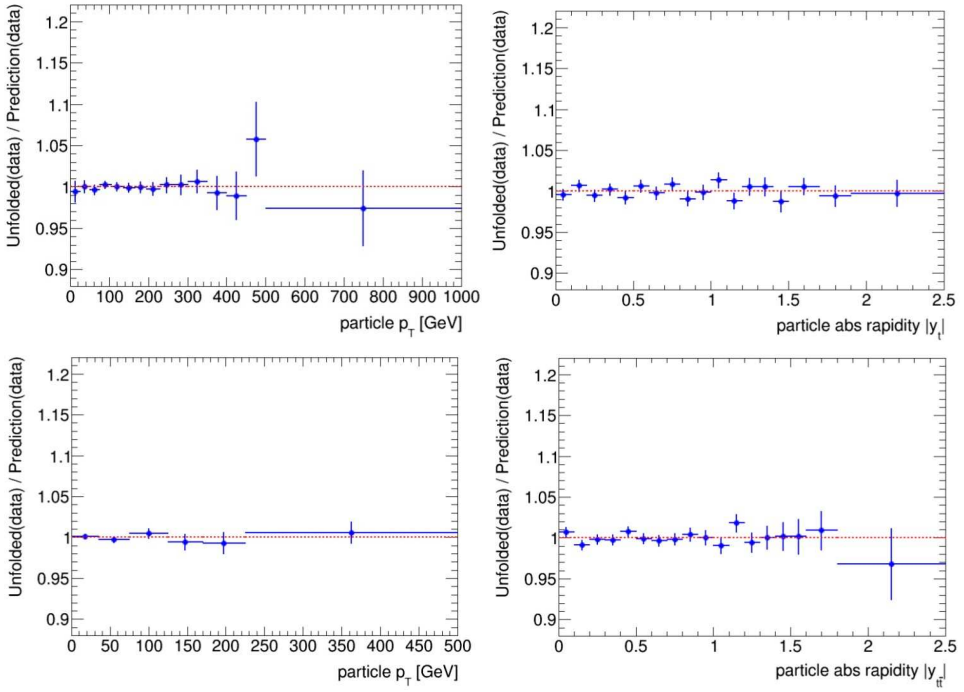

FIGURE 6.10: Closure test for the hadronic top (top) and the $t\bar{t}$ system (bottom), using the bayesian unfolding with $N_{\text{iter}} = 4$. Ratio between the pseudo-data unfolded spectrum and the truth pseudo-data spectrum for the p_{T} (left) and $|y|$ (right).

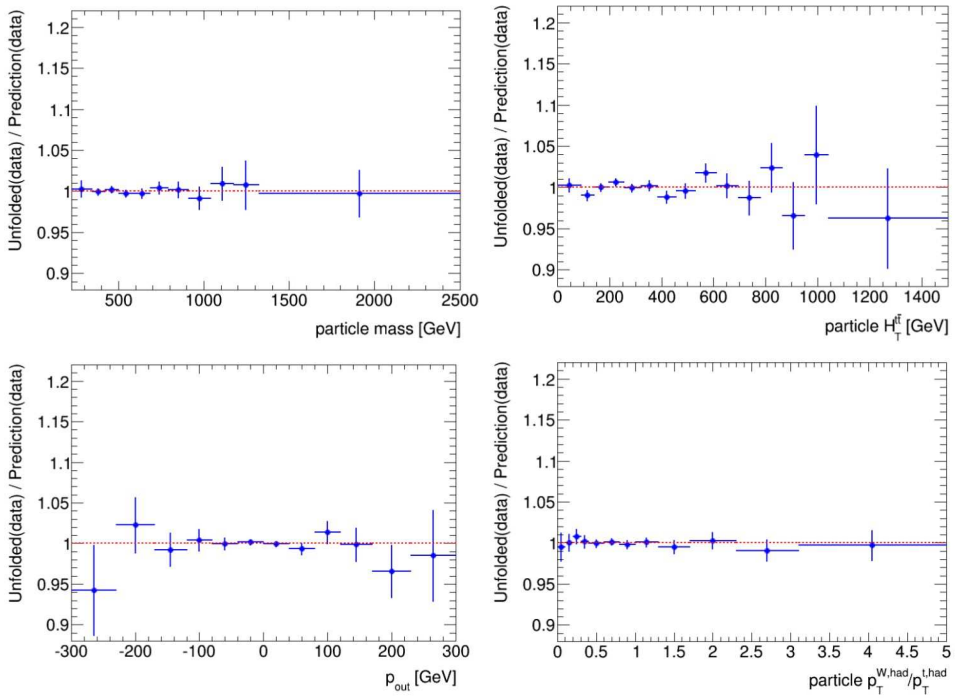

FIGURE 6.11: Closure test for the $t\bar{t}$ system, using the bayesian unfolding with $N_{\text{iter}} = 4$. Ratio between the pseudo-data unfolded spectrum and the truth pseudo-data spectrum for $m^{t\bar{t}}$ (top-left), $H_{\text{T}}^{t\bar{t}}$ (top-right), $p_{\text{out}}^{t\bar{t}}$ (bottom-left) and R_{Wt} (bottom-right).

[htbp]

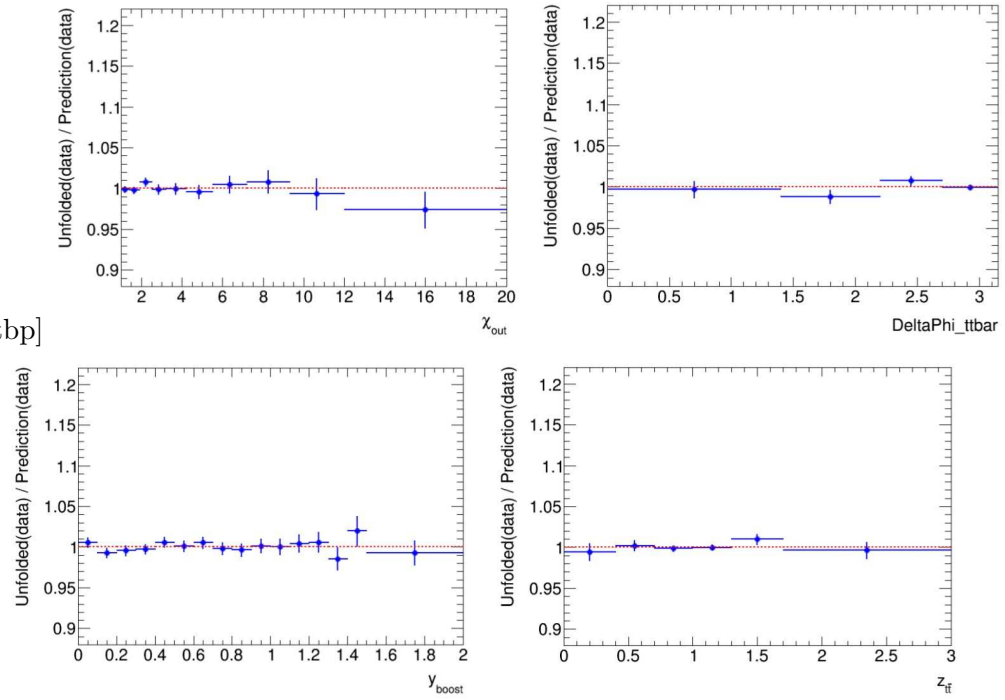

FIGURE 6.12: Closure test for the $t\bar{t}$ system, using the bayesian unfolding with $N_{\text{iter}} = 4$. Ratio between the pseudo-data unfolded spectrum and the truth pseudo-data spectrum for $\chi^{t\bar{t}}$ (top-left), $\Delta\phi_{t\bar{t}}$ (top-right), $y_{\text{boost}}^{t\bar{t}}$ (bottom-left) and $z^{t\bar{t}}$ (bottom-right).

6.3.2 Unfolding to fiducial phase-space

The underlying differential cross-section distributions are obtained from the detector-level events using the Iterative Bayesian method [126] as implemented in RooUnfold [127], that corrects for detector effects. The individual e+jets and μ+jets channels give consistent results and are therefore combined by summing the event yields before the unfolding procedure.

The unfolding starts from the detector-level event distribution (N_{reco}), from which the backgrounds (N_{bg}) are subtracted first. Events where the lepton comes from an intermediate τ lepton decay or where both top quarks decay leptonically are considered as signal. Next, the acceptance correction f_{acc}, shown in Figs. 6.13-6.14, corrects for detector-level events which are not reconstructed at the particle level.

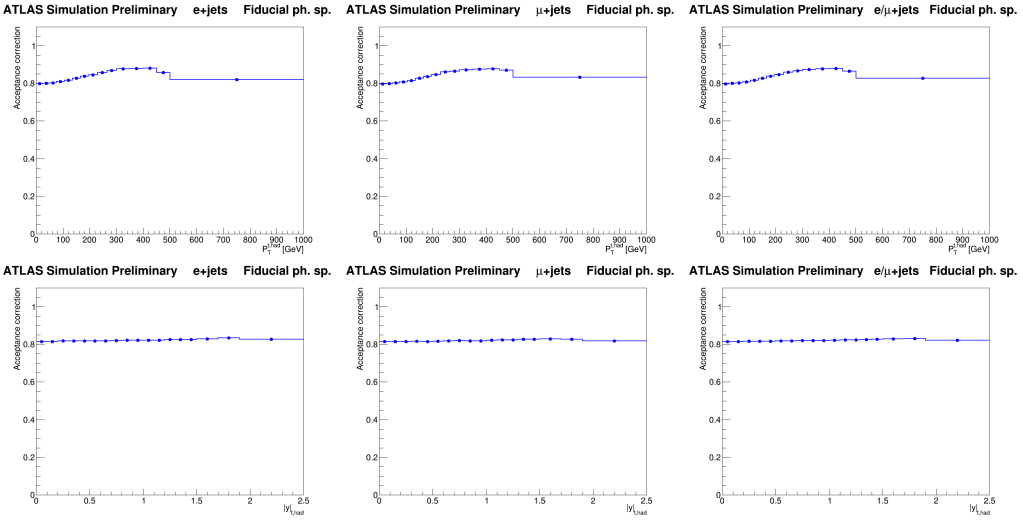

FIGURE 6.13: Acceptance corrections for the hadronic pseudo-top quark p_T (top) and absolute value of rapidity (bottom) in the e+jets (left), μ+jets (middle) and combined ℓ+jets channels in the fiducial phase-space.

In order to separate resolution and combinatorial effects, distributions are corrected to the level where detector- and particle-level objects forming the pseudo-top quarks are angularly well matched. These matching corrections plots are also shown also in Figs. 6.15-6.16, as well as in the App. C.1.4.

The matching correction f_{match} accounts for the corresponding efficiency, by correcting for badly reconstructed signal events. It improves the diagonality of the migration matrix. These corrections are obtained in simulation by taking the ratio between the number of events that pass the reconstructed, particle-level and matching selections to the number of all events that pass reconstructed selection in a particular reconstructed

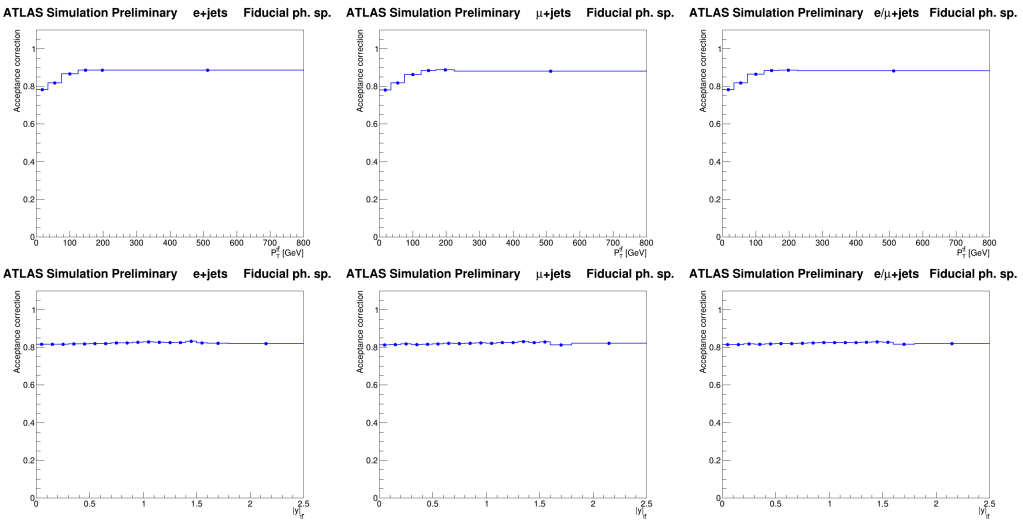

FIGURE 6.14: Acceptance corrections for the top quark pair p_T (top) and absolute value of rapidity (bottom) in the e+jets (left), μ+jets (middle) and combined ℓ+jets channels in the fiducial phase-space.

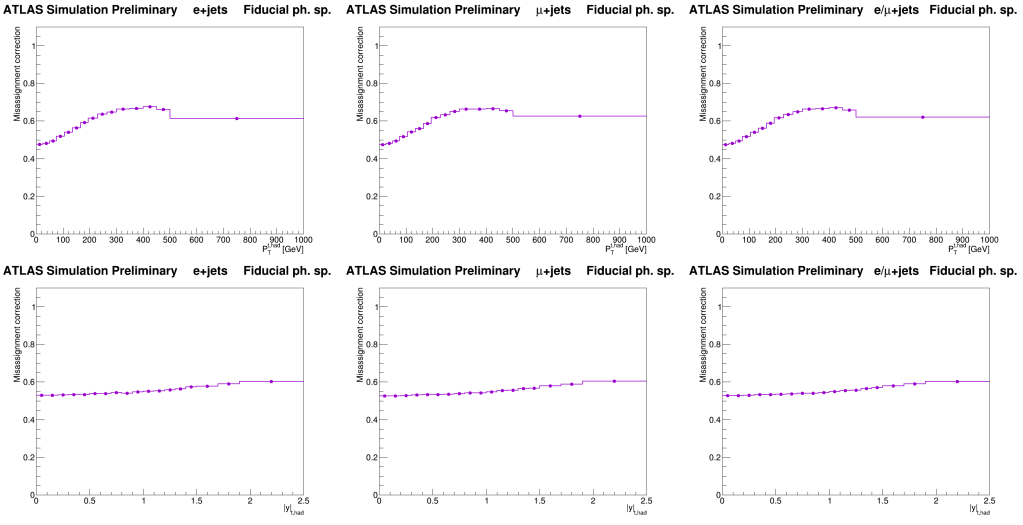

FIGURE 6.15: Matching corrections for the hadronic pseudo-top quark p_T (top) and absolute value of rapidity (bottom) in the e+jets (left), μ+jets (middle) and combined ℓ+jets channels in the fiducial phase-space.

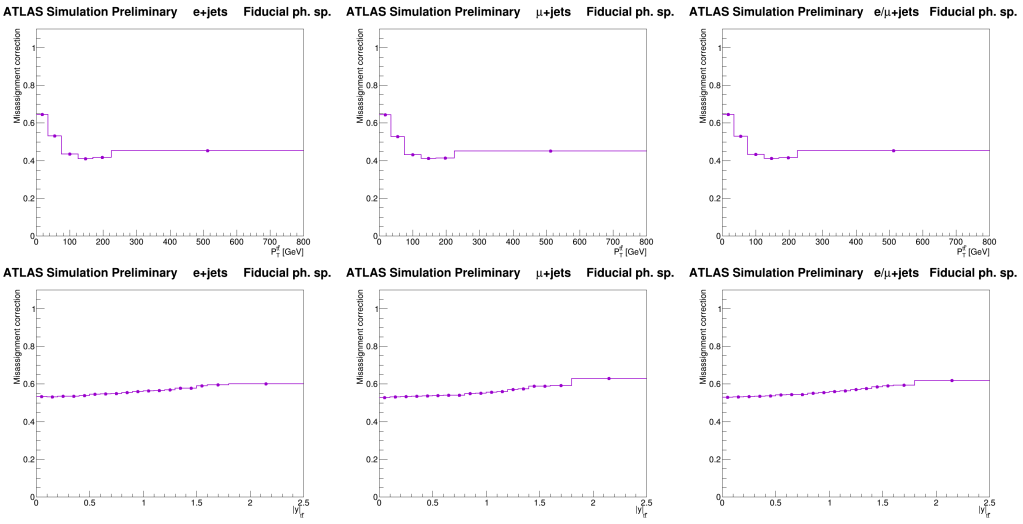

FIGURE 6.16: Matching corrections for the top quark pair p_T (top) and absolute value of rapidity (bottom) in the e+jets (left), μ+jets (middle) and combined ℓ+jets channels in the fiducial phase-space.

bin, binned in the reconstructed quantities:

$$f^j_{\text{acc}} \equiv \left(\frac{N_{\text{reco}\wedge\text{part}}}{N_{\text{reco}}} \right)^j$$

$$f^j_{\text{match}} \equiv \left(\frac{N_{\text{reco}\wedge\text{part}\wedge\text{matched}}}{N_{\text{reco}\wedge\text{part}}} \right)^j$$

$$f^j_{\text{acc}\wedge\text{match}} \equiv \left(\frac{N_{\text{reco}\wedge\text{part}\wedge\text{matched}}}{N_{\text{reco}}} \right)^j = f^j_{\text{acc}} \cdot f^j_{\text{match}}.$$

The acceptance correction is a bin-by-bin factor which corrects for reconstructed events which were not reconstructed at the particle level. These are considered as poorly reconstructed events as they do not belong to the fiducial volume of interest. The matching is performed using geometrical criteria based on the distance ΔR. Each particle e (μ) is matched to the closest detector-level e (μ) within $\Delta R < 0.02$. Particle-level jets are geometrically matched to the closest detector-level jet within $\Delta R < 0.4$. If a detector-level jet is not matched to a particle-level jet, it is assumed to be either from pile-up or matching inefficiency and is treated as background. If two jets are reconstructed as being $\Delta R < 0.4$ from a single particle-level jet, the detector-level jet with smaller ΔR is matched to the particle-level jet and the other detector-level jet is unmatched. In practice, acceptance and matching corrections are applied in a single step. In a more detail, the values of $N^j_{\text{reco}\wedge\text{part}\wedge\text{matched}}$ (reco-level, entering the acceptance correction) and $N^i_{\text{reco}\wedge\text{part}\wedge\text{matched}}$ (particle-level, entering the efficiency correction described below) are obtained as the fully in-range projection of the migration matrix onto the respective axes, in order to respect the restricted analysis bin range, thus excluding over- and

under-flow bins.

The unfolding step uses a migration matrix ($\mathcal{M}$) derived from simulated $t\bar{t}$ events which maps the binned generated particle-level events to the binned detector-level events, that is built from the response matrix by normalizing the detector-level bins (or reco-level) in each particle-level bin to the sum of events in given particle-level bin. The response matrix is constructed from all events that pass both the particle and detector level selection and the matching condition in the nominal $t\bar{t}$ MC sample. The probability for particle-level events to remain in the same bin is therefore represented by the elements on the diagonal, and the off-diagonal elements describe the fraction of particle-level events that migrate into other bins. Therefore, the elements of each row add up to unity as shown in Figs 6.5 and 6.6. A collection of the migration matrices of each spectrum, besides those presented in Sec. 6.2, are also shown in App. C.1.1.

Finally, the efficiency correction f_{eff} is applied to the unfolded spectrum, correcting the result by a bin-by-bin factor to the fiducial phase space. It corrects for events which pass the particle level selection but were not reconstructed at the detector (reco) level. It is defined as the number of events passing the particle level selection, over the number of events passing both the reconstructed, particle and matching selection criteria, binned in the variable of interest:

$$f_{\text{eff}}^{i} \equiv \left(\frac{N_{\text{part}}}{N_{\text{reco}\wedge\text{part}\wedge\text{matched}}} \right)^{i}.$$

The difference in the efficiency between the two channels is due to the difference in the lepton selections between the two channels. The efficiencies for all the spectra are shown in Sec. 6.1, Figs. 6.1-6.2, as well as in App. C.1.2.

The p_{T} of the top quark decaying hadronically is a variable particularly representative since the kinematics of the decay products of the top quark change substantially in the observed range as regards the applied correction factors. Remarkably, the increase in the matching and efficiency correction at high values is primarily due to the increasingly large fraction of non-isolated leptons and close or merged jets in events with high top-quark p_{T}. A similar effect is observed in the tail of the $t\bar{t}$ transverse momentum and rapidity, small $\Delta\phi^{t\bar{t}}$ angle and high $H_{\text{T}}^{t\bar{t}}$ distributions. The matching corrections reach the highest values, of the order of $f_{\text{match}} = 0.6$–0.7, at low $t\bar{t}$ transverse momentum and large $t\bar{t}$ rapidity. Generally, the acceptance corrections are constant and close to unity, indicating very good correlation between the detector- and the particle-level reconstruction. This is also apparent from the high level of diagonality of the migration matrices, with correlations at the level of 85–95%.

The unfolding procedure for an observable X at particle level is summarized by the expression :

$$x^i_{\text{part}} \equiv f^i_{\text{eff}} \cdot \sum_j \mathcal{M}^{-1}_{ij} \cdot f^j_{\text{match}} \cdot f^j_{\text{acc}} \cdot \left(N^j_{\text{reco}} - N^j_{\text{bkg}} \right), \tag{6.11}$$

where the index j iterates over bins of X at detector level while the i index labels bins at particle level; the Bayesian unfolding is symbolized by $\mathcal{M}^{-1}_{ij}$.

Finally, one divides by the bin width and the luminosity, to translate the unfolded result to the differential cross-section.

The master unfolding formula to the fiducial space then reads

$$\frac{\mathrm{d}\sigma^{\text{fid}}}{\mathrm{d}X^i} \equiv \frac{1}{\mathcal{L} \cdot \Delta X^i} \cdot f^i_{\text{eff}} \cdot \sum_j \mathcal{M}^{-1}_{ij} \cdot f^j_{\text{match}} \cdot f^j_{\text{acc}} \cdot \left(N^j_{\text{reco}} - N^j_{\text{bkg}} \right),$$

where ΔX^i is the bin width. The unfolded differential cross-section is integrated to obtain the measured total fiducial cross-section, used to define the normalized differential cross section $\frac{1}{\sigma^{\text{fid}}} \frac{\mathrm{d}\sigma^{\text{fid}}}{\mathrm{d}X^i}$.

6.3.3 Unfolding to full phase-space

To facilitate comparison with theoretical calculations of the $t\bar{t}$ differential cross-section at the exact NNLO, the reconstructed spectra are also unfolded to the parton level. The parton-level top is defined by the status codes 3 and 155 in Pythia and Herwig showered samples, respectively. It represents the top quark approximately after final state radiation and before decay. The method used to correct the measured spectra to the parton level is similar to the one employed in Section 6.3.2. The only difference is in the value used for the binning. The binning used by the CMS experiment in Ref. [29] is used for the observables measured by both experiments to facilitate future combinations. This binning is found to be compatible with the resolution of each observable. The fiducial phase-space binning is used for all the other observables. The measurement is extrapolated to the full phase space via an efficiency correction. The full unfolding procedure can be summarized by the following formula:

$$x^i_{\text{parton}} \equiv f^i_{\text{eff}} \cdot \sum_j \mathcal{M}^{-1}_{ij} \cdot f^j_{\text{acc}} \cdot f_{\text{ljets}} \cdot \left(N^j_{\text{reco}} - N^j_{\text{bkg}} \right), \tag{6.12}$$

where $\mathcal{M}_{ij}$ is the parton-to-reco migration matrix (shown in Figs. 6.17- 6.18, and f^i_{eff} is the selection efficiency correction defined as

$$f^i_{\text{eff}} = \frac{N^i_{\text{parton}}}{N^i_{\text{reco}}} \equiv 1/\epsilon_i,$$

correcting to the full phase-space. The efficiencies are plotted in Figs. 6.19- 6.20.

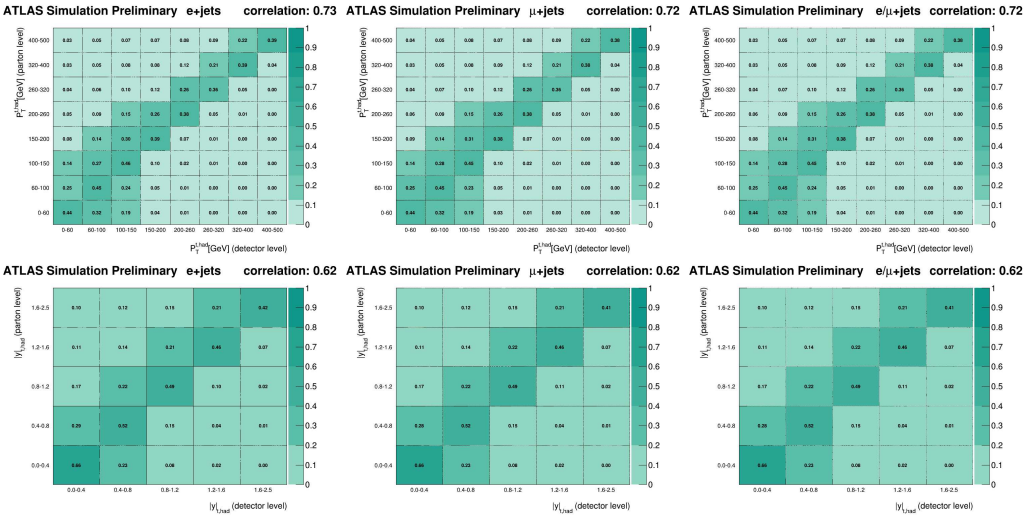

FIGURE 6.17: Migration matrix between detector and parton level for the hadronic pseudo-top quark p_T (top) and absolute value of rapidity (bottom) in the e+jets (left), μ+jets (middle) and combined ℓ+jets channel.

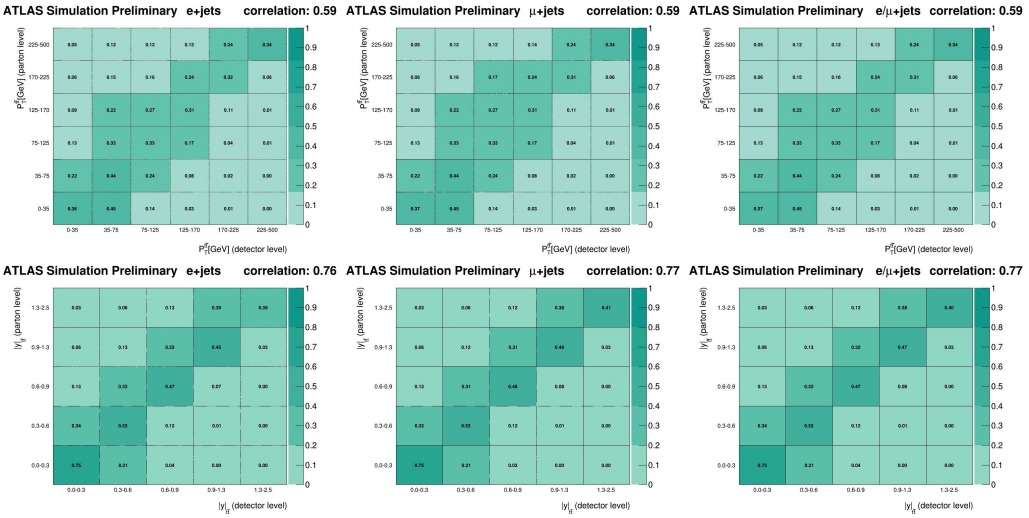

FIGURE 6.18: Migration matrix between detector and parton level for the top quark pair p_T (top) and absolute value of rapidity (bottom) in the e+jets (left), μ+jets (middle) and combined ℓ+jets channel.

In order to unambiguously define leptonic and hadronic top quarks, the contribution of $t\bar{t}$ pairs decaying dileptonically is removed by applying a correction factor f_{ljets} which represents the fraction of $t\bar{t}$ single-lepton events in the nominal sample, shown in Figs 6.21-6.22.

The τ leptons from the leptonically decaying W bosons are considered as signal regardless of the τ decay mode. The cross-section measurements are defined with respect to the

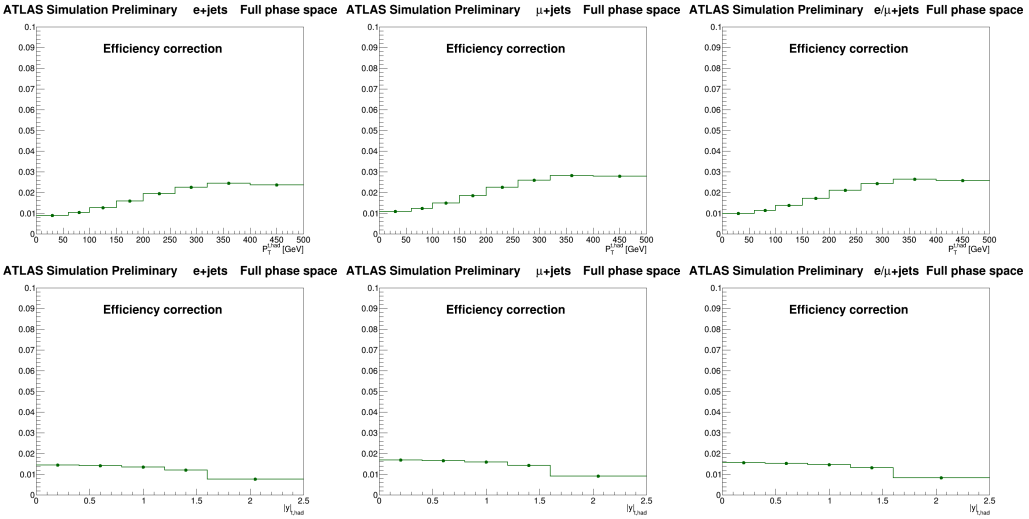

FIGURE 6.19: Efficiency corrections for the hadronic pseudo-top quark p_T (top) and absolute value of rapidity (bottom) in the e+jets (left), μ+jets (middle) and combined ℓ+jets channels in the full phase-space.

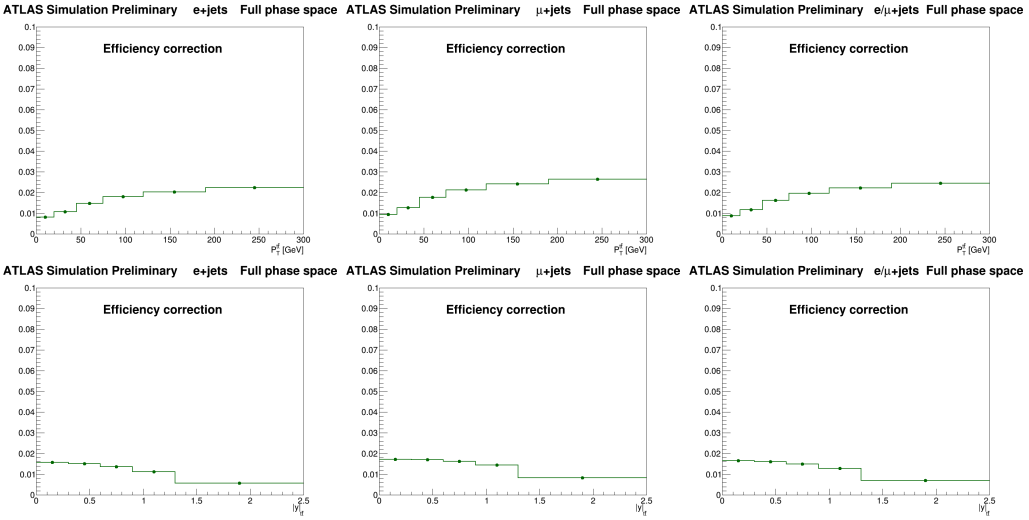

FIGURE 6.20: Efficiency corrections for the top quark pair p_T (top) and absolute value of rapidity (bottom) in the e+jets (left), μ+jets (middle) and combined ℓ+jets channels in the full phase-space.

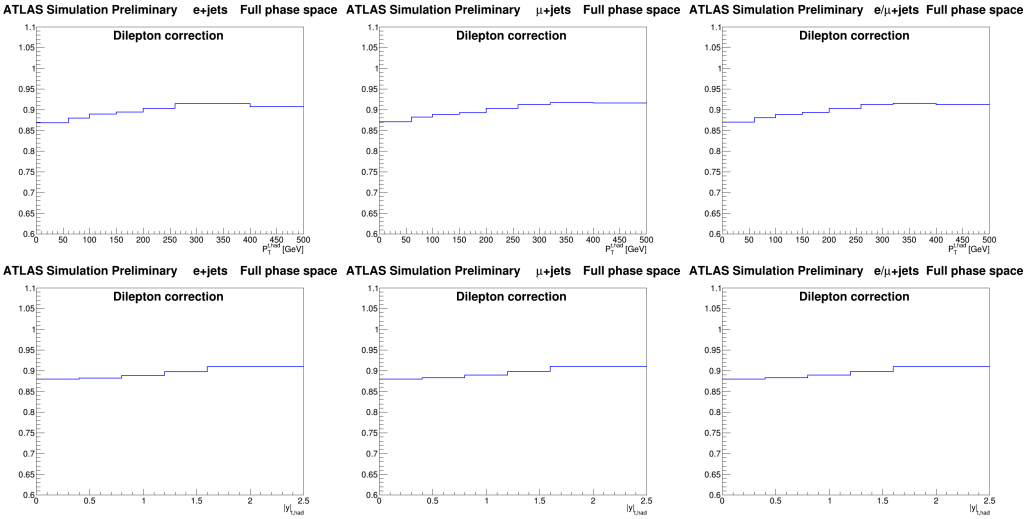

FIGURE 6.21: Dilepton corrections for the hadronic pseudo-top quark p_T (top) and absolute value of rapidity (bottom) in the e+jets (left), μ+jets (middle) and combined ℓ+jets channels in full phase-space.

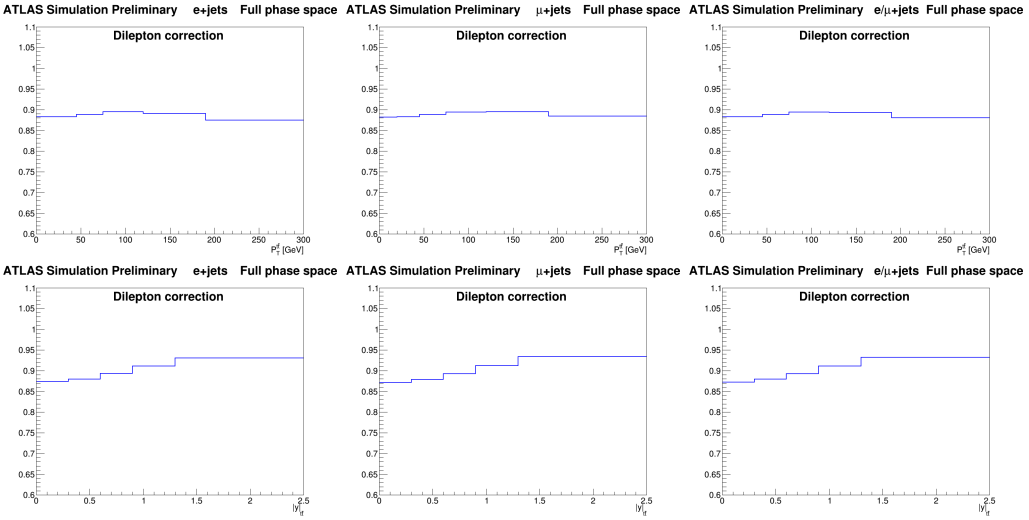

FIGURE 6.22: Dilepton corrections for the top quark pair p_T (top) and absolute value of rapidity (bottom) in the e+jets (left), μ+jets (middle) and combined ℓ+jets channels in full phase-space.

top quarks before the decay (parton level) and after QCD radiation. Observables related to top quarks are extrapolated to the full phase-space starting from top quarks decaying hadronically at the detector level.

The acceptance correction f_{acc} corrects for detector-level events which are reconstructed outside the parton-level bin range for a given variable. Therefore, the f_{acc} correction is defined as the following ratio, taking the fully in-range projection of the parton-to-reco migration matrix onto the reco axis, divided by the reco-level spectrum (which includes the out-of-range parton-level events to be corrected for). The acceptances are plotted in Figures 6.23- 6.24.

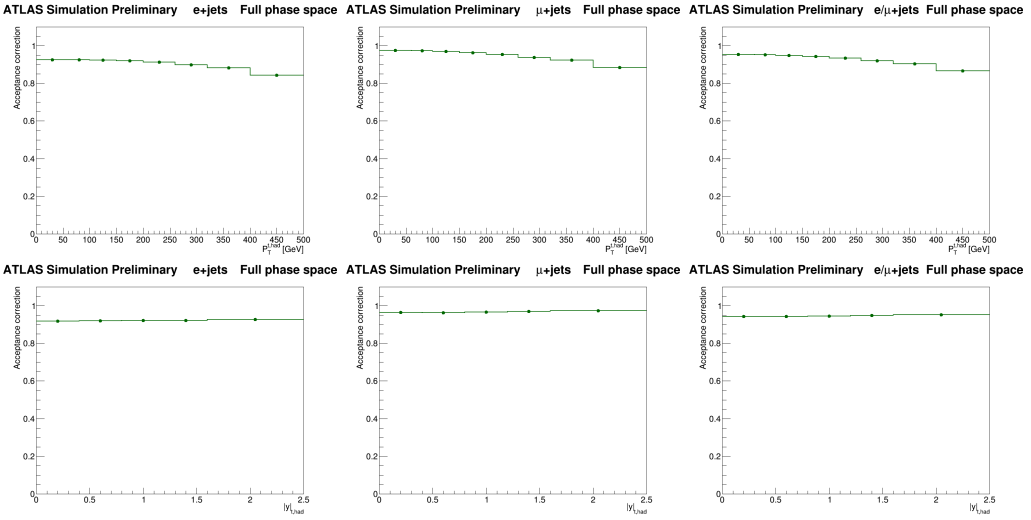

FIGURE 6.23: Acceptance corrections for the hadronic pseudo-top quark p_T (top) and absolute value of rapidity (bottom) in the e+jets (left), μ+jets (middle) and combined ℓ+jets channels in full phase-space.

The migration matrix ($\mathcal{M}$) is derived from simulated $t\bar{t}$ events decaying in the single-lepton channel and the efficiency correction f_{eff} corrects for events which did not pass the detector-level selection.

The master unfolding formula to the full phase space then reads

$$\frac{\mathrm{d}\sigma^{\text{full}}}{\mathrm{d}X^i} \equiv \frac{1}{\text{BR} \cdot \mathcal{L} \cdot \Delta X^i} \cdot f^i_{\text{eff}} \cdot \sum_j \mathcal{M}^{-1}_{ij} \cdot f^j_{\text{acc}} \cdot f_{\text{ljets}} \cdot \left(N^j_{\text{reco}} - N^j_{\text{bkg}} \right),$$

where the index j iterates over bins of observable X at the detector level while the i index labels bins at the parton level; ΔX^i is the bin width, BR = 0.438 is the single-lepton branching ratio, $\mathcal{L}$ is the integrated luminosity and the Bayesian unfolding is symbolized by $\mathcal{M}^{-1}_{ij}$.

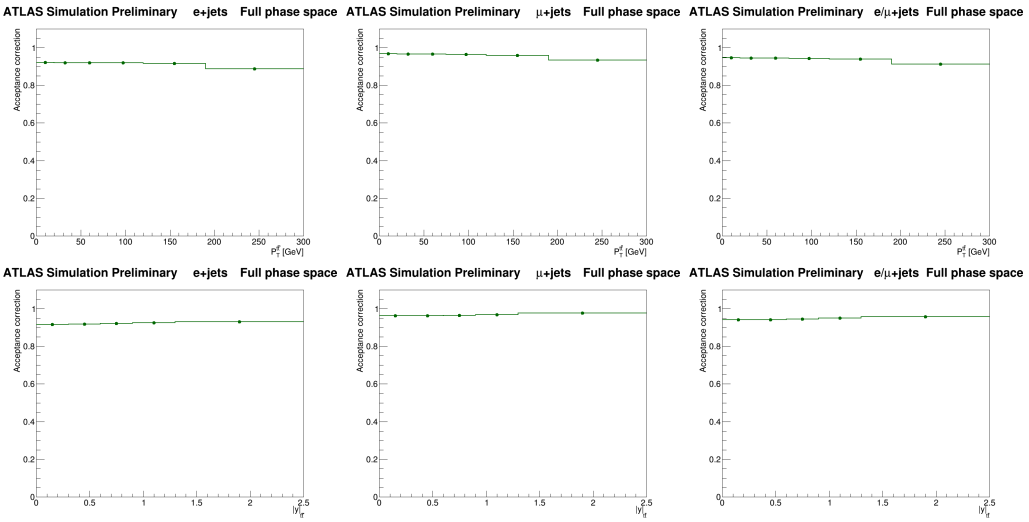

FIGURE 6.24: Acceptance corrections for the top quark pair p_T (top) and absolute value of rapidity (bottom) in the e+jets (left), μ+jets (middle) and combined ℓ+jets channels in full phase-space.

The total cross-section is obtained by integrating the unfolded cross-section over the kinematic bins, and its value is used to compute the normalized differential cross-section $\frac{1}{\sigma^{\text{full}}} \frac{\mathrm{d}\sigma^{\text{full}}}{\mathrm{d}X^i}$.

6.4 Uncertainties

6.4.1 Statistical uncertainty

The statistical uncertainty on the differential cross section measurements is due to the finite number of data events collected. It is evaluated by repeating the same analysis procedure, comprehensive of unfolding, by the use of *pseudo-experiments*, which are simulated distributions obtained by smearing the bin-by-bin value of the background-subtracted data distribution according to a Poissonian distribution. It has been evaluated through the set of 5000 pseudo-experiments according to the following procedure:

1. for each pseudo-experiment, a Poisson fluctuation is applied to the reconstructed spectrum in the data;
2. the nominal background is subtracted from the smeared data;
3. the smeared data-minus-background is unfolded using the nominal efficiency and migration matrix.

The uncertainty on the final distribution in each bin is calculated as the root mean square of the observed cross section distributions for all pseudo-experiments. It will be summed in quadrature with the total systematic uncertainty.

In case of the normalized differential cross sections $1/\sigma d\sigma/dX$, each unfolded toy must be normalized to the same (unit) area, which is then taken as the statistical error on the shape of the observable under study.

6.4.2 Systematic uncertainties

Several sources of systematic uncertainty affect the measured differential cross sections. The systematic uncertainties due to detector effects and the ones related to the modelling of the signal and background MC components, which were found to be the most relevant ones, are described in this section.

Each systematic uncertainty was evaluated before and after the unfolding procedure (described in section 6.3). Deviations from the nominal predictions were evaluated separately for the upward and downward variations (or in the case of a single variation by symmetrising the single deviation) for each bin of each observable and combining the electron and muon channels.

To evaluate the impact of each uncertainty after the unfolding, the reconstructed distribution expected from simulation is varied. Corrections based on the nominal POWHEG-BOX signal sample are used to correct for detector effects and the unfolded distribution is compared to the known particle- or parton-level distribution. While all detector- and background-related systematic uncertainties share the same particle- and parton-level kinematics, alternative models used to assess other systematic uncertainties *e.g.* initial- and final-state radiation uncertainties also have different parton- and particle-level spectra. In these cases, nominal corrections are still used to unfold the detector-level spectra, but the comparison is performed with respect to the corresponding alternative particle- or parton-level spectra. Then, the relative uncertainty from the simulation is assigned to the unfolded data. After the unfolding, each distribution is normalized to unit area.

The detector-related uncertainties are briefly described in section 6.4.2.1 while the uncertainties on the $t\bar{t}$ signal and background modelling are discussed in sections 6.4.2.2 and 6.4.2.3 respectively.

All the components contributing to the total systematic uncertainty of each measured differential cross section (at the particle and parton level), are presented together with

the statistical uncertainties, in graphical form in Sec. 6.4.2.5, as well as in the Appendix D.1.1 (Figs. D.1- D.3) and tabular form Tables D.1- D.22 to the fiducial phase-space, and in the Appendix D.1.2 (Figs. D.4- D.6) and tabular form Tables D.24- D.42 to the full phase-space .

6.4.2.1 Detector systematics

The experimental uncertainties refer to the quality of the detector simulation to describe the detector response in data for each of the reconstructed objects.

Lepton reconstruction

The lepton reconstruction efficiency in simulation is corrected by scale factors derived from measurements of these efficiencies in data using a $Z \to \ell^+\ell^-$ enriched control region. The lepton trigger and reconstruction efficiency scale factors, energy scale and resolution are varied within their uncertainties [128] [129]. These uncertainties are relatively small, dominated by the lepton identification in the e+jets channel and the muon triggering efficiency in the μ+jets channel. They are specific to each lepton flavor and therefore uncorrelated between the channels.

Jet reconstruction

The uncertainties due to the uncertainty on the jet-energy scale was estimated by varying the jet energies according to the uncertainties derived from simulation and in-situ calibration measurements using a model with 22 orthogonal components [130] [131]. The variations in jet energies were also propagated to the $E_{\mathrm{T}}^{\mathrm{miss}}$ value. The uncertainty due to the difference in jet-energy resolution between the data and MC events was evaluated by smearing the MC jet transverse momentum according to the jet resolution as a function of the jet p_{T} and η [132]. The uncertainty due to the jet reconstruction efficiency was estimated by randomly discarding jets according to the difference in jet reconstruction efficiency between the data and MC. The lower value of jet vertex fraction was varied between 0.4 and 0.6 as motivated by the $Z \to ee/\mu\mu$+jets studies [115]. The total jet reconstruction systematic uncertainties are for all the $t\bar{t}$ differential cross-sections at the level of $5-8\%$.

b-tagging

The systematic uncertainties associated with tagging jets originating from b-quarks are separated into three categories. These are the efficiency of the tagging algorithm (b-quark tagging efficiency), the efficiency with which jets originating from c-quarks pass

the b-tag requirement (c-quark tagging efficiency) and the rate at which light-flavour jets are tagged (misidentified tagging efficiency). The efficiencies are estimated from data and parameterised as a function of p_{T} and η. The systematic uncertainties arise from factors used to correct the differences between the simulation and data in each of the categories.

In this analysis the b-tagging calibration *combined_pdf_dijet_7* was used for the combined tagger MV1, with parameters taken from the configuration file *2014-Winter-8TeV-MC12-CDI.root* (CDI file build number 908).

The associated systematic uncertainties are computed by varying the scale factors within their uncertainties [133] [134] [135].

The uncertainty associated to the b-tagging efficiency is a large contributor (5%) to the overall systematic uncertainty and tends to slightly increase with p_{T}^{t}.

Missing transverse momentum

The systematic uncertainties associated with the momenta and energies of reconstructed objects (leptons and jets) were also propagated to the $E_{\mathrm{T}}^{\mathrm{miss}}$ calculation. The $E_{\mathrm{T}}^{\mathrm{miss}}$ reconstruction also receives contributions from the presence of low-p_{T} jets and calorimeter cells not included in reconstructed objects ("soft terms"). The systematic uncertainty on soft terms was evaluated using $Z \to \mu\mu$ events from the $E_{\mathrm{T}}^{\mathrm{miss}}$ data/MC ratio in events without jets and from the balance between soft terms and hard objects using methods similar to those used in Ref. [136]. The $E_{\mathrm{T}}^{\mathrm{miss}}$ measurement is so affected by a small systematic uncertainty (below $\pm 1\%$).

6.4.2.2 Signal modelling systematics

MC generator: matrix element and parton shower models

The choice of MC generator used in the signal modelling affects the kinematic properties of simulated $t\bar{t}$ events and reconstruction efficiencies. In order to address this effect, $t\bar{t}$ events simulated with different settings of Powheg and MC@NLO have been used to assess the impact of different NLO matrix element calculations and parton shower models.

To assess the impact of different NLO subtraction schemes, events simulated with MC@NLO+Herwig are unfolded using the migration matrix and correction factors derived from the Powheg+Herwig sample. The difference between the unfolded distribution and the known particle- or parton-level distribution of the MC@NLO+Herwig

sample is assigned as the relative uncertainty for the fiducial or full phase-space distributions, respectively. This uncertainty is found to be in the range 2–5%, depending on the variable, increasing up to 10% at large p_{T}^{t}, $m^{t\bar{t}}$, $p_{\mathrm{T}}^{t\bar{t}}$ and $\left|y^{t\bar{t}}\right|$. The observable that is most affected by these uncertainties is $m^{t\bar{t}}$ in the full phase space.

To assess the impact of different parton-shower models, unfolded results using events simulated with POWHEG interfaced to PYTHIA are compared to events simulated with POWHEG interfaced to HERWIG, using the same procedure described above to evaluate the uncertainty on the NLO subtraction scheme. The resulting systematic uncertainties, taken as the symmetrized difference, are found to be typically at the 1–3% level.

MC generator: Sample finite statistics To account for the limited statistics of the signal sample, pseudo experiments are used to evaluate the impact of finite statistics. The number of events in each bin is smeared by a gaussian shift with mean equal to the yield of the bin, and standard deviation equal to the uncertainty of the bin. Than the smeared spectrum is unfolded. The procedure is replicated 5000 times, then the final statistical uncertainty is evaluated from the average over the 5000 toys. The resulting systematic uncertainty was found to be typically below 0.5%, increasing to $1-2\%$ in the tails of some distributions such as p_{T}^{t}, $m^{t\bar{t}}$, $p_{\mathrm{T}}^{t\bar{t}}$.

Initial- and final-state QCD radiation ISR/FSR changes the number of jets in the event. In order to evaluate the uncertainty related to the modelling of the ISR/FSR, $t\bar{t}$ MC samples with modified ISR/FSR modelling are used. The MC samples used for the evaluation of this uncertainty are generated using the POWHEG generator interfaced to PYTHIA, where the parameters of the generation (Λ_{QCD}, Q^2_{max} scale, transverse momentum scale for space-like parton-shower evolution, and h_{damp}) were varied to span the ranges compatible with the results of a measurement of $t\bar{t}$ production with a veto on additional central jet activity [82]. To evaluate this uncertainty, for each bin, the largest absolute shift between the two variations is chosen and symmetrized, keeping its sign.

This uncertainty is found to be in the range 2–5%, depending on the variable of the $t\bar{t}$ system considered, and reaching the largest values at high $\left|y^{t}\right|$ and small $p_{\mathrm{T}}^{t\bar{t}}$.

In the App. E the uncertainties obtained with the nominal POWHEG MC are compared with the results obtained with two (upward and downward) variations of the POWHEG parameters affecting the initial- and final-state QCD radiation.

Parton distribution functions

The impact of the uncertainty related to the PDF is assessed by means of $t\bar{t}$ samples

generated with MC@NLO interfaced to HERWIG. An envelope of spectra is evaluated by reweighting the central prediction of the CT10nlo PDF set, using the full set of 52 eigenvectors at 68% CL and removing the events whose weight exceeded 5.0 in absolute value. The uncertainty was then estimated from the ratio of the unfolded spectrum and its particle- or parton-level distribution, and found to be less than 1%.

6.4.2.3 Background modelling systematics

Systematics on the background are modelled by adding to the signal spectrum the difference of the systematics-varied and nominal backgrounds.

W+jet model

The systematic uncertainties due to the overall normalization and the heavy-flavour fraction of W+jets events are obtained by varying the data-driven scale factors within the statistical uncertainty of the W+jets MC sample. The W+jets shape uncertainty is extracted by varying the renormalization and matching scales in ALPGEN. The W+jets MC statistical uncertainty is also taken into account. The overall impact of this uncertainty is less than 1%.

Single top cross-section

The single-top background is assigned an uncertainty associated with the theoretical calculations used for its normalization [96] [97] [98]. The overall impact of this systematic uncertainty is around 0.5%.

Multijet background

Non-prompt leptons and non-leptonic particles present in multijet background events may satisfy the analysis selection criteria, giving rise to so called non-prompt and fake lepton backgrounds. The uncertainty on the background from non-prompt and fake-lepton is evaluated by varying the definition of loose leptons, changing the selection used to form the control region and propagating the statistical uncertainty of parameterizations of the efficiency to pass the tighter lepton requirements for real and fake leptons. The combination of all these components also affects the shape of the background. The overall impact of this systematic uncertainty is less than 1%.

Z+jet model

A 50% uncertainty is applied to the normalization of the Z+jets background, including the uncertainty on the cross-section and a further 48% due to the additional four jets. A

40% uncertainty is applied to the diboson background, including the uncertainty on the cross-section and a further 34% due to the presence of two additional jets. The overall impact of these uncertainties is less than 1%, and the largest contribution is due to the Z+jets background.

6.4.2.4 Unfolding systematics

We evaluated two types of systematic uncertainties related to the unfolding procedure: non-closure and the choice of the regularization parameter.

A non-closure stems from the fact that for some events the value of a given observable falls outside of the range of the histogram. Ignoring the underflows/overflows, one may assume that all reconstructed events have been generated from a non-overflow bin, which of course is not always true. For this reason, a non-closure systematic would take into account the uncertainty due to this assumption. As a matter of fact, the non-closure can be absorbed in the definition of the acceptance correction. With this method, the non-closure is zero by construction.

The second uncertainty is due to the fact that the uncertainty procedure depends on a set of parameters that are chosen according to some criteria, that in turn have some degree of arbitrariness. In the case under consideration, the only parameter that can be tuned is the number of iterations, which has been set equal to 4 for all the observables. While this appears to be a good compromise between the statistical uncertainty and the resulting value of χ^2/NDF, a slightly different choice might have had a different impact in some cases. For this reason, we account for this little arbitrariness by varying the regularization parameter by one unit: $N_{itr} = 4^{+1}_{-1}$. The resulting uncertainty appeared to be below 0.1% in all cases, so it has been removed from the list of systematic uncertainties.

6.4.2.5 Fractional uncertainties

To show visually the impact of all systematic uncertainty sources for each observable, we grouped the systematics in broad groups and plotted their relative impact compared to the nominal prediction, Figs. 6.25 and 6.26. The groups are defined as follows:

Jet Energy Scale b-Tagged jet energy scale, η intercalibration model, Flavor composition, Flavor response, Effective detector, Effective mixed, Effective model, Effective stat., Jet energy resolution, Punch-through, Single particle high-p_T, Pile-up offset ρ topology, Pile-up offset p_T.

Pileup E_T^{miss} Soft Jet Scale, E_T^{miss} Soft Jet Resolution, Jet reconstruction efficiency, Jet vertex fraction, Pile-up offset μ, Pile-up offset N_{PV}.

Flavour tagging c/τ-Tagging efficiency, Light-flavors tagging efficiency, b-Tagging efficiency.

Background Modeling W+jets scale factors, Single top cross-section, Fake lept. MC stat, Fake lept. alternate fake CR, Fake lept. alternate real CR, Fake lept. alternate parametrization for the e+jets and μ+jets channels separately.

Lepton identification Lepton trigger efficiency, Lepton reconstruction efficiency, Lepton identification efficiency, Muon (ID) momentum resolution, Muon momentum scale, Muon (MS) momentum resolution, Electron energy scale, Electron energy resolution.

Modelling Hard scattering, parton shower, MC statistics

Along with these groups, we show also the PDF, IFSR and statistical uncertainties.

As shown in Figs. 6.25 and 6.26, for each spectrum, the systematics uncertainties on the relative differential cross sections are reduced with respect to the absolute ones, because the total cross section by which they are normalized are affected by systematic uncertainties themselves, therefore the total contribution is reduced.

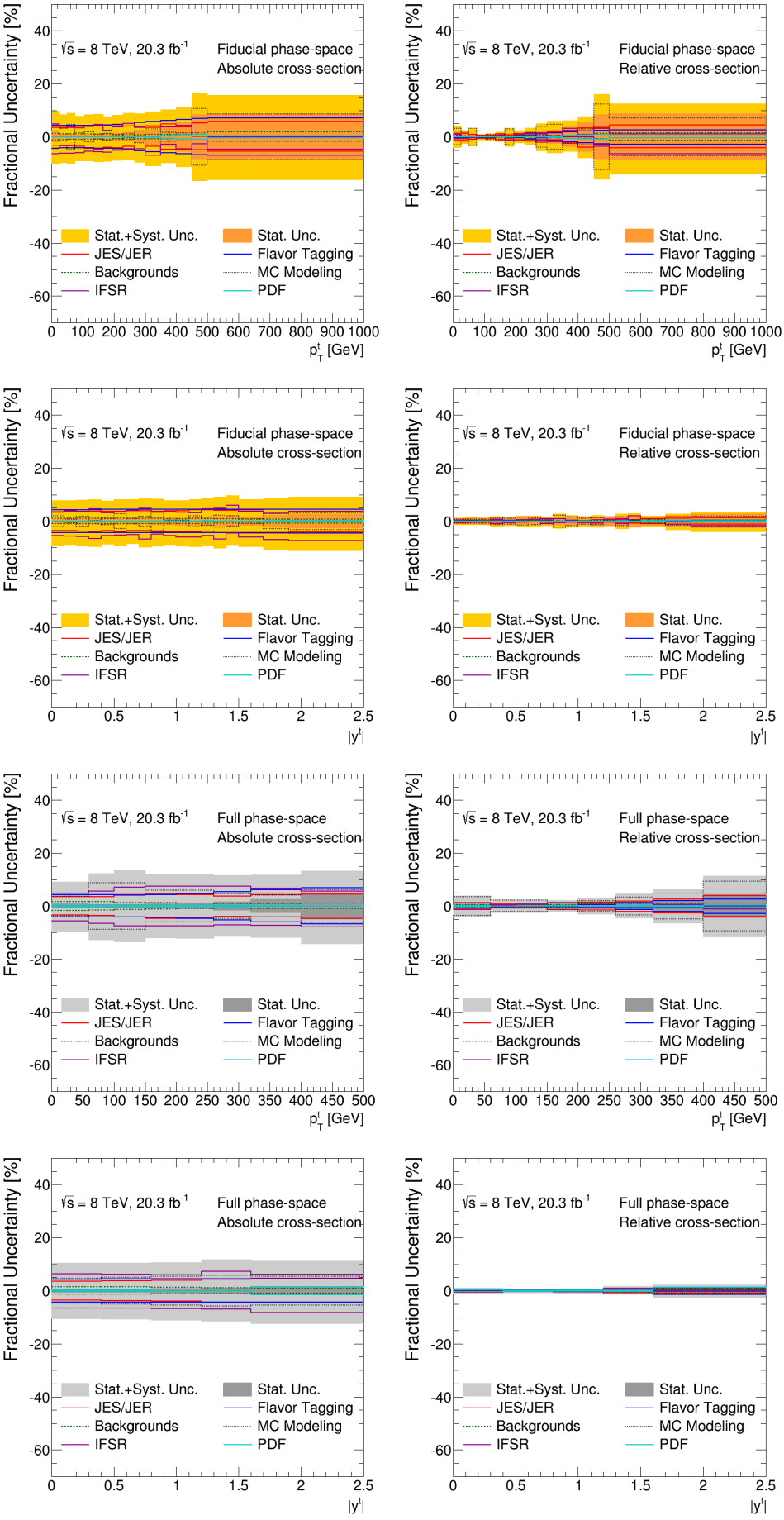

FIGURE 6.25: Fractional uncertainties for the absolute (left) and relative (right) differential cross-sections as a function of $p_{\mathrm{T}}^{t,\mathrm{had}}$ (first row) and $\left|y^{t,\mathrm{had}}\right|$ (second row) in the fiducial phase-space, $p_{\mathrm{T}}^{t,\mathrm{had}}$ (third row) and $\left|y^{t,\mathrm{had}}\right|$ (fourth row) in the full phase-space.

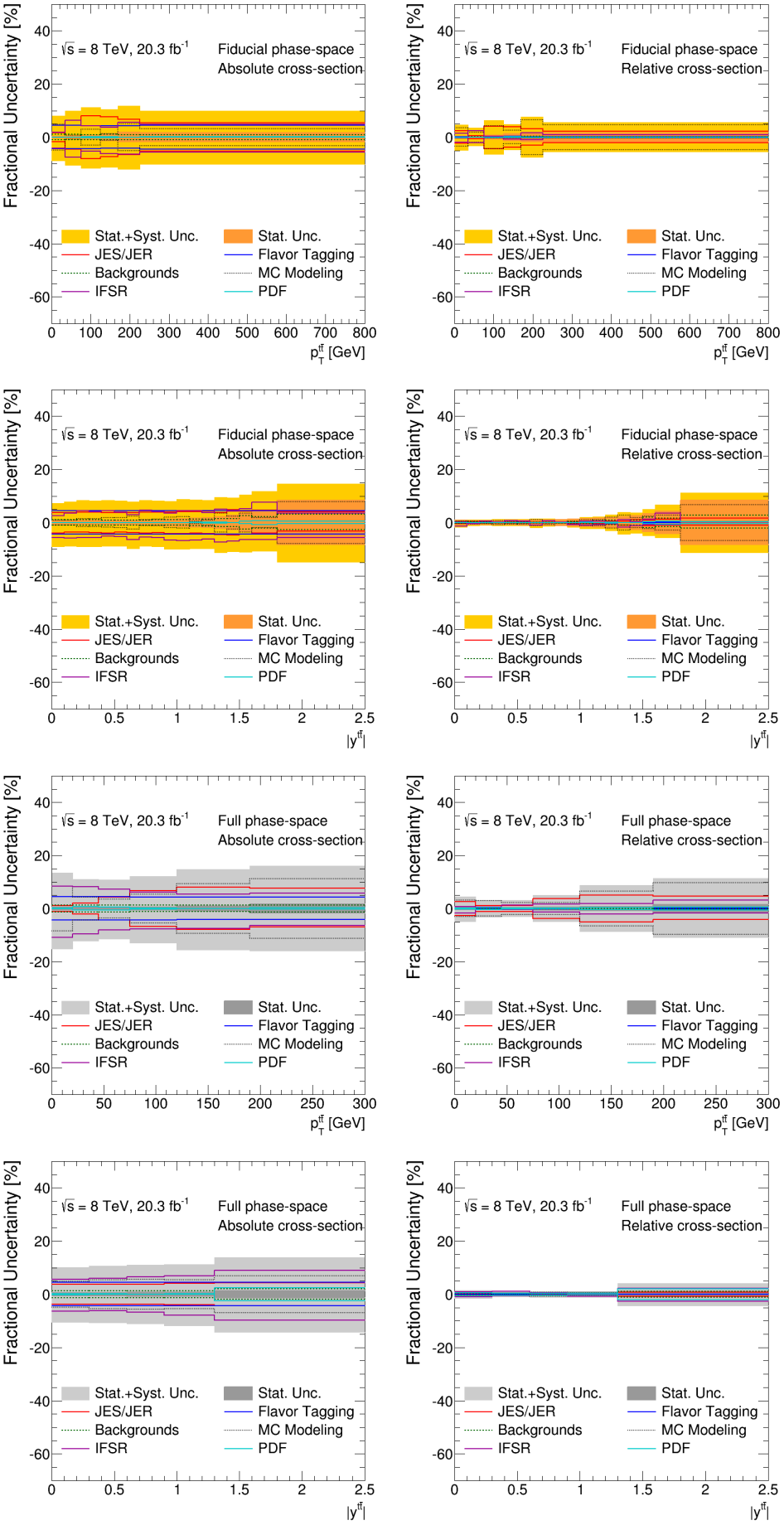

FIGURE 6.26: Fractional uncertainties for the absolute (left) and relative (right) differential cross-sections as a function of $p_{\mathrm{T}}^{t\bar{t}}$ (first row) and $\left|y^{t\bar{t}}\right|$ (second row) in the fiducial phase-space, $p_{\mathrm{T}}^{t\bar{t}}$ (third row) and $\left|y^{t\bar{t}}\right|$ (fourth row) in the full phase-space.

6.4.2.6 Impact of IFSR

To show visually the impact of the increased/decreased initial- and final-state QCD radiation, a series of plots is provided in this section, in which we compare the baseline POWHEG model, along with two upward/downward variation of parameters affecting the initial- and final-state QCD radiation, with respect to the unfolded data. The following Figs. 6.27 and 6.28 show compatibility of increased and decreased IFSR samples for the absolute and relative differential cross-sections as a function of some kinematical quantities. Other plots are shown in App. E.

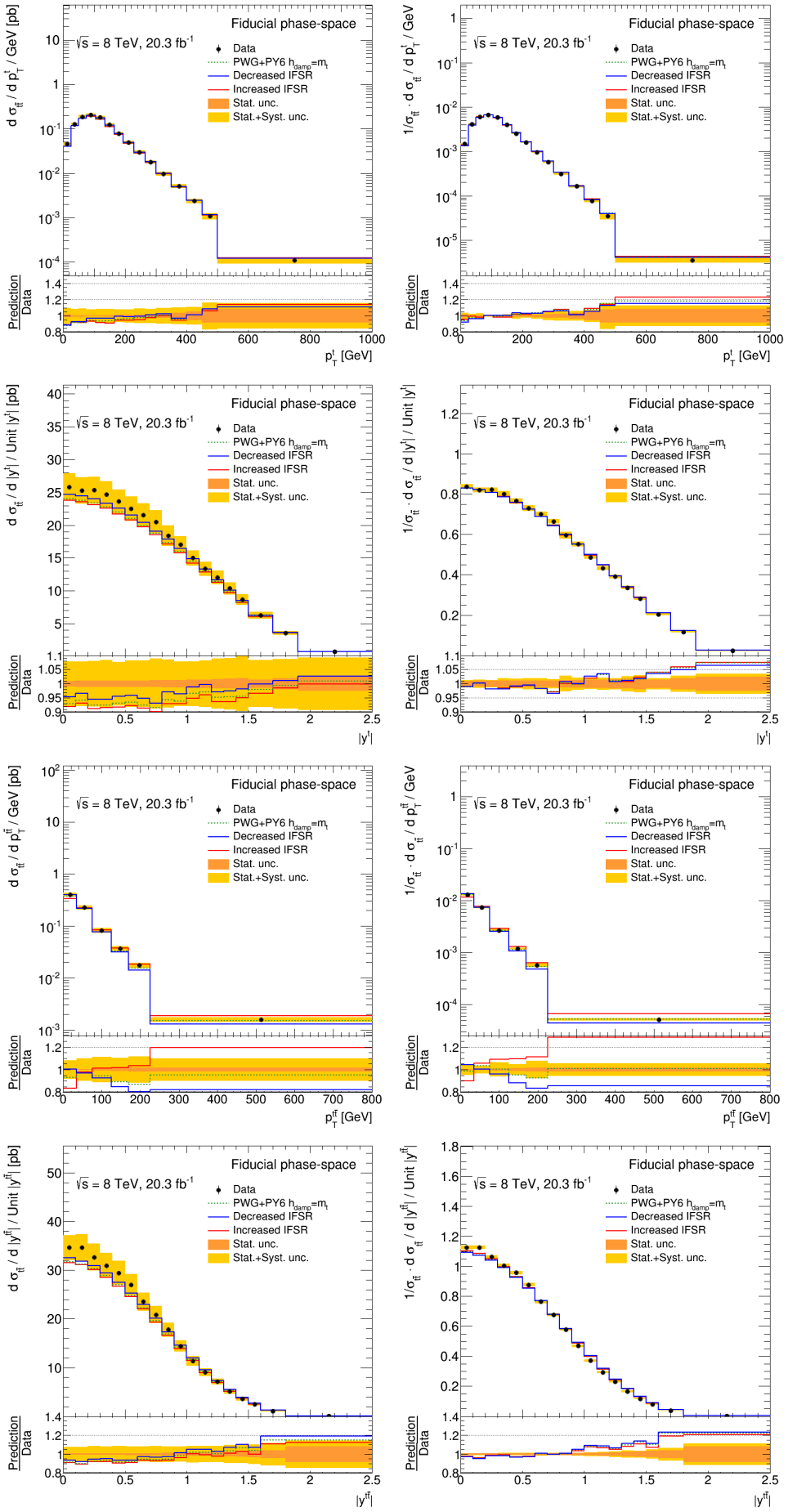

FIGURE 6.27: Compatibility of increased and decreased IFSR samples for the absolute (left) and relative (right) differential cross-sections as a function of the $p_{\mathrm{T}}^{t,\mathrm{had}}$ (first row), $\left|y^{t,\mathrm{had}}\right|$ (second row), $p_{\mathrm{T}}^{t\bar{t}}$ (third row) and $\left|y^{t\bar{t}}\right|$ (fourth row) in the fiducial phase-space.

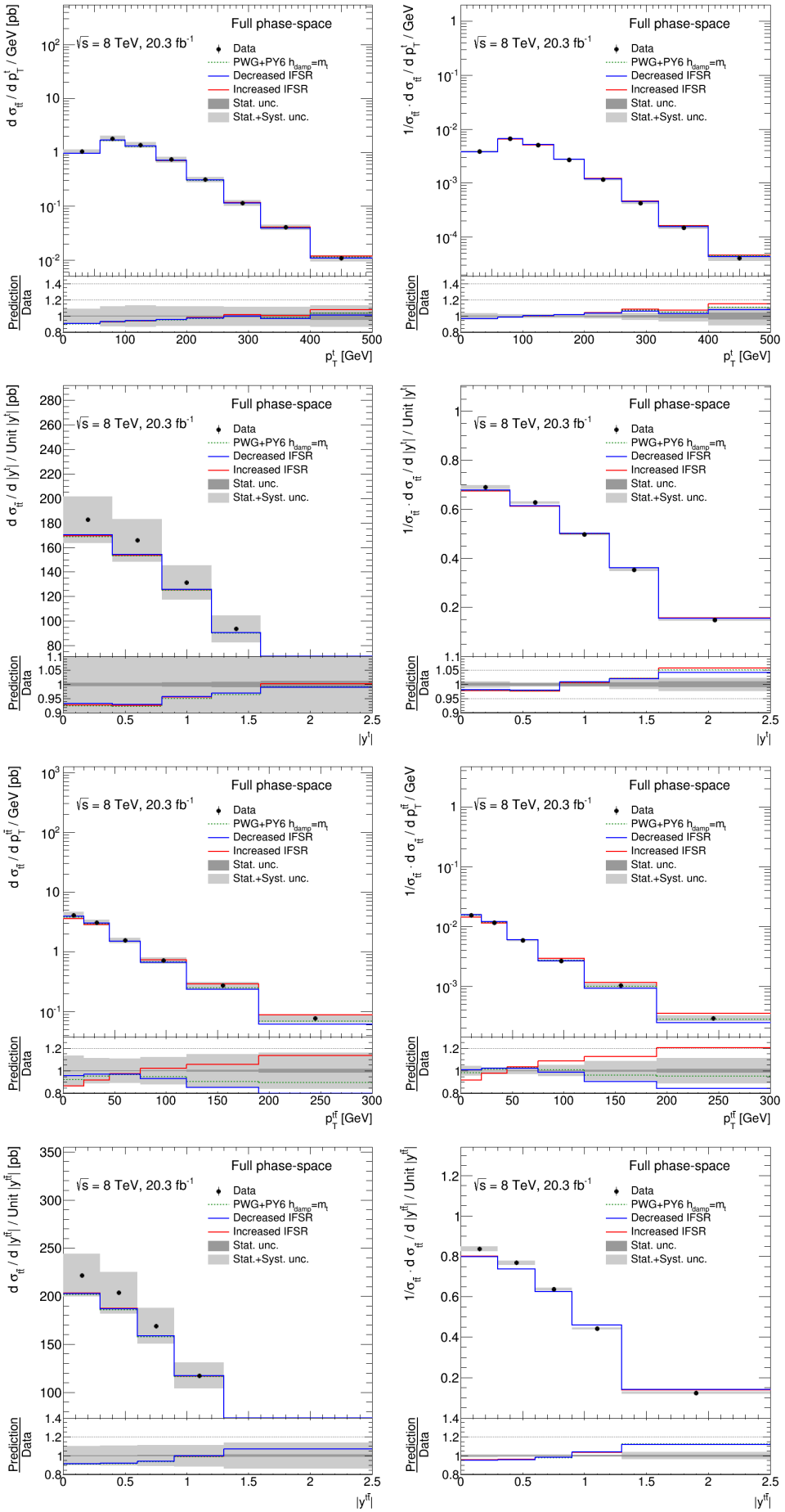

FIGURE 6.28: Compatibility of increased and decreased IFSR samples for the absolute (left) and relative (right) differential cross-sections as a function of the $p_{\mathrm{T}}^{t,\mathrm{had}}$ (first row), $\left|y^{t,\mathrm{had}}\right|$ (second row), $p_{\mathrm{T}}^{t\bar{t}}$ (third row) and $\left|y^{t\bar{t}}\right|$ (fourth row) in the full phase-space.

6.4.3 Correlation matrices

The covariance matrices for the normalized and absolute unfolded spectra due to the statistical and systematic uncertainties are obtained by evaluating the covariance between the kinematic bins using pseudo-experiments. In particular, the correlations due to statistical fluctuations for both data and the signal are evaluated by varying the event counts independently in every bin before unfolding, and then propagating the resulting variations through the unfolding. In Figs 6.29- 6.32 a selection of the covariance matrices for the unfolded spectra in both fiducial and full phase-space are shown. These matrices (see Sec 7.1) are used to quantify the level of agreement between the measured distribution and simulations by calculating χ^2 values and inferred p-values.

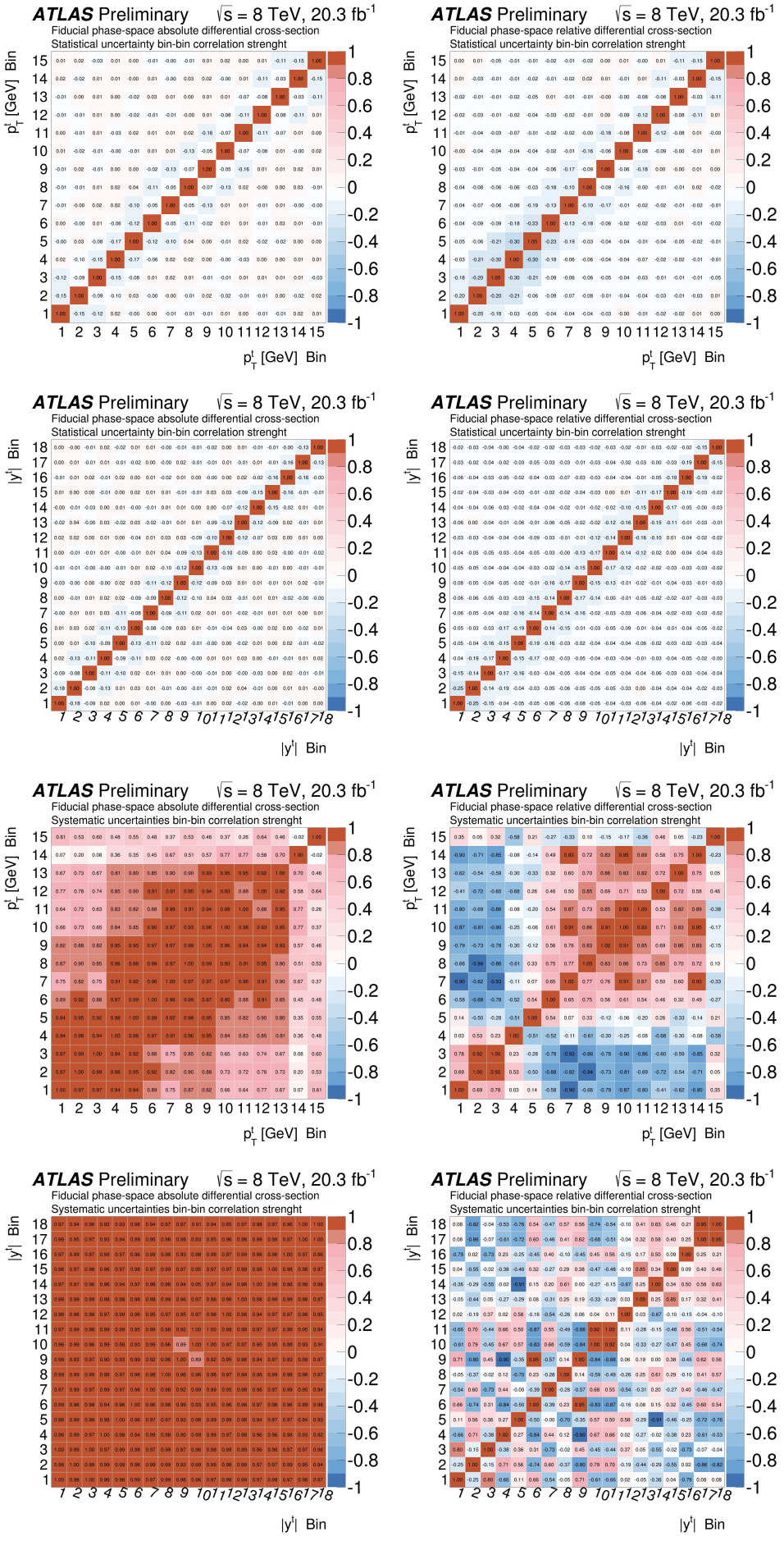

FIGURE 6.29: Absolute (left) and relative (right) correlation matrices of the fiducial phase-space differential cross-sections as a function of the $p_{\mathrm{T}}^{t,\mathrm{had}}$ (top) and $\left|y^{t,\mathrm{had}}\right|$ (bottom) for the statistical uncertainty first and systematic uncertainty then.

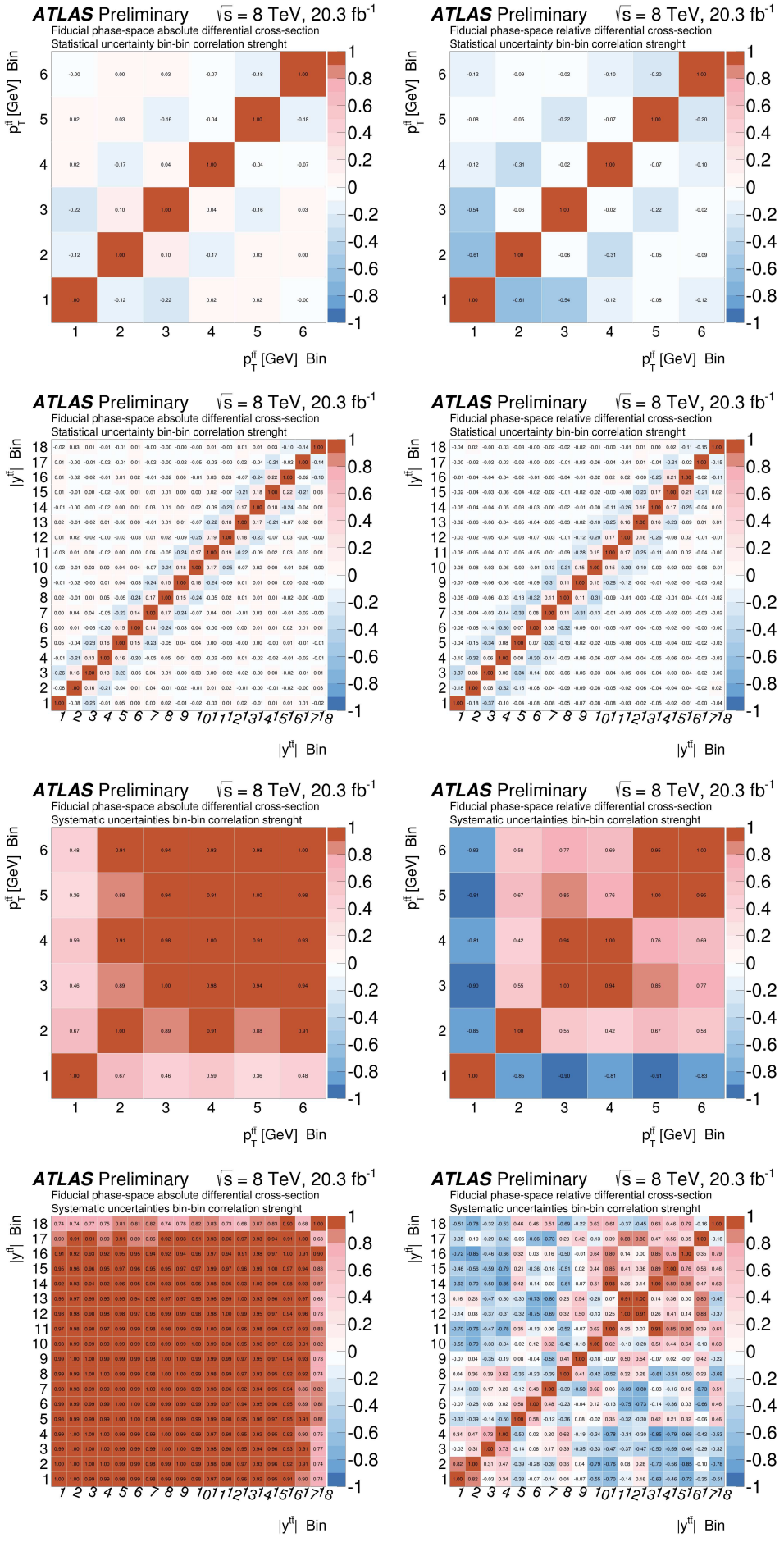

FIGURE 6.30: Absolute (left) and relative (right) correlation matrices of the fiducial phase-space differential cross-sections as a function of the $p_{\mathrm{T}}^{t\bar{t}}$(top) and $\left|y^{t\bar{t}}\right|$ (bottom) for the statistical uncertainty first and systematic uncertanty then.

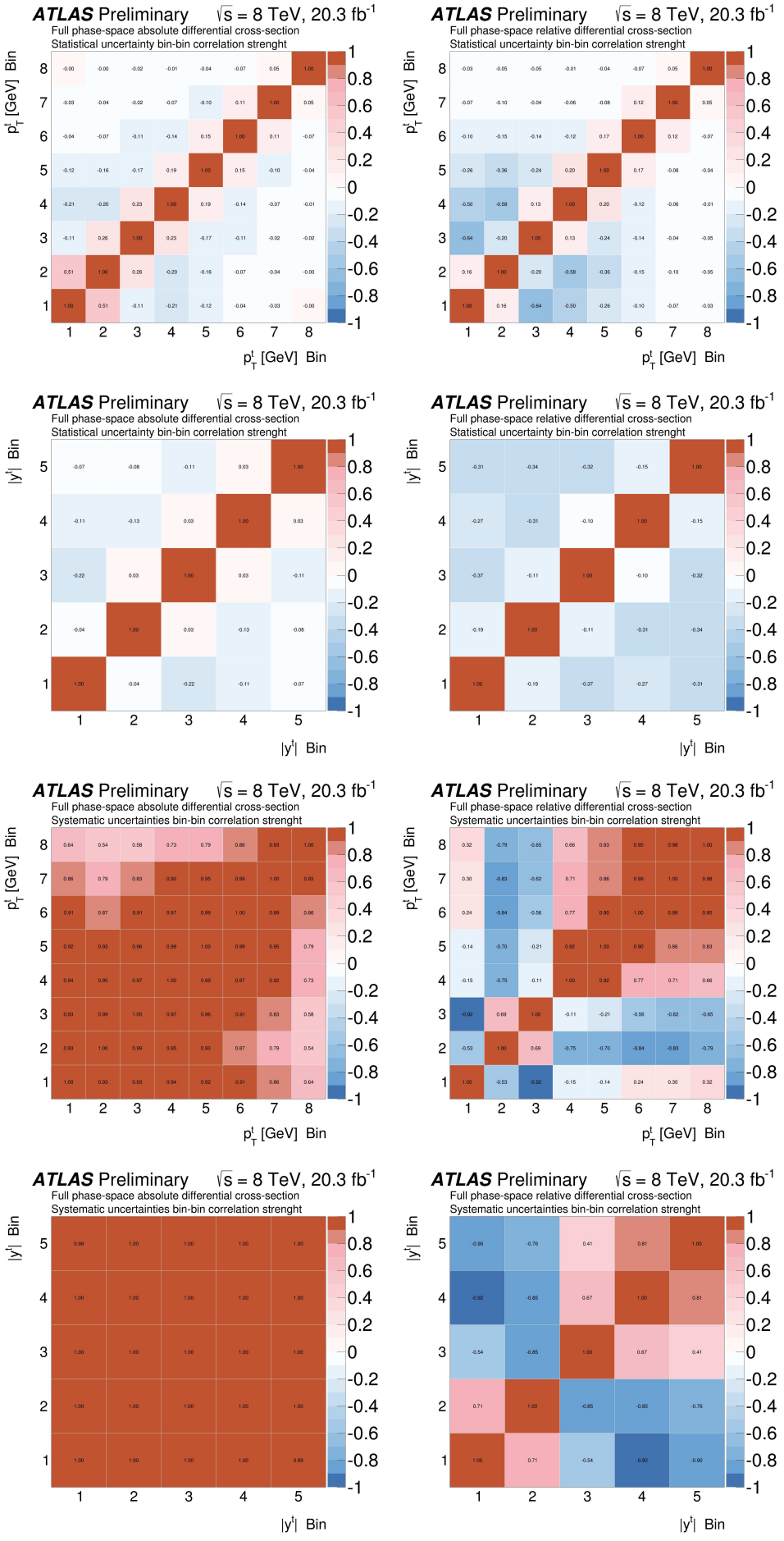

FIGURE 6.31: Absolute (left) and relative (right) correlation matrices of the full phase-space differential cross-sections as a function of the $p_{\mathrm{T}}^{t,\mathrm{had}}$ (top) and $\left|y^{t,\mathrm{had}}\right|$ (bottom) for the statistical uncertainty first and systematic uncertanty then.

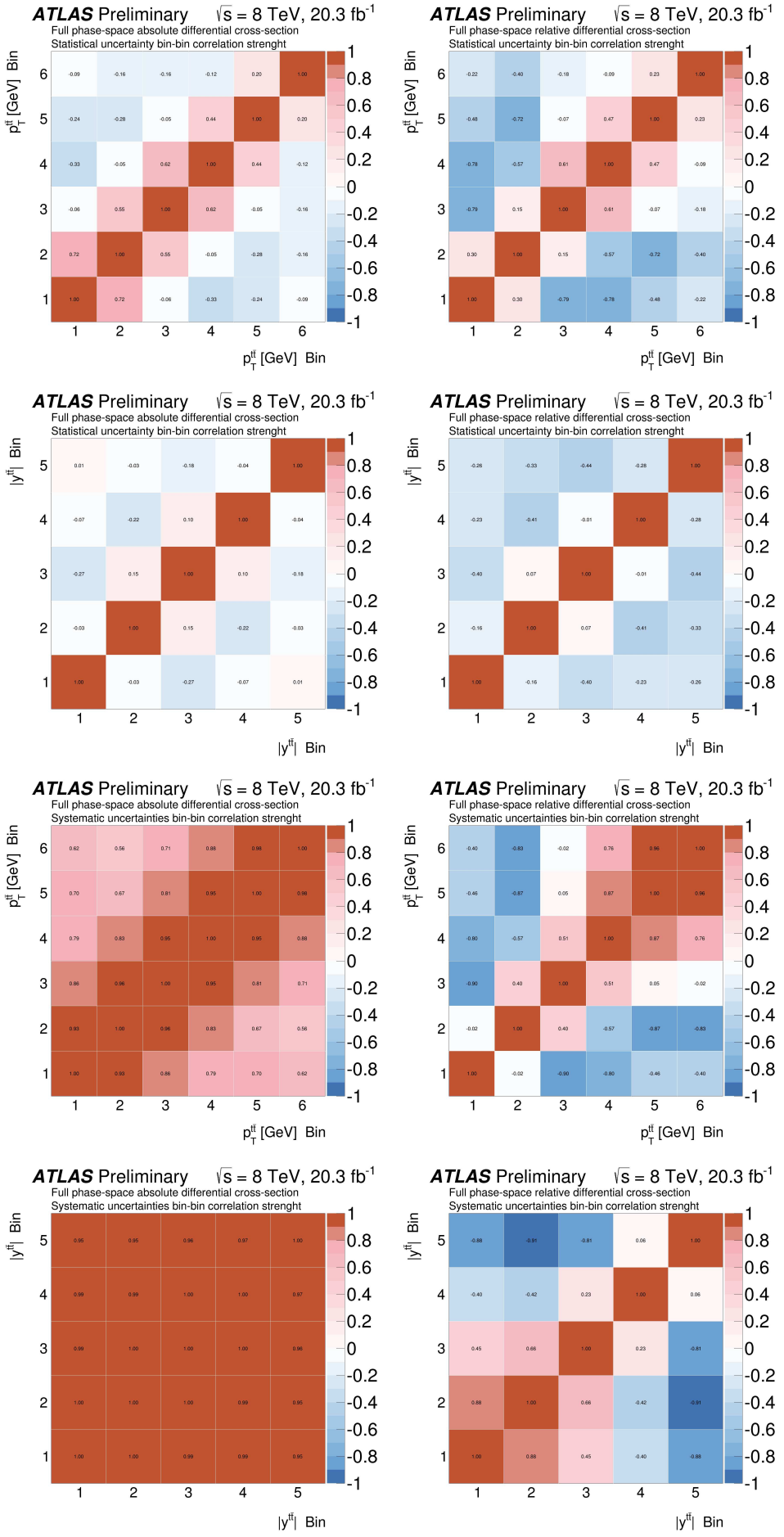

FIGURE 6.32: Absolute (left) and relative (right) correlation matrices of the full phase-space differential cross-sections as a function of the $p_{\mathrm{T}}^{t\bar{t}}$(top) and $\left|y^{t\bar{t}}\right|$ (bottom) for the statistical uncertainty first and systematic uncertanty then.

6.5 Analysis framework

The transfer of knowledge is of fundamental importance within a huge collaboration as ATLAS, for instance by sharing tools for common tasks. This is possible only through a code with a friendly user interface and a high compatibility and flexibility.
The analysis infrastructure used for this analysis is MAMbo [124] (Modular Analysis Made in Bologna), written in C++ object oriented language, it is interfaced with the most common ATLAS top analysis infrastructure named AnalysisTop by using the MoMA package (Modules of MAMbo for ATLAS) that provides a bridge between MAMbo and ATLAS AnalysisTop.
AnalysisTop is derived and inherits from the most general RootCore ATLAS framework, that allows to maintain corrections and scale factors up to date and gives the possibility to use several tools exploited for different analysis tasks already implemented by other groups.
MAMbo has a modular structure through a strong hierarchical coding. The different analysis steps are managed via bash scripts and parameter files, in order to simplify the managing and to be user friendly. It performs the events correction, selection and reconstruction of the physical objects and then produce row histograms. The analysis program covers all the phases of the data analysis: it starts processing data in D3PD format, either on the GRID or using local batch systems, by applying the event selection and by producing slim and easy manageable ntuple files, in which are stored all the needed information in histograms form.
An independent code is given in order to produce final plots in the ATLAS format, as for data/MC comparison. A flexible unfolding tool is also included; it gives the possibility to use different unfolding techniques and to produce cross section measurements; a flexible system to manage statistical and systematic uncertainties is also included. A series of scripts and macros allow data management and storage. The framework is structured in a way that allows to be easily adapted to different top analysis to add new features. The framework is equipped with a documentation describing the different programs included and guiding the analyzer to perform a full basic analysis chain [124].

Chapter 7

Results

In this chapter, comparisons between unfolded data distributions and several SM predictions are presented for the different observables discussed in Sect. 5.3. Events are selected by requiring exactly one lepton and at least four jets with at least two of the jets tagged as originating from a b-quark. Although the normalized differential cross-sections are shown as the main results in order to reduce the systematic uncertainties (see Sec. 7.1), the data/theory comparisons for the absolute spectra are also shown in Sec. 7.2.

7.1 Results

The SM predictions are obtained using different MC generators. The POWHEG-BOX generator [75], denoted "PWG" in the figures, is employed with three different sets of parton shower models, namely Pythia [77] (baseline sample), Pythia8 [137] (newer parton shower) and Herwig [80] (7 TeV ATLAS default sample) . The other NLO generator is MC@NLO [79] interfaced with the Herwig parton shower. Generators at the LO accuracy are represented by MadGraph [138] interfaced with Pythia for parton showering (LO/Multileg generator, CMS default), which calculates $t\bar{t}$ matrix elements with up to three additional partons and implements the matrix-element / parton-shower MLM matching scheme [93].

The level of agreement between the measured distribution and simulations with different theoretical predictions is quantified by calculating χ^2 values, employing the full covariance matrices, and inferring p-values (probabilities that the χ^2 is larger than or equal to the observed value) from the χ^2 and the number of degrees of freedom (NDF). The normalization constraint used to derive the normalized differential cross-sections lowers

by one unit the NDF and the rank of the $N_{\mathrm{b}} \times N_{\mathrm{b}}$ covariance matrix, where N_{b} is the number of bins of the spectrum under consideration. In order to evaluate the χ^2 the following relation is used

$$\chi^2 = V^{\mathrm{T}}_{N_{\mathrm{b}}-1} \cdot \mathrm{Cov}^{-1}_{N_{\mathrm{b}}-1} \cdot V_{N_{\mathrm{b}}-1}\,, \tag{7.1}$$

where $V_{N_{\mathrm{b}}-1}$ is the vector of differences between data and prediction obtained by discarding one of the N_{b} elements and $\mathrm{Cov}_{N_{\mathrm{b}}-1}$ is the $(N_{\mathrm{b}}-1)\times(N_{\mathrm{b}}-1)$ sub-matrix derived from the full covariance matrix, shown in Sec 6.4.3, discarding the corresponding row and column. The sub-matrix obtained in this way is invertible and allows the χ^2 to be computed. The χ^2 value does not depend on the choice of the element discarded for the vector $V_{N_{\mathrm{b}}-1}$ and the corresponding sub-matrix $\mathrm{Cov}_{N_{\mathrm{b}}-1}$.

We present in tabular form the χ^2- and p-values for each studied observable for which will be shown a comparison between the measured fiducial and full phase-space normalized differential cross-sections and the predictions from several MC generators, respectively Tabs. 7.1 and 7.2. Also we show the χ^2- and p-values table for the observables used in comparison between the measured fiducial phase-space normalized differential cross-sections and the predictions from the new PDF sets using the MC@NLO +Herwig generator, Tab. 7.3, and for those used in comparison between the measured full phase-space normalized differential cross-sections and higher-order QCD calculations 7.4. These values are also evaluated in the case of comparison between the measured fiducial and full phase-space absolute differential cross-sections and the predictions from several MC generators, as shown in the App. H.

Variable	PWG+PY8 CT10 $h_{\mathrm{damp}} = m_t$		MC@NLO+HW CT10 AUET2		PWG+PY6 CT10 $h_{\mathrm{damp}} = m_t$		PWG+HW6 CT10 $h_{\mathrm{damp}} = \infty$		MadGraph+PY6 MadGraph+PY6 P2011C	
	χ^2/NDF	p-value	χ^2/NDF	p-value	χ^2/NDF	p-value	χ^2/NDF	p-value	χ^2/NDF	p-value
p_T^t	10.8/14	0.70	16.5/14	0.28	11.5/14	0.65	5.1/14	0.98	47.2/14	<0.01
R_{Wt}	24.9/11	<0.01	26.8/11	<0.01	30.8/11	<0.01	8.8/11	0.64	77.1/11	<0.01
$\chi^{t\bar{t}}$	18.6/9	0.03	28.2/9	<0.01	18.2/9	0.03	39.0/9	<0.01	167.0/9	<0.01
$\lvert y^{t\bar{t}}\rvert$	58.2/17	<0.01	41.8/17	<0.01	51.9/17	<0.01	53.5/17	<0.01	97.5/17	<0.01
$m^{t\bar{t}}$	25.6/10	<0.01	65.5/10	<0.01	14.3/10	0.16	33.2/10	<0.01	33.8/10	<0.01
$y^{t\bar{t}}_{boost}$	42.8/15	<0.01	27.1/15	0.03	38.9/15	<0.01	39.1/15	<0.01	77.8/15	<0.01
$\lvert p^{t\bar{t}}_{out}\rvert$	5.7/5	0.33	11.3/5	0.05	12.5/5	0.03	4.8/5	0.45	8.6/5	0.13
$\lvert y^t\rvert$	23.4/17	0.14	12.7/17	0.76	21.7/17	0.20	15.8/17	0.54	14.6/17	0.63
$p_T^{t\bar{t}}$	10.1/5	0.07	18.3/5	<0.01	16.2/5	<0.01	21.9/5	<0.01	6.7/5	0.24
$H_T^{t\bar{t}}$	14.6/14	0.40	10.0/14	0.76	16.9/14	0.26	9.4/14	0.80	64.4/14	<0.01
$\Delta\phi^{t\bar{t}}$	0.8/3	0.85	26.4/3	<0.01	2.9/3	0.41	24.3/3	<0.01	26.5/3	<0.01

Table 7.1: Comparison between the measured fiducial phase-space normalized differential cross-sections and the predictions from several MC generators. For each variable and prediction a χ^2 and a p-value are calculated using the covariance matrix of each measured spectrum. The number of degrees of freedom (NDF) is equal to $N_{\mathrm{b}} - 1$ where N_{b} is the number of bins in the distribution.

Variable	PWG+PY8 CT10 $h_{\text{damp}} = m_t$		MC@NLO+HW CT10 AUET2		PWG+PY6 CT10 $h_{\text{damp}} = m_t$		PWG+HW6 CT10 $h_{\text{damp}} = \infty$		MadGraph+PY6 MadGraph+PY6 P2011C	
	χ^2/NDF	p-value	χ^2/NDF	p-value	χ^2/NDF	p-value	χ^2/NDF	p-value	χ^2/NDF	p-value
p_T^t	3.1/7	0.87	9.1/7	0.24	6.1/7	0.53	4.9/7	0.67	13.7/7	0.06
$\chi^{t\bar{t}}$	30.3/9	<0.01	51.1/9	<0.01	33.8/9	<0.01	81.2/9	<0.01	200.0/9	<0.01
$\lvert y^{t\bar{t}}\rvert$	17.4/4	<0.01	12.1/4	0.02	17.9/4	<0.01	16.9/4	<0.01	22.3/4	<0.01
$m^{t\bar{t}}$	4.4/6	0.62	4.9/6	0.55	3.1/6	0.80	19.2/6	<0.01	10.1/6	0.12
$y_{boost}^{t\bar{t}}$	25.3/15	0.05	19.0/15	0.21	25.9/15	0.04	23.7/15	0.07	35.8/15	<0.01
$\lvert p_{out}^{t\bar{t}}\rvert$	9.0/5	0.11	11.1/5	0.05	6.3/5	0.28	4.1/5	0.53	17.8/5	<0.01
$\lvert y^t\rvert$	1.4/4	0.84	0.7/4	0.95	1.8/4	0.78	0.8/4	0.94	0.4/4	0.98
$p_T^{t\bar{t}}$	14.6/5	0.01	2.3/5	0.81	6.6/5	0.25	4.1/5	0.53	87.3/5	<0.01
$H_T^{t\bar{t}}$	8.7/14	0.85	14.3/14	0.43	15.5/14	0.34	8.3/14	0.87	29.0/14	0.01
$\Delta\phi^{t\bar{t}}$	2.3/3	0.51	1.0/3	0.80	0.9/3	0.83	29.5/3	<0.01	21.0/3	<0.01

TABLE 7.2: Comparison between the measured full phase-space normalized differential cross-sections and the predictions from several MC generators. For each variable and prediction a χ^2 and a p-value are calculated using the covariance matrix of each measured spectrum. The number of degrees of freedom (NDF) is equal to $N_{\text{b}} - 1$ where N_{b} is the number of bins in the distribution.

Variable	CT14nlo		CJ12mid		MMHT2014nlo68cl		NNPDF30nlo		CT10nlo		METAv10LHC		HERA20NLO	
	χ^2/NDF	p-value	χ^2/NDF	p-value	χ^2/NDF	p-value	χ^2/NDF	p-value	χ^2/NDF	p-value	χ^2/NDF	p-value	χ^2/NDF	p-value
p_T^t	17.3/14	0.24	16.2/14	0.30	16.5/14	0.28	17.2/14	0.24	16.5/14	0.28	16.9/14	0.26	18.1/14	0.20
R_{Wt}	25.2/11	<0.01	24.0/11	0.01	23.9/11	0.01	24.1/11	0.01	26.8/11	<0.01	22.8/11	0.02	15.2/11	0.17
$\chi^{t\bar{t}}$	27.7/9	<0.01	32.3/9	<0.01	31.9/9	<0.01	28.3/9	<0.01	28.2/9	<0.01	31.5/9	<0.01	75.1/9	<0.01
$\lvert y^{t\bar{t}}\rvert$	31.8/17	0.02	25.5/17	0.08	22.2/17	0.18	17.8/17	0.40	41.8/17	<0.01	19.5/17	0.30	24.2/17	0.11
$m^{t\bar{t}}$	55.8/10	<0.01	58.2/10	<0.01	57.7/10	<0.01	55.4/10	<0.01	65.5/10	<0.01	58.0/10	<0.01	80.2/10	<0.01
$y_{boost}^{t\bar{t}}$	18.4/15	0.24	17.7/15	0.28	10.6/15	0.78	8.5/15	0.90	27.1/15	0.03	8.8/15	0.89	20.5/15	0.15
$\lvert y^t\rvert$	12.8/17	0.75	11.4/17	0.83	12.1/17	0.79	11.2/17	0.85	12.7/17	0.76	11.8/17	0.81	31.4/17	0.02
$p_T^{t\bar{t}}$	18.4/5	<0.01	18.9/5	<0.01	19.7/5	<0.01	18.4/5	<0.01	18.3/5	<0.01	19.5/5	<0.01	29.2/5	<0.01
$H_T^{t\bar{t}}$	10.0/14	0.76	9.2/14	0.82	9.2/14	0.82	9.9/14	0.77	10.0/14	0.76	9.3/14	0.81	8.3/14	0.87
$\Delta\phi^{t\bar{t}}$	25.8/3	<0.01	25.1/3	<0.01	25.9/3	<0.01	25.2/3	<0.01	26.4/3	<0.01	25.2/3	<0.01	25.1/3	<0.01

TABLE 7.3: Comparison between the measured fiducial phase-space normalized differential cross-sections and the predictions from new PDF sets using the MC@NLO+HERWIG generator. For each variable and prediction a χ^2 and a p-value are calculated using the covariance matrix of each measured spectrum. The number of degrees of freedom (NDF) is equal to $N_\mathrm{b} - 1$ where N_b is the number of bins in the distribution.

Variable	aN^{3}LO		aNNLO	
	χ^2/NDF	p-value	χ^2/NDF	p-value
p_T^t	18/7	0.01	4.0/7	0.78
$\lvert y^t\rvert$	0.6/4	0.96	9.2/4	0.06

TABLE 7.4: Comparison between the measured full phase-space normalized differential cross-sections and higher-order QCD calculations. For each variable and prediction a χ^2 and a p-value are calculated using the covariance matrix of each measured spectrum. The number of degrees of freedom (NDF) is equal to $N_\mathrm{b} - 1$ where N_b is the number of bins in the distribution.

The Figures 7.1–7.5 present the normalized $t\bar{t}$ fiducial phase-space differential cross-sections as a function of the different variables. In particular, Figures 7.1(a) and 7.1(b) show the distributions of the hadronic top-quark transverse momentum and the absolute value of the rapidity. Figures 7.2(a), 7.2(b) and 7.2(c) present the $t\bar{t}$ system invariant mass, transverse momentum and absolute value of the rapidity, while the additional variables related to the $t\bar{t}$ system and the ratio of the transverse momenta of the hadronically decaying W boson and top quark are shown in Figures 7.3, 7.4 and 7.5.

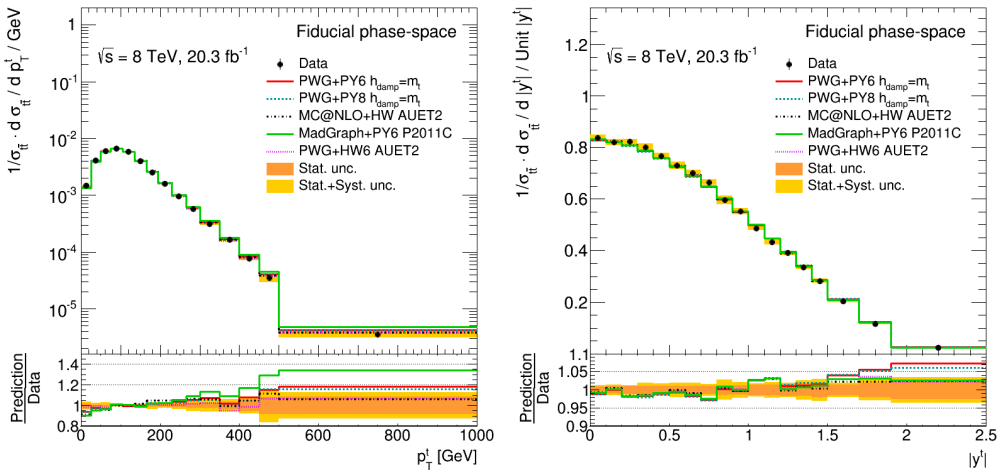

(a) (b)

FIGURE 7.1: Fiducial phase-space normalized differential cross-sections as a function of the (a) transverse momentum ($p_{\mathrm{T}}^{t,\mathrm{had}}$) and (b) absolute value of the rapidity ($\left|y^{t,\mathrm{had}}\right|$) of the hadronic top quark. The yellow bands indicate the total uncertainty on the data in each bin. The POWHEG+PYTHIA generator with $h_{\mathrm{damp}} = m_t$ and the CT10nlo PDF is used as the nominal prediction to correct for detector effects.

In general, the Monte Carlo predictions fairly agree with data in a wide kinematic region at a level of 10-15%.

A few predictions are not able to correctly describe the distributions, as also witnessed by the χ^2 values and the p-values listed in tab. 7.1. In particular, a certain tension between data and all predictions is observed in the case of the hadronic top-quark transverse momentum distribution for values higher than about 400 GeV. No electroweak corrections [139–143] are included in these predictions, as these have been shown to have a measurable impact only at very high values of the top quark transverse momentum, leading to a slightly softer $p_{\mathrm{T}}^{t,\mathrm{had}}$ spectrum as confirmed by the recent ATLAS measurement of the $t\bar{t}$ differential distribution of the hadronic top-quark p_{T} for boosted top quarks [144]. The effect of electroweak corrections alone is not large enough to solve this discrepancy completely [144, 145]. The shape of the $\left|y^{t,\mathrm{had}}\right|$ distribution shows only a modest agreement for all the generators, with larger discrepancies observed in the forward region for POWHEG+PYTHIA and POWHEG+PYTHIA8.

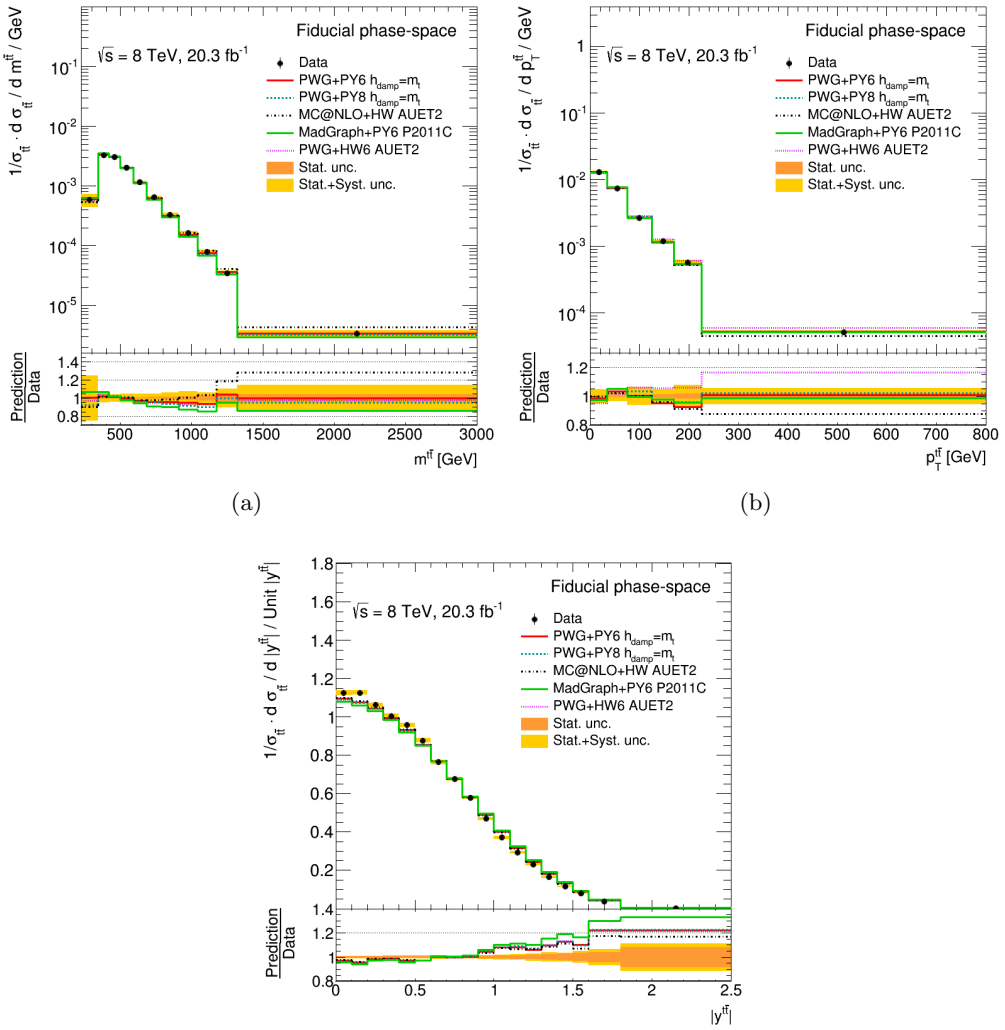

(a) (b)

(c)

FIGURE 7.2: Fiducial phase-space normalized differential cross-sections as a function of the (a) invariant mass ($m^{t\bar{t}}$), (b) transverse momentum ($p_{\mathrm{T}}^{t\bar{t}}$) and (c) absolute value of the rapidity ($\left|y^{t\bar{t}}\right|$) of the $t\bar{t}$ system. The yellow bands indicate the total uncertainty on the data in each bin. The POWHEG+PYTHIA generator with $h_{\mathrm{damp}} = m_t$ and the CT10nlo PDF is used as the nominal prediction to correct for detector effects.

For the $m^{t\bar{t}}$ distribution, the POWHEG+PYTHIA, POWHEG+PYTHIA8 and POWHEG+HERWIG generators are in better agreement with the data. All generators are in good agreement in the $p_{\mathrm{T}}^{t\bar{t}}$ spectrum except for MC@NLO+HERWIG and POWHEG+HERWIG in the last bin. This observation suggests that setting $h_{\mathrm{damp}} = m_t$ in the POWHEG samples improves the agreement at high values of the $t\bar{t}$ transverse momentum. The data at high values of $t\bar{t}$ rapidity is not adequately described by any of the generators considered. The same conclusions hold for the analogous distribution for the absolute spectra (see Sect. 7.2), although the overall agreement estimated with the χ^2 values and the p-values is better due to the larger uncertainties.

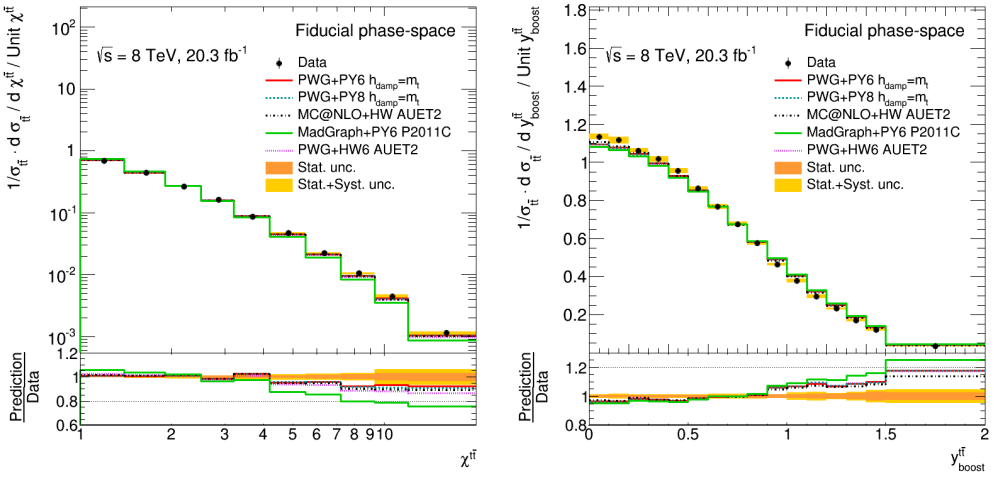

(a) (b)

FIGURE 7.3: Fiducial phase-space normalized differential cross-sections as a function of the $t\bar{t}$ (a) production angle ($\chi^{t\bar{t}}$) and (b) longitudinal boost ($y^{t\bar{t}}_{\text{boost}}$). The yellow bands indicate the total uncertainty on the data in each bin. The POWHEG+PYTHIA generator with $h_{\text{damp}} = m_t$ and the CT10nlo PDF is used as the nominal prediction to correct for detector effects.

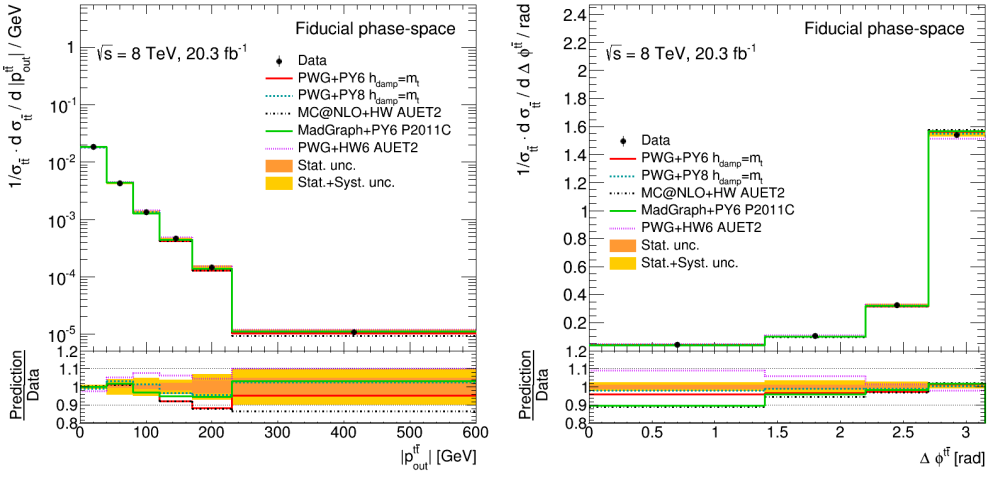

(a) (b)

FIGURE 7.4: Fiducial phase-space normalized differential cross-sections as a function of the $t\bar{t}$ (a) out-of-plane momentum ($\left|p^{t\bar{t}}_{\text{out}}\right|$) and (b) azimuthal angle ($\Delta\phi_{t\bar{t}}$). The yellow bands indicate the total uncertainty on the data in each bin. The POWHEG+PYTHIA generator with $h_{\text{damp}} = m_t$ and the CT10nlo PDF is used as the nominal prediction to correct for detector effects.

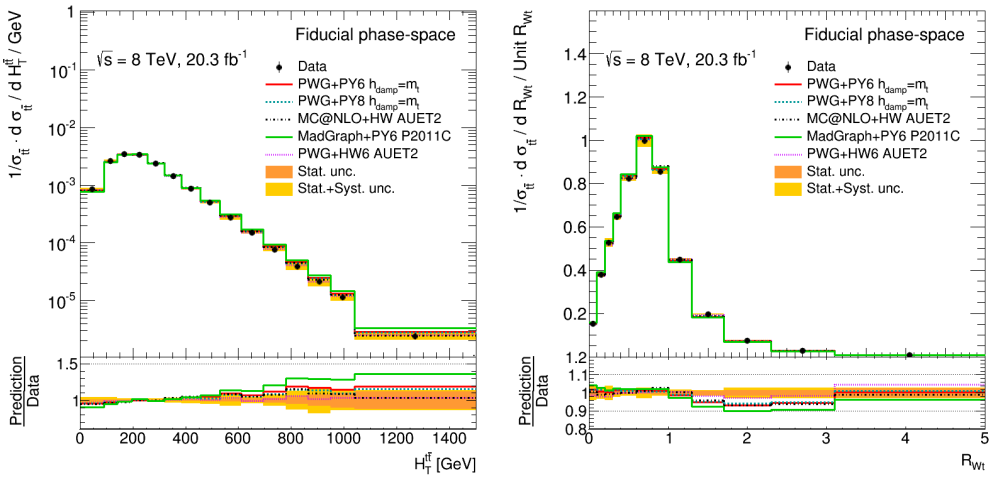

(a) (b)

FIGURE 7.5: Fiducial phase-space normalized differential cross-sections as a function of the (a) scalar sum of the transverse momenta of the hadronic and leptonic top quarks ($H_{\mathrm{T}}^{t\bar{t}}$) and (b) the ratio of the hadronic W and the hadronic top transverse momenta (R_{Wt}). The yellow bands indicate the total uncertainty on the data in each bin. The POWHEG+PYTHIA generator with $h_{\mathrm{damp}} = m_t$ and the CT10nlo PDF is used as the nominal prediction to correct for detector effects.

For the variables describing the hard-scattering interaction, the production angle $\chi^{t\bar{t}}$ is well described in the central region. The forward region, described by the tail of this observable and by the tail of the longitudinal boost $y_{\mathrm{boost}}^{t\bar{t}}$, is not described correctly by any of the generators under consideration. For the variables describing the radiation along the $t\bar{t}$ pair momentum direction, both $\left|p_{\mathrm{out}}^{t\bar{t}}\right|$ and $\Delta\phi_{t\bar{t}}$ indicate that the kinematics of top quarks produced in the collinear region ($\Delta\phi_{t\bar{t}} \lesssim \pi/2$) are described with marginal agreement by all the generators, but the uncertainty is particularly large in this region. The tension observed in the $p_{\mathrm{T}}^{t,\mathrm{had}}$ spectrum is reflected in the tail of the $H_{\mathrm{T}}^{t\bar{t}}$ distribution. Finally, the ratio of the hadronic W boson and top-quark transverse momenta shows a mis-modelling in the range 1.5–3 for all the generators.

The difficulty in correctly predicting the data in the forward region was further investigated by studying the dependence of the predictions from different PDF sets. The study was performed for the rapidity observables $\left|y^{t,\mathrm{had}}\right|$, $\left|y^{t\bar{t}}\right|$ and $y_{\mathrm{boost}}^{t\bar{t}}$, shown in Figures 7.6 7.7 7.8 and comparing the data with the predictions of MC@NLO+HERWIG for more recent sets of parton distribution functions.

The results exhibit a general improvement in the description of the forward region for the most recent PDF sets (CT14nlo [146], CJ12mid [147], MMHT2014nlo [148], NNPDF 3.0 NLO [149], METAv10LHC [150], HERAPDF 2.0 NLO [151]). The improvement with respect to CT10nlo is also clearly shown in Table 7.3 which lists the χ^2 and corresponding

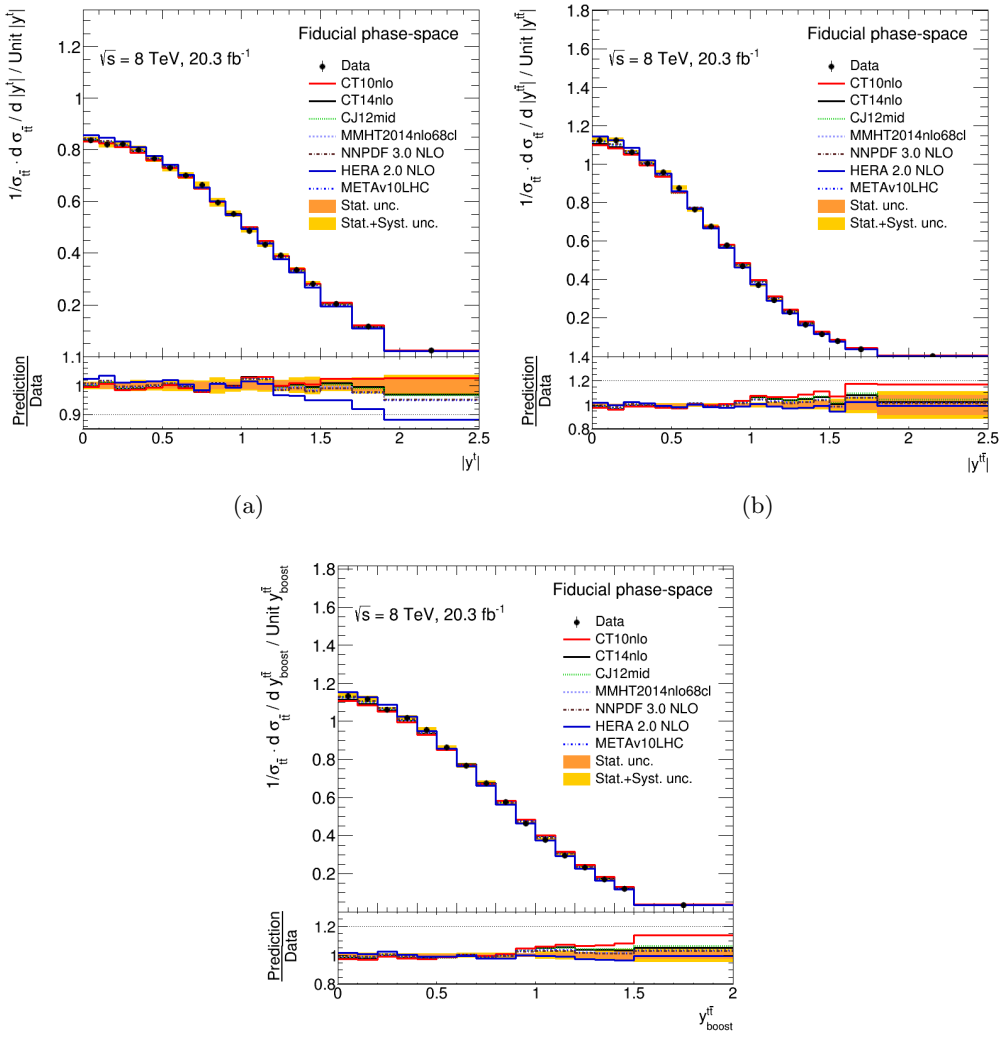

(a) (b)

(c)

FIGURE 7.6: Fiducial phase-space normalized differential cross-sections as a function of the (a) absolute value of the rapidity of the hadronic top quark ($\left|y^{t,\mathrm{had}}\right|$), (b) absolute value of the rapidity ($\left|y^{t\bar{t}}\right|$) of the $t\bar{t}$ system and (c) longitudinal boost ($y^{t\bar{t}}_{\mathrm{boost}}$). The yellow bands indicate the total uncertainty on the data in each bin. The MC@NLO+HERWIG generator is reweighted using the new PDF sets to produce the different predictions. The POWHEG+PYTHIA generator with $h_{\mathrm{damp}} = m_t$ and the CT10nlo PDF is used as the nominal prediction to correct for detector effects.

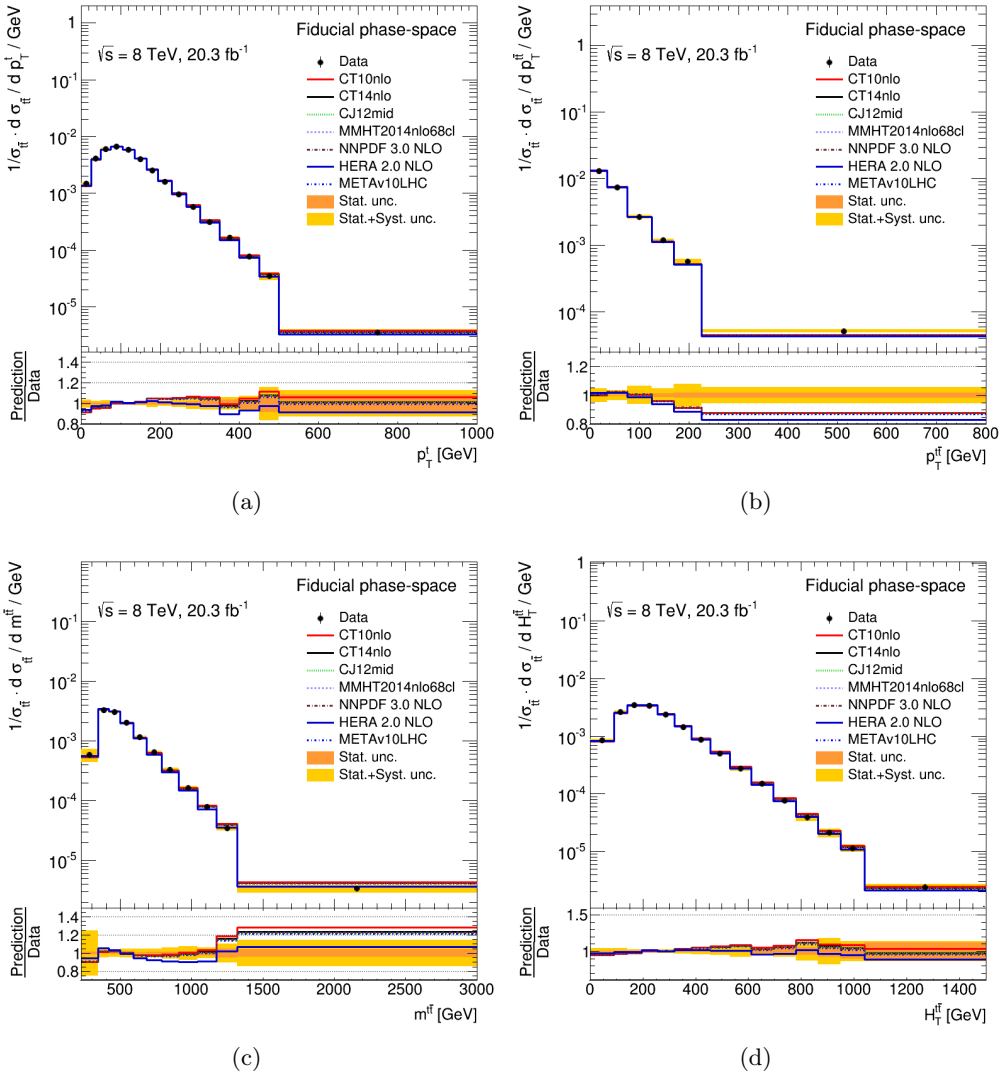

(a) (b)

(c) (d)

FIGURE 7.7: Fiducial phase-space normalized differential cross-sections as a function of the (a) transverse momentum of the hadronic top quark ($p_{\mathrm{T}}^{t,\mathrm{had}}$), (b) transverse momentum ($p_{\mathrm{T}}^{t\bar{t}}$) of the $t\bar{t}$ system, (c) invariant mass ($m^{t\bar{t}}$) of the $t\bar{t}$ system and (d) scalar sum od trasverse momentum ($H_{\mathrm{T}}^{t\bar{t}}$). The yellow bands indicate the total uncertainty on the data in each bin. The MC@NLO+HERWIG generator is reweighted using the new PDF sets to produce the different predictions. The POWHEG+PYTHIA generator with $h_{\mathrm{damp}} = m_t$ and the CT10nlo PDF is used as the nominal prediction to correct for detector effects.

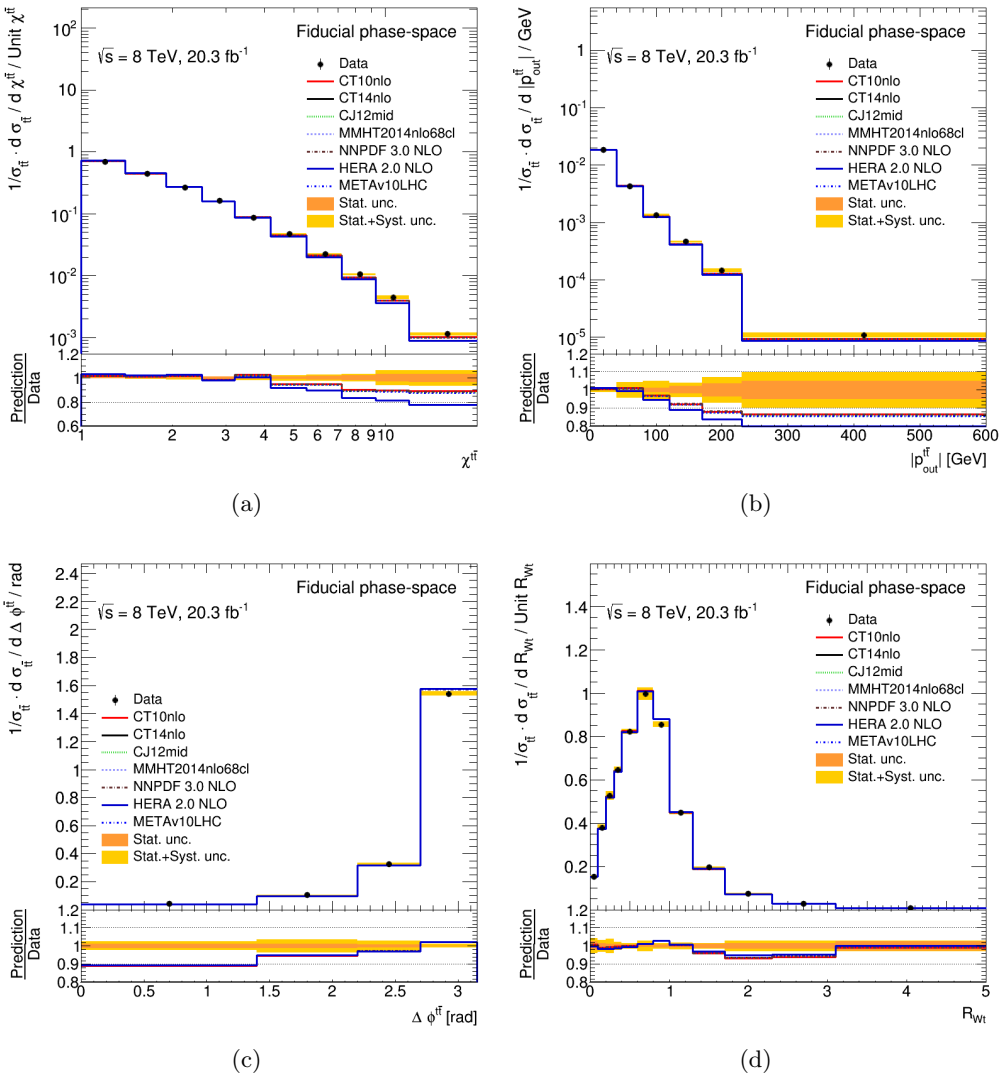

FIGURE 7.8: Fiducial phase-space normalized differential cross-sections as a function of the (a) production angle ($\chi^{t\bar{t}}$), (b) out-of-plane momentum ($|p_{\text{out}}^{t\bar{t}}|$), (c) azimuthal angle ($\Delta\phi_{t\bar{t}}$) and (d) the ratio of the hadronic W and the hadronic top transverse momenta (R_{Wt}). The yellow bands indicate the total uncertainty on the data in each bin. The MC@NLO+HERWIG generator is reweighted using the new PDF sets to produce the different predictions. The POWHEG+PYTHIA generator with $h_{\text{damp}} = m_t$ and the CT10nlo PDF is used as the nominal prediction to correct for detector effects.

p-values for the different sets. The only exception is represented by the $\left|y^{t,\mathrm{had}}\right|$ distribution using HERAPDF 2.0 NLO, for which a large disagreement in the forward region is observed.

The study was performed also for the other observables, but using more recent PDFs has not helped in improving the description of the measurements.

The set of Figures 7.9–7.12 presents the normalized $t\bar{t}$ full phase-space differential cross-sections as a function of the different observables. In particular, Figures 7.9(a) and 7.9(b) show the top-quark transverse momentum and the absolute value of the rapidity; Figures 7.10(a), 7.10(b) and 7.10(c) present the $t\bar{t}$ system invariant mass, transverse momentum and absolute value of the rapidity while the additional observables related to the $t\bar{t}$ system are shown in Figures 7.11 and 7.12.

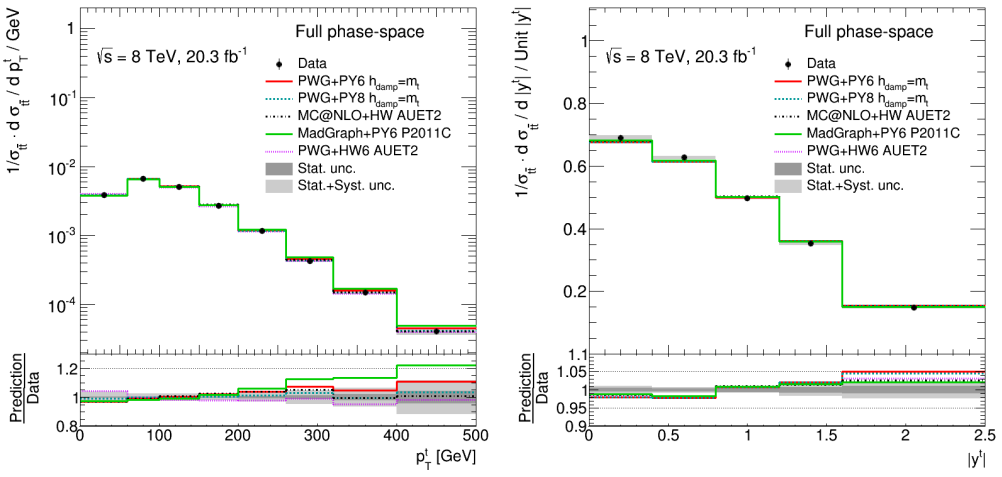

(a) (b)

FIGURE 7.9: Full phase-space normalized differential cross-sections as a function of the (a) transverse momentum (p_{T}^{t}) and (b) the absolute value of the rapidity ($|y^{t}|$) of the top quark. The grey bands indicate the total uncertainty on the data in each bin. The POWHEG+PYTHIA generator with $h_{\mathrm{damp}} = m_t$ and the CT10nlo PDF is used as the nominal prediction to correct for detector effects.

Regarding the comparison between data and predictions, the general picture, already outlined for the fiducial phase-space measurements, is still valid even though the uncertainties are much larger due to the full phase-space extrapolation. In particular, the predictions for the top-quark p_{T} and $H_{\mathrm{T}}^{t\bar{t}}$ tend to be in a better agreement with the data than what is observed in the fiducial phase-space. The χ^2 and corresponding p-values for the different observables and predictions are shown in Table 7.2.

In Figures 7.13–7.16 the normalized $t\bar{t}$ full phase-space differential cross-sections as a function of p_{T}^{t}, $\left|y^{t}\right|$, $m^{t\bar{t}}$ and $\left|y^{t\bar{t}}\right|$ are also compared with theoretical higher-order QCD calculations.

The measurements are compared to calculations that offer beyond–NLO accuracy:

- an approximate next-to-next-to-leading-order (aNNLO) calculation based on QCD threshold expansions beyond the leading logarithmic approximation [152] using the CT14nnlo PDF [146];

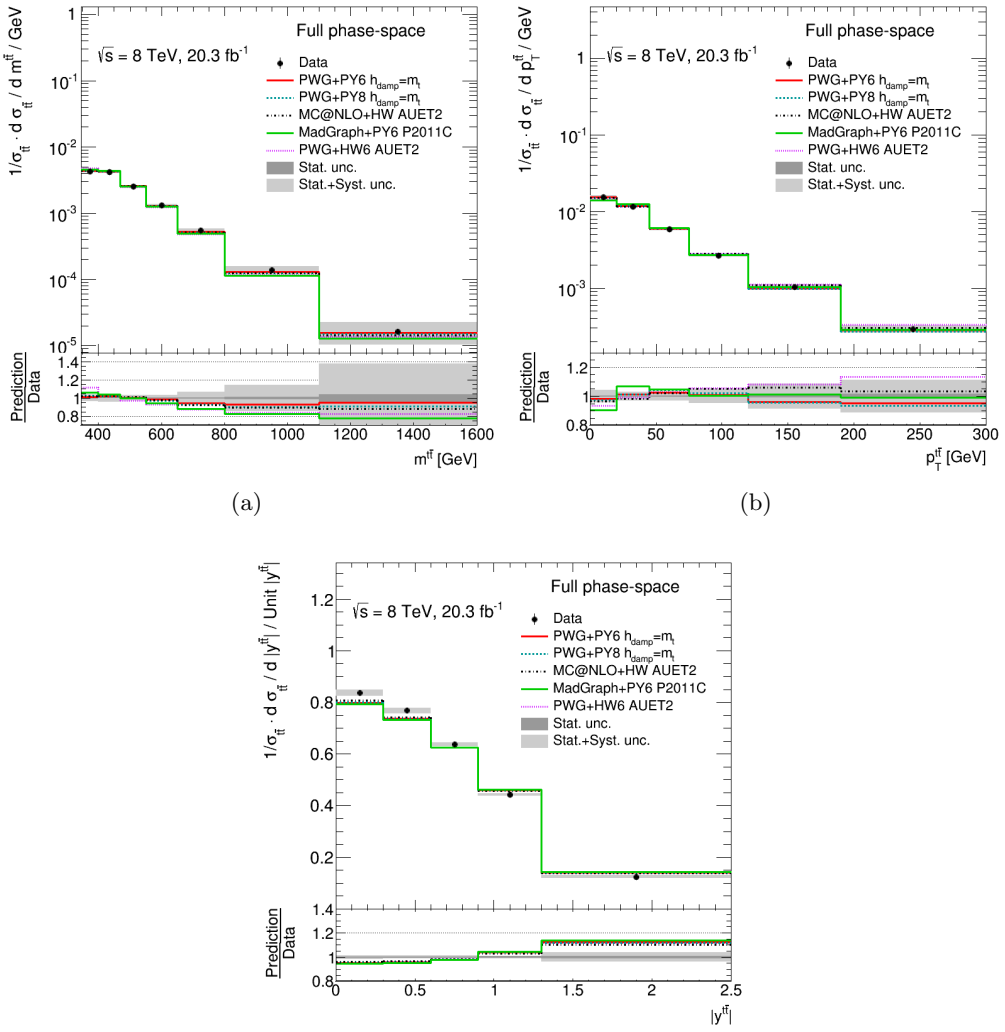

(a) (b)

(c)

FIGURE 7.10: Full phase-space normalized differential cross-sections as a function of the (a) invariant mass ($m^{t\bar{t}}$), (b) transverse momentum ($p_{\mathrm{T}}^{t\bar{t}}$) and (c) absolute value of the rapidity ($\left|y^{t\bar{t}}\right|$) of the $t\bar{t}$ system. The grey bands indicate the total uncertainty on the data in each bin. The POWHEG+PYTHIA generator with $h_{\mathrm{damp}} = m_t$ and the CT10nlo PDF is used as the nominal prediction to correct for detector effects.

- an approximate next-to-next-to-next-to-leading-order (aN^{3}LO) calculation based on the resummation of soft-gluon contributions in the double-differential cross section at next-to-next-to-leading-logarithm (NNLL) accuracy in the moment-space approach in perturbative QCD [153] using the MSTW2008nnlo PDF [154];
- an approximate NLO+NNLL calculation [155] using the MSTW2008nnlo PDF [154].

We have been able to compare our measurements also with the complete NNLO predictions for the differential cross sections recently appeared in the literature [156]. This calculation represents a very important step forward in the study of top pair production.

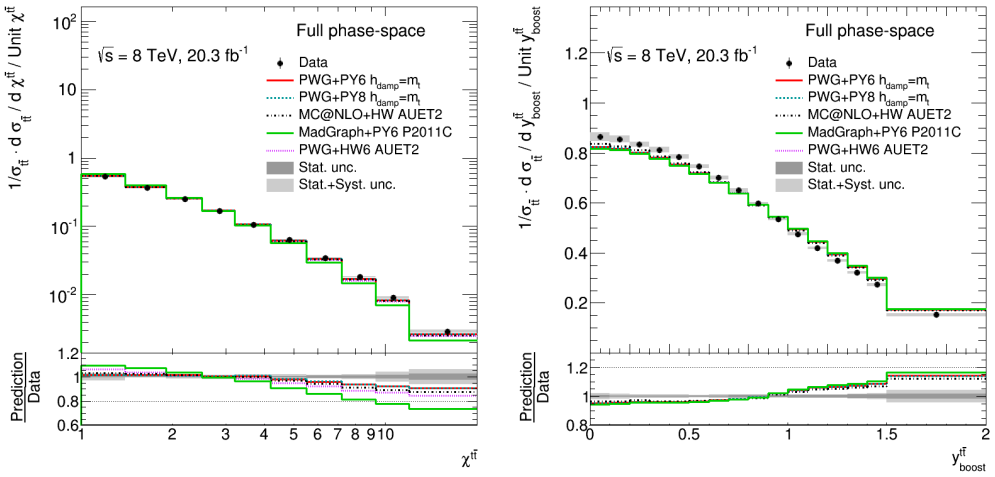

(a) (b)

FIGURE 7.11: Full phase-space normalized differential cross-sections as a function of the (a) production angle ($\chi^{t\bar{t}}$) and (b) longitudinal boost ($y^{t\bar{t}}_{\text{boost}}$) of the $t\bar{t}$ system. The grey bands indicate the total uncertainty on the data in each bin. The POWHEG+PYTHIA generator with $h_{\text{damp}} = m_t$ and the CT10nlo PDF is used as the nominal prediction to correct for detector effects.

These recent calculations use the MSTW2008nnlo PDF [154] and do not cover the highest bins in p^t_{T} and $m^{t\bar{t}}$.

These predictions have been interpolated in order to match the binning of the presented measurements. Table 7.4 shows the χ^2 and p-values for these higher-order QCD calculations.

Figures 7.13 and 7.14 show a comparison of the p^t_{T} and $|y^t|$ distributions to the aNNLO and aN^{3}LO, and to the NNLO calculations respectively. The aN^{3}LO calculation is seen to improve the agreement compared to the POWHEG +PYTHIA generator in $|y^t|$, but not in p^t_{T}. The aNNLO prediction produces a p^t_{T} distribution that is softer than the data at high transverse momentum and does not improve the description of $|y^t|$. The NNLO calculation is in good agreement with both the p^t_{T} and $|y^t|$ distributions, in particular the disagreement seen at high p^t_{T} for the NLO generators is resolved by the NNLO calculation.

The measurement of the invariant mass and transverse momentum of the $t\bar{t}$ system is compared to the NLO+NNLL prediction in Figure 7.15. The NLO+NNLL calculation shows a good agreement in the $m^{t\bar{t}}$ spectrum and a very large discrepancy for high values of the $t\bar{t}$ transverse momentum. Figure 7.16 shows a comparison of the NNLO calculation to the $m^{t\bar{t}}$ and $|y^{t\bar{t}}|$ measurements. For the rapidity of the $t\bar{t}$ system, the NNLO calculation definitively improves the agreement compared to the POWHEG +PYTHIA prediction, although still showing a small shape difference with respect to the data.

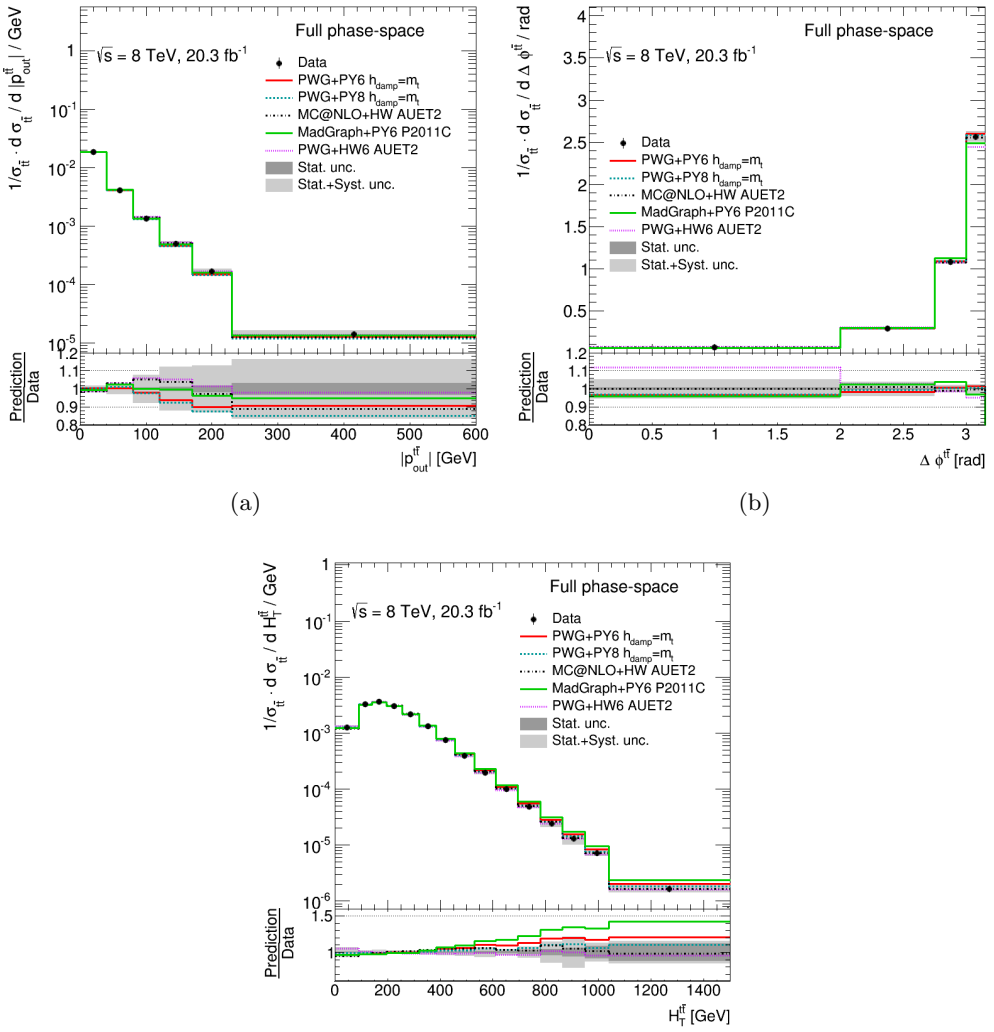

(a) (b)

(c)

FIGURE 7.12: Full phase-space normalized differential cross-sections as a function of the (a) out-of-plane momentum ($|p_{\text{out}}^{t\bar{t}}|$), (b) azimuthal angle ($\Delta\phi_{t\bar{t}}$), and (c) scalar sum of the transverse momenta of the hadronic and leptonic top quarks ($H_{\text{T}}^{t\bar{t}}$)) of the $t\bar{t}$ system. The grey bands indicate the total uncertainty on the data in each bin. The POWHEG+PYTHIA generator with $h_{\text{damp}} = m_t$ and the CT10nlo PDF is used as the nominal prediction to correct for detector effects.

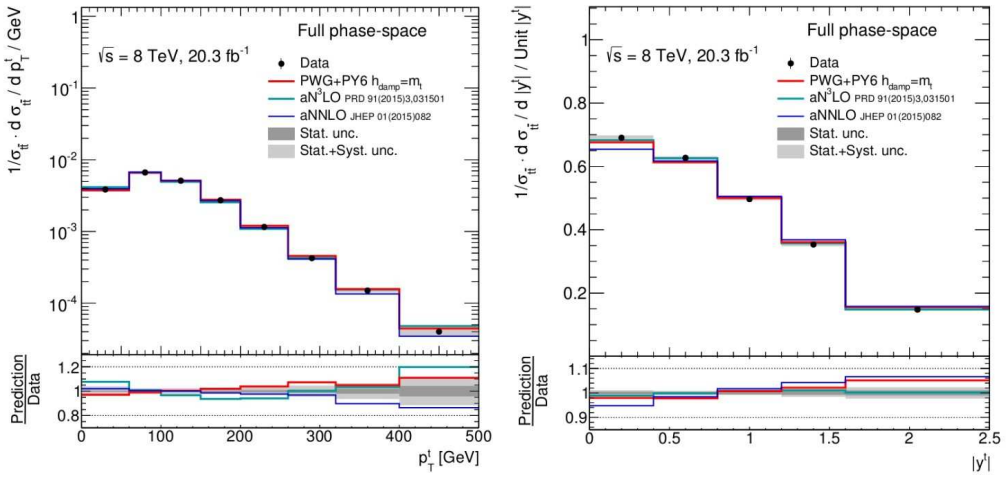

(a) (b)

FIGURE 7.13: Full phase-space normalized differential cross-section as a function of the (a) transverse momentum (p_{T}^{t}) and (b) absolute value of the rapidity of the top quark ($|y^{t}|$) compared to higher-order theoretical calculations. The grey band indicates the total uncertainty on the data in each bin. The POWHEG+PYTHIA generator with $h_{\mathrm{damp}} = m_t$ and the CT10nlo PDF is used as the nominal prediction to correct for detector effects.

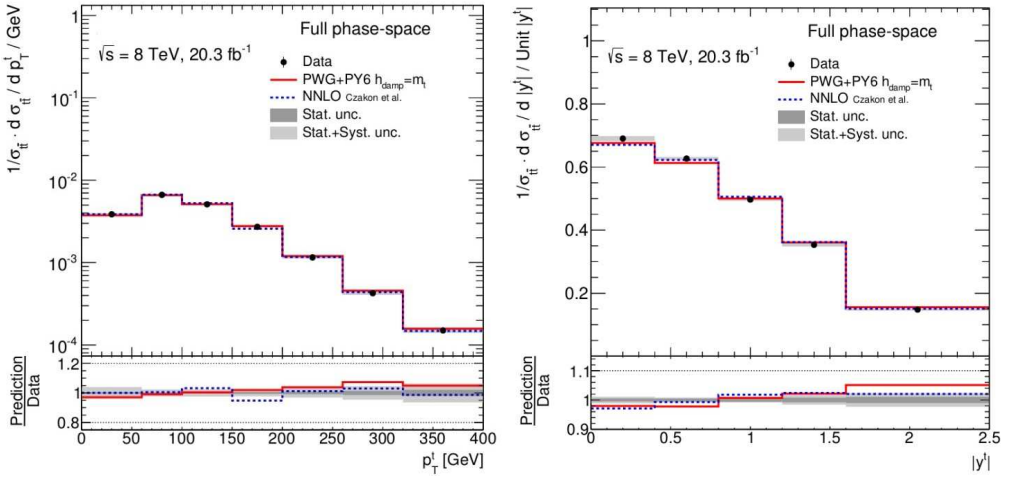

(a) (b)

FIGURE 7.14: Full phase-space normalized differential cross-section as a function of the (a) transverse momentum (p_{T}^{t}) and (b) absolute value of the rapidity of the top quark ($|y^{t}|$) compared to NNLO theoretical calculations using the MSTW2008nnlo PDF set. The grey band indicates the total uncertainty on the data in each bin. The POWHEG+PYTHIA generator with $h_{\mathrm{damp}} = m_t$ and the CT10nlo PDF is used as the nominal prediction to correct for detector effects.

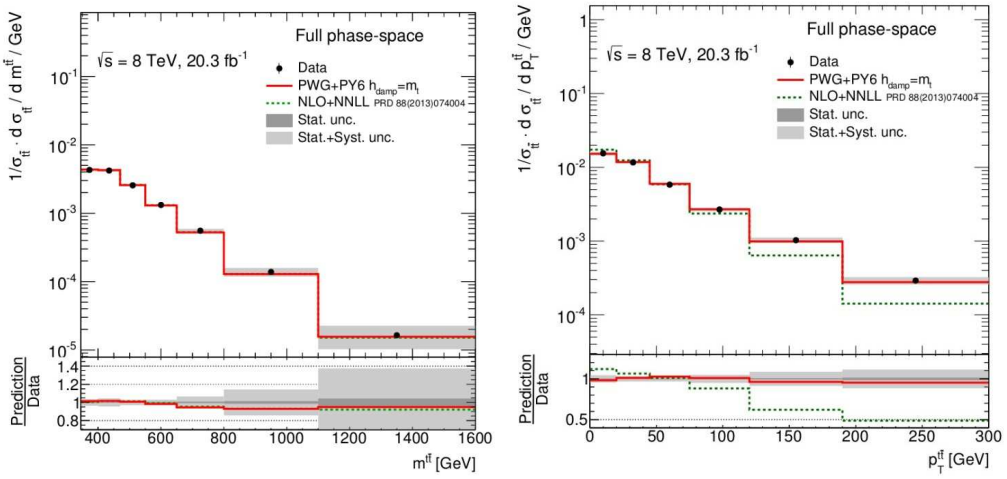

(a) (b)

FIGURE 7.15: Full phase-space normalized differential cross-section as a function of the (a) invariant mass ($m^{t\bar{t}}$) and (b) transverse momentum ($p_{\mathrm{T}}^{t\bar{t}}$) of the $t\bar{t}$ system compared to higher-order theoretical calculations. The grey band indicates the total uncertainty on the data in each bin. The POWHEG+PYTHIA generator with $h_{\mathrm{damp}} = m_t$ and the CT10nlo PDF is used as the nominal prediction to correct for detector effects.

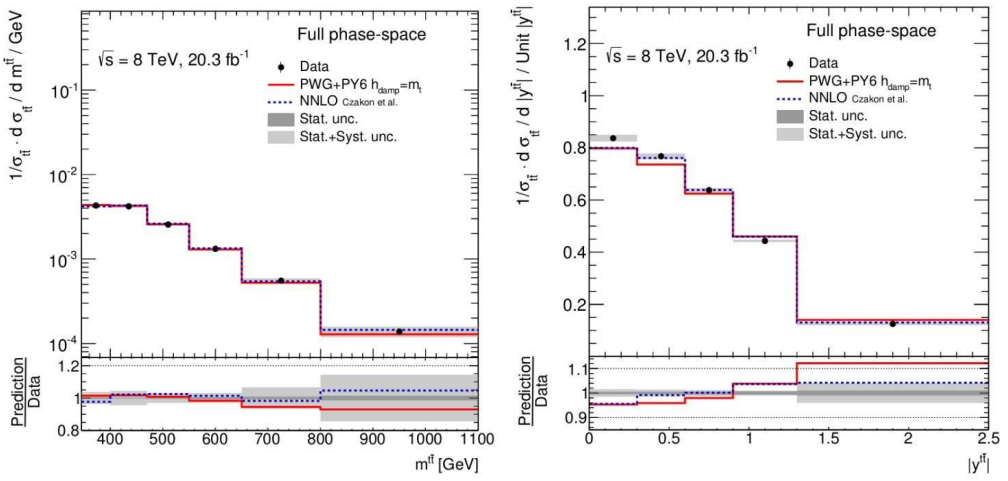

(a) (b)

FIGURE 7.16: Full phase-space normalized differential cross-section as a function of the (a) invariant mass ($m^{t\bar{t}}$) and (b) absolute value of the rapidity ($\left|y^{t\bar{t}}\right|$) of the $t\bar{t}$ system compared to NNLO theoretical calculations using the MSTW2008nnlo PDF set. The grey band indicates the total uncertainty on the data in each bin. The POWHEG+PYTHIA generator with $h_{\mathrm{damp}} = m_t$ and the CT10nlo PDF is used as the nominal prediction to correct for detector effects.

7.2 Absolute cross-sections results

In this section, comparisons between data distributions and several SM predictions are presented for the absolute differential cross-sections.

The set of Figures 7.17–7.21 presents the absolute $t\bar{t}$ fiducial phase-space differential cross-sections as a function of the different variables. In particular, Figures 7.17(a) and 7.17(b) show the distributions of the hadronic top-quark transverse momentum and the absolute value of the rapidity. Figures 7.18(a), 7.18(b) and 7.18(c) present the $t\bar{t}$ system invariant mass, transverse momentum, and absolute value of the rapidity, while the additional variables related to the $t\bar{t}$ system and the ratio of the transverse momenta of the hadronically decaying W boson and top quark are shown in Figures 7.19, 7.20 and 7.21.

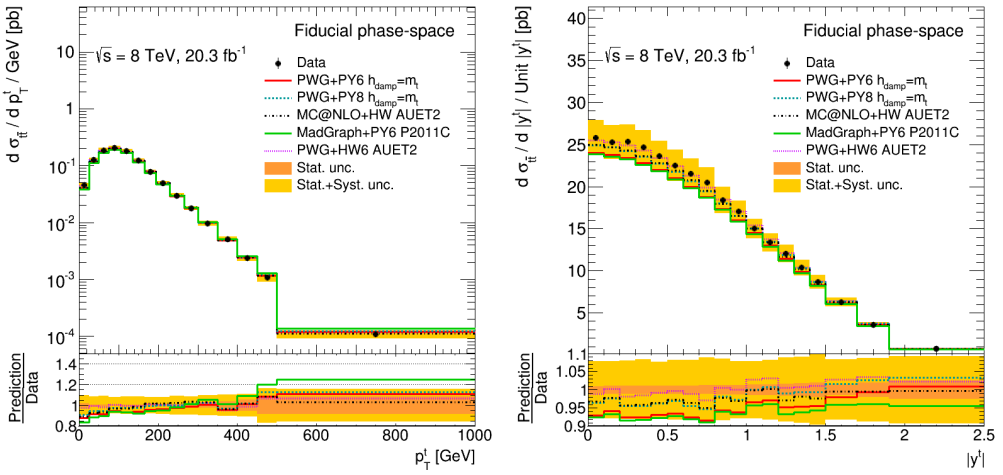

(a) (b)

FIGURE 7.17: Fiducial phase-space absolute differential cross-sections as a function of the (a) transverse momentum ($p_{\mathrm{T}}^{t,\mathrm{had}}$) and (b) absolute value of the rapidity ($\left|y^{t,\mathrm{had}}\right|$) of the hadronic top quark. The yellow bands indicate the total uncertainty on the data in each bin. The POWHEG+PYTHIA generator with $h_{\mathrm{damp}} = m_t$ and the CT10nlo PDF is used as the nominal prediction to correct for detector effects.

Also for the absolute spectra, none of the predictions is able to correctly describe all the distributions, as also witnessed by the χ^2 values and the p-values listed in tab. H.1. Also in the absolute spectra, a tension between data and MADGRAPH predictions is observed in the case of the hadronic top-quark transverse momentum, for values higher than about 400 GeV. The shape of the $\left|y^{t,\mathrm{had}}\right|$ distribution shows only a modest agreement for all the generators, with very large uncertainty.

For the $m^{t\bar{t}}$ distribution, the POWHEG+PYTHIA, POWHEG+PYTHIA8 and POWHEG+HERWIG generators are in better agreement with the data. All generators are in good agreement in the $p_{\mathrm{T}}^{t\bar{t}}$ spectrum except for MC@NLO+HERWIG and POWHEG+HERWIG in the last

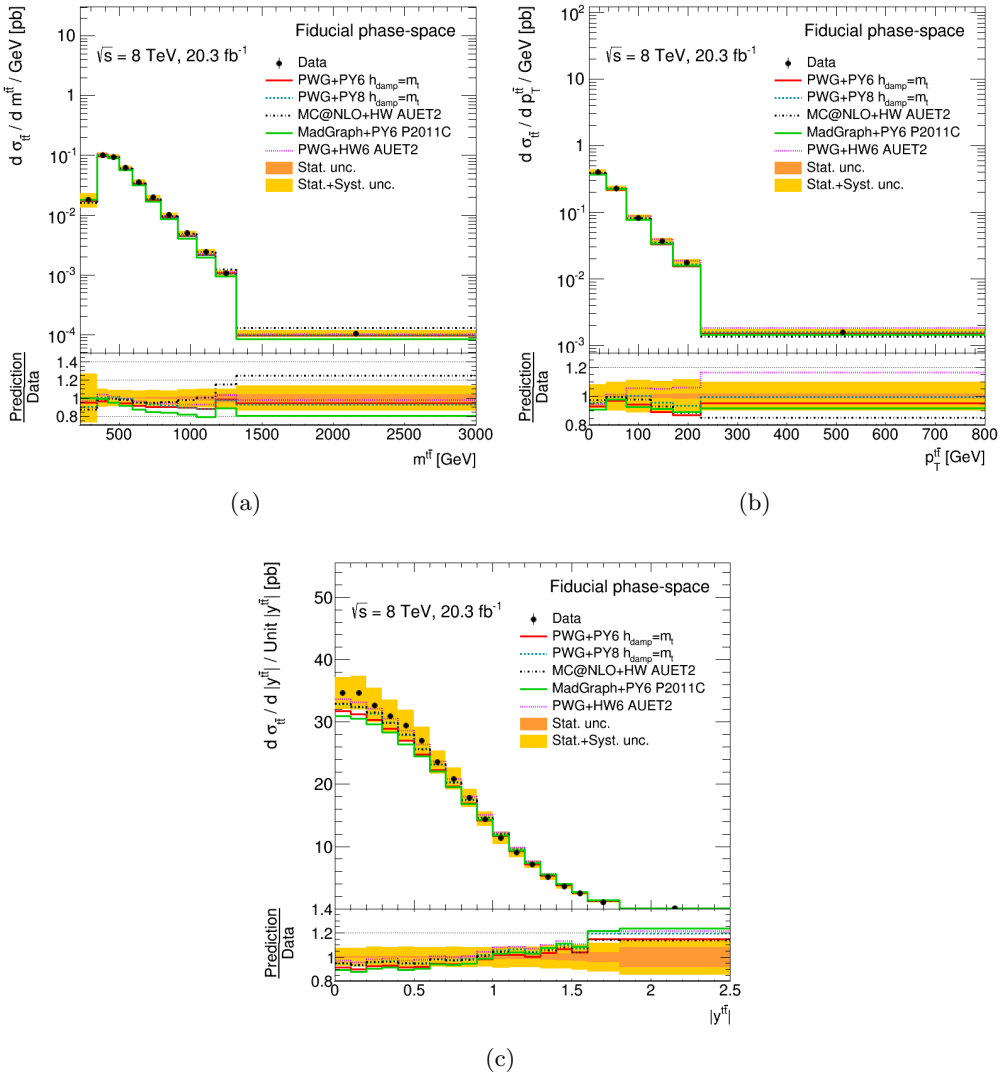

FIGURE 7.18: Fiducial phase-space absolute differential cross-sections as a function of the (a) invariant mass ($m^{t\bar{t}}$), (b) transverse momentum ($p_{\mathrm{T}}^{t\bar{t}}$) and (c) absolute value of the rapidity ($\left|y^{t\bar{t}}\right|$) of the $t\bar{t}$ system. The yellow bands indicate the total uncertainty on the data in each bin. The POWHEG+PYTHIA generator with $h_{\mathrm{damp}} = m_t$ and the CT10nlo PDF is used as the nominal prediction to correct for detector effects.

bin. The data at high values of $t\bar{t}$ rapidity is not adequately described by any of the generators considered.

The production angle $\chi^{t\bar{t}}$ is well described in the central region. The forward region is not described correctly by any of the generators under consideration. Both $\left|p_{\mathrm{out}}^{t\bar{t}}\right|$ and $\Delta\phi_{t\bar{t}}$ spectra show that the kinematics of top quarks produced in the collinear region ($\Delta\phi_{t\bar{t}} \lesssim \pi/2$) are described with marginal agreement by all the generators. The tension observed in the $p_{\mathrm{T}}^{t,\mathrm{had}}$ spectrum is reflected in the tail of the $H_{\mathrm{T}}^{t\bar{t}}$ distribution. Finally, the ratio of the hadronic W boson and top-quark transverse momenta shows a mis-modelling in the range 1.5–3 for all the generators.

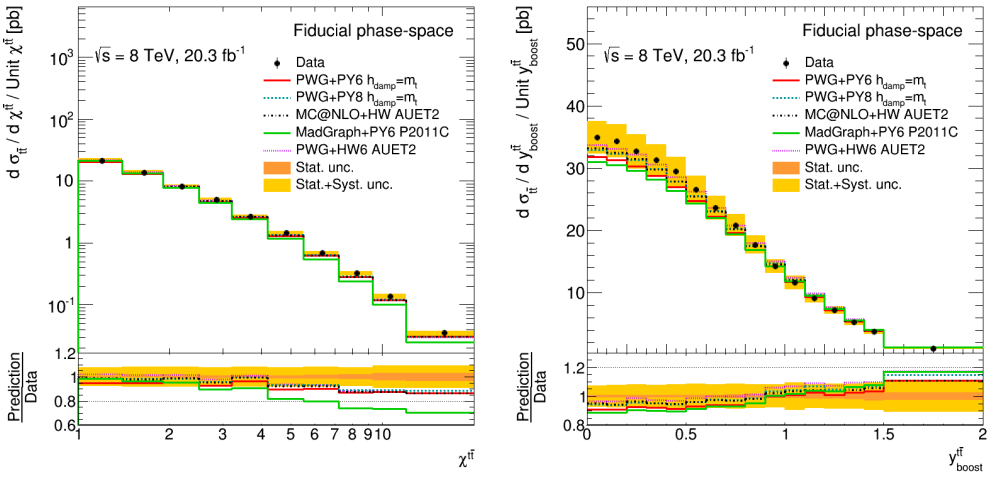

(a) (b)

FIGURE 7.19: Fiducial phase-space absolute differential cross-sections as a function of the $t\bar{t}$ (a) production angle ($\chi^{t\bar{t}}$) and (b) longitudinal boost ($y^{t\bar{t}}_{\text{boost}}$). The yellow bands indicate the total uncertainty on the data in each bin. The POWHEG+PYTHIA generator with $h_{\text{damp}} = m_t$ and the CT10nlo PDF is used as the nominal prediction to correct for detector effects.

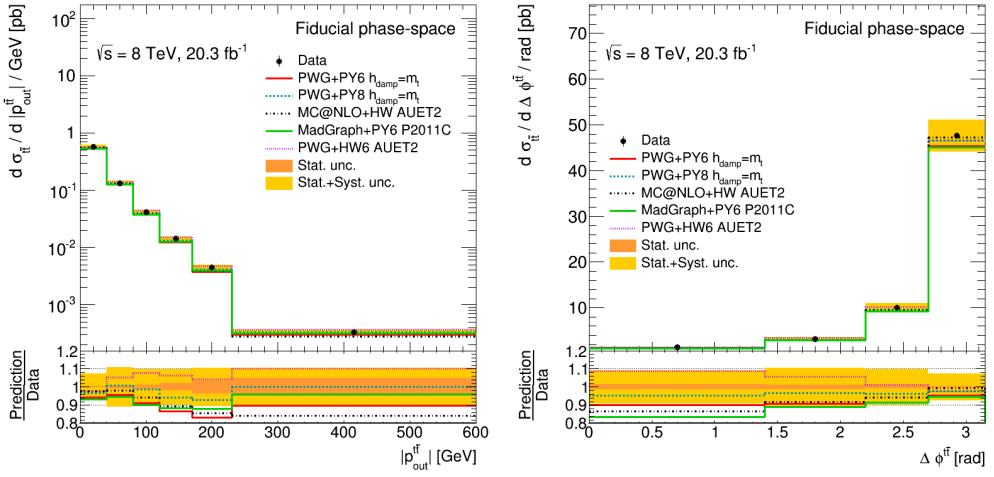

(a) (b)

FIGURE 7.20: Fiducial phase-space absolute differential cross-sections as a function of the $t\bar{t}$ (a) out-of-plane momentum ($|p^{t\bar{t}}_{\text{out}}|$) and (b) azimuthal angle ($\Delta\phi_{t\bar{t}}$). The yellow bands indicate the total uncertainty on the data in each bin. The POWHEG+PYTHIA generator with $h_{\text{damp}} = m_t$ and the CT10nlo PDF is used as the nominal prediction to correct for detector effects.

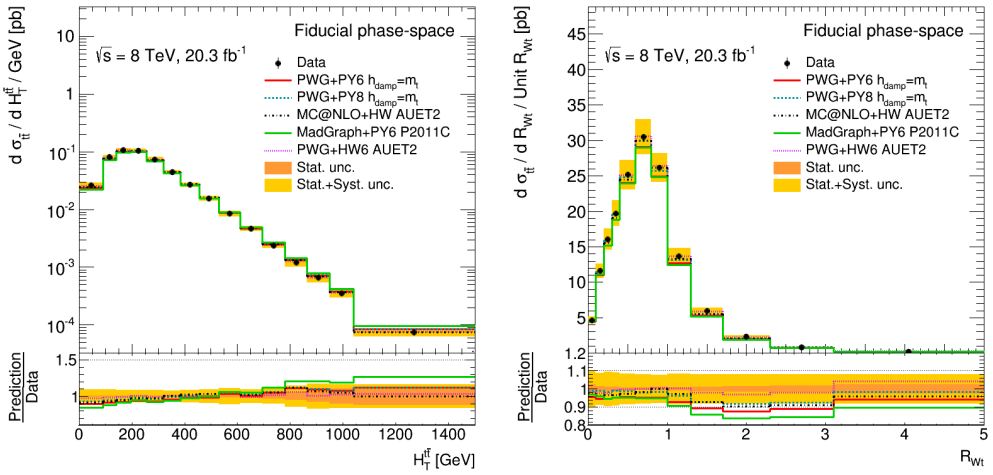

(a) (b)

FIGURE 7.21: Fiducial phase-space absolute differential cross-sections as a function of the (a) scalar sum of the transverse momenta of the hadronic and leptonic top quarks ($H_{\mathrm{T}}^{t\bar{t}}$) and (b) the ratio of the hadronic W and the hadronic top transverse momenta (R_{Wt}). The yellow bands indicate the total uncertainty on the data in each bin. The POWHEG+PYTHIA generator with $h_{\mathrm{damp}} = m_t$ and the CT10nlo PDF is used as the nominal prediction to correct for detector effects.

In analogy to what it is done for the normalized spectra, it was performed a study for the rapidity observables $\left|y^{t,\mathrm{had}}\right|$, $\left|y^{t\bar{t}}\right|$ and $y^{t\bar{t}}_{\mathrm{boost}}$, shown in Figures 7.22 7.23 7.24 and compared the data with the predictions of MC@NLO+HERWIG for more recent sets of parton distribution functions, also for the absolute spectra. The results exhibit a general improvement in the description of the forward region for the most recent PDF sets, as well as the normalized spectra. The improvement with respect to CT10nlo is also clearly shown in Table H.3. The only exception is represented by the MC@NLO+HERWIG prediction reweighted with HERAPDF 2.0 NLO.

As well as the normalized spectra, the reweighting of RunII PDFs set for the other spectra that don't concern the rapidity functions, don't show improvement in the data prediction.

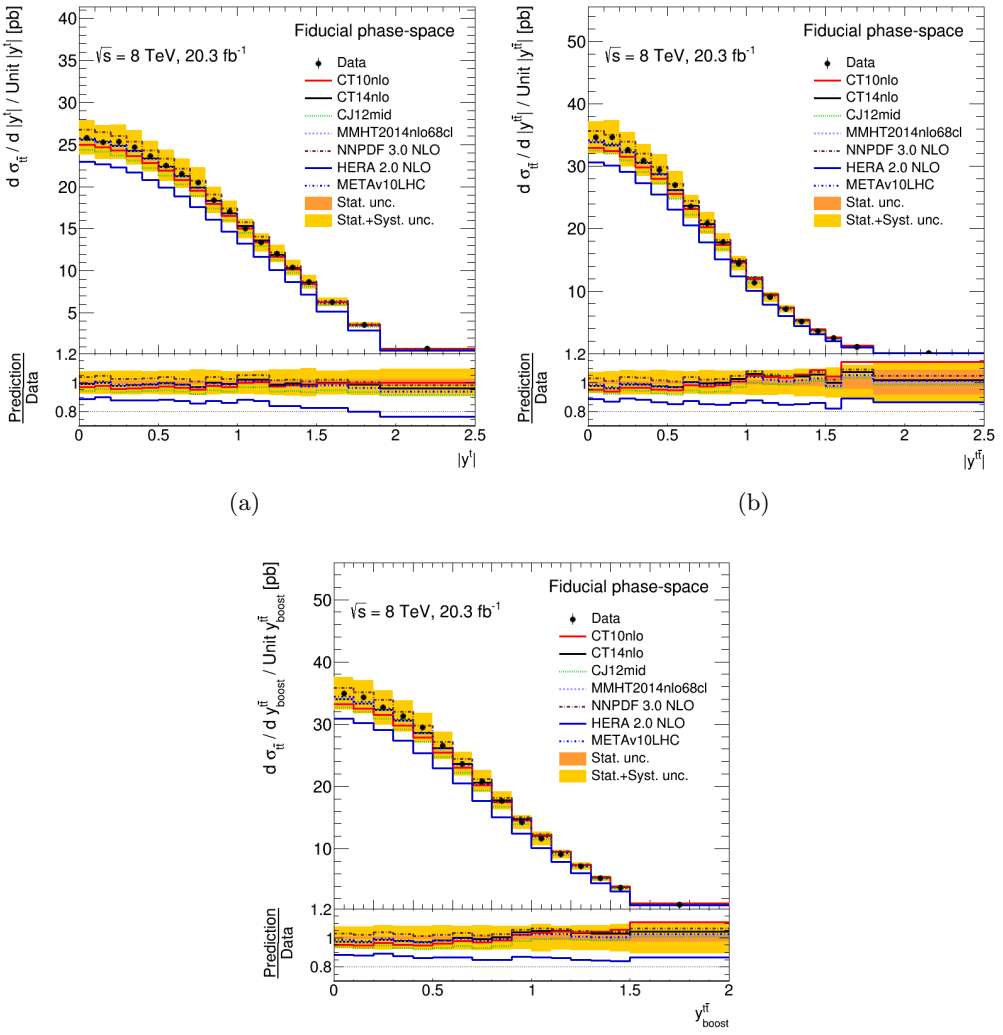

(a) (b)

(c)

FIGURE 7.22: Fiducial phase-space absolute differential cross-sections as a function of the (a) absolute value of the rapidity of the hadronic top quark ($\left|y^{t,\mathrm{had}}\right|$), (b) absolute value of the rapidity ($\left|y^{t\bar{t}}\right|$) of the $t\bar{t}$ system and (c) longitudinal boost ($y^{t\bar{t}}_{\mathrm{boost}}$). The yellow bands indicate the total uncertainty on the data in each bin. The MC@NLO+HERWIG generator is reweighted using the new PDF sets to produce the different predictions. The POWHEG+PYTHIA generator with $h_{\mathrm{damp}} = m_t$ and the CT10nlo PDF is used as the nominal prediction to correct for detector effects.

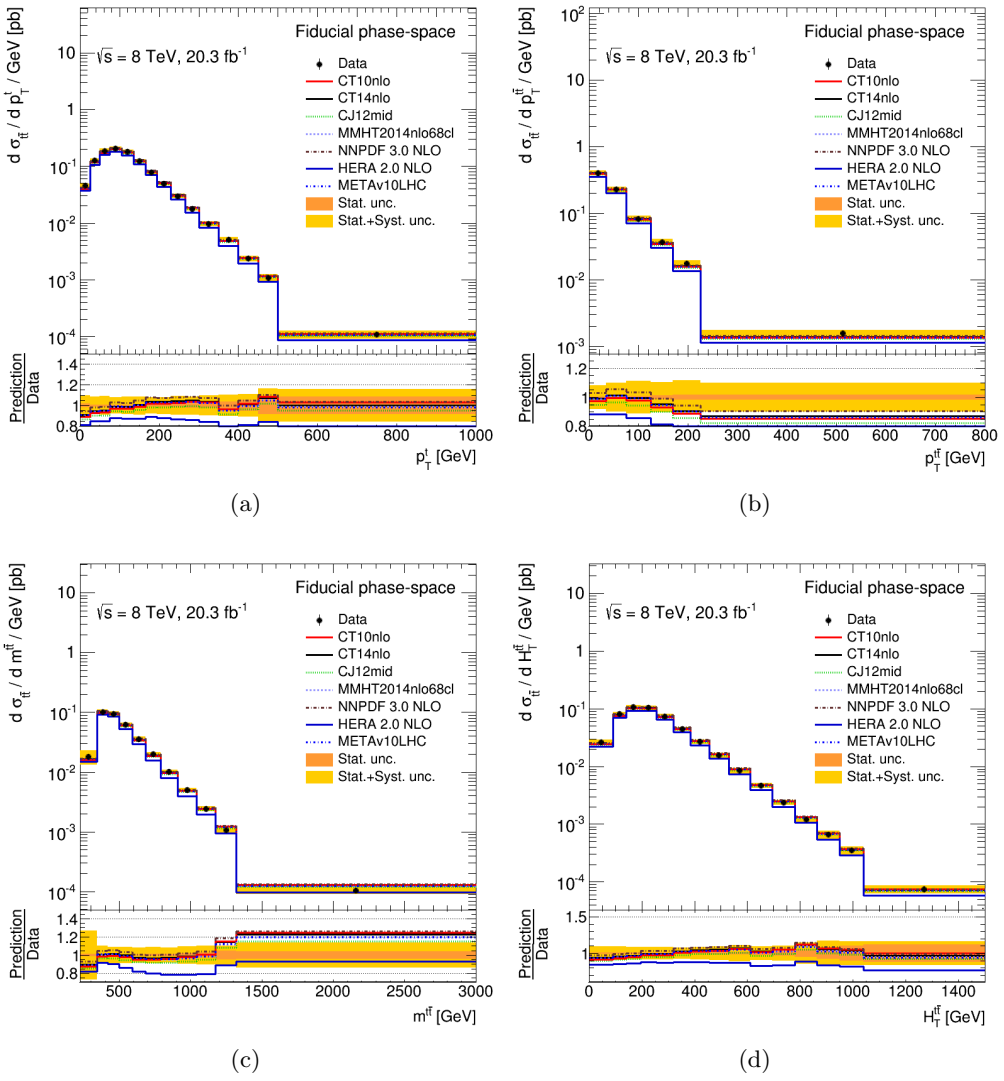

FIGURE 7.23: Fiducial phase-space absolute differential cross-sections as a function of the (a) transverse momentum of the hadronic top quark ($p_{\mathrm{T}}^{t,\mathrm{had}}$), (b) transverse momentum ($p_{\mathrm{T}}^{t\bar{t}}$) of the $t\bar{t}$ system, (c) invariant mass ($m^{t\bar{t}}$) of the $t\bar{t}$ system and (d) scalar sum od trasverse momentum ($H_{\mathrm{T}}^{t\bar{t}}$). The yellow bands indicate the total uncertainty on the data in each bin. The MC@NLO+HERWIG generator is reweighted using the new PDF sets to produce the different predictions. The POWHEG+PYTHIA generator with $h_{\mathrm{damp}} = m_t$ and the CT10nlo PDF is used as the nominal prediction to correct for detector effects.

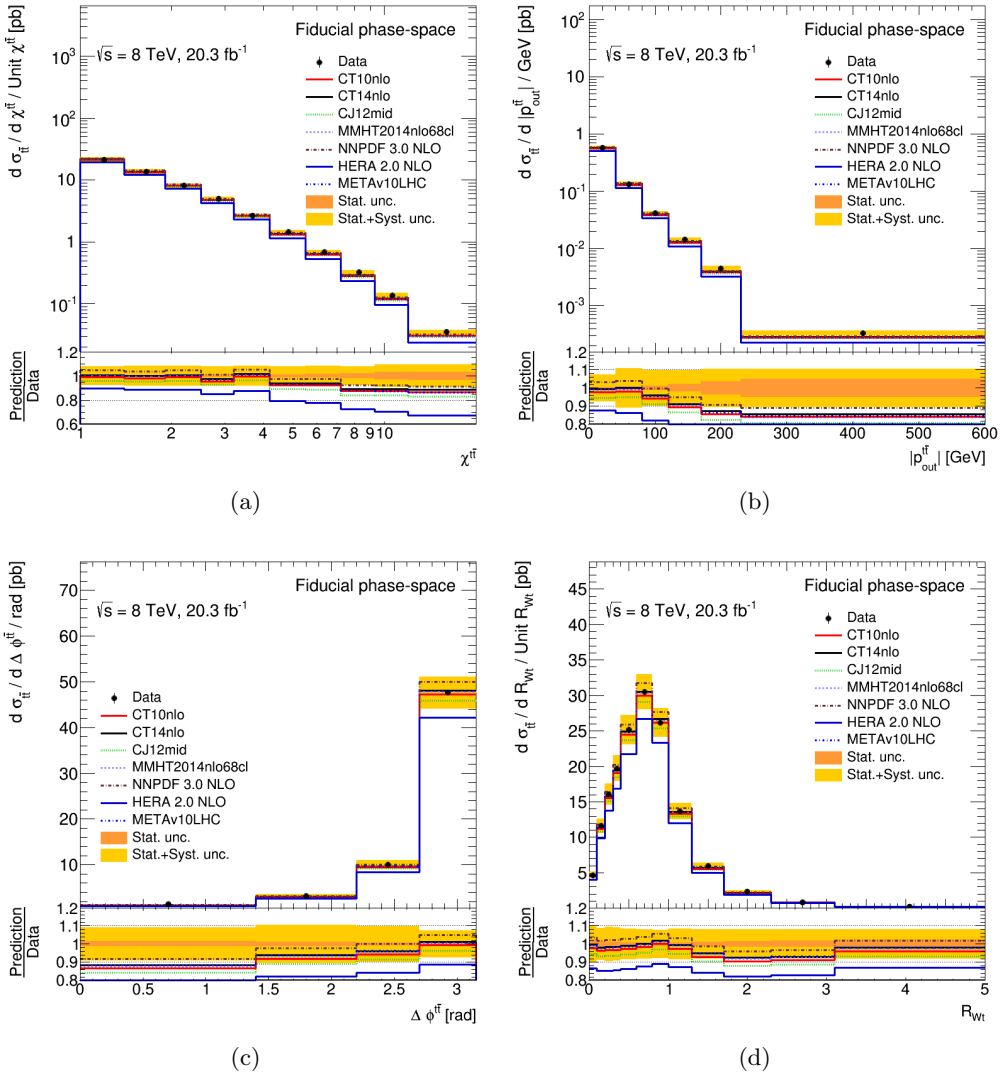

FIGURE 7.24: Fiducial phase-space absolute differential cross-sections as a function of the (a) production angle ($\chi^{t\bar{t}}$), (b) out-of-plane momentum ($|p_{\text{out}}^{t\bar{t}}|$), (c) azimuthal angle ($\Delta\phi_{t\bar{t}}$) and (d) the ratio of the hadronic W and the hadronic top transverse momenta (R_{Wt}). The yellow bands indicate the total uncertainty on the data in each bin. The MC@NLO+HERWIG generator is reweighted using the new PDF sets to produce the different predictions. The POWHEG+PYTHIA generator with $h_{\text{damp}} = m_t$ and the CT10nlo PDF is used as the nominal prediction to correct for detector effects.

The set of Figures 7.25–7.28 presents the absolute $t\bar{t}$ full phase-space differential cross-sections as a function of the different observables. In particular, Figures 7.25(a) and 7.25(b) show the top-quark transverse momentum and the absolute value of the rapidity; Figures 7.26(a), 7.26(b) and 7.26(c) present the $t\bar{t}$ system invariant mass, transverse momentum and absolute value of the rapidity while the additional observables related to the $t\bar{t}$ system are shown in Figures 7.27 and 7.28.

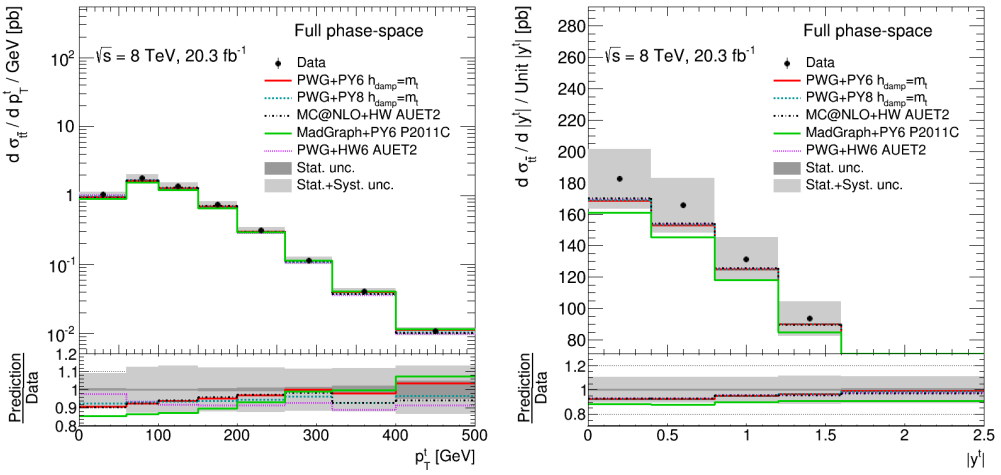

(a) (b)

FIGURE 7.25: Full phase-space absolute differential cross-sections as a function of the (a) transverse momentum (p_{T}^{t}) and (b) the absolute value of the rapidity ($|y^{t}|$) of the top quark. The grey bands indicate the total uncertainty on the data in each bin. The POWHEG+PYTHIA generator with $h_{\mathrm{damp}} = m_t$ and the CT10nlo PDF is used as the nominal prediction to correct for detector effects.

As regards the comparison between data and predictions, the general picture is still valid with respect to what already saw for the fiducial measurements, even though the uncertainties are much larger due to the full phase-space extrapolation. In particular, the predictions for the top-quark p_{T} and $H_{\mathrm{T}}^{t\bar{t}}$ tend to be in a better agreement with the data than what is observed in the fiducial phase-space. The χ^2 and corresponding p-values for the different observables and predictions are shown in Table H.2.

In Figures 7.29–7.31 the absolute $t\bar{t}$ full phase-space differential cross-sections as a function of p_{T}^{t}, $\left|y^{t}\right|$, $m^{t\bar{t}}$ and $\left|y^{t\bar{t}}\right|$ are also compared with theoretical higher-order QCD calculations (the same calculations used in the normalized ones, see Sec. 7.1).

Table H.4 shows the χ^2 and p-values for these higher-order QCD calculations, while Figures 7.29 and 7.30 show a comparison of the p_{T}^{t} and $\left|y^{t}\right|$ distributions to the aNNLO and aN^{3}LO, and to the NNLO calculations respectively. The aN^{3}LO calculation seems to not improve particularly the agreement compared to the POWHEG +PYTHIA generator in $\left|y^{t}\right|$, showing some differences in shapes for the p_{T}^{t} spectrum. The aNNLO prediction produces a p_{T}^{t} distribution that is softer than the data at high transverse momentum

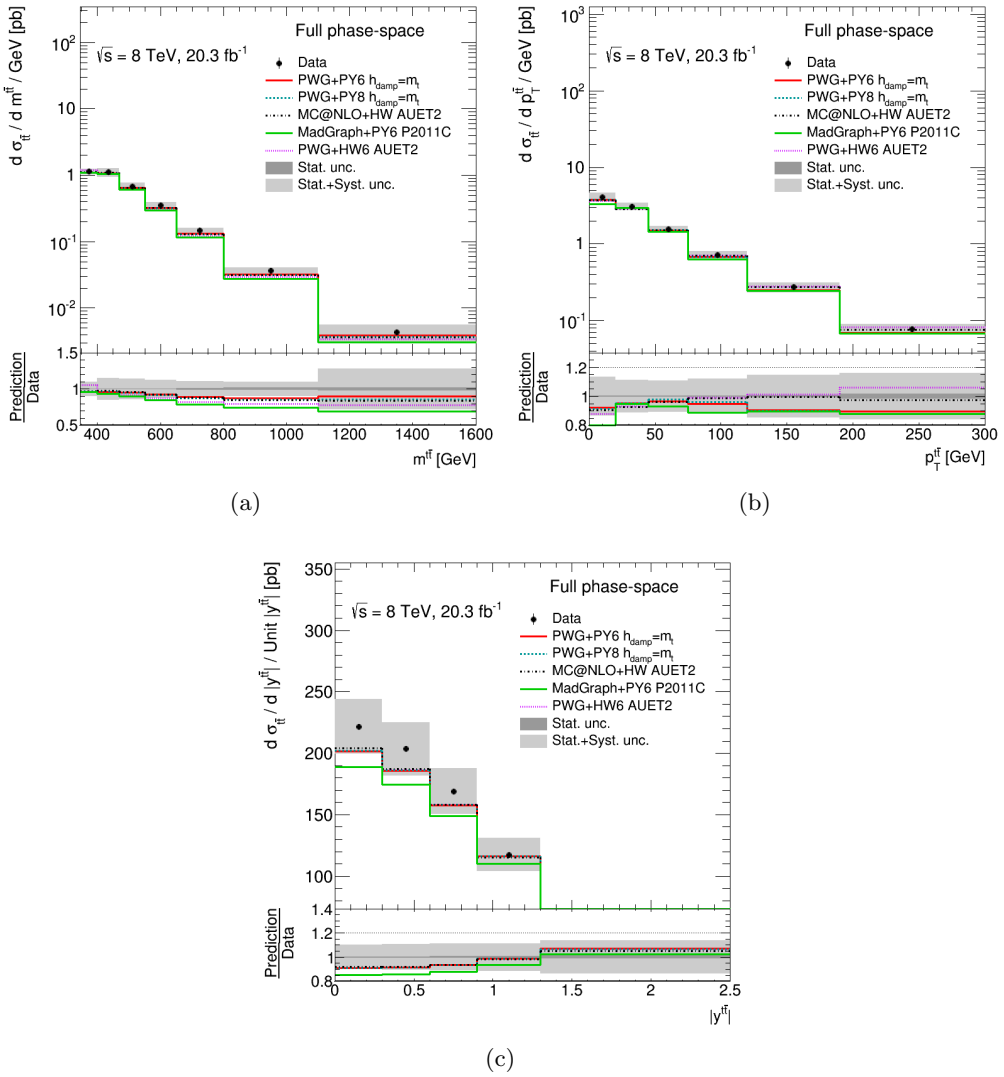

FIGURE 7.26: Full phase-space normalized absolute cross-sections as a function of the (a) invariant mass ($m^{t\bar{t}}$), (b) transverse momentum ($p_{\mathrm{T}}^{t\bar{t}}$) and (c) absolute value of the rapidity ($\left|y^{t\bar{t}}\right|$) of the $t\bar{t}$ system. The grey bands indicate the total uncertainty on the data in each bin. The POWHEG+PYTHIA generator with $h_{\mathrm{damp}} = m_t$ and the CT10nlo PDF is used as the nominal prediction to correct for detector effects.

and does not improve the description of $\left|y^{t}\right|$. The NNLO calculation is in only modest agreement with both the p_{T}^{t} and $\left|y^{t}\right|$ distributions.

For the rapidity of the $t\bar{t}$ system, the NNLO calculation improves the agreement if compared to the POWHEG +PYTHIA prediction, but some shape difference can be seen between the data and the prediction for the $m^{t\bar{t}}$ spectrum.

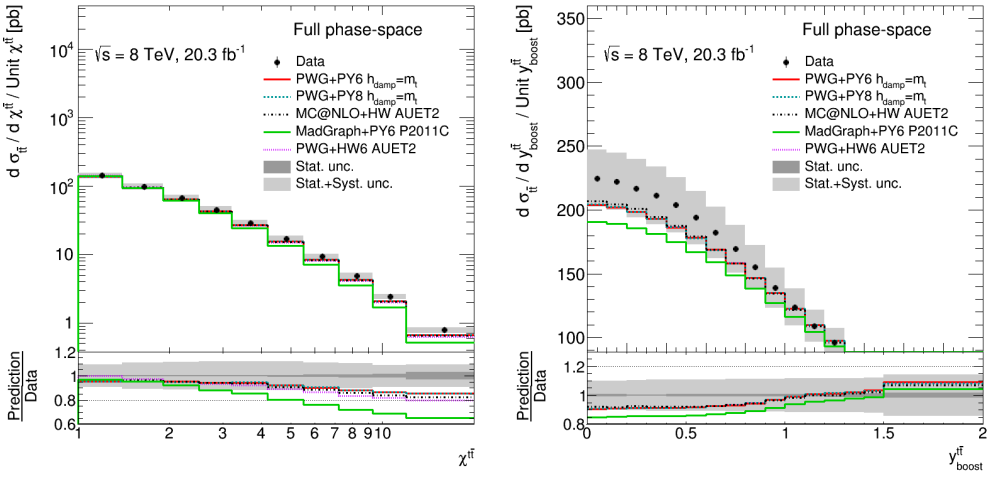

(a) (b)

FIGURE 7.27: Full phase-space absolute differential cross-sections as a function of the (a) production angle ($\chi^{t\bar{t}}$) and (b) longitudinal boost ($y^{t\bar{t}}_{\text{boost}}$) of the $t\bar{t}$ system. The grey bands indicate the total uncertainty on the data in each bin. The POWHEG+PYTHIA generator with $h_{\text{damp}} = m_t$ and the CT10nlo PDF is used as the nominal prediction to correct for detector effects.

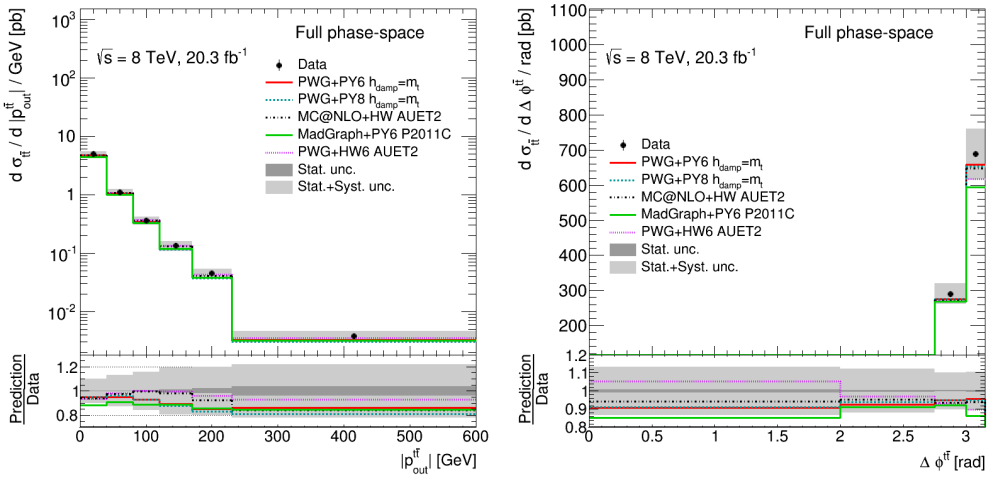

(a) (b)

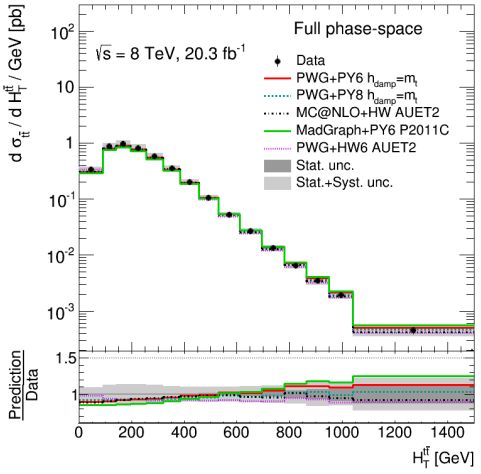

(c)

FIGURE 7.28: Full phase-space absolute differential cross-sections as a function of the (a) out-of-plane momentum ($|p_{\text{out}}^{t\bar{t}}|$), (b) azimuthal angle ($\Delta\phi_{t\bar{t}}$), and (c) scalar sum of the transverse momenta of the hadronic and leptonic top quarks ($H_{\text{T}}^{t\bar{t}}$)) of the $t\bar{t}$ system. The grey bands indicate the total uncertainty on the data in each bin. The POWHEG+PYTHIA generator with $h_{\text{damp}} = m_t$ and the CT10nlo PDF is used as the nominal prediction to correct for detector effects.

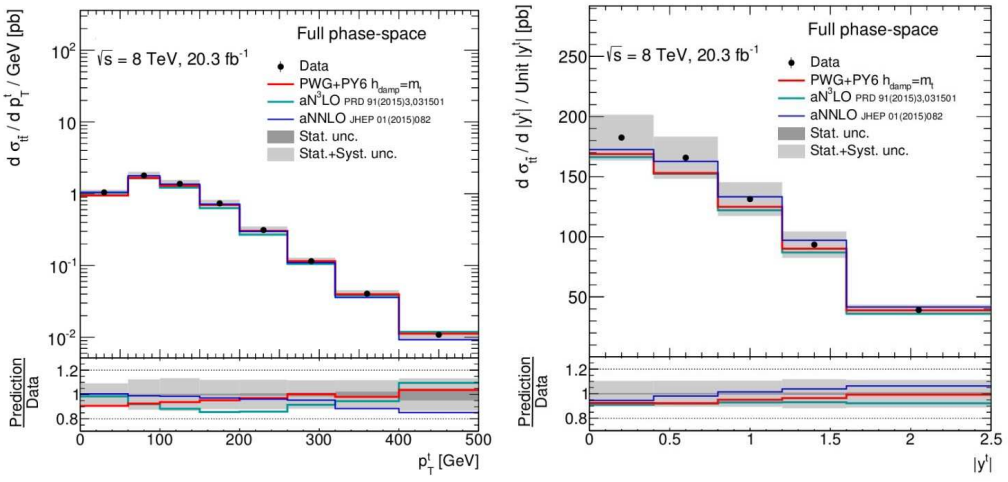

(a) (b)

FIGURE 7.29: Full phase-space absolute differential cross-section as a function of the (a) transverse momentum (p_{T}^{t}) and (b) absolute value of the rapidity of the top quark ($|y^{t}|$) compared to higher-order theoretical calculations. The grey band indicates the total uncertainty on the data in each bin. The POWHEG+PYTHIA generator with $h_{\mathrm{damp}} = m_t$ and the CT10nlo PDF is used as the nominal prediction to correct for detector effects.

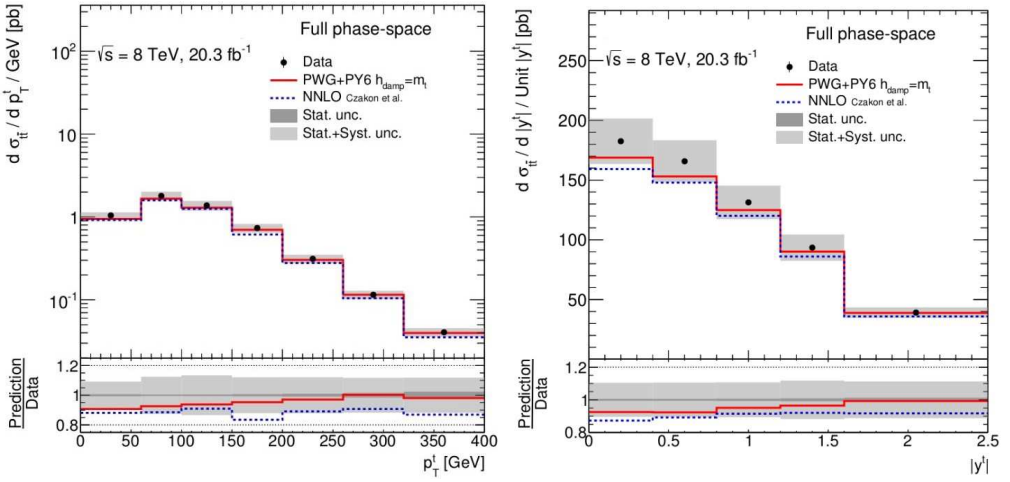

(a) (b)

FIGURE 7.30: Full phase-space absolute differential cross-section as a function of the (a) transverse momentum (p_{T}^{t}) and (b) absolute value of the rapidity of the top quark ($|y^{t}|$) compared to NNLO theoretical calculations using the MSTW2008nnlo PDF set. The grey band indicates the total uncertainty on the data in each bin. The POWHEG+PYTHIA generator with $h_{\mathrm{damp}} = m_t$ and the CT10nlo PDF is used as the nominal prediction to correct for detector effects.

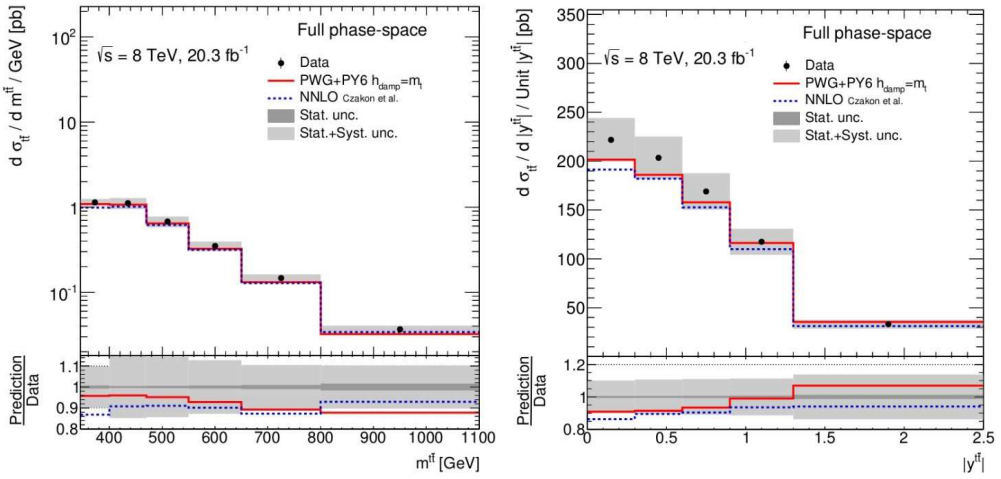

(a) (b)

FIGURE 7.31: Full phase-space absolute differential cross-section as a function of the (a) invariant mass ($m^{t\bar{t}}$) and (b) absolute value of the rapidity ($\left|y^{t\bar{t}}\right|$) of the $t\bar{t}$ system compared to NNLO theoretical calculations using the MSTW2008nnlo PDF set. The grey band indicates the total uncertainty on the data in each bin. The POWHEG+PYTHIA generator with $h_{\text{damp}} = m_t$ and the CT10nlo PDF is used as the nominal prediction to correct for detector effects.

Chapter 8

Conclusions

Since 2010 the data collected by the CERN Large Hadron Collider has given particle physicists an unique opportunity to probe their theories at the highest energies ever achieved by a particle collider, allowing the fundamental discovery of the Higgs boson, and therefore confirmation of the Higgs mechanism, by the ATLAS and CMS experiments in 2012. It also allowed broad and detailed studies of the known SM physics, such as the differential top cross-section analysis presented in this thesis where kinematic distributions of the top quarks in $t\bar{t}$ events, selected in the lepton+jets channel, are measured in the fiducial and full phase space using data from 8 TeV proton–proton collisions collected by the ATLAS detector, corresponding to an integrated luminosity of 20.3 fb^{-1}.

Both normalized and absolute differential cross-sections are measured as a function of the hadronic top-quark transverse momentum and rapidity, and as a function of the mass, transverse momentum, and rapidity of the $t\bar{t}$ system. In addition, a new set of variables describing the hard-scattering interaction ($\chi^{t\bar{t}}$, $y^{t\bar{t}}_{\text{boost}}$) and sensitive to the emission of radiation along with the $t\bar{t}$ pair ($\Delta\phi^{t\bar{t}}$, $\left|p^{t\bar{t}}_{\text{out}}\right|$, $H^{t\bar{t}}_{\text{T}}$, R_{Wt}) are presented.

In general, the Monte Carlo predictions fairly agree with data in a wide kinematic region. However, the tail of the $p^{t,\text{had}}_{\text{T}}$ distribution is harder in all predictions than what is observed in data, an effect previously observed in measurements by ATLAS and CMS. The agreement improves when using the Herwig parton shower with respect to Pythia. The tension observed for Powheg+Pythia, Powheg+Pythia8 and MadGraph+Pythia in the p^{t}_{T} spectrum is reflected in the tail of the $H^{t\bar{t}}_{\text{T}}$ distribution.

Similarly, both aN^{3}LO and aNNLO predictions have a poor agreement in the p^{t}_{T} spectrum in the full phase space. The full NNLO calculation is in good agreement with the p^{t}_{T} distribution, indicating the disagreement seen with the generators and other calculations is due to missing higher-order terms. The NNLO calculation also shows good agreement in the $\left|y^{t}\right|$ and $m^{t\bar{t}}$ distributions.

The $\left|y^{t,\mathrm{had}}\right|$, $\left|y^{t\bar{t}}\right|$ and $y^{t\bar{t}}_{\mathrm{boost}}$distributions are not well modelled by any generator under consideration in the fiducial phase space, however the agreement improves when new parton distribution functions are used with the MC@NLO+Herwig generator.
Finally, all the generators under consideration consistently predict a ratio of the hadronic W boson and top-quark transverse momenta (R_{Wt}) with a mis-modelling in the range 1.5–3.
The measurements presented in this thesis if included in a DGLAP fit have the potential to improve the determination of the gluons density in the proton. Exploiting the full data taking of the Run II period at the Large Hadron Collider, with proton–proton collisions at very high center of mass energy (13 TeV) and large expected integrated luminosity, will provide a unique opportunity to test to an unprecedented level the predictions of the Standard Model and to further explore the physics of the top quark.

Appendix A

Datasets

A.1 $t\bar{t}$ samples

DatasetId	Study	Generator	PS	PDF	h_{damp}	Sim.	X-sec	k-factor	Gen. evts.
110404	nominal	Powheg	Pythia	CT10	m_{top}	Full	114.47	1.1996	14984817
110340	PS	Powheg	Pythia	HERAPDF	m_{top}	AFII	105.86	1.2971	4998495
117050	PS	Powheg	Pythia	CT10	∞	Full	114.49	1.1994	49973332
117046	PS	Powheg	Pythia8	CT10	m_{top}	AFII	114.53	1.1990	14934992
117304	PS	MC@NLO	Herwig	CT10	∞	Full	1.2158	0.57116	118171
117305	PS	MC@NLO	Herwig	CT10	∞	Full	1.2158	0.19707	116833
117306	PS	MC@NLO	Herwig	CT10	∞	Full	1.2158	0.07273	111487
117307	PS	MC@NLO	Herwig	CT10	∞	Full	1.2158	0.05069	113716
105200	PDF	MC@NLO	Herwig	CT10	∞	Full	112.94	1.2158	14997103
110407	IFSR	Powheg	Pythia	CT10	m_{top}	AFII	137.32	1.0000	14922982
110408	IFSR	Powheg	Pythia	CT10	m_{top}	AFII	137.32	1.0000	14969485

A.2 Di boson samples

DatasetId	Channel	Generator	PDF	X-sec	k-factor	Gen. evts.
105985	WW	Herwig	CTEQ6L1	12.416	1.6833	2499890
105986	ZZ	Herwig	CTEQ6L1	0.99081	1.5496	245000
105987	WZ	Herwig	CTEQ6L1	3.6706	1.9011	999998

A.3 Single top samples

DatasetId	Channel	Generator	PS	PDF	X-sec	k-factor	Gen. evts.
110090	t chan	POWHEG	PYTHIA	CT10	17.520	1.0500	4994481
110091	t chan	POWHEG	PYTHIA	CT10	9.3932	1.0616	4999879
110119	s chan	POWHEG	PYTHIA	CT10	1.6424	1.1067	5999781
110140	W chan	POWHEG	PYTHIA	CT10	20.461	1.0933	999692

A.4 W + jets samples

DatasetId	Channel	Generator	PS	PDF	X-sec	k-factor	Gen. evts.
147025	eν + Np0	Alpgen	Pythia	CTEQ6L1	8127.3	1.1330	29464244
147026	eν + Np1	Alpgen	Pythia	CTEQ6L1	1792.7	1.1330	47936004
147027	eν + Np2	Alpgen	Pythia	CTEQ6L1	542.18	1.1330	17495947
147028	eν + Np3	Alpgen	Pythia	CTEQ6L1	147.65	1.1330	4855289
147029	eν + Np4	Alpgen	Pythia	CTEQ6L1	37.736	1.1330	2468793
147030	eν + Np5 incl.	Alpgen	Pythia	CTEQ6L1	11.962	1.1330	799192
147033	$\mu\nu$ + Np0	Alpgen	Pythia	CTEQ6L1	8127.1	1.1330	31965655
147034	$\mu\nu$ + Np1	Alpgen	Pythia	CTEQ6L1	1792.9	1.1330	43622615
147035	$\mu\nu$ + Np2	Alpgen	Pythia	CTEQ6L1	542.24	1.1330	17611454
147036	$\mu\nu$ + Np3	Alpgen	Pythia	CTEQ6L1	147.66	1.1330	4796077
147037	$\mu\nu$ + Np4	Alpgen	Pythia	CTEQ6L1	37.745	1.1330	2551595
147038	$\mu\nu$ + Np5 incl.	Alpgen	Pythia	CTEQ6L1	11.970	1.1330	793898
147041	$\tau\nu$ + Np0	Alpgen	Pythia	CTEQ6L1	8127.1	1.1330	31877158
147042	$\tau\nu$ + Np1	Alpgen	Pythia	CTEQ6L1	1792.2	1.1330	48070179
147043	$\tau\nu$ + Np2	Alpgen	Pythia	CTEQ6L1	542.27	1.1330	17586943
147044	$\tau\nu$ + Np3	Alpgen	Pythia	CTEQ6L1	147.64	1.1330	4982982
147045	$\tau\nu$ + Np4	Alpgen	Pythia	CTEQ6L1	37.781	1.1330	2553295
147046	$\tau\nu$ + Np5 incl.	Alpgen	Pythia	CTEQ6L1	11.959	1.1330	794096
200056	W + c + Np0	Alpgen	Pythia	CTEQ6L1	758.93	1.5200	22999046
200057	W + c + Np1	Alpgen	Pythia	CTEQ6L1	274.47	1.5200	8198769
200058	W + c + Np2	Alpgen	Pythia	CTEQ6L1	71.643	1.5200	2090290
200059	W + c + Np3	Alpgen	Pythia	CTEQ6L1	16.482	1.5200	499498
200060	W + c + Np4 incl.	Alpgen	Pythia	CTEQ6L1	4.7824	1.5200	199499
200156	W + cc + Np0	Alpgen	Pythia	CTEQ6L1	149.39	1.1330	4299592
200157	W + cc + Np1	Alpgen	Pythia	CTEQ6L1	143.90	1.1330	4137891
200158	W + cc + Np2	Alpgen	Pythia	CTEQ6L1	84.227	1.1330	2394394
200159	W + cc + Np3 incl.	Alpgen	Pythia	CTEQ6L1	44.277	1.1330	985295
200256	W + bb + Np0	Alpgen	Pythia	CTEQ6L1	52.237	1.1330	1599997
200257	W + bb + Np1	Alpgen	Pythia	CTEQ6L1	45.628	1.1330	1398396
200258	W + bb + Np2	Alpgen	Pythia	CTEQ6L1	23.955	1.1330	699398
200259	W + bb + Np3 incl.	Alpgen	Pythia	CTEQ6L1	13.633	1.1330	398397

A.5 Z + jets samples

DatasetId	Channel	Generator	PS	PDF	X-sec	k-factor	Gen. evts.
147105	ee + Np0	Alpgen	Pythia	CTEQ6L1	718.89	1.1800	6619984
147106	ee + Np1	Alpgen	Pythia	CTEQ6L1	175.60	1.1800	1329498
147107	ee + Np2	Alpgen	Pythia	CTEQ6L1	58.849	1.1800	404998
147108	ee + Np3	Alpgen	Pythia	CTEQ6L1	15.560	1.1800	109999
147109	ee + Np4	Alpgen	Pythia	CTEQ6L1	3.9322	1.1800	30000
147110	ee + Np5 incl.	Alpgen	Pythia	CTEQ6L1	1.1994	1.1800	10000
147113	$\mu\mu$ + Np0	Alpgen	Pythia	CTEQ6L1	718.91	1.1800	6608490
147114	$\mu\mu$ + Np1	Alpgen	Pythia	CTEQ6L1	175.81	1.1800	1334697
147115	$\mu\mu$ + Np2	Alpgen	Pythia	CTEQ6L1	58.805	1.1800	404995
147116	$\mu\mu$ + Np3	Alpgen	Pythia	CTEQ6L1	15.589	1.1800	110000
147117	$\mu\mu$ + Np4	Alpgen	Pythia	CTEQ6L1	3.9072	1.1800	30000
147118	$\mu\mu$ + Np5 incl.	Alpgen	Pythia	CTEQ6L1	1.1933	1.1800	10000
147121	$\tau\tau$ + Np0	Alpgen	Pythia	CTEQ6L1	718.80	1.1800	6619189
147122	$\tau\tau$ + Np1	Alpgen	Pythia	CTEQ6L1	175.83	1.1800	1334898
147123	$\tau\tau$ + Np2	Alpgen	Pythia	CTEQ6L1	58.630	1.1800	404795
147124	$\tau\tau$ + Np3	Alpgen	Pythia	CTEQ6L1	15.508	1.1800	110000
147125	$\tau\tau$ + Np4	Alpgen	Pythia	CTEQ6L1	3.9526	1.1800	30000
147126	$\tau\tau$ + Np5 incl.	Alpgen	Pythia	CTEQ6L1	1.1805	1.1800	10000C
200332	Z→ ee + bb + Np0	Alpgen	Pythia	CTEQ6L1	6.5083	1.1800	1799992
200333	Z→ ee + bb + Np1	Alpgen	Pythia	CTEQ6L1	3.2948	1.1800	999896
200334	Z→ ee + bb + Np2	Alpgen	Pythia	CTEQ6L1	1.2546	1.1800	994594
200335	Z→ ee + bb + Np3 incl.	Alpgen	Pythia	CTEQ6L1	0.61800	1.1800	885392
200340	Z→ $\mu\mu$ + bb + Np0	Alpgen	Pythia	CTEQ6L1	6.5056	1.1800	1799797
200341	Z→ $\mu\mu$ + bb + Np1	Alpgen	Pythia	CTEQ6L1	3.2909	1.1800	999897
200342	Z→ $\mu\mu$ + bb + Np2	Alpgen	Pythia	CTEQ6L1	1.2585	1.1800	999395
200343	Z→ $\mu\mu$ + bb + Np3 incl.	Alpgen	Pythia	CTEQ6L1	0.61808	1.1800	880894
200348	Z→ $\tau\tau$ + bb + Np0	Alpgen	Pythia	CTEQ6L1	6.5062	1.1800	300000
200349	Z→ $\tau\tau$ + bb + Np1	Alpgen	Pythia	CTEQ6L1	3.2935	1.1800	100000
200350	Z→ $\tau\tau$ + bb + Np2	Alpgen	Pythia	CTEQ6L1	1.2485	1.1800	50000
200351	Z→ $\tau\tau$ + bb + Np3 incl.	Alpgen	Pythia	CTEQ6L1	0.61363	1.1800	49800
200432	Z→ ee + cc + Np0	Alpgen	Pythia	CTEQ6L1	11.763	1.1800	284999
200433	Z→ ee + cc + Np1	Alpgen	Pythia	CTEQ6L1	7.1249	1.1800	499500
200434	Z→ ee + cc + Np2	Alpgen	Pythia	CTEQ6L1	3.3656	1.1800	498997
200435	Z→ ee + cc + Np3 incl.	Alpgen	Pythia	CTEQ6L1	1.7010	1.1800	443697
200440	Z→ $\mu\mu$ + cc + Np0	Alpgen	Pythia	CTEQ6L1	11.795	1.1800	298998
200441	Z→ $\mu\mu$ + cc + Np1	Alpgen	Pythia	CTEQ6L1	7.1254	1.1800	499799
200442	Z→ $\mu\mu$ + cc + Np2	Alpgen	Pythia	CTEQ6L1	3.3694	1.1800	499500
200443	Z→ $\mu\mu$ + cc + Np3 incl.	Alpgen	Pythia	CTEQ6L1	1.7003	1.1800	443999
200448	Z→ $\tau\tau$ + cc + Np0	Alpgen	Pythia	CTEQ6L1	11.760	1.1800	299000
200449	Z→ $\tau\tau$ + cc + Np1	Alpgen	Pythia	CTEQ6L1	7.1410	1.1800	199998
200450	Z→ $\tau\tau$ + cc + Np2	Alpgen	Pythia	CTEQ6L1	3.3582	1.1800	99800
200451	Z→ $\tau\tau$ + cc + Np3 incl.	Alpgen	Pythia	CTEQ6L1	1.7046	1.1800	49400

Appendix B

Control Plots

B.1 Control Plots in signal region

Data distributions of Egamma, Muons and combined streams are compared to predictions using POWHEG+PYTHIA as the $t\bar{t}$ signal model. The hashed area indicates the combined statistical and systematic uncertainties on the total prediction, excluding systematic uncertainties related to the modelling of the $t\bar{t}$ system. The lower parts of the figures show the ratios of data to the predictions. The following figures of this section are related to the signal region in which we have at least of four jets, two of them b-tagged, an isolated lepton and neutrino, in the final state. The W boson transverse mass, which control plots as follow, is defined as $M_T^W = \sqrt{2p_T^l p_T^\nu (1 - cos(\Delta\phi))}$ where p_T^l is the transverse momentum of the charged lepton, p_T^ν is the transverse momentum of the neutrino and $\Delta\phi$ represents the angle between the charged lepton and the neutrino in the trasverse plane, while the effective mass, defined as $m_{eff} = E_T^{miss} + p_T^l + \Sigma_{i=1}^n p_T^{jet,i}$, where E_T^{miss} is the usual missing transverse energy due to the neutrino, p_T^l is the transverse momentum of the lepton, p_T^{jet} is the transverse momentum of the hadronic jet and the i index runs over the number of n jets event by event.

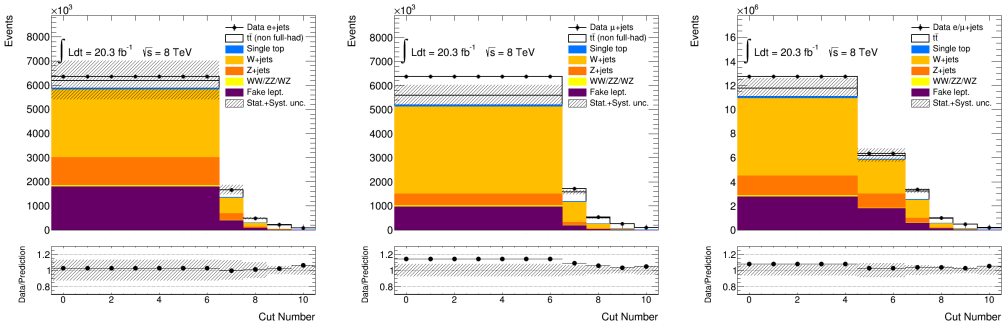

(a) (b) (c)

FIGURE B.1: The number of events as function of the selection cuts for (a) e+jets, (b) μ+jets and (c) combined channels. The shaded area represents the total statistical and systematic uncertainties on the expected number of events.

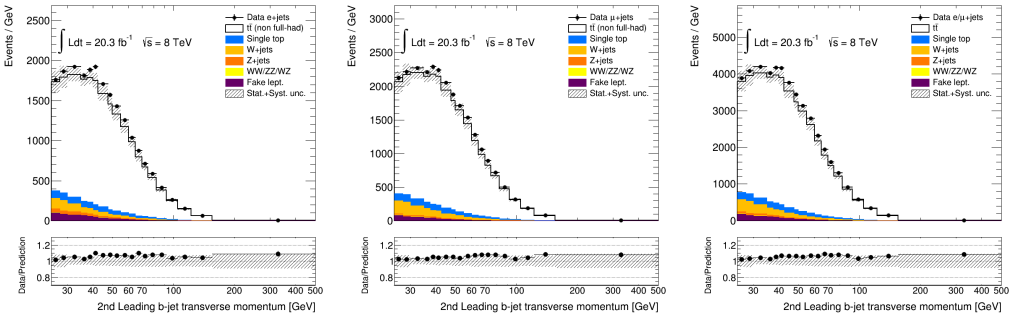

(a) (b) (c)

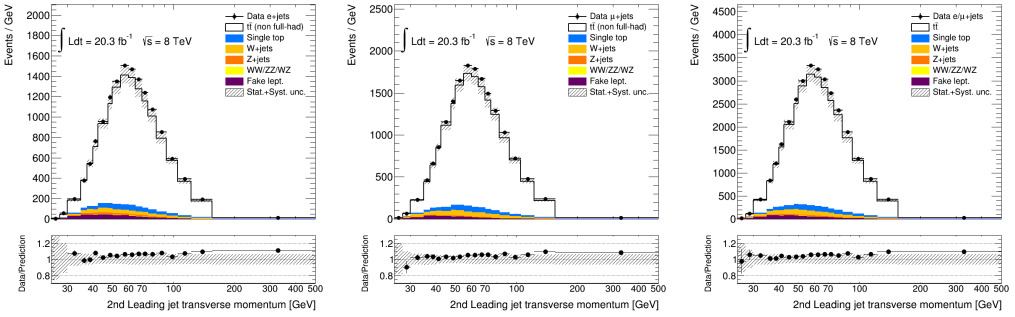

(d) (e) (f)

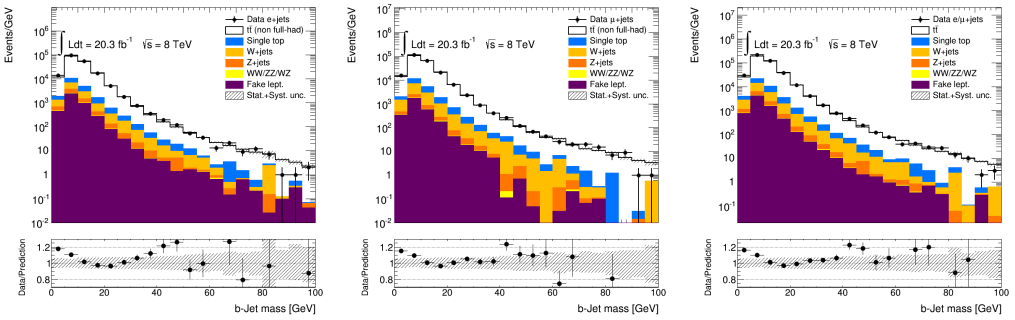

(g) (h) (i)

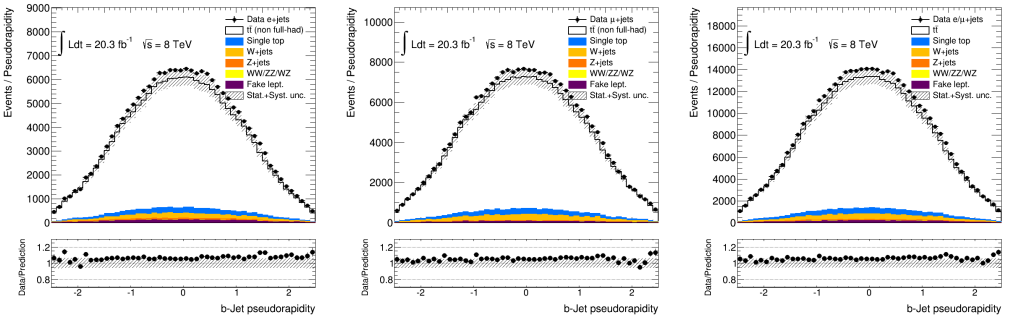

(j) (k) (l)

FIGURE B.2: Kinematic distributions at the detector level: second leading b-tagged jet transverse momentum of B.2(a) Egamma stream, B.2(b) Muons stream and B.2(c) combined; second leading non b-tagged jet transverse momentum of B.2(d) Egamma stream, B.2(e) Muons stream and B.2(f) combined; b-tagged jet invariant mass of B.2(g) Egamma, B.2(h) Muons and B.2(i) combined; b-tagged jet pseudorapidity of B.2(j) Egamma, B.2(k) Muons and B.2(l) combined streams.

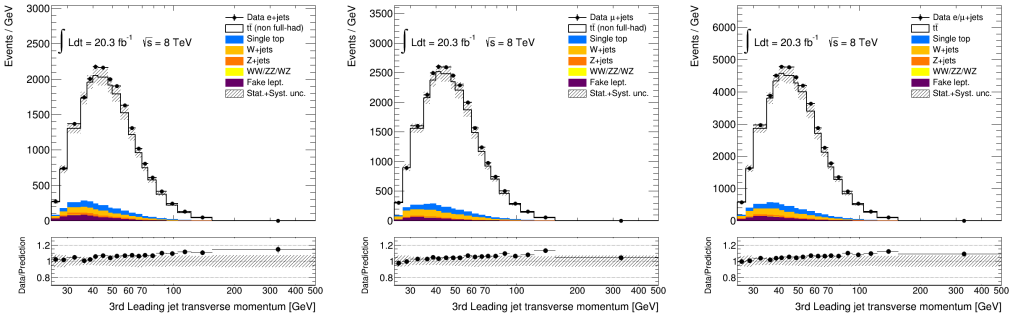

(a) (b) (c)

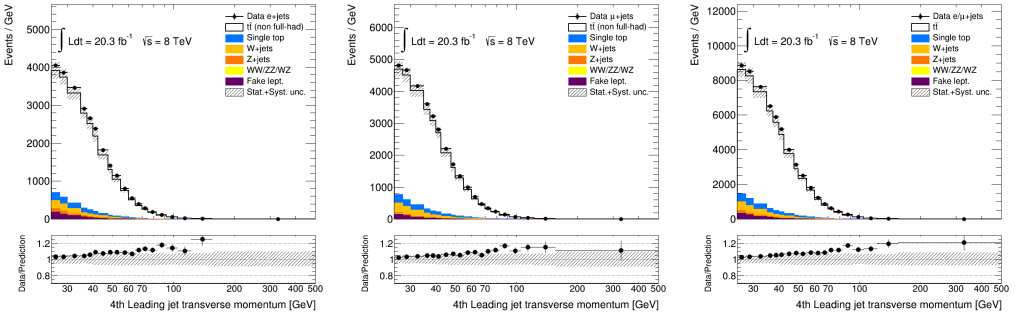

(d) (e) (f)

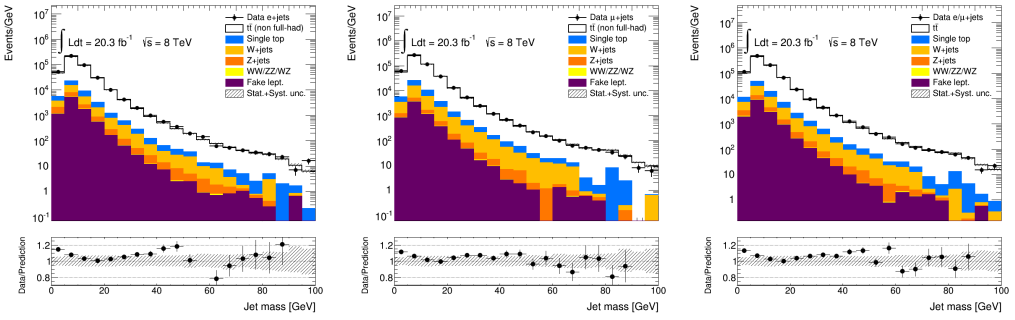

(g) (h) (i)

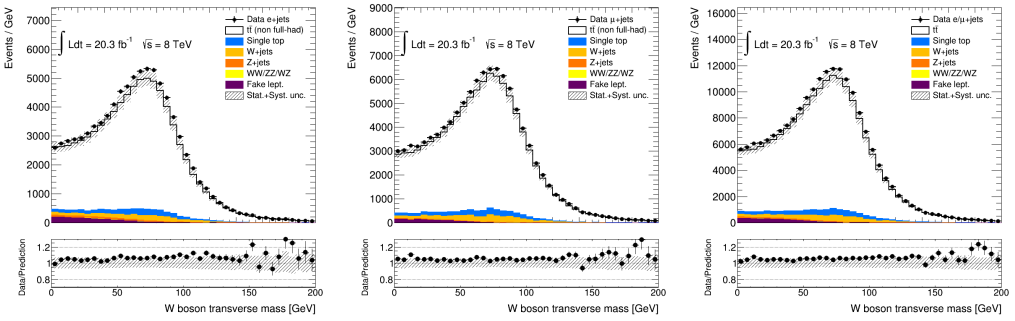

(j) (k) (l)

FIGURE B.3: Kinematic distributions at the detector level: third leading non b-tagged jet transverse momentum of B.3(a) Egamma stream, B.3(b) Muons stream and B.3(c) combined; fourth leading non b-tagged jet transverse momentum of B.3(d) Egamma stream, B.3(e) Muons stream and B.3(f) combined; non b-tagged jet invariant mass of B.3(g) Egamma, B.3(h) Muons and B.3(i) combined; W boson transverse mass of B.3(j) Egamma, B.3(k) Muons and B.3(l) combined streams.

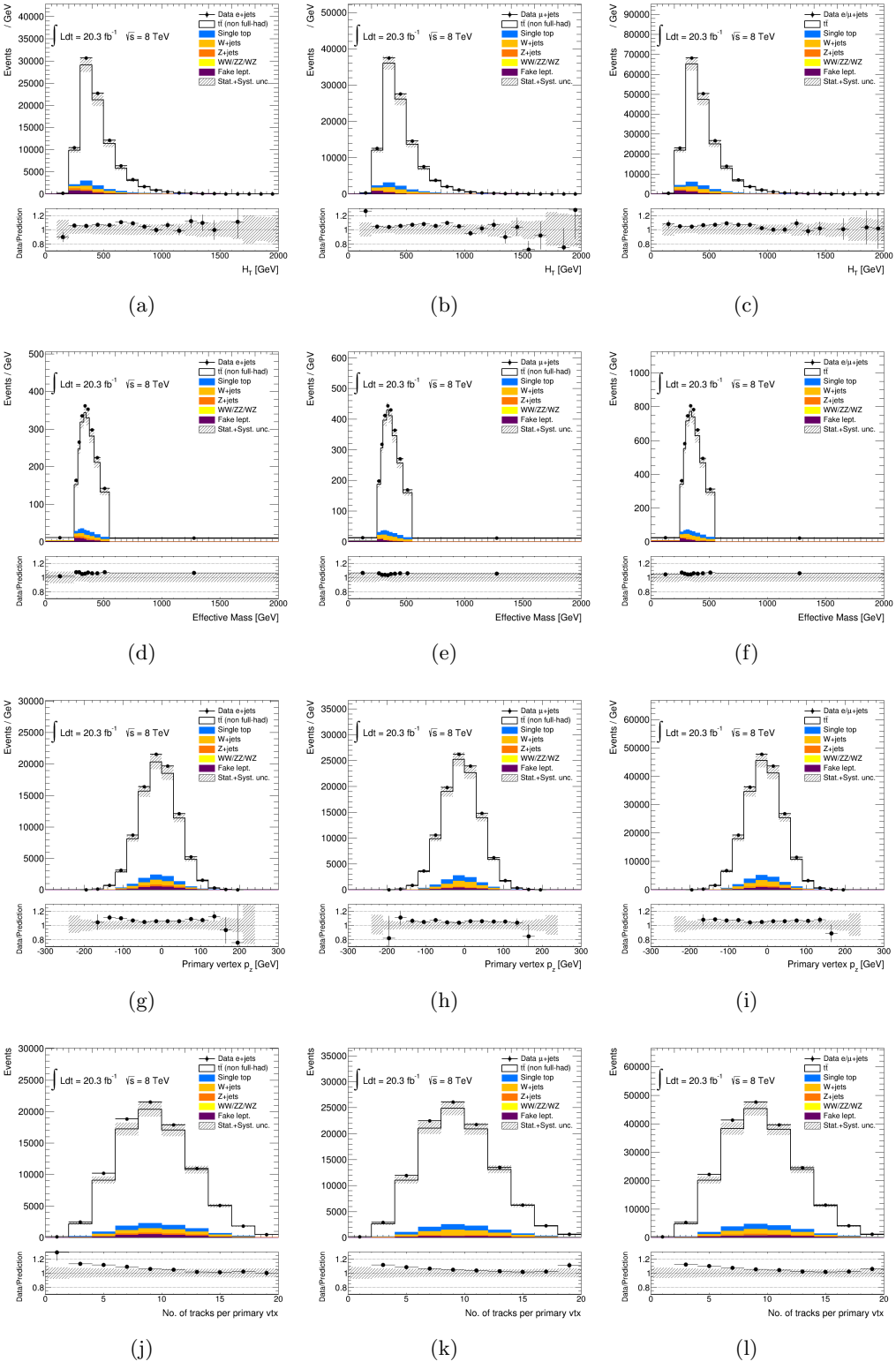

FIGURE B.4: Kinematic distributions at the detector level: scalar sum H_T of transverse momentum of final state particles of B.4(a) Egamma, B.4(b) Muons and B.4(c) combined streams; effective mass of B.4(d) Egamma, B.4(e) Muons and B.4(f) combined streams; momentum along the beam line of tracks related to the primary vertices of B.4(g) Egamma, B.4(h) Muons and B.4(i) combined; number of tracks associated to the primary vertex of B.4(j) Egamma, B.4(k) Muons and B.4(l) combined streams.

B.2 Control Plots in non-signal region

Data distributions of Egamma, Muons and combined streams are compared to predictions using POWHEG+PYTHIA as the $t\bar{t}$ signal model. The hashed area indicates the combined statistical and systematic uncertainties on the total prediction, excluding systematic uncertainties related to the modelling of the $t\bar{t}$ system. The lower parts of the figures show the ratios of data to the predictions. The following figures of this section are related to the non-signal region in which we have at least three jets, with any condition about the number of b-tagged jets, an isolated lepton and neutrino, in the final state.

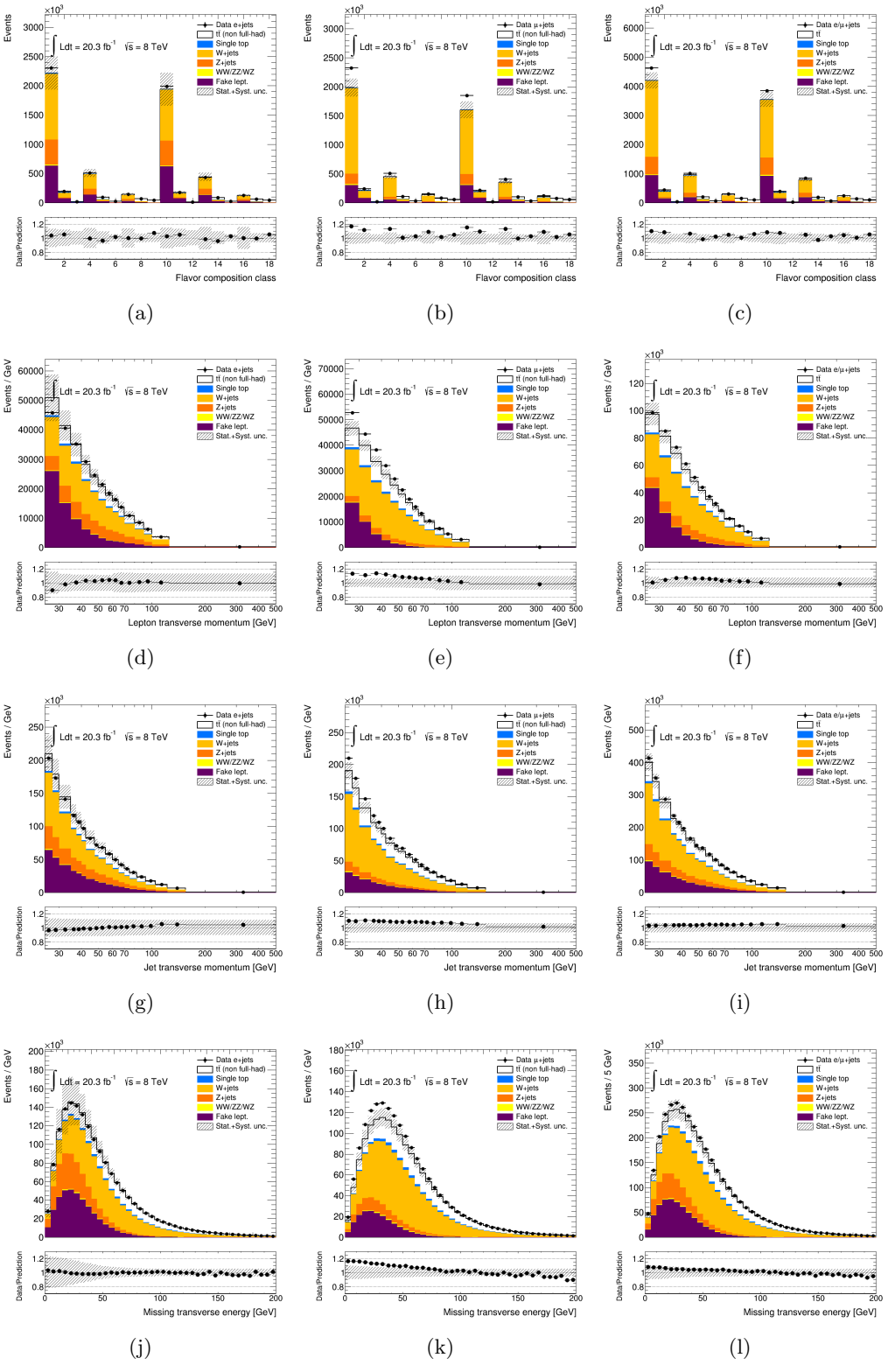

FIGURE B.5: Flavor composition divided in classes according to the charge of the lepton (positive for bins 1-9, negative for bins 10-18), the number of jets ($= 2$, $= 3$, ≥ 4) and the number of b-tagged jets (0, 1, ≥ 2) for each N jets bin. The signal region (4j2b) is represented by bins 9 and 18, of B.5(a) Egamma stream, B.5(b) Muons stream and B.5(c) combined streams. Kinematic distributions at the detector level: lepton transverse momentum of B.5(d) Egamma stream, B.5(e) Muons stream and B.5(f) combined; jets transverse momentum of B.5(g) Egamma, B.5(h) Muons and B.5(i) combined; missing transverse momentum E_T^{miss} of B.5(j) Egamma, B.5(k) Muons and B.5(l) combined streams.

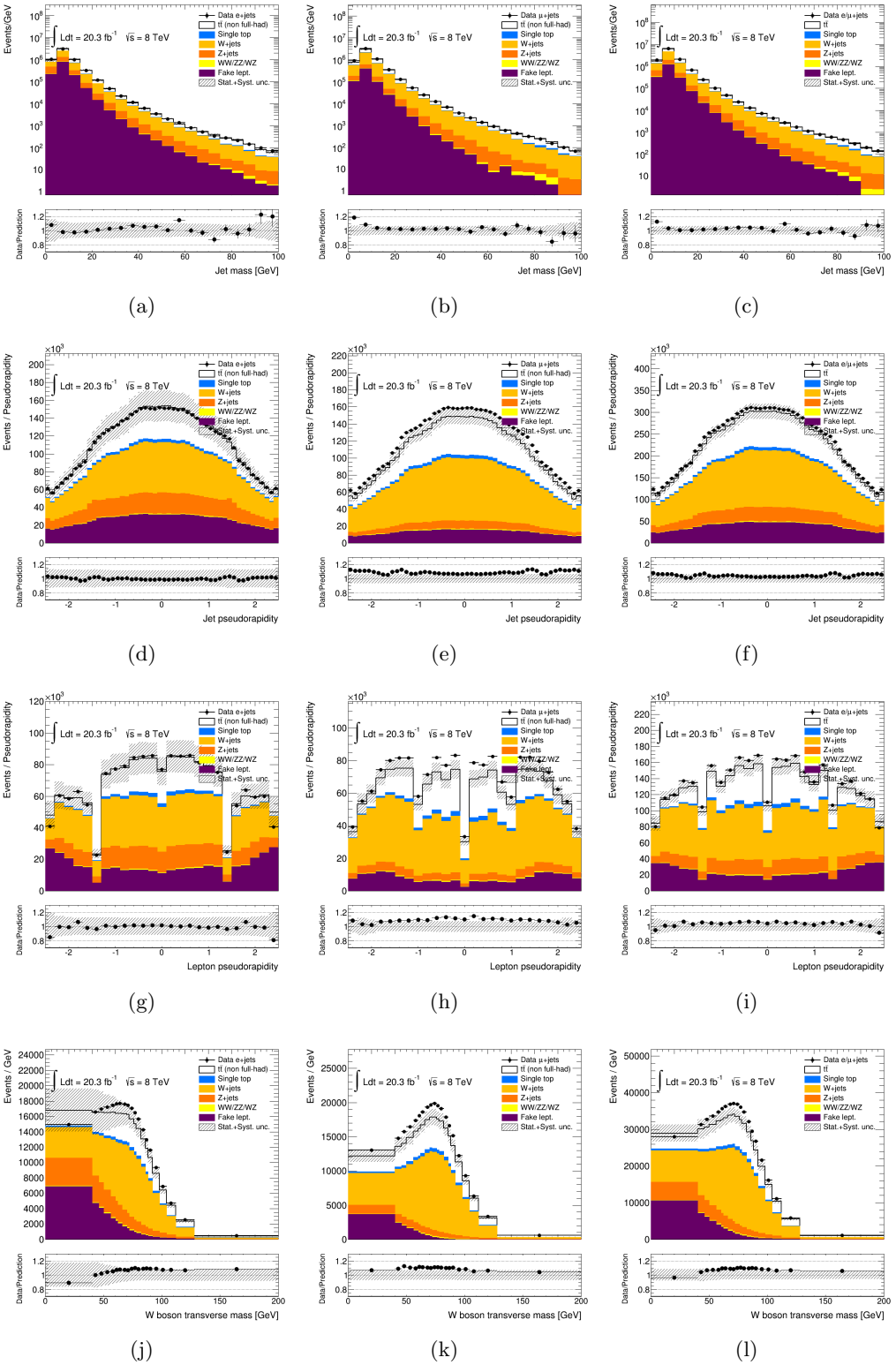

(a) (b) (c)

(d) (e) (f)

(g) (h) (i)

(j) (k) (l)

FIGURE B.6: Kinematic distributions at the detector level: jet mass of B.6(a) Egamma stream, B.6(b) Muons stream and B.6(c) combined; jets pseudorapidity of B.6(d) Egamma, B.6(e) Muons and B.6(f) combined; lepton pseudorapidity of B.6(g) Egamma, B.6(h) Muons and B.6(i) combined; W boson transverse mass of B.6(j) Egamma, B.6(k) Muons and B.6(l) combined streams.

Data distributions of Egamma, Muons and combined streams are compared to predictions using POWHEG+PYTHIA as the $t\bar{t}$ signal model. The hashed area indicates the combined statistical and systematic uncertainties on the total prediction, excluding systematic uncertainties related to the modelling of the $t\bar{t}$ system. The lower parts of the figures show the ratios of data to the predictions. The following figures of this section are related to the non-signal region in which we have at least four jets, with any condition about the number of b-tagged jets, an isolated lepton and neutrino, in the final state.

Data distributions of Egamma, Muons and combined streams are compared to predictions using POWHEG+PYTHIA as the $t\bar{t}$ signal model. The hashed area indicates the combined statistical and systematic uncertainties on the total prediction, excluding systematic uncertainties related to the modelling of the $t\bar{t}$ system. The lower parts of the figures show the ratios of data to the predictions. The following figures of this section are related to the non-signal region in which we have at least four jets, with at least one pf them b-tagged jets, an isolated lepton and neutrino, in the final state.

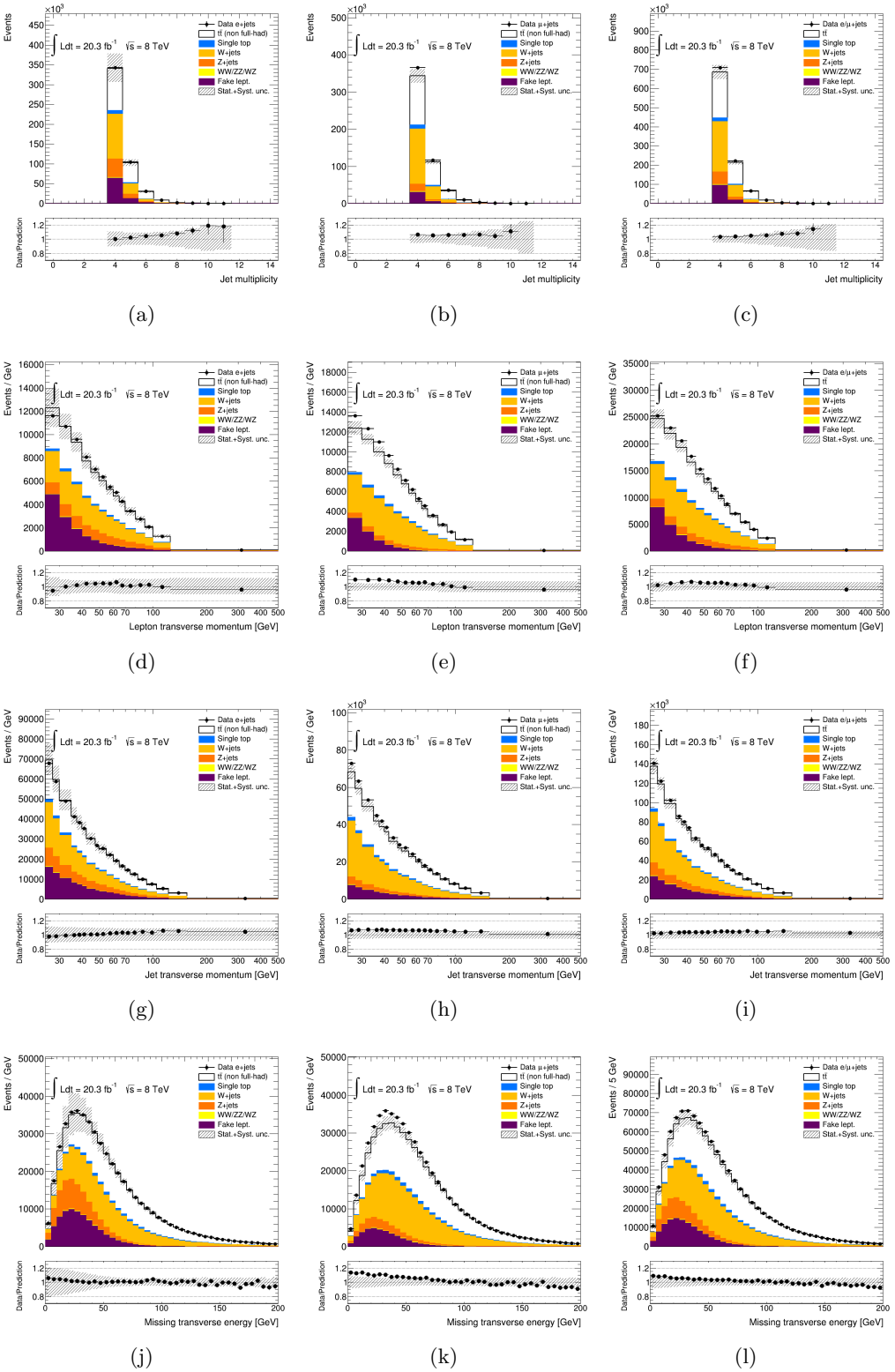

(a) (b) (c)

(d) (e) (f)

(g) (h) (i)

(j) (k) (l)

FIGURE B.7: Jet multiplicity of B.7(a) Egamma stream, B.7(b) Muons stream and B.7(c) combined streams. Kinematic distributions at the detector level: lepton transverse momentum of B.7(d) Egamma stream, B.7(e) Muons stream and B.7(f) combined; jets transverse momentum of B.7(g) Egamma, B.7(h) Muons and B.7(i) combined; missing transverse momentum E_T^{miss} of B.7(j) Egamma, B.7(k) Muons and B.7(l) combined streams.

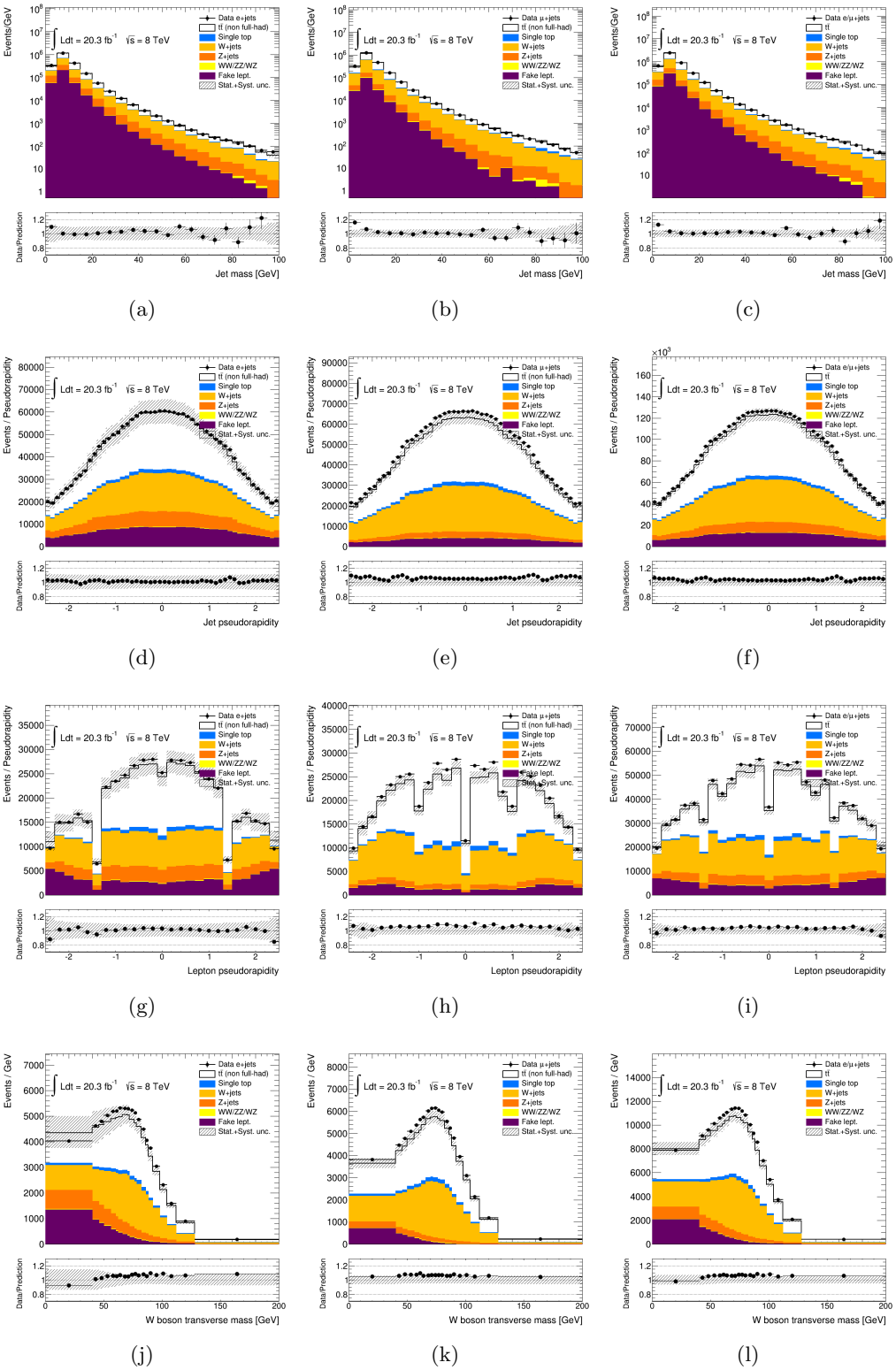

(a) (b) (c)

(d) (e) (f)

(g) (h) (i)

(j) (k) (l)

FIGURE B.8: Kinematic distributions at the detector level: jet mass of B.8(a) Egamma stream, B.8(b) Muons stream and B.8(c) combined; jets pseudorapidity of B.8(d) Egamma, B.8(e) Muons and B.8(f) combined; lepton pseudorapidity of B.8(g) Egamma, B.8(h) Muons and B.8(i) combined; W boson transverse mass of B.8(j) Egamma, B.8(k) Muons and B.8(l) combined streams.

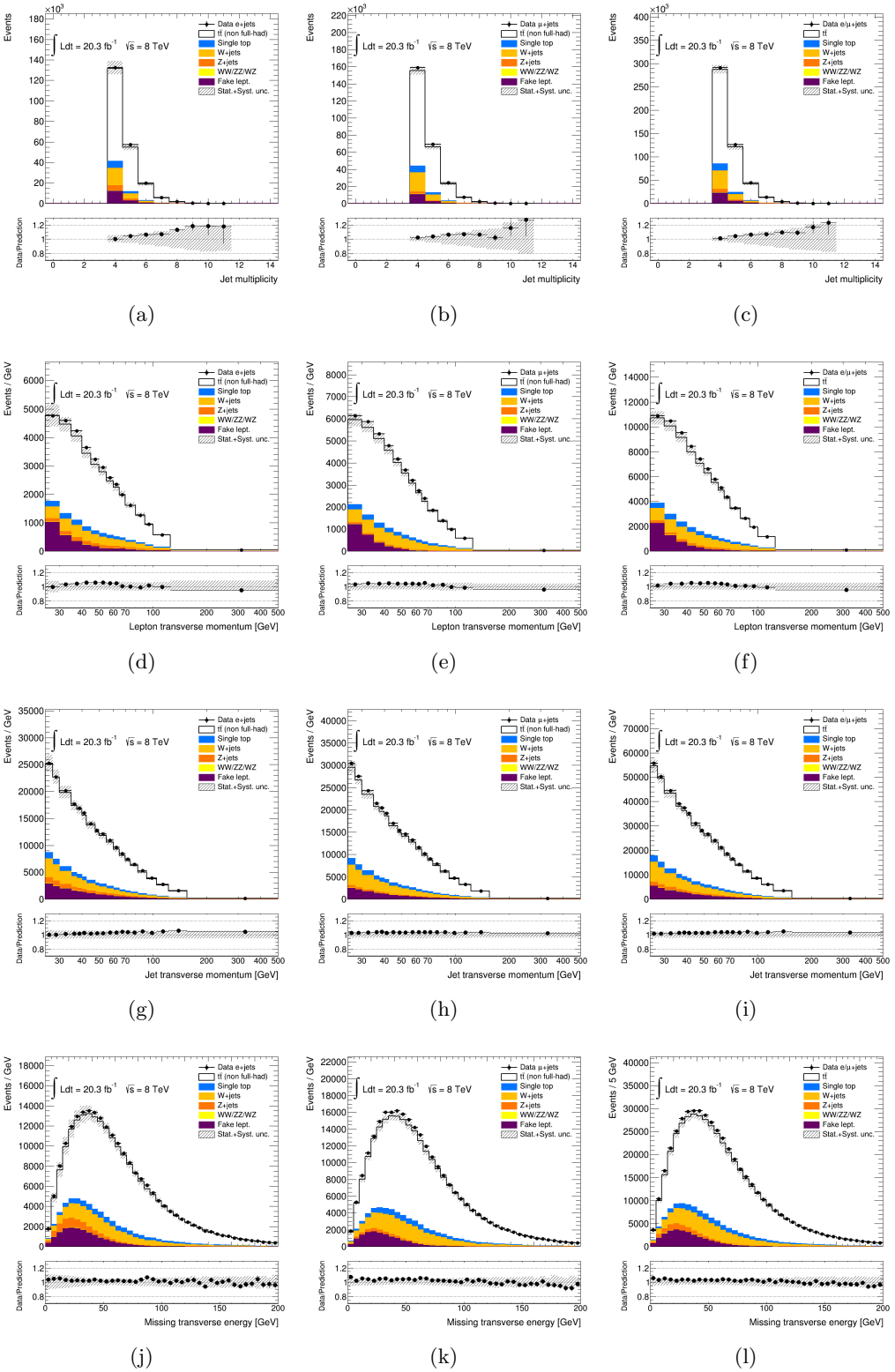

FIGURE B.9: Jet multiplicity of B.9(a) Egamma stream, B.9(b) Muons stream and B.9(c) combined streams. Kinematic distributions at the detector level: lepton transverse momentum of B.9(d) Egamma stream, B.9(e) Muons stream and B.9(f) combined; jets transverse momentum of B.9(g) Egamma, B.9(h) Muons and B.9(i) combined; missing transverse momentum E_T^{miss} of B.9(j) Egamma, B.9(k) Muons and B.9(l) combined streams.

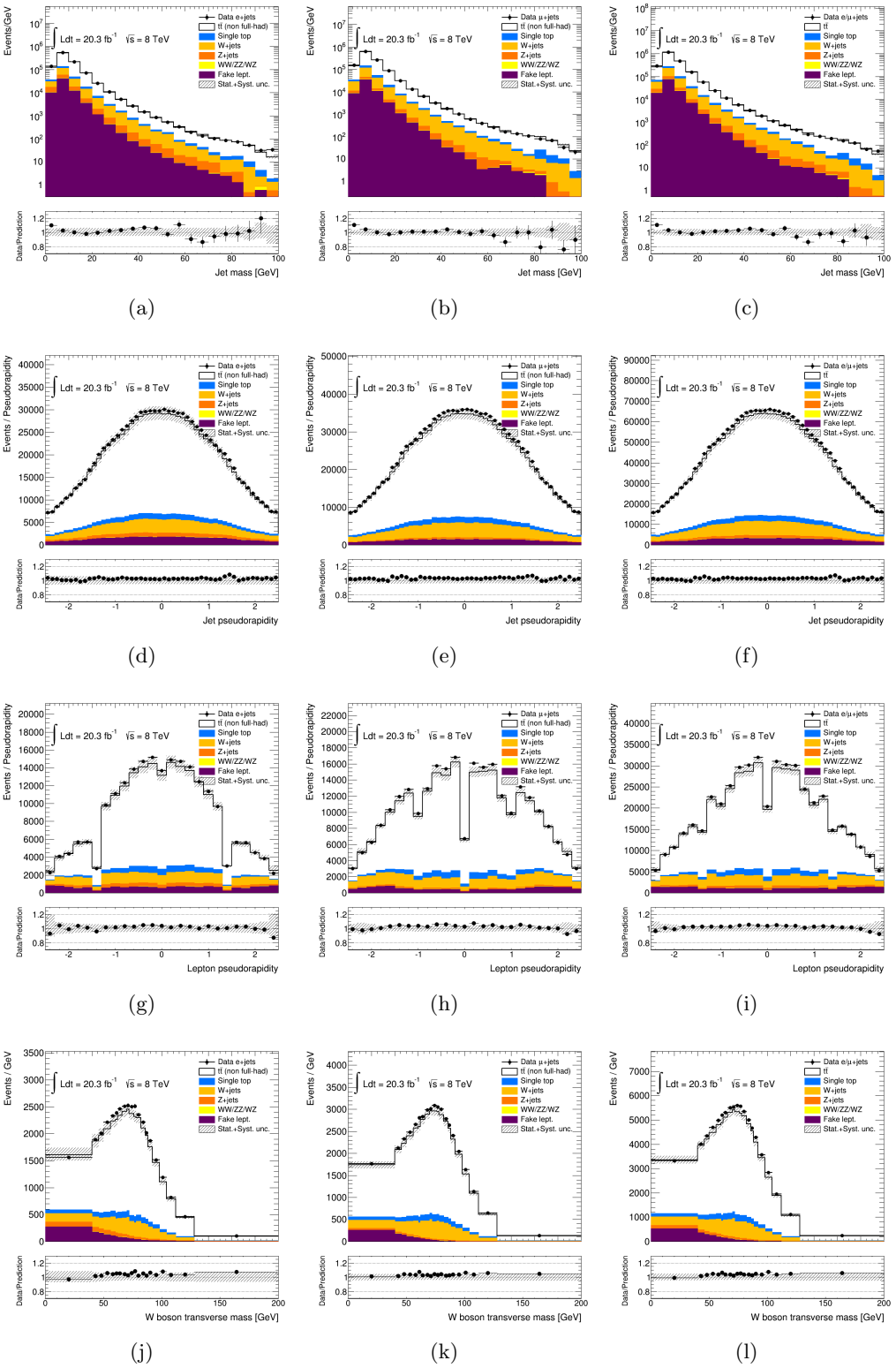

(a) (b) (c)

(d) (e) (f)

(g) (h) (i)

(j) (k) (l)

FIGURE B.10: Kinematic distributions at the detector level: jet mass of B.10(a) Egamma stream, B.10(b) Muons stream and B.10(c) combined; jets pseudorapidity of B.10(d) Egamma, B.10(e) Muons and B.10(f) combined; lepton pseudorapidity of B.10(g) Egamma, B.10(h) Muons and B.10(i) combined; W boson transverse mass of B.10(j) Egamma, B.10(k) Muons and B.10(l) combined streams.

Appendix C

Correction factors and Migration matrices

C.1 Fiducial phase-space

C.1.1 Migration matrices

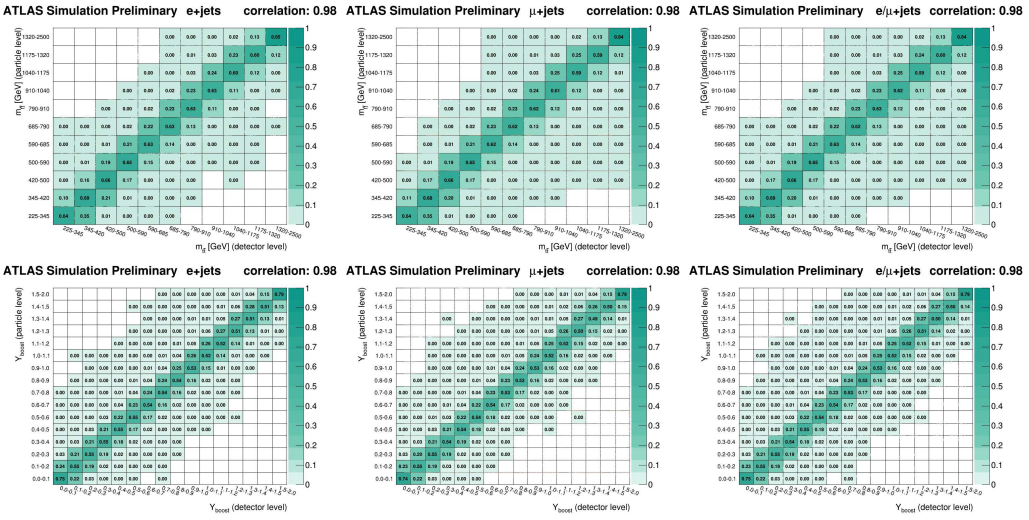

FIGURE C.1: Migration matrix between detector and particle level for the pseudo-top quark pairs $m_{t\bar{t}}$ (top) and longitudinal boost $Y^{t\bar{t}}_{boost}$ (bottom) in the e+jets (left), μ+jets (middle) and combined ℓ+jets channel.

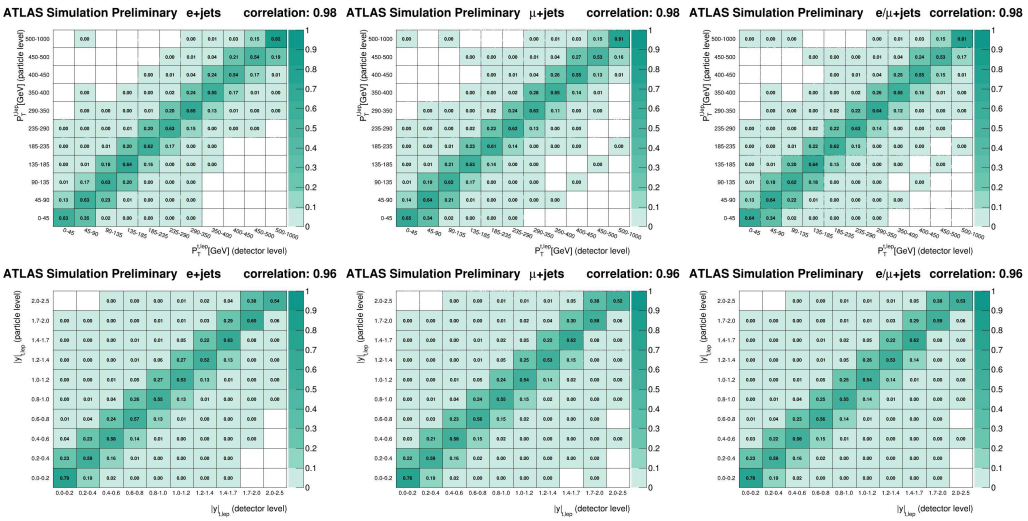

FIGURE C.2: Migration matrix between detector and particle level for the leptonic pseudo-top quark p_T (top) and absolute value of rapidity $|y|$ (bottom) in the e+jets (left), μ+jets (middle) and combined ℓ+jets channel.

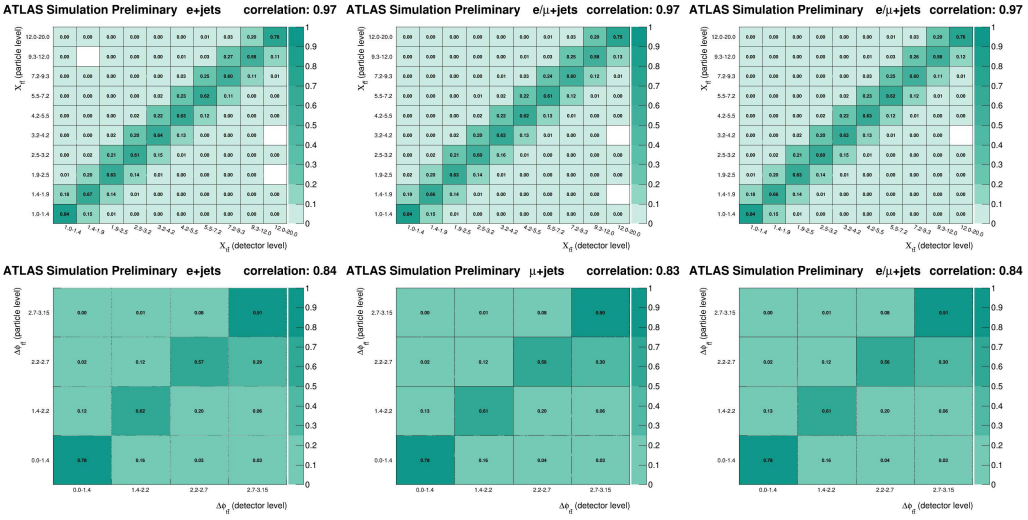

FIGURE C.3: Migration matrix between detector and particle level for the pseudo-top quark pair $\chi_{t\bar{t}}$ (top) and $\Delta\phi_{t\bar{t}}$ (bottom) in the e+jets (left), μ+jets (middle) and combined ℓ+jets channel.

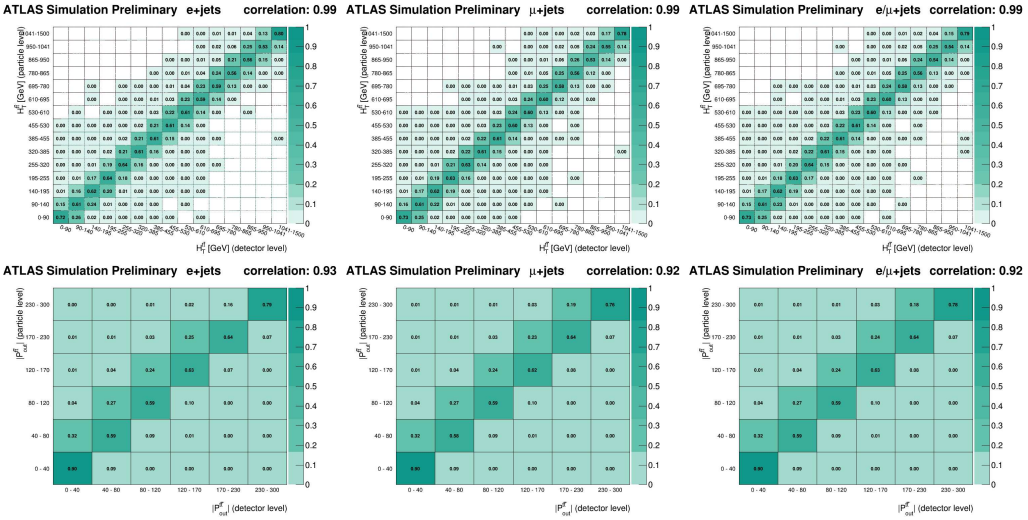

FIGURE C.4: Migration matrix between detector and particle level for the pseudo-top quark pair $H_T^{t\bar{t}}$ (top) and $P_{out}^{t\bar{t}}$(bottom) in the e+jets (left), μ+jets (middle) and combined ℓ+jets channel.

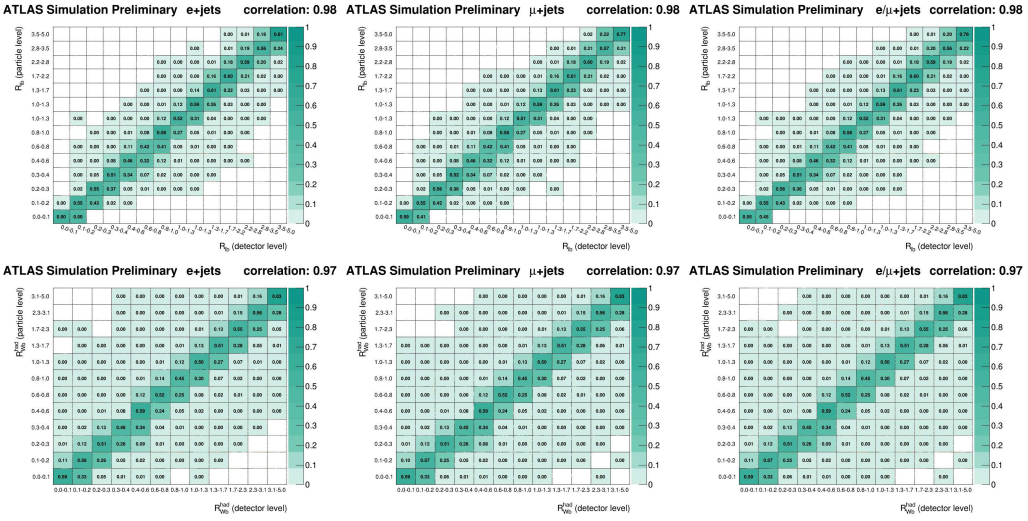

FIGURE C.5: Migration matrix between detector and particle level for the R_{lb} (top) and R_{Wb}^{had} (bottom) in the e+jets (left), μ+jets (middle) and combined ℓ+jets channel.

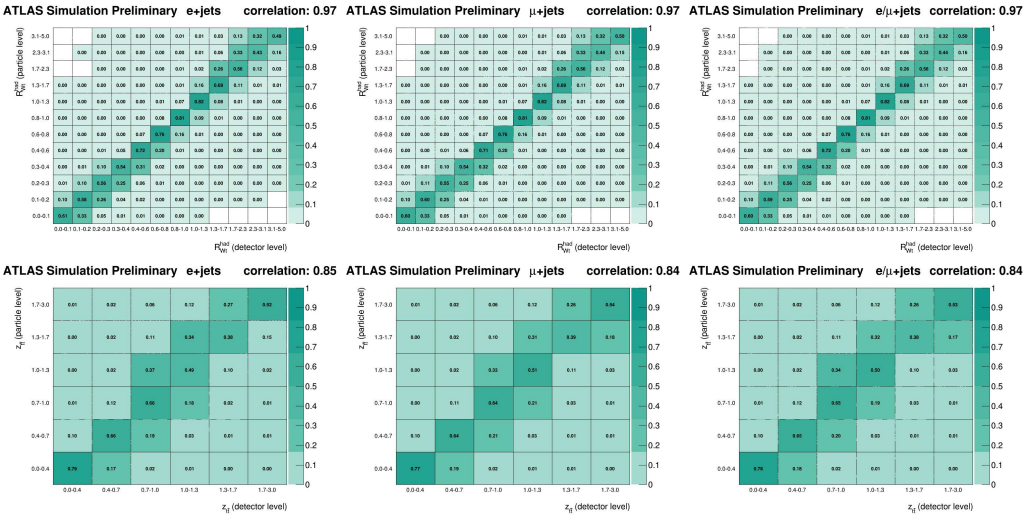

FIGURE C.6: Migration matrix between detector and particle level for the R_{Wt}^{had} (top) and $z_{t\bar{t}}$ (bottom) in the e+jets (left), μ+jets (middle) and combined ℓ+jets channel.

C.1.2 Efficiency correction

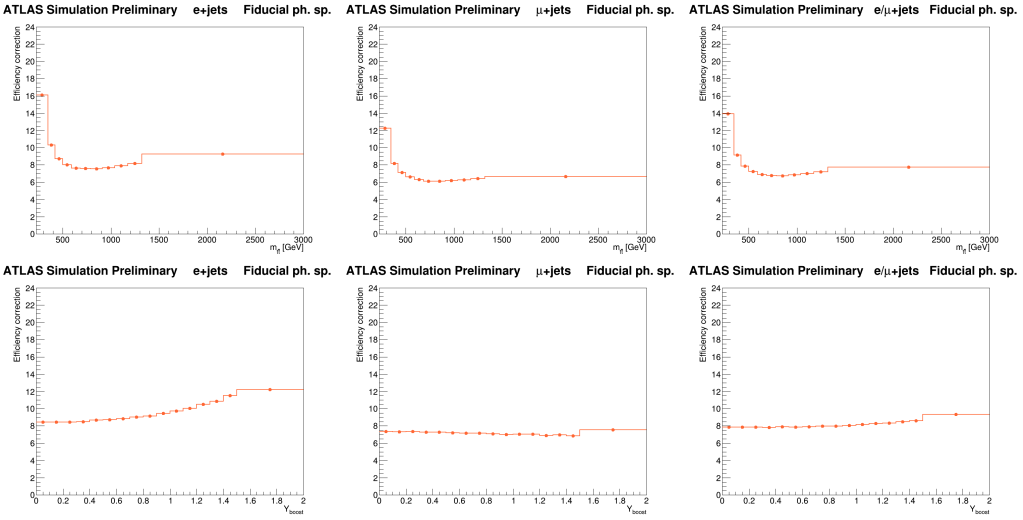

FIGURE C.7: Efficiency corrections for the top quark pair m (top) and longitudinal boost $Y^{t\bar{t}}_{boost}$ (bottom) in the e+jets (left), μ+jets (middle) and combined ℓ+jets channels.

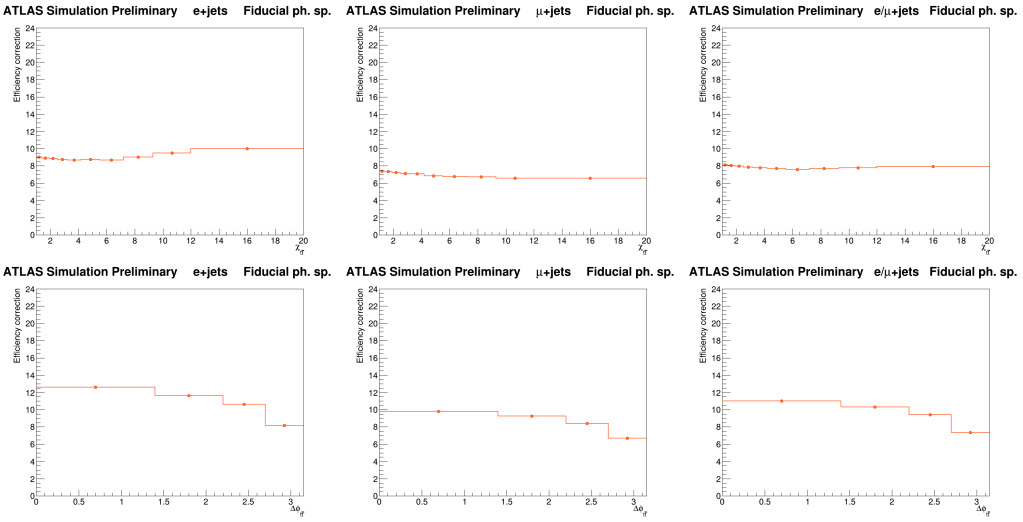

FIGURE C.8: Efficiency corrections for the pseudo-top quark pair $\chi_{t\bar{t}}$ (top) and $\Delta\phi_{t\bar{t}}$ (bottom) in the e+jets (left), μ+jets (middle) and combined ℓ+jets channels in the fiducial phase-space.

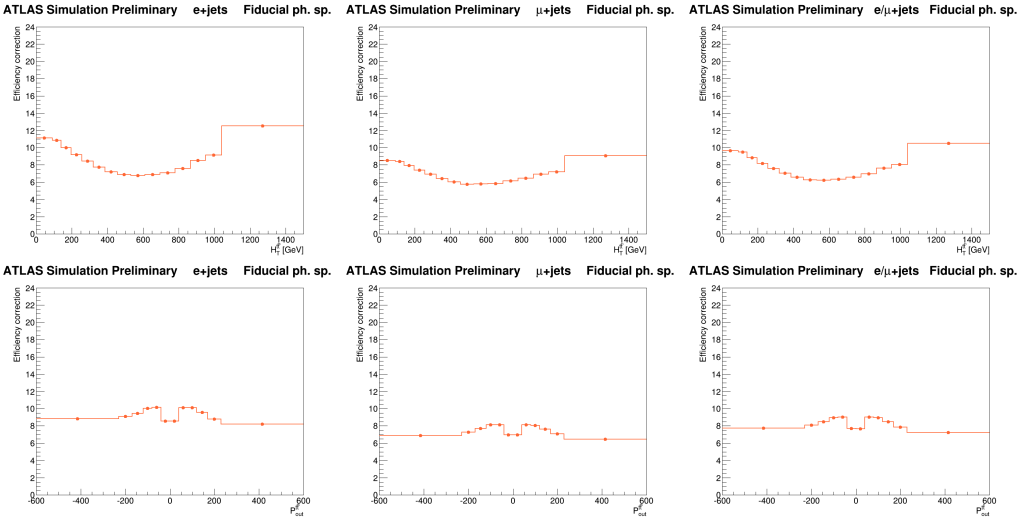

FIGURE C.9: Efficiency corrections for the pseudo-top quark pair $H_T^{t\bar{t}}$ (top) and $P_{out}^{t\bar{t}}$ (bottom) in the e+jets (left), μ+jets (middle) and combined ℓ+jets channels in the fiducial phase-space.

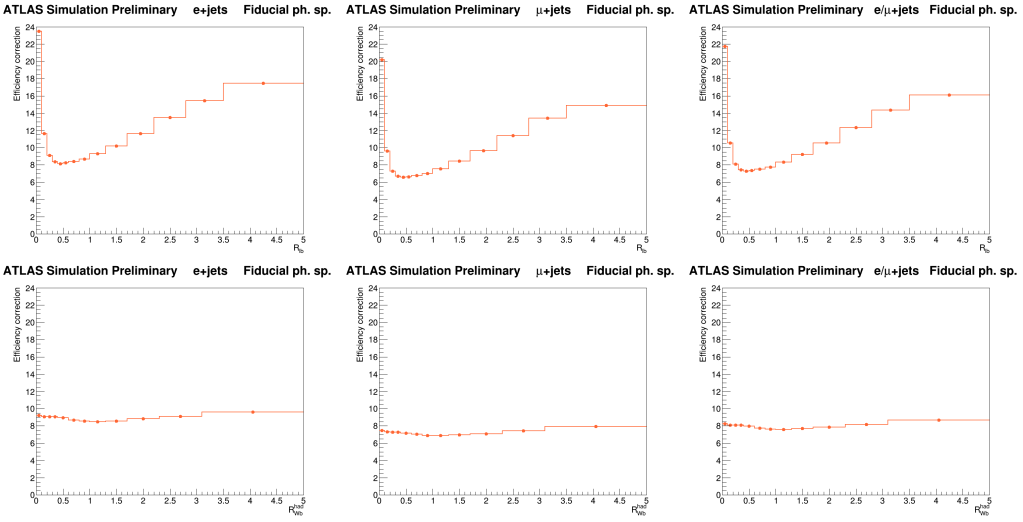

FIGURE C.10: Efficiency corrections for the pseudo-top quark pair R_{lb} (top) and R_{Wb}^{had} (bottom) in the e+jets (left), μ+jets (middle) and combined ℓ+jets channels in the fiducial phase-space.

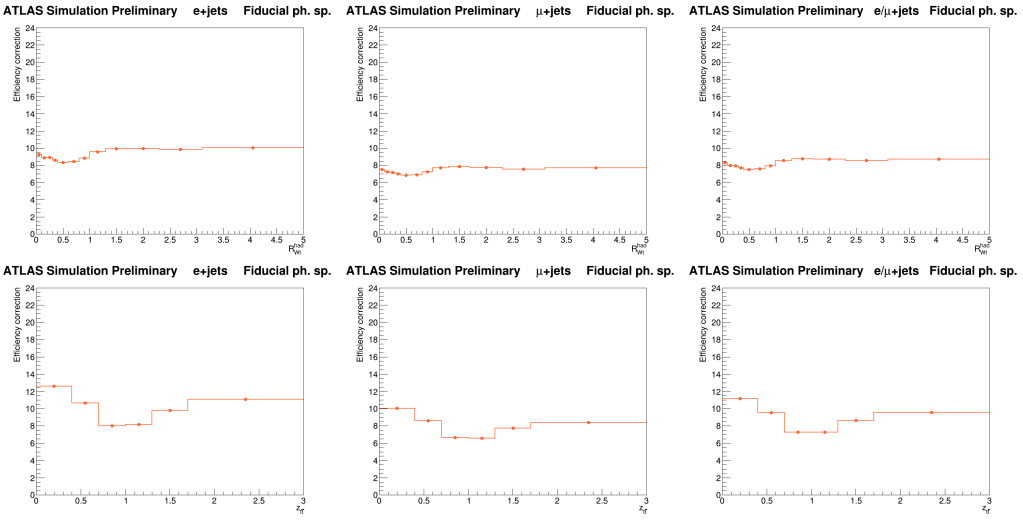

FIGURE C.11: Efficiency corrections for the pseudo-top quark pair R_{Wt}^{had} (top) and $z_{t\bar{t}}$ (bottom) in the e+jets (left), μ+jets (middle) and combined ℓ+jets channels.

C.1.3 Acceptance correction

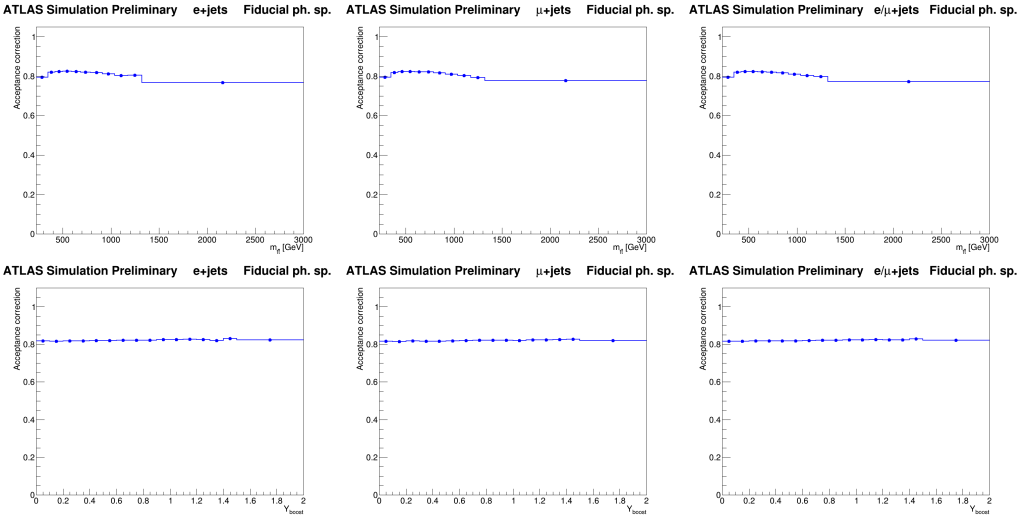

FIGURE C.12: Acceptance corrections for the top quark pair m (top) and longitudinal boost $Y_{boost}^{t\bar{t}}$ (bottom) in the e+jets (left), μ+jets (middle) and combined ℓ+jets channels.

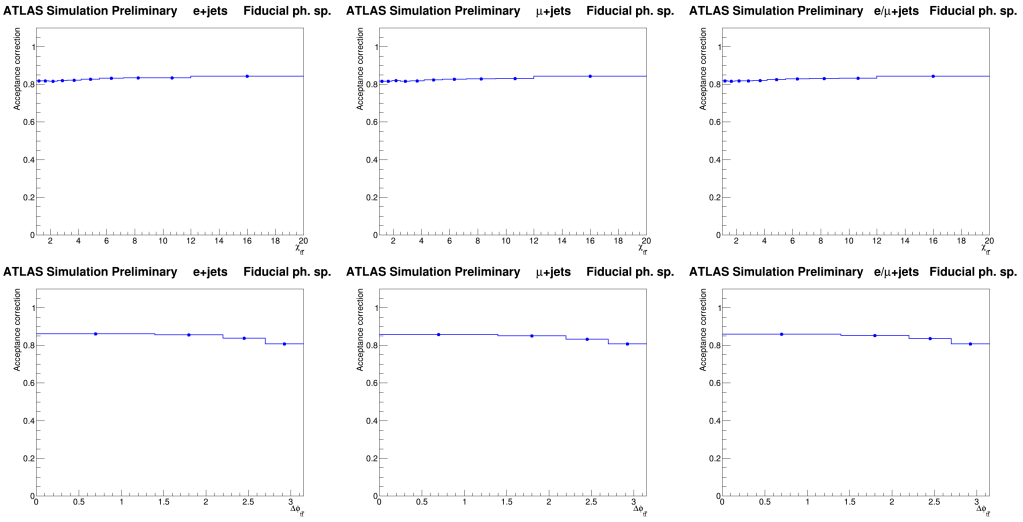

FIGURE C.13: Acceptance corrections for the pseudo-top quark pair $\chi_{t\bar{t}}$ (top) and $\Delta\phi_{t\bar{t}}$ (bottom) in the e+jets (left), μ+jets (middle) and combined ℓ+jets channels in the fiducial phase-space.

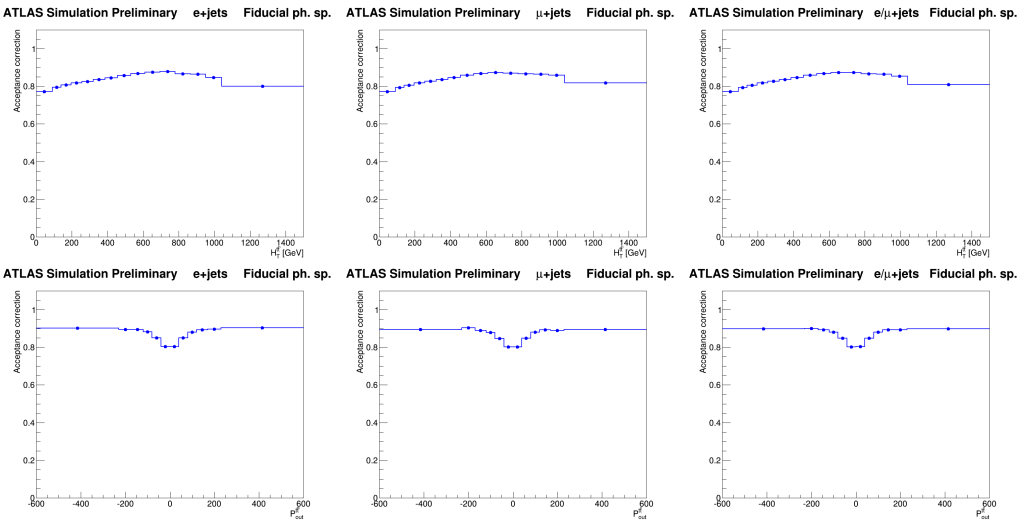

FIGURE C.14: Acceptance corrections for the pseudo-top quark pair $H_T^{t\bar{t}}$ (top) and $P_{out}^{t\bar{t}}$ (bottom) in the e+jets (left), μ+jets (middle) and combined ℓ+jets channels in the fiducial phase-space.

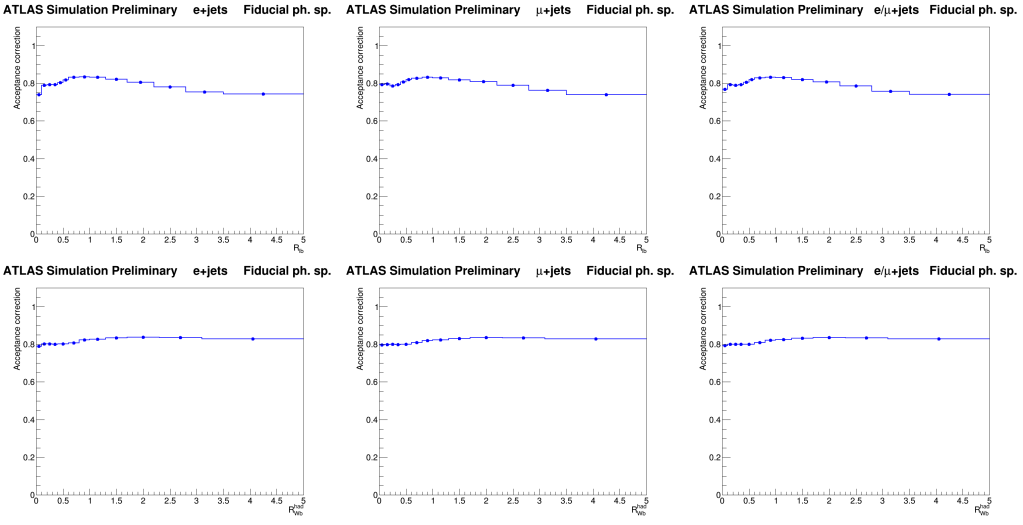

FIGURE C.15: Acceptance corrections for the pseudo-top quark pair R_{lb} (top) and R_{Wb}^{had} (bottom) in the e+jets (left), μ+jets (middle) and combined ℓ+jets channels in the fiducial phase-space.

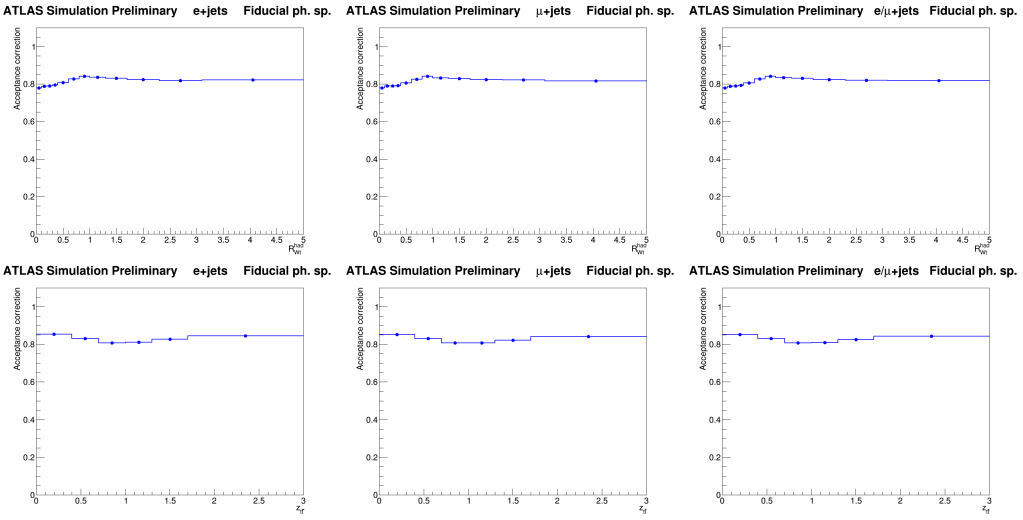

FIGURE C.16: Acceptance corrections for the pseudo-top quark pair R_{Wt}^{had} (top) and $z_{t\bar{t}}$ (bottom) in the e+jets (left), μ+jets (middle) and combined ℓ+jets channels.

C.1.4 Matching correction

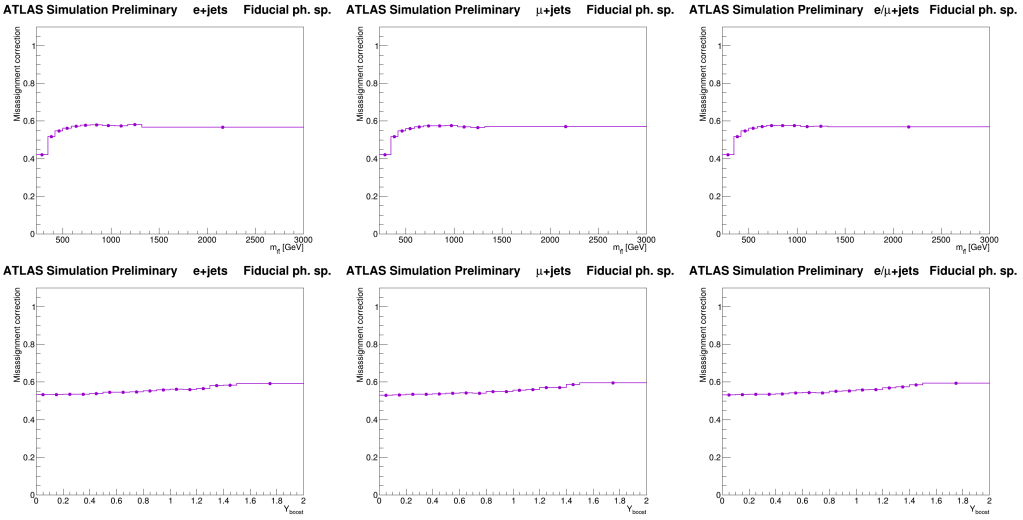

FIGURE C.17: Matching corrections for the top quark pair m (top) and longitudinal boost $Y_{boost}^{t\bar{t}}$ (bottom) in the e+jets (left), μ+jets (middle) and combined ℓ+jets channels.

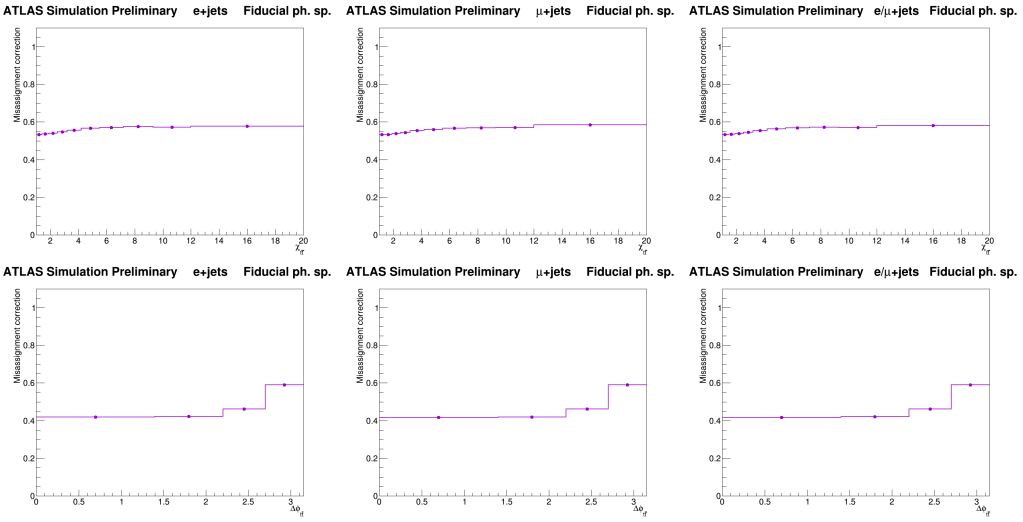

FIGURE C.18: Matching corrections for the pseudo-top quark pair $\chi_{t\bar{t}}$ (top) and $\Delta\phi_{t\bar{t}}$ (bottom) in the e+jets (left), μ+jets (middle) and combined ℓ+jets channels in the fiducial phase-space.

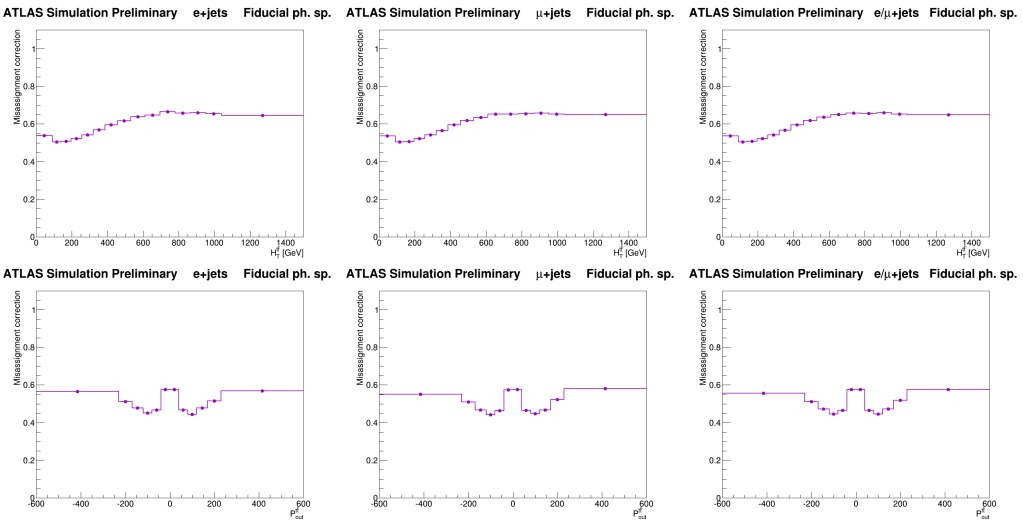

FIGURE C.19: Matching corrections for the pseudo-top quark pair $H_T^{t\bar{t}}$ (top) and $P_{out}^{t\bar{t}}$ (bottom) in the e+jets (left), μ+jets (middle) and combined ℓ+jets channels in the fiducial phase-space.

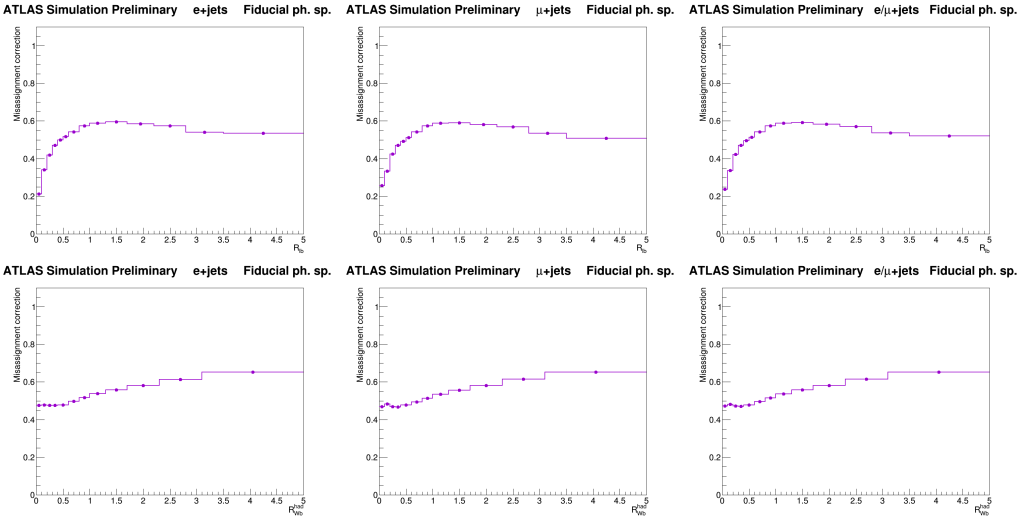

FIGURE C.20: Matching corrections for the pseudo-top quark pair R_{lb} (top) and R_{Wb}^{had} (bottom) in the e+jets (left), μ+jets (middle) and combined ℓ+jets channels in the fiducial phase-space.

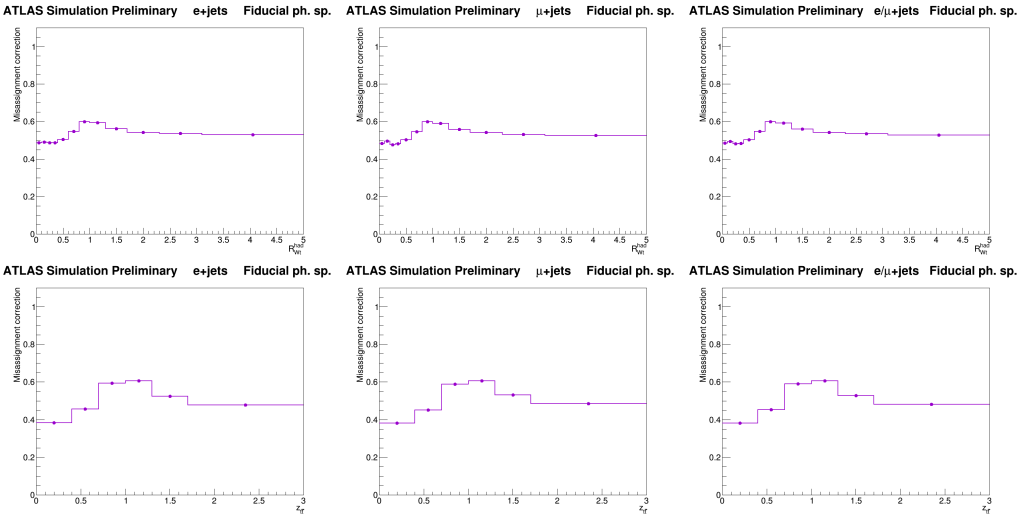

FIGURE C.21: Matching corrections for the pseudo-top quark pair R_{Wt}^{had} (top) and $z_{t\bar{t}}$ (bottom) in the e+jets (left), μ+jets (middle) and combined ℓ+jets channels.

C.2 Full phase-space

C.2.1 Migration matrices

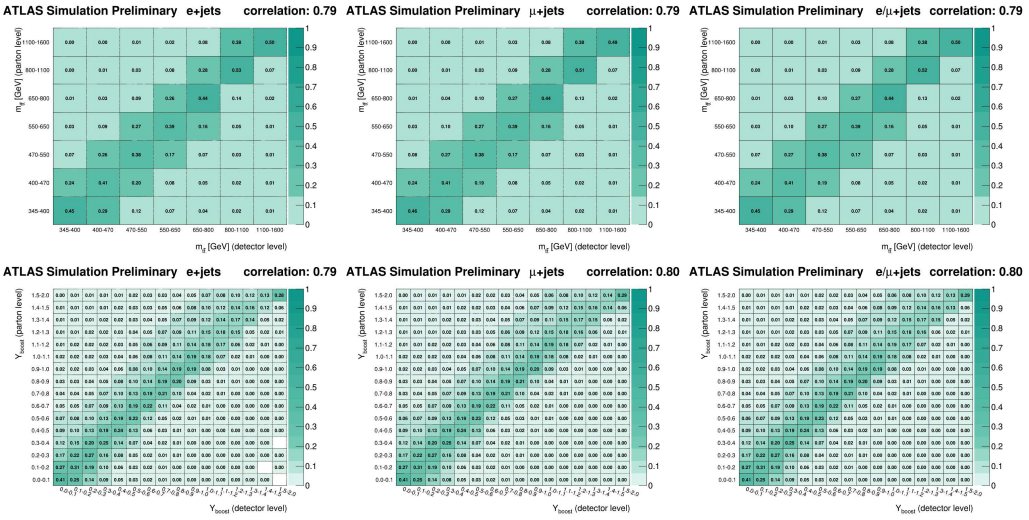

FIGURE C.22: Migration matrix between detector and parton level for the pseudo-top quark pairs $m_{t\bar{t}}$ (top) and longitudinal boost $Y^{t\bar{t}}_{boost}$ (bottom) in the e+jets (left), μ+jets (middle) and combined ℓ+jets channel.

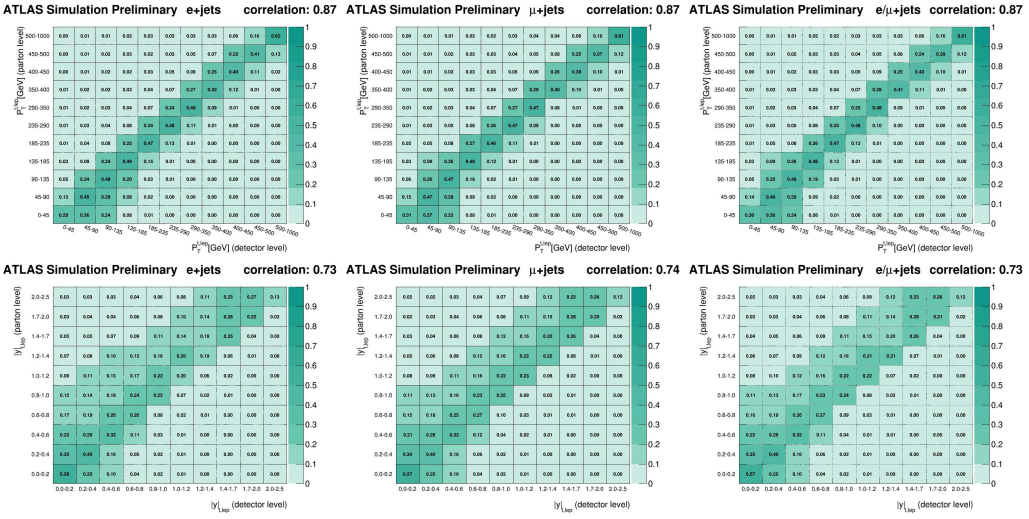

FIGURE C.23: Migration matrix between detector and parton level for the leptonic pseudo-top quark p_T (top) and absolute value of rapidity $|y|$ (bottom) in the e+jets (left), μ+jets (middle) and combined ℓ+jets channel.

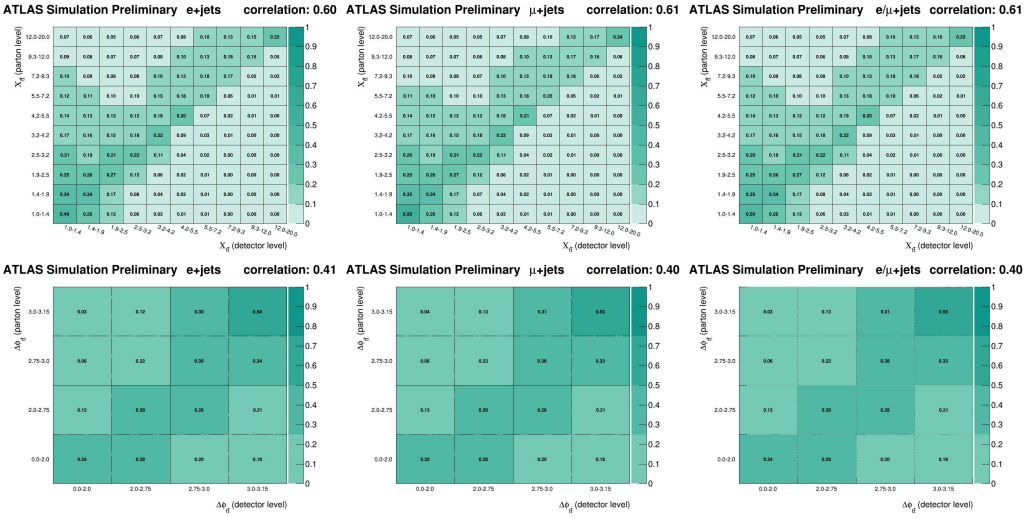

FIGURE C.24: Migration matrix between detector and parton level for the pseudo-top quark pair $\chi_{t\bar{t}}$ (top) and $\Delta\phi_{t\bar{t}}$ (bottom) in the e+jets (left), μ+jets (middle) and combined ℓ+jets channel.

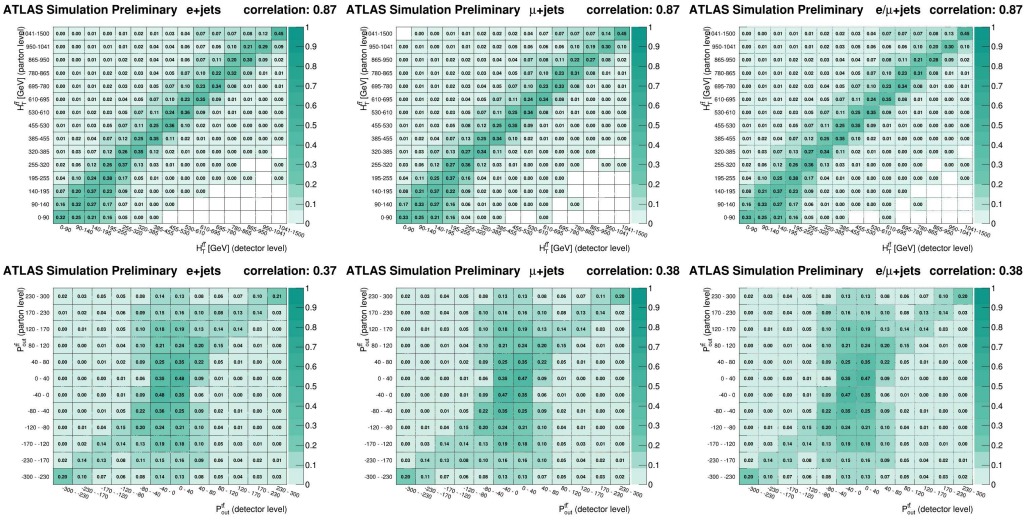

FIGURE C.25: Migration matrix between detector and parton level for the pseudo-top quark pair $H_T^{t\bar{t}}$ (top) and $P_{out}^{t\bar{t}}$(bottom) in the e+jets (left), μ+jets (middle) and combined ℓ+jets channel.

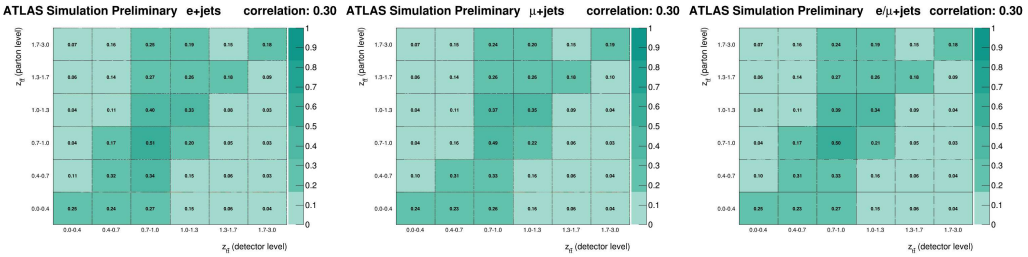

FIGURE C.26: Migration matrix between detector and parton level for the $z_{t\bar{t}}$ in the e+jets (left), μ+jets (middle) and combined ℓ+jets channel.

C.2.2 Efficiency correction

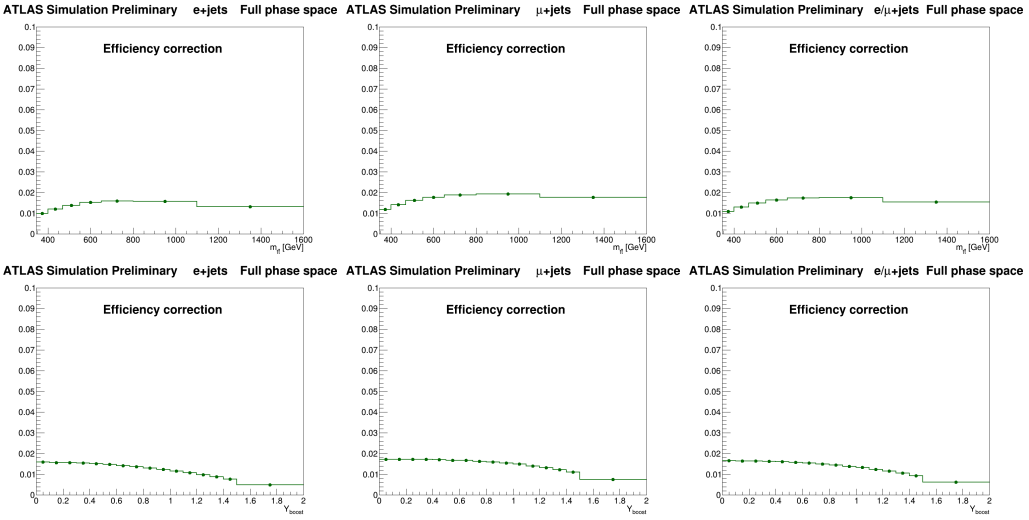

FIGURE C.27: Efficiency corrections for the top quark pair m (top) and longitudinal boost $Y^{t\bar{t}}_{boost}$ (bottom) in the e+jets (left), μ+jets (middle) and combined ℓ+jets channels in the full phase-space.

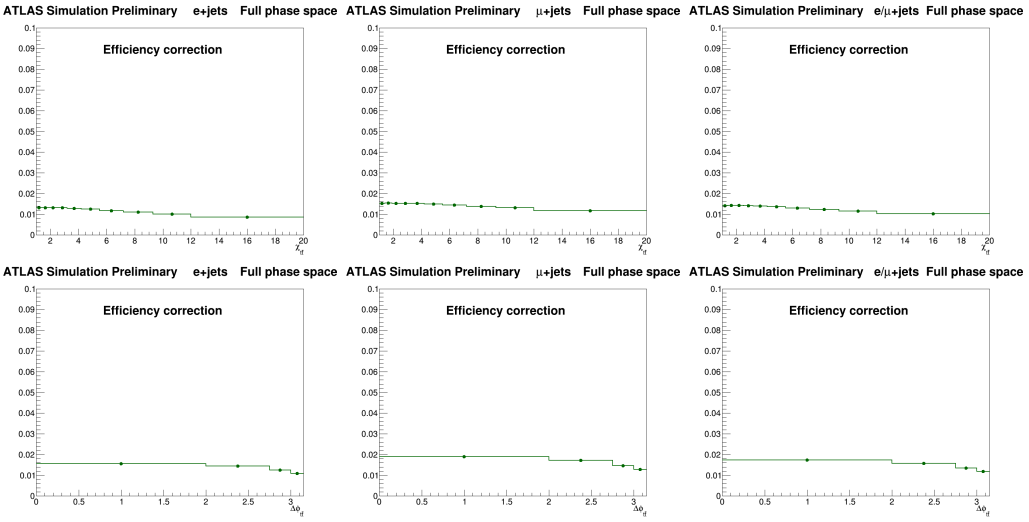

FIGURE C.28: Efficiency corrections for the pseudo-top quark pair $\chi_{t\bar{t}}$ (top) and $\Delta\phi_{t\bar{t}}$ (bottom) in the e+jets (left), μ+jets (middle) and combined ℓ+jets channels in the full phase-space.

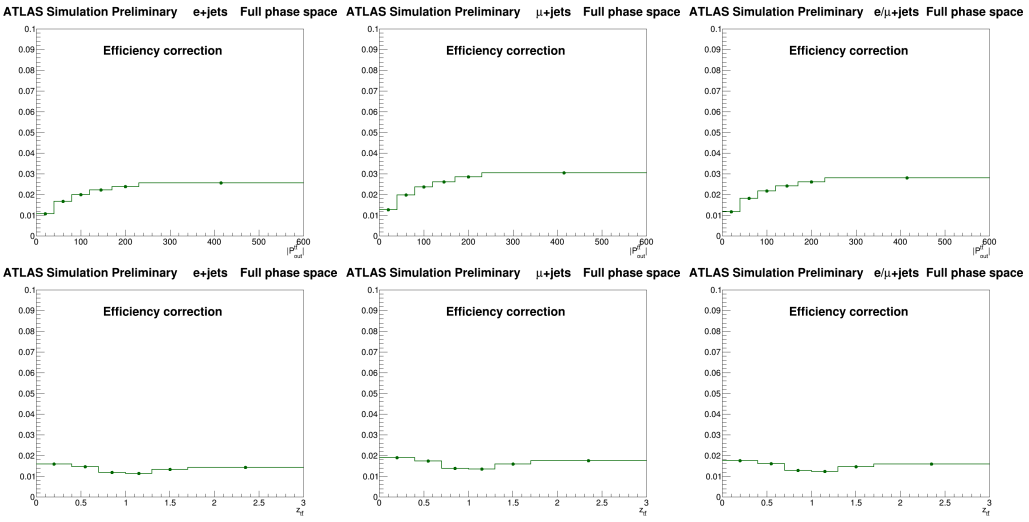

FIGURE C.29: Efficiency corrections for the pseudo-top quark pair $\left|P^{t\bar{t}}_{out}\right|$ (top) and $z_{t\bar{t}}$ (bottom) in the e+jets (left), μ+jets (middle) and combined ℓ+jets channels in the full phase-space.

C.2.3 Acceptance correction

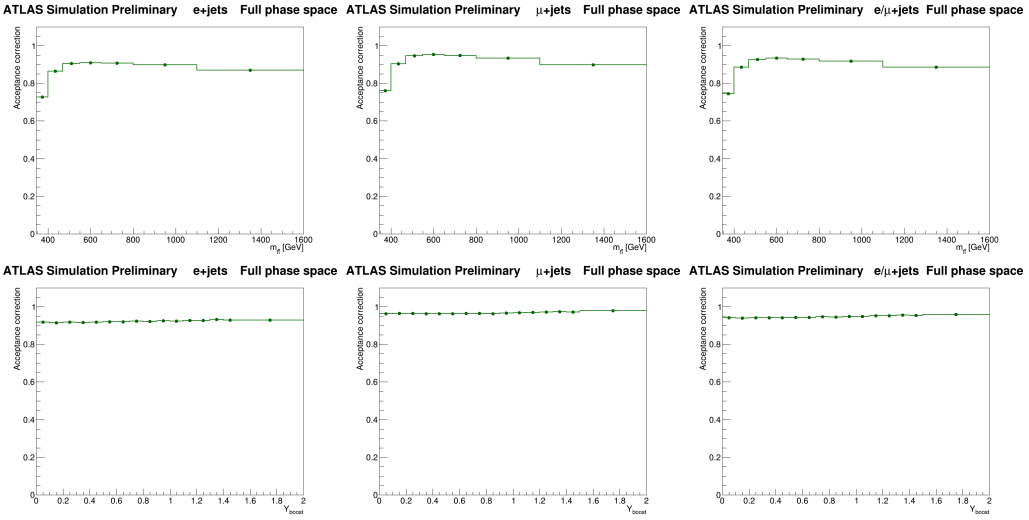

FIGURE C.30: Acceptance corrections for the top quark pair m (top) and longitudinal boost $Y^{t\bar{t}}_{boost}$ (bottom) in the e+jets (left), μ+jets (middle) and combined ℓ+jets channels in the full phase-space.

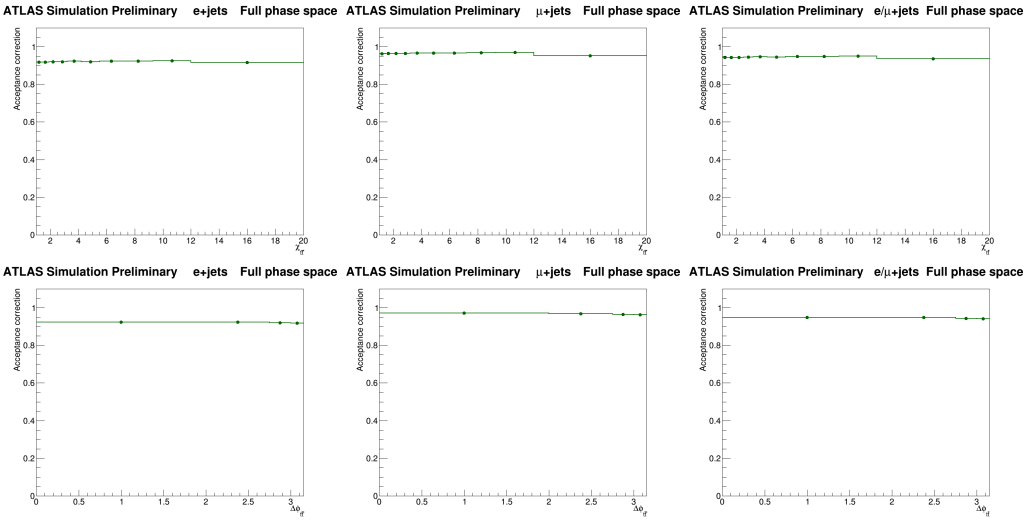

FIGURE C.31: Acceptance corrections for the pseudo-top quark pair $\chi_{t\bar{t}}$ (top) and $\Delta\phi_{t\bar{t}}$ (bottom) in the e+jets (left), μ+jets (middle) and combined ℓ+jets channels in the full phase-space.

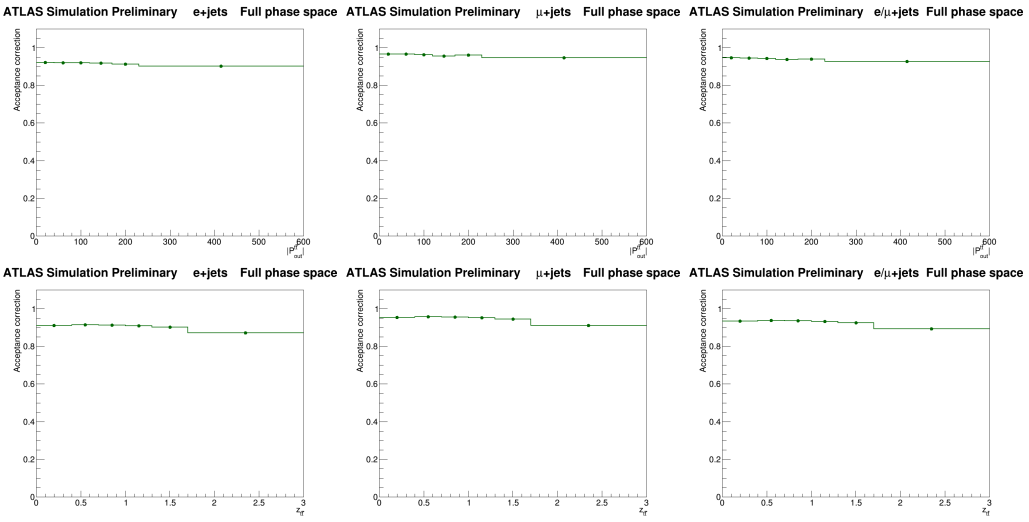

FIGURE C.32: Acceptance corrections for the pseudo-top quark pair $\left|P^{t\bar{t}}_{out}\right|$ (top) and $z_{t\bar{t}}$ (bottom) in the e+jets (left), μ+jets (middle) and combined ℓ+jets channels in the full phase-space.

C.2.4 Dilepton correction

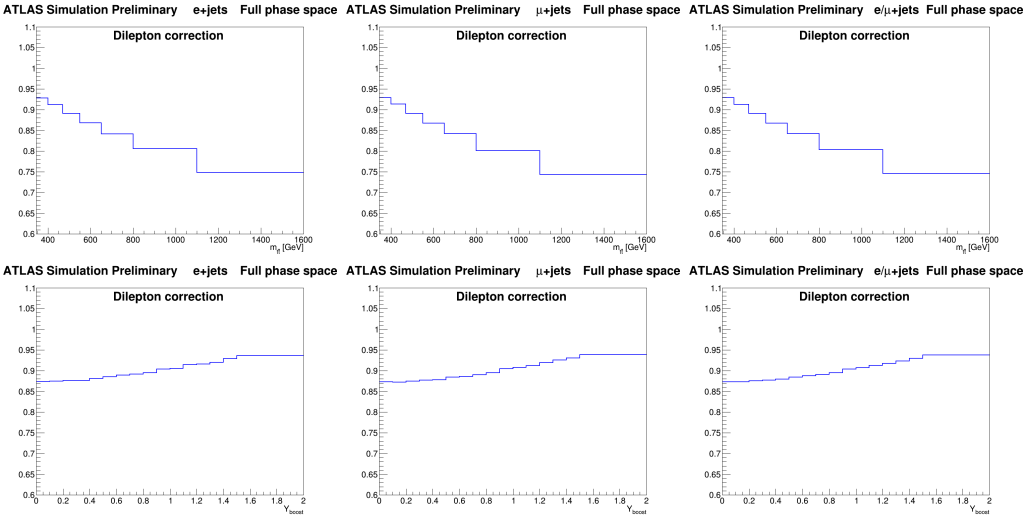

FIGURE C.33: Dilepton corrections for the top quark pair m (top) and longitudinal boost $Y^{t\bar{t}}_{boost}$ (bottom) in the e+jets (left), μ+jets (middle) and combined ℓ+jets channels in the full phase-space.

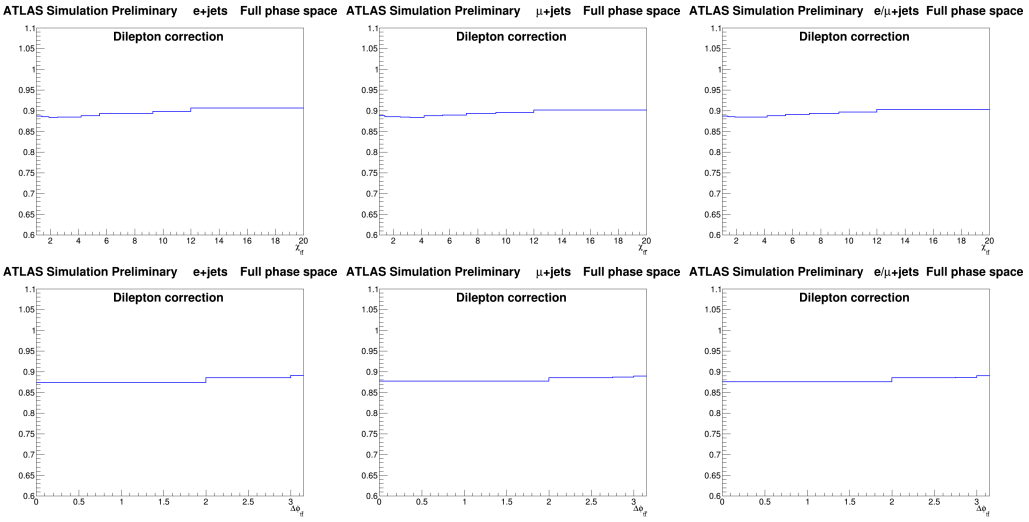

FIGURE C.34: Dilepton corrections for the pseudo-top quark pair $\chi_{t\bar{t}}$ (top) and $\Delta\phi_{t\bar{t}}$ (bottom) in the e+jets (left), μ+jets (middle) and combined ℓ+jets channels in the full phase-space.

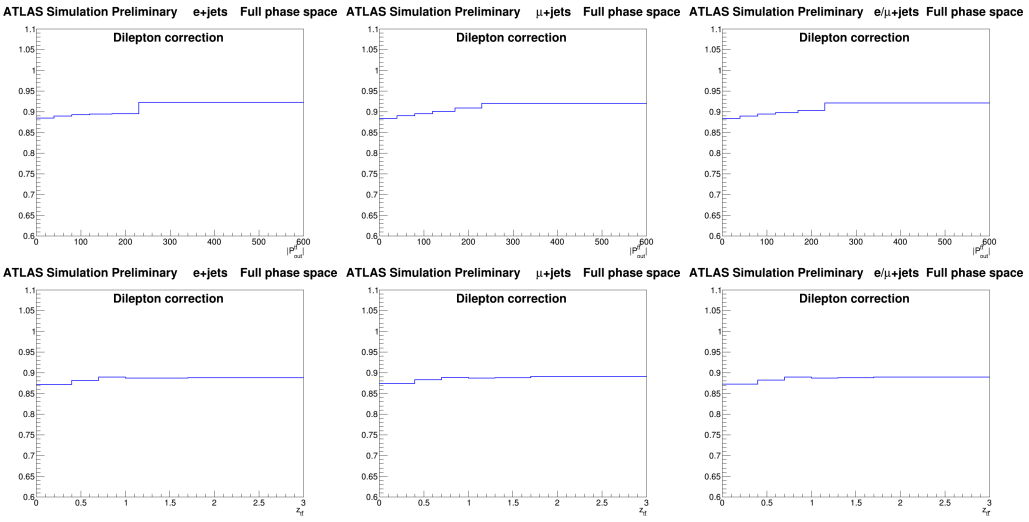

FIGURE C.35: Dilepton corrections for the pseudo-top quark pair $\left|P_{out}^{t\bar{t}}\right|$ (top) and $z_{t\bar{t}}$ (bottom) in the e+jets (left), μ+jets (middle) and combined ℓ+jets channels in the full phase-space.

Appendix D

Uncertainties

D.1 Uncertainties after unfolding

D.1.1 Fractional uncertainties in the fiducial phase-space

D.1.1.1 Graphical form

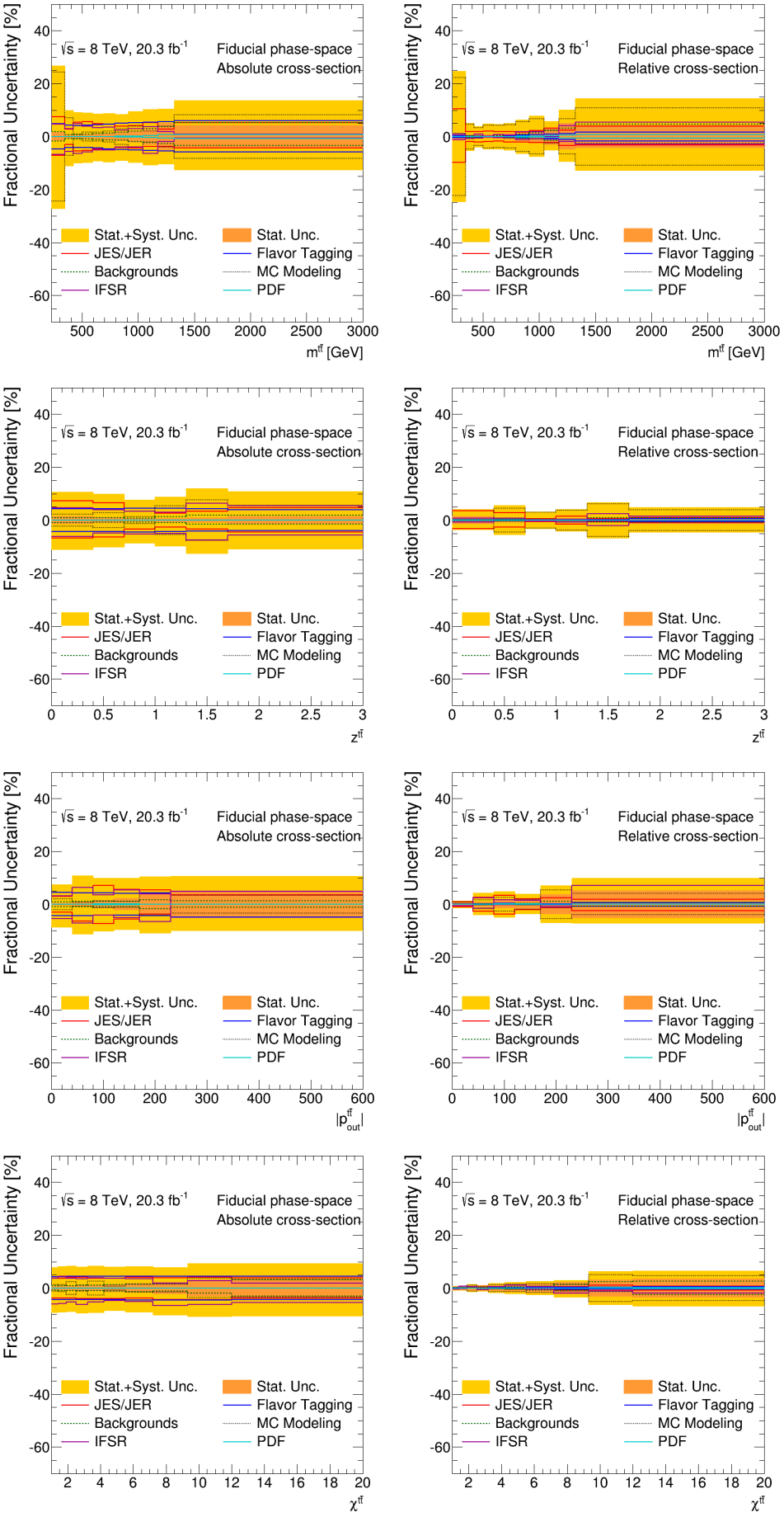

FIGURE D.1: Fractional uncertainties for the absolute (left) and relative (right) differential cross-sections as a function of the mass (first row), $z_{t\bar{t}}$ (second row), $\mid P_{out}^{t\bar{t}} \mid$ (third row) and $\chi_{t\bar{t}}$ (fourth row) of the $t\bar{t}$ system in the fiducial phase-space.

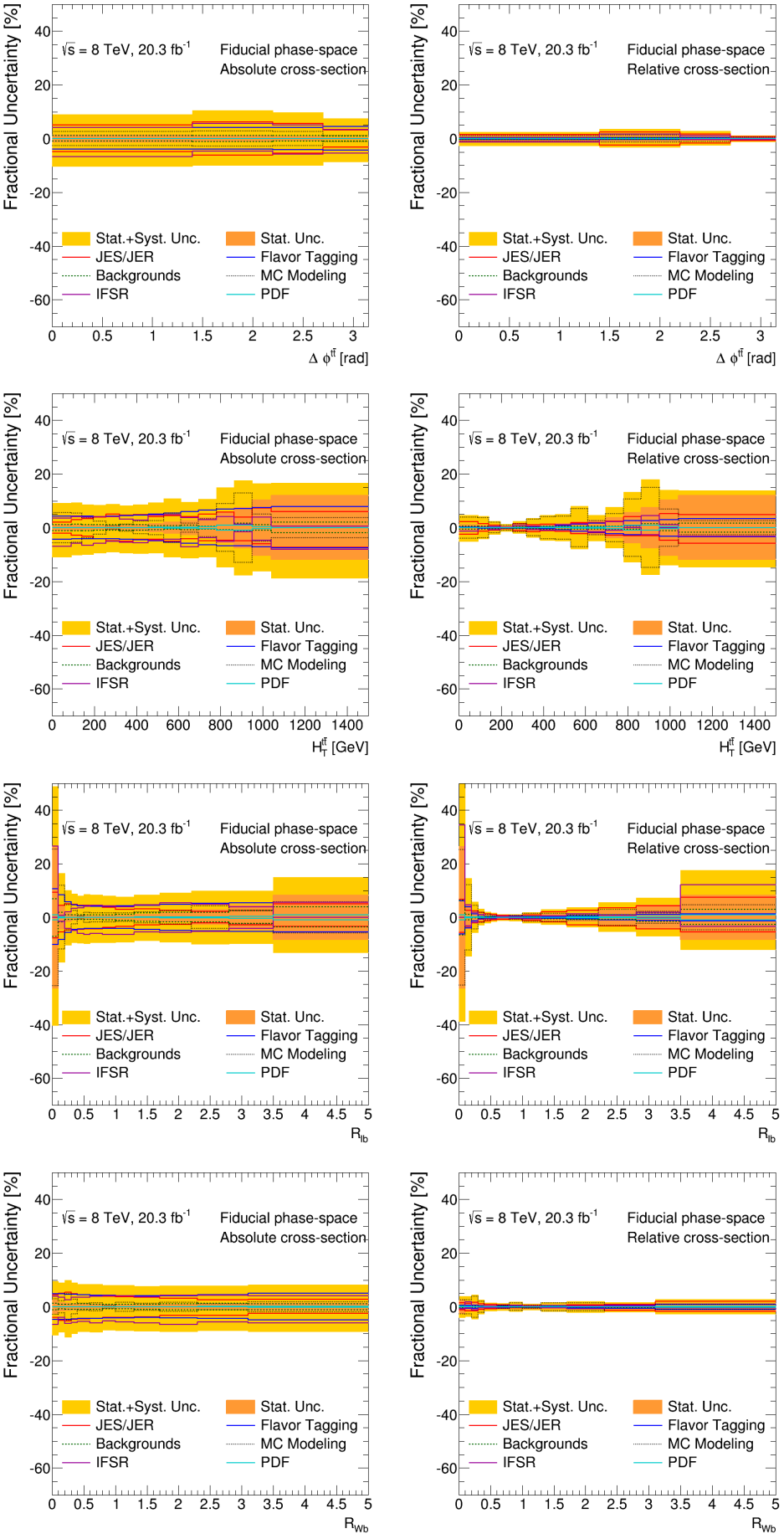

FIGURE D.2: Fractional uncertainties for the absolute (left) and relative (right) differential cross-sections as a function of the $\Delta\phi_{t\bar{t}}$ (first row), $H_{t\bar{t}}$ (second row), R_{lb} (third row) and the R_{Wb} (fourth row) in the fiducial phase-space.

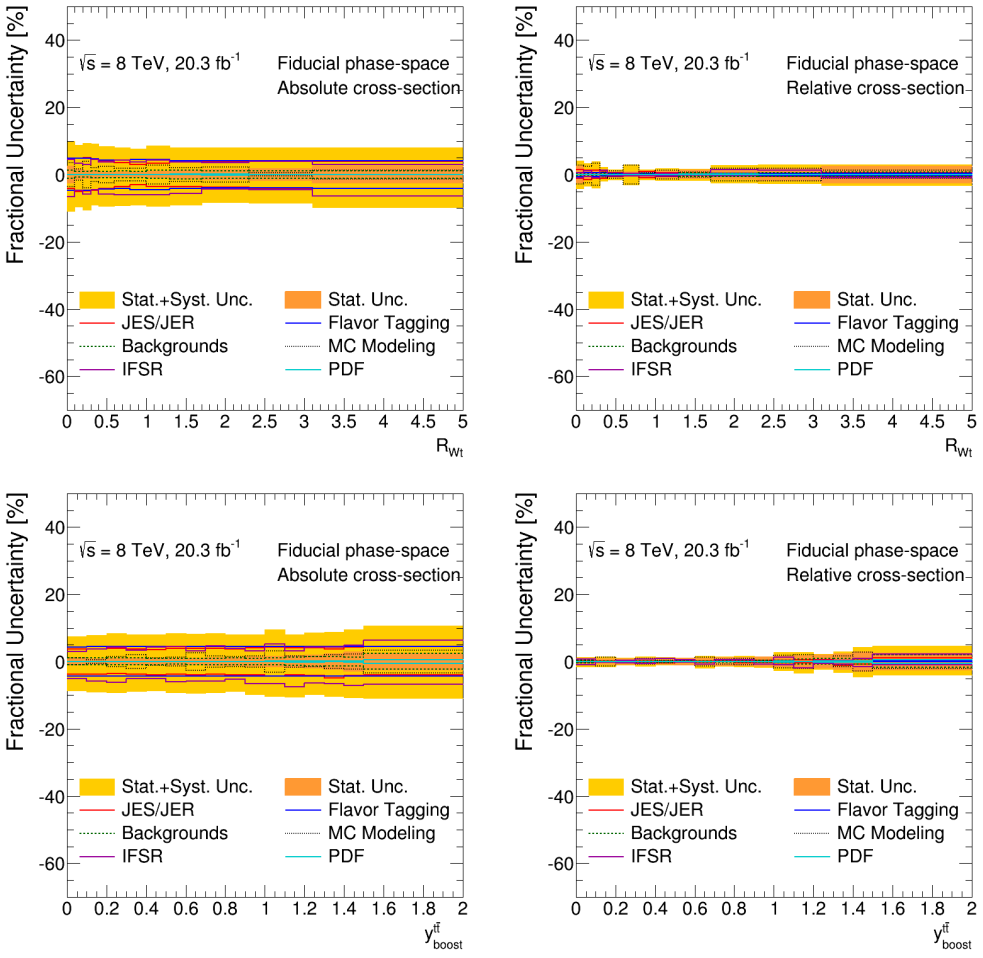

FIGURE D.3: Fractional uncertainties for the absolute (left) and relative (right) differential cross-sections as a function of the R_{Wt} (top) and the $Y^{t\bar{t}}_{boost}$ (bottom) in the fiducial phase-space.

D.1.1.2 Tabular form

Bins [GeV]	0–25	25–50	50–75	75–105	105–135	135–165	165–195	195–230	230–265	265–300	300–350	350–400	400–450	450–500	500–1000
$1/\sigma \cdot \mathrm{d}\sigma$ / d p_T^t	$1.37 \cdot 10^{-3}$	$3.99 \cdot 10^{-3}$	$5.87 \cdot 10^{-3}$	$6.67 \cdot 10^{-3}$	$5.80 \cdot 10^{-3}$	$4.00 \cdot 10^{-3}$	$2.60 \cdot 10^{-3}$	$1.64 \cdot 10^{-3}$	$1.00 \cdot 10^{-3}$	$6.08 \cdot 10^{-4}$	$3.37 \cdot 10^{-4}$	$1.67 \cdot 10^{-4}$	$8.30 \cdot 10^{-5}$	$4.00 \cdot 10^{-5}$	$4.00 \cdot 10^{-6}$
Total Uncertainty [%]	±3.92	±2.46	±3.43	±1.03	±1.33	±1.81	±3.47	±2.28	±3.05	±5.13	±5.97	±5.78	±7.72	±15.9	±13.3
Statistics [%]	±1.7	±0.9	±0.8	±0.6	±0.6	±0.8	±1.0	±1.2	±1.5	±2.0	±2.4	±3.5	±5.3	±8.1	±8.5
Systematics [%]	±3.46	±2.25	±3.33	±0.77	±1.11	±1.59	±3.30	±1.90	±2.57	±4.67	±5.40	±4.46	±5.39	±13.6	±10.0
η intercalibration model (JES) [%]	∓0.10	∓0.22	∓0.16	-	-	±0.22	$^{+0.10}_{-0.16}$	$^{+0.21}_{-0.16}$	±0.12	±0.22	-	±0.21	-	$^{+0.35}_{-}$	-
Single particle high-p_T (JES) [%]	-	-	-	-	-	-	-	-	-	-	-	-	-	-	-
Effective stat. NP set 1 (JES) [%]	$^{+0.17}_{-0.13}$	$^{+0.15}_{-0.10}$	±0.15	-	-	-	$^{-0.20}_{-}$	∓0.27	$^{-0.36}_{+0.51}$	$^{-0.61}_{+0.37}$	∓0.60	∓0.33	∓0.90	∓0.61	$^{-0.22}_{+0.87}$
Effective stat. NP set 2 (JES) [%]	-	-	-	-	-	-	-	-	-	$^{-}_{-0.14}$	±0.12	±0.17	$^{+0.18}_{-0.11}$	$^{+0.25}_{-}$	±0.32
Effective stat. NP set 3 (JES) [%]	±0.31	±0.38	±0.27	±0.12	-	∓0.29	∓0.27	∓0.34	$^{-0.19}_{+0.31}$	$^{-0.37}_{+0.24}$	$^{-0.24}_{+0.15}$	∓0.33	$^{-0.23}_{+0.35}$	$^{+0.36}_{-}$	$^{-}_{+0.36}$
Effective detector NP set 1 (JES) [%]	∓0.45	∓0.52	∓0.46	∓0.32	-	±0.29	±0.31	±0.61	±0.77	±1.23	±1.20	±1.71	±2.46	±2.56	±3.42
Effective detector NP set 2 (JES) [%]	-	-	-	-	-	-	-	-	∓0.11	$^{-0.23}_{+0.14}$	∓0.21	∓0.21	∓0.26	$^{-}_{+0.44}$	∓0.42
Effective detector NP set 3 (JES) [%]	-	-	-	-	-	-	-	-	-	$^{+0.12}_{-0.20}$	-	$^{+0.22}_{-0.30}$	$^{+0.28}_{-0.14}$	$^{+0.17}_{-}$	$^{+0.23}_{-0.10}$
Effective mixed NP set 1 (JES) [%]	∓0.36	∓0.42	∓0.35	∓0.23	-	±0.31	±0.24	±0.44	±0.53	$^{+0.67}_{-0.98}$	$^{+0.73}_{-0.50}$	±1.18	±1.45	±1.51	±1.99
Effective mixed NP set 2 (JES) [%]	-	-	-	-	-	-	-	-	$^{+0.17}_{-}$	$^{-}_{-0.21}$	±0.24	$^{+0.14}_{-}$	±0.36	$^{+0.39}_{-}$	±0.60
Effective model NP set 1 (JES) [%]	$^{-0.43}_{+0.73}$	∓0.58	∓0.35	$^{-0.26}_{+0.15}$	±0.41	±0.66	$^{+0.30}_{-0.19}$	±0.14	-	-	∓0.30	-	$^{-0.75}_{+0.54}$	$^{-}_{-0.32}$	$^{-0.22}_{+0.53}$
Effective model NP set 2 (JES) [%]	-	-	-	-	-	-	-	-	-	±0.21	±0.21	$^{+0.23}_{-0.34}$	±0.75	±0.58	±1.05
Effective model NP set 3 (JES) [%]	±0.33	±0.38	±0.26	±0.14	-	∓0.26	∓0.29	∓0.38	$^{-0.25}_{+0.38}$	$^{-0.46}_{+0.29}$	$^{-0.38}_{+0.29}$	∓0.41	$^{-0.15}_{+0.26}$	$^{-0.20}_{+0.32}$	$^{-}_{+0.40}$
Effective model NP set 4 (JES) [%]	-	-	-	-	-	-	-	$^{+0.16}_{-0.11}$	$^{+0.16}_{-}$	$^{+0.21}_{-0.28}$	±0.18	$^{+0.33}_{-0.48}$	$^{+0.47}_{-0.25}$	±0.36	±0.49
Pile-up offset μ (JES) [%]	-	-	-	-	-	-	-	-	-	-	-	-	$^{+0.23}_{-0.11}$	$^{+0.23}_{-0.11}$	-
Pile-up offset N_{PV} (JES) [%]	-	-	$^{+0.21}_{-}$	-	∓0.13	-	-	-	-	$^{-}_{-0.20}$	$^{+0.11}_{-0.20}$	-	$^{+0.13}_{-0.39}$	$^{-0.19}_{+0.46}$	$^{+0.67}_{-}$
Punch-through (JES) [%]	-	-	-	-	-	-	-	-	-	-	-	-	-	-	-
Pile-up offset ρ topology (JES) [%]	$^{-0.18}_{+0.25}$	∓0.23	$^{-0.10}_{+0.21}$	-	±0.23	±0.36	-	-	$^{-}_{+0.19}$	$^{-}_{-0.24}$	$^{-0.43}_{+0.29}$	-	$^{-1.00}_{+0.71}$	$^{-0.13}_{+0.66}$	$^{-0.24}_{+0.38}$
Pile-up offset p_T (JES) [%]	-	-	-	-	-	-	-	-	-	-	-	-	-	$^{-0.41}_{+0.71}$	-
Flavour composition (JES) [%]	-	-	-	-	$^{+0.18}_{-0.10}$	$^{+0.17}_{-0.27}$	-	∓0.10	$^{-0.29}_{+0.43}$	$^{-0.40}_{+0.17}$	∓0.61	-	$^{-1.54}_{+1.11}$	$^{-0.43}_{+0.22}$	∓0.25
Flavour response (JES) [%]	$^{+0.26}_{-0.16}$	±0.21	$^{+0.20}_{-}$	±0.23	-	∓0.29	-	$^{-0.33}_{+0.23}$	$^{-}_{+0.24}$	$^{-0.48}_{+0.20}$	$^{-0.11}_{+0.26}$	∓0.53	$^{-}_{-0.43}$	$^{-0.16}_{+0.52}$	∓0.51
b-Tagged jet energy scale (JES) [%]	∓0.52	∓0.53	∓0.38	∓0.13	±0.23	±0.35	$^{+0.35}_{-0.24}$	±0.32	$^{+0.31}_{-0.19}$	$^{+0.29}_{-0.39}$	$^{+0.15}_{-0.31}$	±0.53	$^{+0.34}_{-0.56}$	$^{+0.38}_{-}$	±0.54
Jet reconstruction efficiency [%]	-	-	-	-	-	-	-	-	-	-	-	-	-	-	-
Jet energy resolution [%]	-	-	-	-	-	-	-	-	-	-	-	-	-	-	-
b-Quark tagging efficiency [%]	-	∓0.14	∓0.17	∓0.18	∓0.18	-	-	±0.29	±0.62	±1.00	±1.40	±1.84	±2.16	±2.52	±2.69
c-Quark tagging efficiency [%]	-	±0.11	±0.15	±0.10	-	-	∓0.14	∓0.21	∓0.27	∓0.34	∓0.38	∓0.40	∓0.43	∓0.37	∓0.27
Light-jet tagging efficiency [%]	-	-	-	-	-	-	-	-	-	-	-	-	-	-	±0.36
Electron energy scale [%]	-	-	-	-	-	-	-	-	-	-	-	-	-	-	-
Electron energy resolution [%]	-	-	-	-	-	-	-	-	-	-	-	-	-	-	-
Muon momentum scale [%]	-	-	-	-	-	-	-	-	-	-	-	-	-	-	-
Muon (ID) momentum resolution [%]	-	-	-	-	-	-	-	-	-	-	-	-	-	-	-
Muon (MS) momentum resolution [%]	-	-	-	-	-	-	-	-	-	-	-	-	-	-	-
Lepton trigger efficiency [%]	-	-	-	-	-	-	-	-	-	-	-	-	-	-	-
Lepton reconstruction efficiency [%]	-	-	-	-	-	-	-	-	-	-	-	-	-	-	-
Lepton identification efficiency [%]	-	-	-	-	-	-	-	-	-	-	-	-	-	-	-
E_T^{miss} Soft jet scale [%]	-	-	-	-	-	-	-	-	-	-	-	-	-	-	-
E_T^{miss} Soft jet resolution [%]	-	-	-	-	-	-	-	-	-	-	-	-	-	-	-
Jet vertex fraction [%]	∓0.33	∓0.26	$^{-0.29}_{+0.22}$	∓0.14	-	$^{+0.22}_{-0.14}$	$^{+0.32}_{-0.21}$	±0.33	±0.41	±0.51	±0.58	±0.54	$^{+0.75}_{-0.52}$	±0.78	±0.58
Alternate hard-scattering model [%]	∓2.92	∓0.63	∓1.69	±0.28	∓0.57	±0.41	±2.26	±0.49	±1.52	±3.07	±3.79	-	±2.69	±10.5	∓7.00
Alternate parton-shower model [%]	∓1.02	∓1.64	∓2.63	∓0.16	±0.66	±0.90	±2.04	±1.22	±0.88	±2.52	±2.82	±2.20	±1.20	±6.61	∓1.53
Monte Carlo sample statistics [%]	±0.44	±0.23	±0.19	±0.15	±0.17	±0.20	±0.25	±0.30	±0.38	±0.49	±0.57	±0.85	±1.23	±1.81	±1.77
ISR/FSR + scale [%]	$^{-0.66}_{+0.91}$	$^{-0.50}_{+0.14}$	$^{-}_{-0.43}$	$^{-0.26}_{-}$	$^{+0.33}_{-}$	$^{+0.54}_{-}$	$^{-}_{-1.30}$	+0.69	+1.36	+1.26 −0.36	$^{-1.22}_{+0.27}$	$^{+3.10}_{-0.10}$	+0.96 $^{-}$	±3.38	$^{+1.06}_{-6.40}$
Parton distribution functions [%]	-	-	-	-	-	-	-	-	-	-	∓0.22	∓0.56	∓0.74	∓0.88	±0.36
Single top cross-section [%]	-	-	-	-	-	-	-	-	-	-	-	±0.12	±0.23	±0.24	±0.28
W+jets scale factors [%]	±0.15	±0.19	-	-	-	-	-	-	∓0.12	-	-	±0.11	∓0.15	∓0.28	±0.81
Fake lept. MC stat, e+jets ch. [%]	-	$^{-}_{-0.22}$	-	-	-	-	-	-	$^{+0.23}_{-}$	±0.22	$^{+0.31}_{-0.14}$	$^{-}_{-0.25}$	$^{+0.47}_{-0.14}$	$^{+1.08}_{-}$	$^{+0.50}_{-0.19}$
Fake lept. alternate fake CR, e+jets ch. [%]	-	-	-	-	-	-	-	-	∓0.10	∓0.22	∓0.21	∓0.25	∓0.24	±0.15	∓0.24
Fake lept. alternate real CR, e+jets ch. [%]	±0.19	-	-	-	-	-	-	-	-	-	-	-	-	-	-
Fake lept. alternate parametrization, e+jets ch. [%]	-	∓0.10	∓0.21	-	±0.14	-	-	-	-	-	-	∓0.23	∓0.12	±0.35	∓0.30
Fake lept. MC stat, μ+jets ch. [%]	-	-	-	-	-	-	-	-	-	-	-	-	$^{+0.35}_{-}$	-	-
Fake lept. alternate fake CR, μ+jets ch. [%]	±0.12	-	-	-	-	-	∓0.12	∓0.16	-	-	-	∓0.32	-	-	∓0.19
Fake lept. alternate real CR, μ+jets ch. [%]	∓0.33	∓0.22	∓0.19	-	±0.12	±0.15	±0.12	±0.15	±0.39	-	-	-	∓0.28	∓0.32	∓0.81
Fake lept. alternate parametrization, μ+jets ch. [%]	∓0.12	-	-	-	-	-	±0.16	-	±0.22	-	-	-	-	∓0.24	±0.43
Z+jets cross-section [%]	±0.18	±0.17	±0.19	-	-	∓0.18	∓0.14	∓0.22	∓0.22	∓0.30	∓0.22	-	∓0.24	∓0.40	-
Diboson cross-section [%]	-	-	-	-	-	-	-	-	-	-	-	-	-	-	-
Luminosity [%]	-	-	-	-	-	-	-	-	-	-	-	-	-	-	-

TABLE D.1: Fiducial phase-space relative differential cross-sections after combining the e+jets and μ+jets channels for the hadronic top-quark transverse momentum $p_{\mathrm{T}}^{t,\mathrm{had}}$. All uncertainties are quoted as a percentage with respect to the cross-section values in each bin. Dashes are used when the estimated relative systematic uncertainty for that bin is below 0.1%.

Bins [GeV]	0–25	25–50	50–75	75–105	105–135	135–165	165–195	195–230	230–265	265–300	300–350	350–400	400–450	450–500	500–1000.00
$d\sigma$ / d p_T^t [GeV]	$3.99 \cdot 10^{-2}$	$1.16 \cdot 10^{-1}$	$1.70 \cdot 10^{-1}$	$1.93 \cdot 10^{-1}$	$1.68 \cdot 10^{-1}$	$1.16 \cdot 10^{-1}$	$7.54 \cdot 10^{-2}$	$4.77 \cdot 10^{-2}$	$2.90 \cdot 10^{-2}$	$1.76 \cdot 10^{-2}$	$9.77 \cdot 10^{-3}$	$4.86 \cdot 10^{-3}$	$2.40 \cdot 10^{-3}$	$1.17 \cdot 10^{-3}$	$1.21 \cdot 10^{-4}$
Total Uncertainty [%]	±9.99	±9.04	±9.54	±8.45	±8.70	±9.00	±8.44	±8.54	±8.78	±9.16	±10.2	±9.96	±11.2	±16.6	±16.0
Statistics [%]	±1.8	±1.0	±0.8	±0.6	±0.7	±0.8	±1.0	±1.2	±1.6	±2.0	±2.4	±3.5	±5.4	±8.2	±8.5
Systematics [%]	±9.85	±8.98	±9.52	±8.41	±8.66	±8.96	±8.37	±8.45	±8.62	±8.91	±9.91	±9.27	±9.71	±14.2	±13.4
η intercalibration model (JES) [%]	±0.30	±0.18	±0.23	±0.30	±0.46	±0.62	±0.54	±0.59	±0.53	±0.62	±0.48	±0.61	+0.31 −0.51	+0.76 −0.44	+0.37 −0.58
Single particle high-p_T (JES) [%]	-	-	-	-	-	-	-	-	-	-	-	-	-	-	-
Effective stat. NP set 1 (JES) [%]	±1.05	±1.02	±1.05	±0.98	±0.97	±0.91	±0.75	±0.61	+0.54 −0.38	+0.28 −0.52	±0.29	±0.55	-	±0.29	+0.67 -
Effective stat. NP set 2 (JES) [%]	−0.14 +0.19	∓0.12	∓0.12	-	-	-	-	-	-	-	-	-	-	-	±0.24
Effective stat. NP set 3 (JES) [%]	±0.29	±0.36	±0.24	±0.11	∓0.10	∓0.32	∓0.29	∓0.36	−0.21 +0.34	−0.40 +0.26	−0.26 +0.17	∓0.34	−0.25 +0.37	+0.39 -	−0.12 +0.39
Effective detector NP set 1 (JES) [%]	∓0.26	∓0.33	∓0.29	∓0.14	±0.14	±0.47	±0.49	±0.79	±0.96	±1.42	±1.38	±1.89	±2.64	±2.74	±3.59
Effective detector NP set 2 (JES) [%]	+0.26 −0.19	±0.20	±0.21	±0.20	±0.21	±0.20	±0.15	±0.11	-	-	-	-	-	+0.26 -	∓0.24
Effective detector NP set 3 (JES) [%]	-	-	-	-	-	-	-	±0.10	-	+0.16 −0.23	±0.12	+0.25 −0.33	+0.31 −0.17	+0.21 -	+0.26 −0.13
Effective mixed NP set 1 (JES) [%]	-	- +0.15	-	-	±0.31	±0.60	±0.53	±0.74	±0.82	±1.12	+1.04 −0.79	±1.47	±1.74	±1.81	±2.21
Effective mixed NP set 2 (JES) [%]	∓0.44	∓0.42	∓0.41	∓0.39	∓0.42	∓0.43	∓0.31	∓0.29	−0.19 +0.29	−0.32 +0.17	∓0.13	−0.22 +0.33	-	+0.32 -	+0.26 −0.17
Effective model NP set 1 (JES) [%]	±1.70	±1.69	±1.92	±2.06	±2.69	±2.94	±2.53	±2.42	±2.32	±2.30	±1.97	±2.33	±1.62	±2.38	±1.90
Effective model NP set 2 (JES) [%]	- +0.14	-	−0.12 -	- +0.12	∓0.10	-	-	-	-	±0.14	+0.17 −0.12	+0.16 −0.27	±0.69	+0.58 −0.44	±0.98
Effective model NP set 3 (JES) [%]	±0.46	±0.51	±0.40	±0.28	-	∓0.12	−0.17 +0.12	∓0.24	−0.11 +0.24	−0.32 +0.16	−0.24 +0.15	∓0.27	-	- +0.19	+0.27 -
Effective model NP set 4 (JES) [%]	-	-	-	-	-	-	-	+0.18 −0.13	+0.19 -	+0.23 −0.30	±0.21	+0.36 −0.50	+0.49 −0.27	±0.39	±0.52
Pile-up offset μ (JES) [%]	−0.15 +0.36	∓0.17	−0.11 +0.15	∓0.16	∓0.20	∓0.20	∓0.21	- −0.13 +0.17	- +0.23	- −0.24	∓0.17	-	-	-	-
Pile-up offset N_{PV} (JES) [%]	∓0.61	∓0.53	−0.38 +0.61	∓0.55	∓0.74	∓0.70	∓0.62	∓0.66	−0.49 +0.74	−0.65 +0.42	∓0.45	∓0.60	−0.46 +0.22	−0.78 +1.08	+1.03 -
Punch-through (JES) [%]	-	-	-	-	-	-	-	-	-	-	-	-	-	-	- −0.24
Pile-up offset ρ topology (JES) [%]	±1.48	±1.47	±1.54	±1.60	±1.93	±2.06	±1.77	±1.73	±1.56	±1.59	±1.33	±1.73	+0.69 −0.97	+1.57 −1.03	±1.39
Pile-up offset p_T (JES) [%]	-	-	-	-	-	-	-	-	-	-	-	-	-	−0.41 +0.71	-
Flavour composition (JES) [%]	±1.94	±1.90	±1.96	±1.79	±2.02	±2.10	±1.80	±1.77	±1.52	±1.59	±1.27	±1.63	+0.30 −0.78	±1.54	±1.62
Flavour response (JES) [%]	∓0.95	∓0.96	∓1.03	∓0.93	∓1.23	∓1.46	∓1.26	∓1.45	∓1.34	∓1.50	∓1.35	∓1.70	−1.60 +0.95	∓1.51	∓1.67
b-Tagged jet energy scale (JES) [%]	-	-	±0.12	±0.38	±0.73	±0.86	±0.80	±0.83	±0.76	±0.85	±0.74	±1.04	±0.96	+0.89 −0.60	±1.06
Jet reconstruction efficiency [%]	-	-	-	-	-	-	-	-	-	-	-	-	-	-	-
Jet energy resolution [%]	-	-	-	-	-	-	-	-	-	-	-	-	-	-	-
b-Quark tagging efficiency [%]	±4.12	±4.08	±4.05	±4.04	±4.04	±4.14	±4.28	±4.52	±4.86	±5.22	±5.62	±6.07	±6.38	±6.74	±6.92
c-Quark tagging efficiency [%]	±1.02	±1.06	±1.09	±1.04	±0.96	±0.88	±0.80	±0.72	±0.67	±0.59	±0.55	±0.54	±0.50	±0.56	±0.67
Light-jet tagging efficiency [%]	±0.59	±0.55	±0.56	±0.53	±0.49	±0.51	±0.49	±0.45	±0.47	±0.42	±0.42	±0.49	±0.49	±0.54	±0.89
Electron energy scale [%]	+0.12 −0.22	+0.11 −0.21	- −0.16	- −0.15	-	-	-	-	-	-	-	-	-	-	-
Electron energy resolution [%]	-	-	-	-	-	-	-	-	-	-	-	-	-	-	-
Muon momentum scale [%]	-	-	-	-	-	-	-	-	-	-	-	-	-	-	-
Muon (ID) momentum resolution [%]	-	-	-	-	-	-	-	-	-	-	-	-	-	-	-
Muon (MS) momentum resolution [%]	-	-	-	-	-	-	-	-	-	-	-	-	-	-	-
Lepton trigger efficiency [%]	±1.30	±1.30	±1.28	±1.27	±1.26	±1.25	±1.24	±1.24	±1.24	±1.24	±1.24	±1.23	±1.24	±1.23	±1.25
Lepton reconstruction efficiency [%]	±0.22	±0.22	±0.23	±0.23	±0.24	±0.25	±0.26	±0.26	±0.27	±0.28	±0.28	±0.29	±0.29	±0.29	±0.29
Lepton identification efficiency [%]	±1.28	±1.27	±1.28	±1.30	±1.31	±1.33	±1.35	±1.36	±1.38	±1.38	±1.38	±1.39	±1.39	±1.38	±1.35
E_T^{miss} Soft jet scale [%]	-	-	-	-	-	-	-	-	-	-	-	-	-	-	-
E_T^{miss} Soft jet resolution [%]	-	-	-	-	-	-	-	-	-	-	-	-	-	-	-
Jet vertex fraction [%]	∓1.00	∓0.93	∓0.92	∓0.80	∓0.68	∓0.47	∓0.39	∓0.32	−0.32 +0.17	−0.19 +0.11	-	−0.15 -	-	+0.15 -	-
Alternate hard-scattering model [%]	∓4.12	∓1.86	∓2.91	∓0.96	∓1.80	∓0.82	±1.00	∓0.75	±0.26	±1.80	±2.50	∓1.14	±1.42	±9.17	∓8.15
Alternate parton-shower model [%]	∓2.05	∓2.67	∓3.65	∓1.20	∓0.38	∓0.15	±0.97	±0.16	∓0.17	±1.45	±1.74	±1.13	±0.15	±5.50	∓2.56
Monte Carlo sample statistics [%]	±0.45	±0.24	±0.20	±0.16	±0.18	±0.21	±0.26	±0.30	±0.39	±0.49	±0.57	±0.85	±1.23	±1.81	±1.78
ISR/FSR + scale [%]	−6.34 +4.80	−6.19 +4.00	−6.12 +3.57	−5.96 +3.90	−5.40 +3.90	∓5.05	−5.77 +2.49	−5.06 +3.77	∓4.70	−4.52 +3.47	−6.87 +4.14	−2.78 +3.74	∓4.54	−2.68 +0.17	- −4.71
Parton distribution functions [%]	-	-	-	-	-	-	-	-	-	-	∓0.20	∓0.54	∓0.72	∓0.86	±0.38
Single top cross-section [%]	±0.28	±0.26	±0.26	±0.24	±0.26	±0.24	±0.27	±0.30	±0.29	±0.33	±0.33	±0.39	±0.49	±0.52	±0.55
W+jets scale factors [%]	±0.55	±0.60	±0.46	±0.39	±0.35	±0.34	±0.31	±0.31	±0.27	±0.37	±0.47	±0.51	±0.25	±0.11	±1.22
Fake lept. MC stat, e+jets ch. [%]	+0.52 -	∓0.21	- +0.31	−0.12 +0.43	+0.40 -	+0.58 -	+0.53 -	+0.42 -	+0.32 -	+0.26 -	+0.34 -	-	+0.49 -	+1.10 -	+0.53 -
Fake lept. alternate fake CR, e+jets ch. [%]	±0.30	±0.34	±0.37	±0.38	±0.35	±0.43	±0.41	±0.32	±0.25	±0.13	±0.13	±0.10	±0.11	±0.51	±0.11
Fake lept. alternate real CR, e+jets ch. [%]	±0.15	-	-	-	-	-	-	-	-	-	-	-	-	-	-
Fake lept. alternate parametrization, e+jets ch. [%]	±0.29	±0.18	-	±0.34	±0.43	±0.36	±0.37	±0.24	±0.25	±0.20	±0.21	-	±0.16	±0.64	-
Fake lept. MC stat, μ+jets ch. [%]	-	-	-	-	-	-	-	-	+0.24 -	-	-	-	+0.40 -	-	-
Fake lept. alternate fake CR, μ+jets ch. [%]	±0.35	±0.29	±0.31	±0.31	±0.19	±0.18	±0.11	-	±0.24	±0.17	±0.17	-	±0.25	±0.20	-
Fake lept. alternate real CR, μ+jets ch. [%]	∓0.12	-	-	±0.19	±0.34	±0.36	±0.34	±0.37	±0.61	±0.22	±0.12	±0.11	-	∓0.11	∓0.60
Fake lept. alternate parametrization, μ+jets ch. [%]	±0.10	±0.19	±0.15	±0.17	±0.22	±0.31	±0.40	±0.25	±0.46	±0.28	±0.25	±0.29	±0.26	-	±0.66
Z+jets cross-section [%]	±0.69	±0.68	±0.70	±0.59	±0.47	±0.32	±0.36	±0.28	±0.28	±0.19	±0.27	±0.44	±0.25	-	±0.49
Diboson cross-section [%]	-	-	-	-	-	-	-	-	-	-	-	-	-	-	-
Luminosity [%]	±2.80	±2.80	±2.80	±2.80	±2.80	±2.80	±2.80	±2.80	±2.80	±2.80	±2.80	±2.80	±2.80	±2.80	±2.80

TABLE D.2: Fiducial phase-space absolute differential cross-sections after combining the e+jets and μ+jets channels for the hadronic top-quark transverse momentum $p_{\mathrm{T}}^{t,\mathrm{had}}$. All uncertainties are quoted as a percentage with respect to the cross-section values in each bin. Dashes are used when the estimated relative systematic uncertainty for that bin is below 0.1%.

Bins [Unit $\|y^t\|$]	0–0.10	0.10–0.20	0.20–0.30	0.30–0.40	0.40–0.50	0.50–0.60	0.60–0.70	0.70–0.80	0.80–0.90	0.90–1	1–1.10	1.10–1.20	1.20–1.30	1.30–1.40	1.40–1.50	1.50–1.70	1.70–1.90	1.90–2.50
$1/\sigma \cdot \mathrm{d}\sigma \,/\, \mathrm{d}\,\|y^t\|$	$8.28 \cdot 10^{-1}$	$8.21 \cdot 10^{-1}$	$8.07 \cdot 10^{-1}$	$7.86 \cdot 10^{-1}$	$7.58 \cdot 10^{-1}$	$7.25 \cdot 10^{-1}$	$6.88 \cdot 10^{-1}$	$6.47 \cdot 10^{-1}$	$5.98 \cdot 10^{-1}$	$5.51 \cdot 10^{-1}$	$5.00 \cdot 10^{-1}$	$4.48 \cdot 10^{-1}$	$3.95 \cdot 10^{-1}$	$3.41 \cdot 10^{-1}$	$2.86 \cdot 10^{-1}$	$2.12 \cdot 10^{-1}$	$1.24 \cdot 10^{-1}$	$2.49 \cdot 10^{-2}$
Total Uncertainty [%]	±1.37	±1.39	±1.35	±1.93	±1.73	±1.95	±1.91	±1.69	±2.74	±2.21	±1.89	±2.19	±1.81	±2.76	$^{+3.00}_{-2.21}$	±2.01	±3.00	±3.76
Statistics [%]	±0.9	±1.0	±1.0	±1.0	±1.0	±1.1	±1.1	±1.1	±1.2	±1.3	±1.4	±1.4	±1.6	±1.7	±1.9	±1.4	±2.0	±2.5
Systematics [%]	±0.93	±0.87	±0.80	±1.60	±1.32	±1.56	±1.50	±1.15	±2.41	±1.75	±1.22	±1.54	$^{+0.98}_{-0.43}$	±2.12	$^{+2.24}_{-0.96}$	±1.31	±2.15	±2.71
η intercalibration model (JES) [%]	$^{-0.42}_{+0.31}$	∓0.32	∓0.28	∓0.30	$^{-0.21}_{+0.29}$	∓0.17	-	-	-	-	±0.23	±0.31	±0.30	±0.54	±0.57	±0.80	±0.94	±1.18
Single particle high-p_T (JES) [%]	-	-	-	-	-	-	-	-	-	-	-	-	-	-	-	-	-	-
Effective stat. NP set 1 (JES) [%]	-	-	-	-	-	-	-	-	-	-	-	-	-	-	-	-	-	-
Effective stat. NP set 2 (JES) [%]	-	-	-	-	-	-	-	-	-	-	-	-	-	-	-	-	-	-
Effective stat. NP set 3 (JES) [%]	-	-	-	-	-	-	-	-	-	-	-	-	-	-	-	-	-	-
Effective detector NP set 1 (JES) [%]	-	-	-	-	-	-	-	-	-	-	-	-	-	-	-	-	-	-
Effective detector NP set 2 (JES) [%]	-	-	-	-	-	-	-	-	-	-	-	-	-	-	-	-	-	-
Effective detector NP set 3 (JES) [%]	-	-	-	-	-	-	-	-	-	-	-	-	-	-	-	-	-	-
Effective mixed NP set 1 (JES) [%]	-	-	-	-	-	-	-	-	-	-	-	-	-	-	-	-	-	-
Effective mixed NP set 2 (JES) [%]	-	-	-	-	-	-	-	-	-	-	-	-	-	-	-	-	-	-
Effective model NP set 1 (JES) [%]	$^{-0.19}_{+0.13}$	-	-	-	-	-	-	-	-	-	-	-	$^{+0.22}_{-}$	$^{-}_{-0.21}$	-	$^{-}_{-0.21}$	$^{+0.24}_{-0.18}$	-
Effective model NP set 2 (JES) [%]	-	-	-	-	-	-	-	-	-	-	-	-	-	-	-	-	-	-
Effective model NP set 3 (JES) [%]	-	-	-	-	-	-	-	-	-	-	-	-	-	-	-	-	-	-
Effective model NP set 4 (JES) [%]	-	-	-	-	-	-	-	-	-	-	-	-	-	-	-	-	-	-
Pile-up offset μ (JES) [%]	-	-	-	-	-	-	-	-	-	-	-	-	-	∓0.11	$^{-0.15}_{-}$	∓0.21	$^{-0.29}_{+0.22}$	∓0.52
Pile-up offset N_{PV} (JES) [%]	-	-	-	-	-	-	-	-	-	-	-	-	-	-	-	-	-	-
Punch-through (JES) [%]	-	-	-	-	-	-	-	-	-	-	-	-	-	-	-	-	-	-
Pile-up offset ρ topology (JES) [%]	∓0.12	-	-	-	∓0.11	-	-	-	-	-	-	-	-	$^{-}_{-0.23}$	-	±0.17	$^{+0.15}_{-0.20}$	-
Pile-up offset p_T (JES) [%]	-	-	-	-	-	-	-	-	-	-	-	-	-	-	-	-	-	-
Flavour composition (JES) [%]	$^{-0.28}_{+0.16}$	∓0.20	∓0.17	-	∓0.11	-	-	-	-	-	$^{+0.35}_{-0.11}$	-	±0.21	$^{+0.22}_{-0.30}$	±0.20	±0.32	-	-
Flavour response (JES) [%]	$^{+0.10}_{-0.16}$	-	±0.15	-	$^{-}_{+0.16}$	-	-	-	-	-	$^{-}_{+0.20}$	-	$^{-}_{+0.13}$	$^{-}_{-0.22}$	-	∓0.25	∓0.26	$^{+0.27}_{-}$
b-Tagged jet energy scale (JES) [%]	-	-	-	-	-	-	-	-	-	-	-	-	-	-	-	-	-	-
Jet reconstruction efficiency [%]	-	-	-	-	-	-	-	-	-	-	-	-	-	-	-	-	-	-
Jet energy resolution [%]	-	-	-	-	-	-	-	-	-	-	-	-	-	-	-	-	-	-
b-Quark tagging efficiency [%]	-	-	-	-	-	-	-	-	-	-	-	-	-	-	-	-	±0.11	±0.14
c-Quark tagging efficiency [%]	-	-	-	-	-	-	-	-	-	-	-	-	-	-	-	∓0.11	∓0.13	∓0.16
Light-jet tagging efficiency [%]	-	-	-	-	-	-	-	-	-	-	-	-	-	-	-	-	-	±0.20
Electron energy scale [%]	-	-	-	-	-	-	-	-	-	-	-	-	-	-	-	-	-	-
Electron energy resolution [%]	-	-	-	-	-	-	-	-	-	-	-	-	-	-	-	-	-	-
Muon momentum scale [%]	-	-	-	-	-	-	-	-	-	-	-	-	-	-	-	-	-	-
Muon (ID) momentum resolution [%]	-	-	-	-	-	-	-	-	-	-	-	-	-	-	-	-	-	-
Muon (MS) momentum resolution [%]	-	-	-	-	-	-	-	-	-	-	-	-	-	-	-	-	-	-
Lepton trigger efficiency [%]	-	-	-	-	-	-	-	-	-	-	-	-	-	-	-	-	-	-
Lepton reconstruction efficiency [%]	-	-	-	-	-	-	-	-	-	-	-	-	-	-	-	-	-	-
Lepton identification efficiency [%]	-	-	-	-	-	-	-	-	-	-	-	-	-	-	-	-	-	-
E_T^{miss} Soft jet scale [%]	-	-	-	-	-	-	-	-	-	-	-	-	-	-	-	-	-	-
E_T^{miss} Soft jet resolution [%]	-	-	-	-	-	-	-	-	-	-	-	-	-	-	-	-	-	-
Jet vertex fraction [%]	-	-	-	-	-	-	-	-	-	-	-	-	-	-	-	-	-	$^{-}_{-0.16}$
Alternate hard-scattering model [%]	∓0.41	±0.59	-	±1.15	±1.06	∓1.36	±0.30	∓0.53	∓1.83	±1.38	±0.93	±0.77	∓0.10	∓1.22	∓0.49	±0.21	∓1.54	∓1.90
Alternate parton-shower model [%]	∓0.55	±0.43	∓0.67	±0.66	∓0.41	∓0.54	±1.35	-	∓1.33	±0.95	±0.60	∓1.12	∓0.17	±1.19	∓0.33	±0.75	∓0.33	∓0.43
Monte Carlo sample statistics [%]	±0.23	±0.25	±0.25	±0.26	±0.26	±0.27	±0.28	±0.29	±0.30	±0.32	±0.33	±0.35	±0.38	±0.41	±0.47	±0.36	±0.48	±0.60
ISR/FSR + scale [%]	±0.29	-	-	∓0.79	$^{+0.42}_{-0.64}$	$^{+0.53}_{-0.33}$	$^{+0.73}_{-}$	∓0.99	$^{+0.90}_{-0.59}$	±0.39	$^{-}_{-0.56}$	$^{-}_{-0.73}$	$^{-}_{+0.78}$	∓1.01	$^{-}_{+2.02}$	$^{-}_{-0.23}$	$^{-}_{-0.18}$	$^{-}_{-1.72}$
Parton distribution functions [%]	-	-	-	-	-	-	-	-	-	-	-	-	-	-	-	∓0.10	∓0.28	∓0.18
Single top cross-section [%]	-	-	-	-	-	-	-	-	-	-	-	-	-	-	-	-	-	-
W+jets scale factors [%]	-	-	-	-	-	-	-	-	-	-	-	-	-	-	∓0.13	-	-	∓0.13
Fake lept. MC stat, e+jets ch. [%]	-	$^{+0.21}_{-}$	-	-	-	-	-	-	-	$^{+0.14}_{-}$	-	$^{-0.20}_{-}$	$^{+0.21}_{-}$	-	-	-	$^{-}_{-0.30}$	$^{-}_{-0.31}$
Fake lept. alternate fake CR, e+jets ch. [%]	-	-	-	-	-	±0.11	-	-	-	-	-	-	-	∓0.10	-	∓0.13	∓0.19	∓0.22
Fake lept. alternate real CR, e+jets ch. [%]	-	-	-	-	-	-	-	-	-	-	-	-	-	-	-	-	-	-
Fake lept. alternate parametrization, e+jets ch. [%]	-	-	-	-	-	-	-	-	-	∓0.15	-	-	-	-	-	∓0.34	-	-
Fake lept. MC stat, μ+jets ch. [%]	-	-	-	-	-	-	-	-	-	-	-	-	-	-	$^{+0.22}_{-}$	-	-	-
Fake lept. alternate fake CR, μ+jets ch. [%]	-	-	-	-	-	-	-	-	-	-	-	-	-	-	-	-	-	-
Fake lept. alternate real CR, μ+jets ch. [%]	-	-	-	-	-	-	-	-	-	-	-	-	-	-	-	-	-	-
Fake lept. alternate parametrization, μ+jets ch. [%]	-	-	-	-	-	-	-	-	-	-	±0.12	-	-	-	-	-	-	-
Z+jets cross-section [%]	-	-	-	-	-	-	-	-	-	-	-	-	-	-	-	-	-	∓0.13
Diboson cross-section [%]	-	-	-	-	-	-	-	-	-	-	-	-	-	-	-	-	-	-
Luminosity [%]	-	-	-	-	-	-	-	-	-	-	-	-	-	-	-	-	-	-

TABLE D.3: Fiducial phase-space relative differential cross-sections after combining the e+jets and μ+jets channels for the hadronic top-quark absolute rapidity $\left|y^{t,\mathrm{had}}\right|$. All uncertainties are quoted as a percentage with respect to the cross-section values in each bin. Dashes are used when the estimated relative systematic uncertainty for that bin is below 0.1%.

Bins [Unit $\lvert y^t\rvert$]	0–0.10	0.10–0.20	0.20–0.30	0.30–0.40	0.40–0.50	0.50–0.60	0.60–0.70	0.70–0.80	0.80–0.90	0.90–1	1–1.10	1.10–1.20	1.20–1.30	1.30–1.40	1.40–1.50	1.50–1.70	1.70–1.90	1.90–2.50
$\mathrm{d}\sigma$ / d $\lvert y^t\rvert$ [Unit $\lvert y^t\rvert$]	$2.40 \cdot 10^1$	$2.38 \cdot 10^1$	$2.34 \cdot 10^1$	$2.28 \cdot 10^1$	$2.20 \cdot 10^1$	$2.10 \cdot 10^1$	$2.00 \cdot 10^1$	$1.88 \cdot 10^1$	$1.73 \cdot 10^1$	$1.60 \cdot 10^1$	$1.45 \cdot 10^1$	$1.30 \cdot 10^1$	$1.15 \cdot 10^1$	$9.88 \cdot 10^0$	$8.31 \cdot 10^0$	$6.15 \cdot 10^0$	$3.59 \cdot 10^0$	$1.21 \cdot 10^{-1}$
Total Uncertainty [%]	±8.41	±8.39	±8.62	±8.94	±8.21	±8.74	±8.37	±9.28	±8.88	±8.38	±8.55	±8.84	±8.92	±9.63	±9.25	±8.91	±9.63	±10.1
Statistics [%]	±1.0	±1.0	±1.0	±1.0	±1.1	±1.1	±1.1	±1.2	±1.2	±1.3	±1.4	±1.5	±1.6	±1.7	±1.9	±1.5	±2.0	±2.5
Systematics [%]	±8.34	±8.31	±8.54	±8.87	±8.12	±8.66	±8.29	±9.20	±8.77	±8.27	±8.43	±8.71	±8.77	±9.50	±9.03	±8.77	±9.41	±9.77
η intercalibration model (JES) [%]	-	-	±0.15	$^{+0.10}_{-0.15}$	$^{+0.22}_{-0.13}$	±0.25	±0.34	$^{+0.42}_{-0.25}$	$^{+0.30}_{-0.51}$	±0.43	±0.66	±0.74	±0.73	±0.96	±1.00	±1.23	±1.36	±1.60
Single particle high-p_T (JES) [%]	-	-	-	-	-	-	-	-	-	-	-	-	-	-	-	-	-	-
Effective stat. NP set 1 (JES) [%]	±0.86	±0.82	±0.92	±0.92	±0.81	±0.94	±0.91	±0.85	±0.90	±0.89	±0.88	±0.89	±0.92	±1.02	±0.92	±0.95	±0.98	±0.85
Effective stat. NP set 2 (JES) [%]	-	-	-	-	-	-	-	-	-	-	-	-	-	-	-	-	-	-
Effective stat. NP set 3 (JES) [%]	-	-	-	-	-	-	-	-	-	-	-	-	-	-	-	-	-	-
Effective detector NP set 1 (JES) [%]	±0.18	±0.18	$^{+0.21}_{-0.13}$	±0.19	±0.19	$^{+0.25}_{-0.14}$	$^{+0.21}_{-0.14}$	±0.17	$^{+0.15}_{-0.23}$	$^{+0.14}_{-0.10}$	±0.23	±0.18	$^{+0.21}_{-0.11}$	±0.23	±0.22	±0.23	$^{+0.17}_{-0.25}$	±0.24
Effective detector NP set 2 (JES) [%]	±0.17	±0.18	±0.21	±0.19	±0.14	$^{+0.21}_{-0.16}$	±0.17	±0.17	±0.16	±0.17	±0.17	$^{+0.15}_{-0.20}$	$^{+0.21}_{-0.10}$	±0.24	±0.21	±0.17	$^{+0.17}_{-0.24}$	±0.16
Effective detector NP set 3 (JES) [%]	-	-	-	-	-	-	-	-	-	-	-	-	-	-	-	-	-	-
Effective mixed NP set 1 (JES) [%]	±0.29	±0.30	±0.29	±0.29	±0.30	±0.30	$^{+0.36}_{-0.25}$	±0.29	$^{+0.23}_{-0.30}$	±0.27	±0.32	±0.30	$^{+0.34}_{-0.25}$	±0.38	±0.32	±0.40	±0.30	±0.33
Effective mixed NP set 2 (JES) [%]	∓0.36	∓0.37	∓0.38	∓0.38	∓0.35	∓0.41	$^{-0.32}_{+0.42}$	∓0.38	∓0.34	∓0.38	∓0.38	∓0.36	$^{-0.27}_{+0.43}$	$^{-0.55}_{+0.41}$	∓0.41	∓0.42	∓0.39	∓0.38
Effective model NP set 1 (JES) [%]	±2.13	±2.28	±2.26	±2.30	±2.23	±2.30	±2.27	±2.25	±2.30	±2.40	±2.29	±2.33	±2.35	±2.41	±2.39	±2.43	±2.52	±2.36
Effective model NP set 2 (JES) [%]	-	-	-	-	-	-	-	-	-	-	-	-	-	-	-	-	-	-
Effective model NP set 3 (JES) [%]	±0.12	$^{-0.15}$	$^{+0.17}_{-0.11}$	±0.10	±0.14	$^{+0.20}_{-0.13}$	-	$^{+0.14}_{-0.10}$	±0.11	±0.15	$^{+0.16}_{-0.11}$	$^{-0.16}$	±0.14	±0.15	±0.17	-	±0.12	-
Effective model NP set 4 (JES) [%]	-	-	-	-	-	-	-	-	-	-	-	-	-	-	-	-	-	-
Pile-up offset μ (JES) [%]	$^{-0.12}_{-}$	∓0.11	$^{-0.10}_{+0.15}$	-	$^{-}_{+0.17}$	$^{-0.13}_{+0.18}$	∓0.12	$^{-0.10}_{+0.16}$	∓0.16	$^{-0.12}_{+0.18}$	∓0.23	$^{-0.32}_{+0.21}$	$^{-0.13}_{+0.26}$	∓0.29	∓0.29	∓0.39	∓0.43	∓0.70
Pile-up offset N_{PV} (JES) [%]	∓0.56	∓0.53	∓0.68	∓0.60	∓0.58	∓0.67	$^{-0.57}_{+0.78}$	∓0.64	$^{-0.65}_{+0.49}$	$^{-0.71}_{+0.52}$	∓0.67	∓0.62	∓0.58	∓0.59	∓0.55	∓0.58	∓0.56	$^{-0.48}_{+0.65}$
Punch-through (JES) [%]	-	-	-	-	-	-	-	-	-	-	-	-	-	-	-	-	-	-
Pile-up offset ρ topology (JES) [%]	±1.59	±1.66	±1.73	±1.67	±1.60	±1.71	±1.73	±1.71	±1.66	±1.73	±1.75	±1.71	±1.76	±1.86	±1.75	±1.88	±1.88	±1.73
Pile-up offset p_T (JES) [%]	-	-	-	-	-	-	-	-	-	-	-	-	-	-	-	-	-	-
Flavour composition (JES) [%]	±1.66	±1.68	±1.71	±1.90	±1.77	±1.89	±1.84	±1.91	±1.93	±1.97	±1.94	±2.12	±1.97	±2.10	±2.15	±2.08	±2.21	±1.98
Flavour response (JES) [%]	∓1.04	∓1.10	∓1.03	∓1.21	∓1.05	∓1.18	∓1.11	∓1.23	∓1.10	∓1.26	∓1.21	∓1.26	∓1.24	∓1.32	∓1.25	∓1.43	∓1.44	∓1.29
b-Tagged jet energy scale (JES) [%]	±0.52	±0.51	±0.60	±0.45	±0.54	±0.52	±0.57	±0.51	±0.53	±0.49	±0.58	±0.42	±0.56	±0.49	±0.51	±0.48	±0.42	±0.49
Jet reconstruction efficiency [%]	-	-	-	-	-	-	-	-	-	-	-	-	-	-	-	-	-	-
Jet energy resolution [%]	-	-	-	-	-	-	-	-	-	-	-	-	-	-	-	-	-	-
b-Quark tagging efficiency [%]	±4.20	±4.17	±4.19	±4.18	±4.22	±4.21	±4.21	±4.22	±4.24	±4.25	±4.25	±4.24	±4.26	±4.29	±4.26	±4.31	±4.33	±4.37
c-Quark tagging efficiency [%]	±0.97	±1.00	±0.98	±0.96	±0.96	±0.98	±0.95	±0.95	±0.93	±0.89	±0.92	±0.89	±0.89	±0.87	±0.84	±0.82	±0.80	±0.77
Light-jet tagging efficiency [%]	±0.52	±0.51	±0.52	±0.51	±0.51	±0.51	±0.48	±0.50	±0.50	±0.50	±0.49	±0.50	±0.54	±0.49	±0.55	±0.55	±0.58	±0.71
Electron energy scale [%]	-	-	$^{-}_{-0.14}$	$^{-}_{-0.15}$	$^{-}_{-0.14}$	-	$^{-}_{-0.13}$	-	-	-	$^{-}_{-0.13}$	$^{-}_{-0.13}$	-	$^{-}_{-0.14}$	-	$^{-}_{-0.14}$	-	-
Electron energy resolution [%]	-	-	-	-	-	-	-	-	-	-	-	-	-	-	-	-	-	-
Muon momentum scale [%]	-	-	-	-	-	-	-	-	-	-	-	-	-	-	-	-	-	-
Muon (ID) momentum resolution [%]	-	-	-	-	-	-	-	-	-	-	-	-	-	-	-	-	-	-
Muon (MS) momentum resolution [%]	-	-	-	-	-	-	-	-	-	-	-	-	-	-	-	-	-	-
Lepton trigger efficiency [%]	±1.26	±1.26	±1.26	±1.26	±1.26	±1.26	±1.26	±1.26	±1.27	±1.26	±1.27	±1.27	±1.27	±1.27	±1.27	±1.27	±1.27	±1.27
Lepton reconstruction efficiency [%]	±0.24	±0.24	±0.24	±0.24	±0.24	±0.24	±0.24	±0.24	±0.24	±0.24	±0.24	±0.24	±0.24	±0.24	±0.24	±0.25	±0.25	±0.24
Lepton identification efficiency [%]	±1.31	±1.32	±1.32	±1.32	±1.32	±1.31	±1.31	±1.31	±1.31	±1.32	±1.31	±1.31	±1.32	±1.31	±1.31	±1.31	±1.32	±1.32
E_T^{miss} Soft jet scale [%]	-	-	-	-	-	-	-	-	-	-	-	-	-	-	-	-	-	-
E_T^{miss} Soft jet resolution [%]	-	-	-	-	-	-	-	-	-	-	-	-	-	-	-	-	-	-
Jet vertex fraction [%]	∓0.65	∓0.64	∓0.65	∓0.64	∓0.65	∓0.65	∓0.68	∓0.68	∓0.66	∓0.66	∓0.65	∓0.70	∓0.64	$^{-0.78}_{+0.56}$	∓0.67	∓0.62	∓0.60	$^{-0.61}_{+0.43}$
Alternate hard-scattering model [%]	∓1.49	∓0.48	∓1.11	-	-	∓2.42	∓0.77	∓1.60	∓2.89	±0.29	∓0.15	∓0.31	∓1.18	∓2.28	∓1.57	∓0.86	∓2.60	∓2.96
Alternate parton-shower model [%]	∓1.40	∓0.43	∓1.53	∓0.19	∓1.27	∓1.39	±0.48	∓0.91	∓2.18	-	∓0.26	∓1.97	∓1.02	±0.32	∓1.19	∓0.11	∓1.19	∓1.29
Monte Carlo sample statistics [%]	±0.24	±0.26	±0.26	±0.26	±0.27	±0.27	±0.29	±0.30	±0.31	±0.32	±0.33	±0.36	±0.39	±0.42	±0.47	±0.37	±0.48	±0.60
ISR/FSR + scale [%]	$^{-5.47}_{+3.58}$	$^{-5.72}_{+3.88}$	$^{-5.82}_{+3.75}$	$^{-6.60}_{+4.62}$	$^{-5.36}_{+3.21}$	$^{-5.26}_{+3.54}$	∓4.57	$^{-6.75}_{+4.86}$	$^{-4.90}_{+3.27}$	$^{-5.38}_{+3.48}$	$^{-6.07}_{+3.29}$	$^{-6.09}_{+3.12}$	∓5.08	$^{-6.75}_{+4.91}$	$^{-4.53}_{+5.99}$	$^{-5.98}_{+3.80}$	$^{-6.88}_{+3.06}$	$^{-7.39}_{+3.75}$
Parton distribution functions [%]	-	-	-	-	-	-	-	-	-	-	-	-	±0.10	-	-	-	∓0.24	∓0.15
Single top cross-section [%]	±0.30	±0.27	±0.28	±0.29	±0.30	±0.26	±0.27	±0.26	±0.28	±0.26	±0.26	±0.26	±0.23	±0.22	±0.22	±0.22	±0.23	±0.18
W+jets scale factors [%]	±0.48	±0.44	±0.40	±0.44	±0.37	±0.39	±0.44	±0.41	±0.36	±0.36	±0.37	±0.40	±0.36	±0.40	±0.26	±0.33	±0.32	±0.26
Fake lept. MC stat, e+jets ch. [%]	$^{+0.49}_{-}$	$^{+0.43}_{-}$	$^{+0.52}_{-}$	$^{-0.15}_{+0.37}$	$^{+0.37}_{-}$	$^{-}_{+0.55}$	$^{-}_{+0.46}$	$^{-}_{+0.43}$	$^{-}_{+0.44}$	$^{+0.32}_{-}$	$^{+0.40}_{-}$	$^{-0.17}_{+0.45}$	$^{+0.32}_{-}$	$^{+0.22}_{-}$	$^{+0.31}_{-}$	$^{+0.24}_{-}$	$^{-}_{-}$	-
Fake lept. alternate fake CR, e+jets ch. [%]	±0.41	±0.37	±0.39	±0.32	±0.36	±0.47	±0.39	±0.36	±0.40	±0.34	±0.34	±0.37	±0.32	±0.24	±0.27	±0.21	±0.16	±0.13
Fake lept. alternate real CR, e+jets ch. [%]	-	-	-	-	-	-	-	-	-	-	-	-	-	-	-	-	-	∓0.13
Fake lept. alternate parametrization, e+jets ch. [%]	±0.36	±0.37	±0.25	±0.34	±0.27	±0.38	±0.36	±0.27	±0.23	±0.13	±0.31	±0.30	±0.31	±0.28	$^{\pm0.38}_{+0.28}$	-	±0.26	±0.22
Fake lept. MC stat, μ+jets ch. [%]	-	-	-	-	-	-	-	-	-	-	-	-	-	-	-	-	-	-
Fake lept. alternate fake CR, μ+jets ch. [%]	±0.21	±0.19	±0.27	±0.26	±0.21	±0.26	±0.20	±0.22	±0.21	±0.25	±0.21	±0.30	±0.23	±0.24	±0.14	±0.22	±0.23	±0.30
Fake lept. alternate real CR, μ+jets ch. [%]	±0.22	±0.23	±0.25	±0.26	±0.15	±0.24	±0.16	±0.30	±0.16	±0.18	±0.25	±0.26	±0.15	±0.17	±0.27	±0.25	±0.16	±0.25
Fake lept. alternate parametrization, μ+jets ch. [%]	±0.22	±0.22	±0.17	±0.31	±0.21	±0.23	±0.19	±0.21	±0.28	±0.30	±0.16	±0.36	±0.20	±0.18	±0.24	±0.26	±0.27	±0.21
Z+jets cross-section [%]	±0.54	±0.51	±0.55	±0.50	±0.53	±0.56	±0.51	±0.48	±0.52	±0.52	±0.42	±0.41	±0.46	±0.40	±0.41	±0.41	±0.40	±0.35
Diboson cross-section [%]	-	-	-	-	-	-	-	-	-	-	-	-	-	-	-	-	-	-
Luminosity [%]	±2.80	±2.80	±2.80	±2.80	±2.80	±2.80	±2.80	±2.80	±2.80	±2.80	±2.80	±2.80	±2.80	±2.80	±2.80	±2.80	±2.80	±2.80

TABLE D.4: Fiducial phase-space absolute differential cross-sections after combining the e+jets and μ+jets channels for the hadronic top-quark absolute rapidity $\left|y^{t,\mathrm{had}}\right|$. All uncertainties are quoted as a percentage with respect to the cross-section values in each bin. Dashes are used when the estimated relative systematic uncertainty for that bin is below 0.1%.

Bins [GeV]	225–345	345–420	420–500	500–590	590–685	685–790	790–910	910–1040	1040–1175	1175–1320	1320–3000
$1/\sigma \cdot \mathrm{d}\sigma \,/\, \mathrm{d}\, m^{t\bar{t}}$	$5.96 \cdot 10^{-4}$	$3.35 \cdot 10^{-3}$	$3.08 \cdot 10^{-3}$	$2.00 \cdot 10^{-3}$	$1.14 \cdot 10^{-3}$	$6.15 \cdot 10^{-4}$	$3.14 \cdot 10^{-4}$	$1.53 \cdot 10^{-4}$	$7.40 \cdot 10^{-5}$	$3.60 \cdot 10^{-5}$	$3.00 \cdot 10^{-6}$
Total Uncertainty [%]	±24.6	±5.16	±3.99	±4.78	±4.70	±5.04	±6.38	±7.67	±5.41	±9.76	±13.6
Statistics [%]	±1.3	±0.5	±0.5	±0.6	±0.8	±1.0	±1.4	±2.0	±2.9	±4.7	±4.1
Systematics [%]	±24.5	±5.13	±3.95	±4.73	±4.62	±4.92	±6.19	±7.38	±4.46	±8.49	±12.9
η intercalibration model (JES) [%]	∓1.50	∓0.51	$^{+0.10}_{-0.15}$	±0.28	±0.47	±0.64	$^{+0.49}_{-0.69}$	±0.80	$^{+1.36}_{-0.86}$	$^{+0.61}_{-0.87}$	±1.24
Single particle high-p_T (JES) [%]	-	-	-	-	-	-	-	-	-	-	-
Effective stat. NP set 1 (JES) [%]	∓0.93	-	±0.34	$^{+0.15}_{-0.10}$	-	$^{-0.24}_{+0.15}$	∓0.47	∓0.46	$^{-0.50}_{+0.68}$	$^{-1.02}_{+0.75}$	$^{-0.50}_{+0.70}$
Effective stat. NP set 2 (JES) [%]	$^{-}_{+0.12}$	-	-	-	-	±0.11	$^{-}_{-0.12}$	±0.11	$^{+0.22}_{-}$	$^{+0.11}_{-0.35}$	±0.19
Effective stat. NP set 3 (JES) [%]	±1.85	±0.41	∓0.27	∓0.37	∓0.41	∓0.43	∓0.35	∓0.44	$^{-0.39}_{+0.51}$	$^{-0.47}_{+0.32}$	$^{-0.34}_{+0.48}$
Effective detector NP set 1 (JES) [%]	∓2.08	∓0.76	$^{-}_{-0.13}$	±0.42	±0.67	±0.95	±0.99	±1.39	$^{+1.85}_{-1.38}$	$^{+1.01}_{-1.63}$	±2.51
Effective detector NP set 2 (JES) [%]	$^{-0.26}_{+0.35}$	-	±0.10	-	-	-	∓0.15	∓0.12	∓0.20	$^{-0.46}_{+0.18}$	$^{-0.22}_{+0.30}$
Effective detector NP set 3 (JES) [%]	∓0.24	-	-	-	-	-	-	±0.15	-	$^{+0.10}_{-0.36}$	$^{+0.29}_{-0.13}$
Effective mixed NP set 1 (JES) [%]	∓2.08	∓0.61	±0.22	±0.41	±0.55	±0.71	$^{+0.55}_{-0.73}$	±0.92	±1.11	±0.88	±1.49
Effective mixed NP set 2 (JES) [%]	$^{+0.65}_{-0.41}$	-	∓0.15	-	-	-	$^{+0.13}_{-0.20}$	$^{+0.17}_{-0.11}$	±0.23	$^{+0.19}_{-0.41}$	$^{+0.35}_{-0.19}$
Effective model NP set 1 (JES) [%]	∓6.74	∓0.95	±1.33	±1.28	±0.86	±0.78	$^{+0.24}_{-0.42}$	$^{+0.14}_{-0.28}$	$^{+0.59}_{-}$	$^{-0.98}_{+0.20}$	$^{+0.62}_{-}$
Effective model NP set 2 (JES) [%]	±0.11	-	-	-	-	$^{+0.12}_{-}$	$^{+0.12}_{-0.16}$	±0.17	$^{+0.35}_{-0.17}$	$^{+0.34}_{-0.59}$	±0.57
Effective model NP set 3 (JES) [%]	±1.47	±0.41	$^{-0.20}_{+0.15}$	∓0.32	∓0.40	∓0.43	∓0.43	∓0.50	∓0.48	$^{-0.65}_{+0.44}$	∓0.46
Effective model NP set 4 (JES) [%]	∓0.30	∓0.11	-	-	±0.11	±0.15	±0.17	±0.23	$^{+0.32}_{-0.19}$	$^{+0.31}_{-0.46}$	±0.39
Pile-up offset μ (JES) [%]	±0.44	-	-	-	-	-	-	-	$^{-0.11}_{+0.26}$	$^{-}_{-0.25}$	$^{-}_{+0.30}$
Pile-up offset N_{PV} (JES) [%]	±1.37	$^{-}_{-0.12}$	∓0.34	$^{-0.14}_{+0.28}$	$^{-0.15}_{+0.10}$	-	-	±0.16	±0.23	$^{+0.16}_{-0.31}$	$^{+0.37}_{-0.11}$
Punch-through (JES) [%]	-	-	-	-	-	-	-	-	-	±0.15	-
Pile-up offset ρ topology (JES) [%]	∓3.79	∓0.53	±0.79	±0.76	±0.48	$^{+0.33}_{-0.46}$	-	-	$^{+0.25}_{-}$	∓0.76	$^{-0.25}_{+0.49}$
Pile-up offset p_T (JES) [%]	-	-	-	-	-	-	-	-	$^{+0.36}_{-}$	$^{-}_{-0.28}$	-
Flavour composition (JES) [%]	∓2.37	$^{-0.18}_{+0.11}$	±0.66	$^{+0.54}_{-0.41}$	-	-	∓0.49	∓0.65	$^{-0.46}_{+0.85}$	∓1.22	$^{-0.26}_{+0.93}$
Flavour response (JES) [%]	±2.23	±0.36	∓0.43	$^{-0.39}_{+0.51}$	∓0.29	$^{-0.47}_{+0.27}$	-	$^{-0.23}_{+0.13}$	$^{-}_{+0.57}$	$^{+0.14}_{-0.48}$	$^{-}_{+0.50}$
b-Tagged jet energy scale (JES) [%]	∓3.63	∓0.75	±0.55	±0.71	±0.72	±0.76	$^{+0.61}_{-0.83}$	±0.68	$^{+0.86}_{-0.60}$	±0.53	±0.67
Jet reconstruction efficiency [%]	∓0.12	-	-	-	-	-	-	-	±0.10	-	-
Jet energy resolution [%]	-	-	-	-	-	-	-	-	-	-	-
b-Quark tagging efficiency [%]	±0.35	-	∓0.21	∓0.14	-	±0.29	±0.50	±0.71	±0.92	±1.04	±1.25
c-Quark tagging efficiency [%]	±0.29	-	-	-	-	-	±0.12	±0.20	±0.23	±0.24	±0.29
Light-jet tagging efficiency [%]	-	-	∓0.10	-	-	±0.15	±0.27	±0.34	±0.40	±0.46	±1.02
Electron energy scale [%]	∓0.44	$^{-0.17}_{+0.13}$	-	-	$^{+0.15}_{-}$	$^{+0.21}_{-0.15}$	$^{+0.19}_{-0.32}$	±0.27	$^{+0.47}_{-}$	±0.49	±0.26
Electron energy resolution [%]	-	-	-	-	-	-	-	-	-	-	-
Muon momentum scale [%]	-	-	-	-	-	-	-	-	-	-	-
Muon (ID) momentum resolution [%]	-	-	-	-	-	-	-	-	-	-	±0.12
Muon (MS) momentum resolution [%]	-	-	-	-	-	-	-	-	-	-	-
Lepton trigger efficiency [%]	-	-	-	-	-	-	-	-	-	-	±0.11
Lepton reconstruction efficiency [%]	-	-	-	-	-	-	-	-	-	-	-
Lepton identification efficiency [%]	-	-	-	-	-	-	-	-	-	-	-
E_T^{miss} Soft jet scale [%]	-	-	-	-	-	-	-	-	-	-	$^{+0.24}_{-}$
E_T^{miss} Soft jet resolution [%]	-	-	-	-	-	-	-	-	$^{+0.30}_{-}$	-	$^{+0.21}_{-}$
Jet vertex fraction [%]	∓0.57	∓0.30	-	$^{+0.18}_{-0.11}$	±0.29	±0.44	±0.60	±0.68	±0.71	±0.70	$^{+1.03}_{-0.79}$
Alternate hard-scattering model [%]	∓11.5	∓2.80	±1.70	±2.33	±2.52	±2.08	±3.38	±4.06	-	±4.52	±9.47
Alternate parton-shower model [%]	∓19.1	∓3.77	±2.82	±3.58	±3.38	±3.89	±4.43	±5.28	±2.48	±4.89	±5.32
Monte Carlo sample statistics [%]	±0.33	±0.13	±0.13	±0.15	±0.20	±0.26	±0.35	±0.49	±0.67	±1.01	±0.91
ISR/FSR + scale [%]	$^{-1.14}_{+0.87}$	$^{-}_{-0.84}$	$^{-0.65}_{+1.01}$	$^{-0.12}_{+0.20}$	$^{+0.72}_{-0.32}$	$^{+0.59}_{-0.23}$	$^{+1.78}_{-1.23}$	$^{+1.89}_{-0.73}$	$^{-}_{-0.64}$	$^{+4.08}_{-1.82}$	$^{+5.50}_{-2.82}$
Parton distribution functions [%]	-	-	-	-	-	-	∓0.14	∓0.19	∓0.38	∓0.61	∓0.66
Single top cross-section [%]	-	-	-	-	-	±0.11	±0.17	±0.30	±0.43	±0.56	±0.73
W+jets scale factors [%]	±0.17	∓0.13	∓0.17	-	±0.10	±0.18	±0.32	±0.55	±0.95	±1.12	±1.56
Fake lept. MC stat, e+jets ch. [%]	$^{-0.49}_{-}$	-	-	-	-	$^{+0.31}_{-}$	$^{+0.71}_{-}$	$^{+0.95}_{-}$	$^{+1.77}_{-}$	$^{+2.44}_{-}$	$^{+3.76}_{-}$
Fake lept. alternate fake CR, e+jets ch. [%]	±0.32	-	-	-	-	-	-	±0.14	±0.23	±0.48	±0.17
Fake lept. alternate real CR, e+jets ch. [%]	±0.22	-	-	-	-	-	-	-	-	-	±0.22
Fake lept. alternate parametrization, e+jets ch. [%]	-	-	-	-	-	-	±0.16	±0.28	±0.38	±0.17	-
Fake lept. MC stat, μ+jets ch. [%]	-	-	-	-	-	-	-	-	-	$^{+1.08}_{-}$	$^{+0.69}_{-0.14}$
Fake lept. alternate fake CR, μ+jets ch. [%]	±0.60	-	-	∓0.11	-	-	∓0.14	±0.16	-	±0.30	±0.46
Fake lept. alternate real CR, μ+jets ch. [%]	∓0.50	∓0.27	-	-	±0.26	±0.39	±0.39	±0.60	±0.77	±1.09	±1.62
Fake lept. alternate parametrization, μ+jets ch. [%]	∓0.12	-	-	-	±0.10	±0.15	-	±0.37	±0.35	±0.20	±0.56
Z+jets cross-section [%]	±0.56	-	∓0.12	-	-	-	±0.13	±0.12	±0.45	±0.46	±0.86
Diboson cross-section [%]	-	-	-	-	-	-	-	-	-	-	-
Luminosity [%]	-	-	-	-	-	-	-	-	-	-	-

TABLE D.5: Fiducial phase-space relative differential cross-sections after combining the e+jets and μ+jets channels for the $t\bar{t}$ system invariant mass $m^{t\bar{t}}$. All uncertainties are quoted as a percentage with respect to the cross-section values in each bin. Dashes are used when the estimated relative systematic uncertainty for that bin is below 0.1%.

Bins [GeV]	225–345	345–420	420–500	500–590	590–685	685–790	790–910	910–1040	1040–1175	1175–1320	1320–3000
$d\sigma$ / d m^{tt} [GeV]	$1.73 \cdot 10^{-2}$	$9.71 \cdot 10^{-2}$	$8.93 \cdot 10^{-2}$	$5.80 \cdot 10^{-2}$	$3.30 \cdot 10^{-2}$	$1.78 \cdot 10^{-2}$	$9.11 \cdot 10^{-3}$	$4.45 \cdot 10^{-3}$	$2.16 \cdot 10^{-3}$	$1.05 \cdot 10^{-3}$	$9.80 \cdot 10^{-5}$
Total Uncertainty [%]	±27.0	±10.5	±9.59	±9.38	±8.82	±9.13	±8.75	±9.61	±10.4	±10.4	±13.1
Statistics [%]	±1.4	±0.6	±0.6	±0.6	±0.8	±1.1	±1.5	±2.0	±2.9	±4.7	±4.1
Systematics [%]	±26.9	±10.5	±9.59	±9.36	±8.77	±9.05	±8.61	±9.37	±9.93	±9.12	±12.4
η intercalibration model (JES) [%]	∓1.14	∓0.15	±0.48	±0.64	±0.82	±0.99	±0.94	±1.15	$^{+1.73}_{-1.21}$	±1.09	±1.59
Single particle high-p_T (JES) [%]	-	-	-	-	-	-	-	-	-	-	-
Effective stat. NP set 1 (JES) [%]	-	±0.95	±1.23	±1.00	±0.83	±0.68	±0.40	±0.41	$^{+0.38}_{-0.19}$	-	$^{+0.38}_{-0.17}$
Effective stat. NP set 2 (JES) [%]	∓0.18	∓0.16	-	-	-	-	-	-	-	-	$^{+0.14}_{-}$
Effective stat. NP set 3 (JES) [%]	±1.88	±0.43	∓0.23	∓0.34	∓0.38	∓0.41	∓0.32	∓0.41	$^{-0.36}$	$^{-0.27}_{-0.45}$	$^{-0.31}$
Effective detector NP set 1 (JES) [%]	∓1.97	∓0.66	±0.22	±0.53	±0.78	±1.06	±1.09	±1.49	$^{+0.48}_{+1.97}$	$^{+0.30}_{+1.12}$	$^{+0.46}_{\pm 2.62}$
Effective detector NP set 2 (JES) [%]	$^{-}_{+0.17}$	±0.21	±0.28	±0.22	±0.16	±0.11	-	-	$^{-1.48}$	$^{-1.73}_{-0.28}$	-
Effective detector NP set 3 (JES) [%]	∓0.22	-	-	-	-	±0.11	±0.11	±0.17	$^{+0.16}_{-}$	$^{+0.12}_{-0.38}$	$^{+0.32}_{-0.15}$
Effective mixed NP set 1 (JES) [%]	∓1.84	∓0.38	±0.45	±0.64	±0.78	±0.94	±0.87	±1.15	±1.34	±1.11	±1.72
Effective mixed NP set 2 (JES) [%]	$^{+0.29}_{-}$	∓0.38	∓0.53	∓0.45	∓0.36	∓0.33	∓0.20	$^{-0.18}_{+0.26}$	∓0.14	-	-
Effective model NP set 1 (JES) [%]	∓4.61	±1.16	±3.46	±3.40	±2.98	±2.89	±2.45	±2.33	$^{+2.71}_{-1.90}$	$^{+1.09}_{-1.92}$	$^{+2.20}_{-1.51}$
Effective model NP set 2 (JES) [%]	-	∓0.14	∓0.11	-	-	-	-	$^{-}_{-0.12}$	$^{+0.28}_{-0.10}$	$^{+0.27}_{-0.52}$	±0.51
Effective model NP set 3 (JES) [%]	±1.65	±0.59	-	∓0.13	∓0.22	∓0.24	∓0.24	∓0.32	∓0.31	$^{-0.46}$	$^{-0.22}$
Effective model NP set 4 (JES) [%]	∓0.29	∓0.10	-	-	±0.11	±0.16	±0.20	±0.25	$^{+0.33}_{-0.20}$	$^{+0.32}_{-0.47}$	±0.40
Pile-up offset μ (JES) [%]	±0.28	$^{-}_{+0.12}$	∓0.23	$^{-0.18}_{+0.24}$	∓0.23	$^{-0.29}_{+0.22}$	∓0.26	$^{-0.14}_{+0.19}$	$^{-0.27}_{+0.43}$	$^{-0.41}$	$^{-0.17}_{+0.47}$
Pile-up offset N_{PV} (JES) [%]	±0.79	∓0.47	∓0.91	∓0.79	∓0.70	∓0.58	∓0.49	∓0.42	∓0.34	$^{-0.40}_{+0.27}$	$^{-0.19}_{+0.48}$
Punch-through (JES) [%]	-	-	-	-	-	-	-	-	-	±0.15	-
Pile-up offset ρ topology (JES) [%]	∓2.17	±1.08	±2.40	±2.37	±2.09	±2.00	±1.60	±1.50	$^{+1.87}_{-1.34}$	±0.84	±1.24
Pile-up offset p_T (JES) [%]	-	-	-	-	-	-	-	-	$^{+0.36}_{-}$	$^{-}_{-0.28}$	-
Flavour composition (JES) [%]	∓0.53	±1.67	±2.49	±2.31	±1.90	±1.81	±1.33	±1.17	$^{+1.35}_{-0.99}$	$^{+0.50}_{-0.70}$	$^{+1.55}_{-0.91}$
Flavour response (JES) [%]	±1.11	∓0.74	∓1.54	∓1.56	∓1.40	∓1.48	∓1.13	∓1.29	$^{-1.13}_{+1.68}$	$^{-0.97}_{+0.62}$	$^{-1.18}_{+1.62}$
b-Tagged jet energy scale (JES) [%]	∓3.23	∓0.34	±0.96	±1.13	±1.13	±1.17	±1.12	±1.09	±1.14	±0.95	±1.08
Jet reconstruction efficiency [%]	∓0.18	-	-	-	-	-	-	-	-	-	-
Jet energy resolution [%]	-	-	-	-	-	-	-	-	-	-	-
b-Quark tagging efficiency [%]	±4.58	±4.12	±4.01	±4.08	±4.26	±4.51	±4.72	±4.94	±5.14	±5.28	±5.48
c-Quark tagging efficiency [%]	±1.23	±0.90	±0.85	±0.89	±0.95	±0.98	±1.06	±1.14	±1.18	±1.19	±1.24
Light-jet tagging efficiency [%]	±0.60	±0.41	±0.40	±0.50	±0.57	±0.67	±0.78	±0.85	±0.92	±0.97	±1.53
Electron energy scale [%]	∓0.35	-	$^{-}_{-0.17}$	$^{+0.13}_{-0.17}$	±0.21	±0.26	$^{+0.24}_{-0.44}$	$^{+0.30}_{-0.40}$	$^{+0.53}_{-0.17}$	$^{+0.49}_{-0.66}$	±0.34
Electron energy resolution [%]	-	-	-	-	-	-	-	-	-	-	-
Muon momentum scale [%]	-	-	-	-	-	-	-	-	-	-	-
Muon (ID) momentum resolution [%]	-	-	-	-	-	-	-	-	-	-	±0.12
Muon (MS) momentum resolution [%]	-	-	-	-	-	-	-	-	-	-	-
Lepton trigger efficiency [%]	±1.30	±1.27	±1.25	±1.25	±1.25	±1.27	±1.28	±1.29	±1.32	±1.34	±1.38
Lepton reconstruction efficiency [%]	±0.21	±0.22	±0.23	±0.25	±0.26	±0.27	±0.28	±0.29	±0.29	±0.31	±0.32
Lepton identification efficiency [%]	±1.25	±1.28	±1.31	±1.33	±1.34	±1.35	±1.36	±1.37	±1.36	±1.36	±1.37
E_T^{miss} Soft jet scale [%]	-	-	-	-	-	-	-	-	-	-	$^{+0.24}_{-}$
E_T^{miss} Soft jet resolution [%]	-	-	-	-	-	-	-	-	$^{+0.30}_{-}$	-	$^{+0.20}_{-}$
Jet vertex fraction [%]	∓1.26	∓0.99	∓0.76	∓0.54	$^{-0.45}_{+0.34}$	∓0.23	-	-	-	-	$^{+0.28}_{-0.16}$
Alternate hard-scattering model [%]	∓13.2	∓4.62	∓0.19	±0.42	±0.61	±0.18	±1.45	±2.12	∓1.93	±2.57	±7.43
Alternate parton-shower model [%]	∓20.5	∓5.51	±0.96	±1.71	±1.51	±2.01	±2.54	±3.37	±0.63	±2.99	±3.41
Monte Carlo sample statistics [%]	±0.34	±0.15	±0.14	±0.16	±0.21	±0.27	±0.36	±0.49	±0.67	±1.01	±0.91
ISR/FSR + scale [%]	$^{-6.78}_{+4.69}$	$^{-5.72}_{+2.90}$	$^{-6.32}_{+4.83}$	$^{-5.82}_{+3.99}$	$^{-5.02}_{+3.44}$	$^{-5.14}_{+3.53}$	$^{-4.02}_{+2.50}$	∓3.46	$^{-6.31}_{+3.66}$	±1.86	$^{-0.52}_{+0.84}$
Parton distribution functions [%]	-	-	-	-	-	-	∓0.18	∓0.23	∓0.42	∓0.65	∓0.70
Single top cross-section [%]	±0.24	±0.18	±0.20	±0.24	±0.30	±0.38	±0.44	±0.56	±0.70	±0.82	±0.99
W+jets scale factors [%]	±0.57	±0.26	±0.22	±0.34	±0.49	±0.58	±0.72	±0.94	±1.35	±1.51	±1.95
Fake lept. MC stat, e+jets ch. [%]	∓0.48	$^{-0.19}_{+0.31}$	$^{-}_{+0.35}$	$^{-}_{+0.45}$	$^{-}_{+0.40}$	$^{+0.50}_{-}$	$^{+0.72}_{-}$	$^{+0.95}_{-}$	$^{+1.77}_{-}$	$^{+2.44}_{-}$	$^{+3.77}_{-}$
Fake lept. alternate fake CR, e+jets ch. [%]	±0.69	±0.26	±0.29	±0.38	±0.35	±0.42	±0.41	±0.51	±0.60	±0.84	±0.53
Fake lept. alternate real CR, e+jets ch. [%]	±0.18	-	-	-	-	-	-	-	-	-	±0.18
Fake lept. alternate parametrization, e+jets ch. [%]	±0.22	±0.26	±0.22	±0.31	±0.29	±0.35	±0.45	±0.57	±0.67	±0.46	±0.29
Fake lept. MC stat, μ+jets ch. [%]	-	-	-	-	-	-	$^{+0.21}_{-}$	-	-	$^{+1.13}_{-}$	$^{+0.70}_{-}$
Fake lept. alternate fake CR, μ+jets ch. [%]	±0.85	±0.26	±0.15	±0.13	±0.21	±0.20	±0.10	±0.41	±0.26	±0.55	±0.71
Fake lept. alternate real CR, μ+jets ch. [%]	∓0.30	-	±0.13	±0.28	±0.45	±0.59	±0.58	±0.80	±0.97	±1.29	±1.82
Fake lept. alternate parametrization, μ+jets ch. [%]	±0.10	±0.14	±0.17	±0.25	±0.32	±0.38	±0.23	±0.60	±0.58	±0.43	±0.79
Z+jets cross-section [%]	±1.07	±0.44	±0.38	±0.42	±0.49	±0.55	±0.63	±0.63	±0.96	±0.97	±1.37
Diboson cross-section [%]	-	-	-	-	-	-	-	-	-	-	±0.11
Luminosity [%]	±2.80	±2.80	±2.80	±2.80	±2.80	±2.80	±2.80	±2.80	±2.80	±2.80	±2.80

TABLE D.6: Fiducial phase-space absolute differential cross-sections after combining the e+jets and μ+jets channels for the $t\bar{t}$ system invariant mass $m^{t\bar{t}}$. All uncertainties are quoted as a percentage with respect to the cross-section values in each bin. Dashes are used when the estimated relative systematic uncertainty for that bin is below 0.1%.

Bins [GeV]	0–35	35–75	75–125	125–170	170–225	225–800
$1/\sigma \cdot \mathrm{d}\sigma$ / d $p_T^{t\bar{t}}$	$1.29 \cdot 10^{-2}$	$7.60 \cdot 10^{-3}$	$2.68 \cdot 10^{-3}$	$1.14 \cdot 10^{-3}$	$5.29 \cdot 10^{-4}$	$5.20 \cdot 10^{-5}$
Total Uncertainty [%]	±4.74	±3.36	±6.29	±4.83	±7.57	±5.47
Statistics [%]	±0.3	±0.4	±0.7	±1.2	±1.7	±1.6
Systematics [%]	±4.72	±3.33	±6.25	±4.64	±7.34	±5.19
η intercalibration model (JES) [%]	∓0.52	-	±0.93	±0.97	±0.78	±0.43
Single particle high-p_T (JES) [%]	-	-	-	-	-	-
Effective stat. NP set 1 (JES) [%]	∓0.37	±0.18	±0.71	±0.36	$^{+0.13}_{-0.19}$	$^{-0.14}_{+0.25}$
Effective stat. NP set 2 (JES) [%]	-	-	-	-	-	-
Effective stat. NP set 3 (JES) [%]	-	-	∓0.18	∓0.32	∓0.17	-
Effective detector NP set 1 (JES) [%]	∓0.14	$^{-0.12}_{-}$	-	±0.45	±0.76	±1.32
Effective detector NP set 2 (JES) [%]	-	-	±0.15	-	-	$^{-0.12}_{+0.16}$
Effective detector NP set 3 (JES) [%]	-	-	-	-	-	$^{+0.13}_{-}$
Effective mixed NP set 1 (JES) [%]	∓0.19	-	±0.27	±0.47	$^{+0.47}_{-0.62}$	±0.77
Effective mixed NP set 2 (JES) [%]	±0.16	-	∓0.30	∓0.22	∓0.11	$^{+0.14}_{-}$
Effective model NP set 1 (JES) [%]	∓1.17	±0.29	±2.23	±1.73	±1.21	$^{+0.38}_{-0.51}$
Effective model NP set 2 (JES) [%]	-	-	-	-	-	±0.32
Effective model NP set 3 (JES) [%]	-	-	-	$^{-0.27}_{+0.18}$	∓0.16	-
Effective model NP set 4 (JES) [%]	-	-	-	-	$^{-}_{-0.22}$	$^{+0.25}_{-0.18}$
Pile-up offset μ (JES) [%]	±0.16	-	∓0.28	∓0.20	$^{-0.17}_{-}$	-
Pile-up offset N_{PV} (JES) [%]	±0.11	-	∓0.21	$^{-0.20}_{+0.32}$	$^{-0.22}_{+0.47}$	-
Punch-through (JES) [%]	-	-	-	-	-	-
Pile-up offset ρ topology (JES) [%]	∓0.82	±0.25	±1.52	±1.22	±0.89	$^{-}_{-0.18}$
Pile-up offset p_T (JES) [%]	-	-	-	$^{+0.14}_{-}$	-	-
Flavour composition (JES) [%]	∓1.35	±0.29	±2.46	±2.25	±1.75	±0.78
Flavour response (JES) [%]	±0.97	∓0.13	∓1.71	∓1.81	∓1.56	∓0.96
b-Tagged jet energy scale (JES) [%]	-	-	-	-	-	-
Jet reconstruction efficiency [%]	-	-	-	-	-	-
Jet energy resolution [%]	-	-	-	-	-	-
b-Quark tagging efficiency [%]	-	-	∓0.14	∓0.22	∓0.17	±0.17
c-Quark tagging efficiency [%]	-	-	-	-	-	∓0.10
Light-jet tagging efficiency [%]	∓0.12	-	±0.22	±0.17	-	-
Electron energy scale [%]	-	-	-	-	-	-
Electron energy resolution [%]	-	-	-	-	-	-
Muon momentum scale [%]	-	-	-	-	-	-
Muon (ID) momentum resolution [%]	-	-	-	-	-	-
Muon (MS) momentum resolution [%]	-	-	-	-	-	-
Lepton trigger efficiency [%]	-	-	-	-	-	-
Lepton reconstruction efficiency [%]	-	-	-	-	-	-
Lepton identification efficiency [%]	-	-	-	-	-	-
E_T^{miss} Soft jet scale [%]	∓1.39	±1.40	±1.27	±0.27	±0.28	±0.20
E_T^{miss} Soft jet resolution [%]	$^{-}_{-0.31}$	$^{+0.31}_{-}$	$^{+0.33}_{-}$	-	$^{-}_{+0.19}$	-
Jet vertex fraction [%]	-	-	-	-	-	±0.21
Alternate hard-scattering model [%]	∓2.87	±1.76	±2.97	±1.40	±5.97	±3.96
Alternate parton-shower model [%]	∓1.93	±0.59	±3.21	±2.12	±2.61	±2.45
Monte Carlo sample statistics [%]	-	±0.10	±0.19	±0.31	±0.44	±0.40
ISR/FSR + scale [%]	$^{+1.46}_{-1.92}$	∓2.27	$^{+0.42}_{-}$	$^{-}_{-0.68}$	$^{-0.89}_{+1.59}$	$^{-}_{+0.93}$
Parton distribution functions [%]	-	-	-	-	-	-
Single top cross-section [%]	-	-	-	-	-	-
W+jets scale factors [%]	-	-	-	-	±0.14	±0.12
Fake lept. MC stat, e+jets ch. [%]	-	-	-	-	±0.18	-
Fake lept. alternate fake CR, e+jets ch. [%]	-	-	-	-	∓0.14	∓0.13
Fake lept. alternate real CR, e+jets ch. [%]	-	-	-	-	-	-
Fake lept. alternate parametrization, e+jets ch. [%]	-	-	-	-	-	-
Fake lept. MC stat, μ+jets ch. [%]	-	-	-	-	-	-
Fake lept. alternate fake CR, μ+jets ch. [%]	-	-	-	-	-	-
Fake lept. alternate real CR, μ+jets ch. [%]	-	-	-	-	-	-
Fake lept. alternate parametrization, μ+jets ch. [%]	-	-	-	-	-	±0.12
Z+jets cross-section [%]	-	-	-	-	-	-
Diboson cross-section [%]	-	-	-	-	-	-
Luminosity [%]	-	-	-	-	-	-

TABLE D.7: Fiducial phase-space relative differential cross-sections after combining the e+jets and μ+jets channels for the $t\bar{t}$ system transverse momentum $p_{\mathrm{T}}^{t\bar{t}}$. All uncertainties are quoted as a percentage with respect to the cross-section values in each bin. Dashes are used when the estimated relative systematic uncertainty for that bin is below 0.1%.

Bins [GeV]	0–35	35–75	75–125	125–170	170–225	225–800
$d\sigma$ / d $p_T^{t\bar{t}}$ [GeV]	$3.74 \cdot 10^{-1}$	$2.21 \cdot 10^{-1}$	$7.79 \cdot 10^{-2}$	$3.31 \cdot 10^{-2}$	$1.53 \cdot 10^{-2}$	$1.50 \cdot 10^{-3}$
Total Uncertainty [%]	±8.43	±10.2	±11.4	±10.8	±11.8	±10.1
Statistics [%]	±0.4	±0.5	±0.8	±1.2	±1.7	±1.7
Systematics [%]	±8.42	±10.1	±11.3	±10.7	±11.7	±9.95
η intercalibration model (JES) [%]	-	±0.49	±1.35	±1.40	±1.21	±0.86
Single particle high-p_T (JES) [%]	-	-	-	-	-	-
Effective stat. NP set 1 (JES) [%]	±0.53	±1.09	±1.61	±1.27	±1.06	±0.70
Effective stat. NP set 2 (JES) [%]	-	∓0.10	∓0.11	-	-	-
Effective stat. NP set 3 (JES) [%]	-	-	∓0.22	∓0.34	∓0.21	-
Effective detector NP set 1 (JES) [%]	-	-	±0.28	±0.65	±0.95	±1.51
Effective detector NP set 2 (JES) [%]	$^{+0.12}_{-}$	±0.22	±0.34	±0.26	$^{+0.14}_{-0.23}$	-
Effective detector NP set 3 (JES) [%]	-	-	-	-	-	$^{+0.16}_{-0.12}$
Effective mixed NP set 1 (JES) [%]	$^{+0.13}_{-}$	±0.27	±0.57	±0.79	±0.85	±1.07
Effective mixed NP set 2 (JES) [%]	∓0.22	∓0.45	∓0.69	∓0.59	∓0.49	$^{-0.23}_{+0.31}$
Effective model NP set 1 (JES) [%]	±1.15	±2.62	±4.55	±4.05	±3.53	±2.77
Effective model NP set 2 (JES) [%]	-	∓0.10	∓0.16	-	-	±0.24
Effective model NP set 3 (JES) [%]	±0.14	±0.20	-	$^{-0.14}_{-}$	-	-
Effective model NP set 4 (JES) [%]	-	-	-	$^{+0.13}_{-}$	$^{+0.11}_{-0.25}$	±0.24
Pile-up offset μ (JES) [%]	-	∓0.25	∓0.45	∓0.37	$^{-0.34}_{+0.23}$	$^{-}_{+0.21}$
Pile-up offset N_{PV} (JES) [%]	∓0.49	∓0.62	∓0.82	∓0.88	$^{-0.82}_{+1.10}$	∓0.60
Punch-through (JES) [%]	-	-	-	-	-	-
Pile-up offset ρ topology (JES) [%]	±0.89	±1.98	±3.24	±2.94	±2.61	±1.86
Pile-up offset p_T (JES) [%]	-	-	-	$^{+0.14}_{-}$	-	-
Flavour composition (JES) [%]	±0.55	±2.21	±4.36	±4.15	±3.65	±2.69
Flavour response (JES) [%]	∓0.21	∓1.32	∓2.91	∓3.00	∓2.75	∓2.16
b-Tagged jet energy scale (JES) [%]	±0.48	±0.55	±0.58	±0.56	±0.58	±0.43
Jet reconstruction efficiency [%]	-	-	∓0.12	-	-	-
Jet energy resolution [%]	-	-	-	-	-	-
b-Quark tagging efficiency [%]	±4.29	±4.23	±4.08	±4.00	±4.05	±4.41
c-Quark tagging efficiency [%]	±0.90	±0.97	±1.00	±0.96	±0.87	±0.83
Light-jet tagging efficiency [%]	±0.40	±0.57	±0.73	±0.69	±0.56	±0.47
Electron energy scale [%]	$^{-}_{-0.14}$	$^{-}_{-0.13}$	-	$^{-}_{-0.12}$	-	-
Electron energy resolution [%]	-	-	-	-	-	-
Muon momentum scale [%]	-	-	-	-	-	-
Muon (ID) momentum resolution [%]	-	-	-	-	-	-
Muon (MS) momentum resolution [%]	-	-	-	-	-	-
Lepton trigger efficiency [%]	±1.27	±1.26	±1.26	±1.26	±1.25	±1.25
Lepton reconstruction efficiency [%]	±0.24	±0.24	±0.25	±0.25	±0.25	±0.26
Lepton identification efficiency [%]	±1.31	±1.31	±1.32	±1.33	±1.34	±1.35
E_T^{miss} Soft jet scale [%]	∓1.36	±1.44	±1.29	±0.30	±0.30	±0.23
E_T^{miss} Soft jet resolution [%]	$^{-}_{-0.31}$	$^{+0.32}_{-}$	$^{+0.33}_{-}$	-	$^{-}_{+0.20}$	-
Jet vertex fraction [%]	∓0.70	∓0.60	∓0.66	∓0.72	∓0.62	∓0.43
Alternate hard-scattering model [%]	∓3.91	±0.67	±1.86	±0.31	±4.83	±2.84
Alternate parton-shower model [%]	∓2.84	∓0.33	±2.25	±1.17	±1.66	±1.50
Monte Carlo sample statistics [%]	±0.10	±0.12	±0.20	±0.32	±0.44	±0.40
ISR/FSR + scale [%]	$^{-4.13}_{+1.89}$	∓6.96	∓4.79	$^{-6.16}_{+3.70}$	∓5.95	∓5.23
Parton distribution functions [%]	-	-	±0.12	±0.12	-	-
Single top cross-section [%]	±0.28	±0.27	±0.24	±0.24	±0.26	±0.25
W+jets scale factors [%]	±0.44	±0.35	±0.30	±0.39	±0.54	±0.52
Fake lept. MC stat, e+jets ch. [%]	$^{+0.36}_{-}$	$^{+0.46}_{-}$	$^{+0.46}_{-}$	$^{-}_{+0.50}$	$^{+0.22}_{-}$	$^{+0.27}_{-}$
Fake lept. alternate fake CR, e+jets ch. [%]	±0.36	±0.38	±0.35	±0.37	±0.21	±0.21
Fake lept. alternate real CR, e+jets ch. [%]	-	-	-	-	-	-
Fake lept. alternate parametrization, e+jets ch. [%]	±0.25	±0.32	±0.36	±0.33	±0.24	±0.21
Fake lept. MC stat, μ+jets ch. [%]	-	-	-	-	-	-
Fake lept. alternate fake CR, μ+jets ch. [%]	±0.22	±0.25	±0.24	±0.16	±0.18	±0.21
Fake lept. alternate real CR, μ+jets ch. [%]	±0.23	±0.22	±0.19	±0.13	±0.28	±0.22
Fake lept. alternate parametrization, μ+jets ch. [%]	±0.23	±0.20	±0.24	±0.33	±0.29	±0.35
Z+jets cross-section [%]	±0.53	±0.48	±0.45	±0.45	±0.49	±0.50
Diboson cross-section [%]	-	-	-	-	-	-
Luminosity [%]	±2.80	±2.80	±2.80	±2.80	±2.80	±2.80

TABLE D.8: Fiducial phase-space absolute differential cross-sections after combining the e+jets and μ+jets channels for the $t\bar{t}$ system transverse momentum $p_{\mathrm{T}}^{t\bar{t}}$. All uncertainties are quoted as a percentage with respect to the cross-section values in each bin. Dashes are used when the estimated relative systematic uncertainty for that bin is below 0.1%.

Bins [Unit $\lvert y^{tt}\rvert$]	0–0.10	0.10–0.20	0.20–0.30	0.30–0.40	0.40–0.50	0.50–0.60	0.60–0.70	0.70–0.80	0.80–0.90	0.90–1	1–1.10	1.10–1.20	1.20–1.30	1.30–1.40	1.40–1.50	1.50–1.60	1.60–1.80	1.80–2.50
$1/\sigma \cdot \mathrm{d}\sigma$ / d $\lvert y^{tt}\rvert$	$1.09 \cdot 10^{0}$	$1.08 \cdot 10^{0}$	$1.04 \cdot 10^{0}$	$9.96 \cdot 10^{-1}$	$9.32 \cdot 10^{-1}$	$8.55 \cdot 10^{-1}$	$7.68 \cdot 10^{-1}$	$6.76 \cdot 10^{-1}$	$5.82 \cdot 10^{-1}$	$4.89 \cdot 10^{-1}$	$4.01 \cdot 10^{-1}$	$3.18 \cdot 10^{-1}$	$2.45 \cdot 10^{-1}$	$1.83 \cdot 10^{-1}$	$1.31 \cdot 10^{-1}$	$8.92 \cdot 10^{-2}$	$4.47 \cdot 10^{-2}$	$3.89 \cdot 10^{-3}$
Total Uncertainty [%]	$^{+1.07}_{-1.71}$	±1.06	±1.04	±1.20	±1.21	±1.18	±1.67	±1.36	±1.21	±1.61	±2.12	±2.30	±3.05	±4.09	±3.77	±4.97	±6.15	±11.2
Statistics [%]	±0.8	±0.7	±0.8	±0.8	±0.8	±0.8	±0.9	±1.0	±1.1	±1.2	±1.4	±1.6	±1.8	±2.2	±2.7	±3.4	±4.2	±8.3
Systematics [%]	$^{+0.64}_{-1.47}$	±0.72	$^{+0.75}_{-0.49}$	±0.85	$^{+0.98}_{-0.64}$	$^{+0.88}_{-0.56}$	±1.33	$^{+1.01}_{-0.75}$	$^{+0.46}_{-0.30}$	$^{+0.72}_{-1.14}$	±1.50	±1.56	±2.35	±3.40	±2.55	±3.50	$^{+5.15}_{-3.57}$	±7.38
η intercalibration model (JES) [%]	∓0.28	$^{-0.15}_{+0.26}$	$^{-0.21}_{+0.16}$	$^{-0.13}_{+0.17}$	∓0.15	-	-	-	$^{+0.18}_{-}$	$^{+0.21}_{-0.28}$	±0.41	$^{+0.49}_{-0.37}$	±0.54	±0.58	$^{+0.57}_{-0.86}$	±0.95	±0.94	$^{+1.19}_{-0.46}$
Single particle high-p_T (JES) [%]	-	-	-	-	-	-	-	-	-	-	-	-	-	-	-	-	-	-
Effective stat. NP set 1 (JES) [%]	-	-	-	-	-	-	-	-	-	-	-	-	-	-	±0.12	-	$^{-}_{+0.29}$	$^{+0.36}_{-}$
Effective stat. NP set 2 (JES) [%]	-	-	-	-	-	-	-	-	-	-	-	-	-	-	-	-	-	-
Effective stat. NP set 3 (JES) [%]	-	-	-	-	-	-	-	-	-	-	-	-	-	-	-	$^{-0.27}_{+0.14}$	-	-
Effective detector NP set 1 (JES) [%]	-	-	-	-	-	-	-	-	-	-	-	-	-	-	$^{-}_{-0.22}$	$^{+0.11}_{-0.35}$	-	$^{-0.16}_{+0.31}$
Effective detector NP set 2 (JES) [%]	-	-	-	-	-	-	-	-	-	-	-	-	-	-	-	-	-	-
Effective detector NP set 3 (JES) [%]	-	-	-	-	-	-	-	-	-	-	-	-	-	-	-	-	-	-
Effective mixed NP set 1 (JES) [%]	-	-	-	-	-	-	-	-	-	-	-	-	-	-	$^{+0.10}_{-0.15}$	$^{+0.11}_{-0.28}$	-	$^{-0.11}_{+0.34}$
Effective mixed NP set 2 (JES) [%]	-	-	-	-	-	-	-	-	-	-	-	-	-	-	-	-	-	-
Effective model NP set 1 (JES) [%]	-	-	-	-	-	-	-	-	-	$^{-}_{-0.14}$	±0.14	-	-	$^{-}_{-0.23}$	$^{+0.54}_{-0.37}$	-	$^{+0.23}_{-}$	$^{-}_{+0.41}$
Effective model NP set 2 (JES) [%]	-	-	-	-	-	-	-	-	-	-	-	-	-	-	-	-	-	-
Effective model NP set 3 (JES) [%]	-	-	-	-	-	-	-	-	-	-	-	-	-	-	-	$^{-0.23}_{-}$	-	-
Effective model NP set 4 (JES) [%]	-	-	-	-	-	-	-	-	-	-	-	-	-	-	-	-	-	-
Pile-up offset μ (JES) [%]	-	-	-	-	-	-	-	-	-	-	∓0.12	-	∓0.15	$^{-0.23}_{+0.11}$	-	∓0.28	∓0.32	$^{-0.13}_{+0.36}$
Pile-up offset N_{PV} (JES) [%]	-	-	-	-	-	-	-	-	-	-	-	-	-	-	-	$^{-}_{-0.27}$	$^{+0.31}_{-}$	$^{-}_{+0.17}$
Punch-through (JES) [%]	-	-	-	-	-	-	-	-	-	-	-	-	-	-	-	-	-	-
Pile-up offset ρ topology (JES) [%]	-	-	-	-	-	-	-	-	-	-	-	-	$^{+0.12}_{-}$	$^{-}_{-0.26}$	±0.32	-	-	$^{+0.48}_{-}$
Pile-up offset p_T (JES) [%]	-	-	-	-	-	-	-	-	-	-	-	-	-	-	$^{-}_{-0.23}$	-	-	$^{-0.23}_{+0.17}$
Flavour composition (JES) [%]	-	-	-	-	-	-	-	-	-	-	±0.20	-	-	$^{-}_{-0.49}$	±0.40	$^{+0.22}_{-0.15}$	$^{+0.43}_{-}$	$^{-0.62}_{+0.36}$
Flavour response (JES) [%]	-	-	-	-	-	-	-	-	-	-	-	-	$^{-0.21}_{+0.12}$	-	∓0.33	-	$^{-0.14}_{+0.47}$	$^{+0.56}_{-}$
b-Tagged jet energy scale (JES) [%]	-	-	-	-	-	-	-	-	-	-	-	-	-	-	±0.15	-	$^{-}_{+0.30}$	$^{+0.13}_{-0.37}$
Jet reconstruction efficiency [%]	-	-	-	-	-	-	-	-	-	-	-	-	-	-	-	-	-	∓0.12
Jet energy resolution [%]	-	-	-	-	-	-	-	-	-	-	-	-	-	-	-	-	-	-
b-Quark tagging efficiency [%]	-	-	-	-	-	-	-	-	-	-	-	-	-	-	-	-	-	-
c-Quark tagging efficiency [%]	-	-	-	-	-	-	-	-	-	-	-	-	-	-	-	-	-	-
Light-jet tagging efficiency [%]	-	-	-	-	-	-	-	-	-	-	-	-	-	-	-	-	-	±0.29
Electron energy scale [%]	-	-	-	-	-	-	-	-	-	-	-	±0.12	-	±0.16	$^{+0.10}_{-0.32}$	$^{+0.20}_{-}$	±0.26	$^{+0.38}_{-1.22}$
Electron energy resolution [%]	-	-	-	-	-	-	-	-	-	-	-	-	-	-	-	-	-	-
Muon momentum scale [%]	-	-	-	-	-	-	-	-	-	-	-	-	-	-	-	-	-	$^{-}_{-0.22}$
Muon (ID) momentum resolution [%]	-	-	-	-	-	-	-	-	-	-	-	-	-	-	-	-	-	-
Muon (MS) momentum resolution [%]	-	-	-	-	-	-	-	-	-	∓0.11	-	±0.12	-	∓0.18	-	-	-	∓0.49
Lepton trigger efficiency [%]	-	-	-	-	-	-	-	-	-	-	-	±0.11	±0.15	±0.19	±0.23	±0.29	±0.38	±0.63
Lepton reconstruction efficiency [%]	-	-	-	-	-	-	-	-	-	-	-	-	-	-	-	-	±0.11	±0.19
Lepton identification efficiency [%]	-	-	-	-	-	-	-	-	-	-	-	-	-	-	-	-	-	-
E_T^{miss} Soft jet scale [%]	-	-	-	-	-	-	-	-	-	-	-	-	-	-	$^{-0.22}_{-}$	$^{+0.34}_{-}$	-	-
E_T^{miss} Soft jet resolution [%]	-	-	-	-	-	-	∓0.12	-	-	-	-	$^{-}_{+0.16}$	-	$^{-}_{-0.21}$	$^{-}_{-0.26}$	$^{+0.49}_{-}$	$^{-}_{-0.30}$	$^{-}_{-0.28}$
Jet vertex fraction [%]	-	-	-	-	-	-	-	-	-	-	-	-	-	-	-	-	$^{-}_{-0.16}$	-
Alternate hard-scattering model [%]	±0.43	±0.49	±0.16	±0.54	∓0.53	∓0.35	∓0.50	±0.68	±0.13	∓0.44	∓1.01	±0.65	±1.08	∓2.40	∓1.33	∓2.33	±0.83	∓6.47
Alternate parton-shower model [%]	±0.19	±0.19	∓0.28	∓0.54	±0.16	∓0.37	∓1.02	∓0.14	±0.12	∓0.36	±0.42	±0.95	±1.76	±1.41	±1.31	±0.18	±2.74	∓1.62
Monte Carlo sample statistics [%]	±0.20	±0.19	±0.20	±0.20	±0.20	±0.22	±0.23	±0.25	±0.27	±0.30	±0.33	±0.37	±0.44	±0.51	±0.62	±0.80	±0.90	±1.84
ISR/FSR + scale [%]	$^{+0.13}_{-1.31}$	$^{-}_{-0.38}$	$^{+0.53}_{-}$	$^{+0.25}_{-}$	$^{+0.75}_{-}$	$^{+0.63}_{-}$	$^{-}_{-0.91}$	$^{+0.69}_{-}$	$^{+0.21}_{-}$	$^{-}_{-0.81}$	$^{-0.98}_{+0.46}$	$^{-0.73}_{+0.46}$	$^{-}_{-0.45}$	$^{-1.70}_{+1.04}$	$^{-1.15}_{+0.31}$	$^{-0.70}_{+1.22}$	$^{-0.68}_{+3.57}$	$^{+0.13}_{-0.41}$
Parton distribution functions [%]	-	-	-	-	-	-	-	-	-	-	-	-	±0.13	-	-	±0.42	±0.63	±0.42
Single top cross-section [%]	-	-	-	-	-	-	-	-	-	-	-	-	-	-	-	-	-	-
W+jets scale factors [%]	-	-	-	-	-	-	-	-	-	-	-	-	-	-	-	-	-	∓0.21
Fake lept. MC stat, e+jets ch. [%]	-	-	-	-	-	-	-	$^{-}_{-0.14}$	-	-	±0.11	$^{+0.26}_{-}$	$^{+0.35}_{-}$	±0.12	$^{-}_{-0.43}$	±0.13	$^{+0.56}_{-0.15}$	$^{+0.38}_{-0.22}$
Fake lept. alternate fake CR, e+jets ch. [%]	-	-	-	±0.10	-	-	-	-	-	-	-	-	-	-	∓0.23	-	-	∓0.12
Fake lept. alternate real CR, e+jets ch. [%]	-	-	-	-	-	-	-	-	-	-	-	-	±0.11	-	-	-	±0.12	±0.30
Fake lept. alternate parametrization, e+jets ch. [%]	-	-	-	-	-	∓0.10	∓0.12	-	-	-	-	-	-	∓0.26	-	-	∓0.13	-
Fake lept. MC stat, μ+jets ch. [%]	-	-	-	-	-	-	-	-	-	-	-	-	-	$^{+0.24}_{-}$	$^{+0.23}_{-}$	$^{+0.86}_{-}$	$^{+0.57}_{-}$	$^{+1.75}_{-}$
Fake lept. alternate fake CR, μ+jets ch. [%]	-	-	-	-	-	-	-	-	-	-	-	-	∓0.10	-	-	±0.11	±0.28	±0.74
Fake lept. alternate real CR, μ+jets ch. [%]	∓0.24	∓0.25	∓0.20	∓0.13	-	∓0.12	∓0.10	-	-	±0.23	±0.35	±0.58	±0.62	±0.77	±0.64	±1.65	±1.25	±1.94
Fake lept. alternate parametrization, μ+jets ch. [%]	-	-	-	-	-	-	-	-	-	±0.10	-	±0.12	±0.37	±0.54	±0.50	±0.90	±0.78	±0.20
Z+jets cross-section [%]	-	-	-	-	-	-	-	-	-	-	-	-	-	-	-	-	-	-
Diboson cross-section [%]	-	-	-	-	-	-	-	-	-	-	-	-	-	-	-	-	-	-
Luminosity [%]	-	-	-	-	-	-	-	-	-	-	-	-	-	-	-	-	-	-

TABLE D.9: Fiducial phase-space relative differential cross-sections after combining the e+jets and μ+jets channels for the $t\bar{t}$ system rapidity $\left|y^{t\bar{t}}\right|$. All uncertainties are quoted as a percentage with respect to the cross-section values in each bin. Dashes are used when the estimated relative systematic uncertainty for that bin is below 0.1%.

Bins [Unit $\lvert y^{t\bar{t}}\rvert$]	0–0.10	0.10–0.20	0.20–0.30	0.30–0.40	0.40–0.50	0.50–0.60	0.60–0.70	0.70–0.80	0.80–0.90	0.90–1	1–1.10	1.10–1.20	1.20–1.30	1.30–1.40	1.40–1.50	1.50–1.60	1.60–1.80	1.80–2.50
$\mathrm{d}\sigma$ / d $\lvert y^{t\bar{t}}\rvert$ [Unit $\lvert y^{t\bar{t}}\rvert$]	$3.18 \cdot 10^{1}$	$3.12 \cdot 10^{1}$	$3.03 \cdot 10^{1}$	$2.89 \cdot 10^{1}$	$2.70 \cdot 10^{1}$	$2.48 \cdot 10^{1}$	$2.23 \cdot 10^{1}$	$1.96 \cdot 10^{1}$	$1.69 \cdot 10^{1}$	$1.42 \cdot 10^{1}$	$1.16 \cdot 10^{1}$	$9.22 \cdot 10^{0}$	$7.12 \cdot 10^{0}$	$5.31 \cdot 10^{0}$	$3.81 \cdot 10^{0}$	$2.59 \cdot 10^{0}$	$1.30 \cdot 10^{0}$	$13 \cdot 10^{-1}$
Total Uncertainty [%]	±8.18	±8.34	±8.68	±8.59	±8.58	±8.45	±8.84	±8.65	±8.57	±9.01	±9.37	±9.10	±9.05	±10.4	±10.1	±10.7	±11.2	±14.7
Statistics [%]	±0.8	±0.7	±0.8	±0.8	±0.9	±0.9	±1.0	±1.0	±1.1	±1.2	±1.4	±1.6	±1.9	±2.2	±2.7	±3.4	±4.2	±8.3
Systematics [%]	±8.12	±8.30	±8.64	±8.54	±8.53	±8.38	±8.78	±8.58	±8.49	±8.91	±9.27	±8.94	±8.84	±10.1	±9.71	±10.1	±10.4	±11.9
η intercalibration model (JES) [%]	±0.14	$^{+0.27}_{-0.16}$	±0.23	±0.27	±0.28	±0.34	$^{+0.39}_{-0.52}$	±0.51	±0.56	±0.67	±0.83	±0.85	±0.96	±1.01	±1.15	±1.38	±1.36	$^{+1.63}_{-0.88}$
Single particle high-p_T (JES) [%]	-	-	-	-	-	-	-	-	-	-	-	-	-	-	-	-	-	-
Effective stat. NP set 1 (JES) [%]	±0.89	±0.88	±0.89	±0.92	±0.91	±0.86	±0.87	±0.90	±0.90	±0.93	±0.88	±0.86	±0.94	±0.91	±1.02	±0.92	$^{+0.84}_{-0.59}$	$^{+1.20}_{-0.52}$
Effective stat. NP set 2 (JES) [%]	-	-	-	-	-	-	-	-	-	-	-	-	-	-	-	-	-	−0.21
Effective stat. NP set 3 (JES) [%]	-	-	-	-	-	-	-	-	-	-	-	-	-	-	-	$^{-0.31}_{+0.17}$	-	-
Effective detector NP set 1 (JES) [%]	±0.17	±0.22	±0.15	±0.12	±0.22	±0.17	±0.14	±0.19	±0.21	±0.23	$^{+0.18}_{-0.27}$	$^{+0.31}_{-0.20}$	$^{+0.27}_{-0.19}$	±0.19	$^{+0.21}_{-0.40}$	$^{+0.30}_{-0.53}$	$^{+0.35}_{-0.15}$	-
Effective detector NP set 2 (JES) [%]	±0.17	±0.20	±0.18	±0.18	±0.17	±0.18	±0.15	±0.15	±0.17	±0.21	±0.17	$^{+0.19}_{-0.14}$	±0.20	$^{+0.18}_{-0.11}$	±0.20	$^{+0.15}_{-0.30}$	$^{+0.21}_{-}$	-
Effective detector NP set 3 (JES) [%]	-	-	-	-	-	-	-	-	-	-	-	-	-	-	-	-	-	−0.22
Effective mixed NP set 1 (JES) [%]	±0.28	±0.32	±0.27	±0.25	±0.32	±0.29	±0.27	±0.29	±0.28	±0.38	±0.35	±0.35	$^{+0.43}_{-0.32}$	±0.29	±0.42	$^{+0.42}_{-0.58}$	$^{+0.35}_{-0.24}$	-
Effective mixed NP set 2 (JES) [%]	∓0.36	∓0.40	∓0.37	∓0.38	∓0.40	∓0.37	∓0.32	∓0.36	∓0.38	∓0.40	∓0.38	∓0.42	∓0.45	∓0.39	∓0.40	∓0.36	$^{-0.22}_{+0.38}$	∓0.33
Effective model NP set 1 (JES) [%]	±2.29	±2.22	±2.28	±2.30	±2.25	±2.23	±2.30	±2.25	±2.28	±2.42	±2.44	±2.33	±2.38	±2.33	±2.76	±2.36	±2.42	±2.05
Effective model NP set 2 (JES) [%]	-	-	-	∓0.10	-	-	-	-	-	-	-	-	-	-	∓0.12	-	-	-
Effective model NP set 3 (JES) [%]	±0.15	±0.12	±0.12	±0.14	$^{+0.16}_{-0.12}$	±0.11	$^{+0.12}_{-0.16}$	±0.12	$^{+0.16}_{-0.11}$	±0.13	-0.14	-	$^{+0.14}_{-}$	$^{+0.14}_{-0.10}$	-0.16	-	$^{+0.21}_{-}$	−0.21
Effective model NP set 4 (JES) [%]	-	-	-	-	-	-	-	-	-	-	-	-	-	-	-	-	-	−0.18
Pile-up offset μ (JES) [%]	∓0.14	∓0.16	∓0.13	∓0.14	$^{-0.10}_{+0.18}$	$^{-}_{+0.15}$	$^{-0.16}_{+0.12}$	$^{-0.24}_{+0.18}$	∓0.21	∓0.25	∓0.30	$^{-0.17}_{+0.24}$	∓0.33	$^{-0.41}_{+0.30}$	$^{-0.26}_{+0.12}$	∓0.46	∓0.50	$^{-0.31}_{+0.55}$
Pile-up offset N_{PV} (JES) [%]	∓0.57	∓0.61	∓0.62	∓0.61	∓0.62	∓0.58	∓0.66	∓0.66	$^{-0.47}_{+0.62}$	∓0.61	∓0.57	∓0.69	∓0.70	∓0.52	$^{-0.42}_{+0.61}$	$^{-0.83}_{+0.35}$	$^{-0.28}_{+0.56}$	∓0.73
Punch-through (JES) [%]	-	-	-	-	-	-	-	-	-	-	-	-	-	-	-	-	-	-
Pile-up offset ρ topology (JES) [%]	±1.71	±1.67	±1.69	±1.69	±1.71	±1.62	±1.67	±1.72	±1.73	±1.75	±1.75	±1.78	±1.81	±1.75	±2.04	±1.68	±1.80	$^{+1.94}_{-1.22}$
Pile-up offset p_T (JES) [%]	-	-	-	-	-	-	-	-	-	-	-	-	-	-	-0.23	-	-	$^{-0.23}_{+0.16}$
Flavour composition (JES) [%]	±1.85	±1.79	±1.79	±1.92	±1.85	±1.82	±1.86	±1.97	±1.81	±1.91	±2.08	±1.92	±1.98	±2.11	±2.28	±2.07	±2.09	±1.39
Flavour response (JES) [%]	∓1.18	∓1.12	∓1.11	∓1.21	∓1.13	∓1.07	∓1.15	∓1.21	∓1.17	∓1.23	∓1.26	∓1.23	∓1.34	∓1.26	∓1.51	∓1.17	∓1.48	$^{-0.62}_{+1.17}$
b-Tagged jet energy scale (JES) [%]	±0.51	±0.51	±0.55	±0.46	±0.52	±0.53	±0.50	±0.49	±0.56	±0.59	±0.49	±0.54	±0.55	±0.52	±0.67	±0.55	$^{+0.52}_{-0.22}$	$^{+0.66}_{-0.90}$
Jet reconstruction efficiency [%]	-	-	-	-	-	-	-	-	-	-	-	-	-	-	-	-	-	∓0.17
Jet energy resolution [%]	-	-	-	-	-	-	-	-	-	-	-	-	-	-	-	-	-	-
b-Quark tagging efficiency [%]	±4.21	±4.22	±4.23	±4.22	±4.22	±4.24	±4.22	±4.22	±4.23	±4.23	±4.21	±4.24	±4.24	±4.21	±4.25	±4.23	±4.25	±4.29
c-Quark tagging efficiency [%]	±0.96	±0.95	±0.95	±0.96	±0.95	±0.94	±0.93	±0.92	±0.90	±0.92	±0.92	±0.89	±0.89	±0.90	±0.87	±0.86	±0.88	±0.88
Light-jet tagging efficiency [%]	±0.52	±0.48	±0.51	±0.50	±0.50	±0.52	±0.52	±0.50	±0.52	±0.52	±0.54	±0.57	±0.54	±0.55	±0.50	±0.52	±0.58	±0.81
Electron energy scale [%]	-	-	-	-	-	-	-0.17	±0.11	$^{+0.12}_{-0.21}$	-0.24	±0.17	±0.22	-0.20	±0.28	$^{+0.18}_{-0.46}$	$^{+0.28}_{-0.19}$	±0.36	$^{+0.45}_{-1.36}$
Electron energy resolution [%]	-	-	-	-	-	-	-	-	-	-	-	-	-	-	-	-	-	-
Muon momentum scale [%]	-	-	-	-	-	-	-	-	-	-	-	-	-	-	-	-	-	−0.24
Muon (ID) momentum resolution [%]	-	-	-	-	-	-	-	-	-	-	-	-	-	-	-	-	-	-
Muon (MS) momentum resolution [%]	-	-	-	-	-	-	-	-	-	∓0.11	-	±0.12	-	∓0.18	-	-	-	∓0.49
Lepton trigger efficiency [%]	±1.21	±1.21	±1.22	±1.22	±1.23	±1.24	±1.25	±1.27	±1.29	±1.32	±1.35	±1.38	±1.42	±1.46	±1.50	±1.56	±1.65	±1.90
Lepton reconstruction efficiency [%]	±0.23	±0.23	±0.23	±0.23	±0.23	±0.23	±0.24	±0.24	±0.24	±0.25	±0.26	±0.26	±0.28	±0.29	±0.31	±0.33	±0.36	±0.44
Lepton identification efficiency [%]	±1.33	±1.33	±1.33	±1.33	±1.33	±1.32	±1.31	±1.30	±1.30	±1.29	±1.28	±1.27	±1.26	±1.26	±1.26	±1.28	±1.30	±1.41
E_T^{miss} Soft jet scale [%]	-	-	-	-	-	-	-	-	-	-	-	-	-	-	-0.22	$^{+0.34}_{-}$	-	-
E_T^{miss} Soft jet resolution [%]	-	-	-	-	-	-	∓0.12	-	-	-	-	$^{-}_{+0.15}$	-	-	-	$^{+0.48}_{-}$	-	-
Jet vertex fraction [%]	∓0.65	∓0.69	∓0.67	∓0.64	∓0.65	∓0.66	∓0.66	∓0.63	∓0.65	∓0.64	∓0.61	∓0.66	∓0.69	∓0.63	∓0.65	∓0.67	$^{-0.62}_{+0.44}$	$^{-0.71}_{+0.40}$
Alternate hard-scattering model [%]	∓0.68	∓0.61	∓0.94	∓0.57	∓1.64	∓1.45	∓1.61	∓0.43	∓0.98	∓1.54	∓2.11	∓0.46	-	∓3.49	∓2.42	∓3.41	∓0.28	∓7.51
Alternate parton-shower model [%]	∓0.68	∓0.68	∓1.16	∓1.41	∓0.71	∓1.24	∓1.89	∓1.01	∓0.75	∓1.24	∓0.45	-	±0.87	±0.52	±0.42	∓0.69	±1.84	∓2.48
Monte Carlo sample statistics [%]	±0.21	±0.20	±0.20	±0.21	±0.21	±0.23	±0.24	±0.26	±0.28	±0.31	±0.33	±0.38	±0.44	±0.52	±0.62	±0.80	±0.91	±1.84
ISR/FSR + scale [%]	$^{-5.68}_{+2.56}$	$^{-5.74}_{+3.53}$	∓5.10	$^{-5.56}_{+4.09}$	∓4.82	$^{-5.20}_{+3.90}$	$^{-6.47}_{+2.98}$	∓5.03	$^{-5.60}_{+4.06}$	$^{-6.57}_{+3.51}$	$^{-6.73}_{+4.41}$	$^{-6.49}_{+4.41}$	$^{-6.23}_{+3.81}$	$^{-7.41}_{+5.02}$	$^{-6.89}_{+4.26}$	∓5.83	∓7.05	$^{-5.68}_{+3.50}$
Parton distribution functions [%]	-	-	-	-	-	-	-	-	-	-	-	±0.10	±0.18	±0.12	-	±0.48	±0.69	±0.47
Single top cross-section [%]	±0.29	±0.28	±0.28	±0.29	±0.27	±0.26	±0.28	±0.26	±0.23	±0.26	±0.26	±0.22	±0.23	±0.20	±0.17	±0.19	±0.22	±0.23
W+jets scale factors [%]	±0.42	±0.39	±0.40	±0.41	±0.41	±0.44	±0.40	±0.35	±0.35	±0.36	±0.37	±0.39	±0.32	±0.36	±0.43	±0.32	±0.39	±0.18
Fake lept. MC stat, e+jets ch. [%]	$^{-}_{+0.46}$	$^{-}_{+0.48}$	$^{-}_{+0.48}$	$^{-}_{+0.47}$	$^{+0.39}_{-}$	$^{+0.44}_{-}$	$^{-}_{+0.40}$	$^{+0.26}_{-}$	$^{+0.39}_{-}$	$^{+0.33}_{-}$	$^{+0.29}_{-}$	$^{+0.34}_{-}$	$^{+0.39}_{-}$	$^{+0.25}_{-}$	$^{-0.40}_{-}$	$^{+0.26}_{-}$	$^{+0.59}_{-}$	+0.41
Fake lept. alternate fake CR, e+jets ch. [%]	±0.41	±0.39	±0.38	±0.45	±0.36	±0.33	±0.31	±0.30	±0.34	±0.27	±0.32	±0.33	±0.27	±0.25	±0.12	±0.27	±0.27	±0.23
Fake lept. alternate real CR, e+jets ch. [%]	-	-	-	-	-	-	-	-	-	-	-	-	-	-	-	-	-	±0.27
Fake lept. alternate parametrization, e+jets ch. [%]	±0.34	±0.33	±0.34	±0.36	±0.26	±0.19	±0.16	±0.33	±0.34	±0.30	±0.23	±0.21	±0.37	-	±0.35	±0.23	±0.16	±0.33
Fake lept. MC stat, μ+jets ch. [%]	-	-	-	-	-	-	-	-	-	-	-	-	-	$^{-}_{+0.29}$	$^{-}_{+0.28}$	$^{-}_{+0.92}$	$^{-}_{+0.63}$	+1.81
Fake lept. alternate fake CR, μ+jets ch. [%]	±0.26	±0.25	±0.27	±0.20	±0.14	±0.24	±0.32	±0.24	±0.13	±0.21	±0.16	±0.18	±0.13	±0.30	±0.23	±0.35	±0.51	±0.98
Fake lept. alternate real CR, μ+jets ch. [%]	-	-	-	±0.10	±0.14	±0.11	±0.13	±0.21	±0.30	±0.48	±0.59	±0.82	±0.86	±1.01	±0.88	±1.90	±1.50	±2.18
Fake lept. alternate parametrization, μ+jets ch. [%]	±0.15	±0.14	±0.16	±0.16	±0.21	±0.21	±0.20	±0.17	±0.30	±0.34	±0.16	±0.37	±0.61	±0.79	±0.75	±1.15	±1.03	±0.45
Z+jets cross-section [%]	±0.51	±0.47	±0.50	±0.49	±0.51	±0.51	±0.49	±0.52	±0.50	±0.47	±0.46	±0.50	±0.50	±0.49	±0.42	±0.50	±0.41	±0.55
Diboson cross-section [%]	-	-	-	-	-	-	-	-	-	-	-	-	-	-	-	-	-	-
Luminosity [%]	±2.80	±2.80	±2.80	±2.80	±2.80	±2.80	±2.80	±2.80	±2.80	±2.80	±2.80	±2.80	±2.80	±2.80	±2.80	±2.80	±2.80	±2.80

TABLE D.10: Fiducial phase-space absolute differential cross-sections after combining the e+jets and μ+jets channels for the $t\bar{t}$ system rapidity $\lvert y^{t\bar{t}}\rvert$. All uncertainties are quoted as a percentage with respect to the cross-section values in each bin. Dashes are used when the estimated relative systematic uncertainty for that bin is below 0.1%.

Bins [GeV]	0–40	40–80	80–120	120–170	170–230	230–600
$1/\sigma \cdot \mathrm{d}\sigma$ / d $\lvert p_{out}^{tt} \rvert$	$1.85 \cdot 10^{-2}$	$4.37 \cdot 10^{-3}$	$1.29 \cdot 10^{-3}$	$4.23 \cdot 10^{-4}$	$1.28 \cdot 10^{-4}$	$1.00 \cdot 10^{-5}$
Total Uncertainty [%]	± 1.31	± 4.08	± 4.88	± 3.79	± 6.98	$^{+9.89}_{-7.16}$
Statistics [%]	± 0.1	± 0.7	± 1.2	± 2.0	± 3.5	± 5.0
Systematics [%]	± 1.29	± 4.02	± 4.70	± 3.12	± 5.94	$^{+8.40}_{-4.89}$
η intercalibration model (JES) [%]	∓ 0.22	± 0.57	± 0.95	± 0.69	$^{+0.93}_{-0.11}$	$^{-}_{-0.47}$
Single particle high-p_T (JES) [%]	-	-	-	-	-	-
Effective stat. NP set 1 (JES) [%]	∓ 0.10	± 0.42	$^{+0.20}_{-0.37}$	∓ 0.21	$^{-0.16}_{+0.61}$	∓ 0.62
Effective stat. NP set 2 (JES) [%]	-	-	-	-	$^{+0.16}_{-}$	$^{+0.10}_{-0.14}$
Effective stat. NP set 3 (JES) [%]	-	-	∓ 0.35	∓ 0.38	$^{-}_{+0.29}$	$^{-0.37}_{+0.20}$
Effective detector NP set 1 (JES) [%]	∓ 0.11	± 0.12	± 0.49	± 0.76	± 1.19	± 1.39
Effective detector NP set 2 (JES) [%]	-	-	-	$^{-}_{+0.12}$	-	∓ 0.15
Effective detector NP set 3 (JES) [%]	-	-	-	-	$^{+0.18}_{-0.10}$	$^{-}_{-0.15}$
Effective mixed NP set 1 (JES) [%]	∓ 0.11	± 0.21	± 0.51	± 0.52	$^{+0.97}_{-0.56}$	$^{+0.75}_{-0.98}$
Effective mixed NP set 2 (JES) [%]	-	$^{-0.21}_{+0.16}$	$^{-0.25}_{+0.13}$	-	$^{+0.35}_{-}$	$^{+0.14}_{-0.22}$
Effective model NP set 1 (JES) [%]	∓ 0.46	± 1.35	± 1.72	± 0.78	$^{+0.51}_{-}$	$^{-}_{-0.27}$
Effective model NP set 2 (JES) [%]	-	-	-	± 0.10	$^{+0.31}_{-0.10}$	$^{+0.22}_{-0.29}$
Effective model NP set 3 (JES) [%]	-	-	∓ 0.27	∓ 0.42	$^{-0.13}_{+0.34}$	$^{-0.37}_{+0.21}$
Effective model NP set 4 (JES) [%]	-	-	-	$^{+0.13}_{-}$	$^{+0.27}_{-0.19}$	± 0.31
Pile-up offset μ (JES) [%]	-	$^{-0.24}_{+0.13}$	∓ 0.15	$^{-0.11}_{+0.22}$	$^{+0.28}_{-}$	$^{+0.10}_{-0.27}$
Pile-up offset N_{PV} (JES) [%]	-	$^{-0.15}_{+0.20}$	$^{-0.15}_{-}$	$^{-}_{-0.32}$	$^{+0.39}_{-}$	$^{-}_{-}$
Punch-through (JES) [%]	-	-	-	-	-	$^{+0.12}_{-0.17}$
Pile-up offset ρ topology (JES) [%]	∓ 0.31	± 0.95	± 1.12	± 0.45	$^{+0.31}_{-}$	$^{-0.57}_{-}$
Pile-up offset p_T (JES) [%]	-	-	-	-	-	-
Flavour composition (JES) [%]	∓ 0.51	± 1.50	± 1.92	± 0.85	$^{+0.45}_{-}$	$^{-0.59}_{-}$
Flavour response (JES) [%]	± 0.40	∓ 1.06	∓ 1.62	∓ 0.99	$^{-0.15}_{+0.90}$	$^{-}_{-0.79}$
b-Tagged jet energy scale (JES) [%]	-	-	$^{+0.14}_{-0.23}$	$^{+0.23}_{-0.35}$	$^{+0.32}_{-}$	$^{+0.25}_{-0.64}$
Jet reconstruction efficiency [%]	-	-	-	-	± 0.11	-
Jet energy resolution [%]	-	-	-	-	-	-
b-Quark tagging efficiency [%]	-	-	∓ 0.23	∓ 0.21	-	± 0.57
c-Quark tagging efficiency [%]	-	-	-	-	∓ 0.15	∓ 0.30
Light-jet tagging efficiency [%]	-	± 0.14	± 0.18	-	-	-
Electron energy scale [%]	-	-	-	-	-	-
Electron energy resolution [%]	-	-	-	-	-	-
Muon momentum scale [%]	-	-	-	-	-	-
Muon (ID) momentum resolution [%]	-	-	-	-	-	-
Muon (MS) momentum resolution [%]	-	-	-	-	-	-
Lepton trigger efficiency [%]	-	-	-	-	-	-
Lepton reconstruction efficiency [%]	-	-	-	-	-	-
Lepton identification efficiency [%]	-	-	-	-	-	-
E_T^{miss} Soft jet scale [%]	∓ 0.42	± 1.48	± 0.91	$^{+0.54}_{-0.39}$	± 0.21	± 0.11
E_T^{miss} Soft jet resolution [%]	-	$^{+0.28}_{-}$	$^{+0.28}_{-}$	-	-	-
Jet vertex fraction [%]	-	-	$^{+0.15}_{-0.20}$	± 0.31	± 0.48	$^{+0.74}_{-0.51}$
Alternate hard-scattering model [%]	∓ 0.56	± 1.64	± 1.53	± 0.41	± 5.34	∓ 0.13
Alternate parton-shower model [%]	∓ 0.34	± 0.47	± 2.18	± 1.83	± 0.93	± 4.03
Monte Carlo sample statistics [%]	-	± 0.17	± 0.32	± 0.53	± 0.90	± 1.23
ISR/FSR + scale [%]	$^{+0.20}_{-0.60}$	$^{-1.56}_{+2.41}$	$^{+1.70}_{-0.27}$	$^{+1.56}_{-}$	$^{-0.87}_{-}$	$^{+7.03}_{-}$
Parton distribution functions [%]	-	-	-	± 0.10	-	-
Single top cross-section [%]	-	-	-	-	-	-
W+jets scale factors [%]	-	-	-	-	± 0.40	± 0.36
Fake lept. MC stat, e+jets ch. [%]	-	-	-	$^{+0.26}_{-}$	$^{+0.21}_{-0.28}$	± 0.33
Fake lept. alternate fake CR, e+jets ch. [%]	-	-	-	-	∓ 0.31	∓ 0.30
Fake lept. alternate real CR, e+jets ch. [%]	-	-	-	-	-	-
Fake lept. alternate parametrization, e+jets ch. [%]	-	-	-	-	∓ 0.19	∓ 0.18
Fake lept. MC stat, μ+jets ch. [%]	-	-	-	$^{+0.25}_{-}$	-	-
Fake lept. alternate fake CR, μ+jets ch. [%]	-	-	-	∓ 0.17	-	± 0.28
Fake lept. alternate real CR, μ+jets ch. [%]	-	-	-	-	± 0.17	∓ 0.32
Fake lept. alternate parametrization, μ+jets ch. [%]	-	-	-	-	± 0.93	∓ 0.16
Z+jets cross-section [%]	-	-	-	-	± 0.16	± 0.15
Diboson cross-section [%]	-	-	-	-	-	-
Luminosity [%]	-	-	-	-	-	-

TABLE D.11: Fiducial phase-space relative differential cross-sections after combining the e+jets and μ+jets channels for the $t\bar{t}$ system out-of-plane momentum $\left|p_{\mathrm{out}}^{t\bar{t}}\right|$. All uncertainties are quoted as a percentage with respect to the cross-section values in each bin. Dashes are used when the estimated relative systematic uncertainty for that bin is below 0.1%.

Bins [GeV]	0–40	40–80	80–120	120–170	170–230	230–600
$\mathrm{d}\sigma$ / d $\lvert p_{out}^{tt} \rvert$ [GeV]	$5.37 \cdot 10^{-1}$	$1.27 \cdot 10^{-1}$	$3.74 \cdot 10^{-2}$	$1.23 \cdot 10^{-2}$	$3.72 \cdot 10^{-3}$	$2.98 \cdot 10^{-4}$
Total Uncertainty [%]	±8.12	±11.0	±10.1	±9.76	±10.7	±10.2
Statistics [%]	±0.3	±0.7	±1.2	±2.0	±3.5	±5.0
Systematics [%]	±8.11	±11.0	±9.97	±9.52	±10.0	±8.82
η intercalibration model (JES) [%]	±0.18	±0.99	±1.37	±1.10	$^{+1.35}_{-0.53}$	$^{+0.50}_{-0.89}$
Single particle high-p_T (JES) [%]	-	-	-	-	-	-
Effective stat. NP set 1 (JES) [%]	±0.79	±1.31	±1.19	±0.69	$^{+0.73}_{-0.28}$	$^{+0.20}_{-0.35}$
Effective stat. NP set 2 (JES) [%]	-	∓0.10	-	-	-	-
Effective stat. NP set 3 (JES) [%]	-	$^{-0.16}_{+0.11}$	∓0.39	∓0.41	$^{+0.32}$	$^{-0.40}_{+0.24}$
Effective detector NP set 1 (JES) [%]	-	±0.32	±0.68	±0.95	±1.38	±1.58
Effective detector NP set 2 (JES) [%]	±0.15	±0.27	±0.24	-	$^{+0.16}_{-}$	-
Effective detector NP set 3 (JES) [%]	-	-	-	$^{+0.13}_{-}$	$^{+0.21}_{-0.13}$	$^{+0.12}_{-0.18}$
Effective mixed NP set 1 (JES) [%]	±0.19	±0.51	±0.81	±0.83	$^{+1.29}_{-0.85}$	±1.18
Effective mixed NP set 2 (JES) [%]	∓0.33	∓0.57	∓0.57	∓0.30	$^{-}_{+0.29}$	$^{-0.23}_{+0.16}$
Effective model NP set 1 (JES) [%]	±1.84	±3.66	±4.02	±3.08	±2.54	±2.24
Effective model NP set 2 (JES) [%]	-	∓0.12	-	-	$^{+0.24}_{-}$	$^{+0.15}_{-0.22}$
Effective model NP set 3 (JES) [%]	±0.16	$^{-}_{-0.12}$	$^{-0.17}_{+0.12}$	∓0.30	$^{-}_{+0.21}$	$^{-0.24}_{-}$
Effective model NP set 4 (JES) [%]	-	-	-	$^{+0.15}_{-0.11}$	$^{+0.30}_{-0.22}$	±0.34
Pile-up offset μ (JES) [%]	∓0.12	$^{-0.41}_{+0.31}$	∓0.33	$^{-0.29}_{+0.41}$	$^{+0.31}_{-}$	-
Pile-up offset N_{PV} (JES) [%]	∓0.55	∓0.79	∓0.72	$^{-0.92}_{+0.59}$	$^{-0.23}_{+1.02}$	$^{-0.68}_{+0.43}$
Punch-through (JES) [%]	-	-	-	-	-	$^{+0.12}_{-0.17}$
Pile-up offset ρ topology (JES) [%]	±1.40	±2.67	±2.84	±2.17	$^{+2.05}_{-1.42}$	$^{+1.14}_{-1.69}$
Pile-up offset p_T (JES) [%]	-	-	-	-	-	-
Flavour composition (JES) [%]	±1.38	±3.40	±3.80	±2.74	$^{+2.26}_{-1.44}$	$^{+1.28}_{-1.82}$
Flavour response (JES) [%]	∓0.78	∓2.24	∓2.80	∓2.17	$^{-1.33}_{+2.09}$	$^{-1.96}_{+1.16}$
b-Tagged jet energy scale (JES) [%]	±0.47	±0.59	±0.71	±0.81	$^{+0.84}_{-0.41}$	$^{+0.78}_{-1.17}$
Jet reconstruction efficiency [%]	-	∓0.10	-	-	-	-
Jet energy resolution [%]	-	-	-	-	-	-
b-Quark tagging efficiency [%]	±4.26	±4.12	±3.99	±4.00	±4.17	±4.80
c-Quark tagging efficiency [%]	±0.93	±0.97	±0.96	±0.95	±0.78	±0.64
Light-jet tagging efficiency [%]	±0.46	±0.66	±0.69	±0.58	±0.59	±0.44
Electron energy scale [%]	$^{-}_{-0.13}$	-	$^{-}_{-0.12}$	-	-	-
Electron energy resolution [%]	-	-	-	-	-	-
Muon momentum scale [%]	-	-	-	-	-	-
Muon (ID) momentum resolution [%]	-	-	-	-	-	-
Muon (MS) momentum resolution [%]	-	-	-	-	-	-
Lepton trigger efficiency [%]	±1.26	±1.27	±1.27	±1.27	±1.26	±1.25
Lepton reconstruction efficiency [%]	±0.24	±0.24	±0.25	±0.25	±0.25	±0.25
Lepton identification efficiency [%]	±1.32	±1.31	±1.31	±1.32	±1.31	±1.33
E_T^{miss} Soft jet scale [%]	∓0.41	±1.50	±0.92	$^{+0.55}_{-0.40}$	±0.22	±0.11
E_T^{miss} Soft jet resolution [%]	-	$^{+0.29}_{-}$	$^{+0.28}_{-}$	-	-	$^{+0.20}_{-}$
Jet vertex fraction [%]	∓0.71	∓0.55	$^{-0.56}_{+0.39}$	∓0.34	$^{-0.24}_{-}$	-
Alternate hard-scattering model [%]	∓1.64	±0.53	±0.43	∓0.67	±4.19	∓1.21
Alternate parton-shower model [%]	∓1.25	∓0.43	±1.25	±0.90	-	±3.09
Monte Carlo sample statistics [%]	-	±0.18	±0.33	±0.53	±0.90	±1.23
ISR/FSR + scale [%]	$^{-5.47}_{+3.26}$	∓6.77	∓3.83	∓5.25	$^{-6.49}_{+3.90}$	$^{+4.92}_{-}$
Parton distribution functions [%]	-	-	±0.13	±0.14	-	-
Single top cross-section [%]	±0.27	±0.26	±0.23	±0.26	±0.27	±0.33
W+jets scale factors [%]	±0.41	±0.31	±0.42	±0.36	±0.80	±0.76
Fake lept. MC stat, e+jets ch. [%]	$^{+0.38}_{-}$	$^{+0.47}_{-}$	$^{-}_{+0.52}$	$^{+0.46}_{-}$	$^{+0.24}_{-}$	$^{+0.33}_{-}$
Fake lept. alternate fake CR, e+jets ch. [%]	±0.35	±0.37	±0.42	±0.34	-	-
Fake lept. alternate real CR, e+jets ch. [%]	-	-	∓0.10	-	-	-
Fake lept. alternate parametrization, e+jets ch. [%]	±0.27	±0.36	±0.33	±0.24	±0.10	±0.10
Fake lept. MC stat, μ+jets ch. [%]	-	-	-	$^{+0.30}_{-}$	-	-
Fake lept. alternate fake CR, μ+jets ch. [%]	±0.22	±0.28	±0.20	-	±0.19	±0.52
Fake lept. alternate real CR, μ+jets ch. [%]	±0.23	±0.18	±0.19	±0.30	±0.39	-
Fake lept. alternate parametrization, μ+jets ch. [%]	±0.22	±0.24	±0.19	±0.33	±1.17	-
Z+jets cross-section [%]	±0.50	±0.45	±0.52	±0.50	±0.66	±0.65
Diboson cross-section [%]	-	-	-	-	-	-
Luminosity [%]	±2.80	±2.80	±2.80	±2.80	±2.80	±2.80

TABLE D.12: Fiducial phase-space absolute differential cross-sections after combining the e+jets and μ+jets channels for the $t\bar{t}$ system out-of-plane momentum $\left|p_{\mathrm{out}}^{t\bar{t}}\right|$. All uncertainties are quoted as a percentage with respect to the cross-section values in each bin. Dashes are used when the estimated relative systematic uncertainty for that bin is below 0.1%.

Bins [Unit $\Delta\phi^{tt}$]	0–1.40	1.40–2.20	2.20–2.70	2.70–3.15
$1/\sigma \cdot \mathrm{d}\sigma$ / d $\Delta\phi^{tt}$	$4.16 \cdot 10^{-2}$	$1.00 \cdot 10^{-1}$	$3.16 \cdot 10^{-1}$	$1.56 \cdot 10^{0}$
Total Uncertainty [%]	$\pm$2.53	$\pm$3.38	$\pm$2.62	$\pm$1.08
Statistics [%]	$\pm$1.3	$\pm$1.0	$\pm$0.7	$\pm$0.2
Systematics [%]	$\pm$2.12	$\pm$3.19	$\pm$2.50	$\pm$1.06
η intercalibration model (JES) [%]	$\pm$0.34	$\pm$0.57	$\pm$0.39	$\mp$0.17
Single particle high-p_T (JES) [%]	-	-	-	-
Effective stat. NP set 1 (JES) [%]	$^{+0.13}_{-0.17}$	$\pm$0.45	$\pm$0.36	$\mp$0.15
Effective stat. NP set 2 (JES) [%]	-	-	-	-
Effective stat. NP set 3 (JES) [%]	$\pm$0.12	-	-	-
Effective detector NP set 1 (JES) [%]	-	-	$\mp$0.20	-
Effective detector NP set 2 (JES) [%]	-	-	-	-
Effective detector NP set 3 (JES) [%]	-	-	-	-
Effective mixed NP set 1 (JES) [%]	-	-	-	-
Effective mixed NP set 2 (JES) [%]	-	$\mp$0.20	$\mp$0.15	-
Effective model NP set 1 (JES) [%]	$^{+0.30}_{-0.21}$	$\pm$1.00	$\pm$0.75	$\mp$0.30
Effective model NP set 2 (JES) [%]	-	-	-	-
Effective model NP set 3 (JES) [%]	$^{+0.11}_{-0.17}$	$^{+0.14}_{-}$	$^{-}_{-0.12}$	-
Effective model NP set 4 (JES) [%]	-	-	-	-
Pile-up offset μ (JES) [%]	-	$\mp$0.12	$\mp$0.17	-
Pile-up offset N_{PV} (JES) [%]	-	$^{-0.11}_{+0.17}$	-	-
Punch-through (JES) [%]	-	-	-	-
Pile-up offset ρ topology (JES) [%]	$\pm$0.21	$\pm$0.78	$\pm$0.58	$\mp$0.23
Pile-up offset p_T (JES) [%]	-	-	-	-
Flavour composition (JES) [%]	$\pm$0.92	$\pm$1.57	$\pm$1.05	$\mp$0.49
Flavour response (JES) [%]	$\mp$0.66	$\mp$1.02	$\mp$0.65	$\pm$0.32
b-Tagged jet energy scale (JES) [%]	$\mp$0.40	$^{-0.20}_{+0.15}$	$^{-0.14}_{+0.10}$	-
Jet reconstruction efficiency [%]	-	-	-	-
Jet energy resolution [%]	-	-	-	-
b-Quark tagging efficiency [%]	$\mp$0.33	$\mp$0.34	$\mp$0.25	$\pm$0.12
c-Quark tagging efficiency [%]	-	$\pm$0.12	$\pm$0.12	-
Light-jet tagging efficiency [%]	$\pm$0.10	$\pm$0.12	$\pm$0.14	-
Electron energy scale [%]	-	-	-	-
Electron energy resolution [%]	-	-	-	-
Muon momentum scale [%]	-	-	-	-
Muon (ID) momentum resolution [%]	-	-	-	-
Muon (MS) momentum resolution [%]	-	-	-	-
Lepton trigger efficiency [%]	-	-	-	-
Lepton reconstruction efficiency [%]	-	-	-	-
Lepton identification efficiency [%]	-	-	-	-
E_T^{miss} Soft jet scale [%]	$\pm$0.56	$\pm$1.02	$\pm$1.14	$\mp$0.42
E_T^{miss} Soft jet resolution [%]	-	-	$^{+0.22}_{-}$	-
Jet vertex fraction [%]	$^{-}_{+0.14}$	$^{-0.15}_{+0.10}$	-	-
Alternate hard-scattering model [%]	$\mp$0.61	$\mp$0.93	$\mp$0.55	$\pm$0.28
Alternate parton-shower model [%]	$\mp$0.93	$\mp$0.82	$\mp$0.96	$\pm$0.38
Monte Carlo sample statistics [%]	$\pm$0.33	$\pm$0.26	$\pm$0.18	-
ISR/FSR + scale [%]	$^{-1.28}_{+0.25}$	$^{+1.73}_{-}$	$^{-0.30}_{+1.16}$	$^{-}_{-0.48}$
Parton distribution functions [%]	-	-	-	-
Single top cross-section [%]	-	-	-	-
W+jets scale factors [%]	$\pm$0.16	$\pm$0.11	-	-
Fake lept. MC stat, e+jets ch. [%]	-	-	-	-
Fake lept. alternate fake CR, e+jets ch. [%]	-	-	-	-
Fake lept. alternate real CR, e+jets ch. [%]	-	-	-	-
Fake lept. alternate parametrization, e+jets ch. [%]	-	-	-	-
Fake lept. MC stat, μ+jets ch. [%]	-	-	-	-
Fake lept. alternate fake CR, μ+jets ch. [%]	-	$\pm$0.11	-	-
Fake lept. alternate real CR, μ+jets ch. [%]	$\mp$0.27	$\mp$0.25	-	-
Fake lept. alternate parametrization, μ+jets ch. [%]	$\mp$0.10	-	-	-
Z+jets cross-section [%]	$\pm$0.10	$\pm$0.16	-	-
Diboson cross-section [%]	-	-	-	-
Luminosity [%]	-	-	-	-

TABLE D.13: Fiducial phase-space relative differential cross-sections after combining the e+jets and μ+jets channels for the $t\bar{t}$ system azimuthal angle $\Delta\phi^{t\bar{t}}$. All uncertainties are quoted as a percentage with respect to the cross-section values in each bin. Dashes are used when the estimated relative systematic uncertainty for that bin is below 0.1%.

Bins [Unit $\Delta\phi^{t\bar{t}}$]	0–1.40	1.40–2.20	2.20–2.70	2.70–3.15
$d\sigma$ / d $\Delta\phi^{t\bar{t}}$ [Unit $\Delta\phi^{t\bar{t}}$]	$1.21 \cdot 10^{0}$	$2.91 \cdot 10^{0}$	$9.18 \cdot 10^{0}$	$4.53 \cdot 10^{1}$
Total Uncertainty [%]	± 9.67	± 10.2	± 9.89	± 8.03
Statistics [%]	± 1.3	± 1.1	± 0.7	± 0.3
Systematics [%]	± 9.56	± 10.2	± 9.88	± 8.02
η intercalibration model (JES) [%]	± 0.77	± 0.99	± 0.81	± 0.24
Single particle high-p_T (JES) [%]	-	-	-	-
Effective stat. NP set 1 (JES) [%]	± 1.05	± 1.36	± 1.27	± 0.76
Effective stat. NP set 2 (JES) [%]	∓ 0.10	∓ 0.12	∓ 0.11	-
Effective stat. NP set 3 (JES) [%]	-	-	-	-
Effective detector NP set 1 (JES) [%]	± 0.27	± 0.15	-	± 0.23
Effective detector NP set 2 (JES) [%]	± 0.20	± 0.27	± 0.26	± 0.15
Effective detector NP set 3 (JES) [%]	-	-	-	-
Effective mixed NP set 1 (JES) [%]	$^{+0.37}_{-0.28}$	± 0.36	± 0.23	± 0.31
Effective mixed NP set 2 (JES) [%]	∓ 0.45	∓ 0.58	∓ 0.54	∓ 0.32
Effective model NP set 1 (JES) [%]	± 2.57	± 3.32	± 3.07	± 2.00
Effective model NP set 2 (JES) [%]	-	∓ 0.13	∓ 0.13	-
Effective model NP set 3 (JES) [%]	± 0.28	± 0.24	± 0.23	-
Effective model NP set 4 (JES) [%]	-	-	-	-
Pile-up offset μ (JES) [%]	∓ 0.27	∓ 0.30	∓ 0.34	∓ 0.11
Pile-up offset N_{PV} (JES) [%]	∓ 0.68	∓ 0.76	∓ 0.67	∓ 0.57
Punch-through (JES) [%]	-	-	-	-
Pile-up offset ρ topology (JES) [%]	± 1.94	± 2.50	± 2.31	± 1.48
Pile-up offset p_T (JES) [%]	-	-	-	-
Flavour composition (JES) [%]	± 2.84	± 3.49	± 2.96	± 1.42
Flavour response (JES) [%]	∓ 1.85	∓ 2.21	∓ 1.84	∓ 0.88
b-Tagged jet energy scale (JES) [%]	$^{+0.12}_{-}$	± 0.33	± 0.39	± 0.59
Jet reconstruction efficiency [%]	∓ 0.12	-	∓ 0.11	-
Jet energy resolution [%]	-	-	-	-
b-Quark tagging efficiency [%]	± 3.88	± 3.87	± 3.96	± 4.34
c-Quark tagging efficiency [%]	± 1.02	± 1.06	± 1.06	± 0.89
Light-jet tagging efficiency [%]	± 0.62	± 0.64	± 0.66	± 0.46
Electron energy scale [%]	$^{+0.13}_{-0.20}$	$^{+0.10}_{-0.16}$	$^{-}_{-0.17}$	-
Electron energy resolution [%]	-	-	-	-
Muon momentum scale [%]	-	-	-	-
Muon (ID) momentum resolution [%]	-	-	-	-
Muon (MS) momentum resolution [%]	-	-	-	-
Lepton trigger efficiency [%]	± 1.31	± 1.30	± 1.28	± 1.25
Lepton reconstruction efficiency [%]	± 0.23	± 0.23	± 0.23	± 0.25
Lepton identification efficiency [%]	± 1.26	± 1.28	± 1.29	± 1.33
E_T^{miss} Soft jet scale [%]	± 0.58	± 1.04	± 1.16	∓ 0.39
E_T^{miss} Soft jet resolution [%]	-	-	$^{+0.22}_{-}$	-
Jet vertex fraction [%]	∓ 0.77	∓ 0.78	∓ 0.74	∓ 0.61
Alternate hard-scattering model [%]	∓ 1.99	∓ 2.30	∓ 1.92	∓ 1.10
Alternate parton-shower model [%]	∓ 1.81	∓ 1.69	∓ 1.84	∓ 0.49
Monte Carlo sample statistics [%]	± 0.34	± 0.27	± 0.19	-
ISR/FSR + scale [%]	$^{-6.68}_{+4.04}$	∓ 5.16	∓ 5.37	$^{-5.38}_{+3.28}$
Parton distribution functions [%]	-	-	-	-
Single top cross-section [%]	± 0.23	± 0.23	± 0.24	± 0.28
W+jets scale factors [%]	± 0.56	± 0.51	± 0.40	± 0.37
Fake lept. MC stat, e+jets ch. [%]	$^{-}_{+0.42}$	$^{+0.39}_{-}$	$^{-}_{+0.40}$	$^{+0.41}_{-}$
Fake lept. alternate fake CR, e+jets ch. [%]	± 0.38	± 0.34	± 0.39	± 0.35
Fake lept. alternate real CR, e+jets ch. [%]	-	-	-	-
Fake lept. alternate parametrization, e+jets ch. [%]	± 0.24	± 0.28	± 0.29	± 0.29
Fake lept. MC stat, μ+jets ch. [%]	-	-	-	-
Fake lept. alternate fake CR, μ+jets ch. [%]	± 0.32	± 0.34	± 0.29	± 0.20
Fake lept. alternate real CR, μ+jets ch. [%]	-	-	± 0.18	± 0.27
Fake lept. alternate parametrization, μ+jets ch. [%]	± 0.13	± 0.19	± 0.20	± 0.25
Z+jets cross-section [%]	± 0.61	± 0.67	± 0.59	± 0.45
Diboson cross-section [%]	-	-	-	-
Luminosity [%]	± 2.80	± 2.80	± 2.80	± 2.80

TABLE D.14: Fiducial phase-space absolute differential cross-sections after combining the e+jets and μ+jets channels for the $t\bar{t}$ system azimuthal angle $\Delta\phi^{t\bar{t}}$. All uncertainties are quoted as a percentage with respect to the cross-section values in each bin. Dashes are used when the estimated relative systematic uncertainty for that bin is below 0.1%.

Bins [GeV]	0–90	90–140	140–195	195–255	255–320	320–385	385–455	455–530	530–610	610–695	695–780	780–865	865–950	950–1041	1041–1500	1500–2000
$1/\sigma \cdot \mathrm{d}\sigma$ / d H_T^{tt}	$8.14 \cdot 10^{-4}$	$2.56 \cdot 10^{-3}$	$3.41 \cdot 10^{-3}$	$3.39 \cdot 10^{-3}$	$2.38 \cdot 10^{-3}$	$1.48 \cdot 10^{-3}$	$9.03 \cdot 10^{-4}$	$5.31 \cdot 10^{-4}$	$2.99 \cdot 10^{-4}$	$1.62 \cdot 10^{-4}$	$8.70 \cdot 10^{-5}$	$4.60 \cdot 10^{-5}$	$2.50 \cdot 10^{-5}$	$1.30 \cdot 10^{-5}$	$4.00 \cdot 10^{-6}$	$1.00 \cdot 10^{-6}$
Total Uncertainty [%]	±4.86	±4.16	±2.38	±1.24	±2.18	±3.55	±4.61	±4.94	±7.96	±4.76	±7.58	±13.0	±17.7	±14.0	±14.2	±20.
Statistics [%]	±1.1	±0.8	±0.6	±0.6	±0.6	±0.9	±1.1	±1.4	±1.9	±2.6	±3.7	±5.5	±7.4	±10.	±11.	±20.
Systematics [%]	±4.71	±4.08	±2.29	±1.06	±2.06	±3.43	±4.46	±4.71	±7.70	±3.92	±6.53	±11.7	±16.0	±9.23	±7.45	-
η intercalibration model (JES) [%]	∓0.54	$^{-0.22}_{+0.30}$	∓0.20	-	$^{+0.26}_{-0.17}$	$^{+0.20}_{-0.36}$	$^{+0.26}_{-0.17}$	$^{+0.27}_{-0.20}$	$^{+0.24}_{-0.46}$	±0.15	$^{+0.24}_{-0.16}$	$^{+0.29}_{-}$	$^{-}_{-0.42}$	±0.60	$^{-}_{-0.38}$	-
Single particle high-p_T (JES) [%]	-	-	-	-	-	-	-	-	-	-	-	-	-	-	-	-
Effective stat. NP set 1 (JES) [%]	∓0.14	-	$^{+0.12}_{-}$	-	±0.10	-	∓0.20	$^{-0.43}_{+0.24}$	∓0.40	∓0.51	∓0.49	$^{-0.37}_{+0.71}$	$^{-0.62}_{+0.29}$	$^{-0.47}_{+1.01}$	$^{-0.22}_{+0.65}$	-
Effective stat. NP set 2 (JES) [%]	-	-	-	-	-	-	-	-	±0.13	-	±0.16	$^{+0.27}_{-}$	$^{+0.11}_{-0.15}$	$^{+0.34}_{-0.22}$	±0.38	-
Effective stat. NP set 3 (JES) [%]	±0.41	±0.32	±0.21	-	∓0.23	∓0.28	∓0.31	∓0.26	$^{-0.41}_{+0.29}$	∓0.27	$^{-0.26}_{+0.17}$	$^{-}_{+0.62}$	$^{-0.25}_{-}$	$^{-0.25}_{+0.40}$	$^{+0.29}_{+0.45}$	-
Effective detector NP set 1 (JES) [%]	∓0.68	∓0.60	∓0.45	$^{-0.15}_{+0.10}$	$^{+0.27}_{-0.18}$	±0.42	±0.64	±0.78	±1.43	±1.33	±2.01	±2.62	±2.08	±3.53	±4.13	-
Effective detector NP set 2 (JES) [%]	-	-	-	-	-	-	-	∓0.11	∓0.14	$^{-0.26}_{+0.14}$	∓0.24	$^{-0.19}_{+0.43}$	$^{-0.24}_{+0.10}$	$^{-0.25}_{+0.52}$	∓0.26	-
Effective detector NP set 3 (JES) [%]	-	-	-	-	-	-	-	-	$^{+0.11}_{-0.15}$	±0.12	$^{+0.15}_{-0.21}$	$^{+0.50}_{-}$	$^{-}_{-0.31}$	$^{-}_{-0.43}$	$^{+0.40}_{-0.16}$	-
Effective mixed NP set 1 (JES) [%]	∓0.60	∓0.47	∓0.33	-	±0.27	±0.33	±0.49	±0.53	±0.94	±0.79	±1.25	±1.68	±1.25	±2.46	$^{+1.85}_{-2.62}$	-
Effective mixed NP set 2 (JES) [%]	-	-	-	-	-	-	-	±0.10	$^{-}_{-0.15}$	$^{+0.12}_{-0.24}$	$^{+0.15}_{-}$	$^{+0.47}_{-0.33}$	$^{+0.28}_{-0.12}$	$^{+0.29}_{-}$	±0.66	-
Effective model NP set 1 (JES) [%]	∓1.35	∓0.72	∓0.44	$^{+0.14}_{-0.26}$	±0.82	$^{+0.61}_{-0.81}$	$^{+0.55}_{-0.21}$	$^{+0.22}_{-0.12}$	$^{+0.14}_{-0.46}$	-	$^{+0.30}_{-0.16}$	-	$^{-0.58}_{+0.20}$	$^{+0.80}_{-}$	$^{-}_{-0.36}$	-
Effective model NP set 2 (JES) [%]	-	-	-	-	-	-	-	±0.10	±0.26	±0.17	$^{+0.28}_{-0.41}$	$^{+1.07}_{-0.57}$	$^{-}_{-0.45}$	$^{+1.67}_{-1.09}$	$^{+1.33}_{-1.76}$	-
Effective model NP set 3 (JES) [%]	±0.34	±0.32	±0.21	-	∓0.18	∓0.27	∓0.32	∓0.34	∓0.36	∓0.36	∓0.34	$^{-0.23}_{+0.44}$	$^{-0.12}_{+0.17}$	∓0.29	$^{-0.22}_{+0.32}$	-
Effective model NP set 4 (JES) [%]	-	-	-	-	-	-	±0.14	±0.11	±0.27	±0.24	$^{+0.22}_{-0.30}$	$^{+0.76}_{-0.40}$	$^{+0.19}_{-0.52}$	$^{+0.42}_{-}$	$^{+0.84}_{-1.13}$	-
Pile-up offset μ (JES) [%]	-	-	-	-	-	-	-	-	-	-	-	$^{+0.28}_{-0.10}$	$^{+0.13}_{-0.20}$	∓0.16	-	-
Pile-up offset N_{PV} (JES) [%]	±0.24	-	-	-	$^{-0.15}_{+0.21}$	-	-	-	-	$^{+0.41}_{-0.29}$	$^{-}_{-0.32}$	$^{+0.53}_{-}$	$^{+0.24}_{-}$	$^{+0.33}_{-0.23}$	$^{-0.16}_{+0.28}$	-
Punch-through (JES) [%]	-	-	-	-	-	-	-	-	-	-	-	$^{-}_{+0.14}$	$^{-}_{-0.17}$	$^{-}_{-0.24}$	$^{+0.40}_{-}$	-
Pile-up offset ρ topology (JES) [%]	∓0.81	$^{-0.29}_{+0.47}$	∓0.22	$^{-}_{-0.22}$	$^{+0.53}_{-0.40}$	$^{+0.29}_{-0.45}$	$^{+0.26}_{-0.10}$	-	-	$^{-0.25}_{-}$	-	$^{-}_{+0.51}$	$^{-}_{-0.69}$	$^{+0.62}_{-}$	$^{-0.69}_{+0.10}$	-
Pile-up offset p_T (JES) [%]	-	-	-	-	-	-	-	-	-	±0.10	-	$^{-0.13}_{+0.65}$	$^{+0.11}_{-0.18}$	$^{-}_{+0.17}$	$^{-}_{-0.39}$	-
Flavour composition (JES) [%]	∓0.81	∓0.36	$^{-0.12}_{+0.17}$	$^{-}_{-0.16}$	±0.44	$^{+0.22}_{-0.45}$	$^{+0.38}_{-}$	-	$^{-}_{-0.26}$	$^{-0.24}_{+0.36}$	$^{+0.22}_{-}$	∓0.43	$^{-1.03}_{+0.13}$	$^{+0.51}_{-}$	$^{-}_{-0.20}$	-
Flavour response (JES) [%]	±0.83	±0.49	$^{+0.34}_{-0.24}$	-	∓0.36	$^{-0.57}_{+0.37}$	$^{-0.33}_{+0.55}$	∓0.38	∓0.65	∓0.49	∓0.66	∓0.52	$^{-0.70}_{+0.13}$	$^{-0.52}_{+1.26}$	$^{-1.14}_{+0.64}$	-
b-Tagged jet energy scale (JES) [%]	∓0.57	∓0.45	∓0.26	-	±0.36	$^{+0.26}_{-0.34}$	±0.30	$^{+0.19}_{-0.29}$	±0.31	±0.23	$^{+0.28}_{-0.39}$	$^{+0.78}_{-0.51}$	$^{-}_{-0.34}$	$^{+1.06}_{-0.76}$	$^{+0.33}_{-0.73}$	-
Jet reconstruction efficiency [%]	-	-	-	-	-	-	-	-	-	-	-	-	-	∓0.11	-	-
Jet energy resolution [%]	-	-	-	-	-	-	-	-	-	-	-	-	-	-	-	-
b-Quark tagging efficiency [%]	-	∓0.17	∓0.23	∓0.23	∓0.14	-	±0.29	±0.68	±1.17	±1.66	±2.13	±2.52	±2.63	±3.03	±3.37	-
c-Quark tagging efficiency [%]	-	±0.14	±0.13	-	-	∓0.13	∓0.21	∓0.29	∓0.36	∓0.37	∓0.43	∓0.42	∓0.33	∓0.41	∓0.35	-
Light-jet tagging efficiency [%]	-	-	-	-	-	-	-	-	-	-	-	-	∓0.10	-	±0.23	-
Electron energy scale [%]	$^{-}_{-0.13}$	-	-	-	-	-	-	-	-	-	-	-	-	-	-	-
Electron energy resolution [%]	-	-	-	-	-	-	-	-	-	-	-	-	-	-	-	-
Muon momentum scale [%]	-	-	-	-	-	-	-	-	-	-	-	-	-	-	-	-
Muon (ID) momentum resolution [%]	-	-	-	-	-	-	-	-	-	-	-	-	-	-	-	-
Muon (MS) momentum resolution [%]	-	-	-	-	-	-	-	-	-	-	-	-	-	-	∓0.12	-
Lepton trigger efficiency [%]	-	-	-	-	-	-	-	-	-	-	-	-	-	-	-	-
Lepton reconstruction efficiency [%]	-	-	-	-	-	-	-	-	-	-	-	-	-	-	-	-
Lepton identification efficiency [%]	-	-	-	-	-	-	-	-	-	-	±0.10	-	±0.11	-	-	-
E_T^{miss} Soft jet scale [%]	∓0.35	-	-	-	-	-	-	-	-	-	-	$^{+0.26}_{-}$	$^{-}_{-0.53}$	$^{+0.43}_{-}$	$^{-0.25}_{-}$	-
E_T^{miss} Soft jet resolution [%]	-	-	-	-	-	-	-	-	-	-	$^{+0.22}_{-}$	$^{+0.39}_{-}$	$^{-}_{-0.34}$	±0.21	$^{-}_{-0.59}$	-
Jet vertex fraction [%]	∓0.23	$^{-0.24}_{+0.18}$	∓0.17	-	-	$^{+0.26}_{-0.18}$	$^{+0.37}_{-0.26}$	±0.36	±0.45	$^{+0.67}_{-0.51}$	±0.53	±0.52	$^{+0.57}_{-0.89}$	$^{+0.97}_{-0.49}$	±0.64	-
Alternate hard-scattering model [%]	∓2.55	∓1.82	∓1.17	∓0.93	±0.63	±2.21	±3.17	±1.87	±6.56	±0.15	±2.73	±9.10	±11.9	±4.91	∓2.52	-
Alternate parton-shower model [%]	∓2.91	∓3.26	∓1.57	-	±1.29	±2.15	±2.66	±3.92	±2.94	±2.63	±4.40	±5.73	±8.99	±4.84	±0.74	-
Monte Carlo sample statistics [%]	±0.29	±0.19	±0.15	±0.14	±0.17	±0.21	±0.27	±0.34	±0.45	±0.60	±0.84	±1.18	±1.65	±2.27	±2.40	-
ISR/FSR + scale [%]	$^{-}_{-1.29}$	$^{-}_{+0.26}$	$^{-0.80}_{-}$	$^{-}_{+0.20}$	$^{+0.83}_{-}$	$^{+0.47}_{-0.72}$	$^{+0.14}_{-1.04}$	$^{+1.18}_{-}$	$^{+1.49}_{-}$	$^{-}_{-1.42}$	$^{+2.21}_{-0.91}$	$^{+0.80}_{-}$	$^{+4.52}_{-2.55}$	$^{+1.15}_{-}$	$^{-}_{-3.19}$	-
Parton distribution functions [%]	-	-	-	-	-	-	-	∓0.10	∓0.14	∓0.23	∓0.30	∓0.89	∓0.88	∓0.40	-	-
Single top cross-section [%]	-	-	-	-	-	-	-	-	-	-	-	±0.26	±0.41	±0.47	±0.14	-
W+jets scale factors [%]	±0.25	±0.16	-	-	-	-	-	∓0.15	-	-	-	-	∓0.18	∓0.32	±1.29	-
Fake lept. MC stat, e+jets ch. [%]	-	$^{-0.17}_{-}$	$^{-0.18}_{-}$	-	-	-	$^{+0.13}_{-}$	$^{+0.19}_{-0.30}$	$^{-}_{-0.22}$	±0.30	$^{+0.22}_{-0.30}$	-	$^{+0.76}_{-0.23}$	$^{+0.49}_{-}$	$^{+0.53}_{-0.37}$	-
Fake lept. alternate fake CR, e+jets ch. [%]	-	±0.13	-	-	-	-	∓0.10	∓0.26	∓0.26	∓0.33	∓0.34	-	∓0.38	∓0.15	∓0.36	-
Fake lept. alternate real CR, e+jets ch. [%]	±0.15	-	-	-	-	-	-	-	-	-	-	-	-	-	-	-
Fake lept. alternate parametrization, e+jets ch. [%]	-	∓0.21	-	-	±0.13	-	-	-	∓0.10	∓0.15	∓0.23	-	-	∓0.57	-	-
Fake lept. MC stat, μ+jets ch. [%]	-	-	-	-	-	-	-	-	-	-	-	-	$^{+0.73}_{-}$	-	-	-
Fake lept. alternate fake CR, μ+jets ch. [%]	±0.10	±0.17	±0.11	-	∓0.11	∓0.10	∓0.13	∓0.12	∓0.14	-	∓0.10	∓0.14	±0.13	∓0.24	∓0.27	-
Fake lept. alternate real CR, μ+jets ch. [%]	∓0.42	∓0.27	-	-	±0.19	±0.17	±0.32	±0.22	-	-	∓0.14	∓0.36	∓0.40	∓0.67	∓0.91	-
Fake lept. alternate parametrization, μ+jets ch. [%]	∓0.16	∓0.12	-	-	-	±0.12	±0.25	±0.10	-	±0.24	∓0.23	∓0.11	±0.56	-	∓0.17	-
Z+jets cross-section [%]	±0.15	±0.28	±0.18	-	∓0.14	∓0.17	∓0.22	∓0.28	∓0.31	∓0.27	∓0.30	∓0.18	∓0.21	∓0.39	∓0.14	-
Diboson cross-section [%]	-	-	-	-	-	-	-	-	-	-	-	-	-	-	-	-
Luminosity [%]	-	-	-	-	-	-	-	-	-	-	-	-	-	-	-	-

TABLE D.15: Fiducial phase-space relative differential cross-sections after combining the e+jets and μ+jets channels for the scalar sum of the hadronic and leptonic top-quark transverse momenta $H_{\mathrm{T}}^{t\bar{t}}$. All uncertainties are quoted as a percentage with respect to the cross-section values in

Bins [GeV]	0–90	90–140	140–195	195–255	255–320	320–385	385–455	455–530	530–610	610–695	695–780	780–865	865–950	950–1041	1041–1500
$d\sigma$ / d $H_T^{t\bar{t}}$ [GeV]	$2.36 \cdot 10^{-2}$	$7.42 \cdot 10^{-2}$	$9.90 \cdot 10^{-2}$	$9.84 \cdot 10^{-2}$	$6.91 \cdot 10^{-2}$	$4.28 \cdot 10^{-2}$	$2.62 \cdot 10^{-2}$	$1.54 \cdot 10^{-2}$	$8.69 \cdot 10^{-3}$	$4.71 \cdot 10^{-3}$	$2.51 \cdot 10^{-3}$	$1.34 \cdot 10^{-3}$	$7.17 \cdot 10^{-4}$	$3.81 \cdot 10^{-4}$	$1.40 \cdot 10^{-5}$
Total Uncertainty [%]	±9.99	±9.80	±9.21	±8.91	±8.84	±8.79	±9.01	±9.28	±10.9	±10.3	±10.8	±14.8	±17.6	±16.3	±17.7
Statistics [%]	±1.2	±0.8	±0.6	±0.6	±0.7	±0.9	±1.1	±1.4	±1.9	±2.6	±3.7	±5.5	±7.5	±10.	±11.
Systematics [%]	±9.89	±9.73	±9.19	±8.89	±8.80	±8.73	±8.93	±9.16	±10.7	±9.93	±10.0	±13.7	±15.9	±12.4	±12.8
η intercalibration model (JES) [%]	$^{-0.18}_{+0.11}$	$^{+0.18}_{-}$	±0.20	±0.46	±0.61	±0.68	±0.61	±0.64	$^{+0.65}_{-0.85}$	±0.55	±0.60	$^{+0.70}_{-0.44}$	$^{+0.41}_{-0.82}$	±1.00	$^{-}_{-0.52}$
Single particle high-p_T (JES) [%]	-	-	-	-	-	-	-	-	-	-	-	-	-	-	-
Effective stat. NP set 1 (JES) [%]	±0.74	±0.96	±1.00	±0.98	±0.99	±0.87	±0.69	$^{+0.46}_{-0.64}$	±0.49	$^{+0.32}_{-0.45}$	$^{+0.47}_{-0.34}$	$^{+0.52}_{-0.18}$	$^{+0.27}_{-0.59}$	$^{+0.43}_{-}$	$^{+0.67}_{-0.24}$
Effective stat. NP set 2 (JES) [%]	∓0.13	∓0.14	∓0.11	-	-	-	-	-	-	-	-	$^{+0.19}_{-}$	-	$^{+0.27}_{-0.14}$	±0.30
Effective stat. NP set 3 (JES) [%]	±0.39	±0.31	±0.19	-	∓0.25	∓0.30	∓0.33	∓0.28	$^{-0.43}_{+0.32}$	∓0.29	$^{-0.28}_{+0.20}$	$^{-}_{+0.64}$	$^{-0.27}_{-}$	$^{-0.27}_{+0.42}$	$^{+0.31}_{+0.47}$
Effective detector NP set 1 (JES) [%]	∓0.51	∓0.43	∓0.29	-	$^{+0.45}_{-0.34}$	±0.60	±0.81	±0.94	±1.60	±1.50	±2.18	±2.79	±2.25	±3.71	±4.29
Effective detector NP set 2 (JES) [%]	±0.15	±0.21	±0.20	±0.21	$^{+0.25}_{-0.19}$	±0.18	$^{-}_{-0.13}$	-	-	-	-	$^{-}_{+0.25}$	-	$^{-}_{+0.34}$	-
Effective detector NP set 3 (JES) [%]	-	-	-	-	-	-	$^{-}_{-0.12}$	-	±0.16	$^{+0.17}_{-0.13}$	$^{+0.18}_{-0.24}$	$^{+0.53}_{-}$	$^{+0.12}_{-0.34}$	$^{+0.12}_{-0.46}$	$^{+0.43}_{-0.19}$
Effective mixed NP set 1 (JES) [%]	∓0.31	$^{-0.14}_{+0.22}$	-	±0.21	±0.55	±0.62	±0.78	±0.82	±1.23	±1.08	±1.54	±1.96	±1.54	±2.76	$^{+2.15}_{-2.89}$
Effective mixed NP set 2 (JES) [%]	∓0.29	∓0.40	∓0.39	∓0.41	∓0.44	∓0.41	∓0.29	∓0.27	$^{-0.31}_{+0.23}$	$^{-0.24}_{+0.14}$	$^{-0.21}_{+0.30}$	-	$^{-}_{+0.26}$	$^{-}_{+0.30}$	±0.28
Effective model NP set 1 (JES) [%]	±0.91	±1.53	±1.81	±2.46	±3.08	±2.97	±2.65	±2.44	±2.56	±2.23	±2.50	±2.33	±1.86	$^{+3.07}_{-2.30}$	±2.16
Effective model NP set 2 (JES) [%]	-	$^{-0.10}_{+0.14}$	∓0.11	∓0.10	-	-	-	-	±0.19	$^{+0.13}_{-}$	$^{+0.22}_{-0.34}$	$^{+1.01}_{-0.50}$	$^{-}_{-0.38}$	$^{+1.60}_{-1.02}$	$^{+1.26}_{-1.69}$
Effective model NP set 3 (JES) [%]	±0.47	±0.46	±0.35	±0.14	-	$^{-0.16}_{+0.10}$	∓0.18	∓0.20	∓0.22	∓0.23	$^{-0.23}_{+0.16}$	$^{-}_{+0.30}$	-	∓0.15	$^{-}_{+0.18}$
Effective model NP set 4 (JES) [%]	-	-	-	-	-	-	±0.16	±0.14	±0.29	±0.27	$^{+0.24}_{-0.32}$	$^{+0.79}_{-0.42}$	$^{+0.21}_{-0.54}$	$^{+0.44}_{-0.10}$	$^{+0.86}_{-1.15}$
Pile-up offset μ (JES) [%]	-	$^{-}_{+0.17}$	∓0.17	∓0.21	$^{-0.15}_{+0.24}$	∓0.22	∓0.17	∓0.14	$^{-0.25}_{+0.14}$	-	∓0.18	-	-	∓0.34	$^{-0.35}_{-}$
Pile-up offset N_{PV} (JES) [%]	∓0.36	∓0.53	∓0.53	∓0.65	∓0.79	∓0.67	∓0.65	∓0.59	$^{-0.74}_{+0.53}$	$^{-0.18}_{+0.32}$	$^{-0.76}_{+0.29}$	$^{-0.51}_{+1.16}$	$^{-0.49}_{+0.86}$	$^{-0.26}_{+0.38}$	∓0.83
Punch-through (JES) [%]	-	-	-	-	-	-	-	-	-	-	-	$^{+0.14}_{-}$	$^{-}_{-0.17}$	$^{-}_{-0.24}$	$^{+0.40}_{-}$
Pile-up offset ρ topology (JES) [%]	±0.86	±1.30	±1.46	±1.84	±2.16	±2.06	±1.87	±1.73	±1.73	±1.55	±1.60	$^{+1.82}_{-1.17}$	$^{+0.99}_{-1.81}$	$^{+2.25}_{-1.05}$	$^{+1.00}_{-1.56}$
Pile-up offset p_T (JES) [%]	-	-	-	-	-	-	-	-	-	±0.10	-	$^{-0.13}_{+0.65}$	$^{+0.11}_{-0.18}$	$^{-}_{+0.17}$	$^{-}_{-0.39}$
Flavour composition (JES) [%]	±1.04	±1.50	±1.71	±1.98	±2.30	±2.20	±2.06	±1.86	±1.96	±1.56	±1.92	±1.42	$^{+0.81}_{-1.73}$	$^{+1.97}_{-1.36}$	±1.95
Flavour response (JES) [%]	∓0.31	∓0.66	∓0.85	∓1.16	∓1.52	∓1.62	∓1.59	∓1.52	∓1.80	∓1.65	∓1.81	∓1.67	$^{-1.84}_{+1.28}$	$^{-1.67}_{+2.43}$	∓2.04
b-Tagged jet energy scale (JES) [%]	-	-	±0.24	±0.57	±0.87	±0.81	±0.81	±0.74	±0.81	±0.73	±0.84	±1.15	$^{+0.47}_{-0.85}$	±1.42	$^{+0.84}_{-1.23}$
Jet reconstruction efficiency [%]	-	-	-	-	-	-	-	-	-	-	-	-	-	∓0.16	-
Jet energy resolution [%]	-	-	-	-	-	-	-	-	-	-	-	-	-	-	-
b-Quark tagging efficiency [%]	±4.16	±4.04	±3.98	±4.00	±4.08	±4.26	±4.51	±4.90	±5.40	±5.88	±6.37	±6.75	±6.86	±7.26	±7.60
c-Quark tagging efficiency [%]	±1.00	±1.09	±1.08	±1.01	±0.91	±0.80	±0.72	±0.65	±0.57	±0.57	±0.50	±0.51	±0.61	±0.52	±0.58
Light-jet tagging efficiency [%]	±0.48	±0.56	±0.57	±0.52	±0.49	±0.51	±0.46	±0.42	±0.42	±0.45	±0.55	±0.51	±0.41	±0.47	±0.74
Electron energy scale [%]	$^{+0.15}_{-0.27}$	$^{+0.12}_{-0.19}$	$^{-}_{-0.16}$	-	-	-	-	-	-	-	-	-	-	±0.14	-
Electron energy resolution [%]	-	-	-	-	-	-	-	-	-	-	-	-	-	-	-
Muon momentum scale [%]	-	-	-	-	-	-	-	-	-	-	-	-	-	-	-
Muon (ID) momentum resolution [%]	-	-	-	-	-	-	-	-	-	-	-	-	-	-	-
Muon (MS) momentum resolution [%]	-	-	-	-	-	-	-	-	-	-	-	-	-	-	∓0.12
Lepton trigger efficiency [%]	±1.34	±1.31	±1.28	±1.26	±1.24	±1.23	±1.23	±1.23	±1.23	±1.22	±1.22	±1.24	±1.21	±1.25	±1.25
Lepton reconstruction efficiency [%]	±0.22	±0.22	±0.22	±0.23	±0.25	±0.26	±0.27	±0.28	±0.29	±0.29	±0.30	±0.30	±0.30	±0.30	±0.30
Lepton identification efficiency [%]	±1.24	±1.26	±1.28	±1.30	±1.34	±1.36	±1.38	±1.39	±1.41	±1.41	±1.42	±1.40	±1.43	±1.37	±1.34
E_T^{miss} Soft jet scale [%]	∓0.36	-	-	-	-	-	-	-	-	-	-	$^{+0.26}_{-}$	$^{-}_{-0.53}$	$^{+0.43}_{-}$	$^{-0.26}_{-}$
E_T^{miss} Soft jet resolution [%]	-	-	-	-	-	-	-	-	-	-	$^{+0.22}_{-}$	$^{+0.39}_{-}$	$^{-}_{-0.34}$	±0.21	$^{-}_{-0.59}$
Jet vertex fraction [%]	∓0.90	∓0.88	∓0.83	∓0.76	∓0.57	∓0.43	∓0.34	$^{-0.35}_{+0.24}$	$^{-0.27}_{+0.15}$	-	$^{-0.17}_{-}$	∓0.15	$^{-}_{-0.28}$	$^{+0.25}_{-}$	-
Alternate hard-scattering model [%]	∓3.79	∓3.07	∓2.42	∓2.19	∓0.64	±0.91	±1.86	±0.57	±5.20	∓1.12	±1.43	±7.71	±10.5	±3.57	∓3.77
Alternate parton-shower model [%]	∓4.11	∓4.46	∓2.79	∓1.19	-	±0.89	±1.40	±2.63	±1.66	±1.36	±3.11	±4.42	±7.65	±3.55	∓0.49
Monte Carlo sample statistics [%]	±0.30	±0.20	±0.17	±0.15	±0.18	±0.22	±0.27	±0.35	±0.46	±0.60	±0.84	±1.18	±1.65	±2.28	±2.41
ISR/FSR + scale [%]	$^{-7.02}_{+3.60}$	$^{-5.87}_{+4.17}$	$^{-6.56}_{+3.98}$	$^{-5.90}_{+4.11}$	∓4.58	$^{-5.36}_{+3.15}$	$^{-5.67}_{+2.82}$	∓4.64	∓4.61	$^{-7.15}_{+3.65}$	∓3.33	∓4.54	∓1.40	∓4.34	$^{-8.07}_{+0.58}$
Parton distribution functions [%]	-	-	-	-	-	-	-	∓0.10	∓0.13	∓0.23	∓0.30	∓0.88	∓0.87	∓0.39	-
Single top cross-section [%]	±0.29	±0.26	±0.24	±0.24	±0.24	±0.28	±0.29	±0.30	±0.33	±0.32	±0.29	±0.53	±0.68	±0.74	±0.41
W+jets scale factors [%]	±0.66	±0.56	±0.43	±0.35	±0.31	±0.32	±0.31	±0.24	±0.38	±0.46	±0.41	±0.37	±0.22	-	±1.69
Fake lept. MC stat, e+jets ch. [%]	$^{+0.30}_{-}$	$^{-0.14}_{+0.48}$	$^{-0.16}_{+0.47}$	$^{+0.40}_{-}$	$^{+0.46}_{-}$	$^{+0.49}_{-}$	$^{+0.33}_{-}$	$^{+0.21}_{-}$	-	$^{+0.34}_{-}$	$^{+0.24}_{-}$	$^{+0.37}_{-}$	$^{+0.78}_{-}$	$^{+0.52}_{-}$	$^{+0.56}_{-}$
Fake lept. alternate fake CR, e+jets ch. [%]	±0.39	±0.49	±0.44	±0.35	±0.35	±0.36	±0.25	-	-	-	-	±0.28	-	±0.20	-
Fake lept. alternate real CR, e+jets ch. [%]	±0.11	-	-	-	-	-	-	-	-	-	-	-	-	-	-
Fake lept. alternate parametrization, e+jets ch. [%]	±0.21	-	±0.29	±0.38	±0.42	±0.33	±0.26	±0.20	±0.18	±0.13	-	±0.20	±0.32	∓0.28	±0.35
Fake lept. MC stat, μ+jets ch. [%]	-	-	-	-	-	-	-	-	-	-	-	-	$^{+0.78}_{-}$	-	-
Fake lept. alternate fake CR, μ+jets ch. [%]	±0.34	±0.41	±0.35	±0.21	±0.12	±0.13	±0.10	±0.11	-	±0.21	±0.13	-	±0.37	-	-
Fake lept. alternate real CR, μ+jets ch. [%]	∓0.21	-	±0.11	±0.28	±0.40	±0.38	±0.53	±0.43	±0.14	±0.20	-	∓0.15	∓0.19	∓0.46	∓0.70
Fake lept. alternate parametrization, μ+jets ch. [%]	-	±0.10	±0.17	±0.22	±0.25	±0.36	±0.49	±0.33	±0.16	±0.47	-	±0.11	±0.79	±0.20	-
Z+jets cross-section [%]	±0.66	±0.79	±0.69	±0.49	±0.36	±0.33	±0.28	±0.22	±0.18	±0.22	±0.19	±0.31	±0.29	±0.11	±0.36
Diboson cross-section [%]	-	-	-	-	-	-	-	-	-	-	-	-	-	-	-
Luminosity [%]	±2.80	±2.80	±2.80	±2.80	±2.80	±2.80	±2.80	±2.80	±2.80	±2.80	±2.80	±2.80	±2.80	±2.80	±2.80

TABLE D.16: Fiducial phase-space absolute differential cross-sections after combining the e+jets and μ+jets channels for the scalar sum of the hadronic and leptonic top-quark transverse momenta $H_{\mathrm{T}}^{t\bar{t}}$. All uncertainties are quoted as a percentage with respect to the cross-section values in

Bins [Unit y^{tt}_{boost}]	0–0.10	0.10–0.20	0.20–0.30	0.30–0.40	0.40–0.50	0.50–0.60	0.60–0.70	0.70–0.80	0.80–0.90	0.90–1	1–1.10	1.10–1.20	1.20–1.30	1.30–1.40	1.40–1.50	1.50–2
$1/\sigma \cdot \mathrm{d}\sigma$ / d y^{tt}_{boost}	$1.10 \cdot 10^{0}$	$1.08 \cdot 10^{0}$	$1.04 \cdot 10^{0}$	$9.93 \cdot 10^{-1}$	$9.29 \cdot 10^{-1}$	$8.52 \cdot 10^{-1}$	$7.66 \cdot 10^{-1}$	$6.75 \cdot 10^{-1}$	$5.81 \cdot 10^{-1}$	$4.90 \cdot 10^{-1}$	$4.03 \cdot 10^{-1}$	$3.22 \cdot 10^{-1}$	$2.48 \cdot 10^{-1}$	$1.85 \cdot 10^{-1}$	$1.33 \cdot 10^{-1}$	$4.08 \cdot 10^{-2}$
Total Uncertainty [%]	±1.35	±1.53	±1.07	±1.40	±1.18	±1.07	±1.77	±1.46	±1.65	±1.54	±2.67	±3.12	±2.24	±3.11	±4.41	±4.36
Statistics [%]	±0.8	±0.7	±0.8	±0.8	±0.8	±0.9	±0.9	±1.0	±1.1	±1.2	±1.4	±1.6	±1.8	±2.1	±2.8	±2.4
Systematics [%]	±1.04	±1.31	±0.66	±1.10	$^{+0.98}_{-0.55}$	$^{+0.59}_{-0.36}$	±1.46	±0.98	±1.15	$^{+0.58}_{-0.94}$	±2.22	±2.61	±1.18	±2.15	±3.31	±3.54
η intercalibration model (JES) [%]	∓0.22	∓0.20	∓0.16	∓0.15	-	-	-	-	$^{+0.15}_{-0.23}$	±0.29	$^{+0.18}_{-0.24}$	$^{+0.45}_{-0.34}$	±0.48	$^{+0.25}_{-0.56}$	±0.69	±0.84
Single particle high-p_T (JES) [%]	-	-	-	-	-	-	-	-	-	-	-	-	-	-	-	-
Effective stat. NP set 1 (JES) [%]	-	-	-	-	-	-	-	-	-	-	±0.12	-	-	-	$^{+0.11}_{-0.15}$	$^{-}_{+0.21}$
Effective stat. NP set 2 (JES) [%]	-	-	-	-	-	-	-	-	-	-	-	-	-	-	-	-
Effective stat. NP set 3 (JES) [%]	-	-	-	-	-	-	-	-	-	-	-	-	-	-	-	-
Effective detector NP set 1 (JES) [%]	-	-	-	-	-	-	-	-	-	-	-	-	-	-	-	-
Effective detector NP set 2 (JES) [%]	-	-	-	-	-	-	-	-	-	-	-	-	-	-	-	-
Effective detector NP set 3 (JES) [%]	-	-	-	-	-	-	-	-	-	-	-	-	-	-	-	-
Effective mixed NP set 1 (JES) [%]	-	-	-	-	-	-	-	-	-	-	-	-	-	-	-	-
Effective mixed NP set 2 (JES) [%]	-	-	-	-	-	-	-	-	-	-	-	-	-	-	-	-
Effective model NP set 1 (JES) [%]	-	-	-	-	$^{-}_{-0.20}$	-	-	-	-	-	$^{+0.13}_{-0.23}$	-	-	$^{-}_{-0.45}$	$^{+0.26}_{-0.13}$	-
Effective model NP set 2 (JES) [%]	-	-	-	-	-	-	-	-	-	-	-	-	-	-	-	-
Effective model NP set 3 (JES) [%]	-	-	-	-	-	-	-	-	-	-	-	-	-	-	-	-
Effective model NP set 4 (JES) [%]	-	-	-	-	-	-	-	-	-	-	-	-	-	-	-	-
Pile-up offset μ (JES) [%]	-	-	-	-	-	-	-	-	-	∓0.10	-	$^{-0.16}_{+0.11}$	-	-	-	$^{-0.25}_{+0.34}$
Pile-up offset N_{PV} (JES) [%]	-	-	-	-	-	-	-	-	-	-	-	-	-	-	-	$^{+0.10}_{-0.21}$
Punch-through (JES) [%]	-	-	-	-	-	-	-	-	-	-	-	-	-	-	-	-
Pile-up offset ρ topology (JES) [%]	-	-	-	-	-	-	-	-	-	-	±0.15	-	±0.12	$^{-}_{-0.35}$	$^{+0.22}_{-}$	-
Pile-up offset p_T (JES) [%]	-	-	-	-	-	-	-	-	-	-	-	-	-	-	-	-
Flavour composition (JES) [%]	-	-	-	-	-	-	-	-	-	-	±0.21	-	-	$^{-}_{-0.66}$	$^{+0.18}_{-0.11}$	$^{+0.23}_{-0.10}$
Flavour response (JES) [%]	-	-	-	-	-	-	-	-	-	-	-	-	-	$^{-}_{-0.41}$	-	$^{-0.13}_{+0.31}$
b-Tagged jet energy scale (JES) [%]	-	-	-	-	-	-	-	-	-	-	-	-	-	-	-	-
Jet reconstruction efficiency [%]	-	-	-	-	-	-	-	-	-	-	-	-	-	-	±0.10	-
Jet energy resolution [%]	-	-	-	-	-	-	-	-	-	-	-	-	-	-	-	-
b-Quark tagging efficiency [%]	-	-	-	-	-	-	-	-	-	-	-	-	-	-	-	-
c-Quark tagging efficiency [%]	-	-	-	-	-	-	-	-	-	-	-	-	-	-	-	-
Light-jet tagging efficiency [%]	-	-	-	-	-	-	-	-	-	-	-	-	-	-	-	-
Electron energy scale [%]	-	-	-	-	-	-	-	-	-	-	-	$^{+0.24}_{-}$	-	$^{-}_{-0.31}$	±0.24	±0.27
Electron energy resolution [%]	-	-	-	-	-	-	-	-	-	-	-	-	-	-	-	-
Muon momentum scale [%]	-	-	-	-	-	-	-	-	-	-	-	-	-	-	-	-
Muon (ID) momentum resolution [%]	-	-	-	-	-	-	-	-	-	-	-	-	-	-	∓0.11	-
Muon (MS) momentum resolution [%]	-	-	-	-	-	-	-	-	-	-	-	-	±0.10	∓0.13	-	-
Lepton trigger efficiency [%]	-	-	-	-	-	-	-	-	-	-	-	±0.11	±0.15	±0.18	±0.23	±0.36
Lepton reconstruction efficiency [%]	-	-	-	-	-	-	-	-	-	-	-	-	-	-	-	±0.10
Lepton identification efficiency [%]	-	-	-	-	-	-	-	-	-	-	-	-	-	-	-	-
E_T^{miss} Soft jet scale [%]	-	-	-	-	-	-	-	-	-	-	-	-	-	-	$^{-0.14}_{+0.25}$	$^{-}_{+0.14}$
E_T^{miss} Soft jet resolution [%]	-	-	-	-	-	-	-	$^{+0.21}_{-}$	-	-	-	-	-	-	$^{-}_{-0.21}$	-
Jet vertex fraction [%]	-	-	-	-	-	-	-	-	-	-	-	-	-	-	-	-
Alternate hard-scattering model [%]	±0.22	±1.20	±0.18	∓0.20	±0.12	-	∓0.53	±0.45	∓0.39	-	∓1.63	-	∓0.21	∓0.91	∓0.11	∓2.11
Alternate parton-shower model [%]	±0.39	±0.32	∓0.34	∓0.80	±0.35	±0.10	∓1.24	∓0.68	±0.90	∓0.28	∓0.85	±2.09	±0.24	±1.30	±2.81	-
Monte Carlo sample statistics [%]	±0.20	±0.18	±0.20	±0.20	±0.21	±0.22	±0.23	±0.25	±0.27	±0.30	±0.33	±0.39	±0.45	±0.52	±0.67	±0.56
ISR/FSR + scale [%]	$^{+0.71}_{-0.95}$	-	∓0.39	$^{+0.75}_{-0.53}$	$^{+0.86}_{-}$	$^{-0.23}_{+0.52}$	$^{-}_{-0.68}$	$^{-}_{+0.62}$	$^{+0.54}_{-}$	$^{-}_{-0.76}$	$^{-0.88}_{+1.26}$	$^{-}_{-1.89}$	$^{-0.52}_{+0.32}$	$^{-0.80}_{+0.43}$	$^{-1.45}_{+0.94}$	$^{-0.98}_{+2.30}$
Parton distribution functions [%]	-	-	-	-	-	-	-	-	-	-	∓0.13	-	±0.16	∓0.13	±0.12	±0.49
Single top cross-section [%]	-	-	-	-	-	-	-	-	-	-	-	-	-	-	-	-
W+jets scale factors [%]	-	-	-	-	-	-	-	-	-	-	-	-	-	-	-	-
Fake lept. MC stat, e+jets ch. [%]	-	-	-	-	-	-	-	$^{+0.11}_{-0.15}$	$^{+0.31}_{-}$	$^{+0.14}_{-}$	-	$^{+0.24}_{-0.13}$	$^{+0.46}_{-}$	-	$^{-}_{-0.38}$	$^{+0.28}_{-0.10}$
Fake lept. alternate fake CR, e+jets ch. [%]	-	-	-	-	-	-	-	-	-	-	-	∓0.11	-	∓0.10	∓0.21	-
Fake lept. alternate real CR, e+jets ch. [%]	-	-	-	-	-	-	-	-	-	-	-	-	-	-	-	±0.13
Fake lept. alternate parametrization, e+jets ch. [%]	-	-	-	±0.10	-	-	-	-	±0.12	-	-	-	-	∓0.30	-	-
Fake lept. MC stat, μ+jets ch. [%]	-	-	-	-	-	-	-	-	-	-	-	-	-	$^{+0.31}_{-}$	-	$^{-}_{+0.88}$
Fake lept. alternate fake CR, μ+jets ch. [%]	-	-	-	-	-	-	-	-	-	∓0.12	-	-	-	-	-	±0.21
Fake lept. alternate real CR, μ+jets ch. [%]	∓0.25	∓0.21	∓0.15	∓0.18	∓0.15	∓0.11	∓0.10	-	±0.18	±0.17	±0.21	±0.58	±0.65	±0.63	±0.71	±1.55
Fake lept. alternate parametrization, μ+jets ch. [%]	∓0.11	-	-	-	-	-	-	-	-	-	±0.16	±0.25	±0.34	±0.46	±0.13	±0.81
Z+jets cross-section [%]	-	-	-	-	-	-	-	-	-	-	-	-	-	-	-	-
Diboson cross-section [%]	-	-	-	-	-	-	-	-	-	-	-	-	-	-	-	-
Luminosity [%]	-	-	-	-	-	-	-	-	-	-	-	-	-	-	-	-

TABLE D.17: Fiducial phase-space relative differential cross-sections after combining the e+jets and μ+jets channels for $y^{t\bar{t}}_{\mathrm{boost}}$. All uncertainties are quoted as a percentage with respect to the cross-section values in each bin. Dashes are used when the estimated relative systematic uncertainty for that bin is below 0.1%.

Bins [Unit y^{tt}_{boost}]	0–0.10	0.10–0.20	0.20–0.30	0.30–0.40	0.40–0.50	0.50–0.60	0.60–0.70	0.70–0.80	0.80–0.90	0.90–1	1–1.10	1.10–1.20	1.20–1.30	1.30–1.40	1.40–1.50	1.50–2
$d\sigma$ / d y^{tt}_{boost} [Unit y^{tt}_{boost}]	$3.18 \cdot 10^1$	$3.13 \cdot 10^1$	$3.03 \cdot 10^1$	$2.88 \cdot 10^1$	$2.69 \cdot 10^1$	$2.47 \cdot 10^1$	$2.22 \cdot 10^1$	$1.96 \cdot 10^1$	$1.69 \cdot 10^1$	$1.42 \cdot 10^1$	$1.17 \cdot 10^1$	$9.32 \cdot 10^0$	$7.20 \cdot 10^0$	$5.37 \cdot 10^0$	$3.86 \cdot 10^0$	$1.18 \cdot 10^0$
Total Uncertainty [%]	±8.06	±8.38	±8.81	±8.38	±8.34	±8.82	±8.79	±8.83	±8.49	±8.85	±9.91	±9.30	±9.22	±9.57	±10.1	±10.8
Statistics [%]	±0.8	±0.8	±0.8	±0.8	±0.8	±0.9	±1.0	±1.0	±1.1	±1.3	±1.4	±1.6	±1.8	±2.2	±2.8	±2.4
Systematics [%]	±8.01	±8.34	±8.77	±8.33	±8.29	±8.77	±8.73	±8.76	±8.41	±8.74	±9.80	$^{+7.93}_{-10.4}$	±9.01	±9.31	±9.69	±10.4
η intercalibration model (JES) [%]	±0.19	±0.21	±0.26	±0.28	±0.33	±0.35	±0.43	±0.43	±0.61	±0.71	±0.64	±0.82	±0.91	$^{+0.68}_{-0.98}$	±1.11	±1.27
Single particle high-p_T (JES) [%]	-	-	-	-	-	-	-	-	-	-	-	-	-	-	-	-
Effective stat. NP set 1 (JES) [%]	±0.90	±0.84	±0.90	±0.92	±0.86	±0.90	±0.89	±0.88	±0.84	±0.95	±1.01	±0.85	±0.89	±0.99	±1.02	$^{+0.89}_{-0.67}$
Effective stat. NP set 2 (JES) [%]	-	-	-	-	-	-	-	-	-	-	-	-	-	-	$^{-}_{+0.13}$	-
Effective stat. NP set 3 (JES) [%]	-	-	-	-	-	-	-	-	-	-	-	-	-	-	-	-
Effective detector NP set 1 (JES) [%]	±0.20	±0.17	$^{+0.19}_{-0.12}$	±0.22	±0.16	±0.14	±0.21	±0.17	±0.20	±0.20	±0.20	$^{+0.29}_{-0.20}$	$^{+0.33}_{-0.22}$	$^{-}_{-0.21}$	$^{+0.18}_{-0.31}$	±0.27
Effective detector NP set 2 (JES) [%]	±0.20	±0.18	±0.18	±0.18	±0.17	±0.16	±0.16	±0.20	±0.15	±0.20	±0.20	±0.16	±0.20	±0.20	$^{+0.20}_{-0.12}$	±0.17
Effective detector NP set 3 (JES) [%]	-	-	-	-	-	-	-	-	-	-	-	-	-	-	-	-
Effective mixed NP set 1 (JES) [%]	±0.32	±0.27	±0.27	±0.34	±0.28	±0.27	±0.30	±0.29	±0.28	±0.33	±0.35	±0.36	±0.39	$^{+0.22}_{-0.39}$	±0.35	$^{+0.20}_{-0.29}$
Effective mixed NP set 2 (JES) [%]	∓0.40	∓0.36	∓0.37	∓0.39	∓0.36	∓0.36	∓0.34	∓0.38	∓0.35	∓0.39	∓0.42	∓0.39	∓0.43	∓0.45	∓0.39	∓0.33
Effective model NP set 1 (JES) [%]	±2.25	±2.25	±2.26	±2.25	±2.20	±2.37	±2.38	±2.21	±2.29	±2.40	±2.48	±2.33	±2.36	±2.45	±2.50	±2.47
Effective model NP set 2 (JES) [%]	-	-	-	-	-	-	-	-	-	-	-	-	-	$^{-}_{+0.13}$	-	-
Effective model NP set 3 (JES) [%]	±0.14	±0.12	±0.12	±0.14	±0.12	±0.14	±0.12	±0.14	±0.10	±0.13	±0.15	-	-	-	±0.17	-
Effective model NP set 4 (JES) [%]	-	-	-	-	-	-	-	-	-	-	-	-	-	-	-	-
Pile-up offset μ (JES) [%]	∓0.15	∓0.11	∓0.15	$^{-0.10}_{+0.17}$	$^{-0.10}_{+0.14}$	∓0.14	∓0.18	$^{-0.13}_{+0.17}$	∓0.22	∓0.28	∓0.27	∓0.32	∓0.27	∓0.21	$^{-0.29}_{+0.22}$	∓0.48
Pile-up offset N_{PV} (JES) [%]	∓0.54	∓0.60	∓0.64	∓0.62	∓0.60	∓0.63	∓0.69	∓0.62	∓0.54	∓0.60	∓0.67	∓0.59	∓0.65	∓0.59	∓0.57	∓0.45
Punch-through (JES) [%]	-	-	-	-	-	-	-	-	-	-	-	-	-	-	-	-
Pile-up offset ρ topology (JES) [%]	±1.69	±1.67	±1.68	±1.67	±1.62	±1.72	±1.76	±1.68	±1.68	±1.75	±1.85	±1.74	±1.84	±1.82	±1.79	±1.74
Pile-up offset p_T (JES) [%]	-	-	-	-	-	-	-	-	-	-	-	-	-	-	-	-
Flavour composition (JES) [%]	±1.81	±1.79	±1.84	±1.84	±1.87	±1.92	±1.90	±1.88	±1.87	±1.95	±2.09	±1.88	±1.92	$^{+1.83}_{-2.53}$	±2.04	±2.06
Flavour response (JES) [%]	∓1.15	∓1.13	∓1.14	∓1.15	∓1.15	∓1.15	∓1.19	∓1.17	∓1.17	∓1.22	∓1.27	∓1.21	∓1.27	$^{-1.58}_{+1.05}$	∓1.21	∓1.40
b-Tagged jet energy scale (JES) [%]	±0.50	±0.55	±0.48	±0.50	±0.49	±0.53	±0.57	$^{+0.56}_{-0.43}$	±0.52	±0.52	±0.62	±0.54	±0.58	±0.53	±0.54	±0.49
Jet reconstruction efficiency [%]	-	-	-	-	-	-	-	-	-	-	-	-	-	-	-	-
Jet energy resolution [%]	-	-	-	-	-	-	-	-	-	-	-	-	-	-	-	-
b-Quark tagging efficiency [%]	±4.21	±4.22	±4.23	±4.22	±4.22	±4.23	±4.24	±4.21	±4.23	±4.22	±4.22	±4.25	±4.24	±4.24	±4.24	±4.24
c-Quark tagging efficiency [%]	±0.95	±0.95	±0.94	±0.96	±0.94	±0.95	±0.93	±0.92	±0.90	±0.93	±0.93	±0.91	±0.89	±0.90	±0.88	±0.88
Light-jet tagging efficiency [%]	±0.52	±0.48	±0.51	±0.49	±0.50	±0.51	±0.51	±0.51	±0.52	±0.53	±0.55	±0.57	±0.53	±0.56	±0.52	±0.59
Electron energy scale [%]	-	-	-	-	-	-	±0.10	$^{-}_{-0.15}$	±0.11	$^{-}_{-0.28}$	$^{-}_{-0.22}$	$^{+0.32}_{-0.23}$	±0.12	$^{+0.13}_{-0.45}$	±0.34	$^{+0.31}_{-0.42}$
Electron energy resolution [%]	-	-	-	-	-	-	-	-	-	-	-	-	-	-	-	-
Muon momentum scale [%]	-	-	-	-	-	-	-	-	-	-	-	-	-	-	-	-
Muon (ID) momentum resolution [%]	-	-	-	-	-	-	-	-	-	-	-	-	-	-	∓0.11	-
Muon (MS) momentum resolution [%]	-	-	-	-	-	-	-	-	-	-	-	-	±0.10	∓0.13	-	-
Lepton trigger efficiency [%]	±1.21	±1.21	±1.22	±1.22	±1.23	±1.24	±1.26	±1.27	±1.30	±1.32	±1.35	±1.38	±1.42	±1.45	±1.50	±1.63
Lepton reconstruction efficiency [%]	±0.23	±0.23	±0.23	±0.23	±0.23	±0.23	±0.24	±0.24	±0.25	±0.25	±0.26	±0.27	±0.28	±0.29	±0.30	±0.35
Lepton identification efficiency [%]	±1.33	±1.33	±1.33	±1.33	±1.33	±1.32	±1.31	±1.30	±1.30	±1.29	±1.28	±1.27	±1.26	±1.26	±1.26	±1.30
E_T^{miss} Soft jet scale [%]	-	-	-	-	-	-	-	-	-	-	-	-	$^{-}_{+0.20}$	$^{-}_{-0.33}$	$^{-0.15}_{+0.25}$	$^{-}_{+0.14}$
E_T^{miss} Soft jet resolution [%]	-	-	-	-	-	-	-	$^{+0.21}_{-}$	-	-	-	-	-	-	$^{-}_{-0.21}$	-
Jet vertex fraction [%]	∓0.64	∓0.69	∓0.64	∓0.64	∓0.68	∓0.65	∓0.62	∓0.66	∓0.66	∓0.66	∓0.64	∓0.70	∓0.68	∓0.62	∓0.67	$^{-0.69}_{+0.47}$
Alternate hard-scattering model [%]	∓0.89	-	∓0.93	∓1.31	∓0.98	∓1.08	∓1.65	∓0.66	∓1.50	∓1.11	∓2.73	∓1.19	∓1.32	∓2.01	∓1.23	∓3.21
Alternate parton-shower model [%]	∓0.49	∓0.56	∓1.22	∓1.68	∓0.53	∓0.78	∓2.11	∓1.56	-	∓1.16	∓1.73	∓1.19	∓0.64	∓0.40	∓1.90	∓0.88
Monte Carlo sample statistics [%]	±0.21	±0.19	±0.20	±0.21	±0.22	±0.23	±0.24	±0.26	±0.28	±0.31	±0.34	±0.39	±0.45	±0.52	±0.67	±0.56
ISR/FSR + scale [%]	$^{-5.13}_{+2.94}$	$^{-5.81}_{+3.75}$	$^{-6.17}_{+4.35}$	$^{-5.10}_{+3.37}$	∓4.64	$^{-6.03}_{+4.47}$	$^{-5.79}_{+3.21}$	∓5.23	$^{-5.29}_{+3.93}$	$^{-6.51}_{+3.14}$	∓5.94	$^{-7.59}_{+3.21}$	$^{-6.30}_{+4.27}$	$^{-6.57}_{+4.38}$	$^{-7.18}_{+4.91}$	∓6.53
Parton distribution functions [%]	-	-	-	-	-	-	-	-	-	-	-	±0.11	±0.21	-	±0.17	±0.55
Single top cross-section [%]	±0.29	±0.27	±0.29	±0.27	±0.27	±0.28	±0.26	±0.26	±0.24	±0.24	±0.26	±0.24	±0.20	±0.20	±0.20	±0.20
W+jets scale factors [%]	±0.42	±0.39	±0.39	±0.38	±0.42	±0.41	±0.39	±0.41	±0.36	±0.40	±0.39	±0.35	±0.38	±0.42	±0.35	±0.34
Fake lept. MC stat, e+jets ch. [%]	$^{-}_{+0.46}$	$^{-}_{+0.46}$	$^{+0.51}_{-}$	$^{-}_{+0.46}$	$^{-}_{+0.45}$	$^{-}_{+0.38}$	$^{-}_{+0.45}$	$^{+0.25}_{-}$	$^{+0.34}_{-}$	$^{+0.32}_{-}$	$^{-}_{+0.44}$	$^{+0.28}_{-}$	$^{+0.49}_{-}$	$^{-}_{+0.22}$	$^{-0.34}_{-}$	$^{+0.31}_{-}$
Fake lept. alternate fake CR, e+jets ch. [%]	±0.43	±0.34	±0.40	±0.45	±0.42	±0.29	±0.36	±0.30	±0.28	±0.27	±0.42	±0.24	±0.25	±0.25	±0.13	±0.28
Fake lept. alternate real CR, e+jets ch. [%]	-	-	-	-	-	-	-	-	-	-	-	-	-	-	-	-
Fake lept. alternate parametrization, e+jets ch. [%]	±0.33	±0.28	±0.33	±0.39	±0.27	±0.21	±0.20	±0.25	±0.42	±0.26	±0.28	±0.24	±0.25	-	±0.27	±0.32
Fake lept. MC stat, μ+jets ch. [%]	-	-	-	-	-	-	-	-	-	-	-	-	-	$^{-}_{+0.36}$	$^{-}_{+0.23}$	$^{-}_{+0.94}$
Fake lept. alternate fake CR, μ+jets ch. [%]	±0.33	±0.25	±0.25	±0.25	±0.17	±0.22	±0.22	±0.27	±0.15	±0.10	±0.15	±0.14	±0.23	±0.21	±0.29	±0.45
Fake lept. alternate real CR, μ+jets ch. [%]	-	-	-	-	-	±0.13	±0.13	±0.25	±0.42	±0.42	±0.45	±0.82	±0.90	±0.88	±0.95	±1.79
Fake lept. alternate parametrization, μ+jets ch. [%]	±0.13	±0.15	±0.18	±0.16	±0.18	±0.19	±0.24	±0.20	±0.19	±0.26	±0.40	±0.49	±0.59	±0.71	±0.37	±1.26
Z+jets cross-section [%]	±0.48	±0.54	±0.49	±0.51	±0.49	±0.49	±0.48	±0.47	±0.51	±0.53	±0.43	±0.50	±0.50	±0.44	±0.48	±0.45
Diboson cross-section [%]	-	-	-	-	-	-	-	-	-	-	-	-	-	-	-	-
Luminosity [%]	±2.80	±2.80	±2.80	±2.80	±2.80	±2.80	±2.80	±2.80	±2.80	±2.80	±2.80	±2.80	±2.80	±2.80	±2.80	±2.80

TABLE D.18: Fiducial phase-space absolute differential cross-sections after combining the e+jets and μ+jets channels for $y^{t\bar{t}}_{\mathrm{boost}}$. All uncertainties are quoted as a percentage with respect to the cross-section values in each bin. Dashes are used when the estimated relative systematic uncertainty for that bin is below 0.1%.

Bins [Unit χ^{tt}]	1–1.40	1.40–1.90	1.90–2.50	2.50–3.20	3.20–4.20	4.20–5.50	5.50–7.20	7.20–9.30	9.30–12	12–20
$1/\sigma \cdot d\sigma$ / d χ^{tt}	$7.05 \cdot 10^{-1}$	$4.47 \cdot 10^{-1}$	$2.68 \cdot 10^{-1}$	$1.58 \cdot 10^{-1}$	$8.81 \cdot 10^{-2}$	$4.49 \cdot 10^{-2}$	$2.13 \cdot 10^{-2}$	$9.65 \cdot 10^{-3}$	$4.13 \cdot 10^{-3}$	$1.05 \cdot 10^{-3}$
Total Uncertainty [%]	±0.68	$^{+0.96}_{-0.73}$	±1.44	±1.14	±1.75	±2.16	±2.54	±3.11	±6.28	±6.59
Statistics [%]	±0.4	±0.6	±0.7	±0.8	±1.0	±1.2	±1.5	±2.0	±2.9	±3.3
Systematics [%]	$^{+0.37}_{-0.54}$	$^{+0.72}_{-0.36}$	±1.24	±0.72	±1.40	±1.75	±1.96	±2.27	±5.51	±5.59
η intercalibration model (JES) [%]	∓0.15	-	-	-	-	$^{+0.13}_{-0.22}$	±0.32	±0.53	$^{+1.07}_{-0.69}$	$^{+0.57}_{-0.77}$
Single particle high-p_T (JES) [%]	-	-	-	-	$-_{-0.23}$	-	-	-	-	-
Effective stat. NP set 1 (JES) [%]	-	-	-	-	-	-	-	-	-	-
Effective stat. NP set 2 (JES) [%]	-	-	-	-	-	-	-	-	-	-
Effective stat. NP set 3 (JES) [%]	-	-	-	-	-	-	-	-	-	-
Effective detector NP set 1 (JES) [%]	-	-	-	-	-	-	-	-	$-_{-0.20}$	-
Effective detector NP set 2 (JES) [%]	-	-	-	-	-	-	-	-	-	-
Effective detector NP set 3 (JES) [%]	-	-	-	-	-	-	-	-	-	-
Effective mixed NP set 1 (JES) [%]	-	-	-	-	-	-	-	-	$-_{-0.22}$	-
Effective mixed NP set 2 (JES) [%]	-	-	-	-	-	-	-	-	-	-
Effective model NP set 1 (JES) [%]	-	-	-	-	-	-	-	-	$-_{-0.23}$	$^{+0.15}$
Effective model NP set 2 (JES) [%]	-	-	-	-	-	-	-	-	-	-
Effective model NP set 3 (JES) [%]	-	-	-	-	-	-	-	-	∓0.11	-
Effective model NP set 4 (JES) [%]	-	-	-	-	-	-	-	-	-	-
Pile-up offset μ (JES) [%]	-	-	-	-	-	-	-	$^{+0.17}$	$^{+0.26}_{-0.24}$	∓0.33
Pile-up offset N_{PV} (JES) [%]	-	-	-	-	-	±0.11	-	-	-	-
Punch-through (JES) [%]	-	-	-	$^{+0.15}$	-	-	-	-	-	-
Pile-up offset ρ topology (JES) [%]	-	-	-	-	-	-	-	-	-	$-_{-0.24}$
Pile-up offset p_T (JES) [%]	-	-	-	-	-	-	-	-	-	-
Flavour composition (JES) [%]	-	-	-	-	-	-	-	$-_{-0.33}$	$-_{-0.22}$	$^{+0.41}$
Flavour response (JES) [%]	-	-	-	-	-	-	-	$-_{-0.23}$	-	$^{+0.20}$
b-Tagged jet energy scale (JES) [%]	-	-	-	-	-	-	-	-	$^{+0.13}$	-
Jet reconstruction efficiency [%]	-	-	-	-	-	-	-	-	-	$-_{-0.16}$
Jet energy resolution [%]	-	-	-	-	-	-	-	-	∓0.10	-
b-Quark tagging efficiency [%]	-	-	-	-	-	-	-	-	-	-
c-Quark tagging efficiency [%]	±0.11	-	-	-	±0.11	±0.14	±0.16	±0.19	±0.18	±0.17
Light-jet tagging efficiency [%]	-	-	-	-	∓0.12	∓0.21	∓0.28	∓0.30	∓0.30	∓0.42
Electron energy scale [%]	-	-	-	-	-	-	-	-	-	-
Electron energy resolution [%]	-	-	-	-	-	-	$-_{-0.16}$	-	±0.27	±0.30
Muon momentum scale [%]	-	-	-	-	-	-	-	-	-	-
Muon (ID) momentum resolution [%]	-	-	-	-	-	-	-	-	-	-
Muon (MS) momentum resolution [%]	-	-	-	-	-	-	-	-	-	∓0.10
Lepton trigger efficiency [%]	-	-	-	-	-	-	-	-	-	-
Lepton reconstruction efficiency [%]	-	-	-	-	-	-	-	-	±0.15	±0.23
Lepton identification efficiency [%]	-	-	-	-	-	-	-	-	-	-
E_T^{miss} Soft jet scale [%]	-	-	-	-	-	-	-	-	-	-
E_T^{miss} Soft jet resolution [%]	-	-	-	-	-	-	-	-	-	-
Jet vertex fraction [%]	-	-	-	-	-	-	-	-	$-_{-0.15}$	±0.10
Alternate hard-scattering model [%]	±0.18	±0.11	∓1.14	-	∓1.03	±1.40	±1.60	∓0.51	±3.04	±4.32
Alternate parton-shower model [%]	-	-	∓0.21	±0.52	∓0.82	±0.20	∓0.46	±1.10	±3.94	±1.71
Monte Carlo sample statistics [%]	±0.11	±0.14	±0.17	±0.21	±0.24	±0.30	±0.38	±0.52	±0.71	±0.85
ISR/FSR + scale [%]	$-_{-0.35}$	$^{-0.14}_{+0.67}$	$^{+0.53}_{-}$	$-_{-0.57}$	$^{+0.48}_{-}$	$^{+1.13}_{-}$	$^{+0.60}_{-0.37}$	$-_{-1.96}$	$-_{-1.06}$	$^{+0.22}_{-1.88}$
Parton distribution functions [%]	-	-	-	-	-	-	-	-	-	∓0.11
Single top cross-section [%]	-	-	-	-	-	-	-	-	-	-
W+jets scale factors [%]	-	-	-	-	-	-	±0.16	±0.11	±0.32	±0.69
Fake lept. MC stat, e+jets ch. [%]	-	-	-	-	-	$^{+0.29}_{-}$	-	$^{+1.28}_{-0.34}$	$^{+1.99}_{-}$	$^{+0.87}_{-}$
Fake lept. alternate fake CR, e+jets ch. [%]	-	-	-	-	-	-	-	∓0.24	±0.14	±0.12
Fake lept. alternate real CR, e+jets ch. [%]	-	-	-	-	-	-	-	-	±0.13	-
Fake lept. alternate parametrization, e+jets ch. [%]	-	-	-	-	-	±0.13	-	±0.20	±0.74	±0.17
Fake lept. MC stat, μ+jets ch. [%]	-	-	-	-	-	-	-	-	-	-
Fake lept. alternate fake CR, μ+jets ch. [%]	-	-	-	-	-	-	-	∓0.19	∓0.43	-
Fake lept. alternate real CR, μ+jets ch. [%]	∓0.19	∓0.14	-	-	±0.12	±0.43	±0.64	±0.40	±0.82	±2.02
Fake lept. alternate parametrization, μ+jets ch. [%]	-	-	-	-	-	±0.11	±0.19	±0.17	±0.31	±1.28
Z+jets cross-section [%]	-	-	-	-	-	-	-	∓0.10	-	-
Diboson cross-section [%]	-	-	-	-	-	-	-	-	-	-
Luminosity [%]	-	-	-	-	-	-	-	-	-	-

TABLE D.19: Fiducial phase-space relative differential cross-sections after combining the e+jets and μ+jets channels for χ^{tt}. All uncertainties are quoted as a percentage with respect to the cross-section values in each bin. Dashes are used when the estimated relative systematic uncertainty for that bin is below 0.1%.

Bins [Unit χ^{tt}]	1–1.40	1.40–1.90	1.90–2.50	2.50–3.20	3.20–4.20	4.20–5.50	5.50–7.20	7.20–9.30	9.30–12	12–20
$d\sigma$ / d χ^{tt} [Unit χ^{tt}]	$2.04 \cdot 10^{1}$	$1.30 \cdot 10^{1}$	$7.77 \cdot 10^{0}$	$4.58 \cdot 10^{0}$	$2.55 \cdot 10^{0}$	$1.30 \cdot 10^{0}$	$6.18 \cdot 10^{-1}$	$2.79 \cdot 10^{-1}$	$1.20 \cdot 10^{-1}$	$3.03 \cdot 10^{-2}$
Total Uncertainty [%]	±8.53	±8.68	±8.62	±8.75	±8.80	±8.25	±8.59	±8.98	±10.0	±9.91
Statistics [%]	±0.5	±0.6	±0.7	±0.8	±1.0	±1.2	±1.5	±2.0	±2.9	±3.4
Systematics [%]	±8.50	±8.65	±8.59	±8.70	±8.74	±8.14	±8.43	$^{+7.57}_{-9.89}$	±9.53	±9.27
η intercalibration model (JES) [%]	±0.25	±0.33	±0.37	±0.47	±0.56	±0.59	±0.73	±0.95	$^{+1.49}_{-1.10}$	±1.08
Single particle high-p_T (JES) [%]	-	-	-	-	-	-	-	-	-	-
Effective stat. NP set 1 (JES) [%]	±0.89	±0.89	±0.91	±0.92	±0.86	±0.86	±0.92	±0.89	±0.95	±0.90
Effective stat. NP set 2 (JES) [%]	-	-	-	-	-	-	-	-	-	-
Effective stat. NP set 3 (JES) [%]	-	-	-	-	-	-	-	-	-	-
Effective detector NP set 1 (JES) [%]	±0.18	±0.18	±0.18	±0.19	±0.18	±0.21	$^{+0.19}_{-0.14}$	±0.22	$^{+0.19}_{-0.39}$	$^{+0.19}_{-0.26}$
Effective detector NP set 2 (JES) [%]	±0.17	±0.18	±0.19	±0.19	±0.18	$^{+0.18}_{-}$	±0.18	$^{+0.15}_{-0.24}$	$^{+0.10}_{-0.19}$	$^{+0.26}_{-}$
Effective detector NP set 3 (JES) [%]	-	-	-	-	-	-	-	-	-	-
Effective mixed NP set 1 (JES) [%]	±0.30	±0.29	±0.30	±0.30	±0.32	±0.30	±0.30	±0.30	$^{+0.38}_{-0.52}$	$^{+0.25}_{-0.38}$
Effective mixed NP set 2 (JES) [%]	∓0.38	∓0.37	∓0.40	∓0.39	∓0.38	∓0.34	∓0.38	∓0.36	$^{-0.46}_{+0.32}$	∓0.35
Effective model NP set 1 (JES) [%]	±2.30	±2.23	±2.33	±2.38	±2.30	±2.21	±2.29	±2.38	±2.40	±2.17
Effective model NP set 2 (JES) [%]	-	-	-	-	-	-	-	-	-	-
Effective model NP set 3 (JES) [%]	±0.11	±0.14	±0.14	±0.14	±0.14	±0.12	±0.14	±0.13	-	-
Effective model NP set 4 (JES) [%]	-	-	-	-	-	-	-	-	-	-
Pile-up offset μ (JES) [%]	∓0.12	∓0.16	∓0.21	$^{-0.15}_{+0.23}$	∓0.17	∓0.22	$^{-0.35}_{+0.15}$	$^{-0.25}_{+0.35}$	$^{-0.19}_{+0.45}$	∓0.51
Pile-up offset N_{PV} (JES) [%]	∓0.57	∓0.64	$^{-0.54}_{+0.71}$	∓0.68	∓0.58	∓0.50	∓0.61	∓0.64	$^{-0.80}_{+0.37}$	$^{-0.55}_{+0.73}$
Punch-through (JES) [%]	-	-	-	-	-	-	-	-	-	-
Pile-up offset ρ topology (JES) [%]	±1.71	±1.65	±1.71	±1.82	±1.69	±1.63	±1.77	±1.74	±1.65	±1.82
Pile-up offset p_T (JES) [%]	-	-	-	-	-	-	-	-	-	-
Flavour composition (JES) [%]	±1.85	±1.83	±1.94	±1.95	±1.85	±1.88	±1.85	±2.06	±2.00	$^{+2.01}_{-1.47}$
Flavour response (JES) [%]	∓1.15	∓1.15	∓1.19	∓1.22	∓1.16	∓1.19	∓1.16	∓1.29	∓1.28	∓1.08
b-Tagged jet energy scale (JES) [%]	±0.53	±0.51	±0.48	±0.56	$^{+0.46}_{-0.60}$	±0.46	±0.52	±0.53	±0.50	±0.62
Jet reconstruction efficiency [%]	-	-	-	-	-	-	-	-	∓0.15	-
Jet energy resolution [%]	-	-	-	-	-	-	-	-	-	-
b-Quark tagging efficiency [%]	±4.14	±4.17	±4.21	±4.28	±4.33	±4.37	±4.38	±4.42	±4.42	±4.40
c-Quark tagging efficiency [%]	±1.05	±1.01	±0.96	±0.89	±0.81	±0.72	±0.66	±0.63	±0.63	±0.51
Light-jet tagging efficiency [%]	±0.50	±0.51	±0.51	±0.53	±0.54	±0.51	±0.55	±0.51	±0.49	±0.50
Electron energy scale [%]	-	$^{-}_{-0.13}$	-	-	$^{-}_{-0.18}$	$^{+0.16}_{-0.23}$	$^{+0.12}_{-0.29}$	$^{+0.16}_{-0.22}$	±0.37	±0.40
Electron energy resolution [%]	-	-	-	-	-	-	-	-	$^{-}_{+0.13}$	-
Muon momentum scale [%]	-	-	-	-	-	-	-	-	-	-
Muon (ID) momentum resolution [%]	-	-	-	-	-	-	-	-	-	∓0.10
Muon (MS) momentum resolution [%]	-	-	-	-	-	-	-	-	-	-
Lepton trigger efficiency [%]	±1.24	±1.25	±1.25	±1.26	±1.27	±1.29	±1.33	±1.36	±1.42	±1.50
Lepton reconstruction efficiency [%]	±0.23	±0.24	±0.24	±0.24	±0.25	±0.25	±0.26	±0.27	±0.28	±0.30
Lepton identification efficiency [%]	±1.31	±1.32	±1.32	±1.32	±1.32	±1.31	±1.31	±1.30	±1.27	±1.29
E_T^{miss} Soft jet scale [%]	-	-	-	-	-	-	-	-	-	-
E_T^{miss} Soft jet resolution [%]	-	-	-	-	-	-	-	-	$^{-0.15}_{-}$	±0.10
Jet vertex fraction [%]	∓0.66	∓0.66	∓0.64	∓0.67	$^{-0.74}_{+0.55}$	∓0.65	∓0.64	$^{-0.69}_{+0.46}$	∓0.71	∓0.65
Alternate hard-scattering model [%]	∓0.83	∓0.90	∓2.15	∓1.03	∓2.04	±0.37	±0.57	∓1.53	±1.99	±3.26
Alternate parton-shower model [%]	∓0.89	∓0.95	∓1.08	∓0.34	∓1.68	∓0.66	∓1.33	±0.22	±3.04	±0.82
Monte Carlo sample statistics [%]	±0.13	±0.15	±0.18	±0.21	±0.25	±0.31	±0.39	±0.52	±0.72	±0.85
ISR/FSR + scale [%]	$^{-6.07}_{+3.75}$	∓5.22	$^{-5.22}_{+3.80}$	$^{-6.27}_{+3.62}$	$^{-5.27}_{+3.97}$	∓4.24	$^{-5.16}_{+3.49}$	$^{-6.57}_{+1.83}$	$^{-6.14}_{+2.77}$	$^{-5.52}_{+1.92}$
Parton distribution functions [%]	-	-	-	-	-	-	-	-	-	-
Single top cross-section [%]	±0.27	±0.26	±0.27	±0.27	±0.28	±0.28	±0.29	±0.25	±0.33	±0.22
W+jets scale factors [%]	±0.33	±0.35	±0.40	±0.42	±0.45	±0.42	±0.56	±0.51	±0.72	±1.08
Fake lept. MC stat, e+jets ch. [%]	$^{-0.12}_{+0.44}$	$^{-0.11}_{+0.36}$	$^{+0.46}_{-}$	$^{-}_{+0.40}$	$^{+0.39}_{-}$	$^{+0.36}_{-}$	$^{+0.42}_{-}$	$^{+1.30}_{-}$	$^{+2.01}_{-}$	$^{+0.89}_{-}$
Fake lept. alternate fake CR, e+jets ch. [%]	±0.34	±0.34	±0.36	±0.38	±0.39	±0.39	±0.37	±0.11	±0.50	±0.48
Fake lept. alternate real CR, e+jets ch. [%]	-	-	-	-	-	-	-	-	-	-
Fake lept. alternate parametrization, e+jets ch. [%]	±0.26	±0.26	±0.27	±0.22	±0.34	±0.43	±0.34	±0.50	±1.04	±0.47
Fake lept. MC stat, μ+jets ch. [%]	-	-	-	-	-	-	-	-	-	-
Fake lept. alternate fake CR, μ+jets ch. [%]	±0.24	±0.29	±0.22	±0.20	±0.21	±0.21	±0.17	-	∓0.20	±0.21
Fake lept. alternate real CR, μ+jets ch. [%]	-	-	±0.14	±0.28	±0.34	±0.65	±0.86	±0.62	±1.04	±2.25
Fake lept. alternate parametrization, μ+jets ch. [%]	±0.16	±0.16	±0.20	±0.28	±0.26	±0.35	±0.43	±0.41	±0.54	±1.52
Z+jets cross-section [%]	±0.50	±0.51	±0.48	±0.51	±0.47	±0.45	±0.53	±0.39	±0.41	±0.54
Diboson cross-section [%]	-	-	-	-	-	-	-	-	-	-
Luminosity [%]	±2.80	±2.80	±2.80	±2.80	±2.80	±2.80	±2.80	±2.80	±2.80	±2.80

TABLE D.20: Fiducial phase-space absolute differential cross-sections after combining the e+jets and μ+jets channels for $\chi^{t\bar{t}}$. All uncertainties are quoted as a percentage with respect to the cross-section values in each bin. Dashes are used when the estimated relative systematic uncertainty for that bin is below 0.1%.

Bins [Unit R_{Wt}]	0–0.10	0.10–0.20	0.20–0.30	0.30–0.40	0.40–0.60	0.60–0.80	0.80–1	1–1.30	1.30–1.70	1.70–2.30	2.30–3.10	3.10–5
$d\sigma$ / d R_{Wt} [Unit R_{Wt}]	$4.46 \cdot 10^0$	$1.10 \cdot 10^1$	$1.52 \cdot 10^1$	$1.88 \cdot 10^1$	$2.40 \cdot 10^1$	$2.90 \cdot 10^1$	$2.49 \cdot 10^1$	$1.27 \cdot 10^1$	$5.33 \cdot 10^0$	$2.01 \cdot 10^0$	$7.68 \cdot 10^{-1}$	$2.33 \cdot 10^{-1}$
Total Uncertainty [%]	±10.4	±9.17	±9.97	±9.11	±8.90	±8.62	±8.39	±9.00	±8.53	±8.17	±8.18	±8.89
Statistics [%]	±2.4	±1.4	±1.1	±1.0	±0.7	±0.6	±0.8	±0.9	±1.2	±1.4	±1.6	±2.5
Systematics [%]	±10.1	±9.05	±9.88	±9.04	±8.87	±8.59	±8.34	±8.95	±8.43	±8.04	±7.98	±8.51
η intercalibration model (JES) [%]	±0.43	±0.43	±0.54	±0.49	±0.46	±0.36	±0.32	±0.34	±0.45	±0.39	$^{+0.32}_{-0.57}$	$^{+0.74}_{-0.46}$
Single particle high-p_T (JES) [%]	-	-	-	-	-	-	-	-	-	-	-	-
Effective stat. NP set 1 (JES) [%]	±1.19	±1.17	±1.23	±1.19	±1.00	±0.80	±0.62	±0.75	±0.79	±0.91	±0.94	±0.98
Effective stat. NP set 2 (JES) [%]	∓0.14	-	$^{-}_{+0.13}$	-	-	-	-	-	-	-	-	-
Effective stat. NP set 3 (JES) [%]	±0.43	±0.29	-	-	∓0.12	-	-	-	-	∓0.11	$^{-0.15}_{+0.11}$	$^{-0.15}_{+0.21}$
Effective detector NP set 1 (JES) [%]	±0.54	±0.49	±0.38	±0.32	±0.13	-	±0.23	±0.24	$^{+0.14}_{-0.10}$	-	-	-
Effective detector NP set 2 (JES) [%]	±0.18	±0.14	$^{+0.28}_{-0.21}$	±0.23	±0.21	±0.18	±0.12	±0.11	±0.17	$^{+0.15}_{-0.24}$	±0.26	$^{+0.33}_{-0.14}$
Effective detector NP set 3 (JES) [%]	-	-	-	-	-	-	-	-	-	-	-	-
Effective mixed NP set 1 (JES) [%]	±0.47	±0.45	$^{+0.55}_{-0.39}$	±0.44	±0.30	±0.21	±0.27	±0.30	±0.26	$^{+0.17}_{-0.24}$	±0.24	$^{+0.36}_{-0.27}$
Effective mixed NP set 2 (JES) [%]	∓0.54	∓0.47	∓0.55	∓0.48	∓0.41	∓0.34	∓0.27	∓0.29	∓0.34	∓0.38	∓0.44	$^{-0.39}_{+0.57}$
Effective model NP set 1 (JES) [%]	±2.44	±2.83	±2.91	±2.83	±2.60	±2.21	±1.59	±1.95	±2.17	±2.33	±2.51	±2.54
Effective model NP set 2 (JES) [%]	-	-	-	-	∓0.11	-	-	-	-	∓0.12	∓0.12	-
Effective model NP set 3 (JES) [%]	±0.67	±0.43	$^{+0.31}_{-0.23}$	±0.22	-	-	-	-	±0.11	-	-	-
Effective model NP set 4 (JES) [%]	-	-	-	-	-	-	-	-	-	-	-	-
Pile-up offset μ (JES) [%]	$^{-0.20}_{+0.14}$	∓0.24	∓0.23	$^{-0.19}_{+0.25}$	∓0.22	∓0.12	∓0.15	∓0.14	∓0.17	∓0.11	$^{-0.21}_{+0.15}$	$^{-0.18}_{+0.45}$
Pile-up offset N_{PV} (JES) [%]	$^{-0.59}_{+0.84}$	∓0.92	∓0.89	∓0.88	∓0.70	∓0.51	∓0.42	∓0.50	∓0.48	∓0.49	∓0.59	∓0.78
Punch-through (JES) [%]	-	-	-	-	-	-	-	-	-	-	-	-
Pile-up offset ρ topology (JES) [%]	±2.22	±2.29	±2.30	±2.19	±1.88	±1.56	±1.21	±1.48	±1.56	±1.62	±1.72	±1.76
Pile-up offset p_T (JES) [%]	-	-	-	-	-	-	-	-	-	-	-	-
Flavour composition (JES) [%]	±2.08	±2.52	±2.50	±2.27	±1.89	±1.69	±1.60	±1.78	±1.83	±1.80	±1.89	±1.82
Flavour response (JES) [%]	$^{-0.69}_{+1.05}$	∓1.23	∓1.31	∓1.22	∓1.06	∓1.12	∓1.19	∓1.36	∓1.21	∓1.13	∓1.13	∓1.10
b-Tagged jet energy scale (JES) [%]	±0.96	±0.96	±0.84	±0.90	±0.79	±0.45	-	±0.18	±0.36	$^{+0.53}_{-0.39}$	$^{+0.42}_{-0.70}$	$^{+0.58}_{-0.87}$
Jet reconstruction efficiency [%]	∓0.11	-	-	-	-	-	-	-	-	-	-	-
Jet energy resolution [%]	-	-	-	-	-	-	-	-	-	-	-	-
b-Quark tagging efficiency [%]	±4.55	±4.62	±4.54	±4.30	±4.07	±4.07	±4.42	±4.41	±4.04	±3.88	±3.89	±3.93
c-Quark tagging efficiency [%]	±1.31	±1.26	±1.34	±1.35	±1.22	±0.84	±0.49	±0.59	±0.80	±0.92	±0.98	±1.05
Light-jet tagging efficiency [%]	±0.60	±0.56	±0.61	±0.59	±0.55	±0.49	±0.43	±0.47	±0.49	±0.51	±0.54	±0.56
Electron energy scale [%]	-	-	-	-	-	-	-	$^{-}_{-0.14}$	$^{+0.10}_{-0.20}$	$^{+0.11}_{-0.24}$	$^{+0.14}_{-0.27}$	±0.21
Electron energy resolution [%]	-	-	-	-	-	-	-	-	-	-	-	-
Muon momentum scale [%]	-	-	-	-	-	-	-	-	-	-	-	-
Muon (ID) momentum resolution [%]	-	-	-	-	-	-	-	-	-	-	-	-
Muon (MS) momentum resolution [%]	-	-	-	-	-	-	-	-	-	-	-	-
Lepton trigger efficiency [%]	±1.25	±1.26	±1.26	±1.26	±1.25	±1.25	±1.25	±1.27	±1.30	±1.31	±1.31	±1.32
Lepton reconstruction efficiency [%]	±0.24	±0.25	±0.25	±0.25	±0.24	±0.25	±0.25	±0.23	±0.22	±0.22	±0.22	±0.22
Lepton identification efficiency [%]	±1.32	±1.32	±1.32	±1.32	±1.33	±1.33	±1.33	±1.30	±1.28	±1.27	±1.27	±1.27
E_T^{miss} Soft jet scale [%]	-	-	-	-	-	-	-	-	-	-	-	-
E_T^{miss} Soft jet resolution [%]	-	-	-	-	-	-	-	-	-	-	-	-
Jet vertex fraction [%]	∓1.41	∓1.22	∓0.98	∓0.87	∓0.69	∓0.52	∓0.48	∓0.54	∓0.48	∓0.61	∓0.58	∓0.49
Alternate hard-scattering model [%]	∓3.55	∓1.00	∓3.92	∓1.84	∓1.98	±1.68	∓1.46	∓2.02	∓1.79	±0.16	±0.47	∓1.35
Alternate parton-shower model [%]	±0.23	±1.43	±0.54	∓0.75	∓1.49	∓0.67	∓1.23	∓1.91	∓1.11	∓2.27	-	±0.18
Monte Carlo sample statistics [%]	±0.57	±0.34	±0.29	±0.26	±0.17	±0.16	±0.19	±0.23	±0.30	±0.36	±0.41	±0.59
ISR/FSR + scale [%]	$^{-6.60}_{+4.48}$	$^{-4.73}_{+3.31}$	$^{-5.75}_{+2.94}$	∓4.50	$^{-5.87}_{+3.66}$	$^{-6.04}_{+4.36}$	$^{-6.10}_{+3.64}$	$^{-5.96}_{+4.35}$	$^{-5.71}_{+3.65}$	∓3.96	∓4.22	$^{-6.37}_{+2.89}$
Parton distribution functions [%]	-	-	-	-	-	-	-	-	±0.10	±0.11	-	-
Single top cross-section [%]	±0.29	±0.27	±0.26	±0.23	±0.26	±0.26	±0.24	±0.29	±0.32	±0.31	±0.28	±0.27
W+jets scale factors [%]	±0.46	±0.37	±0.26	±0.26	±0.30	±0.34	±0.37	±0.53	±0.63	±0.60	±0.67	±0.75
Fake lept. MC stat, e+jets ch. [%]	$^{-0.10}_{+0.50}$	$^{-}_{+0.33}$	$^{+0.35}_{-}$	$^{+0.56}_{-}$	$^{+0.43}_{-}$	$^{+0.40}_{-}$	$^{+0.35}_{-}$	$^{+0.40}_{-}$	$^{-0.26}_{+0.45}$	∓0.31	$^{-}_{+0.53}$	$^{+0.37}_{-}$
Fake lept. alternate fake CR, e+jets ch. [%]	±0.38	±0.35	±0.37	±0.46	±0.33	±0.35	±0.29	±0.39	±0.45	±0.32	±0.42	±0.31
Fake lept. alternate real CR, e+jets ch. [%]	-	-	-	-	-	-	-	-	-	-	-	-
Fake lept. alternate parametrization, e+jets ch. [%]	±0.50	±0.26	±0.17	±0.29	±0.40	±0.37	±0.30	±0.26	-	-	±0.18	-
Fake lept. MC stat, μ+jets ch. [%]	-	-	-	-	-	-	-	-	-	-	-	-
Fake lept. alternate fake CR, μ+jets ch. [%]	-	±0.31	±0.23	±0.23	±0.21	±0.21	±0.14	±0.33	±0.33	±0.30	±0.15	±0.24
Fake lept. alternate real CR, μ+jets ch. [%]	±0.30	±0.16	±0.24	±0.24	±0.28	±0.32	±0.30	±0.17	-	-	∓0.12	∓0.23
Fake lept. alternate parametrization, μ+jets ch. [%]	±0.46	±0.13	±0.17	±0.39	±0.22	±0.24	±0.30	±0.17	±0.15	±0.20	±0.14	±0.11
Z+jets cross-section [%]	±0.61	±0.40	±0.42	±0.43	±0.42	±0.45	±0.39	±0.71	±0.79	±0.64	±0.57	±0.54
Diboson cross-section [%]	-	-	-	-	-	-	-	-	-	-	-	-
Luminosity [%]	±2.80	±2.80	±2.80	±2.80	±2.80	±2.80	±2.80	±2.80	±2.80	±2.80	±2.80	±2.80

TABLE D.21: Fiducial phase-space absolute differential cross-sections after combining the e+jets and μ+jets channels for R_{Wt}. All uncertainties are quoted as a percentage with respect to the cross-section values in each bin. Dashes are used when the estimated relative systematic uncertainty for that bin is below 0.1%.

Bins [Unit R_{Wt}]	0–0.10	0.10–0.20	0.20–0.30	0.30–0.40	0.40–0.60	0.60–0.80	0.80–1	1–1.30	1.30–1.70	1.70–2.30	2.30–3.10	3.10–5
$1/\sigma \cdot \mathrm{d}\sigma$ / d R_{Wt}	$1.55 \cdot 10^{-1}$	$3.82 \cdot 10^{-1}$	$5.29 \cdot 10^{-1}$	$6.55 \cdot 10^{-1}$	$8.36 \cdot 10^{-1}$	$1.01 \cdot 10^{0}$	$8.66 \cdot 10^{-1}$	$4.41 \cdot 10^{-1}$	$1.85 \cdot 10^{-1}$	$7.00 \cdot 10^{-2}$	$2.67 \cdot 10^{-2}$	$8.12 \cdot 10^{-3}$
Total Uncertainty [%]	±4.15	±3.38	±3.86	±2.05	±1.46	±2.94	±1.47	±1.80	±1.61	±2.64	±2.83	±3.08
Statistics [%]	±2.4	±1.3	±1.1	±1.0	±0.6	±0.6	±0.7	±0.8	±1.2	±1.4	±1.6	±2.4
Systematics [%]	±3.33	±3.05	±3.66	$^{+1.97}_{-1.50}$	±1.27	±2.86	±1.25	±1.56	±1.02	±2.19	±2.24	±1.72
η intercalibration model (JES) [%]	-	-	$^{+0.10}_{-0.16}$	-	-	-	-	-	-	-	-	$^{+0.33}_{-}$
Single particle high-p_T (JES) [%]	-	-	-	-	-	-	-	-	-	-	-	-
Effective stat. NP set 1 (JES) [%]	±0.31	±0.29	±0.36	±0.30	±0.12	-	∓0.24	∓0.12	-	-	-	$^{+0.16}_{-}$
Effective stat. NP set 2 (JES) [%]	-	-	-	-	-	-	-	-	-	-	-	-
Effective stat. NP set 3 (JES) [%]	±0.46	±0.32	±0.10	-	-	-	-	-	-	-	-	$^{-0.12}_{+0.17}$
Effective detector NP set 1 (JES) [%]	±0.35	±0.31	±0.19	$^{+0.17}_{-0.10}$	-	∓0.14	-	-	-	$^{-0.19}_{+0.10}$	$^{-0.20}_{-}$	-
Effective detector NP set 2 (JES) [%]	-	-	-	-	-	-	-	-	-	-	-	-
Effective detector NP set 3 (JES) [%]	-	-	-	-	-	-	-	-	-	-	-	-
Effective mixed NP set 1 (JES) [%]	±0.17	$^{+0.18}_{-0.13}$	$^{+0.24}_{-0.10}$	±0.14	-	-	-	-	-	-	-	-
Effective mixed NP set 2 (JES) [%]	∓0.16	∓0.10	$^{-0.16}_{+0.21}$	∓0.11	-	-	±0.10	-	-	-	-	$^{-}_{+0.19}$
Effective model NP set 1 (JES) [%]	$^{+0.33}_{-}$	±0.57	±0.65	±0.58	±0.34	-	∓0.66	∓0.29	-	-	$^{+0.22}_{-0.29}$	$^{+0.21}_{-0.36}$
Effective model NP set 2 (JES) [%]	-	$^{-}_{-0.12}$	-	-	-	-	-	-	-	-	-	-
Effective model NP set 3 (JES) [%]	±0.55	±0.31	$^{+0.18}_{-0.11}$	-	-	-	-	-	-	-	-	$^{-}_{+0.16}$
Effective model NP set 4 (JES) [%]	-	-	-	-	-	-	-	-	-	-	-	-
Pile-up offset μ (JES) [%]	-	-	-	-	-	-	-	-	-	-	-	$^{-}_{+0.27}$
Pile-up offset N_{PV} (JES) [%]	$^{-}_{+0.23}$	∓0.33	$^{-0.22}_{+0.36}$	$^{-0.22}_{+0.34}$	∓0.11	-	$^{+0.14}_{-0.20}$	-	$^{-}_{-0.14}$	-	-	∓0.18
Punch-through (JES) [%]	-	-	-	-	-	-	-	-	-	-	-	-
Pile-up offset ρ topology (JES) [%]	$^{+0.70}_{-0.38}$	±0.60	±0.63	±0.52	±0.21	∓0.11	∓0.45	∓0.20	$^{-}_{-0.12}$	-	-	-
Pile-up offset p_T (JES) [%]	-	-	-	-	-	-	-	-	-	-	-	-
Flavour composition (JES) [%]	$^{+0.45}_{-}$	$^{+0.56}_{-0.76}$	±0.64	$^{+0.35}_{-0.48}$	-	$^{-0.21}_{+0.13}$	$^{-0.20}_{+0.31}$	-	-	-	-	-
Flavour response (JES) [%]	$^{+0.49}_{-0.12}$	-	$^{-}_{+0.17}$	-	$^{+0.12}_{-}$	-	-	$^{-0.21}_{+0.14}$	-	-	-	-
b-Tagged jet energy scale (JES) [%]	$^{+0.53}_{-0.40}$	$^{+0.40}_{-0.54}$	±0.36	±0.41	±0.30	-	∓0.40	∓0.29	$^{-}_{+0.16}$	-	$^{-}_{-0.21}$	$^{+0.10}_{-0.38}$
Jet reconstruction efficiency [%]	-	-	-	-	-	-	-	-	-	-	-	-
Jet energy resolution [%]	-	-	-	-	-	-	-	-	-	-	-	-
b-Quark tagging efficiency [%]	±0.32	±0.39	±0.31	-	∓0.15	∓0.15	±0.20	±0.17	∓0.18	∓0.34	∓0.34	∓0.29
c-Quark tagging efficiency [%]	±0.41	±0.35	±0.43	±0.45	±0.32	-	∓0.40	∓0.30	∓0.10	-	-	±0.14
Light-jet tagging efficiency [%]	-	-	±0.10	-	-	-	-	-	-	-	-	-
Electron energy scale [%]	-	-	-	-	-	-	-	-	-	-	-	-
Electron energy resolution [%]	-	-	-	-	-	-	-	-	-	-	-	-
Muon momentum scale [%]	-	-	-	-	-	-	-	-	-	-	-	-
Muon (ID) momentum resolution [%]	-	-	-	-	-	-	-	-	-	-	-	-
Muon (MS) momentum resolution [%]	-	-	-	-	-	-	-	-	-	-	-	-
Lepton trigger efficiency [%]	-	-	-	-	-	-	-	-	-	-	-	-
Lepton reconstruction efficiency [%]	-	-	-	-	-	-	-	-	-	-	-	-
Lepton identification efficiency [%]	-	-	-	-	-	-	-	-	-	-	-	-
E_T^{miss} Soft jet scale [%]	-	-	-	-	-	-	-	-	-	-	-	-
E_T^{miss} Soft jet resolution [%]	-	-	-	-	-	-	-	-	-	-	-	-
Jet vertex fraction [%]	∓0.77	∓0.57	∓0.34	∓0.23	-	±0.11	±0.15	-	$^{+0.18}_{-0.11}$	-	-	$^{+0.20}_{-}$
Alternate hard-scattering model [%]	∓2.50	-	∓2.88	∓0.78	∓0.92	±2.78	∓0.39	∓0.96	∓0.73	±1.25	±1.56	∓0.29
Alternate parton-shower model [%]	±1.23	±2.44	±1.55	±0.23	∓0.51	±0.31	∓0.24	∓0.93	∓0.12	∓1.30	±1.05	±1.18
Monte Carlo sample statistics [%]	±0.57	±0.33	±0.28	±0.26	±0.16	±0.15	±0.18	±0.21	±0.30	±0.36	±0.40	±0.59
ISR/FSR + scale [%]	$^{-0.92}_{+0.56}$	$^{+1.06}_{-0.56}$	$^{-}_{-0.92}$	$^{+1.29}_{-}$	$^{-}_{-0.22}$	$^{-0.33}_{+0.44}$	$^{-}_{-0.38}$	$^{-0.24}_{+0.43}$	$^{-}_{-0.23}$	$^{+1.49}_{-0.29}$	$^{+1.34}_{-}$	$^{-}_{-0.97}$
Parton distribution functions [%]	-	-	-	-	-	-	-	-	-	-	-	-
Single top cross-section [%]	-	-	-	-	-	-	-	-	-	-	-	-
W+jets scale factors [%]	-	-	∓0.14	∓0.14	∓0.10	-	-	±0.12	±0.22	±0.20	±0.26	±0.34
Fake lept. MC stat, e+jets ch. [%]	$^{-0.12}_{-}$	-	-	-	-	-	-	-	$^{-0.29}_{-}$	$^{-}_{-0.30}$	∓0.11	$^{+0.17}_{-}$
Fake lept. alternate fake CR, e+jets ch. [%]	-	-	-	±0.10	-	-	-	-	-	-	-	-
Fake lept. alternate real CR, e+jets ch. [%]	-	-	-	-	-	-	-	-	-	-	-	-
Fake lept. alternate parametrization, e+jets ch. [%]	±0.21	-	∓0.11	-	±0.11	-	-	-	∓0.24	∓0.20	∓0.10	∓0.23
Fake lept. MC stat, μ+jets ch. [%]	-	-	-	-	-	-	-	-	-	-	-	-
Fake lept. alternate fake CR, μ+jets ch. [%]	∓0.13	-	-	-	-	-	-	-	±0.10	-	-	-
Fake lept. alternate real CR, μ+jets ch. [%]	-	-	-	-	-	±0.10	-	-	∓0.18	∓0.28	∓0.34	∓0.45
Fake lept. alternate parametrization, μ+jets ch. [%]	±0.23	∓0.10	-	±0.16	-	-	-	-	-	-	-	∓0.12
Z+jets cross-section [%]	±0.10	-	-	-	-	-	∓0.11	±0.20	±0.28	±0.13	-	-
Diboson cross-section [%]	-	-	-	-	-	-	-	-	-	-	-	-
Luminosity [%]	-	-	-	-	-	-	-	-	-	-	-	-

TABLE D.22: Fiducial phase-space relative differential cross-sections after combining the e+jets and μ+jets channels for R_{Wt}. All uncertainties are quoted as a percentage with respect to the cross-section values in each bin. Dashes are used when the estimated relative systematic uncertainty for that bin is below 0.1%.

D.1.2 Fractional uncertainties in the full phase-space

D.1.2.1 Graphical form

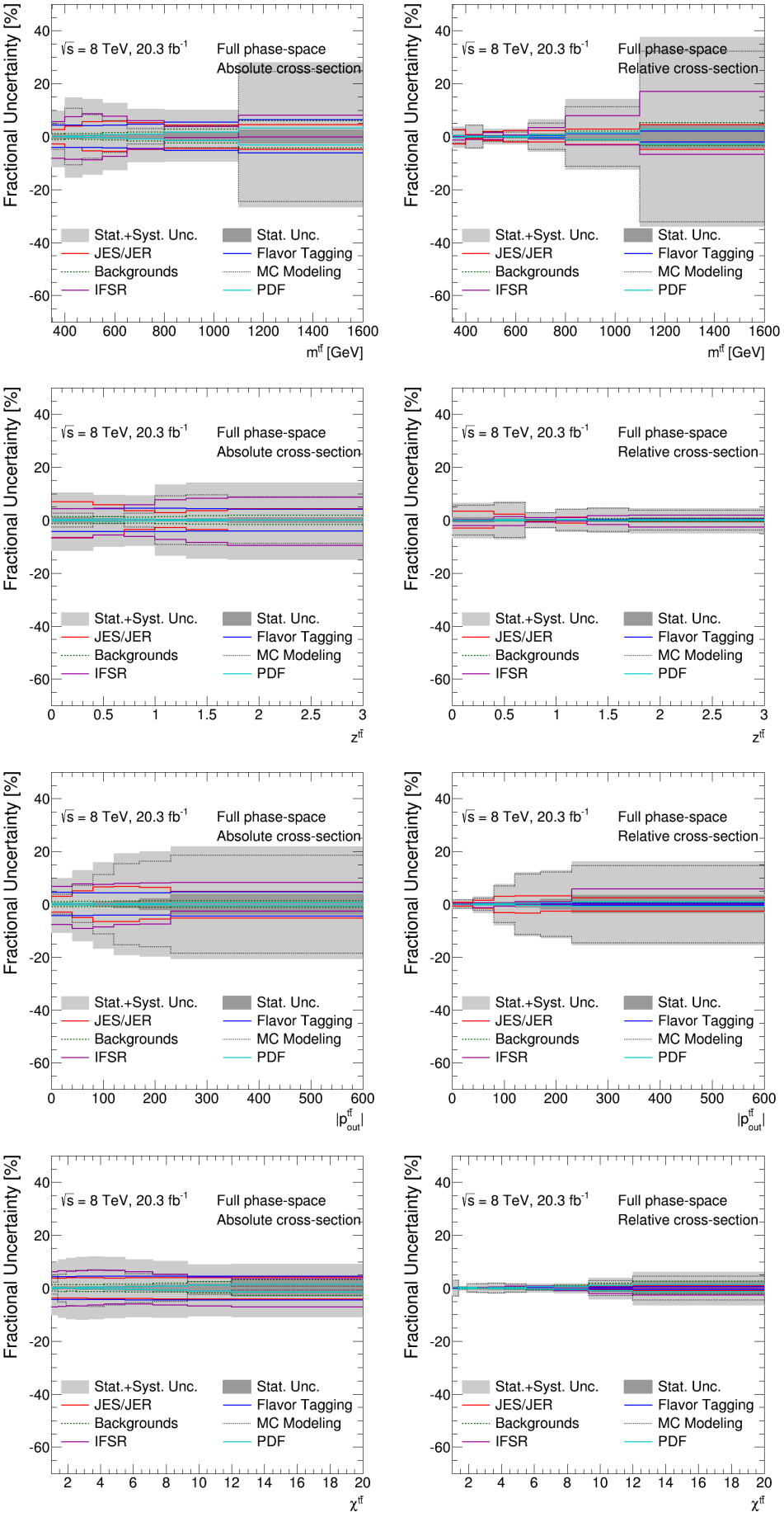

FIGURE D.4: Fractional uncertainties for the absolute (left) and relative (right) differential cross-sections as a function of the mass (first row), $z_{t\bar{t}}$ (second row), $\mid P^{t\bar{t}}_{out} \mid$ (third row) and the $\chi_{t\bar{t}}$ (fourth row) of the $t\bar{t}$ system in the full phase-space.

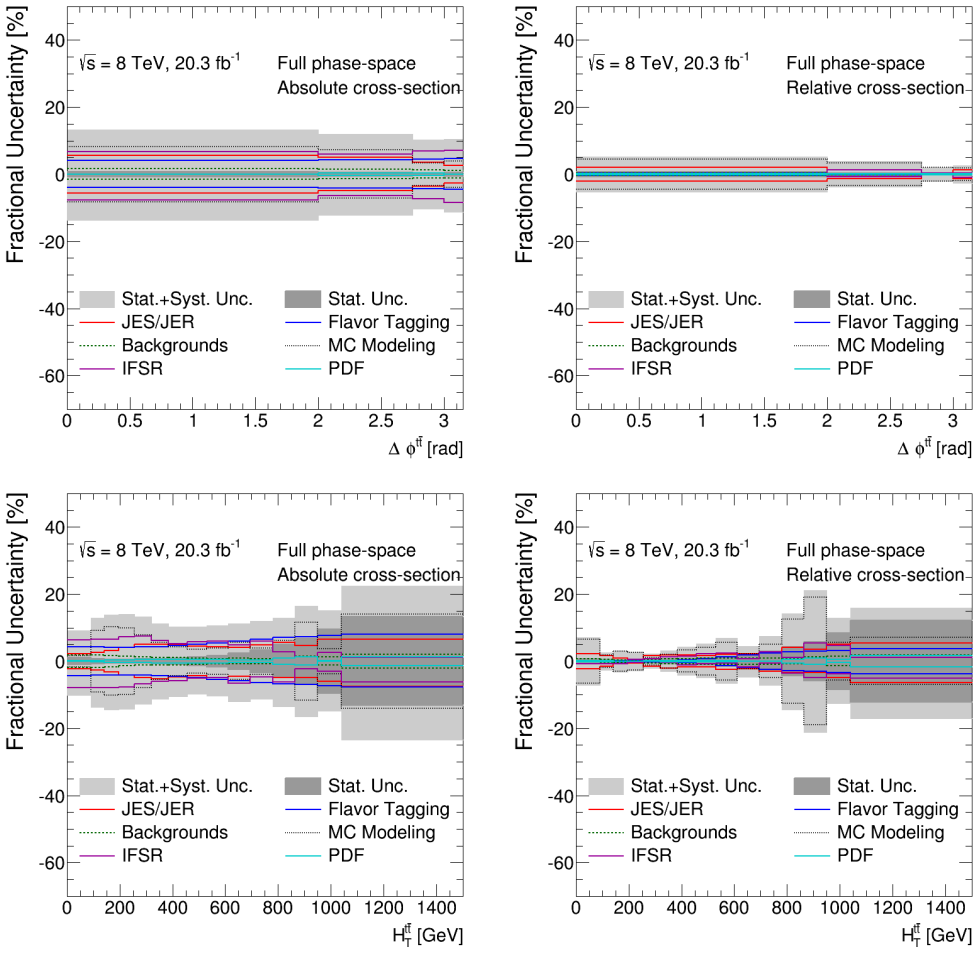

FIGURE D.5: Fractional uncertainties for the absolute (left) and relative (right) differential cross-sections as a function of the $\Delta\phi_{t\bar{t}}$ (top) and the $H_{t\bar{t}}$ (bottom) in the full phase-space.

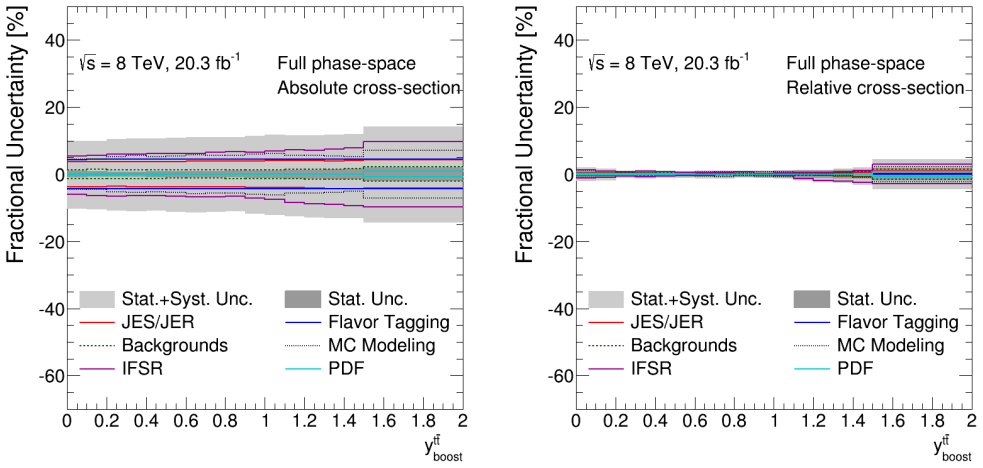

FIGURE D.6: Fractional uncertainties for the absolute (left) and relative (right) differential cross-sections as a function of the $Y^{t\bar{t}}_{boost}$ in the full phase-space.

D.1.2.2 Tabular form

Bins [GeV]	0–60	60–100	100–150	150–200	200–260	260–320	320–400	400–500
$1/\sigma \cdot \mathrm{d}\sigma \,/\, \mathrm{d}\, p_T^t$	$3.75 \cdot 10^{-3}$	$6.59 \cdot 10^{-3}$	$5.12 \cdot 10^{-3}$	$2.78 \cdot 10^{-3}$	$1.20 \cdot 10^{-3}$	$4.57 \cdot 10^{-4}$	$1.58 \cdot 10^{-4}$	$4.50 \cdot 10^{-5}$
Total Uncertainty [%]	±4.00	±2.40	±2.40	±2.24	±3.09	±4.57	±6.38	±11.6
Statistics [%]	±0.5	±0.3	±0.3	±0.6	±0.9	±1.4	±2.0	±4.3
Systematics [%]	±3.97	±2.38	±2.35	±2.15	±2.95	±4.34	±6.02	±10.6
η intercalibration model (JES) [%]	$^{-0.17}_{+0.23}$	∓0.12	-	$^{+0.23}_{-0.30}$	±0.25	±0.20	±0.18	$^{-}_{-0.13}$
Single particle high-p_T (JES) [%]	-	-	-	-	-	-	-	-
Effective stat. NP set 1 (JES) [%]	$^{+0.18}_{-0.11}$	±0.11	-	$^{-0.15}_{-}$	∓0.41	∓0.62	∓0.67	∓0.90
Effective stat. NP set 2 (JES) [%]	-	-	-	-	±0.11	±0.15	±0.17	$^{+0.24}_{-0.14}$
Effective stat. NP set 3 (JES) [%]	±0.34	±0.20	∓0.11	∓0.39	∓0.45	∓0.40	∓0.32	$^{-0.21}_{+0.42}$
Effective detector NP set 1 (JES) [%]	∓0.51	∓0.38	-	±0.52	±0.91	±1.27	±1.83	±2.89
Effective detector NP set 2 (JES) [%]	-	-	-	-	-	∓0.20	∓0.28	$^{-0.24}_{+0.39}$
Effective detector NP set 3 (JES) [%]	-	-	-	-	-	±0.15	±0.19	$^{+0.28}_{-0.15}$
Effective mixed NP set 1 (JES) [%]	∓0.41	∓0.28	-	±0.44	±0.65	±0.80	±1.15	±1.72
Effective mixed NP set 2 (JES) [%]	-	-	-	-	±0.12	±0.18	±0.26	$^{+0.43}_{-0.32}$
Effective model NP set 1 (JES) [%]	∓0.54	∓0.28	±0.38	±0.61	±0.29	$^{-0.16}_{+0.10}$	$^{-}_{+0.23}$	$^{-0.47}_{+0.27}$
Effective model NP set 2 (JES) [%]	-	-	-	-	±0.10	±0.22	±0.32	±0.76
Effective model NP set 3 (JES) [%]	±0.34	±0.21	-	∓0.39	∓0.50	∓0.47	∓0.45	$^{-0.27}_{+0.38}$
Effective model NP set 4 (JES) [%]	-	-	-	-	±0.15	±0.26	±0.35	$^{+0.50}_{-0.38}$
Pile-up offset μ (JES) [%]	-	-	-	-	-	-	-	$^{+0.24}_{-0.11}$
Pile-up offset N_{PV} (JES) [%]	-	-	-	$^{-0.14}_{-}$	-	-	$^{+0.10}_{-0.17}$	-
Punch-through (JES) [%]	-	-	-	-	-	-	-	-
Pile-up offset ρ topology (JES) [%]	$^{-0.19}_{+0.27}$	∓0.12	±0.21	$^{+0.25}_{-0.33}$	-	$^{-0.29}_{+0.21}$	$^{-0.28}_{+0.18}$	∓0.69
Pile-up offset p_T (JES) [%]	-	-	-	-	-	-	-	∓0.18
Flavour composition (JES) [%]	-	-	±0.11	-	$^{-0.22}_{+0.14}$	∓0.53	$^{-0.48}_{+0.71}$	∓1.04
Flavour response (JES) [%]	±0.23	±0.18	-	$^{-0.34}_{+0.25}$	$^{-0.39}_{+0.29}$	∓0.26	∓0.40	$^{-0.45}_{+0.17}$
b-Tagged jet energy scale (JES) [%]	∓0.49	∓0.25	±0.21	±0.51	±0.46	$^{+0.35}_{-0.47}$	±0.45	±0.50
Jet reconstruction efficiency [%]	-	-	-	-	-	-	-	-
Jet energy resolution [%]	-	-	-	-	-	-	-	-
b-Quark tagging efficiency [%]	∓0.14	∓0.16	∓0.14	-	±0.48	±1.18	±1.94	±2.67
c-Quark tagging efficiency [%]	±0.13	±0.11	-	∓0.15	∓0.30	∓0.42	∓0.51	∓0.51
Light-jet tagging efficiency [%]	-	-	-	-	-	∓0.10	-	-
Electron energy scale [%]	-	-	-	-	-	-	-	-
Electron energy resolution [%]	-	-	-	-	-	-	-	-
Muon momentum scale [%]	-	-	-	-	-	-	-	-
Muon (ID) momentum resolution [%]	-	-	-	-	-	-	-	-
Muon (MS) momentum resolution [%]	-	-	-	-	-	-	-	-
Lepton trigger efficiency [%]	-	-	-	-	-	-	-	-
Lepton reconstruction efficiency [%]	-	-	-	-	-	-	-	-
Lepton identification efficiency [%]	-	-	-	-	-	-	-	-
E_T^{miss} Soft jet scale [%]	-	-	-	-	-	-	-	-
E_T^{miss} Soft jet resolution [%]	-	-	-	-	-	-	-	-
Jet vertex fraction [%]	∓0.29	∓0.20	-	$^{+0.35}_{-0.25}$	±0.50	±0.65	±0.71	$^{+0.93}_{-0.70}$
Alternate hard-scattering model [%]	±1.65	∓1.74	∓1.66	±1.26	±1.98	±3.31	±4.84	±9.41
Alternate parton-shower model [%]	±3.09	∓1.28	∓1.36	-	∓0.46	±0.59	±0.75	±0.40
Monte Carlo sample statistics [%]	±0.12	-	-	±0.15	±0.21	±0.33	±0.49	±0.96
ISR/FSR + scale [%]	±1.27	$^{+0.31}_{-0.62}$	∓0.76	$^{-0.67}_{+1.09}$	$^{-0.72}_{+1.10}$	$^{-0.36}_{+1.15}$	∓0.48	$^{-}_{-1.15}$
Parton distribution functions [%]	±0.13	-	-	∓0.10	-	±0.20	±0.26	±0.41
Single top cross-section [%]	-	-	-	-	-	-	±0.10	±0.25
W+jets scale factors [%]	±0.14	-	-	∓0.11	∓0.13	-	-	∓0.12
Fake lept. MC stat, e+jets ch. [%]	-	-	-	-	-	$^{+0.31}_{-0.18}$	±0.26	$^{+0.68}_{-}$
Fake lept. alternate fake CR, e+jets ch. [%]	-	-	-	-	-	∓0.22	∓0.32	∓0.17
Fake lept. alternate real CR, e+jets ch. [%]	-	-	-	-	-	-	-	-
Fake lept. alternate parametrization, e+jets ch. [%]	∓0.14	-	±0.13	±0.12	-	-	∓0.17	-
Fake lept. MC stat, μ+jets ch. [%]	-	-	-	-	-	-	-	$^{+0.21}_{-}$
Fake lept. alternate fake CR, μ+jets ch. [%]	-	-	-	∓0.12	∓0.12	∓0.13	∓0.17	-
Fake lept. alternate real CR, μ+jets ch. [%]	∓0.23	∓0.11	±0.10	±0.23	±0.30	±0.13	-	∓0.32
Fake lept. alternate parametrization, μ+jets ch. [%]	-	-	-	±0.13	±0.15	±0.13	-	-
Z+jets cross-section [%]	∓0.41	∓0.26	±0.11	±0.42	±0.63	±0.72	±0.47	±0.64
Diboson cross-section [%]	-	-	-	-	-	-	-	-
Luminosity [%]	-	-	-	-	-	-	-	-

TABLE D.23: Full phase-space relative differential cross-sections after combining the e+jets and μ+jets channels for the top-quark transverse momentum p_{T}^t. All uncertainties are quoted as a percentage with respect to the cross-section values in each bin. Dashes are used when the estimated relative systematic uncertainty for that bin is below 0.1%.

Bins [GeV]	0–60	60–100	100–150	150–200	200–260	260–320	320–400	400–500
$d\sigma$ / d p_T^t [GeV]	$9.46 \cdot 10^{-1}$	$1.66 \cdot 10^{0}$	$1.29 \cdot 10^{0}$	$7.01 \cdot 10^{-1}$	$3.03 \cdot 10^{-1}$	$1.15 \cdot 10^{-1}$	$3.98 \cdot 10^{-2}$	$1.12 \cdot 10^{-2}$
Total Uncertainty [%]	±9.34	±12.6	±13.4	±12.0	±12.1	±11.5	±11.8	±13.8
Statistics [%]	±0.7	±0.5	±0.5	±0.7	±1.0	±1.5	±2.3	±4.9
Systematics [%]	±9.31	±12.6	±13.4	±12.0	±12.0	±11.4	±11.6	±12.9
η intercalibration model (JES) [%]	$^{+0.20}_{-0.13}$	±0.24	±0.43	±0.64	±0.62	±0.57	±0.55	±0.48
Single particle high-p_T (JES) [%]	-	-	-	-	-	-	-	-
Effective stat. NP set 1 (JES) [%]	±1.09	±1.07	±0.99	±0.82	±0.54	±0.32	$^{+0.21}_{-0.33}$	-
Effective stat. NP set 2 (JES) [%]	∓0.15	∓0.13	-	-	-	-	-	-
Effective stat. NP set 3 (JES) [%]	±0.39	±0.23	-	∓0.35	∓0.41	∓0.36	∓0.29	$^{-0.18}_{+0.39}$
Effective detector NP set 1 (JES) [%]	∓0.46	∓0.33	-	±0.56	±0.95	±1.31	±1.88	±2.94
Effective detector NP set 2 (JES) [%]	±0.22	±0.22	±0.22	±0.17	-	-	-	-
Effective detector NP set 3 (JES) [%]	-	-	-	-	±0.11	±0.16	±0.21	$^{+0.20}_{+0.29}$ $^{-0.17}$
Effective mixed NP set 1 (JES) [%]	$^{-0.17}_{+0.24}$	-	±0.25	±0.64	±0.85	±1.00	±1.35	±1.92
Effective mixed NP set 2 (JES) [%]	∓0.44	∓0.42	∓0.42	∓0.36	∓0.27	∓0.21	∓0.13	-
Effective model NP set 1 (JES) [%]	±1.69	±1.94	±2.61	±2.83	±2.51	±2.09	±2.10	±1.84
Effective model NP set 2 (JES) [%]	∓0.11	∓0.11	∓0.11	-	-	±0.13	±0.23	±0.68
Effective model NP set 3 (JES) [%]	±0.55	±0.41	±0.11	∓0.18	∓0.30	∓0.28	$^{-0.29}_{+0.22}$	- $^{+0.18}$
Effective model NP set 4 (JES) [%]	-	-	-	-	±0.15	±0.26	±0.35	$^{+0.50}_{-0.38}$
Pile-up offset μ (JES) [%]	∓0.16	∓0.17	∓0.19	∓0.21	∓0.17	$^{-0.15}$ -	-	-
Pile-up offset N_{PV} (JES) [%]	∓0.54	∓0.56	∓0.65	∓0.72	∓0.61	∓0.54	∓0.46	∓0.50
Punch-through (JES) [%]	-	-	-	-	-	-	-	-
Pile-up offset ρ topology (JES) [%]	±1.45	±1.56	±1.90	±1.98	±1.73	±1.44	±1.45	±0.99
Pile-up offset p_T (JES) [%]	-	-	-	-	-	-	-	∓0.18
Flavour composition (JES) [%]	±1.93	±1.90	±2.01	±1.96	±1.71	±1.37	±1.31	$^{+0.71}_{-1.00}$
Flavour response (JES) [%]	∓0.88	∓0.94	∓1.20	∓1.42	∓1.46	∓1.38	∓1.52	∓1.43
b-Tagged jet energy scale (JES) [%]	-	±0.18	±0.65	±0.95	±0.91	±0.84	±0.89	±0.94
Jet reconstruction efficiency [%]	-	-	-	-	-	-	-	-
Jet energy resolution [%]	-	-	-	-	-	-	-	-
b-Quark tagging efficiency [%]	±4.00	±3.97	±4.00	±4.19	±4.62	±5.32	±6.08	±6.81
c-Quark tagging efficiency [%]	±1.11	±1.10	±0.99	±0.82	±0.67	±0.55	±0.47	±0.47
Light-jet tagging efficiency [%]	±0.57	±0.55	±0.51	±0.48	±0.45	±0.42	±0.44	±0.52
Electron energy scale [%]	$^{+0.11}_{-0.21}$	$^{-}_{-0.17}$	-	-	-	-	-	-
Electron energy resolution [%]	-	-	-	-	-	-	-	-
Muon momentum scale [%]	-	-	-	-	-	-	-	-
Muon (ID) momentum resolution [%]	-	-	-	-	-	-	-	-
Muon (MS) momentum resolution [%]	-	-	-	-	-	-	-	-
Lepton trigger efficiency [%]	±1.30	±1.28	±1.26	±1.24	±1.23	±1.23	±1.23	±1.24
Lepton reconstruction efficiency [%]	±0.22	±0.22	±0.24	±0.25	±0.27	±0.28	±0.29	±0.30
Lepton identification efficiency [%]	±1.27	±1.28	±1.31	±1.34	±1.37	±1.39	±1.39	±1.39
E_T^{miss} Soft jet scale [%]	-	-	-	-	-	-	-	-
E_T^{miss} Soft jet resolution [%]	-	-	-	-	-	-	-	-
Jet vertex fraction [%]	∓1.02	∓0.92	∓0.69	∓0.42	$^{-0.26}_{+0.19}$	-	-	-
Alternate hard-scattering model [%]	∓3.16	∓6.40	∓6.32	∓3.53	∓2.84	∓1.58	∓0.12	±4.23
Alternate parton-shower model [%]	∓1.96	∓6.12	∓6.19	∓4.91	∓5.34	∓4.33	∓4.18	∓4.51
Monte Carlo sample statistics [%]	±0.17	±0.12	±0.12	±0.17	±0.24	±0.37	±0.55	±1.09
ISR/FSR + scale [%]	∓5.26	∓6.06	∓7.31	∓7.44	∓7.47	∓7.33	∓7.03	$^{-7.87}_{+5.62}$
Parton distribution functions [%]	∓0.22	∓0.35	∓0.45	∓0.45	∓0.39	∓0.15	-	-
Single top cross-section [%]	±0.26	±0.24	±0.24	±0.26	±0.29	±0.33	±0.36	±0.52
W+jets scale factors [%]	±0.56	±0.45	±0.35	±0.30	±0.27	±0.37	±0.48	±0.29
Fake lept. MC stat, e+jets ch. [%]	$^{-0.15}_{+0.30}$	$^{-0.12}_{+0.36}$	$^{+0.47}_{-}$	$^{+0.54}_{-}$	$^{+0.45}_{-}$	$^{+0.30}_{-}$	$^{+0.24}_{-}$	$^{+0.68}_{-}$
Fake lept. alternate fake CR, e+jets ch. [%]	±0.35	±0.37	±0.40	±0.41	±0.32	±0.13	-	±0.18
Fake lept. alternate real CR, e+jets ch. [%]	-	-	-	-	-	-	-	-
Fake lept. alternate parametrization, e+jets ch. [%]	±0.13	±0.23	±0.41	±0.40	±0.27	±0.18	±0.11	±0.26
Fake lept. MC stat, μ+jets ch. [%]	-	-	-	-	-	-	-	$^{+0.26}$ -
Fake lept. alternate fake CR, μ+jets ch. [%]	±0.34	±0.32	±0.22	±0.13	±0.13	±0.11	-	±0.19
Fake lept. alternate real CR, μ+jets ch. [%]	-	-	±0.29	±0.42	±0.49	±0.32	±0.15	∓0.14
Fake lept. alternate parametrization, μ+jets ch. [%]	±0.13	±0.14	±0.22	±0.35	±0.37	±0.34	±0.22	±0.18
Z+jets cross-section [%]	∓1.49	∓1.35	∓0.97	∓0.66	∓0.46	∓0.36	∓0.61	∓0.44
Diboson cross-section [%]	∓0.14	∓0.12	-	-	-	-	-	-
Luminosity [%]	±2.80	±2.80	±2.80	±2.80	±2.80	±2.80	±2.80	±2.80

TABLE D.24: Full phase-space absolute differential cross-sections after combining the e+jets and μ+jets channels for the top-quark transverse momentum p_{T}^{t}. All uncertainties are quoted as a percentage with respect to the cross-section values in each bin. Dashes are used when the estimated relative systematic uncertainty for that bin is below 0.1%.

Bins [Unit $\lvert y^t \rvert$]	0–0.40	0.40–0.80	0.80–1.20	1.20–1.60	1.60–2.50
$1/\sigma \cdot \mathrm{d}\sigma \,/\, \mathrm{d}\,\lvert y^t \rvert$	$6.76 \cdot 10^{-1}$	$6.13 \cdot 10^{-1}$	$5.00 \cdot 10^{-1}$	$3.61 \cdot 10^{-1}$	$1.55 \cdot 10^{-1}$
Total Uncertainty [%]	± 1.10	± 0.76	± 0.85	± 1.48	± 2.50
Statistics [%]	± 0.5	± 0.4	± 0.6	± 0.7	± 1.0
Systematics [%]	± 0.97	$^{+0.65}_{-0.49}$	± 0.57	± 1.25	± 2.25
η intercalibration model (JES) [%]	∓ 0.52	∓ 0.31	-	± 0.52	± 0.97
Single particle high-p_T (JES) [%]	-	-	-	-	-
Effective stat. NP set 1 (JES) [%]	-	-	-	-	-
Effective stat. NP set 2 (JES) [%]	-	-	-	-	-
Effective stat. NP set 3 (JES) [%]	-	-	-	-	-
Effective detector NP set 1 (JES) [%]	-	-	-	-	-
Effective detector NP set 2 (JES) [%]	-	-	-	-	-
Effective detector NP set 3 (JES) [%]	-	-	-	-	-
Effective mixed NP set 1 (JES) [%]	-	-	-	-	-
Effective mixed NP set 2 (JES) [%]	-	-	-	-	-
Effective model NP set 1 (JES) [%]	-	-	-	$^{-}_{-0.13}$	$^{+0.18}_{-}$
Effective model NP set 2 (JES) [%]	-	-	-	-	-
Effective model NP set 3 (JES) [%]	-	-	-	-	-
Effective model NP set 4 (JES) [%]	-	-	-	-	-
Pile-up offset μ (JES) [%]	± 0.11	-	-	-	∓ 0.30
Pile-up offset N_{PV} (JES) [%]	-	-	-	-	-
Punch-through (JES) [%]	-	-	-	-	-
Pile-up offset ρ topology (JES) [%]	-	-	-	± 0.11	$^{+0.17}_{-}$
Pile-up offset p_T (JES) [%]	-	-	-	-	-
Flavour composition (JES) [%]	∓ 0.23	-	-	$^{+0.16}_{-0.26}$	$^{+0.29}_{-0.16}$
Flavour response (JES) [%]	$^{+0.10}_{-0.15}$	-	-	$^{-0.17}_{-}$	$^{-0.12}_{+0.31}$
b-Tagged jet energy scale (JES) [%]	-	-	-	-	-
Jet reconstruction efficiency [%]	-	-	-	-	-
Jet energy resolution [%]	-	-	-	-	-
b-Quark tagging efficiency [%]	-	-	-	-	± 0.10
c-Quark tagging efficiency [%]	-	-	-	-	∓ 0.14
Light-jet tagging efficiency [%]	-	-	-	-	-
Electron energy scale [%]	-	-	-	-	-
Electron energy resolution [%]	-	-	-	-	-
Muon momentum scale [%]	-	-	-	-	-
Muon (ID) momentum resolution [%]	-	-	-	-	-
Muon (MS) momentum resolution [%]	-	-	-	-	-
Lepton trigger efficiency [%]	-	-	-	-	-
Lepton reconstruction efficiency [%]	-	-	-	-	-
Lepton identification efficiency [%]	-	-	-	-	-
E_T^{miss} Soft jet scale [%]	-	-	-	-	-
E_T^{miss} Soft jet resolution [%]	-	-	-	-	-
Jet vertex fraction [%]	-	-	-	-	-
Alternate hard-scattering model [%]	± 0.61	± 0.19	-	∓ 0.81	∓ 0.70
Alternate parton-shower model [%]	-	-	∓ 0.45	-	± 0.54
Monte Carlo sample statistics [%]	± 0.12	± 0.12	± 0.14	± 0.18	± 0.25
ISR/FSR + scale [%]	$^{+0.32}_{-}$	$^{+0.35}_{-0.16}$	$^{+0.15}_{-0.40}$	$^{-}_{+0.95}$	$^{-}_{-1.44}$
Parton distribution functions [%]	± 0.31	± 0.24	± 0.14	± 0.11	∓ 1.36
Single top cross-section [%]	-	-	-	-	-
W+jets scale factors [%]	-	-	-	-	-
Fake lept. MC stat, e+jets ch. [%]	-	-	-	-	$^{-}_{-0.29}$
Fake lept. alternate fake CR, e+jets ch. [%]	-	-	-	-	∓ 0.20
Fake lept. alternate real CR, e+jets ch. [%]	-	-	-	-	-
Fake lept. alternate parametrization, e+jets ch. [%]	-	-	-	-	∓ 0.17
Fake lept. MC stat, μ+jets ch. [%]	-	-	-	-	-
Fake lept. alternate fake CR, μ+jets ch. [%]	-	-	-	-	-
Fake lept. alternate real CR, μ+jets ch. [%]	-	-	-	-	-
Fake lept. alternate parametrization, μ+jets ch. [%]	-	-	-	-	-
Z+jets cross-section [%]	∓ 0.11	-	-	± 0.16	± 0.18
Diboson cross-section [%]	-	-	-	-	-
Luminosity [%]	-	-	-	-	-

TABLE D.25: Full phase-space relative differential cross-sections after combining the e+jets and μ+jets channels for the top-quark absolute rapidity $|y^t|$. All uncertainties are quoted as a percentage with respect to the cross-section values in each bin. Dashes are used when the estimated relative systematic uncertainty for that bin is below 0.1%.

Bins [Unit $\lvert y^t \rvert$]	0–0.40	0.40–0.80	0.80–1.20	1.20–1.60	1.60–2.50
$\mathrm{d}\sigma$ / d $\lvert y^t \rvert$ [Unit $\lvert y^t \rvert$]	$1.69 \cdot 10^2$	$1.53 \cdot 10^2$	$1.25 \cdot 10^2$	$9.01 \cdot 10^1$	$3.88 \cdot 10^1$
Total Uncertainty [%]	±10.4	±10.6	±10.8	±11.6	±11.8
Statistics [%]	±0.6	±0.5	±0.7	±0.9	±1.2
Systematics [%]	±10.4	±10.6	±10.8	±11.6	±11.6
η intercalibration model (JES) [%]	-	$^{+0.22}_{-0.14}$	±0.53	±1.02	±1.46
Single particle high-p_T (JES) [%]	-	-	-	-	-
Effective stat. NP set 1 (JES) [%]	±0.87	±0.87	±0.89	±0.95	±0.95
Effective stat. NP set 2 (JES) [%]	-	-	-	-	-
Effective stat. NP set 3 (JES) [%]	-	-	-	-	-
Effective detector NP set 1 (JES) [%]	±0.18	±0.18	±0.17	±0.21	±0.23
Effective detector NP set 2 (JES) [%]	±0.18	±0.17	±0.17	±0.19	±0.19
Effective detector NP set 3 (JES) [%]	-	-	-	-	-
Effective mixed NP set 1 (JES) [%]	±0.29	±0.30	±0.28	±0.34	±0.35
Effective mixed NP set 2 (JES) [%]	∓0.37	∓0.38	∓0.36	∓0.41	∓0.41
Effective model NP set 1 (JES) [%]	±2.21	±2.25	±2.33	±2.42	±2.44
Effective model NP set 2 (JES) [%]	-	-	-	-	-
Effective model NP set 3 (JES) [%]	±0.12	$^{+0.14}_{-0.10}$	±0.13	±0.14	±0.11
Effective model NP set 4 (JES) [%]	-	-	-	-	-
Pile-up offset μ (JES) [%]	-	$^{-}_{+0.13}$	∓0.18	∓0.29	∓0.50
Pile-up offset N_{PV} (JES) [%]	∓0.59	∓0.65	∓0.62	∓0.59	∓0.54
Punch-through (JES) [%]	-	-	-	-	-
Pile-up offset ρ topology (JES) [%]	±1.65	±1.67	±1.71	±1.83	±1.85
Pile-up offset p_T (JES) [%]	-	-	-	-	-
Flavour composition (JES) [%]	±1.67	±1.83	±2.00	±2.12	±2.13
Flavour response (JES) [%]	∓1.06	∓1.12	∓1.21	∓1.33	∓1.41
b-Tagged jet energy scale (JES) [%]	±0.53	±0.54	±0.51	±0.50	±0.47
Jet reconstruction efficiency [%]	-	-	-	-	-
Jet energy resolution [%]	-	-	-	-	-
b-Quark tagging efficiency [%]	±4.17	±4.21	±4.24	±4.29	±4.34
c-Quark tagging efficiency [%]	±1.00	±0.97	±0.91	±0.85	±0.78
Light-jet tagging efficiency [%]	±0.51	±0.50	±0.49	±0.52	±0.62
Electron energy scale [%]	$^{-}_{-0.13}$	$^{-}_{-0.13}$	$^{-}_{-0.13}$	-	-
Electron energy resolution [%]	-	-	-	-	-
Muon momentum scale [%]	-	-	-	-	-
Muon (ID) momentum resolution [%]	-	-	-	-	-
Muon (MS) momentum resolution [%]	-	-	-	-	-
Lepton trigger efficiency [%]	±1.26	±1.26	±1.27	±1.27	±1.27
Lepton reconstruction efficiency [%]	±0.24	±0.24	±0.24	±0.24	±0.25
Lepton identification efficiency [%]	±1.32	±1.32	±1.31	±1.31	±1.32
E_T^{miss} Soft jet scale [%]	-	-	-	-	-
E_T^{miss} Soft jet resolution [%]	-	-	-	-	-
Jet vertex fraction [%]	∓0.65	∓0.67	∓0.67	∓0.66	∓0.59
Alternate hard-scattering model [%]	∓3.19	∓3.59	∓3.77	∓4.56	∓4.46
Alternate parton-shower model [%]	∓3.50	∓3.56	∓3.98	∓3.52	∓3.02
Monte Carlo sample statistics [%]	±0.15	±0.14	±0.17	±0.22	±0.30
ISR/FSR + scale [%]	∓6.45	∓6.35	∓6.32	∓7.12	$^{-8.21}_{+6.24}$
Parton distribution functions [%]	±0.21	±0.14	-	-	∓1.46
Single top cross-section [%]	±0.29	±0.28	±0.27	±0.22	±0.21
W+jets scale factors [%]	±0.46	±0.41	±0.37	±0.33	±0.30
Fake lept. MC stat, e+jets ch. [%]	$^{+0.48}_{-}$	$^{-}_{+0.47}$	$^{+0.41}_{-}$	$^{+0.29}_{-}$	-
Fake lept. alternate fake CR, e+jets ch. [%]	±0.39	±0.41	±0.38	±0.27	±0.13
Fake lept. alternate real CR, e+jets ch. [%]	-	-	-	-	-
Fake lept. alternate parametrization, e+jets ch. [%]	±0.35	±0.33	±0.24	±0.26	±0.10
Fake lept. MC stat, μ+jets ch. [%]	-	-	-	-	-
Fake lept. alternate fake CR, μ+jets ch. [%]	±0.23	±0.23	±0.24	±0.22	±0.23
Fake lept. alternate real CR, μ+jets ch. [%]	±0.25	±0.21	±0.21	±0.20	±0.21
Fake lept. alternate parametrization, μ+jets ch. [%]	±0.22	±0.21	±0.27	±0.21	±0.27
Z+jets cross-section [%]	∓1.09	∓1.07	∓0.95	∓0.81	∓0.79
Diboson cross-section [%]	-	-	-	-	-
Luminosity [%]	±2.80	±2.80	±2.80	±2.80	±2.80

TABLE D.26: Full phase-space absolute differential cross-sections after combining the e+jets and μ+jets channels for the top-quark absolute rapidity $|y^t|$. All uncertainties are quoted as a percentage with respect to the cross-section values in each bin. Dashes are used when the estimated relative systematic uncertainty for that bin is below 0.1%.

Bins [GeV]	345–400	400–470	470–550	550–650	650–800	800–1100	1100–1600
$1/\sigma \cdot \mathrm{d}\sigma \,/\, \mathrm{d}\, m^{tt}$	$4.36 \cdot 10^{-3}$	$4.28 \cdot 10^{-3}$	$2.58 \cdot 10^{-3}$	$1.30 \cdot 10^{-3}$	$5.24 \cdot 10^{-4}$	$1.29 \cdot 10^{-4}$	$1.60 \cdot 10^{-5}$
Total Uncertainty [%]	±3.93	±4.52	±2.88	±2.94	±6.13	±13.3	±35.8
Statistics [%]	±0.5	±0.3	±0.4	±0.6	±0.8	±1.4	±4.3
Systematics [%]	±3.89	±4.51	±2.85	±2.87	±6.06	±13.2	±35.5
η intercalibration model (JES) [%]	∓0.63	∓0.24	$^{+0.24}_{-0.18}$	±0.53	±0.76	±1.05	±1.46
Single particle high-p_T (JES) [%]	-	-	-	-	-	-	-
Effective stat. NP set 1 (JES) [%]	-	±0.15	±0.16	-	∓0.36	∓0.79	∓1.37
Effective stat. NP set 2 (JES) [%]	-	-	-	-	±0.12	±0.18	±0.29
Effective stat. NP set 3 (JES) [%]	±0.56	±0.14	∓0.28	∓0.46	∓0.49	∓0.49	∓0.42
Effective detector NP set 1 (JES) [%]	∓0.93	∓0.38	±0.28	±0.77	±1.16	±1.71	±2.72
Effective detector NP set 2 (JES) [%]	-	-	-	-	∓0.12	∓0.26	∓0.45
Effective detector NP set 3 (JES) [%]	-	-	-	-	±0.11	±0.15	±0.22
Effective mixed NP set 1 (JES) [%]	∓0.78	∓0.26	±0.30	±0.63	±0.84	±1.06	±1.61
Effective mixed NP set 2 (JES) [%]	-	-	-	-	-	±0.30	±0.58
Effective model NP set 1 (JES) [%]	∓1.65	$^{-0.15}_{-}$	±1.14	±1.18	$^{+0.74}_{-0.52}$	$^{-}_{+0.12}$	∓1.06
Effective model NP set 2 (JES) [%]	-	-	-	-	±0.14	±0.27	±0.66
Effective model NP set 3 (JES) [%]	±0.52	±0.17	∓0.22	∓0.45	∓0.55	∓0.61	∓0.67
Effective model NP set 4 (JES) [%]	∓0.13	-	-	±0.11	±0.20	±0.30	±0.46
Pile-up offset μ (JES) [%]	-	-	-	-	-	-	$^{-0.25}_{-}$
Pile-up offset N_{PV} (JES) [%]	$^{+0.15}_{-0.22}$	-	$^{-0.13}_{+0.24}$	$^{-0.11}_{+0.15}$	-	$^{+0.23}_{-0.34}$	±0.50
Punch-through (JES) [%]	-	-	-	-	-	-	$^{+0.18}_{-0.11}$
Pile-up offset ρ topology (JES) [%]	∓0.94	-	±0.69	±0.69	$^{+0.33}_{-0.22}$	∓0.31	∓1.03
Pile-up offset p_T (JES) [%]	-	-	-	-	-	-	$^{+0.16}_{-}$
Flavour composition (JES) [%]	$^{-0.47}_{+0.33}$	$^{+0.11}_{-0.18}$	±0.44	$^{+0.33}_{-0.16}$	$^{-0.18}_{+0.33}$	∓1.00	∓1.73
Flavour response (JES) [%]	±0.59	-	∓0.38	∓0.45	$^{-0.24}_{+0.32}$	-	±0.21
b-Tagged jet energy scale (JES) [%]	∓1.09	∓0.23	±0.57	±0.85	±0.86	±0.76	±0.73
Jet reconstruction efficiency [%]	-	-	-	-	-	-	±0.10
Jet energy resolution [%]	-	-	-	-	-	-	-
b-Quark tagging efficiency [%]	-	∓0.12	∓0.14	-	±0.36	±0.98	±1.83
c-Quark tagging efficiency [%]	-	-	-	-	-	±0.27	±0.49
Light-jet tagging efficiency [%]	-	-	-	-	±0.22	±0.49	±0.96
Electron energy scale [%]	∓0.19	-	-	±0.15	±0.20	±0.34	±0.49
Electron energy resolution [%]	-	-	-	-	-	-	-
Muon momentum scale [%]	-	-	-	-	-	-	-
Muon (ID) momentum resolution [%]	-	-	-	-	-	-	-
Muon (MS) momentum resolution [%]	-	-	-	-	-	-	-
Lepton trigger efficiency [%]	-	-	-	-	-	-	±0.12
Lepton reconstruction efficiency [%]	-	-	-	-	-	-	±0.10
Lepton identification efficiency [%]	-	-	-	-	-	-	-
E_T^{miss} Soft jet scale [%]	-	-	-	-	-	-	-
E_T^{miss} Soft jet resolution [%]	-	-	-	-	-	-	-
Jet vertex fraction [%]	∓0.34	∓0.21	-	±0.32	±0.59	±0.94	±1.27
Alternate hard-scattering model [%]	±2.40	∓2.79	∓1.72	∓0.44	±1.97	±7.53	±29.1
Alternate parton-shower model [%]	±0.42	∓3.34	∓0.52	±1.69	±4.54	±8.33	±13.9
Monte Carlo sample statistics [%]	±0.13	-	±0.11	±0.15	±0.21	±0.35	±1.02
ISR/FSR + scale [%]	$^{-}_{-1.24}$	$^{-1.12}_{+0.48}$	$^{-1.19}_{+1.55}$	$^{+0.62}_{-}$	$^{+3.39}_{-0.95}$	$^{+7.83}_{-3.12}$	$^{+17.0}_{-6.73}$
Parton distribution functions [%]	±0.45	±0.13	-	∓0.26	∓0.49	∓1.22	∓2.86
Single top cross-section [%]	-	-	-	-	±0.16	±0.39	±0.89
W+jets scale factors [%]	∓0.10	∓0.13	-	-	±0.30	±0.74	±1.85
Fake lept. MC stat, e+jets ch. [%]	$^{-}_{-0.21}$	-	-	-	$^{+0.33}_{-}$	$^{+1.34}_{-}$	$^{+3.99}_{-}$
Fake lept. alternate fake CR, e+jets ch. [%]	-	-	-	-	±0.10	±0.18	±0.60
Fake lept. alternate real CR, e+jets ch. [%]	-	-	-	-	-	-	±0.22
Fake lept. alternate parametrization, e+jets ch. [%]	-	-	-	-	-	±0.26	±0.52
Fake lept. MC stat, μ+jets ch. [%]	-	-	-	-	-	-	$^{+0.51}_{-}$
Fake lept. alternate fake CR, μ+jets ch. [%]	-	-	-	-	-	-	±0.36
Fake lept. alternate real CR, μ+jets ch. [%]	∓0.30	∓0.18	-	±0.25	±0.50	±0.81	±1.54
Fake lept. alternate parametrization, μ+jets ch. [%]	-	-	-	-	±0.17	±0.30	±0.35
Z+jets cross-section [%]	-	±0.10	±0.10	-	∓0.20	∓0.64	∓1.96
Diboson cross-section [%]	-	-	-	-	-	∓0.10	∓0.18
Luminosity [%]	-	-	-	-	-	-	-

TABLE D.27: Full phase-space relative differential cross-sections after combining the e+jets and μ+jets channels for the $t\bar{t}$ system invariant mass $m^{t\bar{t}}$. All uncertainties are quoted as a percentage with respect to the cross-section values in each bin. Dashes are used when the estimated relative systematic uncertainty for that bin is below 0.1%.

Bins [GeV]	345–400	400–470	470–550	550–650	650–800	800–1100	1100–1600
$d\sigma$ / d $m^{t\bar{t}}$ [GeV]	$1.09 \cdot 10^{0}$	$1.07 \cdot 10^{0}$	$6.45 \cdot 10^{-1}$	$3.25 \cdot 10^{-1}$	$1.31 \cdot 10^{-1}$	$3.23 \cdot 10^{-2}$	$3.91 \cdot 10^{-3}$
Total Uncertainty [%]	±10.6	±15.1	±14.3	±12.6	±10.0	±9.76	±27.4
Statistics [%]	±0.7	±0.4	±0.5	±0.7	±0.9	±1.6	±2.4
Systematics [%]	±10.6	±15.1	±14.3	±12.6	±9.96	±9.63	±27.2
η intercalibration model (JES) [%]	$^{-0.30}_{+0.23}$	±0.11	±0.58	±0.90	±1.12	±1.41	±1.83
Single particle high-p_T (JES) [%]	-	-	-	-	-	-	-
Effective stat. NP set 1 (JES) [%]	±0.94	±1.11	±1.14	±0.93	±0.59	$^{+0.12}_{-0.21}$	∓0.40
Effective stat. NP set 2 (JES) [%]	∓0.17	∓0.13	-	-	-	-	±0.21
Effective stat. NP set 3 (JES) [%]	±0.54	±0.11	∓0.30	∓0.50	∓0.53	∓0.52	∓0.45
Effective detector NP set 1 (JES) [%]	∓0.82	∓0.27	±0.39	±0.88	±1.27	±1.83	±2.83
Effective detector NP set 2 (JES) [%]	±0.20	±0.26	±0.26	±0.18	-	-	$^{-0.29}_{+0.20}$
Effective detector NP set 3 (JES) [%]	-	-	-	±0.11	±0.14	±0.17	±0.24
Effective mixed NP set 1 (JES) [%]	∓0.51	-	±0.56	±0.90	±1.11	±1.33	±1.89
Effective mixed NP set 2 (JES) [%]	∓0.38	∓0.46	∓0.48	∓0.42	∓0.31	$^{-0.12}_{-}$	±0.17
Effective model NP set 1 (JES) [%]	$^{+0.58}_{-0.94}$	±2.30	±3.56	±3.60	±3.04	±2.31	±1.34
Effective model NP set 2 (JES) [%]	∓0.15	∓0.15	∓0.11	-	-	±0.18	±0.57
Effective model NP set 3 (JES) [%]	±0.67	±0.32	-	∓0.29	∓0.40	∓0.46	∓0.53
Effective model NP set 4 (JES) [%]	∓0.12	-	-	±0.11	±0.21	±0.32	±0.47
Pile-up offset μ (JES) [%]	∓0.11	∓0.15	∓0.22	∓0.26	∓0.26	∓0.27	$^{-0.43}_{+0.27}$
Pile-up offset N_{PV} (JES) [%]	∓0.47	∓0.69	∓0.85	∓0.80	∓0.58	$^{-0.42}_{+0.32}$	∓0.16
Punch-through (JES) [%]	-	-	-	-	-	-	$^{+0.17}_{-0.11}$
Pile-up offset ρ topology (JES) [%]	±0.83	±1.75	±2.46	±2.47	±2.06	±1.46	±0.74
Pile-up offset p_T (JES) [%]	-	-	-	-	-	-	$^{+0.15}_{-}$
Flavour composition (JES) [%]	±1.56	±2.12	±2.42	±2.22	±1.71	±0.97	±0.24
Flavour response (JES) [%]	∓0.60	∓1.14	∓1.58	∓1.65	∓1.48	∓1.25	∓0.99
b-Tagged jet energy scale (JES) [%]	∓0.55	±0.29	±1.10	±1.38	±1.40	±1.29	±1.27
Jet reconstruction efficiency [%]	-	-	-	-	-	-	-
Jet energy resolution [%]	-	-	-	-	-	-	-
b-Quark tagging efficiency [%]	±4.12	±4.04	±4.03	±4.17	±4.54	±5.15	±6.00
c-Quark tagging efficiency [%]	±0.90	±0.88	±0.87	±0.92	±1.00	±1.18	±1.41
Light-jet tagging efficiency [%]	±0.40	±0.40	±0.44	±0.54	±0.70	±0.98	±1.45
Electron energy scale [%]	$^{-0.15}_{-}$	-	$^{+0.13}_{-0.17}$	±0.24	±0.29	±0.44	±0.58
Electron energy resolution [%]	-	-	-	-	-	-	-
Muon momentum scale [%]	-	-	-	-	-	-	-
Muon (ID) momentum resolution [%]	-	-	-	-	-	-	-
Muon (MS) momentum resolution [%]	-	-	-	-	-	-	-
Lepton trigger efficiency [%]	±1.27	±1.26	±1.25	±1.25	±1.27	±1.30	±1.39
Lepton reconstruction efficiency [%]	±0.22	±0.22	±0.24	±0.26	±0.27	±0.30	±0.34
Lepton identification efficiency [%]	±1.27	±1.29	±1.32	±1.35	±1.36	±1.38	±1.40
E_T^{miss} Soft jet scale [%]	-	-	-	-	-	-	-
E_T^{miss} Soft jet resolution [%]	-	-	-	-	-	-	-
Jet vertex fraction [%]	∓1.04	∓0.91	∓0.66	∓0.38	$^{-0.13}_{-}$	±0.23	±0.56
Alternate hard-scattering model [%]	∓2.47	∓7.42	∓6.40	∓5.18	∓2.87	±2.41	±22.9
Alternate parton-shower model [%]	∓4.23	∓7.83	∓5.14	∓3.02	∓0.31	±3.30	±8.62
Monte Carlo sample statistics [%]	±0.18	±0.11	±0.13	±0.17	±0.24	±0.40	±0.31
ISR/FSR + scale [%]	$^{-8.17}_{+5.65}$	∓8.10	∓8.71	∓7.62	$^{-4.53}_{+5.96}$	$^{-0.43}_{+3.64}$	$^{+8.07}_{-0.21}$
Parton distribution functions [%]	-	∓0.25	∓0.42	∓0.65	∓0.88	∓1.60	∓3.24
Single top cross-section [%]	±0.17	±0.18	±0.22	±0.28	±0.41	±0.64	±1.14
W+jets scale factors [%]	±0.24	±0.22	±0.28	±0.44	±0.65	±1.10	±2.21
Fake lept. MC stat, e+jets ch. [%]	$^{-0.22}_{+0.30}$	$^{-0.15}_{+0.32}$	$^{-}_{+0.39}$	$^{-}_{+0.47}$	$^{+0.51}_{-}$	$^{+1.33}_{-}$	$^{+3.97}_{-}$
Fake lept. alternate fake CR, e+jets ch. [%]	±0.24	±0.26	±0.34	±0.41	±0.43	±0.50	±0.92
Fake lept. alternate real CR, e+jets ch. [%]	-	-	-	-	-	-	±0.17
Fake lept. alternate parametrization, e+jets ch. [%]	±0.25	±0.23	±0.27	±0.32	±0.34	±0.55	±0.81
Fake lept. MC stat, μ+jets ch. [%]	-	-	-	-	-	$^{+0.23}_{-}$	$^{+0.54}_{-}$
Fake lept. alternate fake CR, μ+jets ch. [%]	±0.27	±0.20	±0.15	±0.15	±0.19	±0.27	±0.57
Fake lept. alternate real CR, μ+jets ch. [%]	∓0.12	-	±0.22	±0.43	±0.68	±0.99	±1.72
Fake lept. alternate parametrization, μ+jets ch. [%]	±0.13	±0.15	±0.21	±0.31	±0.39	±0.52	±0.58
Z+jets cross-section [%]	∓0.89	∓0.81	∓0.81	∓0.93	∓1.11	∓1.55	∓2.86
Diboson cross-section [%]	-	-	-	-	∓0.10	∓0.18	∓0.26
Luminosity [%]	±2.80	±2.80	±2.80	±2.80	±2.80	±2.80	±2.80

TABLE D.28: Full phase-space absolute differential cross-sections after combining the e+jets and μ+jets channels for the $t\bar{t}$ system invariant mass $m^{t\bar{t}}$. All uncertainties are quoted as a percentage with respect to the cross-section values in each bin. Dashes are used when the estimated relative systematic uncertainty for that bin is below 0.1%.

Bins [GeV]	0–20	20–45	45–75	75–120	120–190	190–300
$1/\sigma \cdot \mathrm{d}\sigma \,/\, \mathrm{d}\, p_T^{t\bar{t}}$	$1.52 \cdot 10^{-2}$	$1.18 \cdot 10^{-2}$	$5.98 \cdot 10^{-3}$	$2.70 \cdot 10^{-3}$	$9.90 \cdot 10^{-4}$	$2.78 \cdot 10^{-4}$
Total Uncertainty [%]	±4.67	±3.20	±3.08	±4.92	±8.71	±11.1
Statistics [%]	±0.3	±0.1	±0.3	±0.5	±0.7	±1.5
Systematics [%]	±4.65	±3.19	±3.06	±4.88	±8.67	±11.0
η intercalibration model (JES) [%]	∓0.57	∓0.28	±0.23	±0.82	±1.19	±1.11
Single particle high-p_T (JES) [%]	-	-	-	-	-	-
Effective stat. NP set 1 (JES) [%]	∓0.43	∓0.15	±0.27	±0.63	±0.63	$^{+0.33}_{-0.21}$
Effective stat. NP set 2 (JES) [%]	-	-	-	-	-	-
Effective stat. NP set 3 (JES) [%]	-	-	-	∓0.15	∓0.29	$^{-0.19}_{+0.27}$
Effective detector NP set 1 (JES) [%]	∓0.14	∓0.11	-	$^{+0.10}_{-0.14}$	±0.50	±1.04
Effective detector NP set 2 (JES) [%]	-	-	-	±0.14	±0.11	-
Effective detector NP set 3 (JES) [%]	-	-	-	-	-	±0.10
Effective mixed NP set 1 (JES) [%]	∓0.20	∓0.12	-	±0.26	±0.55	$^{+0.86}_{-0.66}$
Effective mixed NP set 2 (JES) [%]	±0.19	-	∓0.11	∓0.27	∓0.30	$^{-0.14}_{+0.21}$
Effective model NP set 1 (JES) [%]	∓1.31	∓0.58	±0.63	±1.94	±2.42	±1.88
Effective model NP set 2 (JES) [%]	-	-	-	-	-	-
Effective model NP set 3 (JES) [%]	-	-	-	-	∓0.17	$^{-0.16}_{+0.23}$
Effective model NP set 4 (JES) [%]	-	-	-	-	-	±0.20
Pile-up offset μ (JES) [%]	±0.17	-	∓0.10	∓0.26	∓0.28	$^{-}_{+0.20}$
Pile-up offset N_{PV} (JES) [%]	$^{-}_{-0.12}$	-	-	∓0.20	$^{-0.21}_{+0.34}$	$^{-}_{+0.40}$
Punch-through (JES) [%]	-	-	-	-	-	-
Pile-up offset ρ topology (JES) [%]	∓0.93	∓0.40	±0.46	±1.35	±1.69	±1.25
Pile-up offset p_T (JES) [%]	-	-	-	-	-	-
Flavour composition (JES) [%]	∓1.50	∓0.70	±0.67	±2.17	±2.96	±2.49
Flavour response (JES) [%]	±1.06	±0.53	∓0.42	∓1.52	∓2.26	∓2.15
b-Tagged jet energy scale (JES) [%]	-	-	-	-	-	-
Jet reconstruction efficiency [%]	-	-	-	-	-	-
Jet energy resolution [%]	-	-	-	-	-	-
b-Quark tagging efficiency [%]	-	-	-	∓0.11	∓0.21	∓0.18
c-Quark tagging efficiency [%]	-	-	-	-	-	-
Light-jet tagging efficiency [%]	∓0.14	-	-	±0.19	±0.22	±0.13
Electron energy scale [%]	-	-	-	-	-	-
Electron energy resolution [%]	-	-	-	-	-	-
Muon momentum scale [%]	-	-	-	-	-	-
Muon (ID) momentum resolution [%]	-	-	-	-	-	-
Muon (MS) momentum resolution [%]	-	-	-	-	-	-
Lepton trigger efficiency [%]	-	-	-	-	-	-
Lepton reconstruction efficiency [%]	-	-	-	-	-	-
Lepton identification efficiency [%]	-	-	-	-	-	-
E_T^{miss} Soft jet scale [%]	∓1.83	-	±1.40	±1.65	±1.23	±0.82
E_T^{miss} Soft jet resolution [%]	$^{-}_{-0.36}$	-	$^{+0.28}_{-}$	$^{+0.39}_{-}$	$^{+0.26}_{-}$	$^{+0.29}_{-}$
Jet vertex fraction [%]	-	-	-	-	-	-
Alternate hard-scattering model [%]	∓0.64	±2.80	±1.59	∓1.61	∓6.41	∓8.99
Alternate parton-shower model [%]	∓3.01	±0.73	±1.61	±1.47	±1.68	±3.70
Monte Carlo sample statistics [%]	-	-	-	±0.13	±0.19	±0.39
ISR/FSR + scale [%]	$^{-1.78}_{+0.80}$	$^{-0.33}_{+0.57}$	$^{+1.21}_{-0.31}$	±1.46	±1.99	$^{+3.11}_{-1.73}$
Parton distribution functions [%]	±0.24	∓0.32	∓0.19	±0.10	±0.37	±0.62
Single top cross-section [%]	-	-	-	-	-	-
W+jets scale factors [%]	-	-	-	-	-	-
Fake lept. MC stat, e+jets ch. [%]	-	-	-	-	-	-
Fake lept. alternate fake CR, e+jets ch. [%]	-	-	-	-	-	∓0.11
Fake lept. alternate real CR, e+jets ch. [%]	-	-	-	-	-	-
Fake lept. alternate parametrization, e+jets ch. [%]	-	-	-	-	-	-
Fake lept. MC stat, μ+jets ch. [%]	-	-	-	-	-	-
Fake lept. alternate fake CR, μ+jets ch. [%]	-	-	-	-	-	-
Fake lept. alternate real CR, μ+jets ch. [%]	-	-	-	-	-	±0.10
Fake lept. alternate parametrization, μ+jets ch. [%]	-	-	-	-	-	±0.17
Z+jets cross-section [%]	-	-	-	-	-	-
Diboson cross-section [%]	-	-	-	-	-	-
Luminosity [%]	-	-	-	-	-	-

TABLE D.29: Full phase-space relative differential cross-sections after combining the e+jets and μ+jets channels for the $t\bar{t}$ system transverse momentum $p_{\mathrm{T}}^{t\bar{t}}$. All uncertainties are quoted as a percentage with respect to the cross-section values in each bin. Dashes are used when the estimated relative systematic uncertainty for that bin is below 0.1%.

Bins [GeV]	0–20	20–45	45–75	75–120	120–190	190–300
$d\sigma$ / d $p_T^{t\bar{t}}$ [GeV]	$3.80 \cdot 10^0$	$2.95 \cdot 10^0$	$1.50 \cdot 10^0$	$6.76 \cdot 10^{-1}$	$2.47 \cdot 10^{-1}$	$6.95 \cdot 10^{-2}$
Total Uncertainty [%]	±14.3	±11.6	±11.2	±12.6	±15.1	±15.9
Statistics [%]	±0.6	±0.4	±0.4	±0.5	±0.8	±1.7
Systematics [%]	±14.3	±11.6	±11.2	±12.6	±15.1	±15.9
η intercalibration model (JES) [%]	∓0.34	-	±0.47	±1.06	±1.44	±1.35
Single particle high-p_T (JES) [%]	-	-	-	-	-	-
Effective stat. NP set 1 (JES) [%]	±0.35	±0.64	±1.06	±1.42	±1.42	±1.06
Effective stat. NP set 2 (JES) [%]	-	-	-	∓0.11	-	-
Effective stat. NP set 3 (JES) [%]	-	-	-	∓0.15	∓0.30	$^{-0.19}_{+0.27}$
Effective detector NP set 1 (JES) [%]	-	-	-	±0.23	±0.61	±1.15
Effective detector NP set 2 (JES) [%]	-	±0.12	±0.22	±0.30	±0.28	±0.17
Effective detector NP set 3 (JES) [%]	-	-	-	-	-	±0.12
Effective mixed NP set 1 (JES) [%]	-	-	±0.26	±0.48	±0.77	±0.99
Effective mixed NP set 2 (JES) [%]	$^{-0.12}_{+0.16}$	∓0.26	∓0.44	∓0.61	∓0.64	∓0.51
Effective model NP set 1 (JES) [%]	±0.61	±1.34	±2.56	±3.87	±4.36	±3.81
Effective model NP set 2 (JES) [%]	-	-	∓0.10	∓0.14	∓0.10	-
Effective model NP set 3 (JES) [%]	±0.15	±0.17	±0.18	±0.11	-	-
Effective model NP set 4 (JES) [%]	-	-	-	-	-	$^{+0.24}_{-0.18}$
Pile-up offset μ (JES) [%]	-	-	∓0.23	∓0.39	∓0.41	$^{-0.18}_{+0.34}$
Pile-up offset N_{PV} (JES) [%]	∓0.46	∓0.48	∓0.60	∓0.78	∓0.85	$^{-0.64}_{+0.98}$
Punch-through (JES) [%]	-	-	-	-	-	-
Pile-up offset ρ topology (JES) [%]	±0.52	±1.06	±1.92	±2.79	±3.15	±2.69
Pile-up offset p_T (JES) [%]	-	-	-	-	-	-
Flavour composition (JES) [%]	-	±0.74	±2.12	±3.62	±4.41	±3.95
Flavour response (JES) [%]	$^{+0.19}_{-0.25}$	∓0.32	∓1.27	∓2.38	∓3.11	∓3.00
b-Tagged jet energy scale (JES) [%]	±0.45	±0.49	±0.55	±0.57	±0.58	±0.55
Jet reconstruction efficiency [%]	-	-	-	∓0.10	-	-
Jet energy resolution [%]	-	-	-	-	-	-
b-Quark tagging efficiency [%]	±4.33	±4.29	±4.23	±4.13	±4.03	±4.06
c-Quark tagging efficiency [%]	±0.89	±0.92	±0.97	±0.99	±0.96	±0.87
Light-jet tagging efficiency [%]	±0.33	±0.43	±0.56	±0.67	±0.70	±0.61
Electron energy scale [%]	$^{-}_{-0.14}$	$^{-}_{-0.14}$	$^{-}_{-0.13}$	-	-	-
Electron energy resolution [%]	-	-	-	-	-	-
Muon momentum scale [%]	-	-	-	-	-	-
Muon (ID) momentum resolution [%]	-	-	-	-	-	-
Muon (MS) momentum resolution [%]	-	-	-	-	-	-
Lepton trigger efficiency [%]	±1.27	±1.27	±1.26	±1.26	±1.26	±1.25
Lepton reconstruction efficiency [%]	±0.24	±0.24	±0.24	±0.24	±0.25	±0.26
Lepton identification efficiency [%]	±1.30	±1.31	±1.31	±1.32	±1.33	±1.34
E_T^{miss} Soft jet scale [%]	∓2.19	∓0.35	±1.06	±1.31	±0.90	±0.48
E_T^{miss} Soft jet resolution [%]	$^{-}_{-0.43}$	-	$^{+0.21}_{-}$	$^{+0.32}_{-}$	-	$^{+0.22}_{-}$
Jet vertex fraction [%]	∓0.70	∓0.66	∓0.62	∓0.64	∓0.67	∓0.59
Alternate hard-scattering model [%]	∓3.16	±0.20	∓0.98	∓4.10	∓8.78	∓11.2
Alternate parton-shower model [%]	∓7.84	∓4.28	∓3.44	∓3.58	∓3.38	∓1.46
Monte Carlo sample statistics [%]	±0.14	±0.10	±0.11	±0.14	±0.21	±0.44
ISR/FSR + scale [%]	∓9.64	∓8.89	∓7.71	∓7.00	$^{-7.54}_{+5.33}$	∓6.08
Parton distribution functions [%]	-	∓0.65	∓0.52	∓0.22	-	±0.29
Single top cross-section [%]	±0.28	±0.28	±0.27	±0.26	±0.24	±0.22
W+jets scale factors [%]	±0.47	±0.41	±0.35	±0.32	±0.37	±0.49
Fake lept. MC stat, e+jets ch. [%]	$^{-}_{+0.36}$	$^{+0.41}_{-}$	$^{+0.44}_{-}$	$^{+0.45}_{-}$	$^{+0.44}_{-}$	$^{+0.31}_{-}$
Fake lept. alternate fake CR, e+jets ch. [%]	±0.36	±0.38	±0.37	±0.35	±0.33	±0.25
Fake lept. alternate real CR, e+jets ch. [%]	-	-	-	-	-	-
Fake lept. alternate parametrization, e+jets ch. [%]	±0.21	±0.27	±0.33	±0.35	±0.33	±0.28
Fake lept. MC stat, μ+jets ch. [%]	-	-	-	-	-	-
Fake lept. alternate fake CR, μ+jets ch. [%]	±0.21	±0.24	±0.26	±0.25	±0.18	±0.17
Fake lept. alternate real CR, μ+jets ch. [%]	±0.23	±0.23	±0.23	±0.20	±0.14	±0.33
Fake lept. alternate parametrization, μ+jets ch. [%]	±0.22	±0.21	±0.21	±0.22	±0.28	±0.40
Z+jets cross-section [%]	∓1.05	∓1.04	∓0.98	∓0.92	∓0.92	∓0.97
Diboson cross-section [%]	∓0.13	∓0.10	-	-	-	-
Luminosity [%]	±2.80	±2.80	±2.80	±2.80	±2.80	±2.80

TABLE D.30: Full phase-space absolute differential cross-sections after combining the e+jets and μ+jets channels for the $t\bar{t}$ system transverse momentum $p_{\mathrm{T}}^{t\bar{t}}$. All uncertainties are quoted as a percentage with respect to the cross-section values in each bin. Dashes are used when the estimated relative systematic uncertainty for that bin is below 0.1%.

Bins [Unit $\lvert y^{t\bar{t}} \rvert$]	0–0.30	0.30–0.60	0.60–0.90	0.90–1.30	1.30–2.50
$1/\sigma \cdot \mathrm{d}\sigma$ / d $\lvert y^{t\bar{t}} \rvert$	$7.98 \cdot 10^{-1}$	$7.36 \cdot 10^{-1}$	$6.25 \cdot 10^{-1}$	$4.60 \cdot 10^{-1}$	$1.40 \cdot 10^{-1}$
Total Uncertainty [%]	± 1.57	$^{+1.39}_{-1.03}$	± 1.13	± 1.13	± 4.15
Statistics [%]	± 0.5	± 0.4	± 0.5	± 0.6	± 1.0
Systematics [%]	± 1.47	$^{+1.30}_{-0.90}$	± 0.95	$^{+0.76}_{-1.01}$	± 4.02
η intercalibration model (JES) [%]	∓ 0.36	∓ 0.27	-	± 0.24	± 0.69
Single particle high-p_T (JES) [%]	-	-	-	-	-
Effective stat. NP set 1 (JES) [%]	-	-	-	-	-
Effective stat. NP set 2 (JES) [%]	-	-	-	-	-
Effective stat. NP set 3 (JES) [%]	-	-	-	-	-
Effective detector NP set 1 (JES) [%]	-	-	-	-	-
Effective detector NP set 2 (JES) [%]	-	-	-	-	-
Effective detector NP set 3 (JES) [%]	-	-	-	-	-
Effective mixed NP set 1 (JES) [%]	-	-	-	-	-
Effective mixed NP set 2 (JES) [%]	-	-	-	-	-
Effective model NP set 1 (JES) [%]	-	-	-	-	$^{+0.11}_{-0.16}$
Effective model NP set 2 (JES) [%]	-	-	-	-	-
Effective model NP set 3 (JES) [%]	-	-	-	-	-
Effective model NP set 4 (JES) [%]	-	-	-	-	-
Pile-up offset μ (JES) [%]	-	-	-	-	∓ 0.16
Pile-up offset N_{PV} (JES) [%]	-	-	-	-	-
Punch-through (JES) [%]	-	-	-	-	-
Pile-up offset ρ topology (JES) [%]	-	-	-	-	-
Pile-up offset p_T (JES) [%]	-	-	-	-	-
Flavour composition (JES) [%]	∓ 0.10	-	-	-	$^{+0.15}_{-0.24}$
Flavour response (JES) [%]	-	-	-	-	∓ 0.14
b-Tagged jet energy scale (JES) [%]	-	-	-	-	-
Jet reconstruction efficiency [%]	-	-	-	-	-
Jet energy resolution [%]	-	-	-	-	-
b-Quark tagging efficiency [%]	-	-	-	-	-
c-Quark tagging efficiency [%]	-	-	-	-	-
Light-jet tagging efficiency [%]	-	-	-	-	-
Electron energy scale [%]	-	-	-	-	$^{+0.16}_{-0.21}$
Electron energy resolution [%]	-	-	-	-	-
Muon momentum scale [%]	-	-	-	-	-
Muon (ID) momentum resolution [%]	-	-	-	-	-
Muon (MS) momentum resolution [%]	-	-	-	-	-
Lepton trigger efficiency [%]	-	-	-	-	± 0.23
Lepton reconstruction efficiency [%]	-	-	-	-	-
Lepton identification efficiency [%]	-	-	-	-	-
E_T^{miss} Soft jet scale [%]	-	-	-	-	-
E_T^{miss} Soft jet resolution [%]	-	-	-	-	-
Jet vertex fraction [%]	-	-	-	-	-
Alternate hard-scattering model [%]	± 0.57	± 0.19	± 0.45	± 0.42	∓ 2.04
Alternate parton-shower model [%]	± 0.49	∓ 0.10	∓ 0.56	∓ 0.32	± 0.41
Monte Carlo sample statistics [%]	± 0.13	± 0.12	± 0.14	± 0.16	± 0.23
ISR/FSR + scale [%]	± 0.98	$^{+1.09}_{-0.60}$	$^{+0.59}_{-0.17}$	$^{-0.72}_{+0.25}$	∓ 2.41
Parton distribution functions [%]	± 0.50	± 0.45	± 0.33	± 0.28	∓ 2.00
Single top cross-section [%]	-	-	-	-	-
W+jets scale factors [%]	-	-	-	-	-
Fake lept. MC stat, e+jets ch. [%]	∓ 0.11	-	-	$^{+0.15}_{-}$	$^{+0.11}_{-0.17}$
Fake lept. alternate fake CR, e+jets ch. [%]	-	-	-	-	∓ 0.10
Fake lept. alternate real CR, e+jets ch. [%]	-	-	-	-	-
Fake lept. alternate parametrization, e+jets ch. [%]	-	-	-	-	-
Fake lept. MC stat, μ+jets ch. [%]	-	-	-	-	$^{+0.39}_{-}$
Fake lept. alternate fake CR, μ+jets ch. [%]	-	-	-	-	-
Fake lept. alternate real CR, μ+jets ch. [%]	∓ 0.37	∓ 0.28	∓ 0.20	± 0.18	± 0.93
Fake lept. alternate parametrization, μ+jets ch. [%]	∓ 0.15	∓ 0.12	∓ 0.10	-	± 0.52
Z+jets cross-section [%]	-	-	-	-	-
Diboson cross-section [%]	-	-	-	-	-
Luminosity [%]	-	-	-	-	-

TABLE D.31: Full phase-space relative differential cross-sections after combining the e+jets and μ+jets channels for the $t\bar{t}$ system rapidity $\left|y^{t\bar{t}}\right|$. All uncertainties are quoted as a percentage with respect to the cross-section values in each bin. Dashes are used when the estimated relative systematic uncertainty for that bin is below 0.1%.

Bins [Unit $\lvert y^{t\bar{t}}\rvert$]	0–0.30	0.30–0.60	0.60–0.90	0.90–1.30	1.30–2.50
$d\sigma$ / d $\lvert y^{t\bar{t}}\rvert$ [Unit $\lvert y^{t\bar{t}}\rvert$]	$2.02 \cdot 10^2$	$1.86 \cdot 10^2$	$1.58 \cdot 10^2$	$1.16 \cdot 10^2$	$3.54 \cdot 10^1$
Total Uncertainty [%]	±10.3	±10.6	±11.1	±11.6	±14.0
Statistics [%]	±0.6	±0.5	±0.6	±0.8	±1.2
Systematics [%]	±10.2	±10.6	±11.0	±11.6	±13.9
η intercalibration model (JES) [%]	±0.14	±0.23	±0.42	±0.74	±1.19
Single particle high-p_T (JES) [%]	-	-	-	-	-
Effective stat. NP set 1 (JES) [%]	±0.88	±0.89	±0.89	±0.91	±0.90
Effective stat. NP set 2 (JES) [%]	-	-	-	-	-
Effective stat. NP set 3 (JES) [%]	-	-	-	-	-
Effective detector NP set 1 (JES) [%]	±0.18	±0.16	±0.17	±0.22	±0.27
Effective detector NP set 2 (JES) [%]	±0.19	±0.18	±0.15	±0.18	±0.17
Effective detector NP set 3 (JES) [%]	-	-	-	-	-
Effective mixed NP set 1 (JES) [%]	±0.29	±0.28	±0.27	±0.35	±0.37
Effective mixed NP set 2 (JES) [%]	∓0.38	∓0.38	∓0.35	∓0.40	∓0.39
Effective model NP set 1 (JES) [%]	±2.26	±2.25	±2.26	±2.38	±2.45
Effective model NP set 2 (JES) [%]	-	-	-	-	-
Effective model NP set 3 (JES) [%]	±0.14	±0.13	±0.14	±0.11	-
Effective model NP set 4 (JES) [%]	-	-	-	-	-
Pile-up offset μ (JES) [%]	∓0.13	$^{-}_{+0.14}$	∓0.16	∓0.25	∓0.36
Pile-up offset N_{PV} (JES) [%]	∓0.60	∓0.60	∓0.62	∓0.65	∓0.55
Punch-through (JES) [%]	-	-	-	-	-
Pile-up offset ρ topology (JES) [%]	±1.69	±1.67	±1.69	±1.77	±1.81
Pile-up offset p_T (JES) [%]	-	-	-	-	-
Flavour composition (JES) [%]	±1.79	±1.85	±1.88	±1.96	±2.10
Flavour response (JES) [%]	∓1.13	∓1.13	∓1.15	∓1.25	∓1.33
b-Tagged jet energy scale (JES) [%]	±0.52	±0.50	±0.51	±0.55	±0.55
Jet reconstruction efficiency [%]	-	-	-	-	-
Jet energy resolution [%]	-	-	-	-	-
b-Quark tagging efficiency [%]	±4.22	±4.22	±4.22	±4.23	±4.24
c-Quark tagging efficiency [%]	±0.96	±0.95	±0.93	±0.91	±0.88
Light-jet tagging efficiency [%]	±0.50	±0.50	±0.51	±0.53	±0.56
Electron energy scale [%]	-	-	±0.12	$^{+0.11}_{-0.19}$	$^{+0.25}_{-0.37}$
Electron energy resolution [%]	-	-	-	-	-
Muon momentum scale [%]	-	-	-	-	-
Muon (ID) momentum resolution [%]	-	-	-	-	-
Muon (MS) momentum resolution [%]	-	-	-	-	-
Lepton trigger efficiency [%]	±1.20	±1.21	±1.25	±1.33	±1.53
Lepton reconstruction efficiency [%]	±0.23	±0.23	±0.23	±0.25	±0.31
Lepton identification efficiency [%]	±1.34	±1.33	±1.31	±1.28	±1.27
E_T^{miss} Soft jet scale [%]	-	-	-	-	-
E_T^{miss} Soft jet resolution [%]	-	-	-	-	-
Jet vertex fraction [%]	∓0.67	∓0.66	∓0.65	∓0.65	∓0.62
Alternate hard-scattering model [%]	∓3.52	∓3.88	∓3.63	∓3.66	∓6.03
Alternate parton-shower model [%]	∓3.25	∓3.82	∓4.27	∓4.03	∓3.33
Monte Carlo sample statistics [%]	±0.15	±0.14	±0.17	±0.19	±0.29
ISR/FSR + scale [%]	∓5.98	∓6.14	∓6.61	∓7.44	∓9.36
Parton distribution functions [%]	±0.13	-	-	-	∓2.36
Single top cross-section [%]	±0.29	±0.28	±0.26	±0.24	±0.20
W+jets scale factors [%]	±0.41	±0.43	±0.38	±0.35	±0.36
Fake lept. MC stat, e+jets ch. [%]	$^{-}_{+0.49}$	$^{-}_{+0.45}$	$^{+0.37}_{-}$	$^{+0.32}_{-}$	$^{+0.21}_{-}$
Fake lept. alternate fake CR, e+jets ch. [%]	±0.41	±0.40	±0.33	±0.29	±0.23
Fake lept. alternate real CR, e+jets ch. [%]	-	-	-	-	-
Fake lept. alternate parametrization, e+jets ch. [%]	±0.35	±0.28	±0.26	±0.29	±0.18
Fake lept. MC stat, μ+jets ch. [%]	-	-	-	-	$^{+0.48}_{-}$
Fake lept. alternate fake CR, μ+jets ch. [%]	±0.27	±0.21	±0.22	±0.17	±0.33
Fake lept. alternate real CR, μ+jets ch. [%]	-	-	±0.13	±0.51	±1.27
Fake lept. alternate parametrization, μ+jets ch. [%]	±0.13	±0.16	±0.18	±0.27	±0.81
Z+jets cross-section [%]	∓0.99	∓1.01	∓1.01	∓0.97	∓0.93
Diboson cross-section [%]	-	-	-	-	-
Luminosity [%]	±2.80	±2.80	±2.80	±2.80	±2.80

TABLE D.32: Full phase-space absolute differential cross-sections after combining the e+jets and μ+jets channels for the $t\bar{t}$ system rapidity $\left|y^{t\bar{t}}\right|$. All uncertainties are quoted as a percentage with respect to the cross-section values in each bin. Dashes are used when the estimated relative systematic uncertainty for that bin is below 0.1%.

Bins [GeV]	0–40	40–80	80–120	120–170	170–230	230–600
$1/\sigma \cdot \mathrm{d}\sigma \,/\, \mathrm{d}\,\lvert p_{out}^{tt}\rvert$	$1.86 \cdot 10^{-2}$	$4.11 \cdot 10^{-3}$	$1.33 \cdot 10^{-3}$	$4.65 \cdot 10^{-4}$	$1.50 \cdot 10^{-4}$	$1.30 \cdot 10^{-5}$
Total Uncertainty [%]	± 1.77	± 3.00	± 7.79	± 12.1	± 12.8	± 15.8
Statistics [%]	± 0.1	± 0.3	± 0.6	± 1.1	± 1.8	± 3.2
Systematics [%]	± 1.77	± 2.99	± 7.75	± 12.0	± 12.6	± 15.4
η intercalibration model (JES) [%]	∓ 0.17	± 0.34	± 0.79	± 0.96	$^{+1.06}_{-0.76}$	± 0.66
Single particle high-p_T (JES) [%]	-	-	-	-	-	-
Effective stat. NP set 1 (JES) [%]	-	± 0.22	± 0.30	$^{-}_{-0.13}$	$^{-}_{+0.23}$	∓ 0.50
Effective stat. NP set 2 (JES) [%]	-	-	-	-	-	± 0.13
Effective stat. NP set 3 (JES) [%]	-	-	∓ 0.25	∓ 0.38	$^{-0.31}_{+0.43}$	∓ 0.38
Effective detector NP set 1 (JES) [%]	-	-	± 0.39	± 0.72	± 1.13	± 1.54
Effective detector NP set 2 (JES) [%]	-	-	-	-	-	∓ 0.13
Effective detector NP set 3 (JES) [%]	-	-	-	-	$^{+0.15}_{-}$	± 0.15
Effective mixed NP set 1 (JES) [%]	-	± 0.14	± 0.40	± 0.60	± 0.82	± 1.02
Effective mixed NP set 2 (JES) [%]	-	$^{-0.12}_{-}$	$^{-0.20}_{+0.13}$	-	-	± 0.16
Effective model NP set 1 (JES) [%]	∓ 0.34	± 0.78	± 1.52	± 1.54	± 1.14	$^{+0.45}_{-0.60}$
Effective model NP set 2 (JES) [%]	-	-	-	-	$^{+0.18}_{-0.10}$	± 0.26
Effective model NP set 3 (JES) [%]	-	-	∓ 0.18	∓ 0.35	∓ 0.39	∓ 0.39
Effective model NP set 4 (JES) [%]	-	-	-	$^{+0.12}_{-}$	$^{+0.23}_{-0.17}$	± 0.32
Pile-up offset μ (JES) [%]	-	$^{-0.13}_{-}$	∓ 0.17	∓ 0.20	$^{+0.20}_{-}$	-
Pile-up offset N_{PV} (JES) [%]	-	-	$^{-0.17}_{+0.12}$	$^{-0.24}_{+0.10}$	$^{-}_{+0.22}$	-
Punch-through (JES) [%]	-	-	-	-	-	-
Pile-up offset ρ topology (JES) [%]	∓ 0.23	± 0.54	± 1.02	± 0.98	$^{+0.76}_{-0.55}$	$^{-}_{-0.24}$
Pile-up offset p_T (JES) [%]	-	-	-	-	-	-
Flavour composition (JES) [%]	∓ 0.38	± 0.87	± 1.69	± 1.68	± 1.09	$^{+0.24}_{-0.37}$
Flavour response (JES) [%]	± 0.30	∓ 0.63	∓ 1.36	∓ 1.54	∓ 1.31	$^{-1.10}_{+0.75}$
b-Tagged jet energy scale (JES) [%]	-	-	$^{+0.12}_{-0.18}$	$^{+0.22}_{-0.29}$	$^{+0.32}_{-0.21}$	$^{+0.34}_{-0.50}$
Jet reconstruction efficiency [%]	-	-	-	-	-	-
Jet energy resolution [%]	-	-	-	-	-	-
b-Quark tagging efficiency [%]	-	-	∓ 0.17	∓ 0.23	∓ 0.15	± 0.30
c-Quark tagging efficiency [%]	-	-	-	-	-	∓ 0.24
Light-jet tagging efficiency [%]	-	-	± 0.16	± 0.16	± 0.13	-
Electron energy scale [%]	-	-	-	-	-	-
Electron energy resolution [%]	-	-	-	-	-	-
Muon momentum scale [%]	-	-	-	-	-	-
Muon (ID) momentum resolution [%]	-	-	-	-	-	-
Muon (MS) momentum resolution [%]	-	-	-	-	-	-
Lepton trigger efficiency [%]	-	-	-	-	-	-
Lepton reconstruction efficiency [%]	-	-	-	-	-	-
Lepton identification efficiency [%]	-	-	-	-	-	-
E_T^{miss} Soft jet scale [%]	∓ 0.30	± 0.78	± 1.16	± 1.08	± 0.84	± 0.49
E_T^{miss} Soft jet resolution [%]	-	-	$^{+0.24}_{-}$	$^{+0.25}_{-}$	$^{-}_{-}$	$^{+0.20}_{-}$
Jet vertex fraction [%]	-	-	± 0.16	± 0.29	± 0.47	± 0.68
Alternate hard-scattering model [%]	± 1.45	∓ 1.87	∓ 6.60	∓ 11.0	∓ 11.5	∓ 13.6
Alternate parton-shower model [%]	± 0.61	∓ 1.20	∓ 2.29	∓ 3.10	∓ 4.27	∓ 5.17
Monte Carlo sample statistics [%]	-	-	± 0.17	± 0.28	± 0.45	± 0.81
ISR/FSR + scale [%]	± 0.24	$^{-1.25}_{+0.64}$	$^{-0.74}_{+0.38}$	$^{+0.88}_{-}$	$^{+0.97}_{-}$	$^{+5.81}_{-}$
Parton distribution functions [%]	-	∓ 0.13	± 0.18	± 0.39	± 0.50	± 0.84
Single top cross-section [%]	-	-	-	-	-	-
W+jets scale factors [%]	-	-	-	-	± 0.19	± 0.36
Fake lept. MC stat, e+jets ch. [%]	-	-	-	-	$^{+0.23}_{-}$	± 0.32
Fake lept. alternate fake CR, e+jets ch. [%]	-	-	-	-	∓ 0.16	∓ 0.30
Fake lept. alternate real CR, e+jets ch. [%]	-	-	-	-	-	-
Fake lept. alternate parametrization, e+jets ch. [%]	-	-	-	-	∓ 0.10	∓ 0.18
Fake lept. MC stat, μ+jets ch. [%]	-	-	-	-	-	-
Fake lept. alternate fake CR, μ+jets ch. [%]	-	-	-	-	-	± 0.15
Fake lept. alternate real CR, μ+jets ch. [%]	-	-	-	-	-	∓ 0.15
Fake lept. alternate parametrization, μ+jets ch. [%]	-	-	-	± 0.10	± 0.47	± 0.19
Z+jets cross-section [%]	-	-	-	-	-	± 0.15
Diboson cross-section [%]	-	-	-	-	-	-
Luminosity [%]	-	-	-	-	-	-

TABLE D.33: Fiducial phase-space relative differential cross-sections after combining the e+jets and μ+jets channels for the $t\bar{t}$ system out-of-plane momentum $\left|p_{\mathrm{out}}^{t\bar{t}}\right|$. All uncertainties are quoted as a percentage with respect to the cross-section values in each bin. Dashes are used when the estimated relative systematic uncertainty for that bin is below 0.1%.

Bins [GeV]	0–40	40–80	80–120	120–170	170–230	230–600
$d\sigma$ / d $\|p_{out}^{t\bar{t}}\|$ [GeV]	$4.71 \cdot 10^{0}$	$1.04 \cdot 10^{0}$	$3.37 \cdot 10^{-1}$	$1.18 \cdot 10^{-1}$	$3.79 \cdot 10^{-2}$	$3.26 \cdot 10^{-3}$
Total Uncertainty [%]	±10.3	±13.4	±16.2	±19.2	±19.9	±21.2
Statistics [%]	±0.3	±0.4	±0.7	±1.2	±2.0	±3.6
Systematics [%]	±10.3	±13.4	±16.2	±19.2	±19.8	±20.9
η intercalibration model (JES) [%]	±0.16	±0.69	±1.14	±1.29	±1.25	±1.00
Single particle high-p_T (JES) [%]	-	-	-	-	-	-
Effective stat. NP set 1 (JES) [%]	±0.80	±1.09	±1.17	±0.98	±0.71	±0.36
Effective stat. NP set 2 (JES) [%]	-	-	-	-	-	-
Effective stat. NP set 3 (JES) [%]	-	-	∓0.27	∓0.39	$^{-0.32}_{+0.44}$	∓0.39
Effective detector NP set 1 (JES) [%]	-	±0.24	±0.53	±0.86	±1.27	±1.69
Effective detector NP set 2 (JES) [%]	±0.16	±0.22	±0.24	±0.17	$^{+0.15}$ -	-
Effective detector NP set 3 (JES) [%]	-	-	-	$^{+0.12}$ -	$^{+0.18}_{-0.12}$	±0.17
Effective mixed NP set 1 (JES) [%]	±0.16	±0.40	±0.66	±0.86	±1.08	±1.28
Effective mixed NP set 2 (JES) [%]	∓0.33	∓0.47	∓0.53	∓0.45	$^{-0.23}_{+0.36}$	∓0.20
Effective model NP set 1 (JES) [%]	±1.81	±2.94	±3.69	±3.71	±3.30	±2.69
Effective model NP set 2 (JES) [%]	-	-	-	-	-	±0.18
Effective model NP set 3 (JES) [%]	±0.18	±0.11	-	∓0.21	$^{-0.19}_{+0.28}$	∓0.24
Effective model NP set 4 (JES) [%]	-	-	-	±0.12	$^{+0.25}_{-0.19}$	±0.33
Pile-up offset μ (JES) [%]	∓0.12	∓0.26	∓0.34	∓0.35	$^{-0.14}_{+0.37}$	-
Pile-up offset N_{PV} (JES) [%]	∓0.55	∓0.69	∓0.74	∓0.76	$^{-0.62}_{+0.83}$	∓0.62
Punch-through (JES) [%]	-	-	-	-	-	-
Pile-up offset ρ topology (JES) [%]	±1.39	±2.16	±2.63	±2.60	±2.28	±1.75
Pile-up offset p_T (JES) [%]	-	-	-	-	-	-
Flavour composition (JES) [%]	±1.35	±2.60	±3.42	±3.42	±2.83	±2.04
Flavour response (JES) [%]	∓0.74	∓1.69	∓2.42	∓2.59	∓2.37	∓1.98
b-Tagged jet energy scale (JES) [%]	±0.46	±0.55	±0.66	±0.76	±0.77	±0.93
Jet reconstruction efficiency [%]	-	-	-	-	-	-
Jet energy resolution [%]	-	-	-	-	-	-
b-Quark tagging efficiency [%]	±4.28	±4.17	±4.05	±4.00	±4.08	±4.54
c-Quark tagging efficiency [%]	±0.93	±0.96	±0.97	±0.95	±0.86	±0.69
Light-jet tagging efficiency [%]	±0.46	±0.58	±0.66	±0.66	±0.63	±0.52
Electron energy scale [%]	$^{-}_{-0.13}$	$^{-}_{-0.13}$	-	-	-	-
Electron energy resolution [%]	-	-	-	-	-	-
Muon momentum scale [%]	-	-	-	-	-	-
Muon (ID) momentum resolution [%]	-	-	-	-	-	-
Muon (MS) momentum resolution [%]	-	-	-	-	-	-
Lepton trigger efficiency [%]	±1.26	±1.27	±1.27	±1.27	±1.27	±1.25
Lepton reconstruction efficiency [%]	±0.24	±0.24	±0.24	±0.25	±0.25	±0.25
Lepton identification efficiency [%]	±1.32	±1.31	±1.31	±1.31	±1.31	±1.33
E_T^{miss} Soft jet scale [%]	∓0.41	±0.67	±1.05	±0.97	±0.73	±0.39
E_T^{miss} Soft jet resolution [%]	-	-	$^{+0.22}$ -	$^{+0.23}$ -	-	-
Jet vertex fraction [%]	∓0.72	∓0.61	∓0.51	∓0.38	$^{-0.25}_{+0.15}$	-
Alternate hard-scattering model [%]	∓1.43	∓4.67	∓9.27	∓13.6	∓14.0	∓16.1
Alternate parton-shower model [%]	∓3.49	∓5.23	∓6.28	∓7.05	∓8.18	∓9.04
Monte Carlo sample statistics [%]	-	±0.11	±0.19	±0.31	±0.50	±0.91
ISR/FSR + scale [%]	∓7.25	∓8.41	∓8.04	∓7.83	∓7.78	$^{-2.65}_{+8.15}$
Parton distribution functions [%]	∓0.27	∓0.40	-	±0.12	±0.23	±0.57
Single top cross-section [%]	±0.27	±0.26	±0.24	±0.25	±0.27	±0.31
W+jets scale factors [%]	±0.40	±0.35	±0.37	±0.40	±0.59	±0.77
Fake lept. MC stat, e+jets ch. [%]	$^{+0.39}$ -	$^{+0.44}$ -	$^{+0.49}$ -	$^{+0.47}$ -	$^{+0.30}$ -	$^{+0.34}$ -
Fake lept. alternate fake CR, e+jets ch. [%]	±0.35	±0.37	±0.39	±0.36	±0.19	-
Fake lept. alternate real CR, e+jets ch. [%]	-	-	-	-	-	-
Fake lept. alternate parametrization, e+jets ch. [%]	±0.28	±0.33	±0.33	±0.29	±0.19	±0.10
Fake lept. MC stat, μ+jets ch. [%]	-	-	-	-	-	-
Fake lept. alternate fake CR, μ+jets ch. [%]	±0.23	±0.25	±0.22	±0.15	±0.16	±0.39
Fake lept. alternate real CR, μ+jets ch. [%]	±0.23	±0.20	±0.20	±0.25	±0.30	-
Fake lept. alternate parametrization, μ+jets ch. [%]	±0.22	±0.22	±0.23	±0.33	±0.70	±0.42
Z+jets cross-section [%]	±0.50	±0.47	±0.49	±0.51	±0.58	±0.65
Diboson cross-section [%]	-	-	-	-	-	-
Luminosity [%]	±2.80	±2.80	±2.80	±2.80	±2.80	±2.80

TABLE D.34: Fiducial phase-space absolute differential cross-sections after combining the e+jets and μ+jets channels for the $t\bar{t}$ system out-of-plane momentum $\left|p_{\mathrm{out}}^{t\bar{t}}\right|$. All uncertainties are quoted as a percentage with respect to the cross-section values in each bin. Dashes are used when the estimated relative systematic uncertainty for that bin is below 0.1%.

Bins [Unit $\Delta\phi^{t\bar{t}}$]	0–2	2–2.75	2.75–3	3–3.15
$1/\sigma \cdot \mathrm{d}\sigma$ / d $\Delta\phi^{tt}$	$6.09 \cdot 10^{-2}$	$2.87 \cdot 10^{-1}$	$1.09 \cdot 10^{0}$	$2.60 \cdot 10^{0}$
Total Uncertainty [%]	$\pm$5.23	$\pm$3.86	$\pm$2.08	$\pm$2.59
Statistics [%]	$\pm$0.7	$\pm$0.3	$\pm$0.1	$\pm$0.3
Systematics [%]	$\pm$5.18	$\pm$3.84	$\pm$2.07	$\pm$2.57
η intercalibration model (JES) [%]	$\pm$0.50	$\pm$0.28	-	$\mp$0.28
Single particle high-p_T (JES) [%]	-	-	-	-
Effective stat. NP set 1 (JES) [%]	$\pm$0.36	$\pm$0.28	-	$\mp$0.27
Effective stat. NP set 2 (JES) [%]	-	-	-	-
Effective stat. NP set 3 (JES) [%]	-	-	-	-
Effective detector NP set 1 (JES) [%]	-	$\mp$0.14	-	$\pm$0.11
Effective detector NP set 2 (JES) [%]	-	-	-	-
Effective detector NP set 3 (JES) [%]	-	-	-	-
Effective mixed NP set 1 (JES) [%]	-	-	-	-
Effective mixed NP set 2 (JES) [%]	$\mp$0.15	$\mp$0.11	-	$\pm$0.11
Effective model NP set 1 (JES) [%]	$\pm$0.76	$\pm$0.56	-	$\mp$0.51
Effective model NP set 2 (JES) [%]	-	-	-	-
Effective model NP set 3 (JES) [%]	$\pm$0.14	-	-	-
Effective model NP set 4 (JES) [%]	-	-	-	-
Pile-up offset μ (JES) [%]	$\mp$0.14	-	-	-
Pile-up offset N_{PV} (JES) [%]	$\mp$0.11	-	-	-
Punch-through (JES) [%]	-	-	-	-
Pile-up offset ρ topology (JES) [%]	$\pm$0.59	$\pm$0.45	-	$\mp$0.41
Pile-up offset p_T (JES) [%]	-	-	-	-
Flavour composition (JES) [%]	$\pm$1.42	$\pm$0.81	$^{-0.14}_{+0.10}$	$\mp$0.81
Flavour response (JES) [%]	$\mp$0.94	$\mp$0.49	-	$\pm$0.49
b-Tagged jet energy scale (JES) [%]	$\mp$0.30	$^{-0.12}_{-}$	-	$\pm$0.12
Jet reconstruction efficiency [%]	-	-	-	-
Jet energy resolution [%]	-	-	-	-
b-Quark tagging efficiency [%]	$\mp$0.38	$\mp$0.21	-	$\pm$0.22
c-Quark tagging efficiency [%]	$\pm$0.12	-	-	-
Light-jet tagging efficiency [%]	$\pm$0.14	$\pm$0.10	-	$\mp$0.10
Electron energy scale [%]	-	-	-	-
Electron energy resolution [%]	-	-	-	-
Muon momentum scale [%]	-	-	-	-
Muon (ID) momentum resolution [%]	-	-	-	-
Muon (MS) momentum resolution [%]	-	-	-	-
Lepton trigger efficiency [%]	-	-	-	-
Lepton reconstruction efficiency [%]	-	-	-	-
Lepton identification efficiency [%]	-	-	-	-
E_T^{miss} Soft jet scale [%]	$\pm$1.08	$\pm$0.98	$\pm$0.14	$\mp$0.97
E_T^{miss} Soft jet resolution [%]	-	-	-	-
Jet vertex fraction [%]	$\mp$0.11	-	-	-
Alternate hard-scattering model [%]	$\mp$4.55	$\mp$3.29	$\pm$1.97	$\pm$1.86
Alternate parton-shower model [%]	$\mp$0.12	$\mp$0.24	$\pm$0.49	$\mp$0.17
Monte Carlo sample statistics [%]	$\pm$0.17	-	-	-
ISR/FSR + scale [%]	-	$^{+1.25}_{-0.73}$	$^{+0.32}_{-}$	$^{-0.88}_{+0.37}$
Parton distribution functions [%]	$\pm$0.22	$\mp$0.10	$\mp$0.22	$\pm$0.14
Single top cross-section [%]	-	-	-	-
W+jets scale factors [%]	$\pm$0.13	-	-	-
Fake lept. MC stat, e+jets ch. [%]	-	-	-	-
Fake lept. alternate fake CR, e+jets ch. [%]	-	-	-	-
Fake lept. alternate real CR, e+jets ch. [%]	-	-	-	-
Fake lept. alternate parametrization, e+jets ch. [%]	-	-	-	-
Fake lept. MC stat, μ+jets ch. [%]	-	-	-	-
Fake lept. alternate fake CR, μ+jets ch. [%]	$\pm$0.10	-	-	-
Fake lept. alternate real CR, μ+jets ch. [%]	$\mp$0.24	-	-	$\pm$0.10
Fake lept. alternate parametrization, μ+jets ch. [%]	-	-	-	-
Z+jets cross-section [%]	$\mp$0.32	$\mp$0.17	-	$\pm$0.17
Diboson cross-section [%]	-	-	-	-
Luminosity [%]	-	-	-	-

TABLE D.35: Fiducial phase-space relative differential cross-sections after combining the e+jets and μ+jets channels for the $t\bar{t}$ system azimuthal angle $\Delta\phi^{t\bar{t}}$. All uncertainties are quoted as a percentage with respect to the cross-section values in each bin. Dashes are used when the estimated relative systematic uncertainty for that bin is below 0.1%.

Bins [Unit $\Delta\phi^{tt}$]	0–2	2–2.75	2.75–3	3–3.15
$d\sigma$ / d $\Delta\phi^{tt}$ [Unit $\Delta\phi^{tt}$]	$1.54 \cdot 10^1$	$7.25 \cdot 10^1$	$2.76 \cdot 10^2$	$6.59 \cdot 10^2$
Total Uncertainty [%]	±13.5	±12.1	±10.3	±10.9
Statistics [%]	±0.8	±0.4	±0.3	±0.5
Systematics [%]	±13.5	±12.1	±10.3	±10.9
η intercalibration model (JES) [%]	±0.88	±0.67	±0.33	±0.11
Single particle high-p_T (JES) [%]	-	-	-	-
Effective stat. NP set 1 (JES) [%]	±1.23	±1.15	±0.86	±0.60
Effective stat. NP set 2 (JES) [%]	∓0.11	∓0.11	-	-
Effective stat. NP set 3 (JES) [%]	-	-	-	-
Effective detector NP set 1 (JES) [%]	±0.15	-	±0.17	±0.32
Effective detector NP set 2 (JES) [%]	±0.25	±0.23	±0.17	±0.11
Effective detector NP set 3 (JES) [%]	-	-	-	-
Effective mixed NP set 1 (JES) [%]	±0.32	±0.25	±0.28	±0.34
Effective mixed NP set 2 (JES) [%]	∓0.53	∓0.48	∓0.36	∓0.26
Effective model NP set 1 (JES) [%]	±3.01	±2.80	±2.20	±1.73
Effective model NP set 2 (JES) [%]	-	∓0.11	-	-
Effective model NP set 3 (JES) [%]	±0.26	±0.21	±0.11	-
Effective model NP set 4 (JES) [%]	-	-	-	-
Pile-up offset μ (JES) [%]	∓0.30	∓0.26	∓0.15	-
Pile-up offset N_{PV} (JES) [%]	∓0.71	∓0.63	∓0.57	∓0.57
Punch-through (JES) [%]	-	-	-	-
Pile-up offset ρ topology (JES) [%]	±2.27	±2.12	±1.64	±1.25
Pile-up offset p_T (JES) [%]	-	-	-	-
Flavour composition (JES) [%]	±3.22	±2.62	±1.67	±0.99
Flavour response (JES) [%]	∓2.05	∓1.61	∓1.02	∓0.62
b-Tagged jet energy scale (JES) [%]	±0.23	±0.42	±0.56	±0.67
Jet reconstruction efficiency [%]	∓0.10	-	-	-
Jet energy resolution [%]	-	-	-	-
b-Quark tagging efficiency [%]	±3.87	±4.03	±4.26	±4.47
c-Quark tagging efficiency [%]	±1.05	±1.02	±0.93	±0.83
Light-jet tagging efficiency [%]	±0.65	±0.61	±0.50	±0.40
Electron energy scale [%]	$^{+0.12}_{-0.18}$	$^{-}_{-0.15}$	-	-
Electron energy resolution [%]	-	-	-	-
Muon momentum scale [%]	-	-	-	-
Muon (ID) momentum resolution [%]	-	-	-	-
Muon (MS) momentum resolution [%]	-	-	-	-
Lepton trigger efficiency [%]	±1.30	±1.28	±1.26	±1.24
Lepton reconstruction efficiency [%]	±0.23	±0.23	±0.24	±0.25
Lepton identification efficiency [%]	±1.27	±1.29	±1.32	±1.34
E_T^{miss} Soft jet scale [%]	±1.00	±0.90	-	∓1.06
E_T^{miss} Soft jet resolution [%]	-	-	-	-
Jet vertex fraction [%]	∓0.76	∓0.71	∓0.64	∓0.58
Alternate hard-scattering model [%]	∓7.28	∓6.05	∓0.93	∓1.04
Alternate parton-shower model [%]	∓3.78	∓3.90	∓3.19	∓3.83
Monte Carlo sample statistics [%]	±0.20	±0.12	-	±0.12
ISR/FSR + scale [%]	∓7.19	∓6.19	∓7.04	∓7.77
Parton distribution functions [%]	-	∓0.31	∓0.44	-
Single top cross-section [%]	±0.23	±0.26	±0.27	±0.29
W+jets scale factors [%]	±0.53	±0.40	±0.37	±0.36
Fake lept. MC stat, e+jets ch. [%]	$^{-}_{+0.42}$	$^{+0.42}_{-}$	$^{+0.42}_{-}$	$^{+0.38}_{-}$
Fake lept. alternate fake CR, e+jets ch. [%]	±0.38	±0.37	±0.36	±0.33
Fake lept. alternate real CR, e+jets ch. [%]	-	-	-	-
Fake lept. alternate parametrization, e+jets ch. [%]	±0.27	±0.28	±0.30	±0.29
Fake lept. MC stat, μ+jets ch. [%]	-	-	-	-
Fake lept. alternate fake CR, μ+jets ch. [%]	±0.33	±0.27	±0.21	±0.18
Fake lept. alternate real CR, μ+jets ch. [%]	-	±0.15	±0.26	±0.33
Fake lept. alternate parametrization, μ+jets ch. [%]	±0.16	±0.21	±0.24	±0.27
Z+jets cross-section [%]	∓1.30	∓1.15	∓0.95	∓0.80
Diboson cross-section [%]	-	-	-	-
Luminosity [%]	±2.80	±2.80	±2.80	±2.80

TABLE D.36: Fiducial phase-space absolute differential cross-sections after combining the e+jets and μ+jets channels for the $t\bar{t}$ system azimuthal angle $\Delta\phi^{t\bar{t}}$. All uncertainties are quoted as a percentage with respect to the cross-section values in each bin. Dashes are used when the estimated relative systematic uncertainty for that bin is below 0.1%.

Bins [GeV]	0–90	90–140	140–195	195–255	255–320	320–385	385–455	455–530	530–610	610–695	695–780	780–865	865–950	950–1041	1041–1500	1500–2000
$1/\sigma \cdot \mathrm{d}\sigma$ / d $H_T^{t\bar{t}}$	$1.22 \cdot 10^{-3}$	$3.19 \cdot 10^{-3}$	$3.54 \cdot 10^{-3}$	$3.06 \cdot 10^{-3}$	$2.18 \cdot 10^{-3}$	$1.36 \cdot 10^{-3}$	$7.82 \cdot 10^{-4}$	$4.21 \cdot 10^{-4}$	$2.17 \cdot 10^{-4}$	$1.09 \cdot 10^{-4}$	$5.50 \cdot 10^{-5}$	$2.90 \cdot 10^{-5}$	$1.50 \cdot 10^{-5}$	$8.00 \cdot 10^{-6}$	$2.00 \cdot 10^{-6}$	$3.00 \cdot 10^{-7}$
Total Uncertainty [%]	±7.06	±2.65	±3.17	±2.80	±2.21	±3.16	±4.18	±5.07	±6.78	±4.63	±7.29	±14.4	±21.1	±12.7	±16.4	±12.
Statistics [%]	±0.8	±0.4	±0.3	±0.4	±0.5	±0.7	±0.8	±1.1	±1.5	±2.1	±3.0	±4.3	±5.8	±8.4	±12.	±19.
Systematics [%]	±7.01	±2.60	±3.14	±2.77	±2.13	±3.07	±4.08	±4.93	±6.58	±4.09	±6.61	±13.7	±20.3	±9.37	±10.8	±19.
η intercalibration model (JES) [%]	∓0.49	∓0.32	∓0.16	-	±0.30	±0.39	±0.34	±0.32	$^{+0.31}_{-0.46}$	±0.26	$^{+0.28}_{-0.20}$	$^{+0.32}_{-0.14}$	$^{+0.18}_{-0.40}$	±0.53	-	-
Single particle high-p_T (JES) [%]	-	-	-	-	-	-	-	-	-	-	-	-	-	-	$^{-}_{-0.26}$	$^{-}_{-0.}$
Effective stat. NP set 1 (JES) [%]	-	-	-	±0.11	-	-	∓0.19	$^{-0.43}_{+0.30}$	∓0.46	∓0.55	∓0.55	$^{-0.45}_{+0.71}$	∓0.54	$^{-0.50}_{+0.88}$	$^{-0.25}_{+0.75}$	$^{-0.}_{+0.}$
Effective stat. NP set 2 (JES) [%]	-	-	-	-	-	-	-	±0.11	±0.15	$^{-}_{-0.15}$	±0.16	$^{+0.25}_{-0.13}$	±0.17	$^{+0.33}_{-0.24}$	±0.41	±0.
Effective stat. NP set 3 (JES) [%]	±0.41	±0.33	±0.18	-	∓0.29	∓0.41	∓0.41	∓0.37	∓0.40	∓0.35	∓0.30	$^{-0.16}_{+0.55}$	∓0.26	$^{-0.29}_{+0.40}$	$^{-0.35}_{+0.51}$	$^{-0.}_{+0.}$
Effective detector NP set 1 (JES) [%]	∓0.66	∓0.56	∓0.38	-	±0.34	±0.61	±0.80	±0.98	±1.48	±1.62	±2.15	±2.75	±2.65	±3.66	±4.58	±5.
Effective detector NP set 2 (JES) [%]	-	-	-	-	-	-	-	∓0.12	∓0.16	$^{-0.27}_{+0.17}$	∓0.27	$^{-0.24}_{+0.40}$	∓0.25	$^{-0.26}_{+0.45}$	∓0.30	∓0.
Effective detector NP set 3 (JES) [%]	-	-	-	-	-	-	-	-	±0.13	±0.15	±0.20	$^{+0.43}_{-0.14}$	$^{+0.22}_{-0.29}$	$^{+0.14}_{-0.42}$	$^{+0.39}_{-0.23}$	$^{+0.}_{-0.}$
Effective mixed NP set 1 (JES) [%]	∓0.57	∓0.46	∓0.29	-	±0.34	±0.52	±0.62	±0.70	±0.99	±1.00	±1.33	±1.75	±1.67	±2.46	±2.58	±3.
Effective mixed NP set 2 (JES) [%]	-	-	-	-	-	-	-	±0.12	$^{-}_{-0.17}$	$^{+0.12}_{-0.24}$	±0.16	$^{+0.42}_{-0.28}$	$^{+0.37}_{-0.18}$	$^{+0.37}_{-0.15}$	±0.67	±0.
Effective model NP set 1 (JES) [%]	∓1.27	∓0.85	∓0.38	±0.31	±0.98	±1.06	$^{+0.81}_{-0.61}$	$^{+0.45}_{-0.29}$	$^{+0.23}_{-0.45}$	$^{-}_{-0.24}$	±0.25	$^{+0.25}_{-}$	$^{-0.19}_{-}$	$^{+0.53}_{-}$	$^{-}_{-0.26}$	$^{-}_{-0.}$
Effective model NP set 2 (JES) [%]	-	-	-	-	-	-	-	±0.13	±0.24	±0.23	±0.36	$^{+0.89}_{-0.57}$	±0.53	±1.28	±1.73	±2.
Effective model NP set 3 (JES) [%]	±0.35	±0.31	±0.18	-	∓0.24	∓0.37	∓0.42	∓0.43	∓0.44	∓0.43	∓0.42	$^{-0.31}_{+0.45}$	$^{-0.20}_{+0.30}$	∓0.30	$^{-0.27}_{+0.36}$	$^{-0.}_{+0.}$
Effective model NP set 4 (JES) [%]	-	-	-	-	-	-	±0.15	±0.17	±0.27	±0.29	±0.32	$^{+0.66}_{-0.43}$	±0.46	$^{+0.47}_{-0.31}$	±1.00	±1.
Pile-up offset μ (JES) [%]	-	-	-	-	-	-	-	-	-	-	-	$^{+0.22}_{-}$	±0.15	-	$^{-}_{-0.23}$	$^{-}_{-0.}$
Pile-up offset N_{PV} (JES) [%]	±0.22	±0.12	-	-	∓0.18	∓0.15	-	-	-	±0.27	$^{-}_{-0.29}$	$^{+0.34}_{-}$	$^{+0.33}_{-}$	$^{+0.23}_{-}$	$^{-0.13}_{+0.28}$	$^{-0.}_{+0.}$
Punch-through (JES) [%]	-	-	-	-	-	-	-	-	-	-	-	±0.12	$^{-}_{-0.17}$	$^{-}_{-0.23}$	$^{+0.38}_{-}$	$^{+0.}_{-0.}$
Pile-up offset ρ topology (JES) [%]	∓0.75	∓0.47	∓0.18	$^{+0.18}_{-0.25}$	±0.56	±0.58	±0.35	±0.14	-	-	-	$^{+0.37}_{-}$	$^{-0.35}_{-}$	$^{+0.41}_{-}$	$^{-0.53}_{+0.12}$	$^{-0.}_{+0.}$
Pile-up offset p_T (JES) [%]	-	-	-	-	-	-	-	-	-	-	-	$^{-}_{+0.45}$	-	-	$^{-}_{-0.38}$	$^{-}_{-0.}$
Flavour composition (JES) [%]	∓0.73	∓0.44	∓0.14	±0.20	±0.52	±0.53	$^{+0.44}_{-0.24}$	±0.11	$^{-}_{-0.22}$	∓0.17	-	∓0.33	$^{-0.79}_{+0.24}$	$^{-0.15}_{+0.35}$	$^{-}_{-0.20}$	$^{-}_{-0.}$
Flavour response (JES) [%]	±0.77	±0.54	±0.27	-	∓0.48	∓0.66	∓0.63	∓0.55	∓0.70	∓0.66	∓0.73	∓0.65	$^{-0.73}_{+0.43}$	$^{-0.71}_{+1.09}$	$^{-1.24}_{+0.85}$	$^{-1.}_{+0.}$
b-Tagged jet energy scale (JES) [%]	∓0.57	∓0.45	∓0.22	±0.11	±0.45	±0.49	±0.44	±0.35	±0.35	±0.32	±0.41	±0.63	$^{+0.35}_{-0.51}$	±0.84	$^{+0.52}_{-0.87}$	$^{+0.}_{-0.}$
Jet reconstruction efficiency [%]	-	-	-	-	-	-	-	-	-	-	-	-	-	-	-	-
Jet energy resolution [%]	-	-	-	-	-	-	-	-	-	-	-	-	-	-	-	-
b-Quark tagging efficiency [%]	-	∓0.11	∓0.17	∓0.18	∓0.11	-	±0.32	±0.71	±1.24	±1.79	±2.31	±2.75	±2.95	±3.27	±3.69	±4.
c-Quark tagging efficiency [%]	-	±0.12	±0.11	-	-	∓0.16	∓0.26	∓0.34	∓0.41	∓0.43	∓0.48	∓0.47	∓0.41	∓0.42	∓0.39	∓0.
Light-jet tagging efficiency [%]	-	-	-	-	-	-	-	∓0.10	∓0.11	-	-	-	-	-	±0.21	±0.
Electron energy scale [%]	-	-	-	-	-	-	-	-	-	-	-	-	-	-	-	-
Electron energy resolution [%]	-	-	-	-	-	-	-	-	-	-	-	-	-	-	-	-
Muon momentum scale [%]	-	-	-	-	-	-	-	-	-	-	-	-	-	-	-	-
Muon (ID) momentum resolution [%]	-	-	-	-	-	-	-	-	-	-	-	-	-	-	-	-
Muon (MS) momentum resolution [%]	-	-	-	-	-	-	-	-	-	-	-	-	-	-	∓0.11	∓0.
Lepton trigger efficiency [%]	-	-	-	-	-	-	-	-	-	-	-	-	-	-	-	-
Lepton reconstruction efficiency [%]	-	-	-	-	-	-	-	-	-	-	-	-	-	-	-	-
Lepton identification efficiency [%]	-	-	-	-	-	-	-	-	±0.11	±0.11	±0.11	±0.11	±0.11	-	-	-
E_T^{miss} Soft jet scale [%]	∓0.23	-	-	-	-	-	-	-	-	-	-	$^{-}_{+0.20}$	$^{-}_{-0.32}$	-	-	-
E_T^{miss} Soft jet resolution [%]	-	-	-	-	-	-	-	-	-	-	-	$^{+0.33}_{-}$	-	$^{-}_{-0.23}$	$^{-}_{-0.56}$	$^{-}_{-0.}$
Jet vertex fraction [%]	∓0.23	∓0.21	∓0.16	-	±0.12	$^{+0.33}_{-0.24}$	$^{+0.45}_{-0.33}$	±0.45	±0.53	±0.65	±0.62	±0.61	±0.76	$^{+0.94}_{-0.66}$	±0.73	±0.
Alternate hard-scattering model [%]	±5.12	∓0.72	∓1.92	∓2.32	∓1.09	±1.14	±2.44	±2.94	±5.37	±2.02	±4.60	±11.5	±17.2	±5.31	∓5.72	∓8.
Alternate parton-shower model [%]	±4.11	∓1.71	∓2.23	∓1.28	±0.43	±1.71	±2.20	±2.89	±1.83	±1.00	±1.85	±4.90	±8.09	±1.90	∓4.05	∓6.
Monte Carlo sample statistics [%]	±0.20	±0.11	-	±0.10	±0.13	±0.17	±0.22	±0.28	±0.36	±0.48	±0.67	±0.94	±1.29	±1.84	±2.44	±3.
ISR/FSR + scale [%]	$^{-}_{-0.74}$	$^{-}_{-0.71}$	$^{-}_{-0.72}$	$^{-0.42}_{+0.63}$	$^{+0.76}_{-}$	$^{+1.31}_{-0.35}$	±1.32	$^{+2.24}_{-0.80}$	$^{+2.51}_{-0.57}$	$^{+0.80}_{-1.61}$	$^{+2.73}_{-0.56}$	$^{+1.18}_{-3.49}$	±5.16	±4.16	$^{+1.07}_{-5.06}$	$^{+2.}_{-6.}$
Parton distribution functions [%]	±0.26	±0.13	-	-	∓0.10	∓0.14	∓0.22	∓0.19	∓0.16	-	-	∓0.63	∓0.86	±0.47	±1.67	±2.
Single top cross-section [%]	-	-	-	-	-	-	-	-	-	-	-	±0.23	±0.42	±0.49	±0.21	±0.
W+jets scale factors [%]	±0.23	±0.15	-	-	∓0.13	∓0.13	∓0.13	∓0.17	-	-	-	-	∓0.19	∓0.20	±1.21	±2.
Fake lept. MC stat, e+jets ch. [%]	-	-	-	-	-	-	$^{+0.15}_{-}$	$^{+0.20}_{-0.27}$	$^{+0.11}_{-0.29}$	±0.30	±0.30	$^{+0.20}_{-0.11}$	$^{+0.64}_{-0.16}$	$^{+0.63}_{-}$	$^{+0.63}_{-0.34}$	$^{+0.}_{-0.}$
Fake lept. alternate fake CR, e+jets ch. [%]	-	-	-	-	-	-	∓0.11	∓0.26	∓0.32	∓0.37	∓0.37	∓0.18	∓0.31	∓0.22	∓0.36	∓0.
Fake lept. alternate real CR, e+jets ch. [%]	±0.11	-	-	-	-	-	-	-	-	-	-	-	-	-	-	-
Fake lept. alternate parametrization, e+jets ch. [%]	∓0.13	∓0.14	-	-	±0.16	±0.10	-	-	∓0.12	∓0.16	∓0.21	∓0.11	-	∓0.39	-	-
Fake lept. MC stat, μ+jets ch. [%]	-	-	-	-	-	-	-	-	-	-	-	-	$^{+0.52}_{-}$	-	-	-
Fake lept. alternate fake CR, μ+jets ch. [%]	±0.14	±0.15	-	-	∓0.13	∓0.16	∓0.17	∓0.16	∓0.16	-	∓0.10	∓0.13	-	∓0.18	∓0.31	∓0.
Fake lept. alternate real CR, μ+jets ch. [%]	∓0.40	∓0.28	∓0.10	-	±0.25	±0.29	±0.37	±0.31	-	-	∓0.12	∓0.32	∓0.44	∓0.69	∓0.97	∓1.
Fake lept. alternate parametrization, μ+jets ch. [%]	∓0.15	∓0.12	-	-	-	±0.16	±0.27	±0.18	-	±0.16	∓0.11	-	±0.38	±0.12	∓0.13	∓0.
Z+jets cross-section [%]	∓0.43	∓0.48	∓0.32	-	±0.37	±0.53	±0.60	±0.70	±0.76	±0.71	±0.70	±0.52	±0.52	±0.75	±0.42	±0.
Diboson cross-section [%]	-	-	-	-	-	-	-	-	-	-	-	-	-	-	±0.10	±0.
Luminosity [%]	-	-	-	-	-	-	-	-	-	-	-	-	-	-	-	-

TABLE D.37: Fiducial phase-space relative differential cross-sections after combining the e+jets and μ+jets channels for the scalar sum of the hadronic and leptonic top-quark transverse momenta $H_{\mathrm{T}}^{t\bar{t}}$. All uncertainties are quoted as a percentage with respect to the cross-section values in each bin. Dashes are used when the estimated relative systematic uncertainty for that bin is below 0.1%.

Bins [GeV]	0–90	90–140	140–195	195–255	255–320	320–385	385–455	455–530	530–610	610–695	695–780	780–865	865–950	950–1041	1041–1500
$\mathrm{d}\sigma$ / d H_T^{tt} [GeV]	$3.08 \cdot 10^{-1}$	$8.06 \cdot 10^{-1}$	$8.96 \cdot 10^{-1}$	$7.74 \cdot 10^{-1}$	$5.50 \cdot 10^{-1}$	$3.43 \cdot 10^{-1}$	$1.98 \cdot 10^{-1}$	$1.07 \cdot 10^{-1}$	$5.49 \cdot 10^{-2}$	$2.75 \cdot 10^{-2}$	$1.39 \cdot 10^{-2}$	$7.24 \cdot 10^{-3}$	$3.91 \cdot 10^{-3}$	$2.14 \cdot 10^{-3}$	$1.11 \cdot 10^{-4}$
Total Uncertainty [%]	±9.65	±13.2	±14.2	±14.1	±13.0	±11.2	±10.4	±10.0	±10.5	±11.6	±11.6	±13.2	±16.5	±15.0	±23.0
Statistics [%]	±1.0	±0.6	±0.5	±0.5	±0.6	±0.8	±1.0	±1.3	±1.7	±2.3	±3.4	±4.9	±6.6	±9.5	±13.
Systematics [%]	±9.61	±13.2	±14.1	±14.1	±13.0	±11.2	±10.4	±9.92	±10.3	±11.4	±11.0	±12.2	±15.0	±11.4	±18.5
η intercalibration model (JES) [%]	∓0.15	-	±0.17	±0.43	±0.64	±0.72	±0.68	±0.66	±0.73	±0.59	±0.57	$^{+0.67}_{-0.47}$	$^{+0.52}_{-0.73}$	±0.87	$^{-}_{-0.58}$
Single particle high-p_T (JES) [%]	-	-	-	-	-	-	-	-	-	-	-	-	-	-	-
Effective stat. NP set 1 (JES) [%]	±0.81	±0.93	±1.00	±1.02	±1.02	±0.91	±0.72	±0.54	±0.45	$^{+0.31}_{-0.41}$	±0.35	$^{+0.47}_{-0.20}$	±0.36	$^{+0.42}_{-}$	$^{+0.67}_{-0.16}$
Effective stat. NP set 2 (JES) [%]	∓0.15	∓0.14	∓0.11	-	-	-	-	-	-	-	-	$^{+0.17}_{-}$	-	$^{+0.25}_{-0.15}$	±0.33
Effective stat. NP set 3 (JES) [%]	±0.46	±0.38	±0.23	-	∓0.24	∓0.35	∓0.37	∓0.33	∓0.35	∓0.30	∓0.24	$^{-}_{-0.11}$	∓0.22	$^{-0.25}_{+0.36}$	$^{+0.30}_{+0.47}$
Effective detector NP set 1 (JES) [%]	∓0.64	∓0.54	∓0.36	-	±0.36	±0.64	±0.82	±1.00	±1.50	±1.64	±2.17	$^{+0.50}_{-}$	±2.67	±3.67	±4.61
Effective detector NP set 2 (JES) [%]	±0.17	±0.20	±0.21	±0.21	±0.23	±0.20	±0.12	-	-	-	-	$^{-}_{+0.21}$	-	$^{-}_{+0.26}$	$^{-}_{+0.12}$
Effective detector NP set 3 (JES) [%]	-	-	-	-	-	-	$^{-}_{-0.12}$	-	±0.15	±0.16	±0.21	$^{+0.45}_{-0.15}$	±0.27	$^{+0.16}_{-0.43}$	$^{+0.41}_{-0.24}$
Effective mixed NP set 1 (JES) [%]	∓0.40	∓0.29	$^{-}_{+0.13}$	±0.17	±0.52	±0.69	±0.80	±0.87	±1.17	±1.17	±1.51	±1.93	±1.84	±2.63	±2.75
Effective mixed NP set 2 (JES) [%]	∓0.32	∓0.37	∓0.40	∓0.42	∓0.45	∓0.41	∓0.32	∓0.26	$^{-0.29}_{+0.21}$	$^{-0.25}_{+0.15}$	∓0.21	-	$^{-}_{+0.21}$	$^{-}_{+0.24}$	±0.28
Effective model NP set 1 (JES) [%]	±0.84	±1.27	±1.73	±2.44	±3.10	±3.19	±2.84	±2.50	±2.46	±2.25	±2.38	±2.29	±1.99	±2.44	±2.19
Effective model NP set 2 (JES) [%]	∓0.10	∓0.11	∓0.11	∓0.11	∓0.10	-	-	-	±0.16	±0.14	±0.28	$^{+0.81}_{-0.48}$	±0.45	$^{+1.35}_{-1.03}$	±1.64
Effective model NP set 3 (JES) [%]	±0.56	±0.52	±0.40	±0.17	-	∓0.16	∓0.22	∓0.22	∓0.23	∓0.23	∓0.21	$^{-0.10}_{+0.25}$	-	-	$^{-}_{+0.16}$
Effective model NP set 4 (JES) [%]	-	-	-	-	-	-	±0.14	±0.16	±0.27	±0.29	±0.31	$^{+0.66}_{-0.43}$	±0.46	$^{+0.46}_{-0.31}$	±1.00
Pile-up offset μ (JES) [%]	-	$^{-}_{+0.14}$	∓0.16	∓0.20	∓0.21	∓0.22	∓0.18	∓0.15	$^{-0.22}_{+0.12}$	$^{-0.14}_{-}$	∓0.15	-	-	∓0.26	$^{-0.39}_{+0.10}$
Pile-up offset N_{PV} (JES) [%]	∓0.36	∓0.46	∓0.53	∓0.65	∓0.78	∓0.73	∓0.67	∓0.61	$^{-0.67}_{+0.50}$	∓0.32	$^{-0.59}_{+0.30}$	$^{-0.55}_{+0.95}$	$^{-0.47}_{+0.94}$	$^{-0.34}_{+0.60}$	∓0.79
Punch-through (JES) [%]	-	-	-	-	-	-	-	-	-	-	-	$^{+0.12}_{-}$	$^{-}_{-0.17}$	$^{-}_{-0.22}$	$^{+0.38}_{-}$
Pile-up offset ρ topology (JES) [%]	±0.86	±1.14	±1.42	±1.83	±2.19	±2.20	±1.97	±1.75	±1.68	±1.54	±1.54	$^{+1.71}_{-1.23}$	±1.41	$^{+1.88}_{-1.19}$	$^{+1.08}_{-1.48}$
Pile-up offset p_T (JES) [%]	-	-	-	-	-	-	-	-	-	-	-	$^{-}_{+0.46}$	-	-	$^{-}_{-0.38}$
Flavour composition (JES) [%]	±1.06	±1.35	±1.65	±1.99	±2.32	±2.33	±2.14	±1.90	±1.88	±1.62	±1.76	±1.46	$^{+0.98}_{-1.55}$	±1.54	±1.92
Flavour response (JES) [%]	∓0.27	∓0.50	∓0.78	∓1.14	∓1.52	∓1.71	∓1.68	∓1.60	∓1.75	∓1.71	∓1.77	∓1.69	∓1.62	∓1.95	∓2.08
b-Tagged jet energy scale (JES) [%]	$^{-0.18}_{+0.12}$	-	±0.19	±0.55	±0.88	±0.93	±0.86	±0.78	±0.78	±0.75	±0.83	±1.06	±0.86	±1.27	$^{+0.94}_{-1.30}$
Jet reconstruction efficiency [%]	-	-	-	-	-	-	-	-	-	-	-	-	-	∓0.12	-
Jet energy resolution [%]	-	-	-	-	-	-	-	-	-	-	-	-	-	-	-
b-Quark tagging efficiency [%]	±4.10	±4.03	±3.96	±3.96	±4.03	±4.20	±4.46	±4.87	±5.39	±5.93	±6.47	±6.89	±7.10	±7.42	±7.85
c-Quark tagging efficiency [%]	±1.07	±1.10	±1.09	±1.04	±0.93	±0.81	±0.71	±0.63	±0.56	±0.54	±0.49	±0.49	±0.57	±0.55	±0.58
Light-jet tagging efficiency [%]	±0.52	±0.55	±0.56	±0.53	±0.50	±0.50	±0.47	±0.42	±0.41	±0.44	±0.53	±0.52	±0.44	±0.48	±0.74
Electron energy scale [%]	$^{+0.15}_{-0.26}$	$^{+0.12}_{-0.22}$	$^{-}_{-0.17}$	-	-	-	-	-	-	-	-	-	-	$^{-}_{-0.13}$	-
Electron energy resolution [%]	-	-	-	-	-	-	-	-	-	-	-	-	-	-	-
Muon momentum scale [%]	-	-	-	-	-	-	-	-	-	-	-	-	-	-	-
Muon (ID) momentum resolution [%]	-	-	-	-	-	-	-	-	-	-	-	-	-	-	-
Muon (MS) momentum resolution [%]	-	-	-	-	-	-	-	-	-	-	-	-	-	-	∓0.11
Lepton trigger efficiency [%]	±1.34	±1.32	±1.29	±1.26	±1.23	±1.22	±1.22	±1.22	±1.22	±1.22	±1.22	±1.23	±1.22	±1.24	±1.26
Lepton reconstruction efficiency [%]	±0.21	±0.21	±0.22	±0.23	±0.25	±0.26	±0.27	±0.28	±0.29	±0.29	±0.30	±0.30	±0.30	±0.30	±0.30
Lepton identification efficiency [%]	±1.23	±1.24	±1.27	±1.30	±1.34	±1.37	±1.38	±1.40	±1.41	±1.41	±1.42	±1.41	±1.42	±1.38	±1.34
E_T^{miss} Soft jet scale [%]	∓0.24	-	-	-	-	-	-	-	-	-	-	$^{-}_{+0.21}$	$^{-}_{-0.33}$	-	$^{-0.19}_{-}$
E_T^{miss} Soft jet resolution [%]	-	-	-	-	-	-	-	-	-	-	-	$^{+0.33}_{-0.13}$	-	$^{-}_{-0.24}$	$^{-}_{-0.57}$
Jet vertex fraction [%]	∓0.96	∓0.93	∓0.88	∓0.78	∓0.59	∓0.43	∓0.32	$^{-0.30}_{+0.23}$	$^{-0.25}_{+0.13}$	-	-	-	-	-	-
Alternate hard-scattering model [%]	-	∓5.61	∓6.76	∓7.14	∓5.97	∓3.84	∓2.60	∓2.13	±0.17	∓3.01	∓0.55	±6.05	±11.4	±0.12	∓10.3
Alternate parton-shower model [%]	∓1.71	∓7.22	∓7.71	∓6.81	∓5.19	∓3.98	∓3.51	∓2.86	∓3.87	∓4.64	∓3.84	∓0.96	±2.03	∓3.79	∓9.42
Monte Carlo sample statistics [%]	±0.26	±0.16	±0.13	±0.13	±0.16	±0.19	±0.24	±0.31	±0.41	±0.54	±0.76	±1.07	±1.47	±2.08	±2.77
ISR/FSR + scale [%]	∓7.12	∓7.18	∓7.25	∓7.45	∓7.09	∓6.12	∓5.60	∓5.45	∓5.44	$^{-6.49}_{+4.86}$	∓5.35	$^{-6.14}_{+2.86}$	$^{-2.20}_{+1.36}$	∓2.79	$^{-6.24}_{+1.19}$
Parton distribution functions [%]	∓0.10	∓0.23	∓0.33	∓0.41	∓0.47	∓0.51	∓0.59	∓0.56	∓0.53	∓0.41	∓0.43	∓0.99	∓1.23	±0.10	±1.30
Single top cross-section [%]	±0.28	±0.26	±0.24	±0.24	±0.24	±0.27	±0.29	±0.30	±0.33	±0.32	±0.30	±0.51	±0.68	±0.76	±0.48
W+jets scale factors [%]	±0.66	±0.58	±0.46	±0.35	±0.29	±0.29	±0.29	±0.25	±0.35	±0.45	±0.43	±0.36	±0.23	±0.22	±1.63
Fake lept. MC stat, e+jets ch. [%]	-	$^{-0.14}_{+0.44}$	$^{-0.14}_{+0.46}$	$^{+0.44}_{-}$	$^{+0.46}_{-}$	$^{+0.48}_{-}$	$^{+0.36}_{-}$	$^{+0.20}_{-}$	-	$^{+0.27}_{-}$	$^{+0.26}_{-}$	$^{+0.30}_{-}$	$^{+0.63}_{-}$	$^{+0.62}_{-}$	$^{+0.62}_{-}$
Fake lept. alternate fake CR, e+jets ch. [%]	±0.44	±0.47	±0.45	±0.38	±0.35	±0.34	±0.27	±0.11	-	-	-	±0.19	-	±0.15	-
Fake lept. alternate real CR, e+jets ch. [%]	-	-	-	-	-	-	-	-	-	-	-	-	-	-	-
Fake lept. alternate parametrization, e+jets ch. [%]	±0.15	±0.13	±0.25	±0.38	±0.44	±0.38	±0.29	±0.20	±0.16	±0.11	-	±0.16	±0.24	∓0.11	±0.28
Fake lept. MC stat, μ+jets ch. [%]	-	-	-	-	-	-	-	-	-	-	-	-	$^{+0.56}_{-}$	-	-
Fake lept. alternate fake CR, μ+jets ch. [%]	±0.40	±0.41	±0.36	±0.23	±0.12	-	-	±0.10	±0.10	±0.18	±0.16	±0.13	±0.29	-	-
Fake lept. alternate real CR, μ+jets ch. [%]	∓0.23	∓0.11	-	±0.26	±0.42	±0.46	±0.54	±0.47	±0.21	±0.16	-	∓0.16	∓0.27	∓0.52	∓0.81
Fake lept. alternate parametrization, μ+jets ch. [%]	-	-	±0.14	±0.21	±0.27	±0.36	±0.47	±0.38	±0.22	±0.37	-	±0.10	±0.58	±0.33	-
Z+jets cross-section [%]	∓1.53	∓1.59	∓1.43	∓1.07	∓0.73	∓0.58	∓0.50	∓0.41	∓0.35	∓0.40	∓0.41	∓0.59	∓0.59	∓0.36	∓0.68
Diboson cross-section [%]	∓0.14	∓0.15	∓0.13	-	-	-	-	-	-	-	-	-	-	-	-
Luminosity [%]	±2.80	±2.80	±2.80	±2.80	±2.80	±2.80	±2.80	±2.80	±2.80	±2.80	±2.80	±2.80	±2.80	±2.80	±2.80

TABLE D.38: Fiducial phase-space absolute differential cross-sections after combining the e+jets and μ+jets channels for the scalar sum of the hadronic and leptonic top-quark transverse momenta $H_{\mathrm{T}}^{t\bar{t}}$. All uncertainties are quoted as a percentage with respect to the cross-section values in each bin. Dashes are used when the estimated relative systematic uncertainty for that bin is below 0.1%.

Bins [Unit $y^{t\bar{t}}_{boost}$]	0–0.10	0.10–0.20	0.20–0.30	0.30–0.40	0.40–0.50	0.50–0.60	0.60–0.70	0.70–0.80	0.80–0.90	0.90–1	1–1.10	1.10–1.20	1.20–1.30	1.30–1.40	1.40–1.50	1.50–2
$1/\sigma \cdot \mathrm{d}\sigma$ / d $y^{t\bar{t}}_{boost}$	$8.23 \cdot 10^{-1}$	$8.16 \cdot 10^{-1}$	$8.02 \cdot 10^{-1}$	$7.81 \cdot 10^{-1}$	$7.53 \cdot 10^{-1}$	$7.20 \cdot 10^{-1}$	$6.82 \cdot 10^{-1}$	$6.38 \cdot 10^{-1}$	$5.93 \cdot 10^{-1}$	$5.45 \cdot 10^{-1}$	$4.96 \cdot 10^{-1}$	$4.45 \cdot 10^{-1}$	$3.94 \cdot 10^{-1}$	$3.45 \cdot 10^{-1}$	$2.97 \cdot 10^{-1}$	$1.74 \cdot 10^{-1}$
Total Uncertainty [%]	±1.90	±1.60	±1.04	±1.19	±1.04	±0.90	±1.07	±1.12	$^{+1.13}_{-0.84}$	±1.04	±1.21	$^{+1.24}_{-1.74}$	$^{+1.31}_{-2.19}$	$^{+1.58}_{-2.54}$	$^{+2.13}_{-3.06}$	±4.41
Statistics [%]	±0.7	±0.5	±0.5	±0.5	±0.5	±0.6	±0.6	±0.6	±0.7	±0.7	±0.8	±0.9	±0.9	±1.0	±1.1	±1.6
Systematics [%]	±1.74	±1.50	±0.91	±1.05	±0.86	±0.66	±0.85	±0.89	$^{+0.87}_{-0.42}$	±0.70	±0.85	$^{+0.82}_{-1.47}$	$^{+0.83}_{-1.94}$	$^{+1.11}_{-2.28}$	$^{+1.75}_{-2.81}$	±4.09
η intercalibration model (JES) [%]	∓0.33	∓0.30	∓0.28	∓0.25	∓0.21	∓0.17	∓0.11	-	-	±0.12	±0.17	±0.24	±0.33	$^{+0.33}_{-0.43}$	±0.50	±0.74
Single particle high-p_T (JES) [%]	-	-	-	-	-	-	-	-	-	-	-	-	-	-	-	-
Effective stat. NP set 1 (JES) [%]	-	-	-	-	-	-	-	-	-	-	-	-	-	-	-	-
Effective stat. NP set 2 (JES) [%]	-	-	-	-	-	-	-	-	-	-	-	-	-	-	-	-
Effective stat. NP set 3 (JES) [%]	-	-	-	-	-	-	-	-	-	-	-	-	-	-	-	-
Effective detector NP set 1 (JES) [%]	-	-	-	-	-	-	-	-	-	-	-	-	-	-	-	-
Effective detector NP set 2 (JES) [%]	-	-	-	-	-	-	-	-	-	-	-	-	-	-	-	-
Effective detector NP set 3 (JES) [%]	-	-	-	-	-	-	-	-	-	-	-	-	-	-	-	-
Effective mixed NP set 1 (JES) [%]	-	-	-	-	-	-	-	-	-	-	-	-	-	-	-	-
Effective mixed NP set 2 (JES) [%]	-	-	-	-	-	-	-	-	-	-	-	-	-	-	-	-
Effective model NP set 1 (JES) [%]	-	-	-	-	-	-	-	-	-	-	-	-	-	-	-	$^{+0.13}_{-}$
Effective model NP set 2 (JES) [%]	-	-	-	-	-	-	-	-	-	-	-	-	-	$^{-}_{-0.20}$	$^{-}_{-0.13}$	-
Effective model NP set 3 (JES) [%]	-	-	-	-	-	-	-	-	-	-	-	-	-	-	-	-
Effective model NP set 4 (JES) [%]	-	-	-	-	-	-	-	-	-	-	-	-	-	-	-	-
Pile-up offset μ (JES) [%]	-	-	-	-	-	-	-	-	-	-	-	-	-	-	-	∓0.21
Pile-up offset N_{PV} (JES) [%]	-	-	-	-	-	-	-	-	-	-	-	-	-	-	-	$^{-}_{-0.13}$
Punch-through (JES) [%]	-	-	-	-	-	-	-	-	-	-	-	-	-	-	-	-
Pile-up offset ρ topology (JES) [%]	-	-	-	-	-	-	-	-	-	-	-	-	-	$^{-}_{-0.19}$	$^{-}_{-0.13}$	-
Pile-up offset p_T (JES) [%]	-	-	-	-	-	-	-	-	-	-	-	-	-	-	-	-
Flavour composition (JES) [%]	$^{-0.14}_{-}$	∓0.11	-	-	-	-	-	-	-	-	-	-	-	$^{-}_{-0.23}$	$^{-}_{-0.23}$	±0.17
Flavour response (JES) [%]	-	-	-	-	-	-	-	-	-	-	-	-	-	-	-	$^{-0.13}_{+0.20}$
b-Tagged jet energy scale (JES) [%]	-	-	-	-	-	-	-	-	-	-	-	-	-	-	-	-
Jet reconstruction efficiency [%]	-	-	-	-	-	-	-	-	-	-	-	-	-	-	-	-
Jet energy resolution [%]	-	-	-	-	-	-	-	-	-	-	-	-	-	-	-	-
b-Quark tagging efficiency [%]	-	-	-	-	-	-	-	-	-	-	-	-	-	-	-	-
c-Quark tagging efficiency [%]	-	-	-	-	-	-	-	-	-	-	-	-	-	-	-	-
Light-jet tagging efficiency [%]	-	-	-	-	-	-	-	-	-	-	-	-	-	-	-	-
Electron energy scale [%]	-	-	-	-	-	-	-	-	-	-	-	-	-	$^{-}_{-0.13}$	$^{+0.13}_{-0.18}$	±0.23
Electron energy resolution [%]	-	-	-	-	-	-	-	-	-	-	-	-	-	-	-	-
Muon momentum scale [%]	-	-	-	-	-	-	-	-	-	-	-	-	-	-	-	-
Muon (ID) momentum resolution [%]	-	-	-	-	-	-	-	-	-	-	-	-	-	-	-	-
Muon (MS) momentum resolution [%]	-	-	-	-	-	-	-	-	-	-	-	-	-	-	-	-
Lepton trigger efficiency [%]	-	-	-	-	-	-	-	-	-	-	-	-	-	±0.12	±0.17	±0.30
Lepton reconstruction efficiency [%]	-	-	-	-	-	-	-	-	-	-	-	-	-	-	-	-
Lepton identification efficiency [%]	-	-	-	-	-	-	-	-	-	-	-	-	-	-	-	-
E_T^{miss} Soft jet scale [%]	-	-	-	-	-	-	-	-	-	-	-	-	-	-	-	-
E_T^{miss} Soft jet resolution [%]	-	-	-	-	-	-	-	-	-	-	-	-	-	-	-	-
Jet vertex fraction [%]	-	-	-	-	-	-	-	-	-	-	-	-	-	-	-	-
Alternate hard-scattering model [%]	±0.62	±0.82	±0.29	±0.28	±0.21	±0.11	±0.22	±0.47	±0.23	∓0.17	∓0.31	∓0.14	∓0.19	∓0.29	∓0.21	∓2.22
Alternate parton-shower model [%]	±0.84	±0.59	±0.11	∓0.31	-	∓0.12	∓0.62	∓0.60	∓0.28	∓0.62	∓0.64	-	-	±0.35	±0.86	±0.27
Monte Carlo sample statistics [%]	±0.18	±0.14	±0.13	±0.13	±0.14	±0.14	±0.15	±0.16	±0.17	±0.18	±0.19	±0.21	±0.23	±0.26	±0.28	±0.36
ISR/FSR + scale [%]	±1.25	±0.94	±0.65	$^{+0.95}_{-0.68}$	$^{+0.82}_{-0.53}$	$^{+0.57}_{-0.40}$	±0.43	$^{+0.53}_{-}$	$^{+0.75}_{-}$	-	∓0.36	$^{-1.39}_{+0.64}$	$^{-1.82}_{+0.47}$	$^{-2.04}_{+0.70}$	$^{-2.44}_{+1.19}$	∓2.82
Parton distribution functions [%]	±0.16	±0.16	±0.18	±0.11	±0.13	±0.10	-	-	-	-	-	-	-	-	-	∓0.82
Single top cross-section [%]	-	-	-	-	-	-	-	-	-	-	-	-	-	-	-	-
W+jets scale factors [%]	-	-	-	-	-	-	-	-	-	-	-	-	-	-	-	-
Fake lept. MC stat, e+jets ch. [%]	-	-	-	∓0.10	-	-	-	-	$^{+0.15}_{-}$	$^{+0.15}_{-}$	-	$^{+0.16}_{-}$	$^{+0.24}_{-}$	±0.12	$^{-}_{-0.20}$	$^{+0.10}_{-0.16}$
Fake lept. alternate fake CR, e+jets ch. [%]	-	-	-	-	-	-	-	-	-	-	-	-	-	-	∓0.13	∓0.10
Fake lept. alternate real CR, e+jets ch. [%]	-	-	-	-	-	-	-	-	-	-	-	-	-	-	-	-
Fake lept. alternate parametrization, e+jets ch. [%]	-	-	-	-	-	-	-	-	-	-	-	-	-	∓0.12	∓0.10	-
Fake lept. MC stat, μ+jets ch. [%]	-	-	-	-	-	-	-	-	-	-	-	-	-	-	-	$^{+0.64}_{-}$
Fake lept. alternate fake CR, μ+jets ch. [%]	-	-	-	-	-	-	-	-	-	-	∓0.11	∓0.11	-	-	-	±0.15
Fake lept. alternate real CR, μ+jets ch. [%]	∓0.35	∓0.33	∓0.30	∓0.30	∓0.28	∓0.26	∓0.23	∓0.16	-	-	-	±0.25	±0.39	±0.49	±0.64	±1.24
Fake lept. alternate parametrization, μ+jets ch. [%]	∓0.16	∓0.14	∓0.13	∓0.12	∓0.11	∓0.10	-	∓0.10	∓0.11	-	-	±0.10	±0.19	±0.28	±0.30	±0.62
Z+jets cross-section [%]	-	-	-	-	-	-	-	-	-	-	-	-	-	-	-	-
Diboson cross-section [%]	-	-	-	-	-	-	-	-	-	-	-	-	-	-	-	-
Luminosity [%]	-	-	-	-	-	-	-	-	-	-	-	-	-	-	-	-

TABLE D.39: Fiducial phase-space relative differential cross-sections after combining the e+jets and μ+jets channels for $y^{t\bar{t}}_{\mathrm{boost}}$. All uncertainties are quoted as a percentage with respect to the cross-section values in each bin. Dashes are used when the estimated relative systematic uncertainty for that bin is below 0.1%.

Bins [Unit y^{tt}_{boost}]	0–0.10	0.10–0.20	0.20–0.30	0.30–0.40	0.40–0.50	0.50–0.60	0.60–0.70	0.70–0.80	0.80–0.90	0.90–1	1–1.10	1.10–1.20	1.20–1.30	1.30–1.40	1.40–1.50	1.50–2
$d\sigma$ / d y^{tt}_{boost} [Unit y^{tt}_{boost}]	$2.04 \cdot 10^2$	$2.02 \cdot 10^2$	$1.98 \cdot 10^2$	$1.93 \cdot 10^2$	$1.86 \cdot 10^2$	$1.78 \cdot 10^2$	$1.69 \cdot 10^2$	$1.58 \cdot 10^2$	$1.47 \cdot 10^2$	$1.35 \cdot 10^2$	$1.23 \cdot 10^2$	$1.10 \cdot 10^2$	$9.76 \cdot 10^1$	$8.53 \cdot 10^1$	$7.35 \cdot 10^1$	$4.31 \cdot 10^1$
Total Uncertainty [%]	±9.98	±10.1	±10.6	±10.7	±10.6	±10.9	±11.1	±11.1	±11.0	±11.5	±11.8	±11.9	±12.1	±12.3	±12.4	±14.2
Statistics [%]	±0.8	±0.6	±0.6	±0.6	±0.6	±0.7	±0.7	±0.7	±0.8	±0.8	±0.9	±1.0	±1.1	±1.2	±1.4	±1.9
Systematics [%]	±9.96	±10.1	±10.6	±10.6	±10.6	±10.9	±11.1	±11.0	±11.0	±11.4	±11.8	±11.9	±12.1	±12.2	±12.4	±14.1
η intercalibration model (JES) [%]	±0.15	±0.17	±0.20	±0.23	±0.27	±0.30	±0.36	±0.41	±0.52	±0.60	±0.65	±0.73	±0.81	±0.86	±0.99	±1.23
Single particle high-p_T (JES) [%]	-	-	-	-	-	-	-	-	-	-	-	-	-	-	-	-
Effective stat. NP set 1 (JES) [%]	±0.89	±0.87	±0.89	±0.90	±0.89	±0.89	±0.89	±0.88	±0.87	±0.91	±0.94	±0.93	±0.93	±0.96	±0.97	±1.36
Effective stat. NP set 2 (JES) [%]	-	-	-	-	-	-	-	-	-	-	-	-	-	-	-	-
Effective stat. NP set 3 (JES) [%]	-	-	-	-	-	-	-	-	-	-	-	-	-	-	-	-
Effective detector NP set 1 (JES) [%]	±0.19	±0.18	$^{+0.20}_{-0.15}$	±0.18	±0.16	±0.15	±0.17	±0.17	±0.18	±0.19	±0.20	±0.22	±0.23	±0.21	±0.23	±0.26
Effective detector NP set 2 (JES) [%]	±0.20	±0.19	±0.18	±0.18	±0.17	±0.16	±0.17	±0.17	±0.17	±0.17	±0.18	±0.18	±0.19	±0.19	±0.18	±0.28
Effective detector NP set 3 (JES) [%]	-	-	-	-	-	-	-	-	-	-	-	-	-	-	-	-
Effective mixed NP set 1 (JES) [%]	±0.30	±0.29	±0.29	±0.30	±0.29	±0.28	±0.28	±0.28	±0.28	±0.30	±0.33	±0.35	±0.36	±0.35	±0.35	±0.54
Effective mixed NP set 2 (JES) [%]	∓0.39	∓0.38	∓0.38	∓0.38	∓0.36	∓0.36	∓0.35	∓0.36	∓0.36	∓0.37	∓0.40	∓0.41	∓0.42	∓0.43	∓0.41	∓0.36
Effective model NP set 1 (JES) [%]	±2.24	±2.24	±2.24	±2.24	±2.23	±2.29	±2.31	±2.27	±2.29	±2.34	±2.40	±2.40	±2.40	±2.42	±2.45	±2.42
Effective model NP set 2 (JES) [%]	-	-	-	-	-	-	-	-	-	-	-	-	-	-	-	-
Effective model NP set 3 (JES) [%]	±0.13	±0.12	±0.13	±0.14	±0.13	±0.13	±0.13	±0.12	±0.12	±0.12	±0.12	±0.11	±0.10	±0.10	±0.11	±0.21
Effective model NP set 4 (JES) [%]	-	-	-	-	-	-	-	-	-	-	-	-	-	-	-	-
Pile-up offset μ (JES) [%]	∓0.14	∓0.13	∓0.13	$^{-0.10}_{+0.14}$	$^{-}_{+0.14}$	∓0.12	∓0.14	∓0.15	∓0.19	∓0.23	∓0.26	∓0.29	∓0.28	∓0.26	∓0.27	∓0.41
Pile-up offset N_{PV} (JES) [%]	∓0.55	∓0.58	∓0.61	∓0.62	∓0.62	∓0.64	∓0.66	∓0.64	∓0.60	∓0.60	∓0.62	∓0.63	∓0.64	∓0.62	∓0.59	∓0.49
Punch-through (JES) [%]	-	-	-	-	-	-	-	-	-	-	-	-	-	-	-	-
Pile-up offset ρ topology (JES) [%]	±1.69	±1.67	±1.67	±1.66	±1.65	±1.69	±1.71	±1.69	±1.70	±1.73	±1.78	±1.79	±1.81	±1.82	±1.81	±1.77
Pile-up offset p_T (JES) [%]	-	-	-	-	-	-	-	-	-	-	-	-	-	-	-	-
Flavour composition (JES) [%]	±1.79	±1.79	±1.81	±1.83	±1.86	±1.89	±1.90	±1.89	±1.88	±1.92	±1.98	±1.96	±1.96	±2.03	±2.05	±2.08
Flavour response (JES) [%]	∓1.14	∓1.13	∓1.13	∓1.13	∓1.14	∓1.15	∓1.17	∓1.16	∓1.17	∓1.19	∓1.22	∓1.23	∓1.25	∓1.27	∓1.27	∓1.36
b-Tagged jet energy scale (JES) [%]	±0.51	±0.52	±0.49	±0.49	±0.49	±0.52	±0.53	±0.52	±0.52	±0.53	±0.56	±0.57	±0.57	±0.56	±0.55	±0.51
Jet reconstruction efficiency [%]	-	-	-	-	-	-	-	-	-	-	-	-	-	-	-	-
Jet energy resolution [%]	-	-	-	-	-	-	-	-	-	-	-	-	-	-	-	-
b-Quark tagging efficiency [%]	±4.21	±4.21	±4.22	±4.22	±4.22	±4.23	±4.23	±4.22	±4.22	±4.22	±4.22	±4.23	±4.24	±4.24	±4.24	±4.24
c-Quark tagging efficiency [%]	±0.95	±0.95	±0.95	±0.95	±0.95	±0.95	±0.94	±0.92	±0.92	±0.92	±0.92	±0.92	±0.91	±0.90	±0.89	±0.88
Light-jet tagging efficiency [%]	±0.51	±0.50	±0.50	±0.49	±0.50	±0.50	±0.51	±0.51	±0.51	±0.52	±0.54	±0.55	±0.55	±0.55	±0.55	±0.57
Electron energy scale [%]	-	-	-	-	-	-	-	-	$^{-}_{-0.14}$	$^{-}_{-0.20}$	$^{+0.10}_{-0.21}$	±0.19	$^{+0.16}_{-0.21}$	$^{+0.16}_{-0.29}$	$^{+0.23}_{-0.33}$	$^{+0.31}_{-0.42}$
Electron energy resolution [%]	-	-	-	-	-	-	-	-	-	-	-	-	-	-	-	-
Muon momentum scale [%]	-	-	-	-	-	-	-	-	-	-	-	-	-	-	-	-
Muon (ID) momentum resolution [%]	-	-	-	-	-	-	-	-	-	-	-	-	-	-	-	-
Muon (MS) momentum resolution [%]	-	-	-	-	-	-	-	-	-	-	-	-	-	-	-	-
Lepton trigger efficiency [%]	±1.20	±1.20	±1.20	±1.21	±1.21	±1.22	±1.24	±1.25	±1.27	±1.29	±1.32	±1.35	±1.38	±1.42	±1.47	±1.60
Lepton reconstruction efficiency [%]	±0.23	±0.23	±0.23	±0.23	±0.23	±0.23	±0.23	±0.24	±0.24	±0.24	±0.25	±0.26	±0.26	±0.28	±0.29	±0.34
Lepton identification efficiency [%]	±1.34	±1.34	±1.34	±1.33	±1.33	±1.33	±1.32	±1.31	±1.30	±1.29	±1.29	±1.27	±1.26	±1.26	±1.26	±1.28
E_T^{miss} Soft jet scale [%]	-	-	-	-	-	-	-	-	-	-	-	-	-	-	-	-
E_T^{miss} Soft jet resolution [%]	-	-	-	-	-	-	-	-	-	-	-	-	-	-	-	-
Jet vertex fraction [%]	∓0.66	∓0.67	∓0.65	∓0.65	∓0.66	∓0.66	∓0.64	∓0.64	∓0.65	∓0.65	∓0.66	∓0.67	∓0.68	∓0.67	∓0.66	∓0.60
Alternate hard-scattering model [%]	∓3.47	∓3.27	∓3.78	∓3.80	∓3.86	∓3.96	∓3.85	∓3.61	∓3.84	∓4.24	∓4.37	∓4.21	∓4.26	∓4.35	∓4.27	∓6.20
Alternate parton-shower model [%]	∓2.91	∓3.15	∓3.61	∓4.02	∓3.63	∓3.83	∓4.31	∓4.30	∓3.99	∓4.32	∓4.34	∓3.67	∓3.73	∓3.38	∓2.89	∓3.46
Monte Carlo sample statistics [%]	±0.21	±0.16	±0.15	±0.15	±0.16	±0.17	±0.18	±0.19	±0.20	±0.21	±0.22	±0.25	±0.27	±0.31	±0.33	±0.44
ISR/FSR + scale [%]	∓5.67	∓5.97	∓6.27	∓6.11	∓6.25	∓6.44	∓6.49	∓6.63	∓6.60	∓6.83	∓7.28	∓7.90	∓8.02	∓8.25	∓8.69	∓9.73
Parton distribution functions [%]	±0.14	±0.14	±0.16	±0.10	±0.11	-	-	-	-	-	-	-	-	-	-	±0.84
Single top cross-section [%]	±0.29	±0.29	±0.29	±0.28	±0.28	±0.27	±0.27	±0.26	±0.26	±0.26	±0.26	±0.24	±0.22	±0.21	±0.20	±0.19
W+jets scale factors [%]	±0.42	±0.40	±0.40	±0.39	±0.40	±0.41	±0.40	±0.40	±0.38	±0.38	±0.38	±0.37	±0.38	±0.39	±0.38	±0.35
Fake lept. MC stat, e+jets ch. [%]	$^{+0.48}_{-}$	$^{+0.49}_{-}$	$^{+0.50}_{-}$	$^{+0.49}_{-}$	$^{+0.47}_{-}$	$^{+0.43}_{-}$	$^{+0.41}_{-}$	$^{+0.33}_{-}$	$^{+0.31}_{-}$	$^{+0.32}_{-}$	$^{+0.36}_{-}$	$^{+0.33}_{-}$	$^{+0.31}_{-}$	$^{+0.26}_{-}$	$^{-}_{-}$	$^{+0.22}_{-}$
Fake lept. alternate fake CR, e+jets ch. [%]	±0.42	±0.39	±0.41	±0.43	±0.41	±0.36	±0.34	±0.31	±0.29	±0.29	±0.33	±0.30	±0.27	±0.25	±0.21	±0.23
Fake lept. alternate real CR, e+jets ch. [%]	-	-	-	-	-	-	-	-	-	-	-	-	-	-	-	-
Fake lept. alternate parametrization, e+jets ch. [%]	±0.33	±0.32	±0.34	±0.35	±0.29	±0.24	±0.22	±0.25	±0.32	±0.31	±0.30	±0.27	±0.23	±0.15	±0.17	±0.25
Fake lept. MC stat, μ+jets ch. [%]	-	-	-	-	-	-	-	-	-	-	-	-	-	-	$^{+0.26}_{-}$	$^{+0.73}_{-}$
Fake lept. alternate fake CR, μ+jets ch. [%]	±0.32	±0.29	±0.26	±0.24	±0.21	±0.21	±0.22	±0.22	±0.18	±0.14	±0.12	±0.12	±0.15	±0.18	±0.23	±0.39
Fake lept. alternate real CR, μ+jets ch. [%]	-	-	-	-	-	-	-	±0.16	±0.26	±0.33	±0.41	±0.58	±0.71	±0.82	±0.97	±1.57
Fake lept. alternate parametrization, μ+jets ch. [%]	±0.12	±0.13	±0.15	±0.15	±0.16	±0.17	±0.19	±0.17	±0.17	±0.20	±0.29	±0.39	±0.48	±0.57	±0.58	±0.91
Z+jets cross-section [%]	∓1.00	∓1.04	∓1.02	∓1.01	∓0.99	∓0.98	∓0.97	∓0.97	∓1.00	∓1.02	∓0.97	∓0.98	∓0.98	∓0.96	∓0.95	∓0.92
Diboson cross-section [%]	-	-	-	-	-	-	-	-	-	-	-	-	∓0.10	∓0.10	∓0.10	-
Luminosity [%]	±2.80	±2.80	±2.80	±2.80	±2.80	±2.80	±2.80	±2.80	±2.80	±2.80	±2.80	±2.80	±2.80	±2.80	±2.80	±2.80

TABLE D.40: Fiducial phase-space absolute differential cross-sections after combining the e+jets and μ+jets channels for $y^{t\bar{t}}_{\mathrm{boost}}$. All uncertainties are quoted as a percentage with respect to the cross-section values in each bin. Dashes are used when the estimated relative systematic uncertainty for that bin is below 0.1%.

Bins [Unit $\chi^{t\bar{t}}$]	1–1.40	1.40–1.90	1.90–2.50	2.50–3.20	3.20–4.20	4.20–5.50	5.50–7.20	7.20–9.30	9.30–12	12–20
$1/\sigma \cdot \mathrm{d}\sigma \,/\, \mathrm{d}\,\chi^{t\bar{t}}$	$5.45 \cdot 10^{-1}$	$3.74 \cdot 10^{-1}$	$2.54 \cdot 10^{-1}$	$1.70 \cdot 10^{-1}$	$1.07 \cdot 10^{-1}$	$6.18 \cdot 10^{-2}$	$3.33 \cdot 10^{-2}$	$1.70 \cdot 10^{-2}$	$8.35 \cdot 10^{-3}$	$2.66 \cdot 10^{-3}$
Total Uncertainty [%]	±3.07	±0.67	±1.67	±1.76	±1.98	±1.81	±1.57	±1.93	±4.08	±6.25
Statistics [%]	±0.4	±0.3	±0.3	±0.4	±0.5	±0.6	±0.8	±1.0	±1.4	±2.5
Systematics [%]	±3.04	±0.57	±1.62	±1.71	±1.91	±1.68	±1.31	±1.58	±3.82	±5.67
η intercalibration model (JES) [%]	∓0.22	∓0.17	-	-	-	$^{+0.14}_{-0.21}$	±0.31	±0.50	±0.73	±0.85
Single particle high-p_T (JES) [%]	-	-	-	-	-	-	-	-	-	-
Effective stat. NP set 1 (JES) [%]	-	-	-	-	-	-	-	-	-	-
Effective stat. NP set 2 (JES) [%]	-	-	-	-	-	-	-	-	-	-
Effective stat. NP set 3 (JES) [%]	-	-	-	-	-	-	-	-	-	-
Effective detector NP set 1 (JES) [%]	-	-	-	-	-	-	-	-	-	-
Effective detector NP set 2 (JES) [%]	-	-	-	-	-	-	-	-	-	-
Effective detector NP set 3 (JES) [%]	-	-	-	-	-	-	-	-	-	-
Effective mixed NP set 1 (JES) [%]	-	-	-	-	-	-	-	-	-	-
Effective mixed NP set 2 (JES) [%]	-	-	-	-	-	-	-	-	-	-
Effective model NP set 1 (JES) [%]	-	-	-	-	-	-	-	-	-	-
Effective model NP set 2 (JES) [%]	-	-	-	-	-	-	-	-	-	-
Effective model NP set 3 (JES) [%]	-	-	-	-	-	-	-	-	-	-
Effective model NP set 4 (JES) [%]	-	-	-	-	-	-	-	-	-	-
Pile-up offset μ (JES) [%]	-	-	-	-	-	-	-	∓0.11	$^{-0.12}_{+0.20}$	∓0.29
Pile-up offset N_{PV} (JES) [%]	-	-	-	-	-	-	-	-	-	-
Punch-through (JES) [%]	-	-	-	-	-	-	-	-	-	-
Pile-up offset ρ topology (JES) [%]	-	-	-	-	-	-	-	-	-	-
Pile-up offset p_T (JES) [%]	-	-	-	-	-	-	-	-	-	-
Flavour composition (JES) [%]	-	-	-	-	-	-	-	-	$^{-}_{-0.15}$	-
Flavour response (JES) [%]	-	-	-	-	-	-	-	-	-	-
b-Tagged jet energy scale (JES) [%]	-	-	-	-	-	-	-	-	-	-
Jet reconstruction efficiency [%]	-	-	-	-	-	-	-	-	-	-
Jet energy resolution [%]	-	-	-	-	-	-	-	-	-	-
b-Quark tagging efficiency [%]	∓0.11	-	-	-	-	±0.13	±0.17	±0.21	±0.21	±0.22
c-Quark tagging efficiency [%]	±0.16	±0.13	-	-	-	∓0.18	∓0.27	∓0.33	∓0.36	∓0.45
Light-jet tagging efficiency [%]	-	-	-	-	-	-	-	-	-	-
Electron energy scale [%]	-	-	-	-	-	-	-	$^{+0.10}_{-0.15}$	±0.21	±0.30
Electron energy resolution [%]	-	-	-	-	-	-	-	-	-	-
Muon momentum scale [%]	-	-	-	-	-	-	-	-	-	-
Muon (ID) momentum resolution [%]	-	-	-	-	-	-	-	-	-	-
Muon (MS) momentum resolution [%]	-	-	-	-	-	-	-	-	-	-
Lepton trigger efficiency [%]	-	-	-	-	-	-	-	-	±0.15	±0.23
Lepton reconstruction efficiency [%]	-	-	-	-	-	-	-	-	-	-
Lepton identification efficiency [%]	-	-	-	-	-	-	-	-	-	-
E_T^{miss} Soft jet scale [%]	-	-	-	-	-	-	-	-	-	-
E_T^{miss} Soft jet resolution [%]	-	-	-	-	-	-	-	-	-	-
Jet vertex fraction [%]	-	-	-	-	-	-	-	-	-	-
Alternate hard-scattering model [%]	±2.02	∓0.17	∓1.26	∓1.28	∓1.20	∓0.59	±0.32	∓0.22	±1.54	±3.25
Alternate parton-shower model [%]	±2.16	-	∓0.98	∓1.10	∓1.44	∓1.37	∓0.71	±0.22	±2.43	±3.13
Monte Carlo sample statistics [%]	±0.10	-	-	±0.10	±0.12	±0.16	±0.20	±0.27	±0.35	±0.63
ISR/FSR + scale [%]	$^{-}_{-0.46}$	∓0.23	-	$^{-}_{+0.24}$	$^{+0.39}_{-}$	$^{+0.79}_{-}$	$^{+0.78}_{-0.11}$	$^{+0.31}_{-1.04}$	$^{-}_{-2.08}$	$^{-}_{-2.56}$
Parton distribution functions [%]	±0.31	±0.25	±0.12	-	∓0.13	∓0.25	∓0.46	∓0.63	∓0.90	∓1.31
Single top cross-section [%]	-	-	-	-	-	-	-	-	-	-
W+jets scale factors [%]	-	-	-	-	-	-	±0.10	±0.15	±0.29	±0.58
Fake lept. MC stat, e+jets ch. [%]	$^{-0.23}_{-}$	$^{-0.21}_{-}$	-	-	-	-	$^{+0.31}_{-}$	$^{+0.89}_{-0.15}$	$^{+1.46}_{-0.10}$	$^{+1.50}_{-}$
Fake lept. alternate fake CR, e+jets ch. [%]	-	-	-	-	-	-	-	-	-	-
Fake lept. alternate real CR, e+jets ch. [%]	-	-	-	-	-	-	-	-	-	-
Fake lept. alternate parametrization, e+jets ch. [%]	-	-	-	-	-	-	-	±0.21	±0.43	±0.41
Fake lept. MC stat, μ+jets ch. [%]	-	-	-	-	-	-	-	-	-	-
Fake lept. alternate fake CR, μ+jets ch. [%]	-	-	-	-	-	-	-	∓0.15	∓0.27	∓0.20
Fake lept. alternate real CR, μ+jets ch. [%]	∓0.30	∓0.25	∓0.16	-	-	±0.31	±0.52	±0.61	±0.89	±1.68
Fake lept. alternate parametrization, μ+jets ch. [%]	∓0.11	-	-	-	-	-	±0.15	±0.21	±0.38	±0.96
Z+jets cross-section [%]	-	-	-	-	-	-	-	±0.10	±0.13	-
Diboson cross-section [%]	-	-	-	-	-	-	-	-	-	-
Luminosity [%]	-	-	-	-	-	-	-	-	-	-

TABLE D.41: Fiducial phase-space relative differential cross-sections after combining the e+jets and μ+jets channels for $\chi^{t\bar{t}}$. All uncertainties are quoted as a percentage with respect to the cross-section values in each bin. Dashes are used when the estimated relative systematic uncertainty for that bin is below 0.1%.

Bins [Unit χ^{tt}]	1–1.40	1.40–1.90	1.90–2.50	2.50–3.20	3.20–4.20	4.20–5.50	5.50–7.20	7.20–9.30	9.30–12	12–20
$d\sigma$ / d χ^{tt} [Unit χ^{tt}]	$1.37 \cdot 10^{2}$	$9.39 \cdot 10^{1}$	$6.37 \cdot 10^{1}$	$4.26 \cdot 10^{1}$	$2.69 \cdot 10^{1}$	$1.55 \cdot 10^{1}$	$8.35 \cdot 10^{0}$	$4.27 \cdot 10^{0}$	$2.10 \cdot 10^{0}$	$6.66 \cdot 10^{-1}$
Total Uncertainty [%]	±9.79	±10.9	±11.6	±11.8	±11.8	±11.5	±10.9	±10.7	±9.78	±10.1
Statistics [%]	±0.5	±0.4	±0.4	±0.5	±0.6	±0.7	±0.9	±1.2	±1.6	±2.9
Systematics [%]	±9.78	±10.9	±11.6	±11.8	±11.8	±11.4	±10.8	±10.6	±9.60	±9.60
η intercalibration model (JES) [%]	±0.19	±0.25	±0.33	±0.42	±0.51	±0.60	±0.73	±0.93	±1.16	±1.28
Single particle high-p_T (JES) [%]	-	-	-	-	-	-	-	-	-	-
Effective stat. NP set 1 (JES) [%]	±0.89	±0.89	±0.90	±0.91	±0.89	±0.88	±0.89	±0.90	±0.92	±0.92
Effective stat. NP set 2 (JES) [%]	-	-	-	-	-	-	-	-	-	-
Effective stat. NP set 3 (JES) [%]	-	-	-	-	-	-	-	-	-	-
Effective detector NP set 1 (JES) [%]	±0.17	±0.18	±0.18	±0.18	±0.19	±0.20	±0.19	±0.21	$^{+0.20}_{-0.29}$	$^{+0.19}_{-0.31}$
Effective detector NP set 2 (JES) [%]	±0.17	±0.18	±0.19	±0.18	±0.18	±0.16	±0.17	$^{+0.15}_{-0.20}$	$^{+0.14}_{-0.19}$	$^{+0.19}_{-0.14}$
Effective detector NP set 3 (JES) [%]	-	-	-	-	-	-	-	-	-	-
Effective mixed NP set 1 (JES) [%]	±0.29	±0.29	±0.30	±0.30	±0.30	±0.30	±0.30	±0.32	±0.36	$^{+0.29}_{-0.43}$
Effective mixed NP set 2 (JES) [%]	∓0.38	∓0.38	∓0.39	∓0.39	∓0.38	∓0.36	∓0.37	∓0.36	∓0.37	∓0.36
Effective model NP set 1 (JES) [%]	±2.28	±2.27	±2.30	±2.33	±2.31	±2.27	±2.28	±2.33	±2.35	±2.28
Effective model NP set 2 (JES) [%]	-	-	-	-	-	-	-	-	-	-
Effective model NP set 3 (JES) [%]	±0.11	±0.12	±0.14	±0.14	±0.14	±0.14	±0.14	±0.12	-	-
Effective model NP set 4 (JES) [%]	-	-	-	-	-	-	-	-	-	-
Pile-up offset μ (JES) [%]	∓0.11	∓0.14	∓0.17	∓0.18	∓0.18	∓0.21	$^{-0.28}_{+0.21}$	∓0.29	$^{-0.29}_{+0.39}$	∓0.46
Pile-up offset N_{PV} (JES) [%]	∓0.59	∓0.62	∓0.64	∓0.65	∓0.60	∓0.56	∓0.57	∓0.60	$^{-0.70}_{+0.51}$	∓0.62
Punch-through (JES) [%]	-	-	-	-	-	-	-	-	-	-
Pile-up offset ρ topology (JES) [%]	±1.69	±1.68	±1.71	±1.75	±1.72	±1.69	±1.72	±1.73	±1.71	±1.77
Pile-up offset p_T (JES) [%]	-	-	-	-	-	-	-	-	-	-
Flavour composition (JES) [%]	±1.83	±1.85	±1.90	±1.92	±1.90	±1.89	±1.89	±1.96	±1.98	±1.87
Flavour response (JES) [%]	∓1.14	∓1.15	∓1.17	∓1.19	∓1.19	∓1.19	∓1.19	∓1.23	∓1.25	∓1.18
b-Tagged jet energy scale (JES) [%]	±0.53	±0.52	±0.52	±0.53	±0.52	±0.49	±0.49	±0.51	±0.52	±0.58
Jet reconstruction efficiency [%]	-	-	-	-	-	-	-	-	-	-
Jet energy resolution [%]	-	-	-	-	-	-	-	-	-	-
b-Quark tagging efficiency [%]	±4.11	±4.14	±4.19	±4.25	±4.31	±4.37	±4.41	±4.44	±4.45	±4.45
c-Quark tagging efficiency [%]	±1.10	±1.06	±1.00	±0.92	±0.83	±0.74	±0.66	±0.59	±0.56	±0.47
Light-jet tagging efficiency [%]	±0.50	±0.50	±0.51	±0.52	±0.53	±0.53	±0.54	±0.52	±0.51	±0.50
Electron energy scale [%]	-	-	-	-	$^{-}_{-0.14}$	$^{+0.11}_{-0.20}$	$^{+0.13}_{-0.26}$	$^{+0.18}_{-0.28}$	±0.32	±0.41
Electron energy resolution [%]	-	-	-	-	-	-	-	-	-	-
Muon momentum scale [%]	-	-	-	-	-	-	-	-	-	-
Muon (ID) momentum resolution [%]	-	-	-	-	-	-	-	-	-	-
Muon (MS) momentum resolution [%]	-	-	-	-	-	-	-	-	-	-
Lepton trigger efficiency [%]	±1.23	±1.24	±1.24	±1.25	±1.27	±1.29	±1.32	±1.36	±1.41	±1.50
Lepton reconstruction efficiency [%]	±0.23	±0.23	±0.24	±0.24	±0.24	±0.25	±0.26	±0.27	±0.28	±0.30
Lepton identification efficiency [%]	±1.31	±1.31	±1.32	±1.32	±1.32	±1.32	±1.31	±1.30	±1.29	±1.28
E_T^{miss} Soft jet scale [%]	-	-	-	-	-	-	-	-	-	-
E_T^{miss} Soft jet resolution [%]	-	-	-	-	-	-	-	-	-	-
Jet vertex fraction [%]	∓0.66	∓0.66	∓0.65	∓0.66	∓0.66	∓0.65	∓0.64	∓0.62	$^{-0.73}_{+0.55}$	∓0.65
Alternate hard-scattering model [%]	∓1.61	∓3.74	∓4.79	∓4.81	∓4.73	∓4.15	∓3.26	∓3.78	∓2.08	∓0.43
Alternate parton-shower model [%]	∓1.55	∓3.72	∓4.58	∓4.70	∓5.03	∓4.96	∓4.33	∓3.42	∓1.29	∓0.62
Monte Carlo sample statistics [%]	±0.13	±0.11	±0.11	±0.13	±0.15	±0.19	±0.24	±0.31	±0.41	±0.73
ISR/FSR + scale [%]	∓6.67	∓6.76	∓6.55	∓6.69	∓6.55	∓6.40	∓6.09	∓5.82	$^{-6.84}_{+4.07}$	$^{-7.09}_{+3.56}$
Parton distribution functions [%]	±0.16	±0.10	-	∓0.15	∓0.28	∓0.39	∓0.60	∓0.77	∓1.05	∓1.46
Single top cross-section [%]	±0.26	±0.26	±0.27	±0.27	±0.28	±0.28	±0.29	±0.28	±0.29	±0.26
W+jets scale factors [%]	±0.31	±0.33	±0.37	±0.40	±0.43	±0.45	±0.51	±0.56	±0.69	±0.98
Fake lept. MC stat, e+jets ch. [%]	$^{-0.19}_{+0.43}$	$^{-0.17}_{+0.41}$	$^{-0.10}_{+0.43}$	$^{-}_{+0.42}$	$^{+0.40}_{-}$	$^{+0.37}_{-}$	$^{+0.35}_{-}$	$^{+0.93}_{-}$	$^{+1.50}_{-}$	$^{+1.54}_{-}$
Fake lept. alternate fake CR, e+jets ch. [%]	±0.33	±0.34	±0.36	±0.37	±0.39	±0.38	±0.36	±0.28	±0.35	±0.44
Fake lept. alternate real CR, e+jets ch. [%]	-	-	-	-	-	-	-	-	-	-
Fake lept. alternate parametrization, e+jets ch. [%]	±0.24	±0.24	±0.24	±0.24	±0.30	±0.36	±0.40	±0.51	±0.73	±0.71
Fake lept. MC stat, μ+jets ch. [%]	-	-	-	-	-	-	-	-	-	-
Fake lept. alternate fake CR, μ+jets ch. [%]	±0.27	±0.28	±0.25	±0.23	±0.22	±0.20	±0.16	-	-	-
Fake lept. alternate real CR, μ+jets ch. [%]	-	-	-	±0.19	±0.32	±0.55	±0.75	±0.85	±1.13	±1.92
Fake lept. alternate parametrization, μ+jets ch. [%]	±0.13	±0.14	±0.17	±0.22	±0.26	±0.32	±0.39	±0.46	±0.63	±1.21
Z+jets cross-section [%]	∓1.02	∓1.02	∓1.00	∓1.00	∓0.97	∓0.94	∓0.96	∓0.89	∓0.86	∓0.95
Diboson cross-section [%]	-	-	-	-	∓0.11	∓0.11	∓0.11	∓0.11	∓0.12	∓0.14
Luminosity [%]	±2.80	±2.80	±2.80	±2.80	±2.80	±2.80	±2.80	±2.80	±2.80	±2.80

TABLE D.42: Fiducial phase-space absolute differential cross-sections after combining the e+jets and μ+jets channels for $\chi^{t\bar{t}}$. All uncertainties are quoted as a percentage with respect to the cross-section values in each bin. Dashes are used when the estimated relative systematic uncertainty for that bin is below 0.1%.

Appendix E

Impact of IFSR in the fiducial and full phase-space

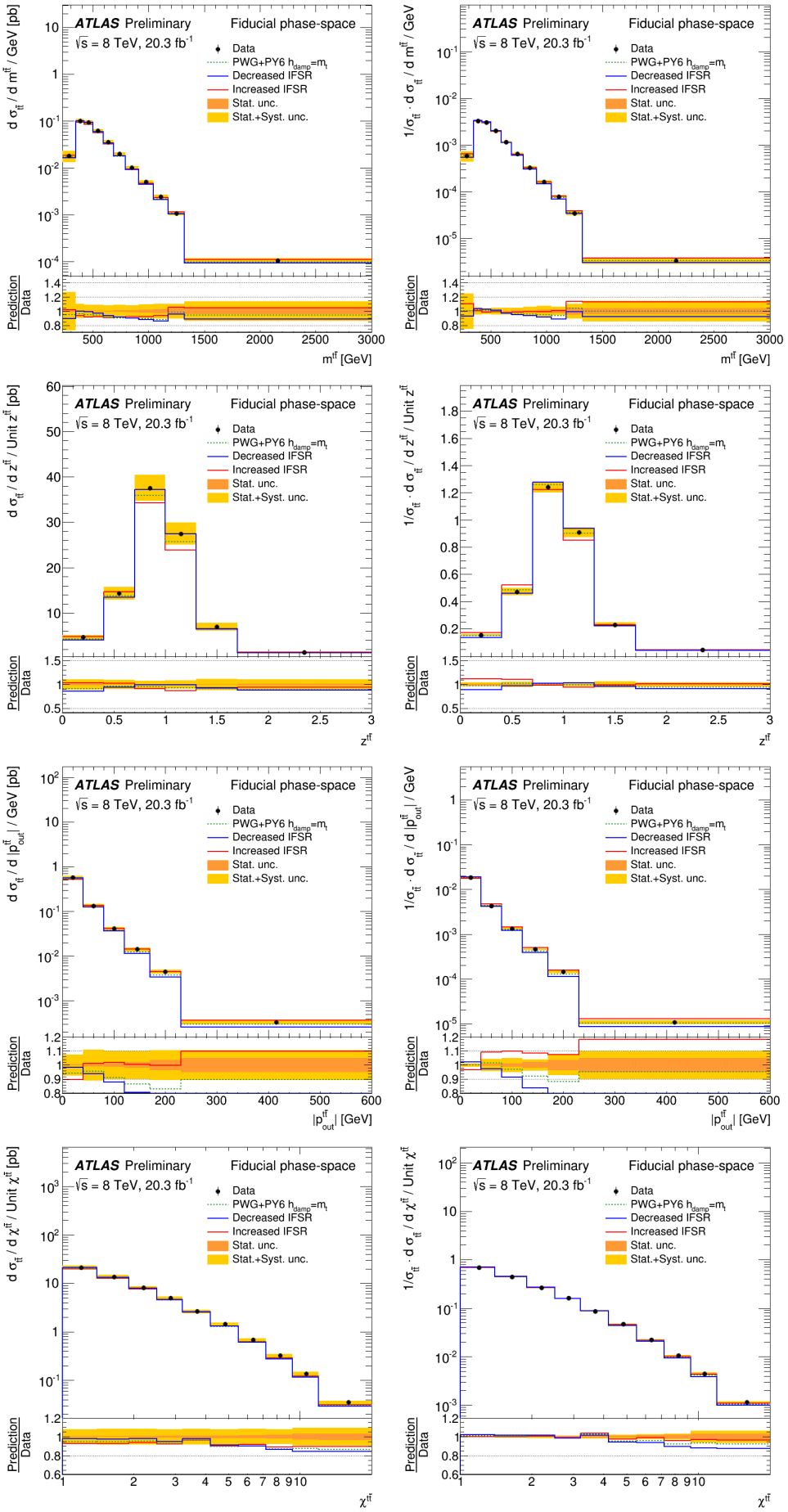

FIGURE E.1: Compatibility of increased and decreased IFSR samples for the absolute (left) and relative (right) differential cross-sections as a function of the mass (first row), $z_{t\bar{t}}$ (second row), $\mid P_{out}^{t\bar{t}} \mid$ (third row) and $\chi_{t\bar{t}}$ (fourth row) of the $t\bar{t}$ system in the fiducial phase-space.

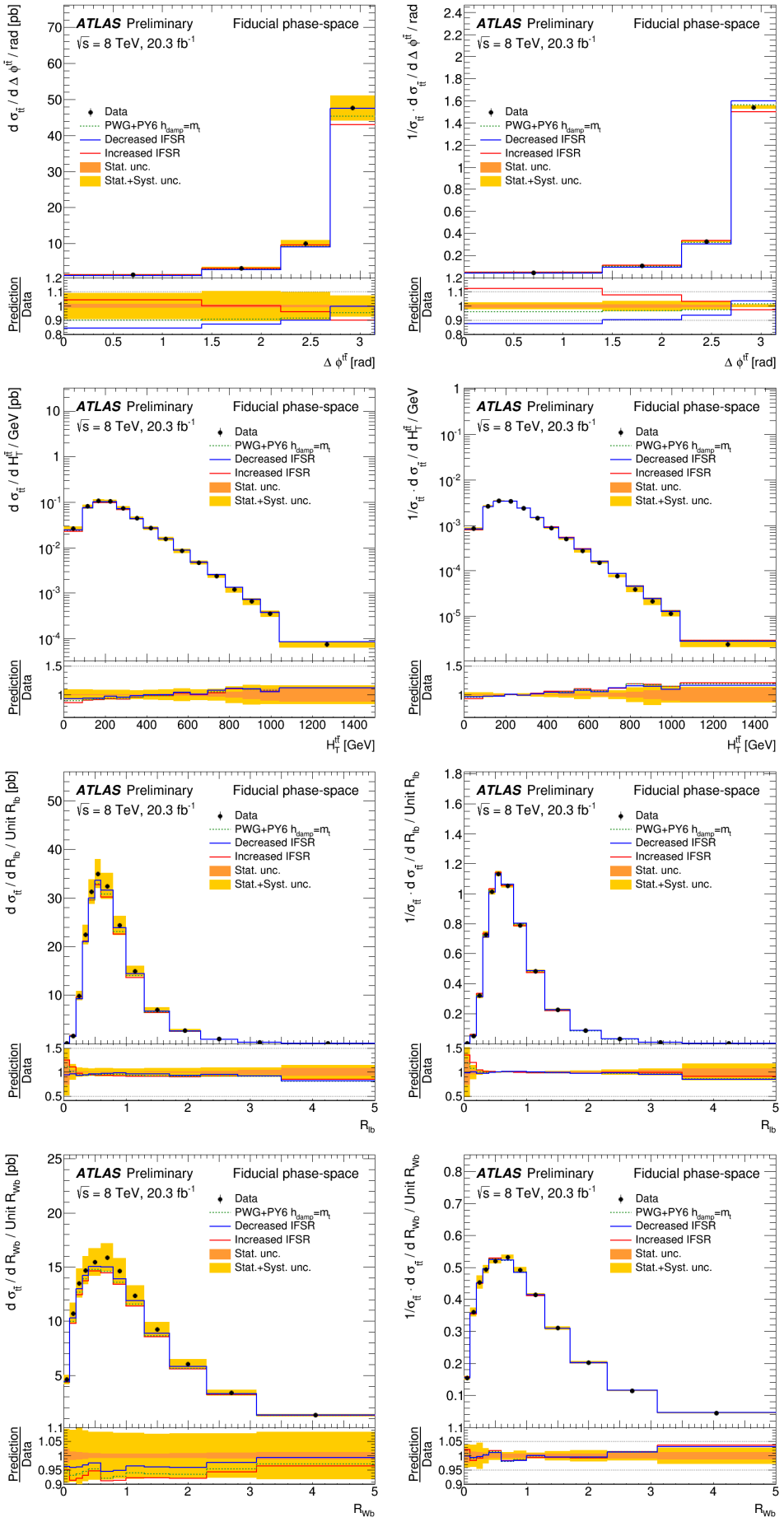

FIGURE E.2: Compatibility of increased and decreased IFSR samples for the absolute (left) and relative (right) differential cross-sections as a function of $\Delta\phi_{t\bar{t}}$ (first row), $H_{t\bar{t}}$ (second row), R_{lb} (third row) and R_{Wb} (fourth row) in the fiducial phase-space.

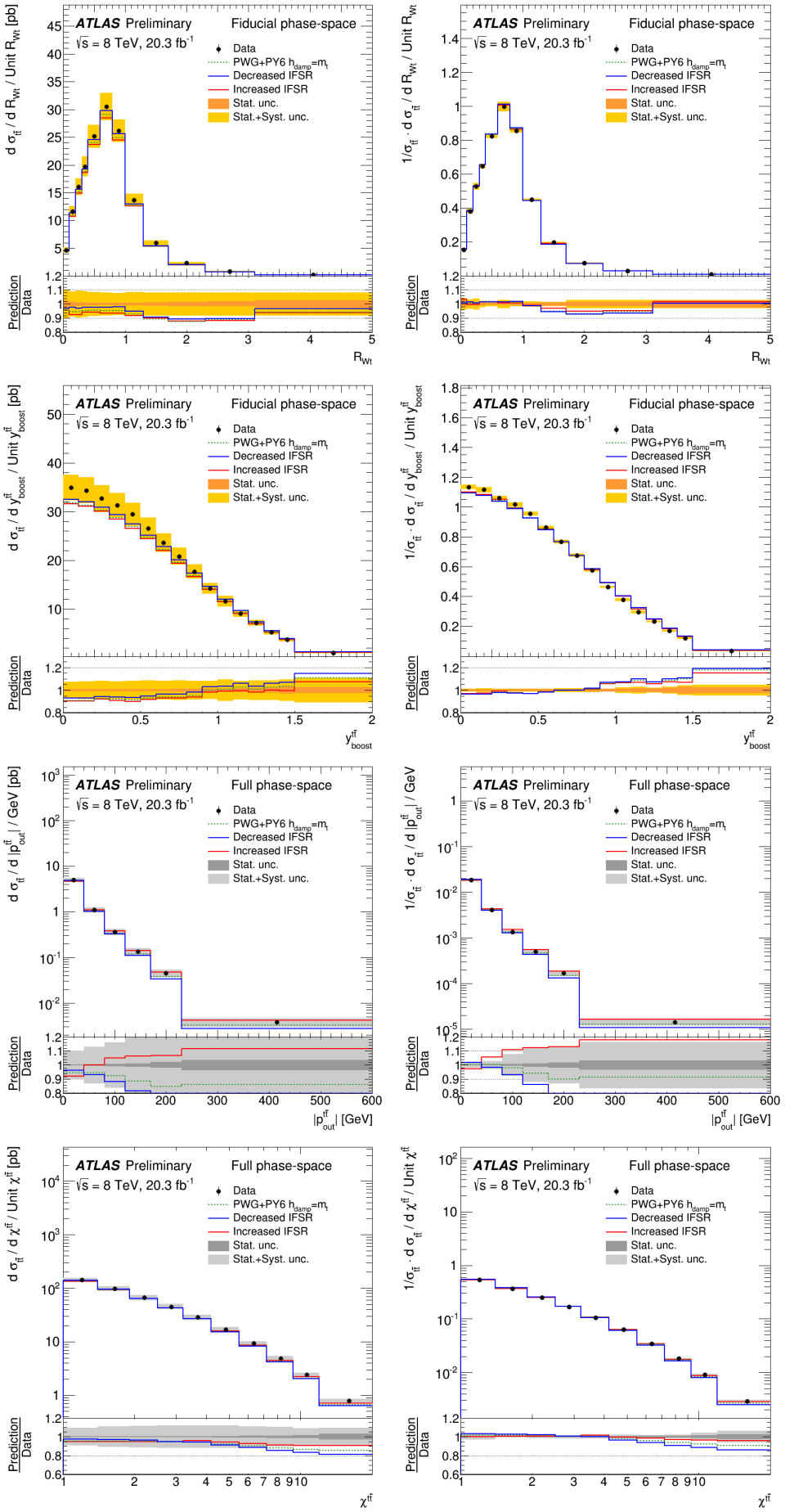

FIGURE E.3: Compatibility of increased and decreased IFSR samples for the absolute (left) and relative (right) differential cross-sections as a function of R_{Wt} (first row) and $Y^{t\bar{t}}_{boost}$ (second row) in the fiducial phase-space, and $|\ P^{t\bar{t}}_{out}\ |$ (third row) and $\chi_{t\bar{t}}$ (fourth row) in the full phase-space.

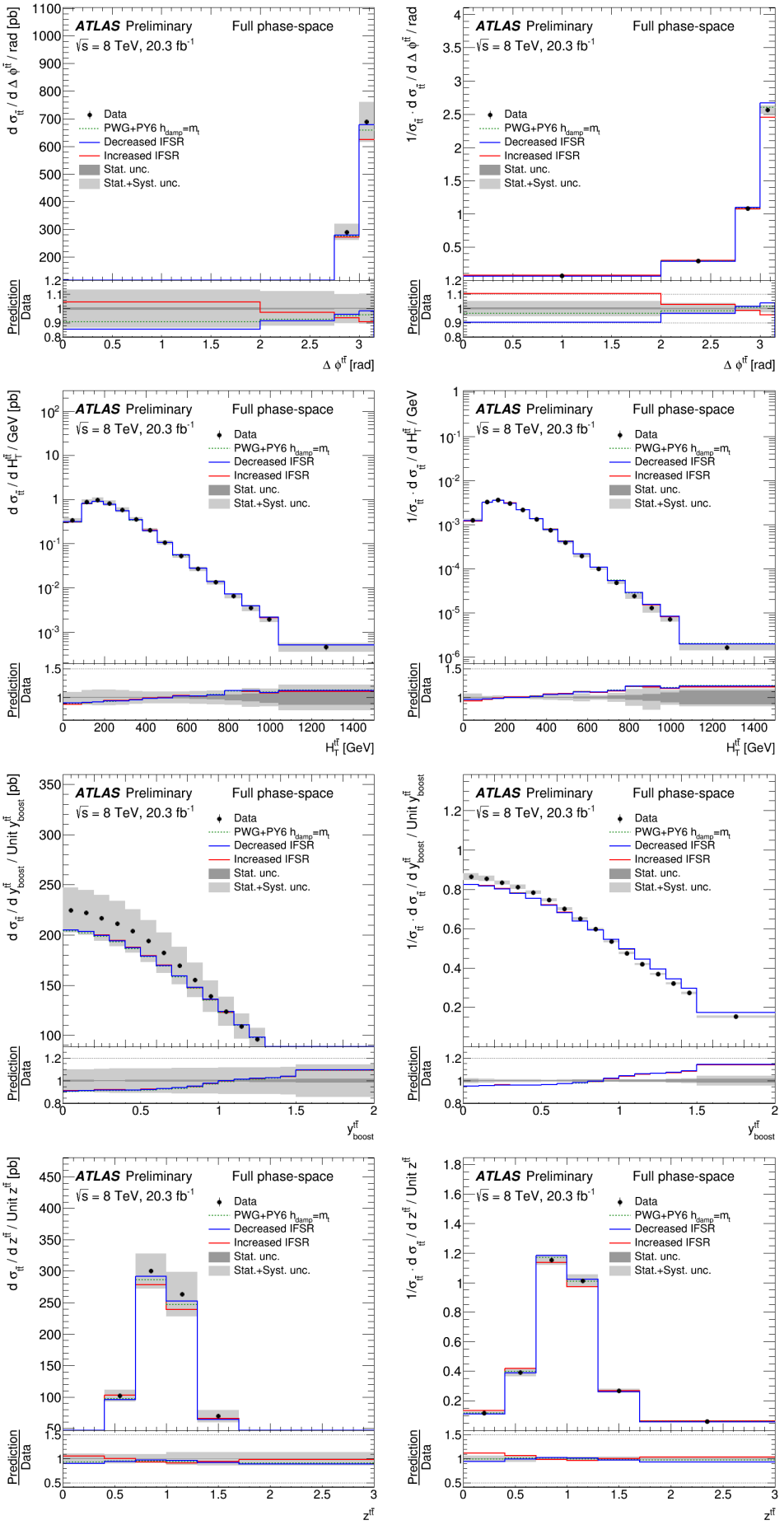

FIGURE E.4: Compatibility of increased and decreased IFSR samples for the absolute (left) and relative (right) differential cross-sections as a function of $\Delta\phi_{t\bar{t}}$ (first row), $H_{t\bar{t}}$ (second row), $Y^{t\bar{t}}_{boost}$ (third row) and $z_{t\bar{t}}$ (fourth row) in the full phase-space.

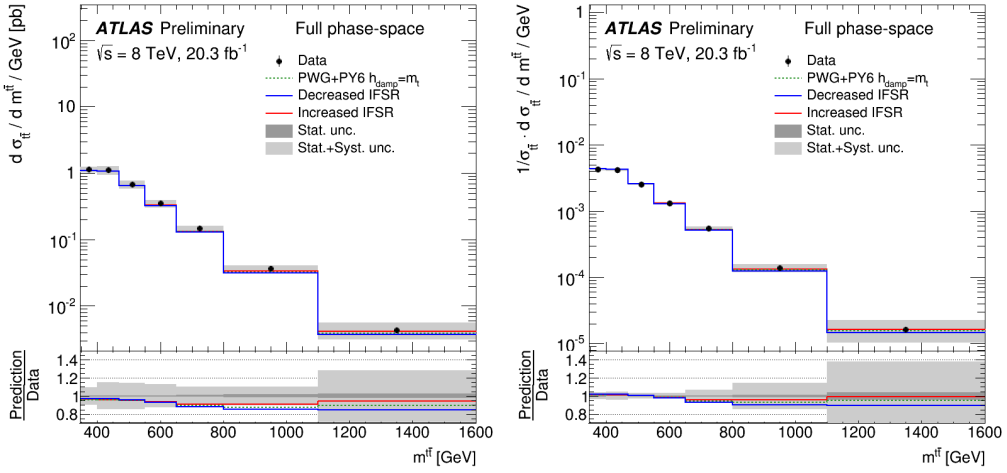

FIGURE E.5: Compatibility of increased and decreased IFSR samples for the absolute (left) and relative (right) differential cross-sections as a function of the mass of $t\bar{t}$ system in the full phase-space.

Appendix F

Covariance matrices

F.1 Fiducial phase-space

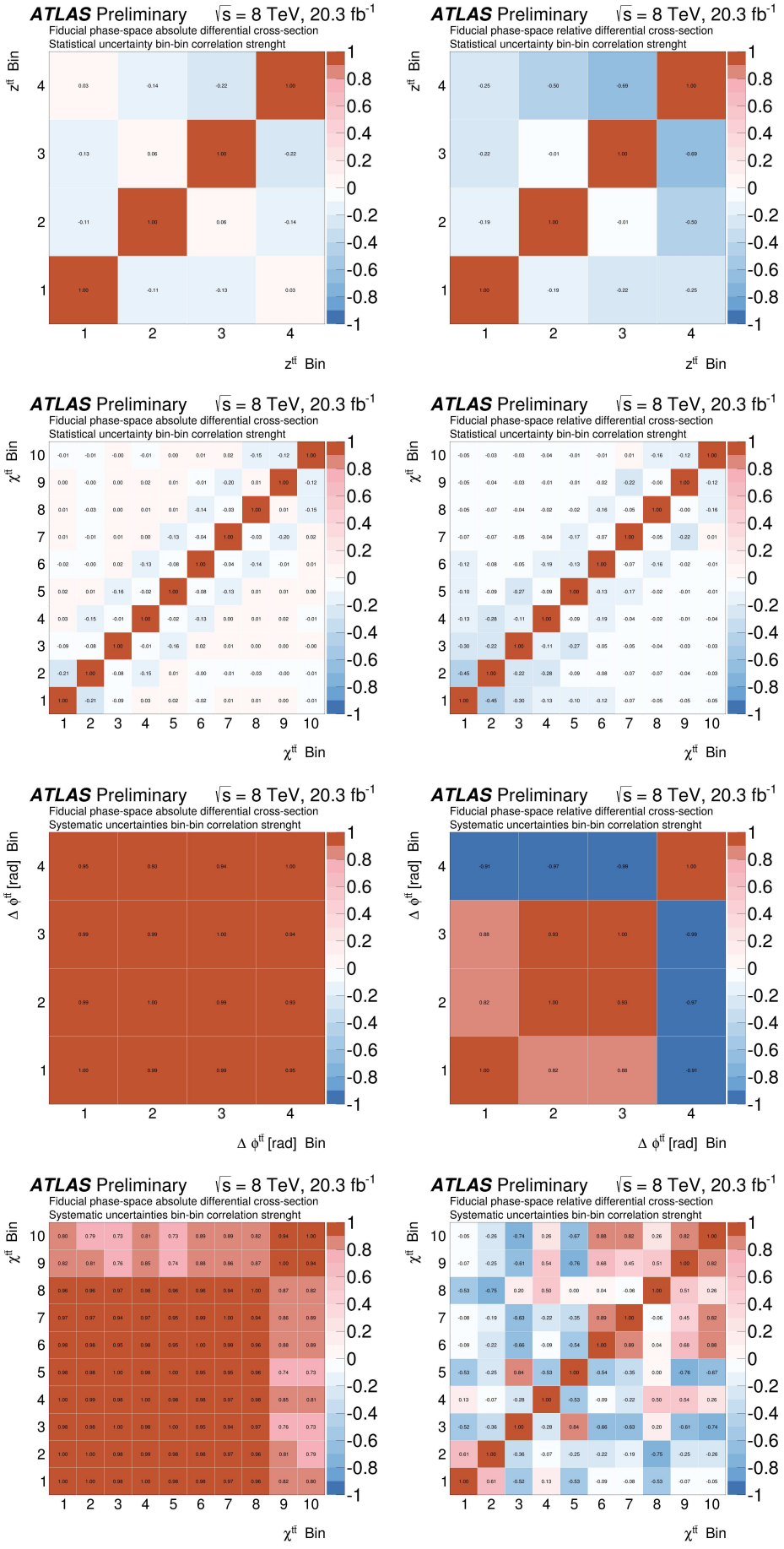

FIGURE F.1: Absolute (left) and relative (right) correlation matrices of the fiducial phase-space differential cross-sections as a function of the $\Delta\phi_{t\bar{t}}$(top) and $\chi^{t\bar{t}}$(bottom) for the statistical uncertainty first and systematic uncertanty then.

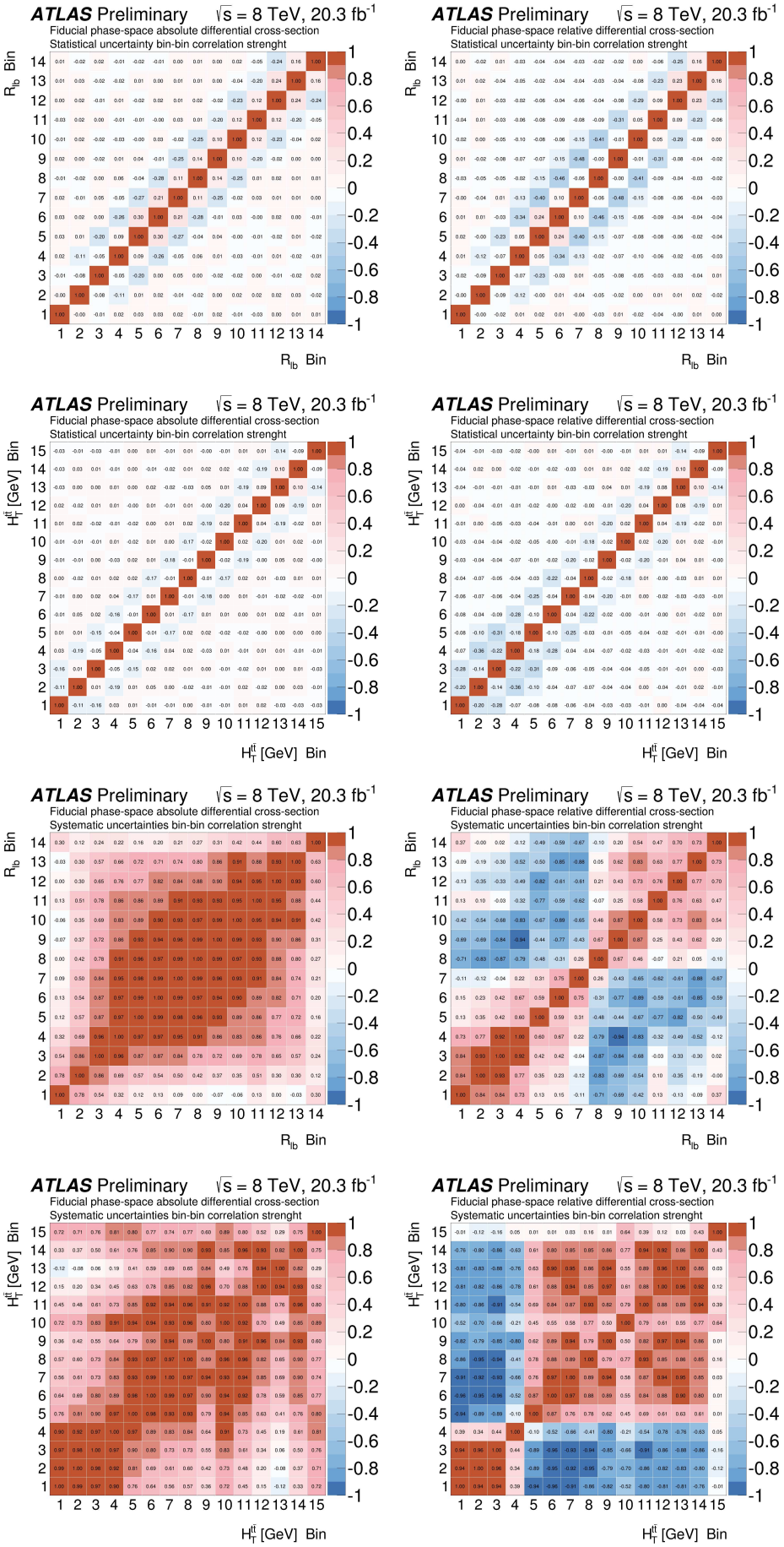

FIGURE F.2: Absolute (left) and relative (right) correlation matrices of the fiducial phase-space differential cross-sections as a function of the R_{lb}(top) and $H_{\mathrm{T}}^{t\bar{t}}$(bottom) for the statistical uncertainty first and systematic uncertanty then.

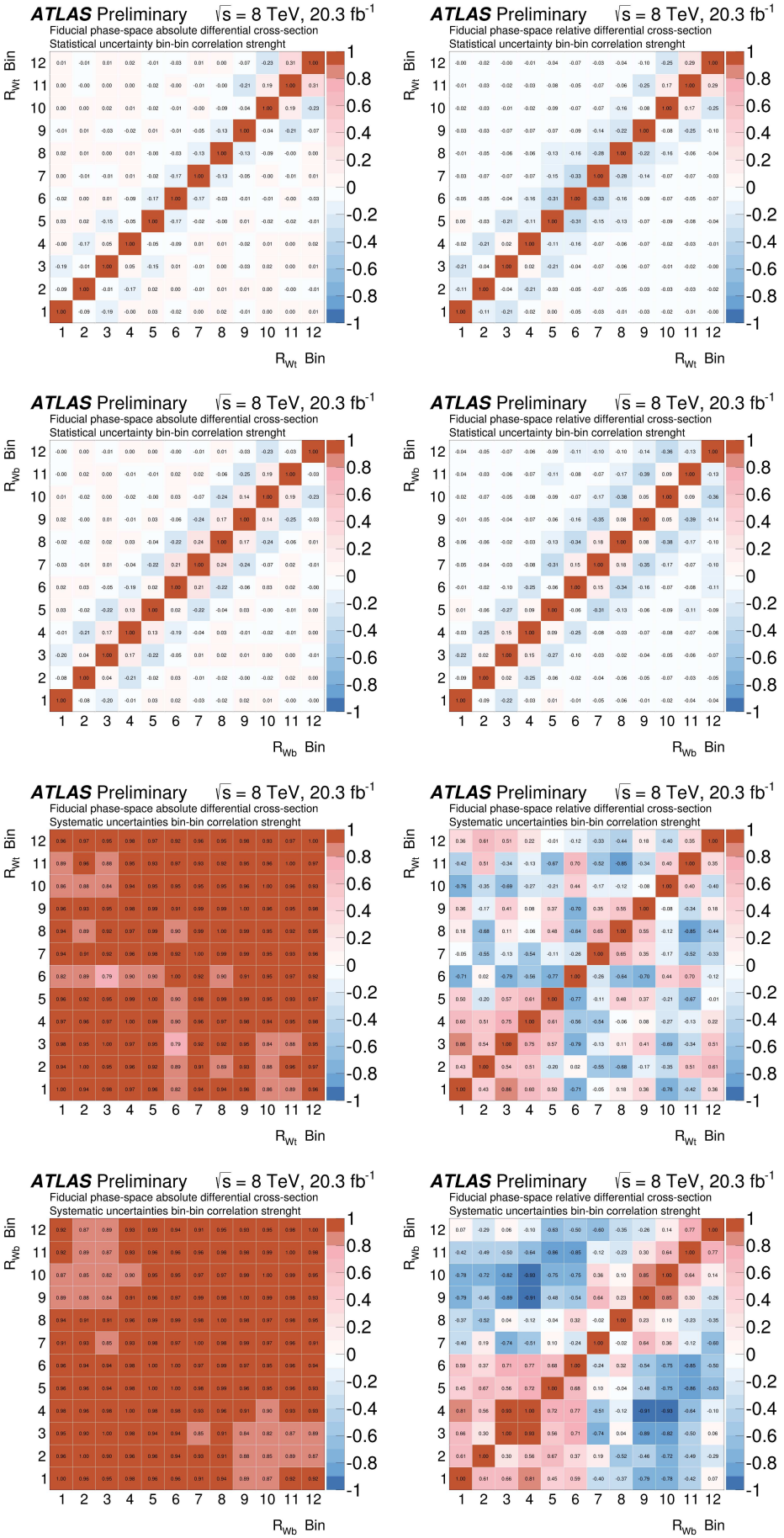

FIGURE F.3: Absolute (left) and relative (right) correlation matrices of the fiducial phase-space differential cross-sections as a function of the R_{Wt}(top) and R_{Wb}(bottom) for the statistical uncertainty first and systematic uncertanty then.

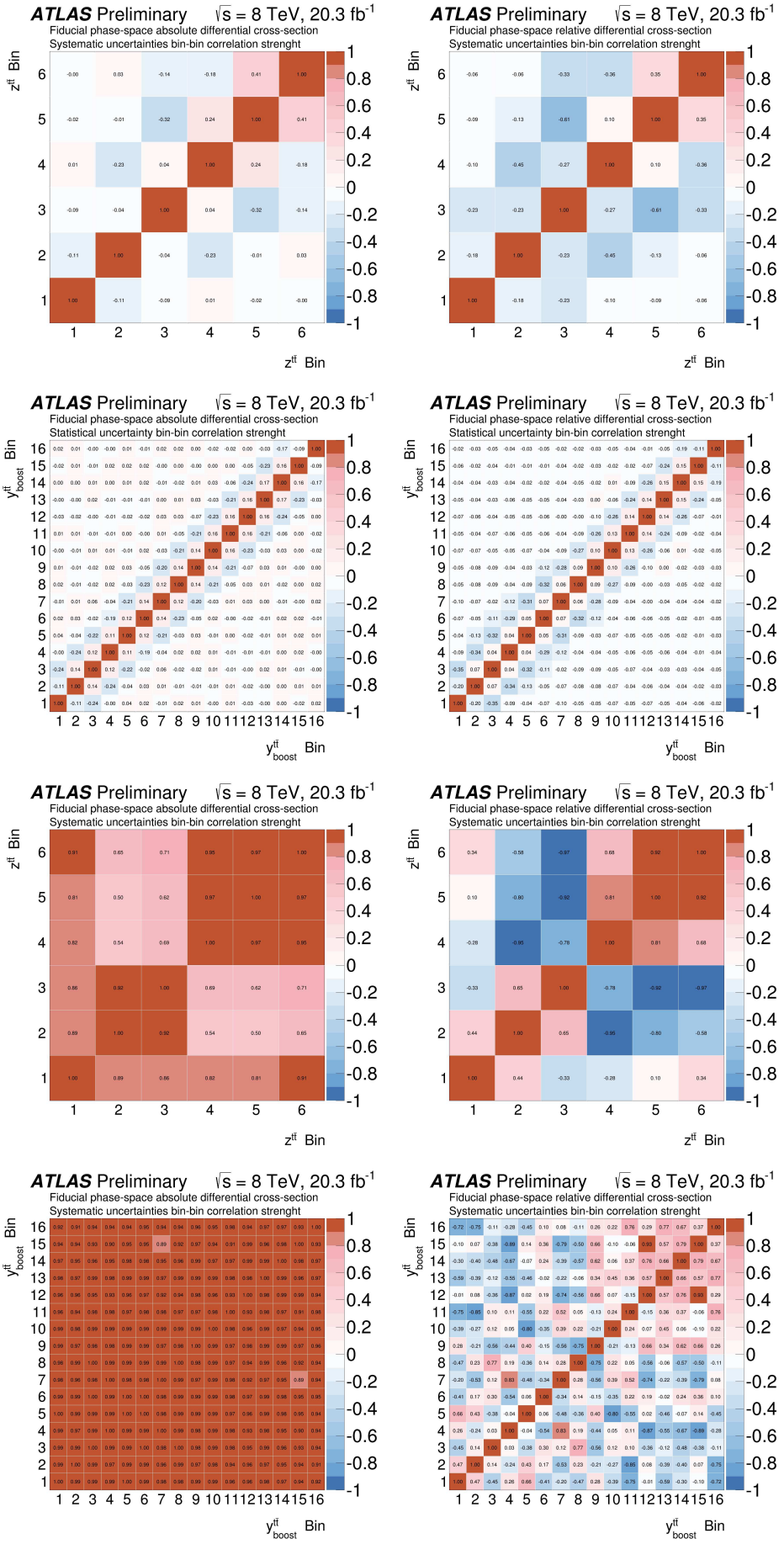

FIGURE F.4: Absolute (left) and relative (right) correlation matrices of the fiducial phase-space differential cross-sections as a function of the $z^{t\bar{t}}$(top) and $y^{t\bar{t}}_{\text{boost}}$(bottom) for the statistical uncertainty first and systematic uncertanty then.

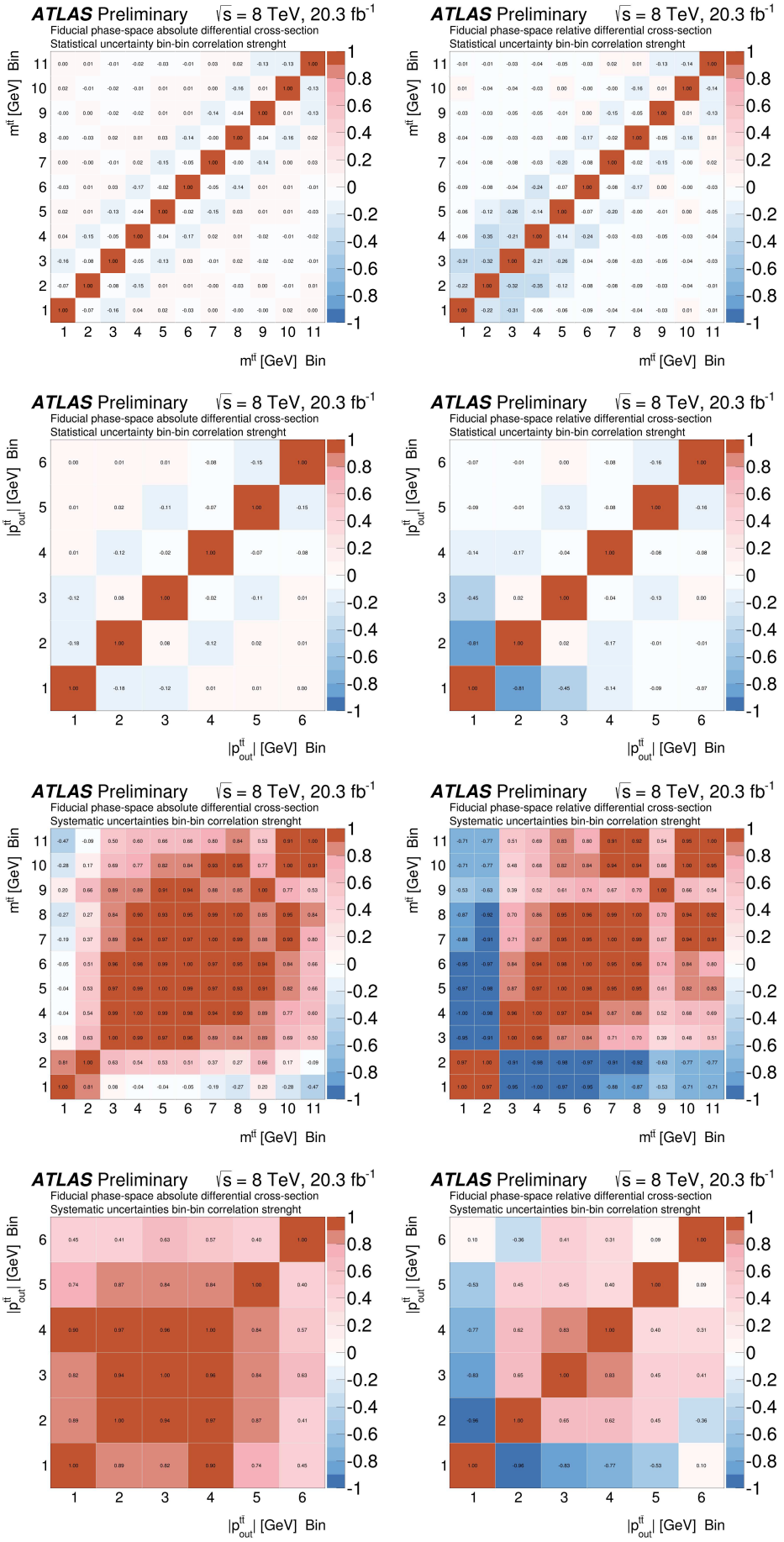

FIGURE F.5: Absolute (left) and relative (right) correlation matrices of the fiducial phase-space differential cross-sections as a function of the $m^{t\bar{t}}$(top) and $\left|p_{\text{out}}^{t\bar{t}}\right|$(bottom) for the statistical uncertainty first and systematic uncertanty then.

F.2 Full phase-space

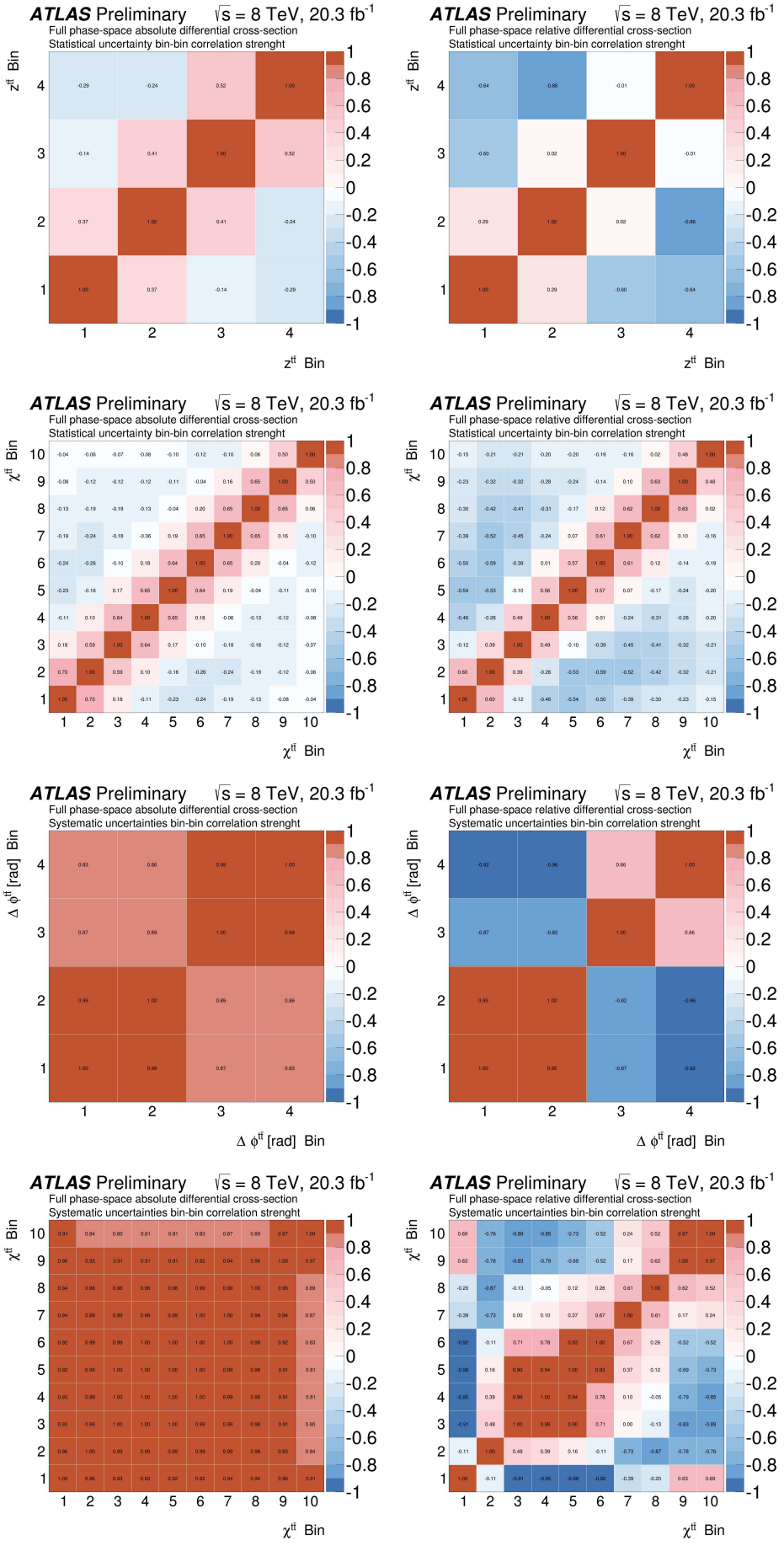

FIGURE F.6: Absolute (left) and relative (right) correlation matrices of the full phase-space differential cross-sections as a function of the $\Delta\phi_{t\bar{t}}$(top) and $\chi^{t\bar{t}}$(bottom) for the statistical uncertainty first and systematic uncertanty then.

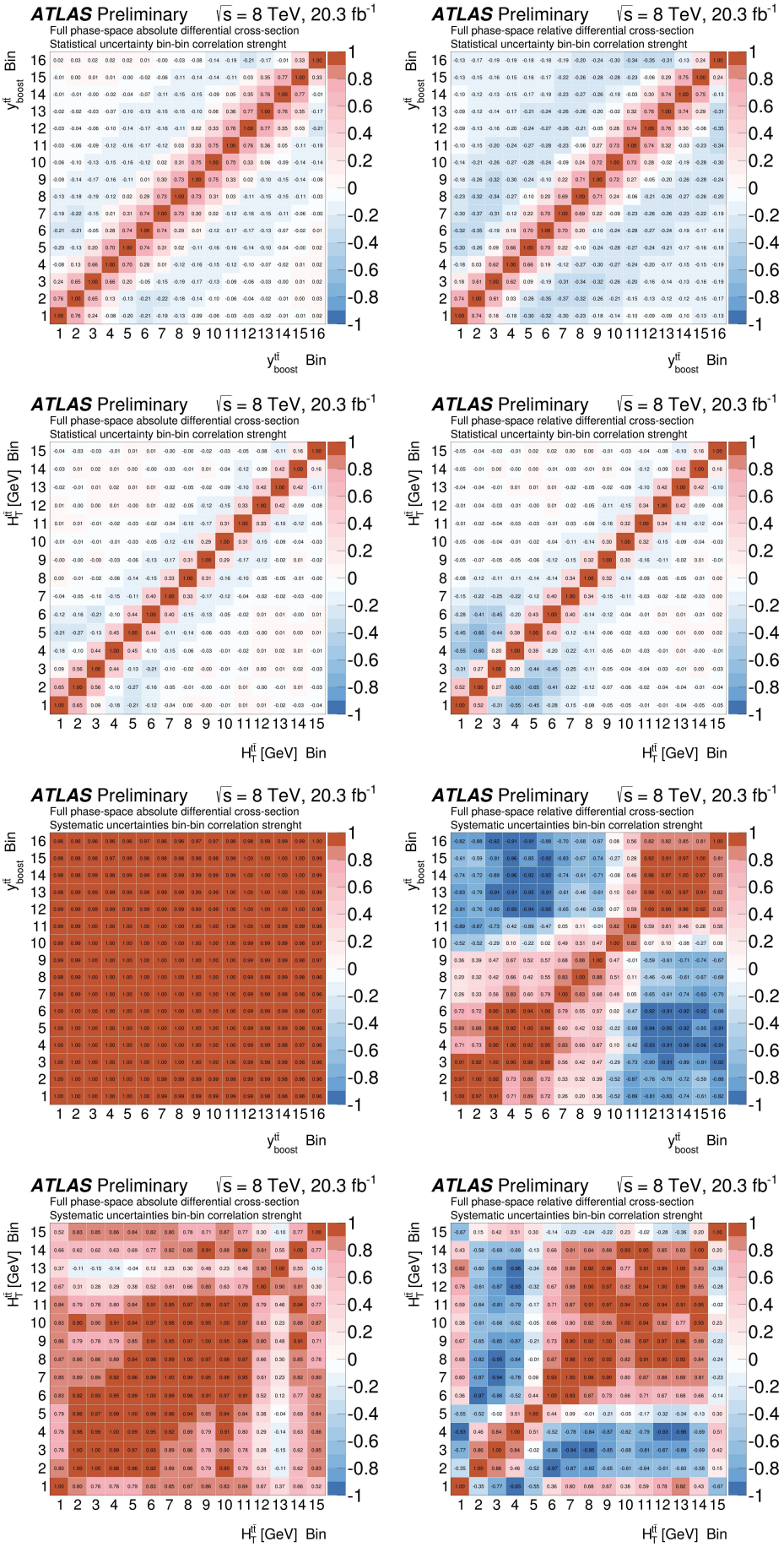

FIGURE F.7: Absolute (left) and relative (right) correlation matrices of the full phase-space differential cross-sections as a function of the $y^{t\bar{t}}_{\text{boost}}$(top) and $H^{t\bar{t}}_{\text{T}}$(bottom) for the statistical uncertainty first and systematic uncertanty then.

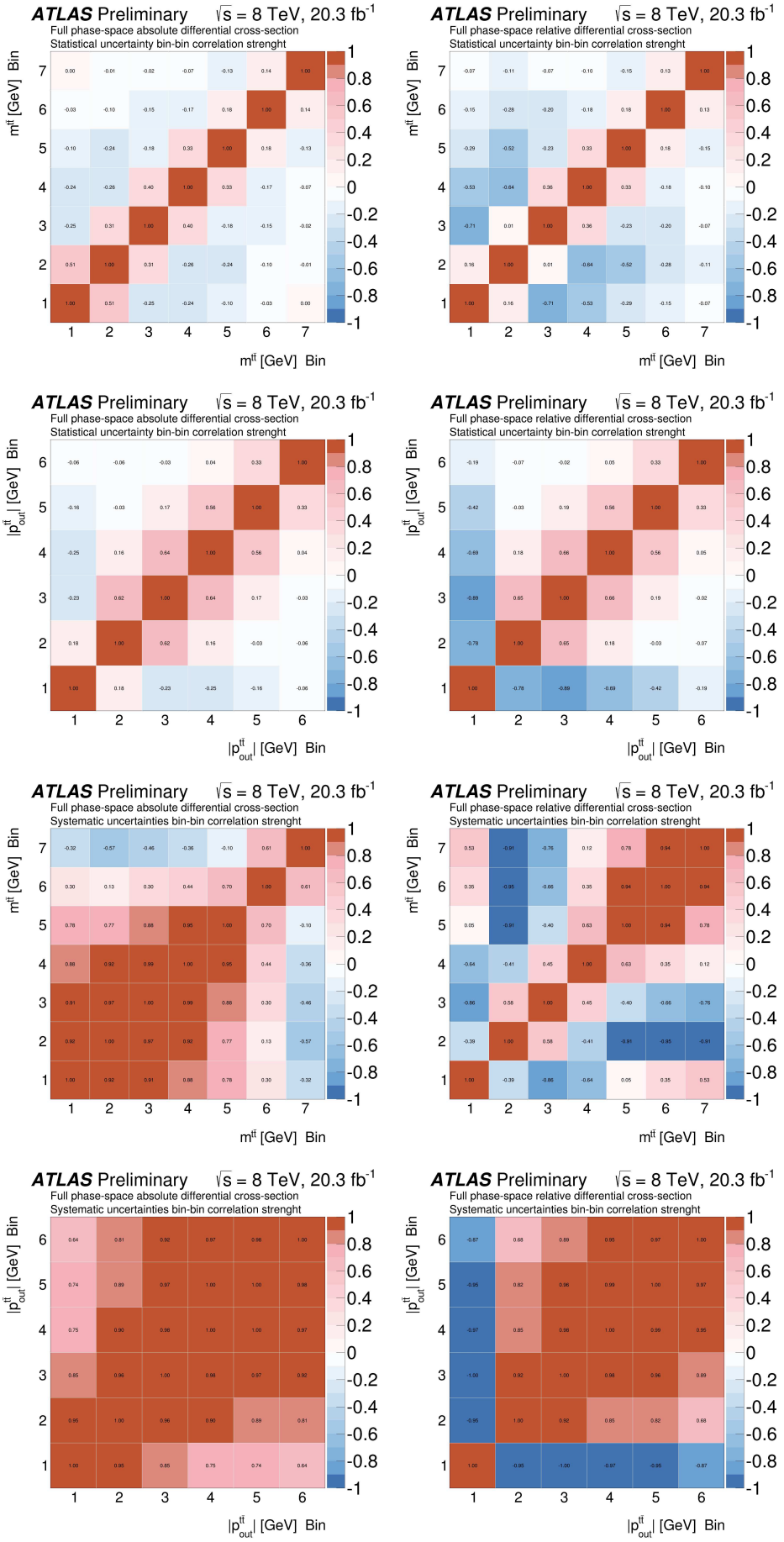

FIGURE F.8: Absolute (left) and relative (right) correlation matrices of the full phase-space differential cross-sections as a function of the $m^{t\bar{t}}$(top) and $\left|p_{\text{out}}^{t\bar{t}}\right|$(bottom) for the statistical uncertainty first and systematic uncertanty then.

Appendix G

Stress tests

Due to the specific choice of the Monte Carlo sample for the training of the unfolding, it is necessary to check whether this choice could introduce a bias via the unfolding. This check is done by reweighting the MC in order to change the shapes of the distributions, and use this varied distribution as pseudo-data. The reweighted MC is then unfolded with the nominal MC response, and the unfolding result is compared to the reweighted MC particle-level. Non-closure would indicate that the unfolding introduces a bias towards the training particle-level spectrum. Different reweight strategies have been used for the different spectra:

- "bump" injection for the $t\bar{t}$ mass spectrum. The bump has been parametrized as:

$$f\left(m_{t\bar{t}}\right) = 1 + k \cdot e^{-\frac{\Delta(m_{t\bar{t}})^2}{\sigma^2}}, \tag{G.1}$$

  where $k = 2$, $\Delta\left(m_{t\bar{t}}\right) = m_{t\bar{t}} - 800\,\text{GeV}$ and $\sigma = 100\,\text{GeV}$;

- linear reweighting as a function for the p_{T} of the $t\bar{t}$ system for the $t\bar{t}$ p_{T}. The reweighting function has been defined as

$$\left(p_{T,t\bar{t}}\right) = 1 + \frac{1}{400\,\text{GeV}} \cdot p_{T,t\bar{t}}; \tag{G.2}$$

- negative Gaussian reweighting as a function of the rapidity of the $t\bar{t}$ system for the $t\bar{t}$, hadronic and leptonic top rapidity spectra. The reweighting function has been defined as

$$f\left(y_{t\bar{t}}\right) = 1 - k \cdot e^{-\frac{y_{t\bar{t}}^2}{\sigma^2}}, \tag{G.3}$$

  where $k = 0.8$ and $\sigma = 0.2$;

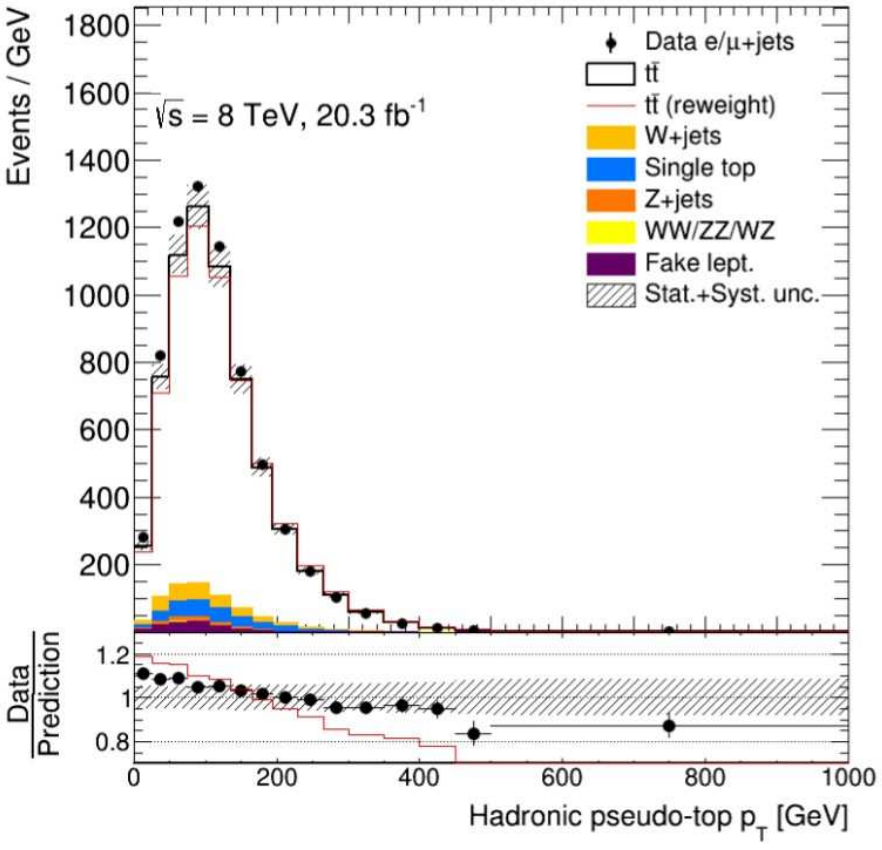

FIGURE G.1: Data-MC comparison for the reconstructed hadronic top p_T using the nominal and reweighted sample as a function of the average top p_T as descrivbed in Eq. G.4.

- combined linear reweighting as a function of the p_{T} of both hadronic and leptonic for the hadronic and leptonic top p_{T} spectra. The reweighting function has been defined as

$$f\left(p_{\mathrm{T}}^{t,\mathrm{had}}, p_{\mathrm{T}}^{t,\mathrm{lep}}\right) = 1 + \frac{1}{750\,\mathrm{GeV}} \cdot \frac{p_{\mathrm{T}}^{t,\mathrm{had}} + p_{\mathrm{T}}^{t,\mathrm{lep}}}{2}. \tag{G.4}$$

- new physics stress test: an exotic model ($Z'(400\,\mathrm{GeV}) \to t\bar{t}$) has been added on top of SM $t\bar{t}$ prediction.

In all cases besides the new physics stress test, the final reweighted histograms have been scaled by $N_{\mathrm{nominal}}/N_{\mathrm{reweighted}}$, where N_{nominal} and $N_{\mathrm{reweighted}}$ are evaluated before any selection cuts, in order to preserve total cross section. For the new physics stress test, the total cross section has been allowed to change. In general, the reweighting shapes have been chosen extreme enough to put the unfolding procedure under a significant stress. For this reason, these shapes are usually unphysical: G.1 shows the comparison of the nominal and reweighted signal to the data for the reconstructed p_T of the hadronic top.

Figs. G.2 G.3 G.4 G.5 G.6 show the results of the stress tests.

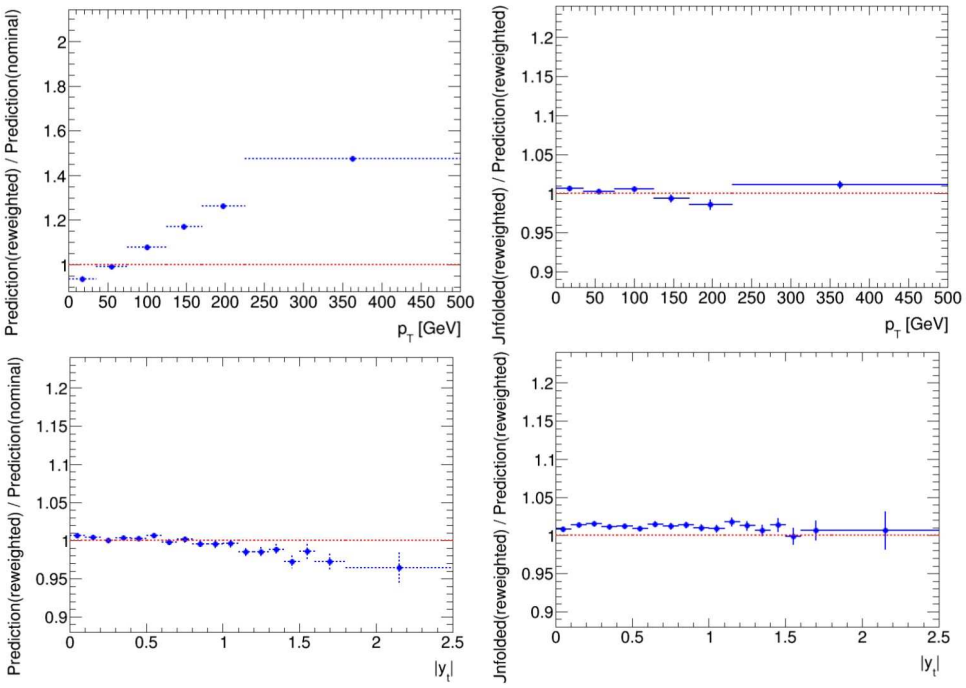

FIGURE G.2: Stress test for the p_{T} (top) and $|y|$ (bottom) of $t\bar{t}$ system, using the Iterative Bayesian unfolding with $N_{\mathrm{iter}} = 4$. Left: shape of the reweighting function (ratio of the truth of the pseudo-data over the truth of the training distributions). Right: ratio of the unfolded pseudo-data over the truth pseudo-data distribution.

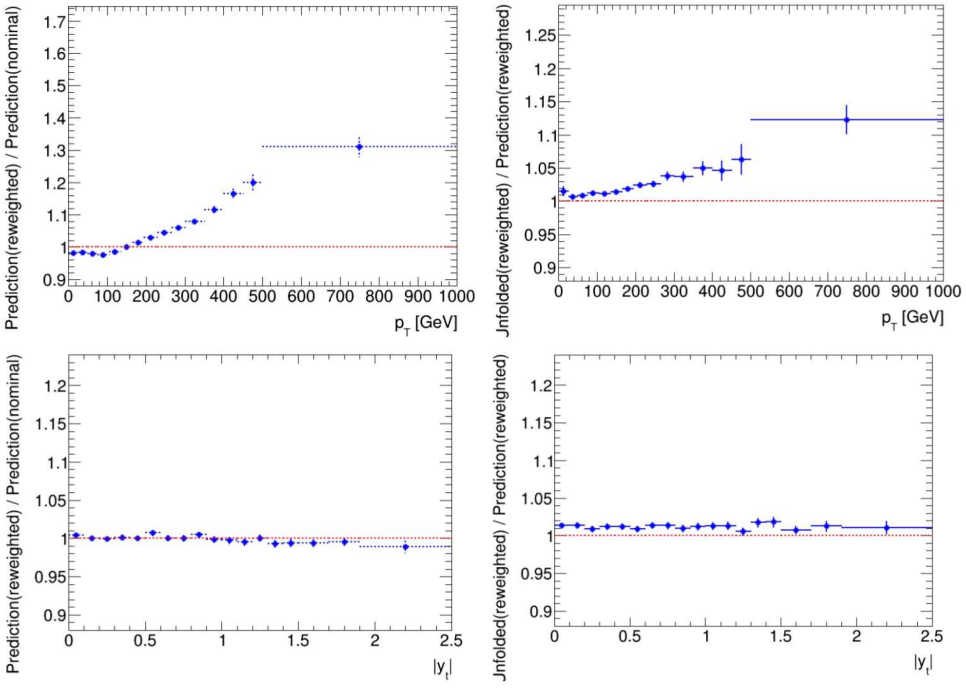

FIGURE G.3: Stress test for the p_{T} (top) and $|y|$ (bottom) of hadronic top, using the Iterative Bayesian unfolding with $N_{\mathrm{iter}} = 4$. Left: shape of the reweighting function (ratio of the truth of the pseudo-data over the truth of the training distributions). Right: ratio of the unfolded pseudo-data over the truth pseudo-data distribution.

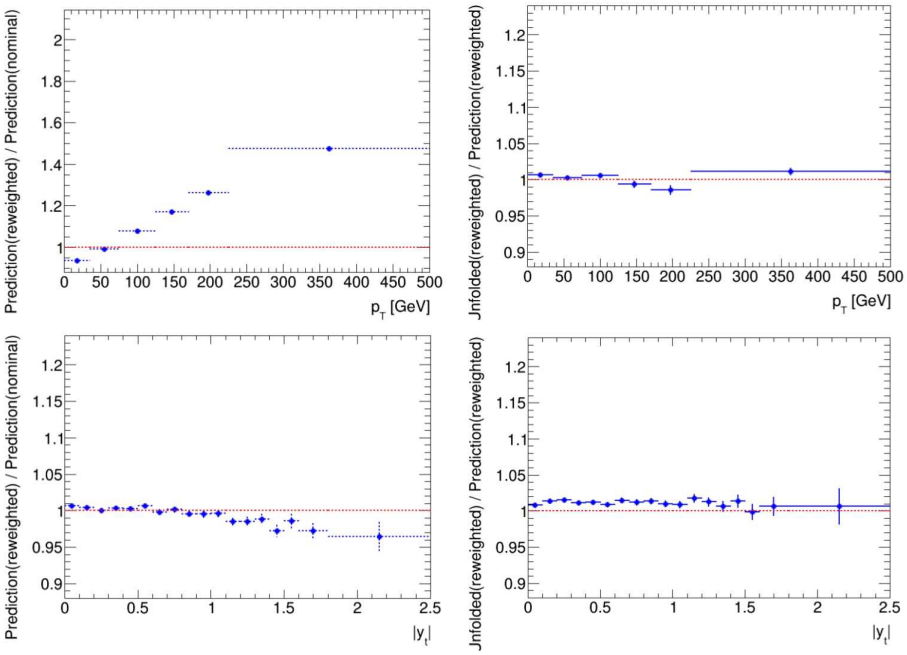

FIGURE G.4: Stress test for the p_{T} (top) and $|y|$ (bottom) of $t\bar{t}$ system with an exotic ($Z' \to t\bar{t}$) model, using the Iterative Bayesian unfolding with $N_{\mathrm{iter}} = 4$. Left: shape of the reweighting function (ratio of the truth of the pseudo-data over the truth of the training distributions). Right: ratio of the unfolded pseudo-data over the truth pseudo-data distribution.

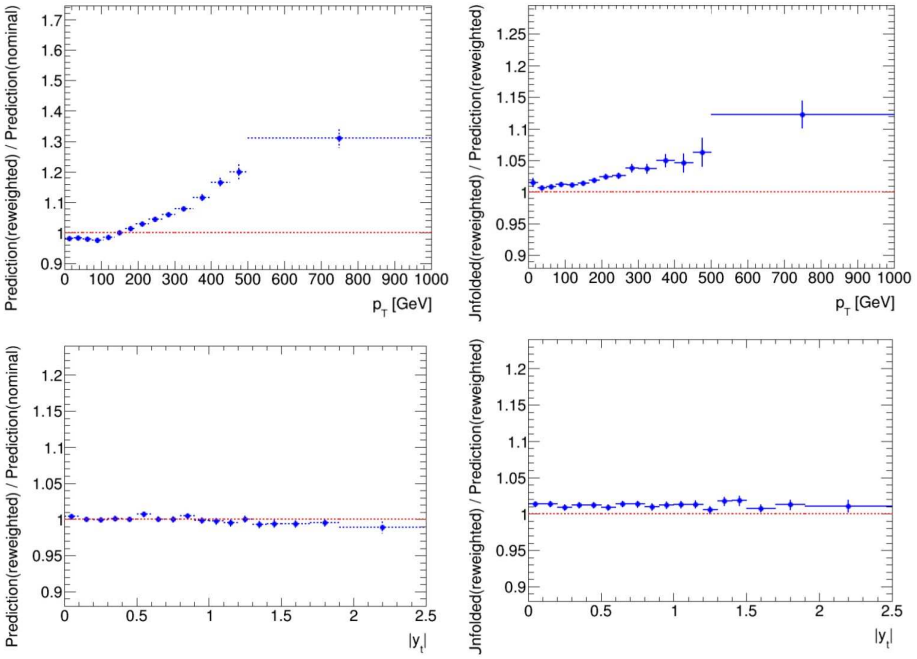

FIGURE G.5: Stress test for the p_{T} (top) and $|y|$ (bottom) of hadronic top with an exotic ($Z' \to t\bar{t}$) model, using the Iterative Bayesian unfolding with $N_{\mathrm{iter}} = 4$. Left: shape of the reweighting function (ratio of the truth of the pseudo-data over the truth of the training distributions). Right: ratio of the unfolded pseudo-data over the truth pseudo-data distribution.

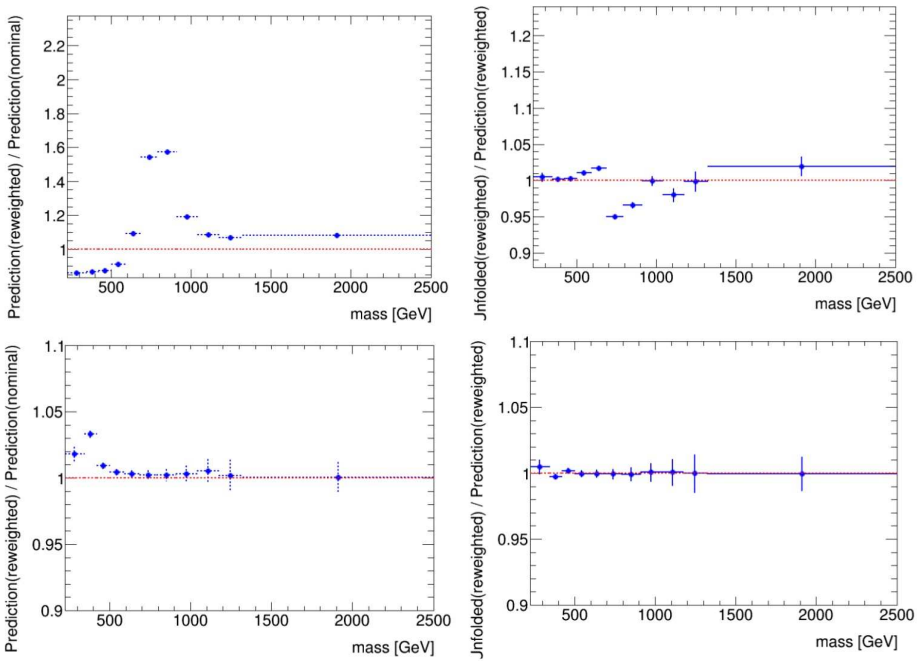

FIGURE G.6: Stress test for the mass of $t\bar{t}$ system, using the Iterative Bayesian unfolding with $N_{\text{iter}} = 4$. Top-Left: shape of the reweighting function (ratio of the truth of the pseudo-data over the truth of the training distributions). Top-Right: ratio of the unfolded pseudo-data over the truth pseudo-data distribution. Bottom-Left: shape of the reweighting function (ratio of the truth of the pseudo-data over the truth of the training distributions). Bottom-Right: ratio of the unfolded pseudo-data over the truth pseudo-data distribution.

In general, the unfolding procedure correctly replicates the reweighting shape. A 5-10% non-closure has been observed in regions where the reweighting function is characterized by high derivatives. For the new physics stress test a good closure is observed for all the variables.

Appendix H

χ^2 test and probability for absolute cross-sections

We present in tabular form the χ^2- and p-values for each studied observable for which will be shown a comparison between the measured fiducial and full phase-space absolute differential cross-sections and the predictions from several MC generators, respectively Tabs. H.1 and H.2. Also we show the χ^2- and p-values table for the observables used in comparison between the measured fiducial phase-space normalized differential cross-sections and the predictions from the new PDF sets using the MC@NLO +Herwig generator, Tab. H.3, and for those used in comparison between the measured full phase-space normalized differential cross-sections and higher-order QCD calculations H.4.

Variable	PWG+PY8 CT10 $h_{\text{damp}} = m_t$		MC@NLO+HW CT10 AUET2		PWG+PY6 CT10 $h_{\text{damp}} = m_t$		PWG+HW6 CT10 $h_{\text{damp}} = \infty$		MadGraph+PY6 MadGraph+PY6 P2011C	
	χ^2/NDF	p-value	χ^2/NDF	p-value	χ^2/NDF	p-value	χ^2/NDF	p-value	χ^2/NDF	p-value
p_T^t	11.4/15	0.72	17.4/15	0.29	12.1/15	0.67	5.6/15	0.98	45.6/15	<0.01
R_{Wt}	30.0/12	<0.01	32.1/12	<0.01	39.0/12	<0.01	9.3/12	0.68	90.4/12	<0.01
$\chi^{t\bar{t}}$	20.2/10	0.03	30.1/10	<0.01	20.4/10	0.03	42.0/10	<0.01	165.0/10	<0.01
$\lvert y^{t\bar{t}}\rvert$	76.6/18	<0.01	56.4/18	<0.01	72.7/18	<0.01	69.7/18	<0.01	130.0/18	<0.01
$m^{t\bar{t}}$	28.0/11	<0.01	67.1/11	<0.01	16.5/11	0.12	35.7/11	<0.01	37.6/11	<0.01
$y_{boost}^{t\bar{t}}$	58.0/16	<0.01	37.8/16	<0.01	57.0/16	<0.01	52.2/16	<0.01	107.0/16	<0.01
$\lvert p_{out}^{t\bar{t}}\rvert$	7.4/6	0.28	15.2/6	0.02	17.4/6	<0.01	5.5/6	0.48	11.9/6	0.06
$\lvert y^t\rvert$	26.2/18	0.09	13.7/18	0.75	25.8/18	0.10	16.8/18	0.54	17.4/18	0.50
$p_T^{t\bar{t}}$	11.0/6	0.09	21.2/6	<0.01	18.0/6	<0.01	23.4/6	<0.01	11.8/6	0.07
$H_T^{t\bar{t}}$	16.4/15	0.36	10.7/15	0.77	19.7/15	0.18	9.8/15	0.83	70.9/15	<0.01
$\Delta\phi^{t\bar{t}}$	0.9/4	0.92	27.8/4	<0.01	3.2/4	0.52	26.5/4	<0.01	25.5/4	<0.01

TABLE H.1: Comparison between the measured fiducial phase-space absolute differential cross-sections and the predictions from several MC generators. For each variable and prediction a χ^2 and a p-value are calculated using the covariance matrix of each measured spectrum. The number of degrees of freedom (NDF) is equal to $N_{\text{b}} - 1$ where N_{b} is the number of bins in the distribution.

Variable	PWG+PY8 CT10 $h_{\text{damp}} = m_t$		MC@NLO+HW CT10 AUET2		PWG+PY6 CT10 $h_{\text{damp}} = m_t$		PWG+HW6 CT10 $h_{\text{damp}} = \infty$		MadGraph+PY6 MadGraph+PY6 P2011C	
	χ^2/NDF	p-value	χ^2/NDF	p-value	χ^2/NDF	p-value	χ^2/NDF	p-value	χ^2/NDF	p-value
p_T^t	3.9/8	0.87	10.1/8	0.26	8.2/8	0.41	4.2/8	0.84	17.4/8	0.03
$\chi^{t\bar{t}}$	28.0/10	<0.01	46.6/10	<0.01	30.7/10	<0.01	73.7/10	<0.01	167.0/10	<0.01
$\lvert y^{t\bar{t}}\rvert$	34.3/5	<0.01	24.4/5	<0.01	35.6/5	<0.01	34.1/5	<0.01	49.9/5	<0.01
$m^{t\bar{t}}$	9.1/7	0.24	10.1/7	0.18	7.0/7	0.43	23.9/7	<0.01	19.9/7	<0.01
$y_{boost}^{t\bar{t}}$	45.0/16	<0.01	34.1/16	<0.01	47.5/16	<0.01	44.9/16	<0.01	68.9/16	<0.01
$\lvert p_{out}^{t\bar{t}}\rvert$	11.6/6	0.07	13.5/6	0.04	7.0/6	0.32	8.1/6	0.23	28.2/6	<0.01
$\lvert y^t\rvert$	12.1/5	0.03	8.1/5	0.15	13.1/5	0.02	9.4/5	0.09	8.2/5	0.14
$p_T^{t\bar{t}}$	16.2/6	0.01	2.8/6	0.83	7.0/6	0.32	4.1/6	0.66	61.5/6	<0.01
$H_T^{t\bar{t}}$	9.8/15	0.83	14.0/15	0.52	16.6/15	0.34	8.2/15	0.91	30.8/15	<0.01
$\Delta\phi^{t\bar{t}}$	2.5/4	0.64	1.3/4	0.87	1.0/4	0.91	37.0/4	<0.01	22.6/4	<0.01

TABLE H.2: Comparison between the measured full phase-space absolute differential cross-sections and the predictions from several MC generators. For each variable and prediction a χ^2 and a p-value are calculated using the covariance matrix of each measured spectrum. The number of degrees of freedom (NDF) is equal to $N_{\text{b}} - 1$ where N_{b} is the number of bins in the distribution.

Variable	CT14nlo		CJ12mid		MMHT2014nlo68cl		NNPDF30nlo		CT10nlo		METAv10LHC		HERA20NLO	
	χ^2/NDF	p-value	χ^2/NDF	p-value	χ^2/NDF	p-value	χ^2/NDF	p-value	χ^2/NDF	p-value	χ^2/NDF	p-value	χ^2/NDF	p-value
p_T^t	18.7/15	0.23	16.3/15	0.36	17.5/15	0.29	20.3/15	0.16	17.4/15	0.29	18.1/15	0.26	17.5/15	0.29
R_{Wt}	29.4/12	<0.01	30.5/12	<0.01	28.2/12	<0.01	26.9/12	<0.01	32.1/12	<0.01	26.7/12	<0.01	25.9/12	0.01
$\chi^{t\bar{t}}$	29.5/10	<0.01	34.6/10	<0.01	34.1/10	<0.01	30.4/10	<0.01	30.1/10	<0.01	33.7/10	<0.01	75.5/10	<0.01
$\lvert y^{t\bar{t}}\rvert$	40.6/18	<0.01	36.6/18	<0.01	28.1/18	0.06	19.8/18	0.34	56.4/18	<0.01	24.0/18	0.16	26.9/18	0.08
$m^{t\bar{t}}$	58.4/11	<0.01	58.8/11	<0.01	60.0/11	<0.01	60.4/11	<0.01	67.1/11	<0.01	60.8/11	<0.01	80.6/11	<0.01
$y_{boost}^{t\bar{t}}$	23.5/16	0.10	24.7/16	0.07	13.7/16	0.62	9.1/16	0.91	37.8/16	<0.01	10.8/16	0.82	18.7/16	0.28
$\lvert y^t\rvert$	13.0/18	0.79	11.4/18	0.88	12.1/18	0.84	13.2/18	0.78	13.7/18	0.75	12.0/18	0.84	23.4/18	0.17
$p_T^{t\bar{t}}$	21.2/6	<0.01	22.2/6	<0.01	22.6/6	<0.01	21.5/6	<0.01	21.2/6	<0.01	22.5/6	<0.01	33.7/6	<0.01
$H_T^{t\bar{t}}$	10.3/15	0.80	10.3/15	0.80	9.6/15	0.85	10.4/15	0.79	10.7/15	0.77	9.6/15	0.85	11.8/15	0.70
$\Delta\phi^{t\bar{t}}$	28.3/4	<0.01	25.0/4	<0.01	27.8/4	<0.01	30.3/4	<0.01	27.8/4	<0.01	27.4/4	<0.01	23.0/4	<0.01

TABLE H.3: Comparison between the measured fiducial phase-space absolute differential cross-sections and the predictions from new PDF sets using the MC@NLO+HERWIG generator. For each variable and prediction a χ^2 and a p-value are calculated using the covariance matrix of each measured spectrum. The number of degrees of freedom (NDF) is equal to $N_\mathrm{b} - 1$ where N_b is the number of bins in the distribution.

Variable	aNNNLO		aNNLO	
	χ^2/NDF	p-value	χ^2/NDF	p-value
p_T^t	5.4/8	0.71	2.4/8	0.97
$\lvert y^t\rvert$	0.5/5	0.99	0.2/5	1.00

TABLE H.4: Comparison between the measured full phase-space absolute differential cross-sections and higher-order QCD calculations. For each variable and prediction a χ^2 and a p-value are calculated using the covariance matrix of each measured spectrum. The number of degrees of freedom (NDF) is equal to $N_\mathrm{b} - 1$ where N_b is the number of bins in the distribution.

Appendix I

Unfolding techniques

I.0.1 Unfolding methods

Bin-by-bin

The bin-by-bin procedure is a very simple method but can not properly considered as an unfolding technique because it does not make into account migration effects. Actually it extracts correction factors for each bin from the ratio of the reconstructed simulation over the theoretical predictions distributions. Anyway, if the response matrix is close to diagonal, it is then useful as a cross check for more complex techniques by providing a good approximation of the true value.

Simple matrix inversion

The simple matrix inversion makes use of the very basic unfolding concepts, seen in the Section 6.3, by using the discretization of Fredholm integral equation, the Equation 6.3, becoming:

$$y_i = M_{ij} \cdot x_j \tag{I.1}$$

where x_j is the vector of true generated events in each bin j and y_i is the vector of measured spectrum in each bin i, related one with the other via the migration matrix M_{ij}.

The measured spectra can be unfolded to the true values simply by numerically inverting the matrix M_{ij}.

SVD

The SVD (Single Value Decomposition) [157], also known as Tichonov regularization, can be considered as an extension of the simple inversion matrix that makes use of a regularization technique in order to reduce possible oscillating solutions due to numerical calculation instabilities and finite samples statistics. The n-dimensions migration matrix can be written as $\mathcal{M} = \mathcal{U}\mathcal{S}\mathcal{V}^T$, in which $\mathcal{U}$ and $\mathcal{V}$ are

$n \times n$ orthogonal matrices and S is an $n \times n$ diagonal matrix. Exploiting basic matrix rules the inverted migration matrix $\mathcal{M}$ can be evaluated as $\mathcal{M}^{-1} = \mathcal{U}\mathcal{S}^{-1}\mathcal{V}^T$. The exact solution of the unfolding system in Equation I.1 leads in most of the cases to a rapidly oscillating distribution. The oscillatory component arises from the suppression of calculation by using some a priori knowledge about the solution, that is achieved by adding a regularization term to the system and minimizing it:

$$(\mathcal{M}x - y)^T (\mathcal{M}x - y) + \tau \cdot (\mathcal{C}x)^T \mathcal{C}x = min \tag{I.2}$$

where the regularization parameter τ determines the relative weight of the a priori condition on the solution, defined by the $\mathcal{C}$ matrix usually chosen from the theoretical distributions from MC simulations, while the optimal value of τ must be determined case by case. Generally if a x distribution is smooth, i.e. with small bin-to-bin variations, can help to reduce the oscillation of the solution. Actually the solution of Eq. I.2 is calculated by rotating vectors and matrices in a different phase space with the following $\mathcal{U}\mathcal{S}\mathcal{V}^T = \mathcal{M}\mathcal{C}^{-1}$, $d = \mathcal{U}^T y$ and $z = \mathcal{V}^T \mathcal{C}x$. The Fourier expansion of the vector d is used in the calculation. In order to have reasonably smooth initial distribution y, only the first few d terms are supposed to be significant. Now introduce the input variable of this method, the k-factor, that is the number of terms that are kept unsuppressed. A small value of the k-factor means a strong regularization, losing information, and giving an higher weight to the MC condition $\mathcal{C}$, viceversa a large value of k gives less importance to the a priori knowledge on the distribution, but allows more oscillating terms in the solutions; it related to the regularization parameter τ through:

$$\tau = \left[\frac{d_k}{z_k}\right]^2 \tag{I.3}$$

A reasonable value of k-factor can be chose equal to the first value of i for which the expansion term d_i starts to become negligible.

Bibliography

[1] "ATLAS Top Working Group". URL https://twiki.cern.ch/twiki/bin/view/AtlasProtected/TopWorkingGroup.

[2] ATLAS Collaboration. "Measurements of top-quark pair differential cross-sections in the lepton+jets channel in pp collisions at $\sqrt{s} = 8$ TeV using the ATLAS detector". *Eur. Phys. J.*, C, 2015. URL http://arxiv.org/abs/1511.04716.

[3] H1 and ZEUS Collaboration. "Combined Measurement and QCD Analysis of the Inclusive $e^{\pm}p$ Scattering Cross Sections at HERA". *JHEP*, 109(1001), 2010. URL http://arxiv.org/abs/0911.0884.

[4] CDF Collaboration. *Conf. Note*, (9913).

[5] D0 Collaboration. *Phys. Rev. D*, 071102(R)(80), 2009. URL http://arxiv.org/abs/0911.4286.

[6] "Combination of CDF and D0 results on the mass of the top quark using up to 5.8 fb^{-1} of data". *Technical Report FERMILAB-TM-2504-E*, 2011.

[7] "Combination of measurements of the top-quark pair production cross section from the Tevatron Collider". *PRD*, 89:072001, 2014. URL http://www-d0.fnal.gov/Run2Physics/WWW/results/final/TOP/T13C/T13C.pdf.

[8] ATLAS Collaboration. *ATLAS-CONF-2011-100*, 2011.

[9] CMS Collaboration. *JHEP*, 049(07), 2011. URL http://arxiv.org/abs/1105.5661.

[10] CMS Collaboration. *PAS TOP-12-006*, 2012.

[11] John M. Campbell and R.K. Ellis. "MCFM for the Tevatron and the LHC". *Nucl.Phys.Proc.Suppl.*, 15(10):205–206, 2010.

[12] V. Abazov et al (D0 Collaboration). *Phys. Lett. B*, 515(693), 2010. URL http://arxiv.org/abs/1001.1900.

[13] T. Aaltonen et al. (CDF Collaboration). *PRL*, 222003(102). URL http://arxiv.org/abs/0903.2850.

[14] The ATLAS collaboration. "Measurements of top quark pair relative differential cross-sections with ATLAS in pp collisions at $\sqrt{s} = 7$ TeV".

[15] The CMS Collaboration. "Measurement of differential top-quark-pair production cross sections in pp collisions at $\sqrt{s} = 7$ TeV". *Eur. Phys. J. C*, (73:2339), 2013.

[16] CDF and D0 Collaborations. "Combination of CDF and D0 results on the mass of the top quark using up to 5.8 fb^{-1} of data". *Technical Report FERMILAB-TM-2504-E*, 2011.

[17] N. Kidonakis. *Phys. Rev. D83*, 091503, 2011.

[18] N. Kidonakis. *Phys. Rev. D82*, 054018, 2010.

[19] N. Kidonakis. *Phys. Rev. D81*, 054028, 2010.

[20] ATLAS Collaboration. "The ATLAS Experiment at the CERN Large Hadron Collider". *JINST*, S08003(3), 2008.

[21] CDF Collaboration. "Observation of top quark production in $p\bar{p}$ collisions". *Phys. Rev. Lett.*, 74:2626–2631, 1995.

[22] D0 Collaboration. "Observation of the top quark". *Phys. Rev. Lett.*, 74, 1995.

[23] "Combination of CDF and D0 results on the mass of the top quark using up to 5.8 $fb^{-}1$ of data". *Technical Report FERMILAB-TM-2504-E*, 2011.

[24] J. Elias-Miro et al. G. Degrassi, S. Di Vita. "Higgs mass and vacuum stability in the Standard Model at NNLO". *JHEP*, 098:1208, 2012. URL http://arxiv.org/abs/1205.6497.

[25] R. Frederix and F. Maltoni. "Top pair invariant mass distribution: a window on new physics". *JHEP*, 01:047, 2009. URL http://arxiv.org/abs/0712.2355.

[26] ATLAS Collaboration. "Measurements of top quark pair relative differential cross-sections with ATLAS in pp collisions at $\sqrt{s} = 7$ TeV". *Eur. Phys. J.*, C 73:2261, 2013. URL http://arxiv.org/abs/1207.5644.

[27] ATLAS Collaboration. "Measurements of normalized differential cross-sections for ttbar production in pp collisions at $\sqrt{s} = 7$ TeV using the ATLAS detector". *Phys. Rev.*, D 90:072004, 2014. URL http://arxiv.org/abs/1407.0371.

[28] ATLAS Collaboration. "Differential top-antitop cross-section measurements as a function of observables constructed from final-state particles using pp collisions at $\sqrt{s} = 7$ TeV in the ATLAS detector". *JHEP hep-ex, CERN-PH-EP-2014-295*, 06:100, 2015. URL http://arxiv.org/abs/1502.05923.

[29] CMS Collaboration. "Measurement of differential top-quark-pair production cross sections in pp collisions at $\sqrt{s} = 7$ TeV". *Eur.Phys.J.*, C 73:2339, 2013. URL http://arxiv.org/abs/1211.2220.

[30] CMS Collaboration. "Measurement of the differential cross section for top quark pair production in *pp* collisions at $\sqrt{s} = 8$ TeV". *Submitted to EPJC*, 2015. URL http://arxiv.org/abs/1505.04480.

[31] ATLAS Collaboration. "Search for New Phenomena in Dijet Angular Distributions in Proton-Proton Collisions at $\sqrt{s} = 8$ TeV Measured with the ATLAS Detector". *Phys. Rev. Lett.*, 114:221802, 2015. URL http://arxiv.org/abs/1504.00357.

[32] L. Apanasevich, J. Bacigalupi, W. Baker, M. Begel, S. Blusk, C. Bromberg, P. Chang, B. Choudhary, W. H. Chung, L. de Barbaro, W. DeSoi, W. Długosz, J. Dunlea, E. Engels, G. Fanourakis, T. Ferbel, J. Ftacnik, D. Garelick, G. Ginther, M. Glaubman, P. Gutierrez, K. Hartman, J. Huston, C. Johnstone, V. Kapoor, J. Kuehler, C. Lirakis, F. Lobkowicz, P. Lukens, S. Mani, J. Mansour, A. Maul, R. Miller, B. Y. Oh, G. Osborne, D. Pellett, E. Prebys, R. Roser, P. Shepard, R. Shivpuri, D. Skow, P. Slattery, L. Sorrell, D. Striley, W. Toothacker, N. Varelas, D. Weerasundara, J. J. Whitmore, T. Yasuda, C. Yosef, M. Zieliński, and V. Zutshi. "Evidence for Parton k_T Effects in High-p_T Particle Production". *Phys. Rev. Lett.*, 81:2642–2645, Sep 1998. doi: 10.1103/PhysRevLett.81.2642.

[33] Celine Degrande, Jean-Marc Gerard, Christophe Grojean, Fabio Maltoni, and Geraldine Servant. "Non-resonant New Physics in Top Pair Production at Hadron Colliders". *JHEP*, 03:125, 2011. URL http://arxiv.org/abs/1010.6304.

[34] A. Denner, S. Dittmaier, S. Kallweit, and S. Pozzorini. "NLO QCD corrections to WWbb production at hadron colliders". *Phys. Rev. Lett.*, 106:052001, 2011. URL http://arxiv.org/abs/1012.3975.

[35] Giuseppe Bevilacqua, Michal Czakon, Andreas van Hameren, Costas G. Papadopoulos, and Malgorzata Worek. "Complete off-shell effects in top quark pair hadroproduction with leptonic decay at next-to-leading order". *JHEP*, 02:083, 2011. URL http://arxiv.org/abs/1012.4230.

[36] ATLAS Collaboration. "Measurements of top-quark pair differential cross-sections in the l+jets channel in pp collisions at $\sqrt{s} = 8$ TeV using the ATLAS detector". *ATL-PHYS-INT-2015-008*, 2015. URL https://cds.cern.ch/record/2011617.

[37] CMS Collaboration. "Observation of a new boson at a mass of 125 GeV with the CMS experiment at the LHC". *Physics Letters B*, 716(1):30–61, 2012. URL http://arxiv.org/abs/1207.7235.

[38] ATLAS Collaboration. "Observation of a new particle in the search for the StandardModel Higgs boson with the ATLAS detector at the LHC". *Physics Letters B*, 716(1):1–29, 2012. URL http://arxiv.org/abs/1207.7214.

[39] D. H. Perkins. *"Introduction to High Energy Physiscs."*.

[40] N. Cabibbo. *Phys. Rev. Lett.*, 531(10), 1963.

[41] M. Kobayashi and T. Maskawa. "CP-Violation in the Renormalizable Theory of Weak Interaction". *Progress of Theoretical Physics*, 49(2):652–657, 1973.

[42] The LEP Collaborations. *Phys. Rept.*, (427):257–454, 2006. URL http://lepewwg.web.cern.ch/LEPEWWG.

[43] Particle Data Group Collaboration. "Review of Particle Physics". *Phys. Rev. D*, 86(010001), 2012.

[44] W. Bernreuther. "Top quark physics at the LHC". *J. Phys.*, 083001(G35), 2008. URL http://arxiv.org/abs/0805.1333.

[45] M. L. Mangano et al. M. Beneke, I. Efthymiopoulos. "Top quark physics".

[46] P. Fiedler M. Czakon and A. Mitov. "Total Top-Quark Pair-Production Cross Section at Hadron Colliders Through $\mathcal{O}(\alpha_s^4)$". *Phys. Rev. Lett.*, 252004(110), 2013. URL http://arxiv.org/abs/1303.6254.

[47] H1 and ZEUS Collaboration. "PDF fits including HERA-II high Q^2 data (HERAPDF1.5)". *H1 and ZEUS reports H1prelim-10-142 ZEUS-prel-10-018*, 2014.

[48] *ATLAS-CONF-2012-149*, 2012.

[49] Valentin Ahrens Andrea Ferroglia Matthias Neubert Ben D. Pecjak and Li-Lin Yang. "RG-improved single-particle inclusive cross sections and forward-backward asymmetry in tt production at hadron colliders". *JHEP, 1109:070*, 2011.

[50] K. Agashe et al. *Top quark working group report*, Nov 2013. URL http://arxiv.org/abs/1311.2028v1.

[51] T. Aaltonen et al. *Phys. Rev. Lett.*, 092002(103), 2009.

[52] V. M. Abazov et al. *Phys. Rev. D*, 112001(84), 2011.

[53] N. Kidonakis. "Differential and total cross sections for top pair and single top production". URL http://arxiv.org/abs/1205.3453.

[54] S. Alioli P. Fernandez J. Fuster et al. "A new observable to measure the top-quark mass at hadron colliders". *Eur.Phys.J. C73*, 2438, 2013. URL http://arxiv.org/abs/1303.6415.

[55] "Precision Electroweak Measurements and Constraints on the Standard Model". *Technical Report CERN-PH-EP-2008-020*, 2008.

[56] V.N. Gribov and L.N. Lipatov. *Sov. J. Nucl. Phys.*, 438(15), 1972.

[57] G. Altarelli and G. Parisi. *Nucl. Phys. B126*, 298, 1977.

[58] Yu.L. Dokshitzer. *Sov. Phys. JETP*, 641(46), 1977.

[59] J. Pumplin A. Belyaev J. Huston D. Stump and W. K. Tung. *JHEP*, 032(0602), 2006.

[60] L. Evans and P. Bryant. "LHC Machine". *JINST*, S08001(3), 2008.

[61] CMS Collaboration. "The CMS experiment at the CERN LHC". *JINST 3*, S08004, 2008.

[62] LHCb Collaboration. "The LHCb Detector at the LHC". *JINST 3*, S08005, 2008.

[63] ALICE Collaboration. "The ALICE experiment at the CERN LHC". *JINST 3*, S08002, 2008.

[64] ATLAS Collaboration. "Readiness of the ATLAS Liquid Argon Calorimeter for LHC Collisions". *Eur. Phys. J. C*, (70):723–753, 2010.

[65] ATLAS Collaboration. "Readiness of the ATLAS Tile Calorimeter for LHC Collisions". *Eur. Phys. J. C*, (70):1193–1236, 2010.

[66] ATLAS collaboration. "Luminosity Determination Using the ATLAS Detector". *ATLAS-CONF-2010-060*, 2010.

[67] A. Sbrizzi. "A Cherenkov Detector for Monitoring ATLAS Luminosity". *ATL-LUM-PROC-2010-004*, 2010.

[68] P. Ruzicka. "Forward physics at the ATLAS experiment". *ATL-LUM-PROC-2010-001*, 2010.

[69] ATLAS Collaboration. "The Trigger for Early Running, ch. in expected performance of the ATLAS experiment: detector, trigger and physics". *CERN-OPEN-2008-020*, pages 550–564, 2008.

[70] ATLAS Collaboration. "Improved luminosity determination in *pp* collisions at $\sqrt{s}$ = 7 TeV using the ATLAS detector at the LHC". *Eur. Phys. J.*, C 73:2518, 2013. doi: 10.1140/epjc/s10052-013-2518-3.

[71] GEANT4 Collaboration. "GEANT4: a simulation toolkit". *nim*, A 506:250, 2003. doi: 10.1016/S0168-9002(03)01368-8. CERN-IT-2002-003.

[72] W. Lucas. "Fast simulation for ATLAS: ATLFAST-II and ISF". *Journal of Physics: Conference Series, IOP Publishing*, 396:p. 022031, 2012.

[73] M. Beckingham et al. "The simulation principle and performance of the ATLAS fast calorimeter simulation FastCaloSim". *Tech. Rep. ATL-PHYS-PUB-2010-013*, Oct 2010.

[74] ATLAS Collaboration. "Performance of the Fast ATLAS Tracking Simulation (FATRAS) and the ATLAS Fast Calorimeter Simulation (FastCaloSim) with single particles". *ATL-SOFT-PUB-2014-001* https://cds.cern.ch/record/1669341, 2014.

[75] Frixione Stefano, Nason Paolo, and Oleari Carlo. "Matching NLO QCD computations with Parton Shower simulations: the POWHEG method". *JHEP*, 11: 070, 2007. doi: 10.1088/1126-6708/2007/11/070.

[76] Lai Hung-Liang, Guzzi Marco, Huston Joey, Li Zhao, Nadolsky Pavel M., et al. "New parton distributions for collider physics". *Phys. Rev.*, D 82:074024, 2010. doi: 10.1103/PhysRevD.82.074024.

[77] T. Sjöstrand S. Mrenna and P.Z. Skands. "PYTHIA 6.4 physics and manual". *JHEP*, 05:026, 2006. doi: 10.1088/1126-6708/2006/05/026.

[78] Skands Peter Zeiler. "Tuning Monte Carlo generators: The Perugia tunes". *Phys. Rev.*, D 82:074018, 2010. doi: 10.1103/PhysRevD.82.074018.

[79] Frixione Stefano, Nason Paolo, and Webber Bryan R. "Matching NLO QCD and parton showers in heavy flavor production". *JHEP*, 08:007, 2003. doi: 10.1088/1126-6708/2003/08/007.

[80] Corcella G. et al. "HERWIG 6: an event generator for hadron emission reactions with interfering gluons (including supersymmetric processes)". *JHEP*, 01:010, 2001. doi: 10.1088/1126-6708/2001/01/010.

[81] Butterworth J.M., Forshaw Jeffrey R., and Seymour M.H. "Multiparton interactions in photoproduction at HERA". *Z. Phys.*, C 72:637, 1996. doi: 10.1007/s002880050286.

[82] ATLAS Collaboration. "Measurement of $t\bar{t}$ production with a veto on additional central jet activity in pp collisions at $\sqrt{s} = 7$ TeV using the ATLAS detector". *Eur.Phys.J.*, C 72:2043, 2012. URL http://arxiv.org/abs/1203.5015.

[83] ATLAS Collaboration. "Measurement of the $t\bar{t}$ production cross-section as a function of jet multiplicity and jet transverse momentum in 7 TeV proton-proton collisions with the ATLAS detector". *JHEP*, 01:020, 2015. doi: 10.1007/JHEP01(2015)020.

[84] ATLAS Collaboration. "Comparison of Monte Carlo generator predictions to ATLAS measurements of top pair production at 7 TeV". *ATL-PHYS-PUB-2015-002 https://cds.cern.ch/record/1981319*, 2015.

[85] Czakon Michal and Mitov Alexander. "Top++: A Program for the Calculation of the Top-Pair Cross-Section at Hadron Colliders". 2011.

[86] Cacciari Matteo, Czakon Michal, Mangano Michelangelo, Mitov Alexander, and Nason Paolo. "Top-pair production at hadron colliders with next-to-next-to-leading logarithmic soft-gluon resummation". *Phys. Lett.*, B710:612–622, 2012. doi: 10.1016/j.physletb.2012.03.013.

[87] Beneke M., Falgari P., Klein S., and Schwinn C. "Hadronic top-quark pair production with NNLL threshold resummation". *Nucl.Phys.*, B855:695–741, 2012. doi: 10.1016/j.nuclphysb.2011.10.021.

[88] Baernreuther Peter, Czakon Michal, and Mitov Alexander. "Percent Level Precision Physics at the Tevatron: First Genuine NNLO QCD Corrections to $q\bar{q} \to t\bar{t} + x$". *Phys. Rev. Lett.*, 109:132001, 2012. doi: 10.1103/PhysRevLett.109.132001.

[89] Czakon Michal and Mitov Alexander. "NNLO corrections to top-pair production at hadron colliders: the all-fermionic scattering channels". *JHEP*, 12:054, 2012. doi: 10.1007/JHEP12(2012)054.

[90] Czakon Michal and Mitov Alexander. "NNLO corrections to top pair production at hadron colliders: the quark-gluon reaction". *JHEP*, 01:080, 2013. doi: 10.1007/JHEP01(2013)080.

[91] Czakon Michal, Fiedler Paul, and Mitov Alexander. "Total Top-Quark Pair-Production Cross Section at Hadron Colliders Through $o(\alpha_s^4)$". *Phys. Rev. Lett.*, 110:252004, 2013. doi: 10.1103/PhysRevLett.110.252004.

[92] Mangano Michelangelo L., Moretti Mauro, Piccinini Fulvio, Pittau Roberto, and Polosa Antonio D. "ALPGEN, a generator for hard multiparton processes in hadronic collisions". *JHEP*, 07:001, 2003. doi: 10.1088/1126-6708/2003/07/001.

[93] Draggiotis Petros D., Kleiss Ronald H. P., and Papadopoulos Costas G. "Multijet production in hadron collisions". *Eur. Phys. J.*, C24:447–458, 2002. doi: 10.1007/s10052-002-0955-5.

[94] Hamberg R., van Neerven W.L., and Matsuura T. "A Complete calculation of the order α_s^2 correction to the Drell-Yan k factor". *Nucl. Phys.*, B359:343, 1991. doi: 10.1016/0550-3213(91)90064-5.

[95] Gavin Ryan, Li Ye, Petriello Frank, and Quackenbush Seth. "W Physics at the LHC with FEWZ 2.1". *Comput. Phys. Commun.*, 184:208, 2013. doi: 10.1016/j.cpc.2012.09.005.

[96] Kidonakis Nikolaos. "Next-to-next-to-leading-order collinear and soft gluon corrections for t-channel single top quark production". *Phys. Rev.*, D 83:091503, 2011. doi: 10.1103/PhysRevD.83.091503.

[97] Kidonakis Nikolaos. "Two-loop soft anomalous dimensions for single top quark associated production with a W^- or H^-". *Phys. Rev.*, D 82:054018, 2010. doi: 10.1103/PhysRevD.82.054018.

[98] Kidonakis Nikolaos. "Next-to-next-to-leading logarithm resummation for s-channel single top quark production". *Phys. Rev.*, D 81:054028, 2010. doi: 10.1103/PhysRevD.81.054028.

[99] Campbell John M, Ellis R. Keith, and Williams Ciaran. "Vector boson pair production at the LHC". 07:018, 2011. doi: 10.1007/JHEP07(2011)018.

[100] C.H. Kom and W. Stirling. "Charge asymmetry in W+jets production at the LHC". *Eur.Phys.J. C69*, (67), 2010.

[101] ATLAS Collaboration. "Measurement of the top quark pair production cross-section with ATLAS in the single lepton channel". *Phys. Lett. B*, 711:244, 2012. doi: 10.1016/j.physletb.2012.03.083.

[102] V. Abazov et al. D0 Collaboration. "Measurement of the $t\bar{t}$ production cross section in pp collisions at $\sqrt{s} = 1.96$ TeV using kinematic characteristics of lepton+jets events". *Phys.Rev. D76*, (092007), 2007.

[103] ATLAS Collaboration. "Performance of primary vertex reconstruction in proton-proton collisions at $\sqrt{s} = 7$ TeV in the ATLAS experiment". *Tech. Rep. ATLAS-CONF-2010-069*, Jul 2010.

[104] W. Waltenberger, R. Frühwirth, and P. Vanlaer. "Adaptive vertex fitting". *Journal of Physics G: Nuclear and Particle Physics*, 34(12):343, 2007.

[105] W. Lampl et al. "Calorimeter Clustering Algorithms: Description and Performance".

[106] ATLAS Collaboration. "Electron performance measurements with the ATLAS detector using the 2010 LHC proton-proton collision data". 2011.

[107] Lagouri et al. "A muon identification and combined reconstruction procedure for the ATLAS detector at the LHC at CERN". *Nuclear Science, IEEE Transactions*, 51(6):3030–3033, 2004.

[108] Rehermann Keith and Tweedie Brock. "Efficient Identification of Boosted Semileptonic Top Quarks at the LHC". *JHEP*, 1103:059, 2011. doi: 10.1007/JHEP03(2011)059.

[109] G. P. Salam. "Elements of QCD for hadron colliders". 2010. URL http://arxiv.org/abs/1011.5131.

[110] Cacciari Matteo, Salam Gavin P., and Soyez Gregory. "The anti-k_t jet clustering algorithm". *jhep*, 04:063, 2008. doi: 10.1088/1126-6708/2008/04/063.

[111] ATLAS Collaboration. "Jet energy measurement with the ATLAS detector in proton-proton collisions at $\sqrt{s} = 7$ TeV". *European Physical Journal C*, 73, Mar 2013.

[112] D. W. Miller et al. "Pile-up jet energy scale corrections using the jet-vertex fraction method". *Tech. Rep. ATL-COM-PHYS-2009-180*, Apr 2009.

[113] Cacciari Matteo, Salam Gavin P., and Soyez Gregory. "Fastjet user manual". *Eur. Phys. J.*, C72:1896, 2012. doi: 10.1140/epjc/s10052-012-1896-2.

[114] Cacciari Matteo, Salam Gavin P., and Soyez Gregory. "The Catchment Area of Jets". *jhep*, 04:005, 2008. doi: 10.1088/1126-6708/2008/04/005.

[115] ATLAS Collaboration. "Pile-up subtraction and suppression for jets in ATLAS". *ATLAS-CONF-2013-083*, 2013.

[116] ATLAS Collaboration. "Jet energy measurement and its systematic uncertainty in proton-proton collisions at $\sqrt{s} = 7$ TeV with the ATLAS detector". *Eur. Phys. J.*, C75:17, 2015. doi: 10.1140/epjc/s10052-014-3190-y.

[117] ATLAS Collaboration. "Commissioning of the ATLAS high-performance b-tagging algorithms in the 7 TeV collision data". *Tech. Rep. ATLAS-CONF-2011-102*, Jul 2011.

[118] G. Piacquadio and C. Weiser. "A new inclusive secondary vertex algorithm for b-jet tagging in ATLAS". *Journal of Physics: Conference Series, IOP Publishing*, 119(p. 032032), 2008.

[119] ATLAS Collaboration. "Measurement of the b-tag Efficiency in a Sample of Jets Containing Muons with 5 fb^{-1} of Data from the ATLAS detector". *ATLAS-CONF-2012-043*, 2012. URL https://cds.cern.ch/record/1435197.

[120] R. Frederix and F. Maltoni. "Top pair invariant mass distribution: a window on new physics". *Journal of High Energy Physics*, vol. 2009(no. 01):p. 047, 2009.

[121] C. T. Hill and S. J. Parke. "Top quark production: Sensitivity to new physics". *Phys. Rev. D*, vol. 49:pp. 4454–4462, May 1994.

[122] "Experimental interplay between the top quark and Supersymmetry at the LHC and Tevatron". *tech. rep., ATL-COM-PHYS-2013-019*, 2013.

[123] K. Nakamura et al. (Particle Data Group). "Review of particle physics". *J.Phys. G37*, page 075021, 2010.

[124] URL https://twiki.cern.ch/twiki/bin/view/Main/MAMbo.

[125] G. D'Agostini. "Improved iterative Bayesian unfolding". 2010. URL http://arxiv.org/abs/1010.0632v1.

[126] G. D'Agostini. "A Multidimensional unfolding method based on Bayes' theorem". *Nucl.Instrum.Meth. DESY-94-099*, A362:487–498, 1995. doi: 10.1016/0168-9002(95)00274-X.

[127] Tim Adye. "Unfolding algorithms and tests using RooUnfold". pages 313–318, 2011. URL http://arxiv.org/abs/1105.1160.

[128] ATLAS Collaboration. "Electron performance measurements with the ATLAS detector using the 2010 LHC proton-proton collision data". *epj*, C 72:1909, 2012. URL http://arxiv.org/abs/1110.3174.

[129] ATLAS Collaboration. "Measurement of the muon reconstruction performance of the ATLAS detector using 2011 and 2012 LHC proton–proton collision data". *Eur. Phys. J.*, C 74:3130, 2014. URL http://arxiv.org/abs/1407.3935.

[130] ATLAS Collaboration. "Jet energy measurement with the ATLAS detector in proton-proton collisions at $\sqrt{s} = 7$ TeV". *Eur.Phys.J.*, C 73(3):2304, 2013. URL http://arxiv.org/abs/1112.6426.

[131] ATLAS Collaboration. "Jet energy measurement and its systematic uncertainty in proton-proton collisions at $\sqrt{s} = 7$ TeV with the ATLAS detector". *Eur.Phys.J.*, C 75(1):17, 2015. URL http://arxiv.org/abs/1406.0076.

[132] ATLAS Collaboration. "Jet energy resolution in proton-proton collisions at $\sqrt{s} = 7$ TeV recorded in 2010 with the ATLAS detector". *Eur.Phys.J.*, C 73(3):2306, 2013. URL http://arxiv.org/abs/1210.6210.

[133] ATLAS Collaboration. "Calibration of b-tagging using dileptonic top pair events in a combinatorial likelihood approach with the ATLAS experiment". *ATLAS-CONF-2014-004*, 2014. URL https://cdsweb.cern.ch/record/1664335.

[134] ATLAS Collaboration. "Measurement of the b-tag Efficiency in a Sample of Jets Containing Muons with 5 fb^{-1} of Data from the ATLAS Detector". *ATLAS-CONF-2012-043, ATLAS-COM-CONF-2012-021*, 2012.

[135] ATLAS Collaboration. "Measurement of the Mistag Rate of b-tagging algorithms with 5 fb^{-1} of Data Collected by the ATLAS Detector". *ATLAS-CONF-2012-040*, 2012. URL https://cds.cern.ch/record/1435194.

[136] ATLAS Collaboration. "Performance of missing transverse momentum reconstruction in proton-proton collisions at $\sqrt{s} = 7$ TeV with ATLAS". *Eur.Phys.J.*, C 72:1844, 2012. URL http://arxiv.org/abs/1108.5602.

[137] S. Mrenna T. Sjöstrand and P.Z. Skands. "A Brief Introduction to PYTHIA 8.1". *Comput. Phys. Commun.*, 178:852–867, 2008. URL http://arxiv.org/abs/0710.3820.

[138] Johan Alwall, Michel Herquet, Fabio Maltoni, Olivier Mattelaer, and Tim Stelzer. "MadGraph 5 : Going Beyond". *JHEP*, 06:128, 2011. URL http://arxiv.org/abs/1106.0522.

[139] J. H. Kühn, A. Scharf, and P. Uwer. "Electroweak corrections to top-quark pair production in quark-antiquark annihilation". *Eur. Phys. J.*, C45:139–150, 2006.

[140] Johann H. Kühn, A. Scharf, and P. Uwer. "Electroweak effects in top-quark pair production at hadron colliders". *Eur. Phys. J.*, C51:37–53, 2007.

[141] Werner Bernreuther, Michael Fucker, and Zong-Guo Si. "Electroweak corrections to t anti-t production at hadron colliders". *Nuovo Cim.*, B 123:1036, 2008. URL http://arxiv.org/abs/0808.1142.

[142] Aneesh V. Manohar and Michael Trott. "Electroweak Sudakov Corrections and the Top Quark Forward-Backward Asymmetry". *Phys. Lett.*, B 711:313, 2012. URL http://arxiv.org/abs/1201.3926.

[143] J. H. Kühn, A. Scharf, and P. Uwer. "Weak Interactions in Top-Quark Pair Production at Hadron Colliders: An Update". *Phys. Rev.*, D91:014020, 2015. URL http://arxiv.org/abs/1305.5773.

[144] ATLAS Collaboration. "Measurement of the differential cross-section of highly boosted top quarks as a function of their transverse momentum in $\sqrt{s} = 8$ TeV proton-proton collisions using the ATLAS detector". 2015. URL http://arxiv.org/abs/1510.03818.

[145] ATLAS Collaboration. "A search for $t\bar{t}$ resonances using lepton-plus-jets events in proton-proton collisions at $\sqrt{s} = 8$ TeV with the ATLAS detector". *JHEP*, 08:148, 2015. URL http://arxiv.org/abs/1505.07018.

[146] Sayipjamal Dulat, Tie Jiun Hou, Jun Gao, Marco Guzzi, Joey Huston, Pavel Nadolsky, Jon Pumplin, Carl Schmidt, Daniel Stump, and C. P. Yuan. "The CT14 Global Analysis of Quantum Chromodynamics". 2015. URL http://arxiv.org/abs/1506.07443.

[147] J. F. Owens, A. Accardi, and W. Melnitchouk. "Global parton distributions with nuclear and finite-Q^2 corrections". *Phys. Rev.*, D87:094012, 2013. URL http://arxiv.org/abs/1212.1702.

[148] L. A. Harland-Lang, A. D. Martin, P. Motylinski, and R. S. Thorne. "Parton distributions in the LHC era: MMHT 2014 PDFs". *Eur. Phys. J.*, C75:204, 2015. URL http://arxiv.org/abs/1412.3989.

[149] NNPDF Collaboration. "Parton distributions for the LHC Run II". *JHEP*, 04:040, 2015. URL http://arxiv.org/abs/1410.8849.

[150] Jun Gao and Pavel Nadolsky. "A meta-analysis of parton distribution functions". *JHEP*, 07:035, 2014. URL http://arxiv.org/abs/1401.0013.

[151] ZEUS and H1 Collaborations. "Combination of Measurements of Inclusive Deep Inelastic $e^{\pm}p$ Scattering Cross Sections and QCD Analysis of HERA Data". *DESY-15-039*, 2015. URL http://arxiv.org/abs/1506.06042.

[152] Marco Guzzi, Katerina Lipka, and Sven-Olaf Moch. "Top-quark pair production at hadron colliders: differential cross section and phenomenological applications with DiffTop". *JHEP*, 01:082, 2015. URL http://arxiv.org/abs/1406.0386.

[153] Nikolaos Kidonakis. "NNNLO soft-gluon corrections for the top-quark p_t and rapidity distributions". *Phys. Rev.*, D91:031501, 2015. URL http://arxiv.org/abs/1411.2633.

[154] A.D. Martin, W.J. Stirling, R.S. Thorne, and G. Watt. "Parton distributions for the LHC". *Eur. Phys. J.*, C 63:189, 2009. URL http://arxiv.org/abs/0901.0002.

[155] Valentin Ahrens, Andrea Ferroglia, Matthias Neubert, Ben D. Pecjak, and Li Lin Yang. "Renormalization-group improved predictions for top-quark pair production at hadron colliders". *JHEP*, 09:097, 2010. URL http://arxiv.org/abs/1003.5827.

[156] Czakon M., Fiedler P., Haymes D., and Mitov A. "Stripper". *Top2015*, 2015. URL https://indico.cern.ch/event/351006/session/10/contribution/34/attachments/1156299/1662250/heymes_TOP2015.pdf.

[157] A. Hocker and V. Kartvelishvili. "SVD approach to data unfolding". *Nucl.Instrum.Meth. A372*, pages 469–481, 1996.